Transactions of the ASME

HEAT TRANSFER DIVISION
Chairman, **R. J. SIMONEAU**
Secretary, **F. A. KULACKI**
Senior Technical Editor, **K. T. YANG**
Technical Editor, **I. CATTON**
Technical Editor, **M. EPSTEIN**
Technical Editor, **G. M. FAETH**
Technical Editor, **R. GREIF**
Technical Editor, **P. J. MARTO**
Technical Editor, **R. H. PLETCHER**
Technical Editor, **R. K. SHAH**
Technical Editor, **R. VISKANTA**

BOARD ON COMMUNICATIONS
Chairman and Vice President
K. N. REID, JR.

Members-at-Large
J. T. COKONIS
W. G. GOTTENBERG
D. KOENIG
M. KUTZ
F. LANDIS
R. E. NICKELL
J. ORTLOFF
C. PHILLIPS
H. C. REEDER

President, **G. KOTNICK**
Executive Director,
PAUL ALLMENDINGER
Treasurer,
ROBERT A. BENNETT

PUBLISHING STAFF
Mng. Dir., Publ., **J. J. FREY**
Dep. Mng. Dir., Pub.,
JOS. SANSONE
Managing Editor,
CORNELIA MONAHAN
Production Editor,
JACK RUMMEL
Editorial Prod. Asst.
MARISOL ANDINO

The Journal of Heat Transfer (ISSN 0022-1481) is published quarterly for $100 per year by The American Society of Mechanical Engineers, 345 East 47th Street, New York, N Y 10017. Second class postage paid at New York, NY and additional mailing offices. POSTMASTER: Send address changes to The Journal of Heat Transfer, c/o THE AMERICAN SOCIETY OF MECHANICAL ENGINEERS, P.O. Box 3199, Grand Central Station, New York, NY 10163.
CHANGES OF ADDRESS must be received at Society headquarters seven weeks before they are to be effective. Please send old label and new address.
PRICES: To members, $24.00, annually; to nonmembers, $100.00.
Add $6.00 for postage to countries outside the United States and Canada.

STATEMENT from By-Laws. The Society shall not be responsible for statements or opinions advanced in papers or . . . printed in its publications (B7.1, para. 3).
COPYRIGHT © 1984 by the American Society of Mechanical Engineers. Reprints from this publication may be made on condition that full credit be given the TRANSACTIONS OF THE ASME, JOURNAL OF HEAT TRANSFER, and the author, and date of publication be stated.

INDEXED by the Engineering Index, Inc.

Journal of Heat Transfer

Published Quarterly by The American Society of Mechanical Engineers

VOLUME 106 • NUMBER 4 • NOVEMBER 1984

ANNOUNCEMENTS

TECHNICAL PAPERS

Downloaded 04 Feb 2011 to 194.85.80.107. Redistribution subject to ASME license or copyright; see http://www.asme.org/terms/Terms_Use.cfm

(Contents continued)

TECHNICAL NOTES

DISCUSSION

The Optical Constants of Coal, Char, and Limestone

M. Q. Brewster[1]

T. Kunitomo

Department of Engineering Science,
School of Mechanical Engineering,
Kyoto University,
Kyoto, Japan

The infrared optical constants, n and k, ($\tilde{n}=n-ik$) of swelling and nonswelling coals, their respective char products, and limestone at room temperature have been obtained by a particle extinction technique using compressed KBr tablets. By assuming spherical particles and using Mie theory for the particle extinction measurements in conjunction with normal specular reflectance measurements from polished specimens, it is possible to obtain more accurate values for n and k than if the usual Fresnel reflectance technique is misapplied to samples that may appear specular but do not satisfy the stringent conditions necessary for invoking the Fresnel equations. Values of k for coal were found to be an order-of-magnitude smaller than previously reported values, with absorption due mainly to molecular vibration. The results for char evidenced that a significant increase in absorption by free electrons takes place upon devolatization and carbonization of coal. The limestone results demonstrated pronounced molecular absorption bands characteristic of $CaCO_3$.

Introduction

Although the complex heat transfer mechanisms in fluidized-bed combustors are far from being well understood, a recent survey of the literature [1] indicates that a 20 to 30 percent contribution by radiation to the total heat transfer would be a conservative estimate for temperatures of 800°C and above. As well, the influence of radiant heat transfer in conventional boilers, furnaces, gasifiers, and other process equipment utilizing coal particles in high-temeprature environments is known to be rather significant. An accurate knowledge of the thermal radiative properties of coal, char, and other particles present in such systems is essential before any meaningful degree of flame modeling [2], heat transfer analysis, or radiation prediction [3, 4] can take place. With this need in mind, a study was undertaken to investigate experimentally the optical constants ($\tilde{n}=n-ik$), which, when used in conjunction with Mie theory for spherical particles, would correctly predict the extinction and emission characteristics of non-spherical polydispersons of coal, char and limestone particles.

Optical Properties of Coal. Previous studies of the optical properties of coal can be generally categorized as being either qualitative or quantitative in nature. The qualitative studies [5-10], which are made in an effort to understand the structure and composition of coal as well as the coalification process itself, have resulted in identification of the general features of visible and infrared spectra of various coals. Generally, it may be noted that coal behaves optically as a dielectric or weak semiconductor, with the tendency to behave like a conductor increasing with coal rank. Below wavelengths of 1.2 μm, electronic absorption by the aliphatic and aromatic constituents dominates. Above 1.2 μm, characteristic absorption bands are observed that may be associated with various chemical bonds [10]. However, absorption by free electrons in this region may, depending on the coal, also be appreciable.

A few quantitative studies that give values of the complex refractive index n for various coals have also been reported. Huntjens and van Krevelen [11], using the Fresnel equations and normal reflectance measurements in two media with differing refractive indices, obtained values for n, ranging from 1.68 to 2.02 and for k from 0.03 to 0.8 at $\lambda = 0.546$ μm. For both n and k the trend from low to high values with increasing carbon content was noticed. McCartney and Ergun [12], using the same technique, obtained very similar values, as did also Gilbert [13]. Values for n and k in the infrared region were obtained by Foster and Howarth [14] using again a Fresnel reflectance technique. They reported values for n similar to those of the previous studies in the visible region. However, the values for k were approximately an order of magnitude larger than those for coals of similar rank. Blokh [15] also obtained values in the infrared region very similar to those of Foster and Howarth.

It is important to note here that unless the sample surfaces used in Fresnel reflectance analyses satisfy extremely stringent homogeneity and smoothness requirements, this technique for determining n and k has been shown [16] to result in erroneous optical constants, especially in the value of k.

Optical Properties of Char. Quantitative studies of carbonized coals have indicated that major changes occur in both swelling and nonswelling coals when heated. Brown [17] noted that most of the change occurs in the temperature range 400-550°C. Upon heating to 800°C, the char became strongly absorbing throughout the infrared region, suggesting that extensive graphitization may have occurred. This observation is also in agreement with the observation that the electrical conductivity of coals increases dramatically upon carbonization [18]. Apparently there have been no quantitative studies of the optical constants of carbonized coals, although graphite, which may have similar values of n and k, has been investigated [12, 19].

Grosshandler and Monteiro have experimentally studied the engineering radiative properties (absorptivity, etc.) of various coals and chars [20]. They conclude that the engineering radiative properties are not sensitive to coal rank, which appears to be in contradiction with the findings of this and many previous studies. One reason could be that every coal reported in [20] had approximately the same carbon content (65 percent). Previous studies of the visible optical properties of coal [11-13] have indicated a strong correlation with carbon content and not necessarily rank.

A second explanation of the apparent contradiction is that there is no contradiction at all. It is probable that k depends strongly on carbon content while n is a weak function of the percent of C. Since the percent of C and coal rank are related (but not equivalent), k also depends strongly on rank. However, for the particular values of n and k for coal

---

[1] Present address: Assistant Professor, Department of Mechanical and Industrial Engineering, University of Utah, Salt Lake City, Utah, 84112. Assoc. Mem. ASME.

Contributed by the Heat Transfer Division for publication in the JOURNAL OF HEAT TRANSFER. Manuscript received by the Heat Transfer Division June 22, 1983.

($n \simeq 1.7$, $k \simeq 0.1$) the engineering radiative properties, e.g., R_N, are strongly determined by the value of n and rather insensitive to the value of k. So it is entirely possible that n and k are strongly dependent on rank while reflectance, absorptance and emittance are not. This point is the essence of this study. Measurements of R_N or any other reflectance or absorptance value are not sufficiently sensitive to variations in k to accurately quantify that parameter.

Theory

Most studies of the optical constants of materials rely on reflectance and/or transmittance measurements using polished specimens. These data are interpreted using the Fresnel equations to infer the optical constants n and k of the specimen. Janzen [16] has shown that misapplication of this technique to surfaces of pressed carbons, which may appear specular but do not satisfy the criteria for application of the Fresnel equations, can lead to results that, although reproducible, are not self-consistent. An alternative technique is to use experimental data for the extinction efficiency $\bar{Q}_{\mathrm{ext}}$ $(\tilde{n}, x, N(r))$ of micron-sized particle suspensions to infer the values of n and k according to Mie theory (assuming spherical particles). In theory, if the particle size and wavelength are known, $\bar{Q}_{\mathrm{ext}}$ will be a function of only n and k. Therefore, measurement of one more independent quantity which is also a function of n and k should allow for their implicit solution.

In this study, the particle extinction technique previously described was employed to determine the optical constants for various coals and limestone, with normal specular reflectance, R_N (n,k) (see Nomenclature), as the second independent quantity. R_N was measured with an infrared prism-type spectrophotometer using polished specimens of coal and limestone. For the char specimens, specular reflectance measurements were not feasible and a dispersion equation curve-fitting technique for $\bar{Q}_{\mathrm{ext}}$ was used to determine n and k instead of R_N measurements. The dispersion equation from optical electron dispersion theory is [21]

$$\tilde{\epsilon}_r = \tilde{n}^2 = \tilde{\epsilon}_{r,\mathrm{opt}} + \sum_j F_j \frac{e^2}{m\epsilon_o} \frac{1}{\omega_{oj}^2 - \omega^2 + i\gamma_j\omega} \tag{1}$$

where the parameters $\tilde{\epsilon}_{r,\mathrm{opt}}$, F_j, and γ_j were determined by a least-squares curve fit of the experimental $\bar{Q}_{\mathrm{ext}}$ data. This approach is justified by the dominant role of electronic absorption in the char samples. Polydispersity of the particles was taken into account by assuming a size distribution of the form [22]

$$N(r) = \frac{N_t \beta^{\alpha+1}}{\Gamma(\alpha+1)} r^{\alpha} e^{-\beta r} \tag{2}$$

with the effective and mean particle diameters defined as

$$d_{\mathrm{eff}} = \frac{2\int_0^\infty \pi r^3 N(r)\,dr}{\int_0^\infty \pi r^2 N(r)\,dr} = \frac{2(3+\alpha)}{\beta} \tag{3}$$

and

$$N'(r_m) = 0; d_m = \frac{2\alpha}{\beta} \tag{4}$$

The optical depth τ for a dispersed slab of thickness L with refractive index n_w of medium then becomes

$$\tau = 1.5 \bar{Q}_{\mathrm{ext}} f_v L / d_{\mathrm{eff}} \tag{5}$$

with

$$\bar{Q}_{\mathrm{ext}}(\tilde{n}/n_w, \lambda, \alpha, \beta) = \frac{\int_0^\infty \pi r^2 Q_{\mathrm{ext}}(\tilde{n}/n_w, x) N(r)\,dr}{\int_0^\infty \pi r^2 N(r)\,dr} \tag{6}$$

Experimental Method

Experimental application of the analytical technique described requires caution in two respects. First, the measured transmission must not include appreciable forward scattering. This was accomplished by keeping the value of x_{eff} $(= \pi d_{\mathrm{eff}} n_w/\lambda)$ small (approximately 1.0 or less) to reduce total scattering as well as the forward scattered component and also by making measurements with a narrow slit double beam spectrometer (Hitachi 260-50). Second, the particle size

Nomenclature

a = absorption coefficient
d = particle diameter
e = electric charge of an electron
$e_{b\lambda}$ = Planck's spectral distribution of emissive power
e_b = hemispherical total emissive power
f_v = particle volume fraction
F_j = intensity coefficient in equation (1)
k = imaginary part of refractive index, $\tilde{n}$
L = slab thickness
m = mass of an electron
$\tilde{n}$ = complex refractive index of particles
n = real part of refractive index, $\tilde{n}$
n_w = refractive index of KBr
$N(r)$ = particle size distribution function, no./vol.
N_t = total number of particles/vol.
$\bar{Q}_{\mathrm{abs,ext}}$ = effective polydispersion absorption or extinction efficiency, equation (6)
R_N = normal specular reflectance, $[(n-1)^2 + k^2]/[(n+1)^2 + k^2]$
r = particle radius
x = particle size parameter, $\pi d/\lambda$
α, β = particle size distribution parameters, equations (2–4)
γ = extinction coefficient
γ_j = attenuation constant in equation (1)
Γ = Gamma function
ϵ_o = dielectric constant of vacuum
$\tilde{\epsilon}_r$ = complex relative dielectric constant of particles
$\tilde{\epsilon}_{r,\mathrm{opt}}$ = contribution to $\tilde{\epsilon}_r$ from optical region
η = wave number, cm^{-1}
ϵ_r' = real part of $\tilde{\epsilon}_r$
ϵ_r'' = imaginary part of $\tilde{\epsilon}_r$
ρ = particle density
σ = Stefan-Boltzmann constant
τ = optical thickness, equation (5)
ω = circular frequency of radiation
ω_{oj} = resonant circular frequency in equation (1)
λ = wavelength in vacuum, μm

Subscripts

abs = absorption
ext = extinction
eff = effective
m = most probable
opt = optical
P = Planck
R = Rosseland

Superscripts

$'$ = derivative
$-$ = average or integrated
$\sim$ = complex quantity

Table 1 Polydispersion properties

Specimen	% C	% H	$d_{\mathrm{eff}}(\mu\mathrm{m})$	$d_m(\mu\mathrm{m})$	α	$\beta(\mu\mathrm{m}^{-1})$	$\rho\left(\frac{\mathrm{gm}}{\mathrm{cc}}\right)$
Saraji coal	83.3	4.69	1.53	1.03	6.25	12.12	1.35
West coal	77.1	5.26	1.53	1.03	6.25	12.12	1.27
Sufco coal	63.9	4.70	1.53	1.03	6.25	12.12	1.31
Saraji char	85.3	0.27	2.00	1.24	4.90	7.90	1.8
West char	85.8	0	1.89	0.939	2.97	6.32	1.8
Sufco char	82.3	0.35	1.25	0.537	2.26	8.42	1.8
Limestone	–	–	0.437	0.265	4.63	34.9	2.71

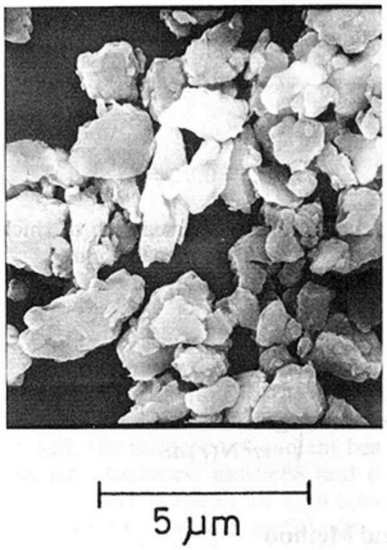

Fig. 1 Photomicrograph of coal (scale = 5 μm)

distribution must be kept sufficiently narrow so that dependence of $\bar{Q}_{\mathrm{ext}}$ on n and k is not overshadowed by polydispersity effects. With these constraints in mind, particles of sufficiently small and uniform size were obtained from crushed samples of the various materials by using a cascade impactor. Scanning electron micrographs of the particles indicated good uniformity of size (Fig. 1). For example, over 98 percent of the coal particles with mean diameter $d_m = 1.03$ had an average diameter between 0.5 and 2.0 μm, where the average particle diameter was taken as an average of the largest and smallest dimensions. A least-squares fit of the assumed size distribution, equation (2), resulted in the properties listed in Table 1.

In this study, three coals (Australian), their respective char products, and limestone were tested. The coals ranged in nature from swelling (Saraji) to nonswelling (Sufco). Carbonization was accomplished by heating the coals in flowing Argon atmosphere to 1070°C and maintaining that temperature for one hour. After crushing and separation, the particles were mixed with infrared transmissive KBr powder and pressed into translucent tablets approximately 0.5 mm thick under vacuum and with a pressure of 120 MPa. Because of the possibility that vacancies in the KBr tablets might contribute to the total scattering, tablets of pure KBr with varying thickness were prepared and their transmittance measured. It was thus found that the effect of reflection at the surface of the tablets was much stronger than scattering within the tablets and this effect, which could be reproducibily predicted, was accounted for in the analysis as follows. Measurement of the transmissivity T of pure KBr pellets allowed calculation of the KBr surface reflectivity ρ using equation (7) with $\tau = 0$.

$$T=\frac{(1-\rho)^2e^{-\tau}}{1-\rho^2e^{-2\tau}} \qquad (7)$$

Then τ was determined from equation (7) using measurements for T made from the sample pellets containing coal, char, or limestone particles.

Specular reflection measurements were carried out on samples that were prepared by graded sanding and diamond paste polishing, the same type of preparation used in [16]. Our experience was that a truly homogeneous, optically smooth surface was, for all practical purposes, impossible to produce. While the diamond particles would polish the harder strata of the coal (at least to within 0.1 μm rms surface roughness as measured with an inference-type surface microscope) the softer layers were merely gouged. Thus the inhomogeneous and inherently soft nature of the coal precluded preparation of a completely satisfactory surface. Nevertheless, the prepared surfaces appeared specular. For various coals the value of normal reflectance R_N, ranged from 6–9 percent according to coal type and wavelength.

In summary, the method for determining n and k for coal and limestone was to solve two simultaneous equations implicitly, $R_N = R_N\ (n,k)$ and $\bar{Q}_{\mathrm{ext}} = \bar{Q}_{\mathrm{ext}}\ (n,k)$, where R_N was measured from polished samples of coal or limestone, and $\bar{Q}_{\mathrm{ext}}$ was measured using the KBr pellets. For the chars $\bar{Q}_{\mathrm{ext}}$ values obtained from the KBr pellets were curve fit as a function of wavelength λ using the Drude model of electron dispersion theory to determine the optimum values of the dispersion parameters.

Results and Discussion

Coal. The optical constants for coal were obtained by both the Fresnel reflectance and particle extinction techniques. Figures 2 and 3 demonstrate how reflectance data for polarized, obliquely-incident radiation could be interpreted using the Fresnel equations to produce values for n and k not far out of agreement with those of other workers who used the same or similar technqiues. The results obtained by the particle extinction technique in Figs. 4 and 5, however, indicate significantly lower values for k, generally between 0.01 and 0.1. Also the trend of increasing k with coal rank which appears unmistakably in the visible region, appears to be not so pronounced in the infrared region and, if anything, reversed in the region of strong absorption bands (1050 cm^{-1} region). The observation of smaller values for k in Fig. 5 finds support in the fact that values for k in the visible region for coals of similar carbon content also range from 0.03 to 0.1 [10], and a sudden increase in going from the visible to near-infrared region as appears in Fig. 3 is not expected (except, perhaps, in the case of anthracite coals) since bound electronic absorption ends near 1.2 μm [10]. Further support comes from a report of transmission measurements of a thin coal maceral layer [5], which indicates that, for that specimen at least, the values of k could not be above 0.005, 0.006, and 0.02 in the wavelength regions near 2, 5, and 10 μm, respectively. It is interesting to note, however, that in [14] the authors had to assume an unreasonably small thickness of 0.5 μm for a thin maceral film in order to predict the correct order of observed transmission using their larger k values. The trend for k to decrease with increasing rank of coal in the infrared

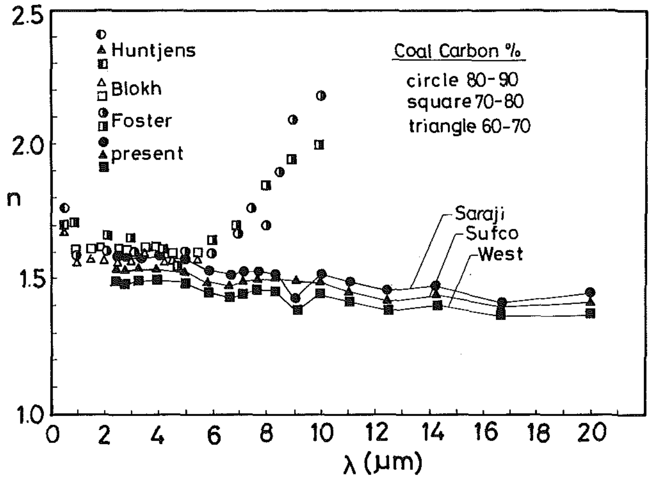

Fig. 2 Summary of real refractive index for coal determined by Fresnel reflectance techniques (see Figure 4 for recommended values)

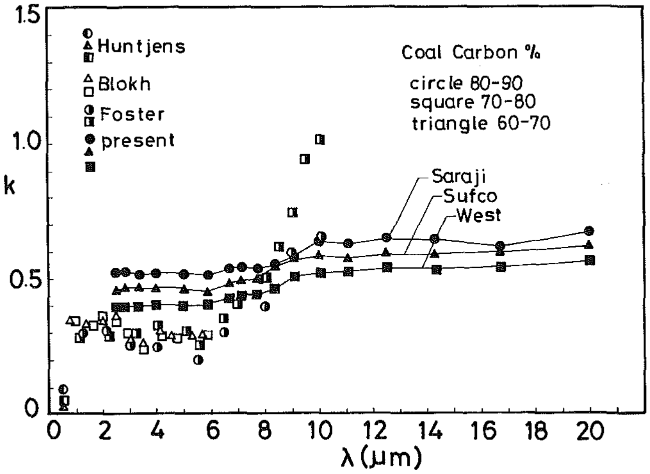

Fig. 3 Summary of imaginary refractive index for coal determined by Fresnel reflectance techniques (see Fig. 5 for recommended values)

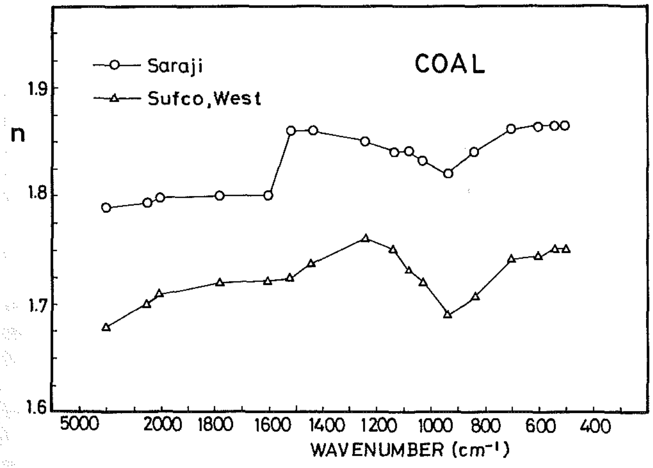

Fig. 4 Real refractive index-coal (particle extinction technique)

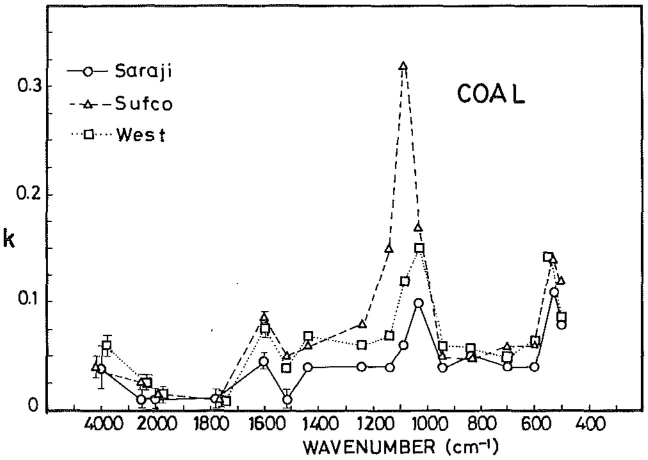

Fig. 5 Imaginary refractive index-coal (particle extinction technique)

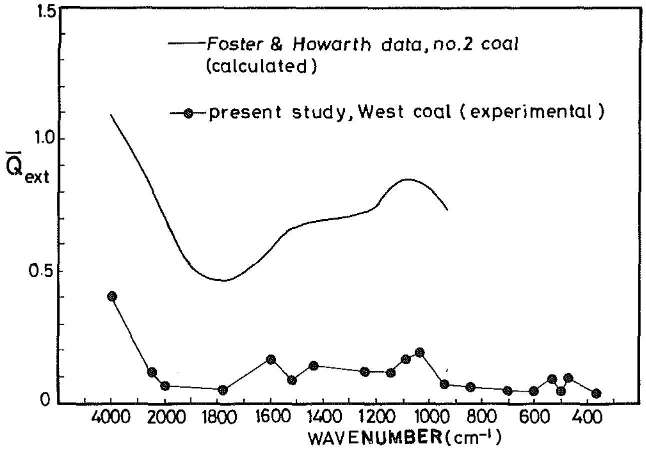

Fig. 6 Comparison of experimental Q_{ext} data with prediction using optical constants of [14], (d = 1 μm)

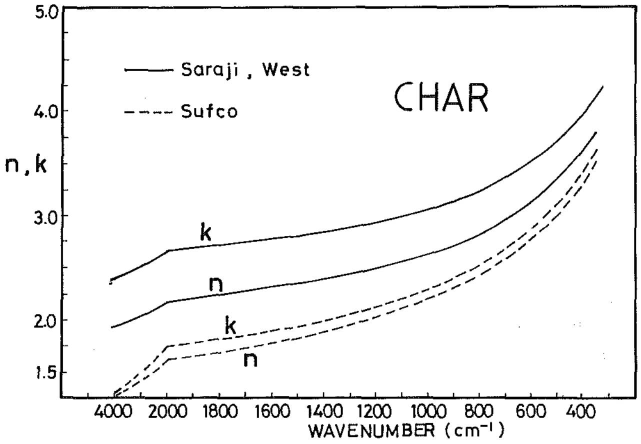

Fig. 7 Optical constants-char (particle extinction technique)

could be explained by the fact that for relatively higher rank coals more of the carbon is present as "fixed carbon" and less as aliphatic and aromatic hydrocarbon molecules, whose vibration appears to be the primary source of absorption in the infrared region. (Stretching by C-O and C=C also occur at approximately 9 μm and 6 μ, respectively.) The discrepancy in k between the present and previously reported values makes no small difference when it comes to radiative transfer calculation. This is demonstrated in Fig. 6 where the experimental values of $\bar{Q}_{ext}$ are shown to be overpredicted by a factor of 3 to 10 using the data for n and k of Foster and Howarth [16] for coals of corresponding carbon and hydrogen contents (no. 2 of [14] and West coal).

Char. Using the dispersion equation (1) and assuming the existence of one type of conduction electron (Drude model), the optical constants of char were obtained as shown in Fig. 7 with the dispersion parameters listed in Table 2. Significantly, both Saraji and West chars, which were found to have nearly

Table 2 Dispersion equation parameters-char

Specimen	$\epsilon'_{r,\mathrm{opt}}$	$\epsilon''_{r,\mathrm{opt}}$	F_i	γ_i
Saraji char	-1.0	8.0	5×10^{20}	1×10^{15}
West char	-1.0	8.0	5×10^{20}	1×10^{15}
Sufco char	1.0	2.0	5×10^{20}	1×10^{15}

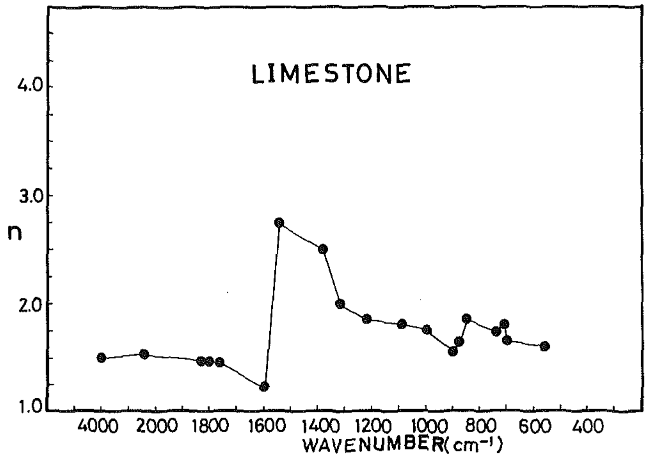

Fig. 8 Real refractive index-limestone (particle extinction technique)

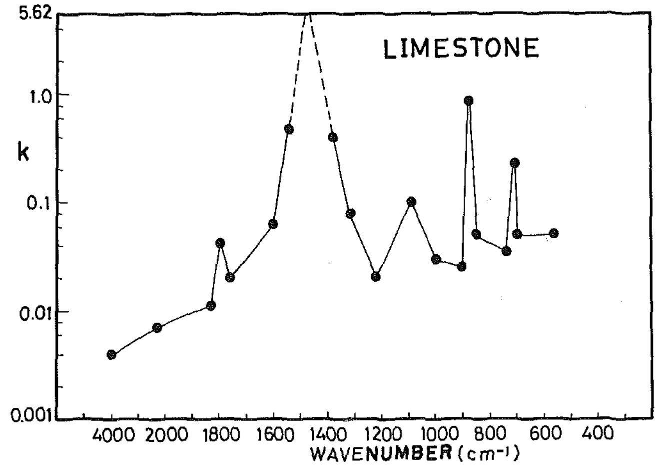

Fig. 9 Imaginary refractive index-limestone (particle extinction technique)

the same composition (Table 1), were fit by the same parameters. Char from Sufco coal also had a very similar composition and exhibited only slightly lower values for n and k even though the appearance of Sufco char was quite different. (Chars from Saraji and West coals demonstrated characteristic swelling and porosity, while Sufco char showed slight shrinkage and cracking.) The characteristic absorption bands of coal are absent in char and a remarkable increase in the value of k, especially, is seen.

Limestone. The optical constants of limestone appear in Figs. 8 and 9. Two fairly strong molecular absorption bands of classical Lorentzian type appear at 6.8 and 11.4 μm, as well as other minor bands which can be assigned as noted in [23]. Otherwise the optical constants are of the same order as those for coal. Since limestone is primarily calcite, $CaCO_3$, which is birefringent, these values represent an average of the values for the extraordinary and ordinary rays.

Extinction and Absorption Coefficients. The Planck and Rosseland mean absorption coefficients are defined by equations (7–9).

$$a_p = \frac{1}{\sigma T^4}\int_0^\infty a_\lambda(\bar{n}) e_{b\lambda}(\lambda,T)d\lambda \tag{7}$$

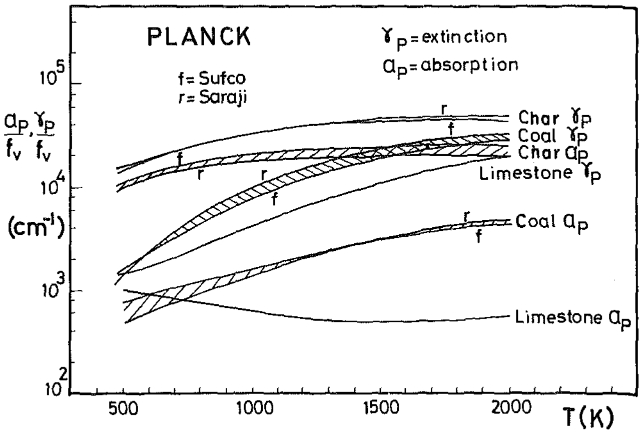

Fig. 10 Planck absorption and extinction coefficients-coal, char, limestone at 300 K (d = 1 μm)

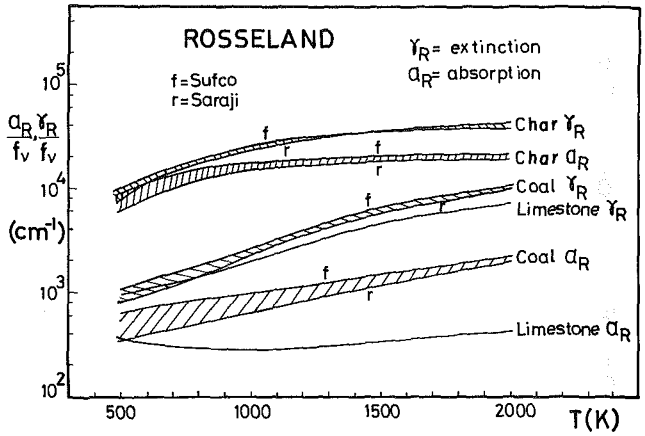

Fig. 11 Rosseland absorption and extinction coefficients-coal, char, limestone at 300 K (d = 1 μm)

$$\frac{1}{a_R} = \int_0^\infty \frac{1}{a_\lambda}\frac{\partial e_{b\lambda}(\lambda,T)}{\partial e_b(T)}d\lambda \Big/ \int_0^\infty \frac{\partial e_{b\lambda}(\lambda,T)}{\partial e_b(T)}d\lambda \tag{8}$$

where

$$a_\lambda = 1.5 f_v \bar{Q}_{\mathrm{abs}}/d_{\mathrm{eff}} \tag{9}$$

and similarly for the corresponding extinction coefficients. These coefficients, normalized by f_v, have been plotted in Figs. 10 and 11 as functions of source temperature for coal, char, and limestone particles of 1 μm diameter. The temperature dependence of the optical constants per se is not included in as much as the values measured at 300 K are used to determine a_λ in equation (9). However, the effect of increasing temperature is included indirectly by accounting for the change in composition that occurs upon heating, that is, by including char measurements also. This change in composition is felt to be a stronger effect than the temperature effect at fixed composition.

Expectedly, the chars demonstrate significantly increased extinction and absorption relative to coal, and the variation in coefficients due to different coal or char types is comparatively minor. Therefore, in fluidized or pulverized coal combustion, the radiative properties of the particles can be expected to change significantly as devolatilization and combustion proceed. It should be noted that the coefficients presented in Figs. 10 and 11 are as much as an order of magnitude smaller than previously reported values [3, 4], based mainly on Foster and Howarth's optical constants. Finally, the results obtained for coal in this paper are felt to be reasonably accurate for most coals as long as the carbon content remains below about 91 percent. At about that carbon

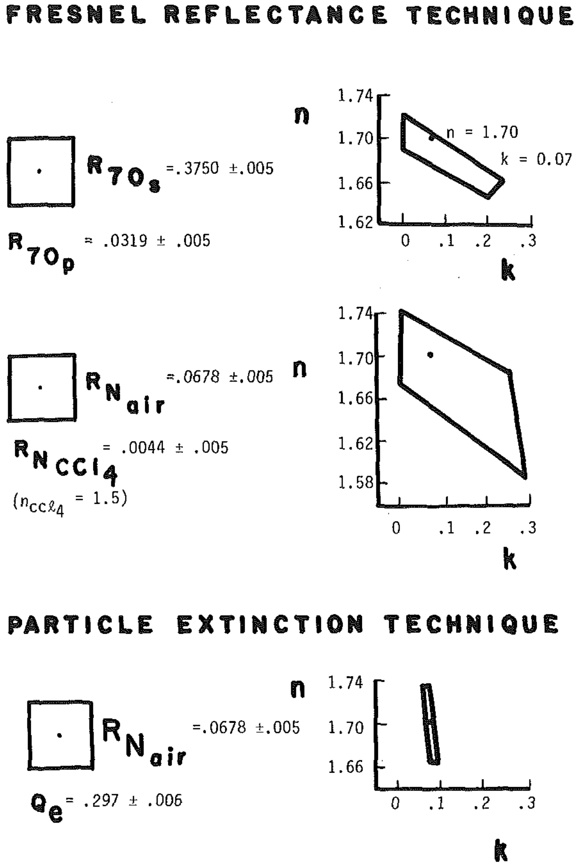

Fig. 12 Typical error regions for determining n (= 1.70) and k (= 0.07) by Fresnel and particle extinction techniques

content it has been shown [10] that continuous (free) electronic absorption increases suddenly, which would result in a significant increase in the value of k especially.

Error Analysis. Figure 12 illustrates the magnitude of the error incurred in determining n and k by the particle extinction technique compared with that for the various Fresnel techniques. For given values of $n = 1.70$, $k = 0.07$ (typical of coal), the three graphs on the right give the error region for the values of n and k determined by three methods. The method for the top case is a Fresnel technique using two polarized reflectance measurements. The middle case is another Fresnel technique using two normal reflectance measurements, one in air and one in carbon tetrachloride. Typical reflectance measurement errors of ±0.5 percent were assumed for both Fresnel techniques. The bottom case corresponds to the particle extinction technique. The usual ±0.5 percent reflectance error gives a similar amount of uncertainty in the value of n. However, the 2.0 percent accuracy attainable for the $\bar{Q}_{\mathrm{ext}}$ measurements ($\bar{Q}_{\mathrm{ext}} = 0.297 \pm 0.006$) substantially decreases the uncertainty in the calculated value of k, thus providing a very accurate means for determining k.

Summary and Conclusions

The optical constants of both swelling and nonswelling coals, their respective char products, and limestone have been measured using a technique that employs both particle extinction data and specular reflectance data. Values of the complex part of the refractive index for coal were found to be about an order of magnitude smaller than previously reported values determined by only Fresnel reflectance techniques [14,15]. A strong absorption band in the wavelength region near 9 μm that increased with decreasing coal rank was observed, as were other minor bands. Dramatically increased values of k, compared with those of coal, and smooth, monotonically increasing wavelength dependence characterized the optical constants of all of the char samples, demonstrating that significant graphitization occurred upon devolatilization. Limestone displayed significant molecular absorption bands, as well as other minor bands, at 6.8 and 11.4 μm. Owing to the extreme difficulty in satisfying the stringent requirements for experimental determination of n and k, even the present technique is subject to inaccuracy. The assumption of spherical particles, polydispersity effects, difficulty in measuring particle density, etc., all introduce error in the analysis. However, because data from two independent and vastly differnt types of measurement are involved, the resulting optical constants are less subject to severe, order-of-magnitude errors, which can easily occur in methods that apply the Fresnel reflectance analysis only.

References

1 Saxena, S. C., and Gabor, J. D., "Mechanisms of Heat Transfer Between a Surface and a Gas-Fluidized Bed for Combustion Applications," *Progress in Energy and Combustion Science*, Vol. 7, 1980, pp. 73-102.

2 Krazinski, J. L., Buckius, R. O., and Krier, H., "A Model for Flame Propagation in Low Volatile Coal Dust-Air Mixtures," ASME JOURNAL OF HEAT TRANSFER, Vol. 100, Feb. 1978, pp. 105-111.

3 Buckius, R. O., and Hwang, D. C., "Radiation Properties for Polydispersions: Application to Coal," ASME JOURNAL OF HEAT TRANSFER, Vol. 102, Feb. 1980, pp. 99-103.

4 Viskanta, R., Ungan, A., and Menguc, M. P., "Predictions of Radiative Properties of Pulverized Coal and Fly-Ash Polydispersions," ASME paper 81-HT-24, 1981.

5 Sutherland, G. B. B. M., Fellgett, P. B., and Willis, H. A., "The Infrared Spectrum of Coal," *Proceedings of Conference on Ultra-fine Structure of Coal and Cokes*, British Coal Utilization Research Association, 1944.

6 Cannon, C. G., and George, W. H., "The Optical Properties of Coals," *Proceedings of Conference on Ultra-fine Structure of Coal and Cokes*, British Coal Utilization Research Association, 1944, pp. 290-321.

7 Brown, J. K., "The Infrared Spectra of Coals," *Journal of Chemical Society*, 1955, pp. 744-752.

8 Friedel, R. A., and Carlson, G. L., "Difficult Carbonaceous Materials and Their Infrared and Raman Spectra. Reassignments for Coal Spectra," *Fuel*, Vol. 51, July, 1972.

9 Rockley, M. G. and Devlin, J. P., "Photoacoustic Infrared Spectra (IR-PAS) of Aged and Fresh-Cleaved Coal Surfaces," *Applied Spectroscopy*, Vol. 34, No. 4, 1980, pp. 407-408.

10 van Krevelen, *Coal*, Elsevier Publishing Comp., 1961, pp. 182-189.

11 Huntjens, F. J., and van Krevelen, D. W., *Fuel*, Vol. 33, 1954, p. 88.

12 McCartney, T. J., and Ergun, S., "Optical Properties of Graphite and Coal," *Proceeding of Third Carbon Conference*, Pergamon Press, 1959, pp. 223-231.

13 Gilbert, L. A., *Fuel*, Vol. 41, 1962, p. 351.

14 Foster, P. J., and Howarth, C. R., "Optical Constants of Carbons and Coals in the Infrared," *Carbon*, Vol. 6, 1968, pp. 719-729.

15 Blokh, A., "The Problem of Flame as a Disperse System," *Heat Transfer in Flames*, Halsted Press, 1974, pp. 111-130.

16 Janzen, J., "The Refractive Index of Colloidal Carbon," *J. Coll. Int. Science*, Vol. 69, No. 3, May 1979, pp. 436-447.

17 Brown, J. K., "Infrared Studies of Carbonized Coals," *Journal of Chemical Society*, 1055, pp. 752-757.

18 Sandor, J., "The Electrical Conductivity of Carbonized Coals," *Proceedings of Conference on Ultrafine Structure of Coal and Cokes*, British Coal Utilization Research Association, 1944, pp. 342-349.

19 Taft, E. A., and Philip, H. R., "The Optical Properties of Graphite," *Physical Review*, 138-1A, 1965, pp. A197-A202.

20 Grosshandler, W. L., and Monteiro, S. L. P., "Attenuation of Thermal Radiation by Pulverized Coal and Char," ASME JOURNAL OF HEAT TRANSFER, Vol. 104, Nov. 1982, pp. 587-593.

21 Slater, J. C., and Frank, N. H., *Electromagnetism*, Ch. IX, Dover, New York, 1947.

22 Hansen, J. E., and Travis, L. D., "Light Scattering in Planetary Atmospheres," *Space Science Review*, Vol. 16, 1974, pp. 527-610.

23 Bhagavantam, S., and Verkatarayudu, T., *Theory of Groups and Its Application to Physical Problems*, Academic Press, New York, 1969, p. 104.

Scaling Rules for Total Absorptivity and Emissivity of Gases

D. K. Edwards
University of California,
Irvine, Calif. 92717

R. Matavosian
Bechtel Power Corporation,
Houston, Texas 77056

Hottel's Rule and Penner's Rule for estimating the total absorptivity of a homogeneous gas from a total emissivity chart or expression are generalized. The generalized rule is developed from an examination of the functional relationships between total and spectral molecular gas radiation properties. It gives a rational prescription for finding the absorptivity or emissivity at arbitrary pressure from the one-atmosphere total emissivity. Calculations of total properties from band absorption data correlations are used to find the needed map of pressure scaling exponent versus path-length-pressure product and gas temperature. Also addressed is the question of allowing for reflecting walls in the calculation of radiation heat transfer between a homogeneous gas and its enclosing walls. Both exact and high-accuracy-approximate calculations are shown to be possible using only total properties.

Introduction

For convenience or speed in computation, many applied heat transfer workers continue to use total (spectrally integrated) radiation properties, e.g., [1-8]. Hottel's Rule or Penner's Rule is used to estimate the total absorptivity of a homogeneous gas from a total emissivity chart or expression [8-10]. The rules prescribe a scaled length L_α' at which a total emissivity chart or functional fit is entered, taking the gas temperature T_g' to be the wall temperature T_w, so that the value of emissivity after multiplication by $(T_g/T_w)^{1/2}$ will be the correct absorptivity for a one-atmosphere gas at temperature T_g and mean beam length L. (Originally the power for T_g/T_w recommended by Hottel was 0.65 for CO_2 and 0.45 for H_2O, but with greater theoretical understanding the single value of 0.5 has become accepted [9]).

$$\alpha_{gw} = (T_g/T_w)^{1/2}\epsilon_g(T_g{}', P_a L_\alpha{}') \qquad (T_g{}' = T_w) \tag{1}$$

The total absorptivity as well as the total emissivity is needed because the heat flux q into a black wall surrounding a homogeneous gas is

$$q = \epsilon_g \sigma T_g{}^4 - \alpha_{gw}\sigma T_w{}^4 \tag{2}$$

Particularly when T_w exceeds T_g, as in some nuclear accident scenarios or in a cavity solar receiver, the fact that gas absorptivity differs from gas emissivity is a significant factor requiring consideration.

Hottel's Rule applies at moderate-to-low temperatures and pressures. It prescribes

$$L_\alpha{}' = (T_w/T_g)L \tag{3a}$$

Penner's Rule applies at high pressures or temperatures when the lines in the infrared spectrum of the gas are overlapped.

$$L_\alpha{}' = (T_w/T_g)^{3/2}L \tag{3b}$$

When to apply one rule, when to apply the other, and what to do when neither rule applies have been left unanswered questions.

Edwards [11] has pointed out that Hottel's and Penner's Rules have implications as to how total absorptivity and emissivity vary with pressure. When the former applies, an L_ϵ' can include the effect of a gas pressure different from one atmosphere, thus avoiding recourse to a pressure correction chart, and when the latter applies no correction for pressure is necessary.

Even when adequate scaling of total absorptivity and emissivity is achieved, another problem is encountered in the use of total properties. That problem is how to modify equation (2) to account for a partially absorbing, partially reflecting wall. For a gray gas, an Oppenheim network [12] or a radiosity-irradiation analysis [13] leads to

$$q = \frac{\epsilon_g \epsilon_w}{1-(1-\epsilon_w)(1-\epsilon_g)}(\sigma T_g^4 - \sigma T_w^4) \tag{4}$$

where ϵ_w is the wall emissivity or absorptivity. This expression is quite unsatisfactory for an actual nongray gas if total emissivity is used in both numerator and denominator. Edwards [14] advocated examining the underlying band behaviors affecting the total gas property behaviors and assigning a "within band" gas transmissivity in place of the $(1-\epsilon_g)$ term in the denominator, putting equation (2) into the form

$$q = \frac{\epsilon_w \epsilon_g \sigma T_g^4}{1-(1-\epsilon_w)\tau_{bg}} - \frac{\epsilon_w \alpha_{gw}\sigma T_w^4}{1-(1-\epsilon_w)\tau_{bgw}} \tag{5}$$

The present paper begins by developing an exact (to the mean beam length approximation) expression to modify equation (2) to account for wall interreflections. The expression contains only total (i.e., spectrally-integrated) radiation properties and is suitable when a functional fit of total properties is used. Alternatively prescriptions are given for τ_{bg} and τ_{bgw} in equation (5) without recourse to spectral or band properties. Both absorptivity and total emissivity are required, emphasizing the need for a general scaling rule. Next, the functional relationships between total properties and the underlying gas absorption band spectral properties are shown to prescribe the need for scaling not only to a path length L_α' but also to a pressure P'. The possibility of scaling from $P' \neq 1$ to a P'' equal to one atmosphere by means of a scaled length L'' is then examined. Comparisons of total properties from band absorption data correlations are made with calculated total properties and those given by the various scaling rules. The two-step (L-to-L'-to-L'') scaling is found to be markedly superior to one-step scaling in the case of H_2O gas.

Total Properties and Transfer Factors

Subject to the mean beam length approximation [9, 15],

Contributed by the Heat Transfer Division for publication in the JOURNAL OF HEAT TRANSFER. Manuscript received by the Heat Transfer Division September 29, 1983. Paper No. 83-HT-36.

known to introduce an uncertainty of well under 10 percent, *the average net spectral radiant heat flux at a wall of uniform* emissivity ϵ_w and temperature T_w, enclosing a homogeneous gas of uniform pressure, composition, and temperature T_g is

$$q=\frac{1}{\dfrac{1-\epsilon_{w\nu}}{\epsilon_{w\nu}}+\dfrac{1}{\alpha_{g\nu}}}[\beta_\nu(T_g)-B_\nu(T_w)] \tag{6}$$

where $B_\nu(T)$ is the Planck black body radiosity. The spectral absorptivity of the gas $\alpha_{g\nu}$ is a function of the gas temperature, composition, pressure, and path length. Integration over the spectrum from wavenumber $\nu=0$ to $\nu=\infty$ gives the total flux. The total integration may be facilitated by introducing the fractional function [16, 17] so that

$$B_\nu(T)d\nu=\sigma T^4 df(\nu/T) \tag{7}$$

First denote the spectral transfer factor F_ν as the lead term on the right of equation (6). It may be put into the form

$$F_\nu=\frac{\epsilon_w\alpha_{g\nu}}{1-\rho_{w\nu}\tau_{g\nu}} \tag{8a}$$

where $\rho_{w\nu}$ is the wall reflectivity and $\tau_{g\nu}$ is the transmissivity of the gas

$$\rho_{w\nu}=1-\epsilon_{w\nu},\tau_{g\nu}=1-\alpha_{g\nu} \tag{9}$$

The form of equation (8*a*) makes obvious the infinity of interreflections

$$F_\nu=\epsilon_{w\nu}\alpha_{g\nu}[1+\rho_{w\nu}\tau_{g\nu}+\rho_{w\nu}^2\tau_{g\nu}^2+\rho_{g\nu}^3\tau_{g\nu}^3+\ .\ .\ .] \tag{8b}$$

Further algebraic manipulation of equations (8*a*) and (9) yields

$$F_\nu=\epsilon_{w\nu}[\alpha_{g\nu}+\rho_{w\nu}(\tau_{g\nu}-\tau_{g\nu}^2)+\rho_{w\nu}^2(\tau_{g\nu}^2-\tau_{g\nu}^3)+\ .\ .\ .] \tag{8c}$$

Only on a high-resolution spectral basis is equation (8*c*) correct. But on a high-resolution spectral basis Bouguer's Law holds

$$\tau_{g\nu}=e^{-k_\nu L},\tau_{g\nu}^n(L)=\tau_{g\nu}(nL) \tag{10}$$

Adopt the notation

$$\tau_{g\nu}(nL)=\tau_{g\nu n},\alpha_{g\nu n}=1-\tau_{g\nu n} \tag{11}$$

Then equation (8*c*) can be written

$$F_\nu=\epsilon_{w\nu}[\alpha_{g\nu 1}+\rho_{w\nu}(\alpha_{g\nu 2}-\alpha_{g\nu 1})+\rho_{w\nu}^2(\alpha_{g\nu 3}-\alpha_{g\nu 2})+\ .\ .\ .] \tag{8d}$$

With the aid of equation (7), the definitions of the total emissivity and absorptivity can be expressed as

$$\epsilon_g=\int_0^1\alpha_{g\nu}df(\nu/T_g) \tag{12}$$

$$\alpha_{gw}=\int_0^1\alpha_{g\nu}df(\nu/T_w) \tag{13}$$

Accordingly, when equation (8*d*) is substituted into equation (6), and the spectral equation is integrated, the result is

$$q=F_g\sigma T_g^4-F_{gw}\sigma T_w^4 \tag{14}$$

where, for a gray wall with $\epsilon_{w\nu}$ = constant = ϵ_w, the total transfer factors for emission and absorption are

$$F_g = \epsilon_w[\epsilon_{g1}+\rho_w(\epsilon_{g2}-\epsilon_{g1})+\rho_w^2(\epsilon_{g3}-\epsilon_{g2})+\ .\ .\ .] \tag{15a}$$

$$F_{gw} = \epsilon_w[\alpha_{gw1}+\rho_w(\alpha_{gw2}-\alpha_{gw1})+\ .\ .\ .] \tag{15b}$$

Equation (14) with (15) is very convenient to use when a fit expression for total emissivity and absorptivity is available. For hand calculation in the case of a low reflecting wall, it is thus reasonable to approximate equations (15*a*, *b*) with expressions in the form of equation (8)

$$F_g=\frac{\epsilon_w\epsilon_g}{1-\rho_w\tau_{gb}},F_{gw}=\frac{\epsilon_w\alpha_{gw}}{1-\rho_w\tau_{gbw}} \tag{16a, b}$$

where, in view of equation (15*a*, *b*), the indicated within-band total transmissivities τ_{gb} and τ_{gwb} are

$$\tau_{gb} = (\epsilon_{g2}-\epsilon_{g1})/\epsilon_{g1} \tag{17a}$$

$$\tau_{gbw} = (\alpha_{gw2}-\alpha_{gw1})/\alpha_{gw1} \tag{17b}$$

Comparisons of equations (15*a*, *b*) and (16*a*, *b*) are presented with the calculated results.

Scaling of Total Absorptivity

Equations (15*a*, *b*) or (16*a*, *b*) require total absorptivity. With the assignment of a nominal set of band limits for the *k*th absorption band, e.g., [11, 18], equations (12) and (13) pass to the form

$$\epsilon_g = \sum_k\alpha_{g\nu k}\Delta f_{gk} \tag{18}$$

$$\alpha_{gw} = \sum_k\alpha_{g\nu k}\Delta f_{wk} \tag{19}$$

where

$$\alpha_{g\nu k}=\omega_k A^*(\tau_{Hk},\eta_k)/\Delta\nu_k \tag{20}$$

Nomenclature

A = band absorptance, dimensionless
b = self broadening coefficient, dimensionless
B = Planck black body spectral radiosity, W/m
f = fractional function, dimensionless
F = transfer factor, dimensionless
k = absorption coefficient, m^{-1}
L = mean beam length, m
m = pressure exponent, equations (30 *a*,*b*)
n = integer; also broadening exponent
P = pressure, atm
q = heat flux W/m^2
r = temperature exponent, equation (24)
s = temperature exponent, equation (25)
T = temperature

Greek

α = absorptivity
β = line width to spacing pressure coefficient
ϵ = emissivity
η = line width to spacing parameter
ν = wavenumber, m^{-1}
ρ = reflectivity
σ = Stefan Boltzmann constant, W/m^{2}K^4
τ = transmissivity
τ_H = optical depth at band head, dimensionless
τ_H^* = optical depth P_aL coefficient, (atm-m)$^{-1}$
ω = spectral band width parameter, m^{-1}

Subscripts

a = absorbing species
b = within-band
e = equivalent
g = gas; gas temperature
k = kth spectral absorption band
o = reference value
w = wall; wall temperature
α = value for absorptivity
ϵ = value for emissivity
ν = value at wavenumber

The quantity ω_k is the rotation band width parameter known on theoretical grounds with experimental verification to vary as $T_g{}^{1/2}$. The quantity τ_{Hk} is the line-averaged spectral optical depth at the band head or peak and varies directly with partial-pressure-path-length product P_aL. The constant of proportionality is denoted τ_{Hk}^* so that

$$\tau_{Hk} = \tau_{Hk}^* P_a L \tag{21}$$

The quantity η_k is the line width-to-spacing parameter which varies with equivalent broadening pressure P_e

$$\eta_k = \beta_k P_{ek}^*, P_{ek}^* = (P_e/P_o)^{n_k} \tag{22}$$

where the equivalent broadening pressure makes provision for self-broadening (absorbing-molecule collisions) being stronger than foreign gas broadening (foreign-molecule-absorbing-molecule collisions),

$$P_e = P - P_a + bP_a \tag{23}$$

where b is the self-broadening coefficient. The quality A^* is the dimensionless band absorptance.

Consequently to "scale" α_{gw} to ϵ_g one would look up or calculate $\epsilon_g{}'$ at conditions $T_g{}'$, $L_\alpha{}'$ and P' such that the set of $f_{gk}{}' = f_{wk}$ (requiring $T_g{}' = T_w$), such that the set of $\tau_{Hk}^*{}'$ P_aL' is $\tau_{Hk}^* P_aL$, and such that the set of $\beta_k P_{ek}^*{}'$ is β_k P_{ek}^*. The value of $\epsilon_g{}'$ would then be multiplied by $(T_g/T_w)^{1/2}$ to correct the values of ω_k back to the true gas conditions. Clearly, for a multiband real gas, it may not be possible to ensure near equality for every member in the k-set. Table 1 examines this question.

Shown in Table 1 are values of τ_{Hk}^* and β_k for the principal bands of H_2O and CO_2 for temperatures of 800, 1200, 1600, and 2000 K, calculated according to [19]. The calculated values may be fit by

$$\tau_{Hk}^* = \tau_{Hok}^*[T_g/T_o]^{-r} \tag{24}$$

$$\beta_k = \beta_{ok}[T_g/T_o]^s \tag{25}$$

Shown in parentheses for each band in Table 1 are values of r and s for a log-log straight-line fit between 800 and 2000 K. Values of $r = 1.5$ and $s = 1.6$ represent well the two major H_2O bands, for which $\eta_k = 1$. For CO_2, because of "hot bands" at 10.4, 9.4, and 2.7 microns, the value of r varies markedly from band to band, but one might try a value of $r = 1$.

Note that the far infrared rotational band of H_2O is not shown in the table because high temperature data at wavenumbers below 500 cm^{-1} are lacking, making it impossible to validate a theoretical model. In the total emissivity and absorptivity calculations to follow, an arbitrary model similar to that suggested by Modak [20] has been used with assumed center at 70 μm and an exponential tail matching known high-temperature data. Calculations of ϵ_g or α_{gw} for T_g or T_w below 800 K are not presented, because, at lower temperatures, uncertainty about this band makes the calculations speculative. At 800 K and higher temperatures the results are sound because of the unimportance of the far infrared spectrum to the high temperature total property.

Accordingly, the absorptivity scaling rule proposed for trial is

$$\alpha_{gw} = (T_g/T_w)^{1/2} \epsilon_g(T_g{}', P_aL_\alpha{}', P_e{}') \tag{26}$$

where

$$T_g{}' = T_w \tag{27}$$

$$P_aL_\alpha{}' = P_aL[T_w/T_g]^r \tag{28}$$

$$P_e{}' = P_e[T_g/T_w]^s \tag{29}$$

Equations (26–28) are seen to be the same as proposed by Hottel and Penner. Equation (29) is new.

Table 1 Temperature variations of absorption band parameters

Gas	Band (μm)	T_g (K)	τ_H^* (atm-m)$^{-1}$	β
H_2O	6.3	800	70.82	0.74
	($r = 1.5$)	1200	38.55	.122
	($s = 1.6$)	1600	25.04	.199
		2000	17.92	.310
	2.7	800	40.26	.093
	($r = 1.5$)	1200	21.95	.152
	($s = 1.6$)	1600	14.29	.254
		2000	10.25	.408
	1.87	800	7.16	.066
	($r = 1.1$)	1200	4.35	.115
	($r = 1.7$)	1600	3.22	.199
		2000	2.62	.325
	1.38	800	7.59	.082
	($r = 1.4$)	1200	4.22	.138
	($s = 1.7$)	1600	2.88	.240
		2000	2.20	.397
CO_2	15	400	1002.8	.098
	($r = 1.5$)	800	354.6	.293
	($s = 2.2$)	1200	193.0	.685
		1600	125.4	1.322
		2000	89.7	2.244
	10.4	400	0.26	.058
	($r = 0$)	800	0.96	.190
	($s = 2.5$)	1200	1.11	.502
		1600	1.06	1.065
		2000	0.97	1.940
	9.4	400	.35	.172
	($r = 0$)	800	1.28	.565
	($s = 2.5$)	1200	1.48	1.492
		1600	1.41	3.167
		2000	1.29	5.771
	4.3	400	6583	.343
	($r = 1.5$)	800	2327	1.036
	($s = 2.4$)	1200	1267	2.576
		1600	823	5.240
		2000	589	9.254
	2.7	400	115.01	.198
	($r = 1.0$)	800	44.78	.685
	($s = 2.6$)	1200	28.69	1.841
		1600	22.15	3.916
		2000	18.63	7.111

[a] Values of r and s in parentheses were calculated from:

$r = \ln(\tau_{H,800}^*/\tau_{H,2000}^*)/\ln(2000/800)$ and $s = \ln(\beta_{2000}/\beta_{800})/\ln(2000/800)$, respectively.

Scaling for Pressure

When band absorptance A^* (τ_{Hk}, η_k) is a function of η_k, the functional dependency is primarily on the product $\tau_{Hk}\eta_k$. This fact suggests that the desired emissivity, ϵ_g or $\epsilon_g{}'$ at a pressure P_e or $P_e{}'$ not equal to one atmosphere, can be found from a one atmosphere total emissivity chart or fit. The scaled path length L'' is then simply $L'(P'_eP_o)^{n_k}$. However, this simple rule applies only when all the major bands are in the strong band region, that is, only when τ_{Hk} is large and η_k small. When the opposite is true, there is no pressure dependency at all. What can be done is to scale for pressure by modifying the path length. For emissivity

$$P_aL_\epsilon{}' = P_aL[P_e/P_o]^m \tag{30a}$$

and for the second step of two-step scaling

$$P_aL'' = P_aL_\alpha{}'[P_e{}'/P_o]^{m'} \tag{30b}$$

The exponent m is simply fit to calculated values of total emissivity and is a function of gas temperature T_g, pressure path-length product P_aL, and pressure P_e. When two-step scaling is used to find absorptivity, the exponent m' is understood to be a function $T_g{}'$, $P_aL_\alpha{}'$, and $P_e{}'$.

Results and Comparison

Tables 2, 3, and 4 present the maps of pressure scaling exponent m for H_2O, CO_2, and an equimolar H_2O-CO_2 mixture, respectively. In the case of the mixture, the pressure scaling is understood to apply to the total pressure, since the gas composition was fixed at 10 percent H_2O, 10 percent

Table 2 Pressure scaling exponent for H_2O

T_g (K)	P_e (atm)	Exponent m (dimensionless) $P_aL=0.01$ (atm-m)	$P_aL=0.10$ (atm-m)	$P_aL=1.0$ (atm-m)	$P_aL=10$ (atm-m)
800	.1	.70	.91	.96	1.00
	.3	.70	.85	.92	.97
	3.0	.63	.90	.83	.80
	10.0	.46	.72	.70	.60
1200	.1	.47	.80	.92	.94
	.3	.45	.87	.95	.87
	3.0	.20	.72	.76	.63
	10.0	.17	.51	.57	.52
1600	.1	.26	.60	.87	.89
	.3	.21	.58	.85	.87
	3.0	.18	.48	.54	.54
	10.0	.15	.27	.32	.26
2000	.1	.14	.46	.77	.82
	.3	.14	.41	.68	.70
	3.0	.14	.25	.40	.34
	10.0	.13	.15	.20	.15

Table 3 Pressure scaling exponent for CO_2

T_g (K)	P_e (atm)	Exponent m (dimensionless) $P_aL=0.001$ (atm-m)	$P_aL=0.01$ (atm-m)	$P_aL=0.10$ (atm-m)	$P_aL=1.0$ (atm-m)
400	.1	.47	.64	.65	.65
	.3	.45	.66	.62	.60
	3.0	.41	.61	.45	.45
	10.0	.35	.49	.38	.38
800	.1	.30	.40	.40	.40
	.3	.21	.41	.30	.30
	3.0	0	.09	.11	.11
	10.0	0	.05	.06	.06
1200	.1	.08	.10	.15	.18
	.3	0	0	0	0
	3.0	0	0	0	0
	10.0	0	0	0	0
1600	.1	0	.02	.02	.03
	.3	0	0	0	0
	3.0	0	0	0	0
	10.0	0	0	0	0
2000	.1	0	0	0	0
	.3	0	0	0	0
	3.0	0	0	0	0
	10.0	0	0	0	0

Table 4 Pressure scaling exponent for equimolar H_2O-CO_2 in nitrogen $x_{H_2O} = x_{CO_2} = 0.10, x_{N_2} = 0.80$

T_g (K)	P (atm)	Exponent m (dimensionless) $P_aL=0.001$ (atm-m)	$P_aL=0.01$ (atm-m)	$P_aL=0.1$ (atm-m)	$P_aL=1.0$ (atm-m)
800	.1	.33	.53	.68	.81
	.3	.28	.54	.67	.76
	3.0	.24	.43	.56	.63
	10.0	.18	.30	.50	.51
1200	.1	.08	.29	.50	.71
	.3	.11	.30	.49	.70
	3.0	.09	.13	.44	.51
	10.0	.07	.10	.36	.36
1600	.1	.03	.12	.35	.65
	.3	.04	.12	.32	.63
	3.0	.07	.08	.26	.21
	10.0	.08	.08	.22	.21
2000	.1	.02	.07	.29	.61
	.3	0	.07	.27	.58
	3.0	0	.06	.10	.20
	10.0	0	.06	.08	.13

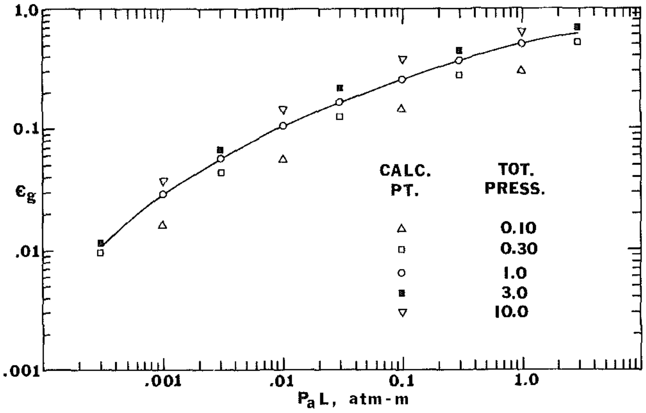

Fig. 1 Total emissivity of a gas mixture at 800 K 10 percent H_2O, 10 percent CO_2, 80 percent N_2

Table 5 Total emissivities from band absorption correlations

Gas	P-Path Product P_aL (atm-m)	$T_g=400$ (K)	Emissivity (dimensionless) $T_g=800$ (K)	$T_g=1200$ (K)	$T_g=1600$ (K)	$T_g=2000$ (K)
H_2O	.001		.0073	.0033	.0017	.0010
($P=1.0$)	.01		.0421	.0275	.0165	.0098
	.1		.1414	.1140	.0949	.0750
	1.		.3505	.3203	.2947	.2634
	10.		.5780	.5427	.5222	.4871
	100.		.7271	.7362	.7319	.6572
CO_2	.0001	.0028	.0026	.0014	.0007	.0004
($P=1.0$)	.001	.0141	.0211	.0137	.0070	.0039
	.01	.0444	.0578	.0462	.0311	.0207
	.1	.0945	.1156	.1074	.0827	.0611
	1.	.1510	.1916	.1900	.1576	.1242
	10.	.2257	.2913	.2960	.2365	.2227
Mix	.001		.0288	.0170	.0088	.0049
($x_{H_2O}=.1$,	.003		.0564	.0368	.0222	.0136
	.01		.1037	.0748	.0467	.0304
$x_{CO_2}=1$,	.03		.1668	.1291	.0914	.0619
	.1		.2564	.2107	.1679	.1297
$x_{N_2}=.8$	.3		.3667	.3206	.2715	.2189
$P=1.0$)	1.		.4971	.4510	.3837	.3249

CO_2, and 80 percent N_2. In the case of the single radiatively active species, the scaling applies to P_e in equation (23). The absorbing species partial pressure P_a is that of the H_2O or CO_2 gas in the mixtures. Note that in the case of the equimolar mixture, P_a is the partial pressure of one of the absorbing species, and not the sum of both.

Figure 1 shows a sample plot of total emissivity versus path-length-pressure product P_aL at a fixed gas temperature T_g. Shown are the calculated one atmosphere curve and a number of points calculated for elevated and reduced pressures. The calculations were made from band absorption correlations as explained in [18]. To find the values of m shown in the tables, the scale factor needed to be applied to L was observed from the horizontal distance on the log-log plot, and m was extracted from equation (30).

With the m-map and one atmosphere total emissivity for the gases, Table 5, it is possible to test equation (26–29) against calculations of total absorptivity. Table 6 shows the

Table 6 Comparison of table absorptivity scaling rules

Gas	Gas Temp T_g (K)	Wall Temp T_w (K)	*P*-Path Product P_aL (atm-m)	Scaling Exp. m'	Absorptivity α_{gw} (dimensionless)			
					Hottel Rule	Penner Rule	Present Rule	True Value
H_2O	2000	800	.01	.30	.034	.024	.033	.033
			.10	.72	.147	.115	.194	.195
$(r = 1.5)$* $(s = 1.6)$			1.00	.83	.403	.337	.527	.528
	800	2000	.01	.31	.015	.022	.015	.015
			.10	.59	.084	.108	.066	.060
			1.00	.72	.218	.247	.182	.171
CO_2	2000	800	.01	.03	.064	.053	.066	.057
			.10	.06	.139	.122	.145	.143
(-1.0) $(s = 2.4)$			1.00	.06	.248	.221	.253	.265
	800	2000	.01	0	.022	.026	.022	.022
			.10	0	.052	.060	.052	.053
			1.00	0	.098	.111	.098	.096
Mix	2000	800	.01	.31	.104	.081	.103	.091
			.10	.45	.288	.242	.310	.317
$r = 1.5)$ $(s = 1.6)$			1.00	.56	.625	.546	.696	.644
	800	2000	.01	.19	.035	.047	.039	.038
			.10	.46	.129	.153	.116	.108
			1.00	.60	.259	.285	.234	.238

*Values of *r* and *s* in parentheses are those recommended and used in the present rule.

Table 7 Comparison of total transfer factors for $\epsilon_w = 0.50$, $T_w = 800$ K, $P = 1$ atm, 10 percent H_2O, 10 percent CO_2, 80 percent N_2 gas mixture

T_g (K)	L (m)	Factor Type	Gray Approx. Eq. (5)	Rule of Thumb Eq. (31)	Transfer Factor Spectral Block Ref. (18)	Within-Band Approx. Eq. (17)	Exact Value Eq. (15)
2000	1	F_g	.1148	.0973	.0889	.0825	.0855
		F_{gw}	.2409	.2381	.2045	.1909	.1979
	2	F_g	.1562	.1388	.1221	.1098	.1142
		F_{gw}	.2980	.3185	.2627	.2434	.2495
1600	1	F_g	.1437	.1259	.1081	.1032	.1075
		F_{gw}	.2317	.2262	.1885	.1790	.1869
	2	F_g	.1874	.1730	.1450	.1351	.1396
		F_{gw}	.2840	.2975	.2461	.2290	.2350

comparison. Shown are calculations made according to Hottel's Rule, Penner's Rule, the two-step scaling rule, and the true value taken to be equation (19) calculated according to [18]. Particularly in the case of H_2O, the recommended two-step scaling is superior to the one-step scaling results.

Table 7 compares values of total transfer factor F_g and F_{gw} computed five ways. In the first of the five columns are values obtained from equation (5) with the transmissivity in the denominator taken to be one minus the total emissivity or absorptivity respectively. Next, out of curiosity, is Hottel's rule of thumb

$$F_g = \left(\frac{1+\epsilon_w}{2}\right)\epsilon_g, \; F_{gw} = \left(\frac{1+\epsilon_w}{2}\right)\alpha_{gw} \qquad (31)$$

Third are results obtained via the Bevans-Dunkle spectral block scheme with Edwards' block limit selection criteria. Fourth is the total property approximate relation, equations (16) and (17). Finally presented are the exact results according to equations (15*a*, *b*).

The gray gas formula gives results 34–37 percent too high for F_g and 21–24 percent too high for F_{gw}. The rule-of-thumb does better for F_g, 14–24 percent too high. The detailed spectral calculations agree with the exact values usually within 4 percent, and the worst case is 7 percent too high. The within-band transmissivity approximation proposed here runs three or four percent low and thus gives values comparable in accuracy to the spectral block method.

The appendix presents a sample calculation illustrating both the two-step scaling rule, equations (27–29) and (30 *a*, *b*) and the within-band transmissivity approximation, equations (16) and (17).

Summary

Scaling rules have been advanced which permit the application of one-atmosphere total-spectrum gas emissivity data to finding (*a*) gas emissivity for pressures other than one atmosphere, (*b*) gas absorptivity for wall temperature below or above the gas temperature, and for pressures other than one atmosphere, and (*c*) total gas-to-wall transfer factors when the wall surrounding the gas is gray-reflecting. Tables 2, 3, and 4 give the needed maps of pressure-scaling exponent *m* needed for (*a*) and (*b*) above. Exact equation (15*a*, *b*) can be used for item (*c*) above, or, with an error of any 4 percent, the within-band gas transmissivity can be estimated from equation (17*a*, *b*) for use in equation (16*a*, *b*). The maps in Tables 2–4 and the scaling rules are thus useful auxiliaries to total gas emissivity charts and fits.

References

1 Bueters, K. Q., Cogole, J. G., and Habelt, W. W., "Performance Prediction of Tangentially Fired Utility Furnaces by Computer Model," *Proceedings Fifteenth Symposium (Int'l.) on Combustion*, 1974, pp. 1245–1260.

2 Cess, R. D., and Lian, M. S., "A Simple Parameterization for Water Vapor Emissivity," ASME JOURNAL OF HEAT TRANSFER, Vol. 98, 1976, pp. 676–678.

3 Nakra, N. K., and Smith, T. F., "Combined Radiation-Convection for a Real Gas," ASME Journal of Heat Transfer, Vol. 99, 1977, pp. 60-65.

4 Abou-Ellail, M. M. M., Gosman, A. D., Lockwood, F. C., and Megahed, I. E. A., "Description and Validation of a Three-Dimensional Procedure for Combustion Chamber Flows," AIAA *J. Energy*, Vol. 2, 1978, pp. 71-80.

5 Grosshandler, W. L., and Modak, A. T., "Radiation from Nonhomogeneous Combustion Products," *Proceedings Eighteenth Symposium (Int'l.) on Combustion*, 1981, pp. 601-609.

6 Farag, I. H., and Allam, T. A., "Gray-Gas Approximation of Carbon Dioxide Standard Emisivity," ASME Journal of Heat Transfer, Vol. 103, 1981, pp. 403-405.

7 Tien, C. L., and Lee, S. C., "Flame Radiation," *Prog. Energy Combustion Sci.*, Vol. 8, 1982, pp. 41-59.

8 Smith, T. F., Shen, Z. F., and Friedman, J. N., "Evaluation of Coefficients for the Weighted Sum of Gray Gases Model," ASME Journal of Heat Transfer, Vol. 104, 1982, pp. 602-608.

9 Hottel, H. C., and Sarofim, A. F., *Radiative Transfer*, McGraw-Hill, 1967, pp. 221-223.

10 Penner, S. S., *Quantitative Molecular Spectroscopy and Gas Emissivities*, Addison-Wesley, 1959, pp. 359-369.

11 Edwards, D. K., *Radiation Heat Transfer Notes*, Hemisphere, 1981.

12 Oppenheim, A. K., "The Engineering Radiation Problem—An Example of the Interaction between Engineering and Mathematics," *Zeits, angew. Math. Mechanik*, Vol. 36, 1956, pp. 81-93.

13 Bevans, J. T., and Dunkle, R. V., "Radiant Interchange within an Enclosure," ASME Journal of Heat Transfer, Vol. 82, 1960, pp. 1-19.

14 Edwards, D. K., "On the Use of Total Radiation Properties of Gases," Argonne National Laboratory Reactor Analysis and Safety Division Report ANL/RAS 75-12, 1975.

15 Dunkle R. V., "Geometric Mean Beam Lengths for Radiant Heat Transfer Calculations," ASME Journal of Heat Transfer, Vol. 86, 1964, pp. 75-80.

16 Dunkle, R. V., "Thermal Radiation Tables and Applications," ASME *Transactions*, Vol. 76, 1954, pp. 549-552.

17 Czerny, M., and Walther A., *Tables of Fractional Functions for the Planck Distribution Law*, Springer, 1961.

18 Edwards, D. K., "Molecular Gas Radiation," *Advances in Heat Transfer*, Vol. 12, 1976, pp. 115-193.

19 Edwards, D. K., and Balakrishnan, A., "Thermal Radiation by Combustion Gases," *International Journal of Heat and Mass Transfer*, Vol. 16, 1973, pp. 25-40.

20 Modak, A. T., "Exponential Wide Band Parameters for the Pure Rotational Band of Water Vapor," *Journal of Quant. Spectr. Radiat. Transfer*, Vol. 21, 1979, pp. 131-142.

APPENDIX

Sample Calculation

Suppose that one wants to use total radiation properties to estimate the radiation heat transfer at an 800 K wall emissivity 0.55 from a mixture of 10 percent H_2O, 10 percent CO_2, and 80 percent N_2 and O_2 of six atmospheres total pressure and 1600 K within say a sphere 0.82 m in diameter. One begins by finding the geometric mean beam length, four times the volume divided by the surface area, and correcting it to the mean beam length by multiplying by 0.91 (See Table 6-1 of [11]). The result in $L = 0.5$ m.

Next one finds ϵ_{g1} and ϵ_{g2} needed for equation (17*a*). To find ϵ_{g1} the values of $P_aL = (0.1)(6)(.5) = 0.3$ and $P = 6$ are used to enter Table 4 to find $m = 0.225$. Then equation (30*a*) gives

$$P_aL_\epsilon{}' = (0.3)(6)^{.225} = 0.45 \text{ atm } m$$

Table 5 thereupon gives $\epsilon_{g1} = 0.331$. Similarly, $\epsilon_{g2} = 0.372$. Note that only one-step scaling was needed for these values. Equation (17*a*) yields $\tau_{gb} = 0.124$, and equation (16*a*) gives

$$F_g = \frac{(.55)(.331)}{1 - (.45)(.124)} = 0.193$$

Values of α_{gw1} and α_{gw2} are needed for equation (17*b*). Equations (27–29) with values of $r = 1.5$ and $s = 1.6$ from Table 6 indicate that $T_g{}' = 800$ K and

$$P_aL_\alpha{}' = 0.3(800/1600)^{1.5} = .106 \text{ atm } m$$

$$P' = 6(1600/800)^{1.6} = 18.2 \text{ atm}$$

Table 4 indicates $m' = 0.47$. Equation (30*b*) is the second step of the two-step scaling. It gives

$$P_aL'' = (0.106)(18.2)^{.47} = 0.415 \text{ atm } m$$

Table 5 thereupon gives $\epsilon_g{}'' = .378$ and equation (26) gives

$$\alpha_{gw1} = (1600/800)^{1/2}(.378) = 0.535$$

Similary $\alpha_{gw2} = 0.671$. Equation (17*b*) gives $\tau_{gwb} = 0.253$, and *equation (16b) gives*

$$F_{gw} = \frac{(.55)(.535)}{1 - (.45)(.253)} = 0.332$$

Finally, equation (14) indicates the net radiant heat flux into the wall to be

$$q = 0.193\,(5.67 \times 10^{-8})(1600)^4$$
$$- 0.332\,(5.67 \times 10^{-8})(800)^4$$
$$q = 71700 - 7700 = 64000 \text{ W/m}^2$$

M. H. N. Naraghi*
Research Associate.
Assoc. Mem. ASME

B. T. F. Chung
Professor.
Mem. ASME

Department of Mechanical Engineering,
The University of Akron,
Akron, Ohio 44325

A Stochastic Approach for Radiative Exchange in Enclosures With Nonparticipating Medium

A stochastic method is developed for calculating radiation interchange in enclosures with a finite number of isothermal surfaces but without a participating medium. Different types of surface properties are considered. They are diffuse and specular surfaces. In this work, a stochastic n *model is proposed that is based on the Markov chain theory and leads to some explicit matrix relationships for the absorption factor from which the heat transfer characteristics of the enclosure can be determined. The present approach provides an exact solution as long as the necessary view factors can be determined. The accuracy of approximate solutions can be improved as* n *increases.*

Introduction

In the calculation of radiant exchange between surfaces, it is commonly assumed that the surfaces obey Lambert's cosine law. However, in spacecraft technology and solar radiation applications, it has been recognized that radiant heat transfer between surfaces of a specular character is the more common situation. Consequently, a number of papers [1-12] have been published dealing with radiant transfer between surfaces with either fully specular idealization or with specular and diffused reflectance components. The methods of treating enclosures with specularly reflecting surfaces are based on the radiosity concept [1, 2, 10]. In these methods the exchange factor $E_{i,j}$, which is the fraction of energy emitted from surface i arriving at surface j by direct radiation and all possible specular irradiation through other surfaces, is employed. The calculation of specular view factors becomes a tedious task when the geometry of enclosure is complicated or when the number of consecutive specular reflections is large. The exact solution for these enclosures exists only for very simple geometries in which the specular view factors can be expressed by a general formula in terms of the reflection number.

Bevans and Edwards [4] introduced three approximate methods for calculating the radiant exchange within a multisurface enclosure made up of real surfaces. The first approximation does not include specular interreflections. The second method incorporates an approximation for specular reflection as well as the directional behavior of real materials. The third approximation, while more exact, involves two bounces of energy bundles in the energy balance equation. It is found that the third approximation provides a reasonable solution when the specular reflectivity of the participating surfaces are in the order of 0.5 or less.

The present work develops a new approach for calculating radiative exchange in enclosures. This approach, similar to the Monte Carlo method [13, 14], is based on the tracing of energy bundles. However, in the Monte Carlo method, the dispatch direction of the energy bundles is determined by the random numbers generated by a random number generator. The stochastic approach used in this work eliminates the use of a random number generator, but is based on the Markov chain theory. The destination of energy bundles in this method is determined by transition probabilities. Recently Fan and co-workers [15-17] have demonstrated that the Markov chain is a powerful tool for simulating chemical reactor systems. This approach will now be further extended for solving various thermal radiation problems. Consideration is given to radiation in enclosures with a finite number of isothermal surfaces and with the following surface properties: (*i*) All surfaces are reflecting and emitting diffusely. (*ii*) The participating surfaces emit diffusely but some reflect fully specularly and some fully diffusely. (*iii*) The reflectivity of the participating surfaces is in the form of $\rho = \rho^d + \rho^s$, and the surfaces emit diffusely.

The objective of this work is to determine the absorption factors matrix, **B** of the aforementioned enclosures using stochastic approach, where the absorption factor $B_{i,j}$ is defined as the fraction of the emission of surface i that is absorbed by surface j.

Once the absorption factor matrix is known, the radiant heat transfer from each surface can be easily calculated. Furthermore, other commonly used radiation variables, such as Hottel's total exchange area $\overline{S_iS_j}$ and Bobco's script F, $\mathcal{F}_{i,j}$, can be also obtained from the relationships: $\overline{S_iS_j} = \epsilon_i A_i B_{i,j}$ and $\mathcal{F}_{i,j} = \epsilon_i B_{i,j}$.

Preliminary Background

The stochastic process is a description of random phenomena that change with respect to time. A stochastic process may be thought of as a set of random variables x_t depending on a parameter $t \epsilon T$. Here the parameter set T may be interpreted as the time. For example, x_t can be the coordinate of the reflecting point on an enclosure surface from which the radiating energy bundle reflects. A stochastic process can be represented by short notation $X = \{x_t, t \epsilon T\}$. The random variable, x_t and the time parameter t can be either continuous or discrete.

For the problem under consideration, the time parameter is discrete and is in terms of reflection number. Since we are dealing with a number of isothermal surfaces in the enclosure, the random variable is also discrete and may be represented by the surface number. The stochastic processes used in this work are in the form of $X = \{x_n, n \epsilon N\}$ or $X = \{x_0, x_1, x_2 \ldots\}$ in which x_n's have numerical values equal to the surface numbers of the enclosure. If we let $i_1, i_2, i_3, \ldots$ be surface numbers that the energy bundle reflects consecutively, then the stochastic process $X = \{x_0 = i_0, x_1 = i_1, x_2 = i_2 \ldots\}$ represents a radiation process in which the radiating energy bundle is initially emitted from surface i_0 and then reflected from surfaces, $i_1, i_2, \ldots$ etc. The symbol $P\{x_0 = i_0, x_1 = i_1, x_2 = i_2, \ldots, x_n = i_n\}$ represents the probability that radiation initially emitted from surface i_0 and having reflected from surfaces $i_1, i_2, \ldots i_{n-1}$ has finally reached surface i_n.

---

*Presently Visiting Assistant Professor.

Contributed by the Heat Transfer Division for publication in the JOURNAL OF HEAT TRANSFER. Manuscript received by the Heat Transfer Division February 22, 1982.

In order to formulate the aforementioned stochastic process, the Markov chain theory is employed. A Markov chain is a stochastic process in which the following property holds

$$P\{x_n | x_0, x_1, x_2, \ldots x_{n-1}\} = P\{x_n | x_{n-1}\} \quad (1)$$

i.e., the probability of each succeeding event in the chain is not influenced by prior events. The radiation transport process in enclosures with only the diffuse surface reflection property form a Markov chain. This is because the future of radiation transport after diffuse reflection is independent of its past history. The probability $P\{x_n = j | x_{n-1} = i\} = P_{i,j}$ is called the transition probability. The transition probability for a k-state Markov chain can be shown as

$$\mathbf{P} = \begin{bmatrix} P_{1,1} & P_{1,2} & \ldots & P_{1,k} \\ P_{2,1} & P_{2,2} & \ldots & P_{2,k} \\ \cdot & \cdot & & \cdot \\ \cdot & \cdot & & \cdot \\ \cdot & \cdot & & \cdot \\ P_{k,1} & P_{k,2} & \ldots & P_{k,k} \end{bmatrix}$$

When the reflection is nondiffuse, i.e., specular or bidirectional, the future of the radiation transport process is no longer independent of its past history. The degree of dependence on the previous reflections of the radiation process depends on the maximum number of specular or bidirectional reflections. In the case of infinite number of specular or bidirectional reflections, the future of the radiation process can be approximated as being dependent on a finite number of past steps. For example, if the future of the process depends on its past l steps, then

$$P\{x_n | x_0, x_1, x_2, \ldots x_{n-1}\} = P\{x_n | x_{n-l}, \ldots, x_{n-2}, x_{n-1}\} \quad (2)$$

This process is called multiple or l-dependent Markov chains [18-19]. The ordinary Markov chain theory can be applied to multiple Markov chain if we define a new random variable as

$$y_n = (x_n, x_{n+1}, \ldots, x_{n+l-1}) \quad (3)$$

Then $Y = \{y_n; n \epsilon N\}$ is a stochastic process which holds the Markovian property, i.e.,

$$P\{y_n | y_0, y_1, y_2 \ldots y_{n-1}\} = P\{y_n | y_{n-1}\} \quad (4)$$

A Markov chain whose transition probability does not change with time, i.e.,

$$P\{x_2 | x_1\} = P\{x_3 | x_2\} = \ldots = P\{x_n | x_{n-1}\} \quad (5)$$

is called time-homogeneous Markov chain.

$$P_{i,j} = P\{x_{n+1} = j | x_n = i\} \quad (6)$$

is called single step transition probability. An m-step transition probability is defined by

$$P_{i,j}^{(m)} = P\{x_{n+m} = j | x_n = i\} \quad (7)$$

For a time-homogeneous Markov chain, we can state

$$[P_{i,j}^{(m)}] = \underbrace{\mathbf{PPP} \ldots \mathbf{P}}_{m \text{ times}} = \mathbf{P}^m \quad (8)$$

In the following analysis, the concept of a time-homogeneous Markov chain is used to calculate the probabilities that radiation was emitted from surface i of an enclosure and then absorbed by surface j in the same enclosure. These probabilities are equivalent to the absorption factor of [20, 21].

Analysis

(*i*) Enclosures With Fully Diffuse Surface Properties. Let the random variable x_n be the surface number that radiation (energy bundle) strikes on at the nth transition. For example, an enclosure consisting of five isothermal surfaces x_n can be 1, 2, 3, 4, or 5. As pointed out before, the diffuse radiation is a Markovian process, i.e., the future of the process only depends on its immediate previous step. The transition probability matrix (probability that radiation is transferred directly from one surface to another) is identical to the view factor matrix, $\mathbf{F} = [F_{i,j}]$, where i is the emitting and j the receiving surface. At each surface the radiation may be absorbed or reflected depending on the values of surface absorptivity and reflectivity. The absorptivities and reflectivities are represented by two diagonal matrices $\mathbf{A} = [\alpha_i \delta_{i,j}]$ and $\mathbf{R} = [\rho_i \delta_{i,j}]$, respectively, for a diffuse enclosure.

We define $\mathbf{B}^{(k)} = [B_{i,j}{}^{(k)}]$ where $B_{i,j}{}^{(k)}$ is the probability that radiation emitting from surface i is absorbed by surface j in exactly k transitions. Since the radiation process in this enclosure form a time-homogeneous Markov chain, using equation (8), we can write

$$\mathbf{B}^{(1)} = \mathbf{FA}, \mathbf{B}^{(2)} = \mathbf{FRFA}, \mathbf{B}^{(3)} = \mathbf{FRFRFA} = (\mathbf{FR})^2\mathbf{FA}, \ldots$$

$$\mathbf{B}^{(k)} = (\mathbf{FR})^{(k-1)}\mathbf{FA} \ldots \quad (9)$$

FR and **FA** stand for the probability that the radiative energy bundle emitting from one surface striking directly upon another surface is reflected and absorbed by the receiving surface, respectively. The absorption factor is a summation of all $\mathbf{B}^{(k)}$'s, i.e.,

$$\mathbf{B} = \sum_{k=1}^{\infty} \mathbf{B}^{(k)} = \mathbf{FA} + \mathbf{FRFA} + (\mathbf{FR})^2\mathbf{FA} + \ldots$$

$$= [\mathbf{I} + (\mathbf{FR}) + (\mathbf{FR})^2 + \ldots]\mathbf{FA}$$

or

$$\mathbf{B} = [\mathbf{I} - \mathbf{FR}]^{-1}\mathbf{FA} \quad (10)$$

This simple, explicit matrix relation gives the identical expression derived by Gebhart [20, 21], based on radiant energy balance in an enclosure.

Nomenclature

$\mathbf{A}$ = absorptivity matrix
A_i = area of surface i
$\mathbf{B}$ = absorption factor matrix
B_{ij} = absorption factor (fraction of energy that originally emits from surface i and finally is absorbed by surface j by direct emission or multireflections)
$\mathbf{C}$ = matrix defined by equation (23)
$E_{i,j}$ = exchange factor between surfaces i and j
$\mathbf{F}$ = view factor matrix
$F_{i,j}$ = view factor from surface i to j
$\mathbf{I}$ = identity matrix
P = probability
$\mathbf{P}$ = transition probability matrix
$\mathbf{R}$ = reflectivity matrix
T = temperature
$\dot{q}$ = average heat flux
q = entries of matrix $\mathbf{Q}$ defined by equations (20) and (31)
$\mathbf{Q}$ = matrix defined by equation (21)
x = random variable
X = stochastic process
y = random variable vector
Y = stochastic process

Greek Symbols

α = absorptivity
δ = Kronecker delta $\delta(i_1, i_2 \ldots, i_l), (j_1, j_2 \ldots, j_l) = 1$ if $(i_1, i_2 \ldots, i_l) = (j_1, j_2 \ldots, j_l)$ otherwise $\delta(i_1, i_2 \ldots, i_l), (j_1, j_2 \ldots, j_l) = 0$
ϵ = emissivity
ρ = reflectivity
σ = Stefan-Boltzmann constant

Superscripts

d = diffuse
s = specular

(*ii*) Enclosures with Specular and Diffuse Reflecting Surfaces. Consideration is now given to an enclosure consisting of a finite number of both specularly and diffusely reflecting surfaces. These surfaces can all be specularly reflecting, or a number of them specular and the rest diffuse. The emissivity of all participating surfaces are assumed to be diffuse.

As pointed out before, the destination of the radiating energy bundle after specular reflection is no longer independent of its past history. Consider the stochastic process $X = \{x_n, n \epsilon N\}$, which represents the radiation process in the enclosure. Assume that the random variable x_{n+1} depends on the random variables x_n, x_{n-1}, and x_{n-2}. Then the stochastic process $Y = \{y_n, n \epsilon N\}$ where $y_n = (x_n, x_{n+1}, x_{n+2})$ forms a Markov chain, i.e., the multiple Markov chain $X = \{x_0, x_1, x_2 \ldots\}$ is transformed to the ordinary Markov chain

$$Y = \{(x_0,x_1,x_2),(x_1,x_2,x_3),(x_2,x_3,x_4),\ldots\} = \{y_0,y_1,y_2\ldots\} \tag{11}$$

Because this Markov chain is time-homogeneous, we can write [18, 19]

$$\begin{aligned} P\{(x_1,x_2,x_3) \mid (x_0,x_1,x_2)\} &= P\{(x_2,x_3,x_4) \mid (x_1,x_2,x_3)\} \\ &= P\{(x_3,x_4,x_5) \mid (x_2,x_3,x_4)\} \\ &= \ldots = P_{(i_1,i_2,i_3),(j_1,j_2,j_3)} \end{aligned} \tag{12}$$

It should be noted that the value of the first random variable x_1 depends on the intitial random variable x_0, and x_2 depends on x_0 and x_1. Only after the second transition is there enough past history to apply the ordinary Markov chain concept to the stochastic process represented by equation (11).

The arrangement of the specular and diffuse surfaces in the enclosure might be in such a way that the destination of the energy bundle after specular reflections at most be influenced by the immediate previous l reflections, i.e., the maximum number of consecutive specular reflections is $l-1$. If the locations of the specular surfaces in the enclosure are such that an infinite number of consecutive reflection occurs, then, the process can be approximated by the one in which the destination of the radiating energy bundle after reflection is a function of an l-past reflection. Therefore, assuming $y_n = (x_n, x_{n+1}, \ldots, x_{n+l-1})$ the multiple Markov chain X can be transformed to the regular Markov chain Y. The transition probability matrix for this case can be represented by

$$\mathbf{P} = [P_{(i_1,i_2,\ldots,i_l),(j_1,j_2,\ldots,j_l)}] \tag{13}$$

The transition from $(i_1, i_2, \ldots, i_l)$ to $(j_1, j_2, \ldots, j_l)$ is possible only if

$$i_2 = j_1, i_3 = j_2, \ldots, i_l = j_{l-1}$$

or in general $i_k = j_{k-1}$ for $2 \leq k \leq l$. This can be realized from two consecutive random variables $y_n = (x_n, x_{n+1}, \ldots, x_{n+l-1})$ and $y_{n+1} = (x_{n+1}, x_{n+2}, \ldots, x_{n+l-1}, x_{n+l})$. At the first $l-1$ transitions of stochastic process X, there are less than l past random variables; therefore, we need to let the process go on for $l-1$ transitions in order to be able to form the initial vector $y_0 = (x_0, x_1, x_2, \ldots x_{l-1})$. The concept of the multiple Markov chain can be applied after the $(l-1)th$ transition has occurred, i.e., when the initial vector of stochastic process Y can be formed. Other techniques are necessary to calculate the energy absorbed by surfaces of the enclosure at first, second, $\ldots$, and $(l-1)th$ transitions. Based on the above argument, the absorption factor can be formulated by

$$\mathbf{B} = \mathbf{B}^{(1)} + \mathbf{B}^{(2)} + \ldots + \mathbf{B}^{(l-1)} + \mathbf{B}^{(l+)} \tag{14}$$

where $\mathbf{B}^{(k)} = [B_{i,j}{}^{(k)}]$ $(k < l)$, and $B_{i,j}{}^{(k)}$ is the probability that radiation initially emitted from surface i is absorbed by surface j in exactly k steps. The multiple Markov chain is only used to calculate the last term, i.e., $B^{(l+)}$ in equation (14). $B_{i,j}{}^{(l+)}$ is defined as the probability that radiative energy bundle initially emitted from surface i is absorbed by surface j at the lth or later transitions.

For $k < l$, we can write

$$B_{i,j}^{(k)} = \sum_{i_1,i_2\ldots i_{k-1}} \rho_{i_1}\rho_{i_2}\ldots\rho_{i_{k-1}} P\{x_0 = i, x_1 = i_1, x_2 = i_2 \ldots x_{k-1} = i_{k-1}, x_k = j\}\alpha_j \tag{15}$$

The term $P\{x_0 = i, x_1 = i_1, x_2 = i_2, \ldots, x_{k-1} = i_{k-1}, x_k = j\}$ represents the probability that radiation initially emitted from surface i, reflected from surfaces $i_1, i_2, \ldots i_{k-1}$, and finally striking on surface j. This term is identical to the specular radiation view factor $F_{i(i_1,i_2,\ldots,i_{k-1}),j}$, if surfaces $i_1, i_2, \ldots, i_{k-1}$ reflect specularly. If one of the foregoing surfaces, e.g., i_m $(m \leq k-1)$ reflects diffusely then the above probability can be decomposed into $P\{x_0 = i, x_1 = i_1, \ldots, x_m = i_m\}$ $P\{x_m = i_m, \ldots, x_{k-1} = i_{k-1}, x_k = j\}$. This can be done because the random variables after x_m are independent of the ones before it. In other words, the diffuse property of i_m makes $\{x_0 = i, x_1 = i_1, \ldots, x_m = i_m\}$ and $\{x_m = i_m, \ldots, x_{k-1} = i_{k-1}, x_k = j\}$ independent of each other. Under this situation we can write

$$P\{x_0 = i, x_1 = i_1, \ldots, x_{k-1} = i_{k-1}, x_k = j\} = F_{i(i_1,i_2,\ldots i_{m-1}),i_m} F_{i_m(i_{m+1}\ldots,i_{k-1}),j} \tag{16}$$

If more than one intermediate diffuse surfaces exist, the foregoing probability would have to be broken into the product of more than two probabilities of random variable sequences. If all of the intermediate surfaces are diffuse, then we have

$$P\{x_0 = i, x_1 = i_1, \ldots, x_{k-1} = i_{k-1}, x_k = j\} = F_{i,i_1} F_{i_1,i_2} F_{i_2,i_3} \ldots F_{i_{k-2},i_{k-1}} F_{i_{k-1},j} \tag{17}$$

The idea of multiple Markov chain is used to calculate $\mathbf{B}^{(l+)}$. It has been shown [18, 19] that the multiple Markov chain $X = \{x_0, x_1, x_2 \ldots\}$ can be reduced to the regular Markov chain $Y = \{y_0, y_1, y_2 \ldots\}$ by letting $y_n = (x_n, x_{n+1}, \ldots x_{n+l-1})$. We now calculate the probability that the radiative energy bundle is absorbed in the first, second, third $\ldots$ transitions of stochastic process Y. The matrix of these probabilities $\mathbf{C}$ should have the same dimension as the transition probability matrix given by equation (13), i.e.,

$$\mathbf{C} = [C_{(i_1,i_2,\ldots,i_l),(j_1,j_2,\ldots,j_l)}]$$

Similarly, matrices of absorptivities and reflectivities should have the same dimension, and the numerical values of each entry corresponding to the absorptivity and reflectivity of surface j_l (last surface in the transition probability matrix) are

$$\mathbf{A} = [\alpha_{j_l} \delta_{(i_1,i_2,\ldots,i_l),(j_1,j_2,\ldots,j_l)}] \tag{18}$$

and

$$\mathbf{R} = [\rho_{j_l} \delta_{(i_1,i_2,\ldots,i_l),(j_1,j_2,\ldots,j_l)}] \tag{19}$$

respectively.

The term

$$q_{(i_1,i_2,\ldots,i_l)} = \rho_{i_2}\rho_{i_3}\ldots\rho_{i_l} P\{x_0 = i_1, x_1 = i_2, \ldots x_{l-1} = i_l\} \tag{20}$$

is the probability that the radiative energy bundle is not absorbed by states $x_1 = i_2, x_2 = i_3, \ldots, x_{l-1} = i_l$, i.e., the entries of vector $y_0 = (x_0, x_1, x_2, \ldots, x_{l-1})$. Equation (20) also represents the probability that the initial state of stochastic process Y is formed. We define an associated diagonal matrix $\mathbf{Q}$ as

$$\mathbf{Q} = [q_{(i_1,i_2,\ldots,i_l)} \delta_{(i_1,i_2,\ldots,i_l),(j_1,j_2,\ldots,j_l)}] \tag{21}$$

As mentioned earlier, $Y = \{y_0, y_1, y_2 \ldots\}$ forms a time-homogeneous Markov chain; therefore, based on equation (8), the following infinite series can be formed

$$\mathbf{C}=\mathbf{Q}[\mathbf{PA}+\mathbf{PRPA}+\mathbf{PRPRPA}+\ldots] \tag{22}$$

or

$$\mathbf{C}=\mathbf{Q}[\mathbf{I}-\mathbf{PR}]^{-1}\mathbf{PA} \tag{23}$$

The interpretation of each term in equation (22) is as follows: **Q** is the probability that the initial state of stochastic processes Y is formed; the terms **QPA**, **QPRPA**, **QPRPRPA**, . . . , represent the probabilities that the radiative energy bundle is absorbed at the first, second, third, . . . transitions of stochastic process Y, respectively. The first transition of stochastic process Y is equivalent to the lth transition of stochastic process X. This is because the transition from y_0 to y_1 is equivalent to the transition from the last entry of $(x_0, x_1, \ldots, x_{l-1})$ to the last entry of $(x_1, x_2, \ldots x_l)$, i.e., transition from x_{l-1} to x_l; but the transition from x_{l-1} to x_l is the lth transition of stochastic process X. Similarly, it can be shown that the second transition of stochastic process Y is equivalent to the $(l+1)$th transition of stochastic process X and so on. Matrix **C** gives the probabilities that the radiative energy bundle is absorbed by the states of stochastic process Y; therefore, we need to transform matrix **C** into the original stochastic process X. This can be realized from the following relationship

$$B_{i,j}^{(l+)}=\sum_{\substack{\text{all } i_2, i_3, \ldots, i_l\\ j_1, j_2, \ldots j_{l-1}}} C_{(i,i_2,i_3,\ldots i_l),(j_1,j_2,\ldots,j_{l-1},j)} \tag{24}$$

which gives entries of the last matrix in equation (14), i.e., $\mathbf{B}^{(l+)}$.

The elements of the transition probability matrix given by equation (13) are set equal to zero if either of the following inequalities is true: $i_2 \neq j_1$, $i_3 \neq j_2$, . . . $i_l \neq j_{l-1}$; otherwise, they form a conditional probability and we can write

$$P_{(i_1,i_2,i_3,\ldots,i_l),(i_2,i_3,\ldots,i_l,j_l)}= P\{x_{l+1}=j_l \mid x_1=i_1, x_2=i_2, \ldots, x_l=i_l\} \tag{25}$$

Mathematically, the conditional probability is defined by [18, 19]

$$P\{x_2=b \mid x_1=a\}=P\{x_2=b, x_1=a\}/P\{x_1=a\} \tag{26}$$

Applying this relation, we can rewrite equation (26) in terms of

$$P\{x_{l+1}=j_l \mid x_1=i_1, x_2=i_2, \ldots, x_l=i_l\} = \frac{P\{x_1=i_1, x_2=i_2, \ldots, x_l=i_l, x_{l+1}=j_l\}}{P\{x_1=i_1, x_2=i_2, \ldots, x_l=i_l\}} \tag{27}$$

or

$$P_{(i_1,i_2,\ldots,i_l),(i_2,i_3,\ldots,j_l)} = \frac{P\{x_1=i_1, x_2=i_2, \ldots, x_l=i_l, x_{l+1}=j_l\}}{P\{x_1=i_1, x_2=i_2, \ldots, x_l=i_l\}} \tag{28}$$

It would be unwise to use the multiple Markov chain to solve enclosures with all surfaces being diffuse; however, for comparison purposes the absorption factors of a diffuse enclosure by both regular and multiple Markov chains were computed. It was found [22] that the final results based on both methods are identical.

To demonstrate the application of the Markov chain, we consider the radiant exchange betweeen two infinite parallel plates shown in Fig. 1. The plates reflect specularly but emit diffusely. The two plates have identical thermophysical properties and are maintained at the same uniform temperature, i.e., $T_1 = T_2 = T$. Due to the symmetry of the system, the unknown heat fluxes must satisfy $\dot{q}_1 = \dot{q}_2 = \dot{q}$. This example has been considered in [1] and [4]. Table 1 compares the calculated $\dot{q}/\sigma T^4 L$ obtained by various approaches for this problem.

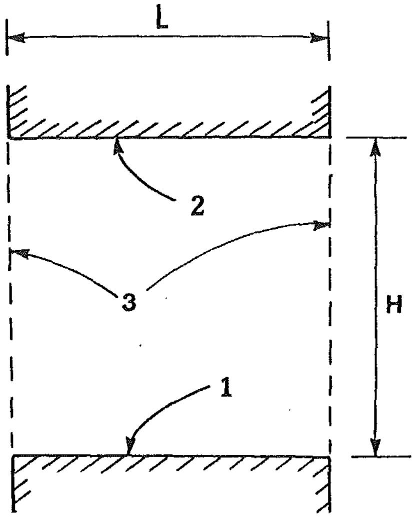

Fig. 1

The numerical values of specular exact, diffuse-reflection approximate solutions II and III are reproduced from [4]. The exact solution was obtained by Eckert and Sparrow [1] from an infinite series. The diffuse reflection solution is given in [23]. As can be seen, the present method in its simplest form, stochastic 2 model, yields results with the same accuracy as the best method in [4]. The strength of the present "stochastic n" model is that the solution can always be improved by using a higher order of n. However, when the specular reflectivity of all surfaces approach unity, the solution converges very slowly. As n approaches infinity, the destination of the energy bundle is influenced by all previous reflections of the energy bundle; therefore, the model yields the exact solution for a specular enclosure. Details of computation procedures for the numerical results of Table 1 are presented in [22].

Additional application of the stochastic approach for determining radiant exchange in a triangular enclosure is presented in Appendix A. In this example, the three surfaces are assumed to have different properties and be at different temperatures. Four different surface conditions are considered. The predicated heat fluxes agree well with that using the method of [10]. It is further shown in this appendix that the stochastic 2 model is quite adequate for the problem under consideration.

Case IV of Appendix A deals with radiant loss in an enclosure with all three surfaces reflecting specularly, a problem for which the solution has not been previously attempted. Theoretically, the destination of the radiative energy bundle, after each specular reflection depends on all the previous reflections, however, as shown in this case, the assumption of dependence on two previous reflections yields a reasonable approximation. The major difficulty in radiative calculations of specular enclosure is to take into account all possible specular reflections. It was pointed out in [24] that omitting the triple specular reflection terms in the exchange factor $E_{1,1}$ causes an error in heat flux even larger than that using the diffuse reflection assumption, when the method of [10] is used. The calculation procedures for the existing methods become even more involved when the number of consecutive specular reflections is very large or when the geometry of the enclosure is complicated. Therefore, a scheme which only includes a small number of consecutive specular reflections would be very desirable from an engineering design point of

Table 1 Comparisons of predicted radiant heat flux, $\dot{q}/\sigma T^4 L$ for various methods

		$\epsilon = 0.1$		$\epsilon = 0.5$		$\epsilon = 0.9$	
H/L	Method	$\dot{q}/\sigma T^4 L$	error,%	$\dot{q}/\sigma T^4 L$	error,%	$\dot{q}/\sigma T^4 L$	error,%
1.0	Specular-exact [1]	0.08826	0.0	0.3503	0.0	0.5439	0.00
	Diffuse reflection [23]	0.09340	5.8	0.3694	5.5	0.5500	1.10
	Approx II [4]	0.09225	4.5	0.3586	2.4	0.5445	0.10
	Approx III [4]	0.09150	3.7	0.3552	1.4	0.5442	0.05
	Stochastic 2[a]	0.09150	3.7	0.3552	1.4	0.5442	0.05
	Stochastic 3	0.09029	2.3	0.3515	0.3	0.5439	0.00
	Stochastic 4	0.08959	1.5	0.3506	0.1	0.5439	0.00
	Stochastic 5	0.08917	1.0	0.3504	0.0	0.5439	0.00
	Stochastic 6	0.08890	0.7	0.3503	0.0	0.5439	0.00
0.5	Specular-exact [1]	0.07948	0.0	0.2622	0.0	0.3632	0.00
	Diffuse reflection [23]	0.08607	8.3	0.2764	5.4	0.3664	0.80
	Approx II [4]	0.08509	7.1	0.2699	2.9	0.3636	0.10
	Approx III [4]	0.08443	6.2	0.2676	2.1	0.3634	0.05
	Stochastic 2	0.08443	6.2	0.2676	2.1	0.3634	0.05
	Stochastic 3	0.08292	4.3	0.2639	0.6	0.3632	0.00
	Stochastic 4	0.08187	3.0	0.2627	0.2	0.3632	0.00
	Stochastic 5	0.08116	2.1	0.2623	0.0	0.3632	0.00
	Stochastic 6	0.08069	1.5	0.2622	0.0	0.3632	0.00
0.1	Specular-exact [1]	0.04735	0.0	0.08575	0.0	0.09393	0.00
	Diffuse reflection [23]	0.05122	8.2	0.08677	1.2	0.09402	0.10
	Approx II [4]	0.05110	7.9	0.08654	0.9	0.09395	0.02
	Approx III [4]	0.05101	7.7	0.08643	0.8	0.09394	0.00
	Stochastic 2	0.05101	7.7	0.08643	0.8	0.09394	0.00
	Stochastic 3	0.05067	7.0	0.08614	0.5	0.09394	0.00
	Stochastic 4	0.05028	6.2	0.08596	0.2	0.09394	0.00
	Stochastic 5	0.04988	5.3	0.08585	0.1	0.09394	0.00
	Stochastic 6	0.04950	4.5	0.08580	0.06	0.09394	0.00

[a] "Stochastic n" designates a stochastic method in which the future of the radiation process depends on n previous reflections. It will be referred to a "stochastic n model" for convenience.

view. As is shown in Appendix A, the present stochastic technique yields a reasonable approximate solution even when only one specular reflection is considered. The calculation steps involved in the stochastic 2 model are straightforward. They are listed as follows for the convenience of thermal designers.

- Step 1. Compute $\mathbf{B}^{(1)}$. The elements of which are obtained from

$$\mathbf{B}^{(1)}_{i,j} = F_{i,j}\alpha_j$$

- Step 2. Find all possible combinations of (i_1, i_2) for which i_1 can "see" i_2 where i_1 and i_2 are surface numbers in the enclosure.
- Step 3. Set up the Matrix **P**. The elements of **P** are given by

$$\begin{aligned} P_{(i_1,i_2),(i_1,j_2)} &= 0 \text{ if } i_2 \neq j_1, \\ P_{(i_1,i_2),(j_2,j_2)} &= F_{i_1(i_2),j_2}/F_{i_1,i_2} \\ &\qquad \text{if } i_2 \text{ is specular} \qquad (29) \\ P_{(i_1,i_2),(i_2,j_2)} &= F_{i_2,j_2} \\ &\qquad \text{if } i_2 \text{ is diffuse} \end{aligned}$$

- Step 4. Compute the matrix **C** according to

$$\mathbf{C} = [C_{(i_1,i_2),(j_1,j_2)}] = \mathbf{Q}[\mathbf{I} - \mathbf{PR}]^{-1}\mathbf{PA}$$

where

$$\mathbf{Q} = [(\rho_{i_2} F_{i_1,i_2})\delta_{(i_1,i_2),(j_1,j_2)}]$$

$$\mathbf{R} = [\rho_{j_2}\delta_{(i_1,i_2),(j_1,j_2)}]$$

$$\mathbf{A} = [\alpha_{j_2}\delta_{(i_1,i_2),(j_1,j_2)}]$$

and

$$\mathbf{I} = [\delta_{(i_1,i_2),(j_1,j_2)}]$$

- Step 5. Determine $\mathbf{B}^{(2+)}$ with its elements being

$$\mathbf{B}^{(2+)}_{i,j} = \sum_{\substack{\text{all possible} \\ i_2 \text{ and } j_1}} C_{(i,i_2),(j_1,j)}$$

- Step 6. Calculate the absorption factor matrix, **B**

$$\mathbf{B} = \mathbf{B}^{(1)} + \mathbf{B}^{(2+)}$$

Note that the only specular view factor employed in the foregoing calculation steps is $F_{i_1(i_2),j_2}$ which involves one specular reflection only. Calculation steps for stochastic 3 and 4 models are omitted here to conserve space; interested readers may refer to [22]. The same computation steps can be used for the enclosure with the reflection property in terms of the sum of diffuse and specular components.

(*iii*) Enclosures With Surface Reflection Property in Terms of $\rho = \rho^d + \rho^s$. The dependence of the radiation process on its past history in an enclosure with a finite number of isothermal surfaces and with $\rho = \rho^d + \rho^s$ is determined by the maximum number of specular reflections involved. The calculation procedures for this type of enclosure are the same as the previous case. The only difference lies in the expressions for $\mathbf{B}^{(k)}$, **Q**, and **P**, which are represented by equations (15), (20), and (28), respectively.

The reflection at each surface in the enclosure under consideration is either specular or diffuse; therefore, radiation that originally emitted from surface i_1 can reach surface j_l in 2^{l-1} different possible combinations of specular and diffuse reflections.

For convenience, we let i_n^d and i_n^s represent diffuse and specular reflection from surface i_n, respectively. Therefore, the random variable x_n may have two different values, either i_n^d or i_n^s. For example, $\{x_1 = i_1, x_2 = i_2^d, x_3 = i_3^d, x_4 = i_4^s, \ldots, x_l = i_l^d\}$ represents diffuse reflection from i_2 and i_3, consecutively, then specular reflection from $i_4, \ldots$, and finally diffuse reflection from the surface i_l. Taking into account all possible ways, then $B_{i,j}^{(k)}$ would be

$$B_{i,j}^{(k)} = \sum_{n_1,n_2,\ldots n_{k-1}} \sum_{i_1,i_2,\ldots i_{k-1}} \rho_{i_1}^{n_1}\rho_{i_2}^{n_2}\cdots\rho_{i_{k-1}}^{n_{k-1}} P\{x_0 = i, x_1 = i_1^{n_1}, x_2 = i_2^{n_2}, \ldots, x_{k-1} = i_{k-1}^{n_{k-1}}, x_k = j\}\alpha_j \qquad (30)$$

Where the superscripts $n_1, n_2, \ldots n_{k-1}$ denote either s or d. The entries of matrix **Q** can be represented by

$$q_{(i_1,i_2,\ldots,i_l)} = \sum_{n_2,n_3,\ldots n_{l-1}} \rho_{i_2}^{n_2}\rho_{i_3}^{n_3} \ldots \rho_{i_{l-1}}^{n_{l-1}}\rho_{i_l}$$

$$P\{x_1=i_1, x_2=i_2^{n_2}, x_3=i_3^{n_3}, \ldots, x_{l-1}=i_{l-1}^{n_{l-1}}, x_l=i_l\} \tag{31}$$

The transition probability is

$$P_{(i_1,i_2,\ldots,i_l),(i_2,\ldots,i_l,j_l)} =$$

$$\sum_{n_2,n_3,\ldots n_l} \frac{\rho_{i_2}^{n_2}\rho_{i_3}^{n_3}\rho_{i_4}^{n_4}}{\rho_{i_2}\rho_{i_3}\rho_{i_4}} \ldots \frac{\rho_{i_{l-1}}^{n_{l-1}}}{\rho_{i_{l-1}}}\frac{\rho_{i_l}^{n_l}}{\rho_{i_l}} \cdot \frac{P\{x_1=i_1, x_2=i_2^{n_2}, \ldots, x_l=i_l^{n_l}, x_{l+1}=j_l\}}{P\{x_1=i_1, x_2=i_2^{n_2}, \ldots, x_{l-1}=i_{l-1}^{n_{l-1}}, x_l=i_l\}} \tag{32}$$

The calculation procedure for the probabilities in the right-hand side of equations (30-32) are the same as the procedure explained in the previous section, and these probabilities can be written in terms of appropriate view factors.

The right-hand side of equation (32) is the summation of probabilities that radiation reaches surface j_k by all combinations of specular and diffuse reflections. The terms ρ^d/ρ and ρ^s/ρ are fractions of specularly and diffusely reflected energy of the total energy reflected.

Appendix B further illustrates the application of the previous formulation to an enclosure consisting of three surfaces which are reflecting diffusely, specularly, and with a surface reflectivity $\rho = \rho^d + \rho^s$. The exact solution, which has not been previously available, is obtained using the stochastic 4 model. However, as is shown in this appendix, the use of the stochastic 2 model also yields a reasonable approximation. The computation steps for the stochastic 2 model listed at the end of the previous section can also be applied here. The only modification is the formulation of $P_{(i_1,i_2),(i_2,j_2)}$ in Step 3. For the present case, it should read

$$P_{(i_1,i_2),(i_2,j_2)} = \frac{\rho_{i_2}^d}{\rho_{i_2}} F_{i_2,j_2} + \frac{\rho_{i_2}^s}{\rho_{i_2}} \frac{F_{i_1(i_2),j_2}}{F_{i_1,i_2}} \tag{33}$$

Conclusion

A stochastic method is developed for formulating the absorption factors of enclosures with diffuse and specular surface properties. The results obtained based on this method, agree with that of [4] and also agree reasonably well with those using methods of [10]. Numerical computations reveal that for a specular reflectivity less than 0.5, the use of stochastic 2 model leads to satisfactory results. For enclosures with highly specular reflective surfaces, a higher-order model may become necessary. Calculation of specular view factors for enclosures with an infinite or large number of specular reflections can be extremely laborious. The solution exists only for simple geometries in which the specular view factors change according to a known pattern [1, 2]. It is noteworthy that the present approach provides a reliable solution by taking into account a finite number of specular reflections; furthermore, the absorption factors obtained from the present scheme automatically satisfy the following relations

$$\sum_{j=1}^{n} B_{i,j} = 1 \quad \text{and} \quad A_i\epsilon_i B_{i,j} = A_j\epsilon_j B_{j,i}$$

It should be pointed out that these two relations are not employed in the formulation of the absorption factor in this work. Hence they can serve as good checks for our numerical results. This method provides exact solutions as long as the necessary specular view factors can be calculated. Furthermore, it gives reasonable approximate solutions when the view factors for direct radiation and several specular reflections are known. The accuracy of the calculations can be improved by choosing a higher-order stochastic n model. Therefore, the proposed stochastic approach provides a useful tool for determining radiative exchange in enclosures involving specular surfaces. However, the method has the same shortcomings as the conventional method with regard to dealing with blocked or partial views between surfaces.

Acknowledgment

The authors gratefully acknowledge the helpful discussion with Dr. D. P. Story of the Mathematics and Statistics Department, The University of Akron. This work is partially supported by NSF under grant MEA 8314478.

References

1 Eckert, E. R. G., and Sparrow, E. M., "Radiative Heat Exchange Between Surfaces with Specular Reflection," *International Journal of Heat and Mass Transfer*, Vol. 3, No. 1, 1961, pp. 42-54.

2 Sparrow, E. M., Eckert, E. R. G., and Jonsson, V. K., "An Enclosure Theory for Radiative Exchange Between Specularly and Diffusely Reflecting Surfaces," ASME JOURNAL OF HEAT TRANSFER, Vol. 84, No. 4, 1962, pp. 294-300.

3 Bobco, R. P., "Radiative Heat Transfer in Semigray Enclosures With Specularly and Diffusely Reflecting Surfaces," ASME JOURNAL OF HEAT TRANSFER, Vol. 86, No. 1, 1964, pp. 123-130.

4 Bevans, J. T., and Edwards, D. K., "Radiation Exchange in an Enclosure With Directional Wall Properties," ASME JOURNAL OF HEAT TRANSFER, Vol. 87, No. 3, 1965, pp. 388-396.

5 Sparrow, E. M., and Lin, S. L., "Radiation Heat Transfer at a Surface Having Both Specular and Diffuse Reflectance Components," *International Journal of Heat and Mass Transfer*, Vol. 8, No. 5, 1965, pp. 769-779.

6 Sarofim, A. F., and Hottel, H. C., "Radiative Exchange Among Non-Lambert Surfaces," ASME JOURNAL OF HEAT TRANSFER, Vol. 88, No. 1, 1966, pp. 37-44.

7 Schornhorst, J. R., and Viskanta, R., "An Experimental Examination of the Validity of the Commonly Used Methods of Radiant Heat Transfer Analysis," ASME JOURNAL OF HEAT TRANSFER, Vol. 90, No. 4, 1968, pp. 429-436.

8 Hering, R. G., and Smith, T. F., "Surface Roughness Effects on Radiant Transfer Between Surfaces," *International Journal of Heat and Mass Transfer*, Vol. 13, No. 4, 1970, pp. 725-739.

9 Bobco, R. P., "A Script-F Matrix Formulation for Enclosures with Arbitrary Surface Emission and Reflection Characteristics," ASME JOURNAL OF HEAT TRANSFER, Vol. 93, No. 1, 1971, pp. 33-40.

10 Sparrow, E. M., and Cess, R. D., *Radiation Heat Transfer*, augmented ed., Hemisphere Publishing, 1978.

11 Rabl, A., "Radiation Transfer Through Specular Passages—A Simple Approximation," *International Journal of Heat and Mass Transfer*, Vol. 20, No. 4, 1977, pp. 323-330.

12 Mahan, J. R., Kingsolver, J. B., and Mears, D. T., "Analysis of Diffuse Specular Axisymmetric Surfaces with Application to Parabolic Reflectors," ASME JOURNAL OF HEAT TRANSFER, Vol. 101, No. 4, 1979, pp. 689-694.

13 Siegel, R., and Howell, J. R., *Thermal Radiation Heat Transfer*, 2d ed., McGraw-Hill, 1980.

14 Howell, J. R., and Perlmutter, M., "Monte Carlo Solution of Thermal Transfer Through Radiant Media Between Gray Walls," ASME JOURNAL OF HEAT TRANSFER, Vol. 86, No. 1, 1964, pp. 116-122.

15 Fan, L. T., and Shin, S. H., "Stochastic Diffusion Model of Non Ideal Mixing in a Horizontal Drum Mixer," *Chemical Engineering Science*, Vol. 34, No. 6, 1979, pp. 811-820.

16 Nassar, R., Fan, L. T., and Too, J. R., "A Stochastic Treatment of Unimolecular Reactions in an Unsteady State Continuous Flow System," *Chemical Engineering Science*, Vol. 36, No. 8, 1981, pp. 1307-1317.

17 Too, J. R., Fan, L. T., Rubison, R. M., and Lai, F. S., "Applications of Nonparametric Statistics to Multicomponent Solid Mixing," *Powder Technology*, Vol. 26, No. 2, 1980, pp. 131-146.

18 Doob, J. L., *Stochastic Processes*, John Wiley & Sons, 1953.

19 Cinlar, E., *Introduction to Stochastic Processes*, Prentice-Hall, 1975.

20 Gebhart, B., *Heat Transfer*, 2d ed., McGraw-Hill, New York, 1971, pp. 150-163.

21 Gebhart, B., "Unified Treatment for Thermal Radiation Transfer Processes—Gray, Diffuse Radiators and Absorbers," ASME Paper No. 57-A-34, Dec. 1957.

22 Naraghi, M. H. N., "A Stochastic Approach for Radiative Exchange in Enclosures," Ph.D. dissertation, Department of Mechanical Engineering, The University of Akron, 1984.

23 Sparrow, E. M., Gregg, J. L., Szel, J. V., and Manos, P., "Analysis, Results, and Interpretation for Radiation Between Some Simply Arranged Gray Surfaces," ASME JOURNAL OF HEAT TRANSFER, Vol. 83, No. 2, 1961, pp. 207-214.

24 Naraghi, M. H. N., and Chung, B. T. F., "A Stochastic Approach for Radiation Exchange in Enclosures with Non-participating Medium" ASME Paper 83-HT-52, presented at 21st National Heat Transfer Conference, Seattle, Wash., July 1983.

APPENDIX A

Consideration is given to an infinitie triangular enclosure. The temperature and the emissivity of each surface are specified in Fig. 2. Four different surface conditions are considered.

Case I.

All surfaces reflect diffusely. Application of equation (10) yields

$$\mathbf{B}=\begin{bmatrix} 0.49446 & 0.11973 & 0.38581 \\ 0.59867 & 0.06874 & 0.33259 \\ 0.64302 & 0.11086 & 0.24612 \end{bmatrix} \qquad \text{(A1)}$$

Case II.

Surface 3 reflects specularly, and surfaces 1 and 2 reflect diffusely. Since the maximum number of specular reflections is 1, then the condition with $l = 2$ in equation (14) or the use of the stochastic 2 model will yield the exact solution, i.e.,

$$\mathbf{B}=\mathbf{B}^{(1)}+\mathbf{B}^{(2+)}$$

Matrix $\mathbf{B}^{(1)}$ is

$$\mathbf{B}^{(1)}=\mathbf{FA}=\begin{bmatrix} F_{1,1} & F_{1,2} & F_{1,3} \\ F_{2,1} & F_{2,2} & F_{2,3} \\ F_{3,1} & F_{3,2} & F_{3,3} \end{bmatrix}\begin{bmatrix} \alpha_1 & 0 & 0 \\ 0 & \alpha_2 & 0 \\ 0 & 0 & \alpha_3 \end{bmatrix}$$

Substitution of numerical values of view factor ($F_{i,j} = 0.5$ when $i \neq j$ and $F_{i,i} = 0$) and absorptivity ($\alpha_i = \epsilon_i$) yields

$$\mathbf{B}^{(1)}=\begin{bmatrix} 0 & 0.05 & 0.15 \\ 0.25 & 0 & 0.15 \\ 0.25 & 0.05 & 0 \end{bmatrix} \qquad \text{(A2)}$$

To evaluate $\mathbf{B}^{(2+)}$, we need to find **P**, **Q**, and **A**.

The states of the Markov process is in the form of (i,j). The possible states are (1,2), (1,3), (2,1), (2,3), (3,1), (3,2).

Using equation (29) the transition probabilities matrix results in the following form

$$\mathbf{P}=\begin{array}{c} \\ (1,2) \\ (1,3) \\ (2,1) \\ (2,3) \\ (3,1) \\ (3,2) \end{array}\begin{array}{c} \begin{array}{cccccc} (1,2) & (1,3) & (2,1) & (2,3) & (3,1) & (3,2) \end{array} \\ \begin{bmatrix} 0 & 0 & F_{2,1} & F_{2,3} & 0 & 0 \\ 0 & 0 & 0 & 0 & F_{1(3),1}/F_{1,3} & F_{1(3),2}/F_{1,3} \\ F_{1,2} & F_{1,3} & 0 & 0 & 0 & 0 \\ 0 & 0 & 0 & 0 & F_{2(3),1}/F_{2,3} & F_{2(3),2}/F_{2,3} \\ F_{1,2} & F_{1,3} & 0 & 0 & 0 & 0 \\ 0 & 0 & F_{2,1} & F_{2,3} & 0 & 0 \end{bmatrix} \end{array}$$

Using equations (20) and (21), we get

$$\mathbf{Q}=\begin{array}{c} \\ (1,2) \\ (1,3) \\ (2,1) \\ (2,3) \\ (3,1) \\ (3,2) \end{array}\begin{array}{c} \begin{array}{cccccc} (1,2) & (1,3) & (2,1) & (2,3) & (3,1) & (3,2) \end{array} \\ \begin{bmatrix} F_{1,2}\rho_2 & 0 & 0 & 0 & 0 & 0 \\ 0 & F_{1,3}\rho_3 & 0 & 0 & 0 & 0 \\ 0 & 0 & F_{2,1}\rho_1 & 0 & 0 & 0 \\ 0 & 0 & 0 & F_{2,3}\rho_3 & 0 & 0 \\ 0 & 0 & 0 & 0 & F_{3,1}\rho_1 & 0 \\ 0 & 0 & 0 & 0 & 0 & F_{3,2}\rho_2 \end{bmatrix} \end{array}$$

Matrix **A** is obtained from equation (18)

$$\mathbf{A}=\begin{array}{c} \\ (1,2) \\ (1,3) \\ (2,1) \\ (2,3) \\ (3,1) \\ (3,2) \end{array}\begin{array}{c} \begin{array}{cccccc} (1,2) & (1,3) & (2,1) & (2,3) & (3,1) & (3,2) \end{array} \\ \begin{bmatrix} \alpha_2 & 0 & 0 & 0 & 0 & 0 \\ 0 & \alpha_3 & 0 & 0 & 0 & 0 \\ 0 & 0 & \alpha_1 & 0 & 0 & 0 \\ 0 & 0 & 0 & \alpha_3 & 0 & 0 \\ 0 & 0 & 0 & 0 & \alpha_1 & 0 \\ 0 & 0 & 0 & 0 & 0 & \alpha_2 \end{bmatrix} \end{array}$$

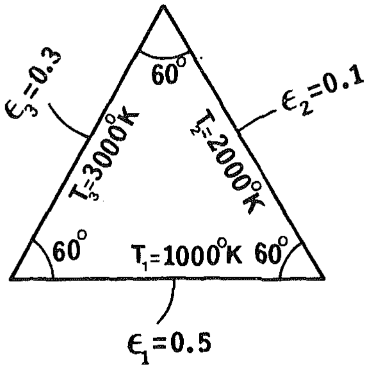

Fig. 2

Note that $\mathbf{R} = \mathbf{I} - \mathbf{A}$. Implementing equation (23), we get

$$\mathbf{C}=\begin{array}{c} \\ (1,2) \\ (1,3) \\ (2,1) \\ (2,3) \\ (3,1) \\ (3,2) \end{array}\begin{array}{c} \begin{array}{cccccc} (1,2) & (1,3) & (2,1) & (2,3) & (3,1) & (3,2) \end{array} \\ \begin{bmatrix} .01383 & .04148 & .17426 & .10455 & .10226 & .01362 \\ .01057 & .03174 & .10226 & .06136 & .10921 & .03488 \\ .01860 & .05580 & .06913 & .04148 & .05287 & .01212 \\ .01212 & .03637 & .06811 & .04087 & .17438 & .01815 \\ .01860 & .05580 & .06913 & .04148 & .05287 & .01212 \\ .01383 & .04148 & .17426 & .10455 & .10226 & .01362 \end{bmatrix} \end{array}$$

and

$$B_{i,j}^{(2+)} = \sum_{i_2, j_1} C_{(i,i_2),(j_1,j)}$$

for example,

$$\begin{aligned} B_{1,1}^{(2+)} &= C_{(1,2),(2,1)} + C_{(1,2),(3,1)} + C_{(1,3),(2,1)} + C_{(1,3),(3,1)} \\ &= .17426 + .10226 + .10226 + .10921 = .48799 \end{aligned}$$

$$\mathbf{B}^{(2+)}=\begin{bmatrix} 0.48799 & 0.07290 & 0.23911 \\ 0.36449 & 0.06099 & 0.17452 \\ 0.39852 & 0.05817 & 0.24331 \end{bmatrix}$$

$$\mathbf{B}=\mathbf{B}^{(1)}+\mathbf{B}^{(2+)}=\begin{bmatrix} 0.48799 & 0.12290 & 0.38911 \\ 0.61449 & 0.06099 & 0.32452 \\ 0.64852 & 0.10817 & 0.24331 \end{bmatrix}$$

For $T_1 = 1000$ K, $T_2 = 2000$ K, and $T_3 = 3000$ K. The net heat loss due to radiation per unit area on each surface is

$$\dot{q}_1 = -944493.3 \frac{W}{m^2}, \ \dot{q}_2 = -68036.0 \frac{W}{m^2},$$

$$\dot{q}_3 = 1012530.9 \frac{W}{m^2}$$

Using the classical approach presented in [10], we obtain the identical solutions for the surface heat flux [22].

Case III.

Surfaces 2 and 3 reflect specularly, and surface 1 reflects diffusely. The use of the stochastic 2 model yields

$$\mathbf{B}=\begin{bmatrix} 0.47467 & 0.12285 & 0.40247 \\ 0.61425 & 0.06099 & 0.32475 \\ 0.67079 & 0.10825 & 0.22096 \end{bmatrix} \qquad \text{(A3)}$$

If the stochastic 3 model is employed, there is obtained

$$\mathbf{B}=\begin{bmatrix} 0.47253 & 0.12378 & 0.40369 \\ 0.61892 & 0.06141 & 0.31967 \\ 0.67281 & 0.10656 & 0.22062 \end{bmatrix} \tag{A4}$$

Finally, the stochastic 4 model yields the following exact solution

$$\mathbf{B}=\begin{bmatrix} 0.47252 & 0.12378 & 0.40369 \\ 0.61892 & 0.06141 & 0.31967 \\ 0.67282 & 0.10656 & 0.22062 \end{bmatrix} \tag{A5}$$

It is seen that the stochastic 3 and the stochastic 4 models almost yield identical results for matrix **B**. In fact, even the stochastic 2 model yields a reasonably accurate solution.

Using the same known surface temperatures, the corresponding heat fluxes are

$$\dot{q}_1=-978287.4\frac{W}{m^2},\ \dot{q}_2=-65857.9\frac{W}{m^2},$$

$$\dot{q}_3=1044145.5\frac{W}{m^2}$$

Again the method of Sparrow and Cess [10] yields identical answers. Numerical computations have shown that [24] if the triple specular reflection is omitted, the method of Sparrow et al. [1, 10] would give an error of 9.57 percent for $\dot{q}_1$, while the error is 4.22 percent by using diffuse reflection assumption. Therefore, ignoring the triple specular reflection in Sparrow's method causes a large error in $\dot{q}$. Surprisingly, this error is even twice as large as that using the diffuse reflection assumption. However, the present method in its simplest form, i.e., stochastic 2 model, yields an error of 0.33 percent.

Case IV.

All three surfaces are specular: This represents a general case. The solution of which has not been attempted previously. Assuming the future of the radiation processes depends on two past steps, i.e., using the stochastic 2 model, we obtain

$$\mathbf{B}=\begin{bmatrix} 0.47434 & 0.12245 & 0.40321 \\ 0.61225 & 0.05860 & 0.32915 \\ 0.67202 & 0.10972 & 0.21826 \end{bmatrix} \tag{A6}$$

Applying the stochastic 3 model, we arrive at

$$\mathbf{B}=\begin{bmatrix} 0.47236 & 0.12282 & 0.40481 \\ 0.61413 & 0.05790 & 0.32798 \\ 0.67468 & 0.10933 & 0.21599 \end{bmatrix} \tag{A7}$$

Comparing matrices (A1), (A6), and (A7) reveals that the present stochastic approach converges very fast for this problem.

APPENDIX B

Consider an enclosure with the same geometry shown in Fig. 2 but with the following surface reflectivity properties: $\rho^d{}_1=0.5, \rho^s{}_1=0, \rho^d{}_2=0.5, \rho^s{}_2=0.4, \rho^d{}_3=0, \rho^s{}_3=0.7$. We attempt to solve for absorption factor matrix **B** using the stochastic *n* model with *n* equal to 2, 3, and 4. Case I, Stochastic 2 model: Assuming that the future of the process depends on two steps past, the possible states of this process are: (1,2), (1,3), (2,1), (2,3), (3,1), (3,2). The absorption factor matrix for this case is

$$\mathbf{B}=\mathbf{B}^{(1)}+\mathbf{B}^{(2+)} \tag{B1}$$

$\mathbf{B}^{(1)}$ is given by equation (A2). The transition probability for this case is

$$\mathbf{P}=[P_{(i_1,i_2),(j_1,j_2)}]$$

Using equation (33) for computing the elements of the above matrix gives

$$P_{(i_1,i_2),(i_2,j_2)}=\frac{\rho^d_{i_2}}{\rho_{i_2}}F_{i_2,j_2}+\frac{\rho^s_{i_2}}{\rho_{i_2}}\frac{F_{i_1(i_2),j_2}}{F_{i_1,j_2}}$$

$$=\frac{1}{2}\frac{\rho^d_{i_2}}{\rho_{i_2}}+\frac{2\rho^s_{i_2}}{\rho_{i_2}}F_{i_1(i_2),j_2}$$

and

$$P_{(i_1,i_2),(j_1,j_2)}=0 \quad \text{if} \quad i_2\neq j_1$$

Matrices **Q** and **A** are identical to those presented in Appendix A. Using equation (23), one can obtain

$$\mathbf{C}=$$

$$\begin{array}{c|cccccc} & (1,2) & (1,3) & (2,1) & (2,3) & (3,1) & (3,2) \\ (1,2) & .01324 & .03971 & .15139 & .11816 & .11333 & .01417 \\ (1,3) & .01086 & .03258 & .11333 & .05477 & .10385 & .03461 \\ (2,1) & .01852 & .05557 & .06618 & .04323 & .05430 & .01220 \\ (2,3) & .01220 & .03659 & .07085 & .03923 & .17305 & .01808 \\ (3,1) & .01852 & .05557 & .06618 & .04323 & .05430 & .01220 \\ (3,2) & .01441 & .04323 & .19694 & .09106 & .09128 & .01308 \end{array}$$

which results

$$\mathbf{B}^{(2+)}=\begin{bmatrix} 0.48190 & 0.07280 & 0.24522 \\ 0.36438 & 0.06099 & 0.17462 \\ 0.40870 & 0.05821 & 0.23310 \end{bmatrix} \tag{B2}$$

From equation (A2) and (B2), we arrive at

$$\mathbf{B}=\mathbf{B}^{(1)}+\mathbf{B}^{(2+)}=\begin{bmatrix} 0.48190 & 0.12288 & 0.39522 \\ 0.61438 & 0.06099 & 0.32462 \\ 0.65870 & 0.10821 & 0.23310 \end{bmatrix} \tag{B3}$$

Case II, Stochastic 3 Model: If the future of the process depends on three past reflection steps, we have

$$\mathbf{B}=\mathbf{B}^{(1)}+\mathbf{B}^{(2)}+\mathbf{B}^{(3+)} \tag{B4}$$

where $\mathbf{B}^{(1)}$ is given by equation (A2)

$$\mathbf{B}^{(2)} \quad = \quad [B^{(2)}_{i,j}]$$

$$\mathbf{B}^{(2)}_{i,j} \quad = \quad \sum_{i_2}\sum_{n_2}\rho^{n_2}_{i_2}P\{x_0=i, x=i^{n_2}_2, x_2=j\}$$

where

$$P\{x_0=i, x_1=i^d_2, x_2=j\}=F_{i,i_2}F_{i_2,j}$$

$$P\{x_0=i, x_1=i^s_2, x_2=j\}=F_{i(i_2),j}$$

which gives

$$\mathbf{B}^{(2)}=\begin{bmatrix} 0.13619 & 0.02562 & 0.08142 \\ 0.12811 & 0.02188 & 0.03750 \\ 0.13571 & 0.01250 & 0.09108 \end{bmatrix} \tag{B5}$$

The matrix **C** is computed from equation (23)

$$\mathbf{C}=\mathbf{Q}[\mathbf{I}-\mathbf{PR}]^{-1}\mathbf{PA}$$

where

$$\mathbf{Q}=[q_{(i_1,i_2,i_3)}\delta_{(i_1,i_2,i_3),(j_1,j_2,j_3)}]$$

$$q_{(i_1,i_2,i_3)}=\rho^d_{i_2}\rho_{i_3}F_{i_1,i_2}F_{i_2,i_3}+\rho^s_{i_2}\rho_{i_3}F_{i_1(i_2),i_3}$$

and

$$\mathbf{P}=[P_{(i_1,i_2,i_3),(j_1,j_2,j_3)}]$$

$$P_{(i_1,i_2,i_3),(j_1,j_2,j_3)}=0$$

$$\text{if } i_2\neq j_1, \quad \text{or} \quad i_3\neq j_2$$

and

$$P_{(i_1,i_2,i_3),(i_2,i_3,J_3)} = \frac{\rho_{i_2}^{d}}{\rho_{i_2}}\frac{\rho_{i_3}^{d}}{\rho_{i_3}}F_{i_3,j_3} + \frac{\rho_{i_2}^{s}}{\rho_{i_2}}\frac{\rho_{i_3}^{d}}{\rho_{i_3}}F_{i_3,j_3} + \frac{\rho_{i_2}^{d}}{\rho_{i_2}}\frac{\rho_{i_3}^{s}}{\rho_{i_3}}\frac{F_{i_2(i_3),j_3}}{F_{i_2,i_3}} + \frac{\rho_{i_2}^{s}}{\rho_{i_2}}\frac{\rho_{i_3}^{s}}{\rho_{i_3}}\frac{F_{i_1(i_2,i_3),j_3}}{F_{i_1(i_2),i_3}}$$

$$\mathbf{A} = [\alpha_{j_3}\,\delta_{(i_1,i_2,i_3),(j_1,j_2,j_3)}]$$

Using the preceding matrices, we can compute the matrix **C**, which yields $\mathbf{B}^{(3+)}$ as

$$\mathbf{B}^{(3+)} = \begin{bmatrix} 0.34500 & 0.04718 & 0.16458 \\ 0.23901 & 0.03884 & 0.13466 \\ 0.27517 & 0.04462 & 0.14093 \end{bmatrix} \tag{B6}$$

Substituting equations (A2), (B5), and (B6) into equation (B4) gives

$$\mathbf{B} = \begin{bmatrix} 0.48119 & 0.12280 & 0.39600 \\ 0.61712 & 0.06072 & 0.32216 \\ 0.66088 & 0.10712 & 0.23201 \end{bmatrix} \tag{B7}$$

Case III, Stochastic 4 Model: Following the similar approach, we obtain

$$\mathbf{B} = \mathbf{B}^{(1)} + \mathbf{B}^{(2)} + \mathbf{B}^{(3)} + \mathbf{B}^{(4+)} = \begin{bmatrix} 0.48100 & 0.12294 & 0.39606 \\ 0.61681 & 0.06094 & 0.32226 \\ 0.66082 & 0.10716 & 0.23203 \end{bmatrix} \tag{B8}$$

The foregoing solution is exact, because the maximum number of specular reflections in the given enclosure is 3. Note that the results given in (B7) are very close to the exact solution, and also, the absorption factors given by equation (B3) are close enough to the exact solution. Therefore, the use of the stochastic 2 model appears to be quite adequate for this case. Additional examples may be found in [22].

Discrete-Ordinates Solutions of the Radiative Transport Equation for Rectangular Enclosures

W. A. Fiveland
The Babcock & Wilcox Company,
Research and Development Division,
Alliance Research Center,
Alliance, Ohio 44601
Mem. ASME

The S_n discrete-ordinates method is used to find numerical solutions in a two-dimensional rectangular enclosure with a gray absorbing, emitting, and isotropically scattering medium. Results are obtained for the S_2, S_4, and S_6 approximations that correspond to 4, 12, and 24 flux approximations, respectively, and are compared with exact solutions, numerical Hottel's zone results, P3 differential approximations, and an approximation method developed by Modest. The S_2 approximation solutions were found to be applicable only for several specific cases and are not recommended for general use. The S_4 and S_6 solutions compare favorably with other methods and can be used to predict radiant intensity and surface heat transfer rate for various surface and optical conditions.

Introduction

In recent years, considerable interest has been given to the study of one- and two-dimensional radiative heat transfer in participating media. The motivation for these studies has been prompted by the numerous practical applications in boilers, furnaces, and other gas-solid suspensions.

A good deal of work has been reported in the literature, but most has been confined to the one-dimensional case only. These studies range from investigations of isotropic scattering [1, 2, 3] to more realistic treatments of scattering phase functions [4-8]. Since one-dimensional analysis of radiative heat transfer is often not suitable, there has been interest in developing methods applicable to multidimensional geometries. Monte Carlo methods [9, 10], Hottel's zonal methods [11, 12], and approximate methods [13-16] have been developed for multidimensional geometries. Monte Carlo and Hottel's zone methods are too time consuming and tedious to apply for scattering problems. Approximate methods are often developed for selective cases of radiative heat transfer. Consequently, alternate schemes of radiative heat transfer are required for practical applications.

One method that has received little attention in the heat transfer community is the discrete-ordinates method. The discrete-ordinates method has been developed by a number of researchers [17, 18, 19] and applied to multidimensional radiative heat transfer only on a limited basis [20, 21]. In this paper, numerical solutions of the radiative transport equations are presented using the S_n discrete-ordinates method [18] in which S_2, S_4, and S_6 solutions are studied corresponding to 4, 12, and 24 flux approximations, respectively. Numerical solutions are found by solving the exact transport equation for a set of discrete directions spanning the range of 4π-solid angle. Angular integrals of intensity are discretized by numerical quadrature. The resulting S_n discrete-ordinate equations are spatially discretized using the control volume technique applied extensively to the general transport problem by Spalding [22] and co-workers [23, 24]. The advantage in using the control volume approach is quite clear: The discrete-ordinates method can be used not only to study radiative heat transfer alone, but can also be easily integrated with existing computer codes [23, 24] based on the control volume method and used to study the complex transport processes involved in many reacting and nonreacting convective transport problems.

Analysis

Governing Equations. Consider the radiative transfer equation for the two-dimensional rectangular enclosure shown in Fig. 1. The balance of energy passing in a specified direction $\mathbf{\Omega}$ through a small differential volume in an emitting–absorbing and scattering gray medium can be written as follows

$$(\mathbf{\Omega}\cdot\nabla)I(\mathbf{r},\mathbf{\Omega}) = -(\kappa+\sigma)I(\mathbf{r},\Omega) + \kappa I_b(\mathbf{r}) + \frac{\sigma}{4\pi}\int_{\Omega'=4\pi} I(\mathbf{r},\mathbf{\Omega})\,\phi(\mathbf{\Omega}'\rightarrow\mathbf{\Omega})\,d\Omega' \qquad (1)$$

where $\phi(\mathbf{\Omega}'\rightarrow\mathbf{\Omega})$ is the phase function of energy transfer from the incoming Ω' direction to the outgoing direction Ω (see Fig. 1); $I(\mathbf{r},\mathbf{\Omega})$ is the radiation intensity, which is a function of position and direction; $I_b(\mathbf{r})$ is the intensity of blackbody radiation at the temperature of the medium; and κ and σ are the gray absorption and scattering coefficients of the medium, respectively. The expression on the left-hand side represents the gradient of the intensity in the specified direction $\mathbf{\Omega}$. The three terms on the right represent the changes in intensity due to absorption and out-scattering, emission and in-scattering, respectively.

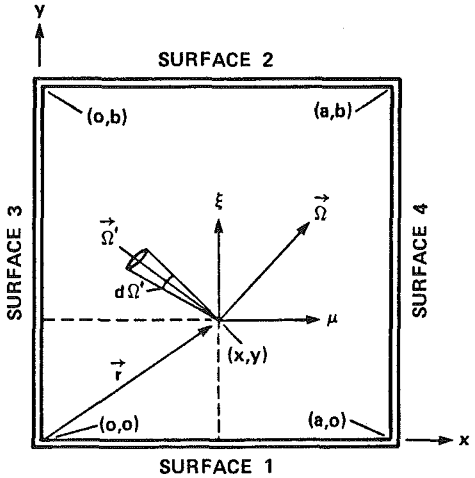

Fig. 1 Schematic of rectangular geometry

Contributed by the Heat Transfer Division for publication in the JOURNAL OF HEAT TRANSFER. Manuscript received by the Heat Transfer Division December 7, 1983. Paper No. 83-HT-51.

If the surface bounding the medium is assumed gray and emits and reflects diffusely, then the radiative boundary condition for equation (1) is given by

$$I(\mathbf{r},\Omega)=\epsilon I_b(\mathbf{r})+\frac{\rho}{\pi}\int_{\mathbf{n}\cdot\Omega'<0}|\mathbf{n}\cdot\Omega|I(\mathbf{r},\Omega')\,d\Omega' \tag{2}$$

where $I(\mathbf{r},\Omega)$ is the intensity of radiant energy leaving a surface at a boundary location, ϵ is the surface emissivity, ρ is the surface reflectivity, and $\mathbf{n}$ is the unit normal vector at the boundary location.

The terms on the right-hand side of equation (2) represent contributions to the outgoing intensity due to emission from the surface and reflection of incoming radiation.

Discrete-Ordinate Equations. Chandrasekar [17] has described derivations of the discrete-ordinate equations. Simply, equations (1) and (2) are replaced by a discrete set of equations for a finite number of ordinate directions. Integrals are replaced by a quadrature summed over each ordinate. These equations can be written

$$\mu_m\frac{\partial I_m}{\partial x}+\xi_m\frac{\partial I_m}{\partial y}=-\beta I_m+\kappa I_b+\frac{\sigma}{4\pi}\sum_{m'}w_{m'}\,\phi_{m'm}\,I_{m'} \tag{3}$$

The conditions at the boundary are given as

$$I_m=\epsilon I_b+\frac{\rho}{\pi}\sum_{\substack{m'\\ \mu'<0}}w_{m'}\,|\mu_{m'}|\,I_{m'}\quad;\ \mu_m>0\qquad \text{at } x=0 \tag{4}$$

$$I_m=I_{m'}\qquad \mu_{m'}=-\mu_m\quad;\ \mu_m>0\qquad \text{at } x=a/2 \tag{5}$$

$$I_m=\epsilon I_b+\frac{\rho}{\pi}\sum_{\substack{m'\\ \xi_{m'}<0}}w_{m'}\,|\xi_{m'}|\,I_{m'}\quad;\ \xi_m>0\qquad \text{at } y=0 \tag{6}$$

$$I_m=\epsilon I_b+\frac{\rho}{\pi}\sum_{\substack{m'\\ \xi_{m'}>0}}w_{m'}\,|\xi_{m'}|\,I_{m'}\quad;\ \xi_m<0\qquad \text{at } y=b \tag{7}$$

In equations (3–7), the values m and m' denote outgoing and incoming directions, respectively. For a discrete direction Ω_m, the values μ_m and ξ_m are the direction cosines of Ω_m. These equations represent m coupled partial differential equations for the m intensities, I_m. The radiant heat flux at any location can be written as follows

$$\mathbf{q}(\mathbf{r})=\int_{\Omega=4\pi}\Omega I(\mathbf{r},\Omega)\,d\Omega=\sum_i w_i\Omega_i I(\mathbf{r},\Omega_i) \tag{8}$$

A control volume form of equation (3) can be obtained by multiplying equation (3) by $dx\cdot dy$ and integrating over the control volume shown in Fig. 2 as follows

$$\mu_m(A_N I_{mN}-A_S I_{mS})+\xi_m(B_E I_{mE}-B_W I_{mW})$$
$$=-\beta\mathcal{V}_p\,I_{mp}+\kappa\mathcal{V}_p\,I_{bp}+\mathcal{V}_p\frac{\sigma}{4\pi}\sum_{m'}w_{m'}\,\phi_{m'm}\,I_{m'p} \tag{9}$$

The source term from in-scattering contains shape parameters $\phi_{m'm}$. The ϕ values can be computed knowing the phase function and ordinate directions. For example, if linear anisotropic scattering is assumed

$$P(\theta)=1+a_o\cos\theta \tag{10}$$

the coefficients can be written as follows

$$\phi_{m'm}=1.0+a_o[\mu_m\mu_{m'}+\xi_m\xi_{m'}+\eta_m\eta_{m'}] \tag{11}$$

The value a_o is the asymmetry factor that lies between $-1\le a_o\le 1$, where the values -1, 0, and 1 denote backward, isotropic, and forward scattering, respectively.

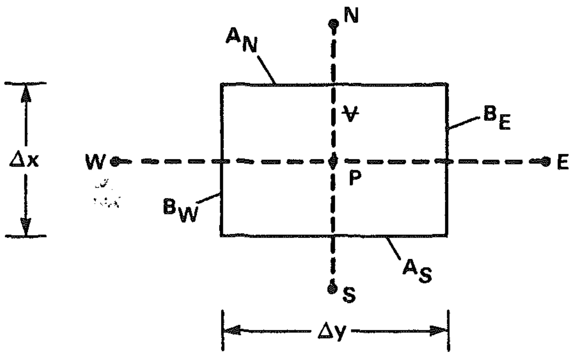

Fig. 2 Arbitrary control volume

Nomenclature

A = north–south areas, m^2
a = height of enclosure, m
B = east–west areas, m^2
b = width of enclosure, m
E = emissive power $(=\tilde{\sigma}T^4)\pi I$, W/m^2
G = incident energy, $\int_{4\pi}Id\Omega$, W/m^2
$\hat{G}$ = nondimensional incident radiant energy, G/E_b
I = radiant intensity, W/(m$^2\cdot$Sr)
$\mathbf{n}$ = unit normal
$\mathbf{q}$ = heat flux, W/m^2
$\hat{Q}$ = nondimensional surface heat transfer rate, q/E_b
$\mathbf{r}$ = position vector, m
$\mathcal{V}_p$ = volume of pth control volume, m^3
w_m = weight function in a direction $-$m (fractional area of a unit sphere), m^2
x = coordinate, m
$\hat{x}$ = nondimensional coordinate, x/a
y = coordinate, m
$\hat{y}$ = nondimensional coordinate, y/b
α = aspect ratio, a/b
Ω = outgoing direction of radiation
ϕ = phase function
θ = angle of scattered energy, measured from the forward direction
σ = scattering coefficient, m^{-1}
$\tilde{\sigma}$ = Boltzmann's constant, 5.669×10^{-8} W/(m$^2\cdot$°K^4)
κ = absorption coefficient, m^{-1}
β = extinction coefficient, $\sigma+\kappa$, m^{-1}
τ = optical thickness
ϵ = surface emissivity
ρ = surface reflectivity
μ,ξ,η = ordinates (there are $n(n+2)$ ordinate directions based on the S_n concept; i.e., $S_4=24$)
ω = relaxation factor
ω_0 = albedo for single scatter, σ/β
∇ = gradient/vector

Subscripts

b = blackbody
g = gas
m = outgoing ordinate direction
m' = incoming ordinate direction
o = wall value
p = control volume center
N,S,E,W = compass directions

Superscripts

$\hat{}$ = nondimensional
$'$ = (prime) incoming value

Boldface

vectorial quantity

Solution of the Discrete-Ordinates Equations

Solutions of equation (3) for each of the m-directions are iterative, because the in-scattering source terms and the boundary conditions depend on incoming intensity. Calculations are initiated by assuming the boundaries are black ($\epsilon = 1$) and the in-scattering source terms are zero. With these assumptions, the radiant intensities can be computed. On subsequent iterations, the full form of equations (4-7) was used together with the in-scattering source term.

At a particular iteration, a solution of equation (9) together with the boundary conditions is found for x and y using a point-by-point method. The solution proceeds by stepping to a new value of y. At that value of y, the intensity is solved for a point x over all of the m-directions before proceeding to the new x-value. After all x-values have been scanned for the y-position, a new y-position is established and the process is repeated. All y-values are scanned repeatedly until the intensity and wall fluxes are within preselected tolerances.

Table 1 Ordinates and weights for S_2 approximation (ordinate values taken from [25])

Direction number	Ordinates			Weight[a]
	(μ_m)	(ξ_m)	(η_m)	(w_m)
1	−.57735026	−.57735026	.57735026	1
2	.57735026	−.57735026	.57735026	1
3	−.57735026	.57735026	.57735026	1
4	.57735026	.57735026	.57735026	1

[a] Multiply weights by the factor π

Table 2 Ordinates and weights for S_4 approximation (ordinate values taken from [25])

Direction number	Ordinates			Weight[a]
	(μ_m)	(ξ_m)	(η_m)	(w_m)
1	−.33333333	−.88191710	.33333333	1/3
2	.33333333	−.88191710	.33333333	1/3
3	−.88191710	−.33333333	.33333333	1/3
4	−.33333333	−.33333333	.88191710	1/3
5	.33333333	−.33333333	.88191710	1/3
6	.88191710	−.33333333	.33333333	1/3
7	−.88191710	.33333333	.33333333	1/3
8	−.33333333	.33333333	.88191710	1/3
9	.33333333	.33333333	.88191710	1/3
10	.88191710	.33333333	.33333333	1/3
11	−.33333333	.88191710	.33333333	1/3
12	.33333333	.88191710	.33333333	1/3

[a] Multiply weights by the factor π

Table 3 Ordinates and weights for S_6 approximation (ordinate values taken from [25])

Direction number	Ordinates			Weight[a]
	(μ_m)	(ξ_m)	(η_m)	(w_m)
1	−.25819889	−.93094934	.25819889	.16086125
2	.25819889	−.93094934	.25819889	.16086125
3	−.68313005	−.68313005	.25819889	.17247209
4	−.25819889	−.68313005	.68313005	.17247209
5	.25819889	−.68313005	.68313005	.17247209
6	.68313005	−.68313005	.25819889	.17247209
7	−.93094934	−.25819889	.25819889	.16086125
8	−.68313005	−.25819889	.68313005	.17247204
9	−.25819889	−.25819889	.93094934	.16086125
10	.25819889	−.25819889	.93094934	.16086125
11	.68313005	−.25819889	.68313005	.17247204
12	.93094934	−.25819889	.25819889	.16086125
13	−.93094934	.25819889	.25819889	.16086125
14	−.68313005	.25819889	.68313005	.17247204
15	−.25819889	.25819889	.93094934	.16086125
16	.25819889	.25819889	.93094934	.16086125
17	.68313005	.25819889	.68313005	.17247204
18	.93094934	.25819889	.25819889	.16086125
19	−.68313005	.68313005	.25819889	.17247204
20	−.25819889	.68313005	.68313005	.17247204
21	.25819889	.68313005	.68313005	.17247204
22	.68313005	.68313005	.25819889	.17247204
24	−.25819889	.93094934	.25819889	.16086125
25	.25819889	.93094934	.25819889	.16086125

[a] Multiply weights by the factor π

Consider the point-by-point iterative process when the direction cosines are both positive. The number of unknowns in equation (9) is reduced by relating cell edge radiant fluxes to the cell center radiant flux. For example, a spatially weighted approximation can be written as follows

$$I_{mp} = \omega I_{mN} + (1-\omega) I_{mS} = \omega I_{mE} + (1-\omega)_{mW} \quad (12)$$

and was used with a value ω of 1/2 which yields the "diamond difference" relations proposed by Carlson and Lathrop [18]. If I_{mS}, I_{mW} are assumed known, where the calculations are proceeding in a direction of positive cosines and increasing index, then equation (12) can be used to eliminate the intensities I_{mN} and I_{mE} in equation (9). Substituting the following equation (13) into equation (9) and solving for the intensity I_{mp} yields

$$I_{mp} = \frac{\mu_m A I_{mS} + \xi_m B I_{mW} + S_1 + S_2}{\mu_m A_N + \xi_m B_E + \omega \beta \vartheta_p} \quad (13)$$

where:

$$A = A_N(1-\omega) + A_S \omega$$

$$B = B_E(1-\omega) + B_w \omega$$

$$S_1 = \kappa \vartheta_p I_{bp}$$

$$S_2 = \vartheta_p \frac{\sigma}{4\pi} \sum_{m'} w_{m'} \phi_{m'm} I_{m'p}$$

Equation (13) is appropriate when both direction cosines are positive and the direction of integration proceeds in a direction of increasing x and y. If negative direction cosines occur, however, the direction of integration is reversed. For example, if $\xi < 0$, then integration proceeds top to bottom, or in a direction of large-to-small y. It follows that the subscript S is replaced by N. Similar arguments hold if μ is negative or if μ and ξ are negative.

Several additional guidelines have been recommended [18] to prevent physically unrealistic solutions and minimize errors. Because equation (12) represents an extrapolation across a control volume, negative intensities can result when scattering and/or absorption cross sections are large or when inadequate spatial resolution is used. On physical grounds, negative fluxes are impossible and are set to zero. Fluxes are recalculated with $\omega = 1$ and the solution proceeds. In addition, one possible set of ordinate directions is shown in Tables 1, 2, and 3 for the S_2, S_4, and S_6 approximations and the ordinate directions are ordered as shown to prevent unrealistic coupling between the equations.

Results

The geometry studied in this paper is the rectangular enclosure previously depicted in Fig 1. For this geometry, three cases are examined

- Scattering in a black enclosure
- Scattering in a gray enclosure
- Radiative transfer in a black enclosure with an absorbing medium

These examples were chosen to benchmark the discrete-ordinates method against other exact solutions and approximate methods.

The radiative transport equation was solved by the discrete-ordinates S_n method documented in several references [17-21], and it requires the selection of $n(n + 2)$ ordinate directions and associated weights. Because there is geometrical symmetry, only one-half the number of ordinates is required. Solutions for radiative transfer in the enclosure have been found using the S_2, S_4, and S_6 approximations proposed in [18]. Tables 1, 2, and 3 summarize these values. Ordinate sets for higher approximations can also be found in [25].

The enclosure in Fig. 1 was divided into 20 control volumes in each direction with the grid points centered in the control volume and spaced uniformly throughout the enclosures. Discrete-ordinate solutions were found and convergence was checked using a tolerance on wall heat flux and radiant intensity of 0.1 percent. Further spatial subdivisions were found not to yield more accurate results. Results are presented using nondimensional values; surface heat transfer and radiant intensities are normalized using a characteristic emissive power, while coordinate directions are normalized with a characteristic length.

Pure Scattering in Black Enclosures. The objective of studying these cases was to provide a benchmark for the discrete-ordinates method against exact solutions and other approximate methods for problems involving scattering of radiant energy. Initial studies focused on isotropic radiative transfer in a square enclosure with black walls and scattering cross section of unity. This geometry, initially analyzed in [26], was reconsidered because the boundary conditions have an influence throughout the medium when the opacity ($\sigma \Delta x$) is moderate. The emissive power of Surface 1 is unity, while the emissive powers of Surfaces 2, 3, and 4 are zero.

Figures 3 and 4 show the mean radiant intensity and heat transfer in the enclosure. Discrete-ordinate solutions for the S_2 and S_4 approximations are compared in the figures with results from a zonal analysis and with the P3 differential approximation reported in [26]. The discrete-ordinates S_4 approximation in Figs. 3(*a*), 3(*b*), and 3(*c*) compares well with the zonal solution for the positions chosen. The S_2 and S_4 approximations overestimate the mean radiant intensity near the hot surface and underestimate the mean radiant intensity near the cold surface. Errors are largest near the centerline and diminish toward the side walls. Although the S_2 and S_4 trends are similar, S_4 results are more accurate. Table 4 indicates the times required to obtain the S_n solutions. The S_4 method compares with the zonal results about as well as the P3 differential approximation. However, it is interesting to note that the S_4 solution errors are opposite the P3 errors; where the S_4 methods overestimate the mean radiant intensity, the P3 method underestimates the intensity; and the converse is true. An S_6 approximation did not improve the results significantly and, therefore, is not shown. Higher-order S_n approximations would be required to match zonal results, that is, S_8, S_{10}, S_{12}, etc. These higher-order approximations are costly to execute, and an S_4 solution is an adequate alternative.

Surface heat transfer predicted using the discrete-ordinates method is compared in Fig. 4 to the zonal method and to the P3 approximation. The S_2 and S_4 methods slightly underpredict the surface heat transfer when compared to the zonal method. The underprediction in surface heat transfer arises as a result of the overprediction in incident radiant energy at a fixed surface emissive power. Large errors in the P3 solution near the side walls are nonexistent in the discrete-ordinates solution. Rather the deviation between the zonal solution and the discrete-ordinates solution is nearly constant, because the discrete-ordinates method uniformly overpredicts mean radiant intensity near the hot surface. Ratzel and Howell [26] accounted for the P3 surface heat transfer errors as a result of finite-differencing inaccuracies in the heat transfer calculations and because the moments of intensity lose accuracy near the surfaces. They also cited similar arguments in [9] and [27], and found similar errors in the P3 approximations when different aspect ratio enclosures were examined [28]. Based on these studies, the S_4 approximate clearly estimates the surface heat transfer more accurately.

Centerline distributions of radiant intensity from the discrete-ordinates method are compared with results presented by Modest [16] and with P3 solutions in Fig. 5 for different rectangular enclosures. Discrete-ordinate S_4

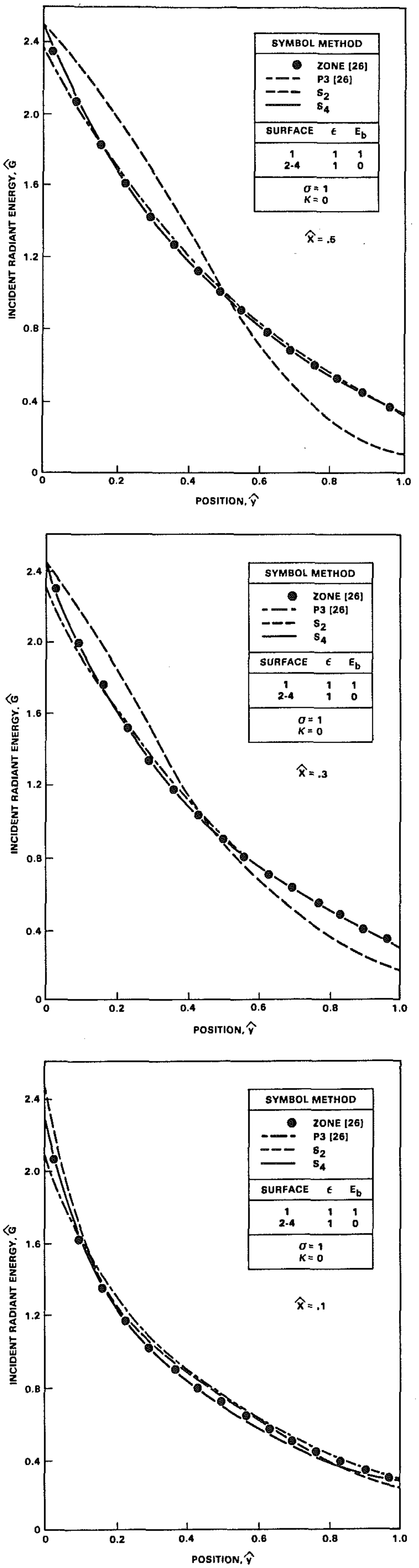

Fig. 3 Incident radiant energy in a square enclosure with a scattering medium

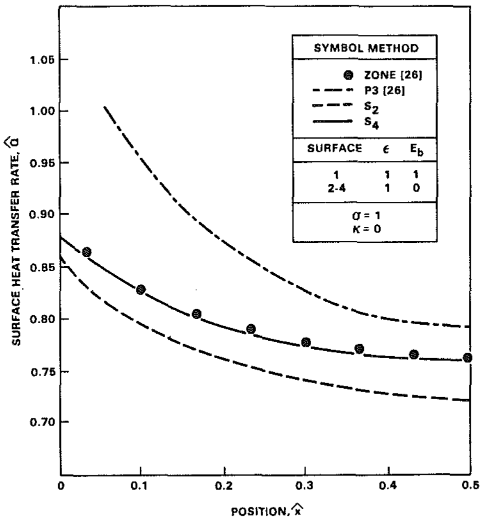

Fig. 4 Surface test transfer rates in a square enclosure with a scattering medium

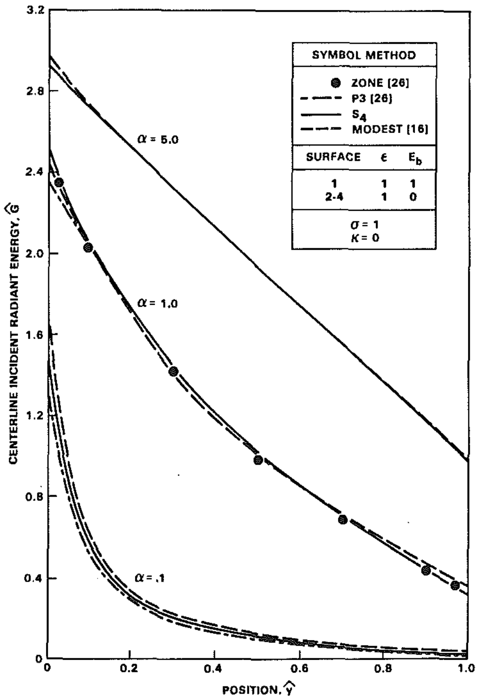

Fig. 5 Incident radiant energy for different aspect ratios in an enclosure with a scattering medium

Table 4 S_n CPU-times (s) for scattering[a]

Emissivity (ε)	S_2	S_4	S_6
1.0	18	43	85
0.5	23	57	113
0.1	64	152	303

[a] Machine calculations performed on VAX-11/780

solutions are comparable with P3 results. At large aspect ratio, when the enclosure approximates two black, parallel plates, the mean radiant intensity results are nearly identical to the one-dimensional solution in which the radiant intensity is linear. The largest deviation between the discrete-ordinates solution and the results reported by Modest occurs at small aspect ratios. In this case, the side walls significantly affect the radiant intensity throughout the medium, and errors arising from the low-order S_n approximation will be magnified. Changes in the aspect ratio did not affect the times listed in Table 4 to obtain solutions.

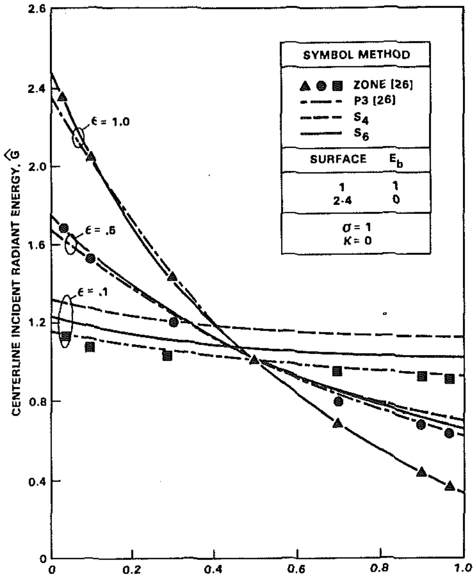

Fig. 6 Incident radiant energy in a square gray enclosure with a scattering medium

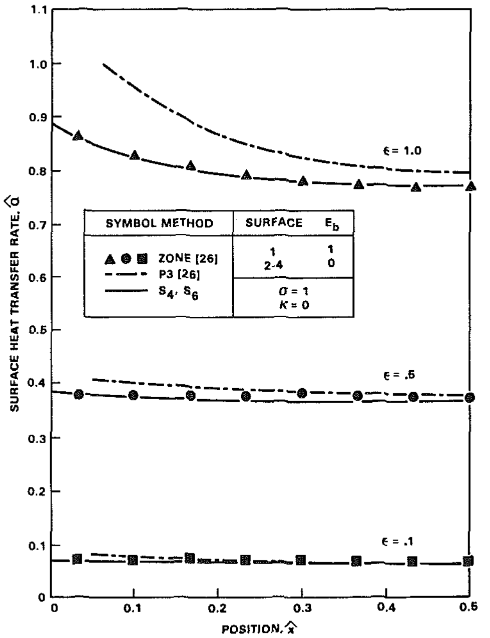

Fig. 7 Surface heat transfer rates in a square gray enclosure with a scatttering medium

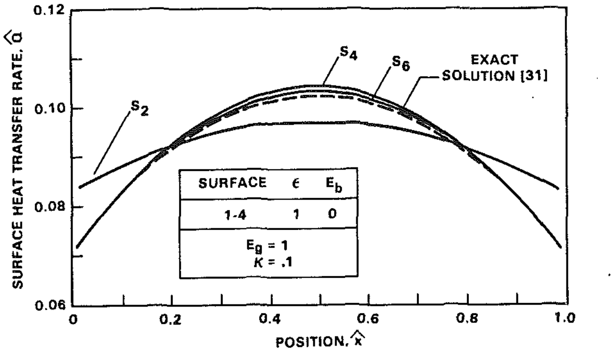

Fig. 8 Surface heat transfer rates for a square enclosure with cold black walls and absorbing medium

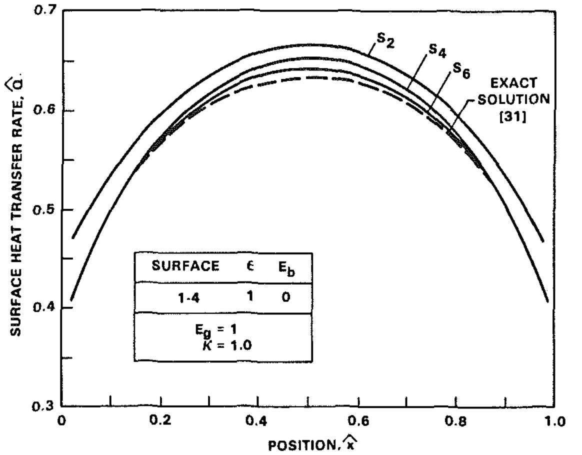

Fig. 9 Surface heat transfer rates for a square enclosure with cold black walls and absorbing medium

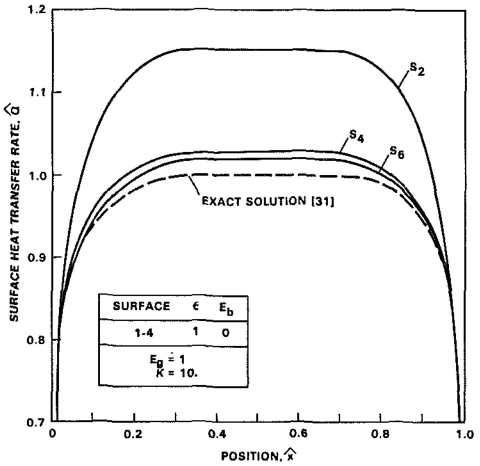

Fig. 10 Surface heat transfer rates for a square enclosure with cold black walls and absorbing medium

Pure Scattering in a Gray Enclosure. Mean radiant intensity and surface heat transfer were predicted using the discrete-ordinates method for a radiatively gray square enclosure with isotropic scattering. The medium is assumed to have a scattering cross section of unity. This case is important because the boundary conditions are not only a function of the surface emissive power but of the incident radiant energy.

Figure 6 compares centerline mean radiant intensity between the discrete-ordinates S_n solutions, Hottel's zonal method, and the P3 differential results. At black body conditions ($\epsilon = 1$), the discrete-ordinates and P3 solutions both compare well with the zonal results reported in [26]. However, at a gray condition, $\epsilon = 0.5$, the S_4 and S_6 approximations overpredict mean radiant intensity at the cold surface. Mean radiant intensity is overpredicted everywhere at $\epsilon = 0.1$ for both S_n solutions presented. The reason for this error is that as the walls become more reflective ($\epsilon \rightarrow 0$), the boundary conditions are more strongly a function of the incident energy and not the emissive power. Therefore, errors in the incident energy at the boundary propagate error into the boundary condition and finally into the field of radiant intensities. Errors in the radiant intensity arise because solutions are found using only a finite number of ordinates. These errors are termed "ray effects" by Lathrop [29] and are discussed in more detail later because they are maximum for problems involving absorption only. Table 5 lists the CPU time required to obtain solutions for the gray enclosure. As higher approximations are computed ($n \rightarrow \infty$), numerical results are expected to approach the zonal results. However, the reader is forewarned that the approach to a limiting solution may not be monotonic as reported by Clark [30] and is cautioned that computational times may become excessive for higher S_n approximations: a twofold increase in problem CPU time was found here between S_4 and S_6 solutions.

In Fig. 7, heat transfer rates for the hot surfaces predicted from the S_4 and S_6 discrete-ordinates method are compared with the zonal method and the P3 approximation. At surface emissivity $\epsilon = 0.5$, the S_4 heat transfer rates compare well with the zone method. At low emissivity, the error in heat flux is about 10 percent at $\epsilon = 0.1$ and is difficult to resolve. The error occurs because the hot-surface radiant intensity (see, for example, Fig. 5) is overpredicted, which leads to a lower value of wall radiant heat transfer. Surface heat transfer in Fig. 7 is adequately predicted by the S_n method. Edwards and Bobco [1] found that while flux methods predict surface heat flux well, radiant intensities can often be in error. At very gray conditions, improved solutions can be expected as higher-order S_n solutions are used but at the expense of computational efficiency. Therefore, S_4 and S_6 solutions adequately predict surface heat transfer rates and the qualitative trends of the radiant intensity.

Black Enclosure With an Absorbing Medium. Many practical problems involve enclosures that absorb radiant energy. Therefore, the discrete-ordinates method was applied to a rectangular enclosure with cold, black walls and a purely absorbing medium maintained at an emissive power of unity.

This geometry was chosen since an exact solution of the radiative transport equation exists and can be compared to the solutions of the discrete-ordinates equations. In Figs. 8, 9, and 10, surface heat transfer rates have been predicted for three optical conditions using the discrete-ordinates method and are compared to an exact solution presented in [31]. The curve representing the exact solution in the figures was found from the relation

$$\frac{q}{\sigma T^4} = \frac{2}{\pi}\kappa\int_0^a \{L|\kappa(\xi-x)|-L[\kappa\{(\xi-x)^2+b^2\}^{1/2}]\}d\xi \quad (14)$$

where the function $L(\xi)$ is defined as $L(Z) = k_o(Z) - k_{i_2}(Z)$. Here, k_o is the modified Bessel function of order zero, and k_{i_2} is the twice-repeated integral of the modified Bessel function k_o.

In Figs. 8, 9, and 10, surface heat transfer is examined for three attenuation coefficients—$\kappa = 0.1$, 1, and 10. The S_2 method predicts surface heat transfer rates which deviate significantly with the exact solution for each of the optical conditions and at all points along the wall in the enclosure. The S_4 and S_6 discrete-ordinate approximations clearly predict the surface heat transfer rate more accurately, with the largest deviations from the exact solution occurring near the center of the surface. For all of the cases, the S_6 approximation provided the closest agreement with the exact solution. As noted in Table 5, however, the required time to obtain an S_6 solution is twice the time required to obtain an S_4 solution.

The deviation between the numerical results and the exact solution in Figs. 8, 9, and 10 occurs because of the "ray effect" presented in [29]. The ray effect is a defect in the discrete-ordinates method arising from the finite discretization of the angular variable of the divergence operator in the radiative transport equation. Regardless of whether numerical approximations are made for spatial variables (for example, finite differences), the discrete-ordinates method replaces a continuously varying differential operator by a discrete and finite set of equations. Radiation is allowed to stream only along these discrete directions. Radiation from an isolated source may be unseen by a point unless the point and source lie along an ordinate direction. In problems with absorbing media and few ordinate directions, this source of error is particularly troublesome because the points in the enclosure are not well coupled to neighboring points. The ray effect can be reduced—but not eliminated by increasing the number of ordinate directions; however, Lathrop [29] reports the increasing ordinate directions mitigate the ray effects slowly, and Clark [30] has shown that discrete-ordinate errors may not diminish monotonically. Remedies to diminish this error are being studied. Fortunately for most problems of practical interest, scattering is important. This error, while present, is less a problem since in-scattering source terms connect a point to its neighbors.

Table 5 S_n **CPU-times (s) for scattering**[a]

Absorption coefficient (κ)	S_2	S_4	S_6
0.1	10	21	41
1.0	15	30	43
10.0	11	22	45

[a] Machine calculations performed on VAX-11/780

Based on the current discrete-ordinates formulation, an S_2 approximation should not be used for radiative calculations with only absorbing media. An S_6 solution should be used; if time is a factor then an S_4 solution is adequate.

Summary and Conclusions

A novel discrete-ordinates method has been presented in this paper. This method can be applied as an alternative in predicting radiative heat transfer in a rectangular enclosure. Solutions have been found using the S_n approximations (n = 2, 4, and 6) for the ordinate directions and a point-by-point iterative scheme in solving the two-dimensional radiative transport equation. With the method presented here, higher-order, discrete-ordinate approximations are quite easily implemented.

Discrete-ordinates solutions were compared to other solution methods in the paper. In black or gray rectangular enclosures, the S_4 and S_6 solutions for heat transfer and radiant intensity were found to compare favorably with the exact zonal solution [26]. In general, heat transfer rates predicted with the discrete-ordinates method compare better with the exact solution than a similar comparison between the P3 approximation [26] and the zone method. In a black square enclosure with an absorbing medium, the S_4 and S_6 solutions compared well with an exact solution developed in [31]. The S_2 discrete-ordinates solution did not compare well for any case considered and, if used, should be applied cautiously.

The discrete-ordinates method can easily be adapted to combined absorption and scattering problems without the need for a calculation of complex configuration factors as required by the zone method. In addition, the method is economical and requires a maximum 304 CPU seconds for the largest case considered. This compares with much longer time estimates cited in the literature [26] for the zone method and P-N differential approximations.

References

1 Edwards, R. H., and Bobco, R. P., "Radiant Heat Transfer From Isothermal Dispersions With Isotropic Scattering," ASME JOURNAL OF HEAT TRANSFER, Vol. 89, 1967, pp. 300-308.

2 Armaly, B. F., and El-Baz, H. S., "Influence of the Refractive Index on the Radiative Source Functions of an Isotropically Scattering Medium," *J. Quant. Spectrosc. Radiat. Transfer*, Vol. 18, 1977, pp. 419-424.

3 Usiskin, C. M., and Sparrow, E. M., "Thermal Radiation Between Parallel Plates Separated by an Absorbing-Emitting Nonisothermal Gas," *International Journal of Heat and Mass Trans.*, Vol. 1, 1960, pp. 28-36.

4 Dayan, A., and Tien, C. L., "Heat Transfer in Gray Medium With Linear Anisotropic Scattering," ASME JOURNAL OF HEAT TRANSFER, Vol. 97, 1975, pp. 391-396.

5 Buckius, R. O., and Tseng, M. M., "Radiative Heat Transfer in a Planar Medium With Anisotropic Scattering and Directional Boundaries," *J. Quant. Spectrosc. Radiat. Transfer*, Vol. 20, 1978, pp. 385-402.

6 Buckius, R. O., and King, R., "Diffuse Solar Radiation on a Horizontal Surface for a Clear Sky," *Solar Energy*, Vol. 21, 1978, pp. 503-509.

7 Bergquam, J. B., and Seban, R. A., "Heat Transfer by Conduction and Radiation in Absorbing and Scattering Materials," ASME Journal of Heat Transfer, Vol. 93, 1971, pp. 236–239.

8 Love, T. J., and Grosh, R. J., "Radiative Heat Transfer in Absorbing, Emitting, and Scattering Media," ASME Journal of Heat Transfer, Vol. 87, 1965, pp. 161–166.

9 Siegel, R., and Howell, J. R., *Thermal Radiation Heat Transfer*, 2nd ed., McGraw-Hill, New York, 1981.

10 Taniguchi, H., "The Radiative Heat Transfer of Gas in a Three-Dimensional System Calculated by Monte Carlo Method," *Bull. JSME*, Vol. 12, 1969, pp. 67–78.

11 Hottel, H. C., and Sarofim, A. F., *Radiative Transfer*, McGraw-Hill, New York, 1967.

12 Hottel, H. C., and Cohen, E. S., "Radiant Heat Exchange in a Gas-Filled Enclosure: Allowance for Nonuniformity of Gas Temperature," *AIChE Journal*, Vol. 4, No. 1, 1958, pp. 3–14.

13 Breig, W. F., and Crosbie, A. I., "Two-Dimensional Radiative Equilibrium," *Journal of Mathematical Analysis and Applications*, Vol. 46, No. 1, 1974, pp. 104–125.

14 Modest, M. F., "Two-Dimensional Radiative Equilibrium of a Gray Medium in a Plane Layer Bounded by Gray Nonisothermal Walls," ASME Journal of Heat Transfer, Vol. 96, No. 4, 1974, pp. 483–488.

15 Yuen, W. W., and Tien, C. L., "A Successive Approximation Approach to Problems in Radiative Transfer With a Differential Approximation," ASME Journal of Heat Transfer, Vol. 102, No. 1, 1980, pp. 86–91.

16 Modest, M. F., "Radiative Equilibrium in a Rectangular Enclosure Bounded by Gray Walls," *J. Quant. Spectrosc. Radiat. Transfer*, Vol. 15, No. 6, 1975, pp. 445–461.

17 Chandrasekar, S., *Radiative Transfer*, Oxford at the Clarendon Press, 1950.

18 Carlson, B. G., and Lathrop, K. D., *Transport Theory—The Method of Discrete-Ordinates in Computing Methods in Reactor Physics*, edited by Greenspan, Kelber, and Okrent; Gordon and Breach, New York, 1968.

19 Lathrop, K. D., "Use of Discrete-Ordinate Methods for Solution of Photon Transport Problems," *Nuclear Science and Engineering*, Vol. 24, 1966.

20 Khalil, E., and Truelove, J., "Calculation of Radative Heat Transfer in a Large Gas-Fired Furnace," *Letters in Heat and Mass Transfer*, Vol. 4, Pergamon Press, 1977.

21 Fiveland, W. A., "A Discrete-Ordinates Method for Predicting Radiative Heat Transfer in Axisymmetric Enclosures," ASME Paper No. 82-HT-20, 1982.

22 Spalding, D. B., *GENMIX—A General Computer Program for Two-Dimensional Parabolic Phenomena*, Pergamon Press, New York, 1977.

23 Gosman, A. D., and Pun, W. M., "Documentation for TEACH, A Program for Calculating Laminar or Turbulent Elliptic Flows," Department of Mechanical Engineering, Imperial College, London, 1973.

24 Patankar, S. V., *Numerical Heat Transfer and Fluid Flow*, McGraw-Hill, New York, 1980.

25 Lee, C. E., "The Discrete S_n Approximation to Transport Theory," *Lawrence Livermore Laboratory Report LA2595*, 1962.

26 Ratzel, A., and Howell, J., "Two-Dimensional Radiation in Absorbing-Emitting-Scattering Media Using the P-N Approximation," ASME Paper No. 82-HT-19, 1982.

27 Bayazitoglu, Y., and Higenyi, J., "Higher-Order Differential Equations of Radiative Transfer: P3 Approximation," *AIAA Journal*, Vol. 17, No. 4, 1979.

28 Ratzel, A. C., "P-N Differential Approximation for Solution of One- and Two-Dimensional Radiation and Conduction Energy Transfer in Gray Participating Media," Ph.D. dissertation, Department of Mechanical Engineering, University of Texas at Austin, Austin, Texas, Dec. 1981.

29 Lathrop, K. D., "Ray Effects in Discrete-Ordinates Equations," *Nuclear Science and Engineering*, Vol. 32, 1968.

30 Clark, B. A., "The Development and Application of the Discrete-Ordinates—Transfer Matrix Hybrid Method for Deterministic Streaming Calculations," *Los Alamos Report No. LA9357-T*, Los Alamos National Laboratory, New Mexico, 1982.

31 Shah, N., "New Method of Computation of Radiation Heat Transfer in Combustion Chambers," Ph.D. dissertation, Department of Mechanical Engineering, Imperial College of Science and Technology, University of London, 1979.

K. Sato
Assistant.

K. Miki
Student.

T. Hirano
Associate Professor.

Engineering Research Institute,
Faculty of Engineering,
University of Tokyo,
Tokyo 113, Japan

Flame Spread Over Paper in an Air Stream With a Velocity Change

The behavior of downward flame spread over a sheet of filter paper during and after an increase in ambient air velocity was examined. It was shown that the behavior depends not only on the free-stream velocity but also on its rate of change. The extinction mechanisms when the free-stream velocity is instantaneously increased from that for steady flame spread to that above the steady flame spread limit are discussed, and the conditions for continued flame spreading in an air stream with a velocity fluctuation are pointed out.

Introduction

Flame spread over solid combustibles is a fundamental process during fire growth, so that various groups interested in fire research have been concerned with this subject. As a result of efforts of these groups, flame spread over solid combustibles was found to depend strongly on mass and heat transfer phenomena near the leading flame edge.

Since convection is an important mode of mass and heat transfer near the leading flame edge, many studies have been performed on the effects of the ambient air velocity on the flame spread phenomena [1-13]. In these studies, the flame spread experiments have been performed for a steady, laminar air stream.

Under real fire conditions, however, the ambient air stream rarely remains steady. Thus knowledge of flame spread in a steady, laminar air stream cannot be directly applied to the prediction of real fire hazards without assuming the effect of an unsteady air stream. Unfortunately, there are few available data concerning such effects.

The present study has been conducted to examine the behavior of downward flame spread over a sheet of filter paper in an upward air stream during and after a velocity change. The extinction mechanisms when the free-stream velocity is instantaneously increased from that for stable flame spread to that above the stable flame-spread limit are discussed and the conditions for flame spreading in an air stream with velocity fluctuations are pointed out.

Experiment

The experiment was conducted in 25-cm-long vertical duct having a 10 cm × 10 cm cross section. The duct was mounted on the top of the converging nozzle of a wind tunnel (Fig. 1) [3-6]. The flame spread phenomena were observed through two optical Pyrex plates serving as duct walls parallel to the paper surface.

The air stream flowing upward in the duct was generated by a blower. The flow rate, i.e., the stream velocity in the duct, was controlled by changing the suction area of the blower. By using this control system, the air stream velocity in the duct could be changed easily with appropriate accuracy. The changing velocity was measured by a hot wire anemometer with the paper removed.

The sheets of filter paper used for the experiments had a surface area of 15 cm × 23 cm and were 0.017 cm, 0.026 cm, and 0.036 cm thick. These sheets were dried for more than 48 hrs in a desiccator and placed along the center of the duct.

Each paper sheet was ignited within 3 min after being taken from the desiccator. An electrically heated nichrome wire was used as an ignition system to simultaneously ignite the top edge of the paper [3-6]. The ignition system was removed just after the paper was ignited to minimize disturbance of the ambient atmosphere during the test.

The air stream velocity was changed when the leading flame edge reached a position 14 cm from the upstream end of the paper sheet. The flame spread phenomena were recorded by using a motor-driven, 35-mm camera and a video camera with a video recorder.

Results and Discussion

Behavior of Spreading Flames. It is obvious that for a very slow change of the free-stream velocity u_∞, the flame spread phenomenon is independent of the changing rate du_∞/dt and depends only on u_∞. In this case, the flame spread phenomenon depends on u_∞ similar to that in a steady, laminar air stream. As an example, the variation of the mean flame spread rate $\bar{V}$ with u_∞ for typical filter paper is shown in Fig. 2. Besides this example, various aspects of the flame spread over solid combustibles in a steady, laminar air stream have been elucidated in many previous studies [1-11] and are well known.

As du_∞/dt was increased, its effects on flame spread phenomena became evident. When u_∞ was instantaneously increased from $u_{\infty 1}$ for stable spread to $u_{\infty 2}$, the behavior of

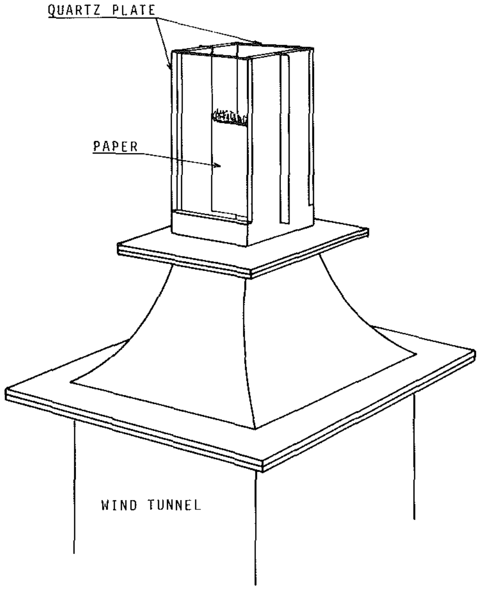

Fig. 1 Vertical duct

Contributed by the Heat Transfer Division and presented at the 21st National Heat Transfer Conference, Seattle, Washington, July 24-27, 1983. Manuscript received by the Heat Transfer Division October 10, 1983.

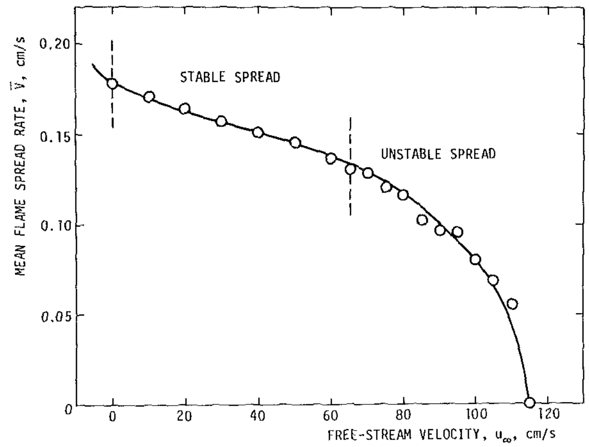

Fig. 2 Variation of mean flame spread rate with free-stream velocity; paper thickness $\delta = 0.026$ cm

the spreading flame was observed to depend on the value of $u_{\infty 2}$ (Fig. 3).

After an instantaneous change of u_∞ between two values for steady flame spread, i.e., both $u_{\infty 1}$ and $u_{\infty 2}$ being for stable flame spread, it took a few seconds until the flame spread phenomena became almost the same as those for $u_{\infty 2}$ under steady conditions. An example of this process is shown in Fig. 3(*a*) as a series of photographs. The time needed to change the flame spread phenomena from those for $u_{\infty 1}$ to those for $u_{\infty 2}$ under steady conditions was observed to increase with the paper sheet thickness.

When u_∞ was instantaneously increased from $u_{\infty 1}$ to $u_{\infty 2}$ for unstable flame spread, the leading flame edge remained horizontal just after the velocity change. At this instant, the brightness of the residual carbon zone just behind the pyrolysis zone was observed to increse. Then the flame became small. At a few seconds after the velocity change, extinction occurred over a large part of the paper sheet. A typical series of photographs representing the extinction process in this case is shown in Fig. 3(*b*).

For an instantaneous change of u_∞ from $u_{\infty 1}$ to $u_{\infty 2}$ just above the flame spread limit, similar extinction behavior was observed. Complete extinction occurred a few seconds after the velocity change. For larger values of $u_{\infty 2}$, the extinction time τ_e from the time of velocity change to extinction was reduced and the pyrolysis zone length, the distance between leading and trailing edges, increased.

At still larger values of $u_{\infty 2}$, the flame was blown off and stopped spreading at the instant of the velocity change. In this case, after blow-off the residual carbon continued to glow and consume the trailing part of the pyrolysis zone. A typical series of photographs representing the extinction process in this case is shown in Fig. 3(*c*).

For convenience of interpretation, $u_{\infty *}$, $u_{\infty **}$, $u_{\infty ***}$, Δt_d, and $(du_\infty/dt)_+$ are introduced.

Figure 4 illustrates typical transitions from stable flame spread to extinction for a sudden increase of the ambient air velocity ($(du_\infty/dt) >> (du_\infty/dt)_+$). Figure 4(*a*) shows the observed delayed extinction for $u_{\infty ***} > u_{\infty 2} > u_{\infty *}$. In this case, as one also observes from the experimental studies of liquid fuel combustion in an air stream [14, 15], following the velocity change the leading flame edge shifts slightly downstream and the flame approaches to the pyrolysis zone surface. Subsequently, the pyrolysis zone length s_p decreases and the flame becomes shorter. Finally, extinction occurs. Figure 4(*b*) shows the events for extinction at $u_{\infty 2} > u_{\infty ***}$. In this case, the leading flame edge is blown off at the instant of velocity change. Although the trailing part of the pyrolysis zone as well as the residual carbon continued to glow after the blow off, most of the pyrolysis zone remained.

The extinction process must be closely related to the temperature and fuel gas concentration profiles near the leading flame edge, which are expected to depend mainly on $u_{\infty 2}$ and the pyrolysis zone length s_{p01} before the velocity change. Since s_{p01} depends on u_∞ and δ, the extinction process is considered to depend on $u_{\infty 1}$, $u_{\infty 2}$, and δ. The time τ_e from

Nomenclature

D = Damköhler number
D_* = critical Damköhler number
$\left(\frac{du_\infty}{dt}\right)_+$ = critical rate of the free-stream velocity change for $\Delta t_d = 0$
$\left(\frac{du_\infty}{dt}\right)_{\mathrm{I,II}}$ = $(u_{\infty 2} - u_{\infty 1})/(t_2 - t_1)$
g_t = function of δ and $u_{\infty 2}$
l_e = extinction width
l_t = initial burning zone width
m = constant
$\dot{q}_p''$ = heat flux to the pyrolysis zone
s_p = pyrolysis zone length, the distance between leading and trailing edges
s_{p0} = pyrolysis zone length for steady flame spread
s_{p*} = critical pyrolysis zone length for blow off
T = period much greater than the characteristic time for fluctuations of u_∞
t = time
u_∞ = free-stream velocity
$u_{\infty *}$ = free-stream velocity beyond which a series of local blow-offs was observed resulting significant distortion of the leading flame edge
$u_{\infty **}$ = free-stream velocity beyond which extinction eventually occurs
$u_{\infty ***}$ = free-stream velocity beyond which immediate extinction occurs
$\bar{V}$ = mean flame spread rate
V_l = spread rate of the leading pyrolysis zone edge
V_t = spread rate of the trailing pyrolysis zone edge
Δt_d = time from the finish of the free-stream velocity increase to the initiation of extinction
δ = thickness of paper
ρ = density of paper
τ_{ch} = characteristic time for a reaction
τ_e = time from the velocity change to extinction
τ_{re} = characteristic residence time for some gaseous element in the flow

Subscripts

1 = before free-stream velocity increase
2 = after free-stream velocity increase
3 = after free-stream velocity decrease from $u_{\infty 2}$
I = state before free-stream velocity increase
II = state after free-stream velocity increase
III = state after free-stream velocity decrease from $u_{\infty 2}$

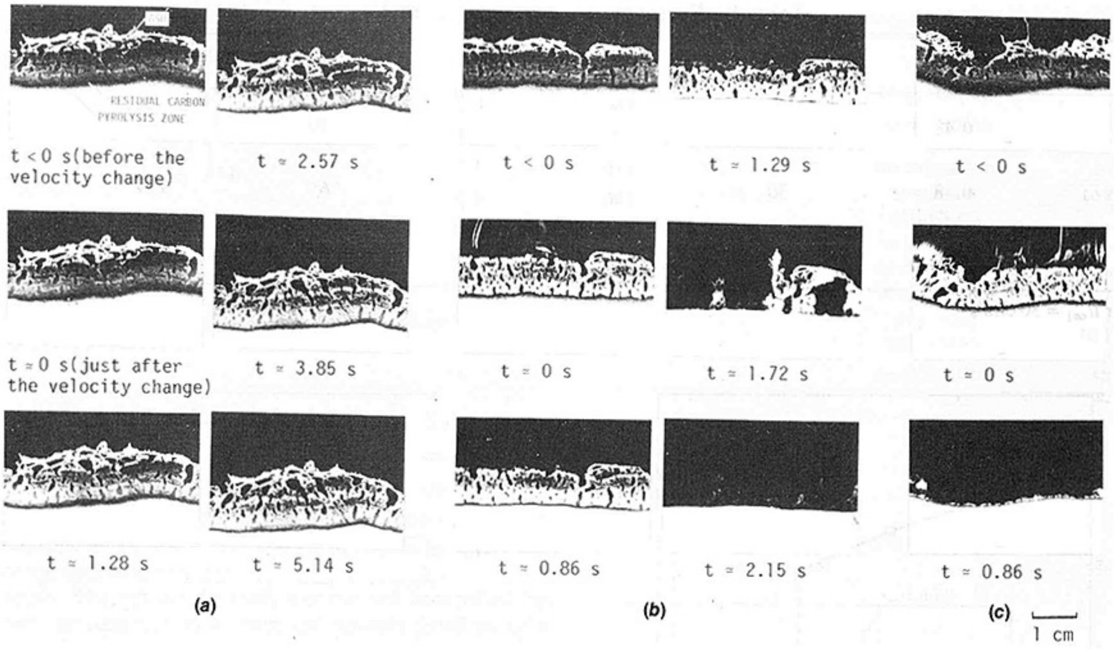

Fig. 3 Typical series of photographs of burning paper sheets when the free-stream velocity u_∞ was instantaneously increased from 30 to (*a*) 50 cm/s; to (*b*) 100 cm/s; and to (*c*) 160 cm/s; $\delta = 0.026$ cm

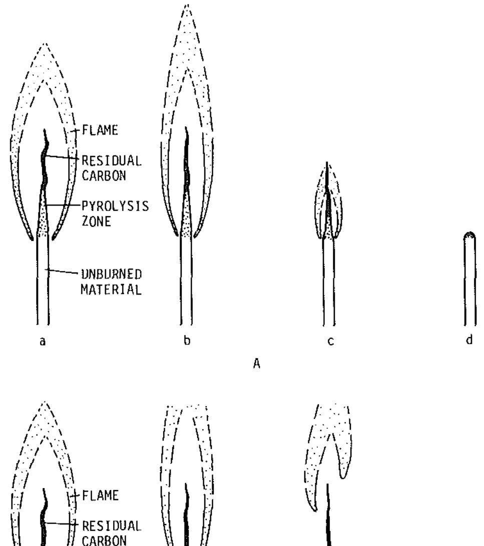

Fig. 4 Processes from stable flame spread to extinction, A: $u_{\infty *} \geq u_{\infty 1}, U_{\infty ***} \geq u_{\infty 2} > u_{\infty *}, (du_\infty/dt) >> (du_\infty/dt)_+$; B: $u_{\infty *} \geq u_{\infty 1}, u_{\infty 2} > U_{\infty ***}, (du_\infty/dt) >> (du_\infty/dt)_+$; a: before the velocity change; b: just after the velocity change; c, d: subsequent processes

the velocity change to extinction is a measurable quantity that is representative of the extinction process. Thus the effects of $u_{\infty 1}$, $u_{\infty 2}$, and δ on τ_e were examined, and the results are shown in Figs. 5 and 6, and Table 1.

Figure 5 shows how τ_e decreases with the increase of $u_{\infty 1}$. In this case, $u_{\infty 1}$ is lower than $u_{\infty *}$. Figure 6 shows that τ_e also decreases with the increase of $u_{\infty 2}$ and suddenly becomes negligibly small (i.e., the transition from the delayed extinction to instantaneous extinction occurs). Typical measured values of τ_e under various conditions are presented in Table 1. The measured value of $u_{\infty *}$, $u_{\infty **}$, and $u_{\infty ***}$ are also presented in the table. Apparently, the increase of τ_e with δ under similar conditions is related to the continued consumption of the pyrolysis zone after the velocity change.

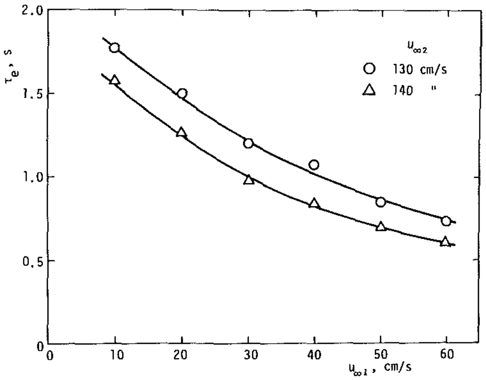

Fig. 5 Dependence of τ_e on $u_{\infty 1}$; $\delta = 0.026$ cm

In general, real fires involve various rates of change of the ambient air velocities. Accordingly, we examined the effects of the velocity rate du_∞/dt on flame spread phenomena. Figure 7 shows some typical results. In each case, u_∞ was increased from $u_{\infty 1}$ for stable flame spread to $u_{\infty 2}$ for unstable flame spread, i.e., $u_{\infty **} \geq u_{\infty 2} > u_{\infty *}$.

We examined the ratio of the extinction width l_e to the initial burning zone width l_t away from the side walls as a measure of the effects of du_∞/dt. One cm from each side wall was excluded from the observations of l_t, so that $l_t = 8$ cm. u_∞, at which extinction starts, depends on du_∞/dt. For a large value of du_∞/dt, extinction starts to occur after the finish of the velocity change. The time Δt_d from the finish of the velocity change to the initiation of local extinction decreases for smaller values of du_∞/dt. For even smaller values extinction starts to occur during the velocity change itself.

Since for small values of du_∞/dt, the flame spread

Table 1 Examples of τ_e, $u_{\infty *}$, $u_{\infty **}$, and $u_{\infty ***}$

thickness δ,cm	density ρ,g/cm^3	$u_{\infty 1}$ cm/s	$u_{\infty 2}$ cm/s	τ_e s	$u_{\infty *}$ cm/s	$u_{\infty **}$ cm/s	$u_{\infty ***}{}^a$ cm/s
0.017	0.48	30	160	0.5	90	140	210–220
			200	0.4			
0.026	0.48		110	1.5	65	115	140–150
			140	1.0			
0.036	0.46		120	2.9	60	95	>240
			200	1.0			

^{a}value for $u_{\infty 1} = 30$ cm/s

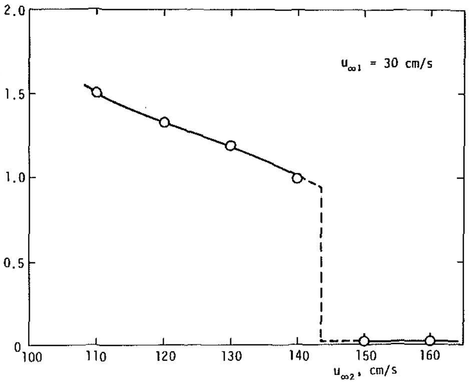

Fig. 6 Dependence of τ_e on $u_{\infty 2}$; $\delta = 0.026$ cm

phenomena obviously depend only on u_∞ as mentioned previously, the flame after the velocity change must continue to spread if $u_{\infty 2} \leq u_{\infty **}$. On the other hand, for a large value of du_∞/dt, complete extinction occurs in some cases even though $u_{\infty 2} \leq u_{\infty **}$. This can be understood by considering the stability for horizontal burning zone [5, 16].

Extinction Mechanisms. It is well known that extinction must occur if the Damköhler number D is reduced from D for a state of continuing combustion to a value below D$_*$ for extinction [17, 18]. D is generally defined as the ratio of the residence time τ_{re} for some gaseous element in the flow to the chemical time τ_{ch} for a reaction, i.e.,

$$D = \frac{\tau_{re}}{\tau_{ch}} \qquad (1)$$

Thus extinction may occur due to either the decrease of τ_{re} or the increase of τ_{ch}.

At the leading flame edge, where the whole flame is anchored, the decrease of τ_{re} must be caused by the velocity increase across the leading flame edge and the increase of τ_{ch} must be caused by the temperature decrease and/or the fuel gas concentration departure from that for the peak chemical reaction rate. When the ambient air velocity is increased, the gas velocity at the leading flame edge may increase and the temperature and the fuel gas concentration at the leading flame edge may decrease due to the flame shifting and quenching. Thus when the ambient velocity increases, one expects D to decrease. Delayed extinction presumably occurs when D remains above D$_*$ just after the velocity change but subsequently becomes less than D$_*$. On the other hand, instantaneous extinction presumably occurs when D becomes less than D$_*$ just after the velocity change.

For steady flame spread over a solid combustible, the conditions at the leading flame edge depend on u_∞ and are closely related to the pyrolysis zone length s_p. The critical pyrolysis zone lengths s_{p*} for blow-off for each value of u_∞ are shown in Fig. 8. The figure also shows the variation of s_{p0} for steady flame spread.

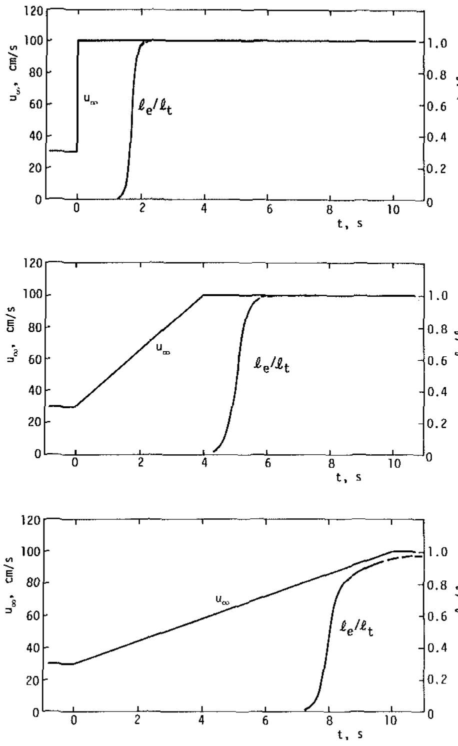

Fig. 7 Extinction aspects for various rates of the free-stream velocity change; $\delta = 0.026$ cm

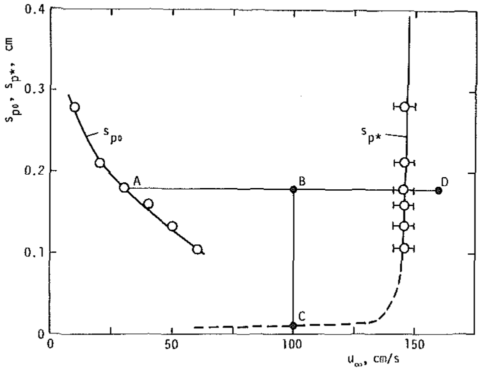

Fig. 8 Examples of experimentally observed values of s_{p0} and s_{p*}; $\delta = 0.026$ cm

When u_∞ is instantaneously increased from $u_{\infty 1}$ to a value of $u_{\infty 2}$ lying between $u_{\infty *}$ and $u_{\infty ***}$, the state will change along a line $\overline{AB}$ and $\overline{BC}$ shown in Fig. 8. In this case, the delayed extinction will occur at the point C, and τ_e corresponds to the time needed to consume the pyrolysis zone from the point B to the point C. When u_∞ is instantaneously

Table 2 A typical example of the results of discussion on the conditions for continued flame spreading

State I	$(du_\infty/dt)_{I,II}$ [a]	$u_{\infty 2}$	Δt_{II} [b]	State II	State III
stable spread $u_{\infty 1} < u_{\infty *}$	$\left(\frac{du_\infty}{dt}\right)_{I,II} >> \left(\frac{du_\infty}{dt}\right)_+$	$u_{\infty 2} > u_{\infty ***}$	—	to extinction	—
		$u_{\infty ***} \geq u_{\infty 2} > u_{\infty **}$	$\Delta t_{II} \geq \Delta t_d$	to extinction	—
			$\Delta t_{II} < \Delta t_d$	no extinction	stable spread
		$u_{\infty **} \geq u_{\infty 2} > u_{\infty *}$	$\Delta t_{II} \geq \Delta t_d$	to partial extinction	to stable spread
			$\Delta t_{II} < \Delta t_d$	no extinction	stable spread
		$u_{\infty 2} \leq u_{\infty *}$	—	no extinction	stable spread
	$\left(\frac{du_\infty}{dt}\right)_{I,II} << \left(\frac{du_\infty}{dt}\right)_+$	$u_{\infty 2} > u_{\infty **}$	—	to extinction	—
		$u_{\infty **} \geq u_{\infty 2} > u_{\infty *}$	—	to partial extinction	to stable spread
		$u_{\infty 2} \leq u_{\infty *}$	—	no extinction	stable spread

[a] $(du_\infty/dt)_{I,II} = (u_{\infty 2} - u_{\infty 1})/(t_2 - t_1)$

[b] $\Delta t_{II} = t_3 - t_2$

increased from $u_{\infty 1}$ to a value of $u_{\infty 2}$ larger than $u_{\infty ***}$, the state will change along a line $\overline{AD}$ shown in Fig. 8. In this case, instantaneous extinction occurs.

In principle, the extinction mechanisms are controlled by the detailed temperature and chemical species profiles in a volume including the spreading flame. However, one has insufficient information for predicting these profiles. Fortunately, as one might expect from the foregoing discussion, the extinction mechanisms can be further elucidated by considering the variation of s_p. In the analysis, the following assumptions are made on the basis of the experimental results or for the simplification of the analysis.

(*i*) The leading pyrolysis zone edge is horizontal and straight.

(*ii*) u_∞ increases instantaneously from $u_{\infty 1}$ to $u_{\infty 2}$.

(*iii*) When s_p becomes less than s_{p*}, blow-off occurs.

(*iv*) Both the velocity V_l of the leading pyrolysis zone edge and that V_t of the trailing pyrolysis zone edge are functions of s_p, δ, and $u_{\infty 2}$.

The changing rate ds_p/dt of s_p can be expressed as

$$\left.\begin{aligned} \frac{ds_p}{dt} &= V_l - V_t \qquad \text{for } s_p \geq s_{p*} \\ &= 0 \qquad\qquad\quad \text{for } s_p < s_{p*}\,. \end{aligned}\right\} \tag{2}$$

The right-hand side of equation (2) is independent of t (Assumption (*iv*)), so that τ_e, which corresponds to the time needed to change s_p from s_{p01}, defined as s_{p0} at $u_{\infty 1}$, to s_{p*} can be calculated as

$$\left.\begin{aligned} \tau_e &= \int_{s_{p01}}^{s_{p*}} \left(\frac{1}{V_l - V_t}\right) ds_p \qquad \text{for } s_{p01} \geq s_{p*} \\ &= 0 \qquad\qquad\qquad\qquad\quad\; \text{for } s_{p01} < s_{p*} \end{aligned}\right\} \tag{3}$$

As $u_{\infty 2} > u_{\infty *}$, the heat removed from the solid surface just in front of the leading pyrolysis zone edge increases rapidly and becomes larger than the heat transferred to the same zone from the flame or through the solid interior, so that V_l becomes almost 0. In this case, V_l can be assumed to be 0. Furthermore, V_t is assumed to be expressed as

$$V_t = s_p{}^m g_t(\delta, u_{\infty 2}), \tag{4}$$

where m is a constant. m must depend on heat flux $\dot{q}_p''$ to the pyrolysis zone, so that m is related to the flame location. In the present case, the absolute value of m is assumed to be much less than unity [15, 19]. Then the right-hand side of equation (3) can be easily integrated and the following relation is obtained.

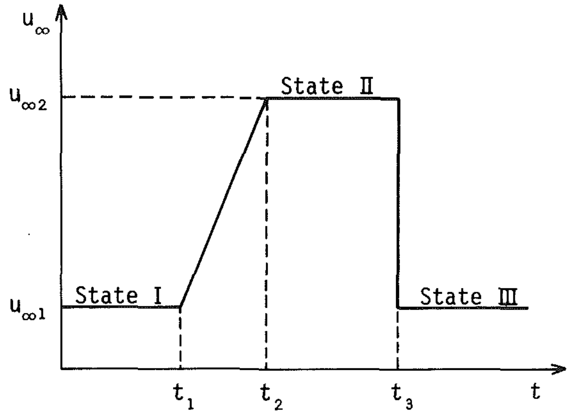

Fig. 9 Simple model of velocity fluctuation

$$\left.\begin{aligned} \tau_e &= \frac{1}{(1-m)g_t}\left(s_{p01}{}^{1-m} - s_{p*}{}^{1-m}\right) \qquad \text{for } s_{p01} \geq s_{p*} \\ &= 0 \qquad\qquad\qquad\qquad\qquad\qquad\quad\; \text{for } s_{p01} < s_{p*} \end{aligned}\right\} \tag{5}$$

Since V_t is positive, g_t must be positive. Thus equation (5) means that τ_e increases with s_{p01}.

s_{p01} increases as $u_{\infty 1}$ decreases or as δ increases. Therefore, it can be inferred from equation (5) that τ_e increases with the decrease of $u_{\infty 1}$ or the increase of δ. These results are qualitatively consistent with the observations shown in Fig. 5 and Table 1.

V_t must increase with increasing heat flux $\dot{q}_p''$. As u_∞ increases, $\dot{q}_p''$ increases until blow-off, because the flame approaches the pyrolysis zone surface. Thus g_t must increase with $u_{\infty 2}$. From this fact and equation (5), it can be inferred that τ_e decreases as $u_{\infty 2}$ increases. These results are again consistent with those shown in Figs. 5 and 6 as well as those shown in Table 1.

Conditions for Continued Flame Spreading. To increase the knowledge of flame spread over solid combustibles in an unsteady or turbulent air stream, it seems very important to explore the conditions for continued flame spreading in a fluctuating air stream.

If the extinction conditions discussed in the previous sections never occur during flame spread, the flame will continue to spread. For example, the flame continues to spread when a simple fluctuation of the ambient air stream occurs as shown in Fig. 9. The conditions for continued flame spreading are shown in Table 2.

The ambient air stream velocity $u_{\infty 1}$ is below $u_{\infty *}$ (State I in Fig. 9). From time t_1, it steadily increases until it reaches $u_{\infty 2}$

at time t_2 (State II). Then, at the time t_3, the ambient air stream velocity decreases instantaneously to $u_{\infty 1}$ (for State III).

When $(du_\infty/dt)_{\mathrm{I,II}}$, during the transition from the State I to the State II, is much larger than $(du_\infty/dt)_+$, extinction at State II occurs not only for $u_{\infty 2} > u_{\infty ***}$, but also for $u_{\infty ***} \geq u_{\infty 2} > u_{\infty **}$, and sometimes, even for $u_{\infty **} \geq u_{\infty 2} > u_{\infty *}$, provided $\Delta t_{\mathrm{II}} = t_3 - t_2 > \Delta t_d$. Under other conditions the flame continues to spread after reaching the State III.

The most significant cases are for $u_{\infty ****} \geq u_{\infty 2} > u_{\infty ***}$ and $\Delta t_{\mathrm{II}} < \Delta t_d$ and for $u_{\infty **} \geq u_{\infty 2} > u_{\infty *}$ and $\Delta t_{\mathrm{II}} > \Delta t_d$. The former is the case of a short duration high velocity, when the flame can continue to spread even for $u_{\infty 2} > u_{\infty ***}$. The latter is the case of a long duration high velocity, when extinction may occur even if $u_{\infty **} > u_{\infty 2}$. As mentioned in the previous section, sometimes complete extinction occurs in this case.

In a recent theoretical study for flame spread along polymeric solids, Carrier et al. proposed the possibility of resumption of burning after short interval of enhanced flow (causing extinction of flame) [20].

When $(du_\infty/dt)_{\mathrm{I,II}}$ is much smaller than $(du_\infty/dt)_+$, the flame spread phenomena are similar to those of steady spread [5].

If extinction does not occur the flame spread rate must be evaluated. The flame spread rate can be considered approximately equal to V_l. If u_∞ is given as a function of t, V_l must be given as a function of t and δ. Consequently, the mean flame spread rate $\bar{V}$ must be calculated as follows.

$$\bar{V} = \frac{1}{T}\int_0^T V_l dt \tag{6}$$

where T is a period much greater than the characteristic time for fluctuations of u_∞. The dependence of V_l on t for each value of δ can be elucidated only when the temperature and chemical species profiles at every instant are revealed. Unfortunately, available data at present are not sufficient, so that $\bar{V}$ cannot be predicted.

Conclusions

Behavior of downward flame spread over a sheet of filter paper during and after a change in velocity of the upward ambient air stream has been explored.

When the free-stream velocity u_∞ was instantaneously increased from that for stable flame spread, two modes of extinction were observed. One was delayed extinction caused by the consumption of the pyrolysis zone, and the other was instantaneous extinction caused by the high air stream velocity near the leading flame edge. The time τ_e from the instantaneous velocity change to extinction was found to increase with the decrease of $u_{\infty 1}$ or $u_{\infty 2}$ (i.e., u_∞, respectively, before or after the velocity change), or with an increase of the paper thickness δ.

For a small rate of increase in velocity, du_∞/dt, flame spread phenomena were shown to depend only on u_∞. The flame after the velocity change was observed to continue spreading if $u_{\infty **} \geq u_{\infty 2}$, i.e., u_∞ after the velocity change was below that of the flame-spread limit in a steady, laminar air stream. On the other hand, for a large value of du_∞/dt, complete extinction occurred even in some cases when $u_{\infty **} \geq u_{\infty 2}$.

The extinction mechanisms were discussed in terms of the Damköhler number, and the conditions at the leading flame edge, where the whole flame is anchored, and were shown to be closely related to u_∞ and the pyrolysis zone length s_p. According to this discussion, a brief analysis was performed on the pyrolysis zone behavior. Most of the experimentally observed results were shown to be consistent with results of this analysis.

The conditions for continued flame spread have been inferred by using a simple velocity fluctuation model of the ambient air stream. For a short duration of high velocity, the flame was shown to spread even when the peak velocity was above the flame-spread limit for steady spread.

Acknowledgment

The authors are indebted to Messrs. H. Ohtani, R. Dobashi, T. Tsuruda, and M. Minami for their discussions and help in conducting this study.

References

1 Perrins, L. E., and Pettet, K., "Measurement of Flame Spread Velocities," *Journal of Fire and Flammability*, Vol. 5, 1974, pp. 85–102.

2 Sibulukin, M., Hetelhut, W., and Feldman, S., "Effect of Orientation and External Flow Velocity on Flame Spreading Over Thermally Thin Paper Strips," *Combustion Science and Technology*, Vol. 9, 1974, pp. 75–77.

3 Hirano, T., and Sato, K., "Effects of Radiation and Convection on Gas Velocity and Temperature Profiles of Flames Spreading Over Paper," *Proceedings of the Fifteenth Symposium (International) on Combustion*, The Combustion Institute, Pittsburgh, Pa., 1975, pp. 233–241.

4 Hirano, T., and Tazawa, K., "Effect of Thickness on Downward Flame Spread Over Paper," *Bulletin of Japanese Association of Fire Science and Engineering*, Vol. 26, 1976, pp. 7–13.

5 Hirano, T., Sato, K., and Tazawa, K., "Instability of Downward Flame Spread Over Paper in an Air Stream," *Combustion and Flame*, Vol. 26, 1976, pp. 191–200.

6 Tazawa, K., and Hirano, T., "Upward Flame Spread Over Paper in an Air Stream," *Bulletin of Japanese Association of Fire Science and Engineering*, Vol. 27, 1977, pp. 9–16.

7 Fernandez-Pello, A. C., Ray, S. R., and Glassman, I., "Downward Flame Spread in an Opposed Forced Flow," *Combustion Science and Technology*, Vol. 19, 1978, pp. 19–30.

8 Kayayan, K. M., "Flame Spread in Opposed Laminar Flow," Master's thesis, University of California, Berkeley, 1978.

9 Fernandez-Pello, A. C., "Flame Spread in a Forward Forced Flow," *Combustion and Flame*, Vol. 36, 1979, pp. 63–78.

10 Fernandez-Pello, A. C., and Mao, C. P., "A Unified Analysis of Concurrent Modes of Flame Spread," *Combustion Science and Technology*, Vol. 26, 1981, pp. 147–155.

11 Fernandez-Pello, A. C., Ray, S. R., and Glassman, I., "Flame Spread in an Opposed Flow: The Effect of Ambient Oxygen Concentration," *Proceedings of the Eighteenth Symposium (International) on Combustion*, The Combustion Institute, Pittsburgh, Pa., 1981, pp. 579–589.

12 Wichman, I. S., Williams, F. A., and Glassman, I., "Theoretical Aspects of Flame Spread in an Opposed Flow Over Flat Surfaces of Solid Fuels," *Proceedings of the Nineteenth Symposium (International) on Combustion*, The Combustion Institute, Pittsburgh, Pa., 1983, pp. 835–845.

13 Borgeson, R. A., "Flame Spread and Spread Limits," NBS. GCR, 82-396, July, 1982.

14 Udelson, D. G., "Geometrical Considerations in the Burning of Liquid Drops," *Combustion and Flame*, Vol. 6, 1962, pp. 93–102.

15 Hirano, T., and Kinoshita, M., "Gas Velocity and Temperature Profiles of a Diffusion Flame Stabilized in the Stream Over Liquid Fuel," *Proceedings of the Fifteenth Symposium (International) on Combustion*, The Combustion Institute, Pittsburgh, Pa., 1975, pp. 379–387.

16 Emmons, H. W., and Shen, T., "Fire Spread in Paper Arrays," *Proceedings of the Thirteenth Symposium (International) on Combustion*, The Combustion Institute, Pittsburgh, Pa., 1971, pp. 917–926.

17 Fendell, F. E., "Ignition and Extinction in Combustion of Initially Unmixed Reactants," *J. Fluid Mechanics*, Vol. 21, 1965, pp. 281–303.

18 Tsuji, H., "Counter Flow Diffusion Flames," *Progress of Energy and Combustion Science*, Vol. 8, 1982, pp. 93–119.

19 Hirano, T., Koshida, T., and Akita, K., "Flame Spread Mechanisms Over PMMA Surfaces," *Bulletin of Japanese Association of Fire Science and Engineering*, Vol. 27, 1977, pp. 33–39.

20 Carrier, G, Fendell, F., Feldman, P., and Fink, S., "Forced-Convection Extinction of a Diffusion Flame Sustained by a Charing Body," *Combustion Science and Technology*, Vol. 28, 1982, pp. 271–304.

C. H. Chen

J. S. T'ien
Mem. ASME

Department of Mechanical
and Aerospace Engineering,
Case Western Reserve University,
Cleveland, Ohio 44106

Fire Plume Along Vertical Surfaces: Effect of Finite-Rate Chemical Reactions

Fire plume along a vertical wall is analyzed using a laminar boundary layer model, including finite-rate, gas-phase chemical kinetics. The chemical reactions include two semiglobal steps: In the first, fuel is oxidized to form carbon monoxide and water vapor, and in the second, carbon monoxide is oxidized to form carbon dioxide. Several important nondimensional kinetic parameters are identified and a parametric study is given. The computed results indicate that by slowing down the relative kinetic rates in the gas-phase reactions, the total surface heat transfer rate and the preheating distance are decreased. Furthermore, slowing down the kinetics also increases the amount of unreacted combustibles that escape from the flame.

Introduction

A fire burning on an upright surface can be divided into three regions: (*i*) a pyrolysis region, where the wall material is gasified and partly burned in the gas phase adjacent to the surface; (*ii*) the combustion plume region, where combustion is maintained by the gaseous fuels convected from the upstream pyrolysis zone; and (*iii*) the thermal plume region, where combustion reactions cease and the reaction products are cooled by mixing with the ambient gas and heat loss to the surface. The latter two regions constitute the fire plume. The fire plume plays an important role in fire growth and upward flame spreading processes because it determines the heat flux level to the unburnt fuel surface, which, in turn, controls the fire growth rate. Furthermore, the quenching of chemical reactions near the tip of the combustion plume results in the escape of the unburnt fuel or combustion intermediates from the flame that produces them. These escaped pyrolyzates can either constitute as air pollutants or serve as fuels to be burnt later elsewhere (such as in the smoke layer in a room). Thus the study of the fire plume can have a number of practical implications to fire research.

The present investigation of fire plumes is triggered by the work of Ahmad and Faeth [1] on the same subject. In that work, the laminar overfire region along upright surfaces was investigated both theoretically and experimentally. In the experiment, the pyrolysis zone was simulated by burning fuel-soaked wicks. Heat flux to the wall and flame shapes were measured. The corresponding theory assumed naturally convective laminar boundary layer flow and infinite-fast chemical reaction. Nonsimilar solutions were obtained numerically. Comparisons between theory and experiment on wall heat flux were in general good, but the authors noted that the largest discrepency occurred near the flame tip where flame quenching occurred. Photographs also showed that the visible flame failed to reattach itself to the wall in the downstream as predicted by the thin-diffusion-flame theory. Ahmad and Faeth [1] suggested that finite rate chemical effects should be important in the flame tip region.

Pagni and Shih [2] formulated and solved a boundary layer model for excess pyrolyzates. Excess pyrolyzates are defined as the gaseous fuels which are not consumed by the flame at the location of their generation but are convected downstream. In [2], Pagni an Shih computed the ratio of excess pyrolyzates to the total amount of fuel pyrolyzed using an infinite-fast chemical kinetic model. They found that excess pyrolyzates were a strong function of the mass consumption number, and they also depended on the mass transfer number although to a much less extent.

The point to be noted is that the amount of excess pyrolyzates at the end of the pyrolysis zone and the amount of unreacted combustibles escaped from the whole flame zone (including the fire plume) cannot be related to each other without specifying additional fundamental parameters. Normally, not all the excess pyrolyzates entering into the fire plume will be oxidized, a portion of them may leave the flame unreacted or partially reacted. The analysis of these unburnt combustibles, referred here as the "escaped pyrolyzates," requires the inclusion of finite-rate chemical kinetics.

In the present work, fire plume along a vertical surface is studied using a laminar boundary layer diffusion flame model. Finite-rate, gas-phase chemical reactions are included. Since the behavior of fire plumes in the infinite-kinetic limit has been discussed in [1] and [2], the emphasis of the present work is on those aspects where finite rate chemical kinetics play an essential role.

Fire Plume Model

The flow configuration to be analyzed is shown schematically in Fig. 1. To illustrate the difference between this and the previous works, the infinite kinetic representation is shown on the left-hand side of Fig. 1. The flame sheet is originated at the leading edge of the pyrolysis zone and reattaches itself to the wall in the downstream. Inside the flame surface, the oxygen mass fraction Y_O is zero and outside the flame sheet, the fuel mass fraction Y_F is zero. With finite-rate kinetics, the right-hand side of Fig. 1 shows that the visible flame is originated in a flame stabilization zone near the leading edge of the pyrolysis region; it ends in the downstream without touching the wall. Normally, the height of visible flames is shorter than that predicted by the thin flame theory [1]. The majority of escaped pyrolyzates is expected to be from the quenched flame tip region. The origin of the coordinate system is at the leading edge of the pyrolysis zone. The length of the pyrolysis region is shown to be l. The focus of our attention will be on the fire plume region, i.e., $x > l$.

Mathematical Formulation. The assumptions of the analysis are as follows:

- The plume flow can be described by a two-dimensional, steady, naturally-convected, laminar boundary layer; viscous dissipation and radiation are negligible.
- The flow is an ideal gas mixture constant and equal

Contributed by the Heat Transfer Division for publication in the JOURNAL OF HEAT TRANSFER. Manuscript received by the Heat Transfer Division October 4, 1983.

specific heats, equal binary diffusion coefficients, constant Prandtl and Schmidt numbers, and constant value of $\rho\mu$.

- The surface in the plume region is chemically inert and the surface temperature is assumed to be the same as that in the pyrolysis zone.
- The gas phase chemistry are described by a couple of sub-global reactions to be discussed later.

Employing these assumptions, the conservation equations are

$$\frac{\partial(\rho u)}{\partial x}+\frac{\partial(\rho v)}{\partial y}=0 \tag{1}$$

$$\rho u\frac{\partial u}{\partial x}+\rho v\frac{\partial u}{\partial y}=\frac{\partial}{\partial y}\left(\mu\frac{\partial u}{\partial y}\right)+g(\rho_\infty-\rho) \tag{2}$$

$$\rho C_p u\frac{\partial T}{\partial x}+\rho C_p v\frac{\partial T}{\partial y}=\frac{\partial}{\partial y}\left(k\frac{\partial T}{\partial y}\right)-\dot{Q}^* \tag{3}$$

$$\rho u\frac{\partial Y_i}{\partial x}+\rho v\frac{\partial Y_i}{\partial y}=\frac{\partial}{\partial y}\left(\rho D\frac{\partial Y_i}{\partial y}\right)+\dot{\omega}_i^* \tag{4}$$

The boundary conditions at the wall are

$$u=v=\frac{\partial Y_i}{\partial y}=0, T=T_w; y=0 \tag{5}$$

far from the wall

$$u=0, T=T_\infty, Y_O=Y_{O\infty}, Y_i=0;\ y\to\infty \tag{6}$$

Defining the modified Grashof number as

$$\mathrm{Gr}_x=\frac{g(T_f-T_\infty)x^3}{4T_\infty\nu_\infty^2} \tag{7}$$

where T_f is the adiabatic flame temperature and introducing the Howarth-Dorodnitzyn similarity variables

$$\xi=\frac{x}{l}$$

$$\eta=\frac{\mathrm{Gr}_x^{1/4}}{x}\int_0^y\frac{\rho}{\rho_\infty}dy \tag{8}$$

a stream function of the form

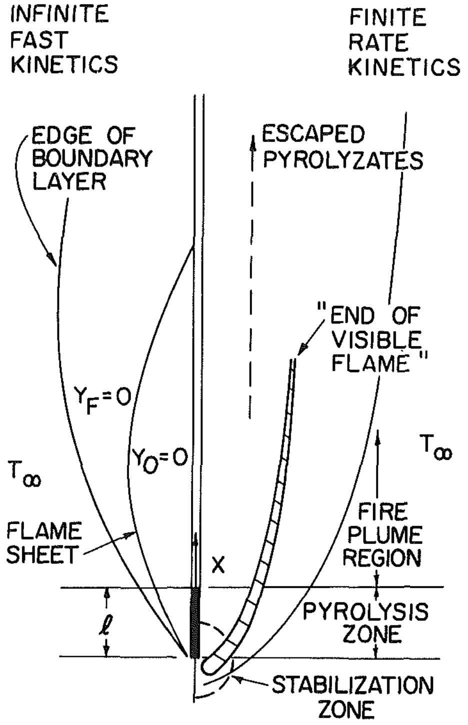

Fig. 1 Schematic configurations of the flame and the fire plume

$$\psi=4\nu_\infty\mathrm{Gr}_x^{1/4}f(\xi,\eta) \tag{9}$$

is used to satisfy equation (1).

$$\rho u=\rho_\infty\frac{\partial\psi}{\partial y}$$

$$\rho v=-\rho_\infty\frac{\partial\psi}{\partial y} \tag{10}$$

Introducing equations (7–10) into equations (1–6) yields the following

Nomenclature

B_i^* = frequency factor for species i oxidation reaction
B_i = nondimensional frequency factor for species i oxidation reaction equations (23) and (24)
B = mass transfer driving potential, $Y_{O\infty}Q^*/M_O\nu_O'L - C_pT_w/L$
C_p = average specific heat
D = diffusion coefficient
E^* = activation energy
E = dimensionless activation energy, E^*/RT_∞
f = dimensionless stream function
Gr_x = modified Grashof number, equation (7)
g = acceleration of gravity
k = thermal conductivity
L = effective heat of vaporization
l = length of pyrolysis zone
N = stoichiometric mass ratio of fuel to oxygen in reaction (R.1)
N_0 = stoichiometric mass ratio of CO to fuel
Pr = Prandtl number
Q^* = overall heat of combustion per unit volume per unit time
q_1^* = heat of reaction per unit mass of fuel in Reaction (R.1)
q_2^* = heat of reaction per unit mass of CO in Reaction (R.2)
$\dot{q}''$ = wall heat flux
T = temperature
R = universal gas constant
Sc = Schmidt number
u = velocity parallel to the fuel surface
v = velocity normal to the fuel surface
$\dot{\omega}^*_i$ = reaction rate for species i
$\dot{\omega}_i$ = nondimensional reaction rate for species i, equations (23) and (24)
x = distance along the fuel surface
Y_i = mass fraction for species i
y = distance normal to fuel surface
η = nondimensional distance normal to the fuel surface, equation (8)
ξ = non-dimensional distance parallel to the fuel surface, equation (8)
θ = nondimensional temperature
μ = dynamic viscosity
ν = kinematic viscosity
ρ = density
ψ = stream function

Subscripts

f = adiabatic flame temperature
F = fuel
O = oxygen
CO = carbon monoxide
w = wall
∞ = ambient
ref = reference

Superscripts

$*$ = dimensional quantity

$$f''' + 3ff'' - 2(f')^2 + \frac{\theta - 1}{\theta_f - 1} = 4\xi\left(f' \frac{\partial f'}{\partial \xi} - f'' \frac{\partial f}{\partial \xi}\right) \tag{11}$$

$$\frac{1}{\mathrm{Pr}}\theta'' + 3f\theta' = 4\xi\left(f' \frac{\partial \theta}{\partial \xi} - \theta' \frac{\partial f}{\partial \xi}\right) + \xi^{1/2}\dot{Q} \tag{12}$$

$$\frac{1}{\mathrm{Sc}}Y_i'' + 3fY_i' = 4\xi\left(f' \frac{\partial Y_i}{\partial \xi} - Y_i' \frac{\partial f}{\partial \xi}\right) - \xi^{1/2}\dot{\omega}_i \tag{13}$$

where the nondimensional heat release rate and reaction rates are given by

$$\dot{Q} = \sqrt{\frac{4l}{g(\theta_f - 1)}}\,\frac{Q^*}{\rho C_p T_\infty} \tag{14}$$

$$\dot{\omega}_i = \sqrt{\frac{4l}{g(\theta_f - 1)}}\,\frac{\dot{\omega}_i^*}{\rho} \tag{15}$$

at the wall ($\eta = 0$)

$$f' = 0,\ f(\xi,0) = \xi^{-3/4} f(1,0), \theta = \theta_w, \frac{\partial Y_i}{\partial \eta} = 0 \tag{16}$$

far from the wall ($\eta \to \infty$)

$$f' = 0, \theta = 1, Y_O = Y_{O\infty}, Y_i = 0 \tag{17}$$

where $(') = \partial/\partial\eta$ and $\theta = T/T_\infty$.

In order to complete the description for the system, the chemical reaction terms in equations (12) and (13) have to be specified.

Finite-Rate Chemical Kinetics. The gas-phase reactions will be represented by two semi global steps. In the first step, the fuel is oxidized to form carbon monoxide and water vapor and, in the second step, carbon monoxide is oxidized to form carbon dioxide. For a fuel with molecular formula $C_n H_m O_p$, the first semiglobal reaction is given by

(R.1):

$$C_n H_m O_p + 1/2(n + m/2 - p)O_2 \to n\mathrm{CO} + m/2H_2O \tag{18}$$

and its reaction rate is assumed to be

$$\frac{\dot{\omega}_F^*}{\rho} = -B_F^* Y_F Y_O \ \mathrm{EXP}\left(-\frac{E_F^*}{RT}\right) \tag{19}$$

Although this reaction rate expression is first order with respect to both the fuel and the oxidizer, generalization to other arbitrary orders presents no difficulty.

The second semiglobal reaction is

(R.2):

$$CO + 1/2O_2 \to CO_2 \tag{20}$$

with rate equation given by [3]

$$\frac{\dot{\omega}_{CO}^{*\prime}}{\rho} = -pB_{CO}^* Y_{CO} Y_O^{1/2} Y_{H_2O}^{1/2} \ \mathrm{EXP}\left(-\frac{E_{CO}^*}{RT}\right) \tag{21}$$

The numerical values of B_{CO}^* and E_{CO}^* can be found from [3]. However, the data gathered in [3] indicate that equation (21) is only good for temperature less than approximately 1280 K. For higher temperatures, the reverse reaction of R.2 (i.e., CO_2 decomposes into CO and O_2) can become significant with the net CO oxidation rate significantly lower than that predicted by equation (21). Therefore, in the present analysis we adopt the following strategy. For temperature below 1280 K, the CO oxidation rate is given by equation (21), and for temperature above 1280 K, the exponential temperature term in equation (21) is set to be equal to that at 1280 K. This limits the unrealisticly high CO oxidation rate at higher temperature. An alternative approach is to include a reverse reaction or reactions. But this has not been tried yet.

Since CO is produced by reaction R.1 and consumed by reaction R.2, the net rate of CO production is

$$\frac{\dot{\omega}_{CO}^*}{\rho} = \frac{\dot{\omega}_{CO}^{*\prime\prime}}{\rho} - N_0 \frac{\dot{\omega}_F^*}{\rho} \tag{22}$$

where N_0 is the stiochiometric mass ratio of CO to fuel in reaction R.1.

Using equations (19), (21), and (22), the nondimensional reaction rates defined in equation (15) become, for fuel,

$$\dot{\omega}_F = -B_F Y_F Y_O \ \mathrm{EXP}\left(-\frac{E_F}{\theta}\right) \tag{23}$$

where

$$B_F = \sqrt{\frac{4l}{g(\theta_f - 1)}}\,B_F{}^*$$

is the nondimensional frequency factor for reaction (R.1), and for CO

$$\dot{\omega}_{CO} = -\frac{B_{CO}}{\theta} Y_{CO} Y_O^{1/2} Y_{H_2O}^{1/2} \ \mathrm{EXP}\left(-\frac{E_{CO}}{\theta}\right) + N_0 B_F Y_F Y_O \ \mathrm{EXP}\left(-\frac{E_F}{\theta}\right) \tag{24}$$

where

$$B_{CO} = \sqrt{\frac{4l}{g(\theta_f - 1)}}\,B_{CO}{}^*$$

is the nondimensional frequency factor for reaction R.2.

The total heat release is the sum of heat of reaction for reactions R.1 and R.2

$$\dot{Q}^* = \dot{\omega}_F^*(q_1^*) + \dot{\omega}_{CO}^{*\prime}(q_2^*)$$

The nondimensional heat release rate is

$$\dot{Q} = -q_1 B_F Y_F Y_O \ \mathrm{EXP}\left(-\frac{E_F}{\theta}\right) - q_2 \frac{B_{CO}}{\theta} Y_{CO} Y_O^{1/2} Y_{H_2O}^{1/2} \ \mathrm{EXP}\left(-\frac{E_{CO}}{\theta}\right) \tag{25}$$

where $q_1 = q_1{}^*/C_p T_\infty$ and $q_2 = q_2{}^*/C_p T_\infty$.

Note that the previous remark on CO oxidation rate above 1280 K is applicable to the first term on the RHS of equation (24) and to the second term on the RHS of equation (25).

Since we will be interested in the escaped pyrolyzates from the flame, an expression for mass flux is derived here. Integrating equation (4) in y and utilizing boundary conditions given by equations (5) and (6), it is found that for fuel and carbon monoxide

$$\frac{\partial}{\partial x}\int_0^\infty \rho u Y_i dy = \int_0^\infty \dot{\omega}_i^* dy \tag{26}$$

The foregoing equation says that the rate of change of mass flux of species i in the x-direction is directly related to its reaction rate. When the reaction rate vanishes (chemically-frozen), the mass flux become constant. Normalized by the mass flux across the initial plane of the fire plume ($\xi = 1$), equation (26), in dimensionless form, becomes

$$\frac{\partial}{\partial \xi}\left[\frac{\left(\int_0^\infty \xi^{3/4} f' Y_i d\eta\right)_\xi}{\left(\int_0^\infty f' Y_i d\eta\right)_{\xi=1}}\right] = \frac{1}{4}\,\frac{\left(\int_0^\infty \dot{\omega}_i d\eta\right)_\xi}{\left(\int_0^\infty f' Y_i d\eta\right)_{\xi=1}} \tag{27}$$

Equation (27) will be used later to find the position in the plume zone where the escaped pyrolyzates can be evaluated.

Numerical Scheme. The system consisting of equations

Table 1 Numerical values of methanol properties

Property	Symbol	Value	Units
Molecular weight	M	32.0	g/Mole
Boiling surface temperature	T_w	337.7	K
Ambient temperature	T_∞	298.0	K
Adiabatic flame temperature	T_f	2070.0	K
Effective heat of vaporization	L	1226.0	J/g
Average specific heat	C_p	1.37	J/g - K
Mass transfer driving potential	$\bar{B}$	2.6	---
Heat of reaction (R1)	q_1^*	12,300.0	J/g-CH_3OH
Heat of reaction (R2)	q_2^*	10,100.0	J/g-CO
Stream function	f(1,0)	-0.3182	---

Table 2 Nondimensional parameters

Parameter	Symbol	Values	Definition
Prandtl number	Pr	0.73	$\mu C_p/k$
Schmidt number	Sc	0.73	$\mu/\rho D$
Adiabatic flame temperature	θ_f	6.95	$\frac{T_f}{T_\infty}$
Surface temperature	θ_w	1.13	$\frac{T_w}{T_\infty}$
Mass Fraction for oxygen in Free Stream	$Y_{O\infty}$	0.231	
Stoichiometric mass ratio of CO to fuel in reaction (R.1)	N_O	0.875	
Stoichiometric mass ratio of O_2 to fuel in reaction (R.2)	N	1	
Heat of reaction (R.1)	q_1	30.12	$\frac{q_1^*}{C_p T_\infty}$
Heat of reaction (R.2)	q_2	24.74	$\frac{q_2^*}{C_p T_\infty}$
Activation energy for Fuel	E_F	variable	$\frac{E_F}{R\ T_\infty}$
Activation energy for CO	E_{CO}	51	$\frac{E_{CO}^*}{R\ T_\infty}$
Frequency factor of fuel oxidation	B_F	variable	$\sqrt{\frac{4\ell}{g(\theta_f-1)}}\ B_F^*$
Frequency factor of CO oxidation	B_{CO}	variable	$\sqrt{\frac{4\ell}{g(\theta_f-1)}}\ B_{CO}^*$

(11-13), (16), (17), (23-25), and initial conditions at $\xi = 1$ (to be discussed later) is mathematically well specified. The boundary layer flow is nonsimilar in nature because (*i*) the initial profiles are derived from the upstream pyrolysis zone where a surface fuel mass flux exists, but in the plume region, the flux drops to zero suddenly; and (*ii*) the gas-phase reactions are finite rate. This system of partial differential equation is solved using a finite difference scheme, marching from upstream to downstream. Details of the numerical scheme and its accuracy check can be found in [4].

Results and Discussion. In the computation performed, many of property values are those for methanol [1] (see Table 1). There are thirteen nondimensional parameters in this system (see Table 2), plus the initial profiles to be specified at $\xi = 1$. Many of the dimensionless parameters are held constant in this study, and their numerical values can be found in Table 2 (they are consistent with the dimensional numbers given in Table 1). The several parameters varied in the parametric study are: B_F and B_{CO}, the nondimensional frequency factors for the fuel and the carbon monoxide oxidation reactions; and E_F, the activation energy for the fuel oxidation reaction.

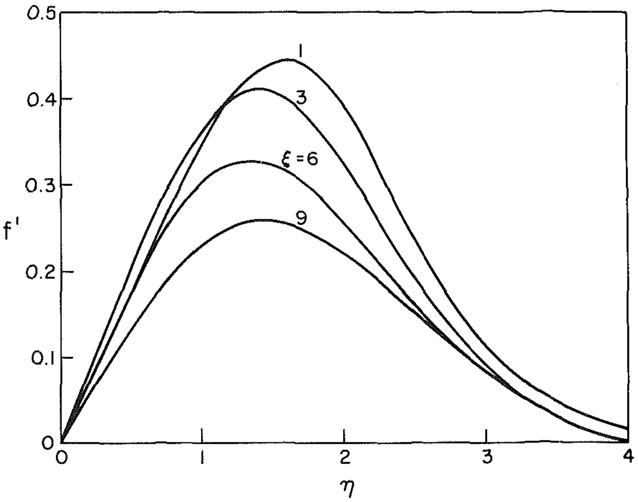

Fig. 2 Velocity profiles (reference case)

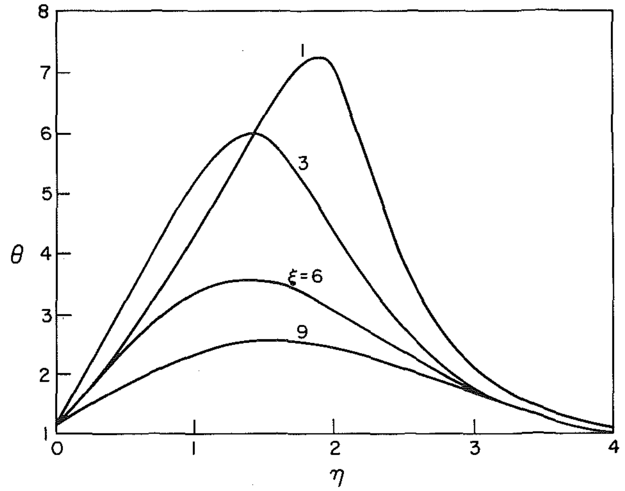

Fig. 3 Temperature profiles (reference case)

The initial profiles specified at $\xi = 1$ require an explanation. The flow properties at $\xi = 1$ depend on the processes occurring upstream. Referring to Fig. 1, the flame is initiated in the stabilization zone. In this zone, the heat conduction to upstream is essential for reaction initiation. Since the flat-plate boundary layer system given by equations (1-4) does not contain this streamwise heat conduction term, it is not appropriate for the flame stabilization region. Therefore, with finite-rate kinetics, we cannot integrate equations (1-4) from the leading edge ($x = 0$) to downstream such as that has been done in Refs. 1 and 2. In the absence of a leading edge model, the initial conditions at $\xi = 1$ for the plume are obtained somewhat arbitrarily [4]. They are shown in Fig. 2 (velocity f'), Fig. 3 (temperature), and Fig. 4 (fuel, oxidizer and CO mass fraction) with a surface fuel blowing factor $f(1,0) = -.3182$. Comparing them with the calculations in [1], it is found that the temperature, fuel, and oxidizer profiles are similar except near the temperature peak region. In the peak zone, there is an overlap of fuel and oxidizer in the present case, which gives a distributed reaction rate rather than a Delta function. In addition, because of the use of two-step kinetics, CO is presented in the flame. The CO profile at $\xi = 1$ has the same shape as that measured in [6]. These initial conditions are held constant in the present parametric study. The readers are referred to [4] for the effect of changing initial conditions and how the initial profiles are obtained.

Table 3 lists the cases studied. First a reference case is chosen and the results of parametric variations are compared with those of the reference case. In cases 1(*a*) and 1(*b*), the value of the dimensionless B_F is changed, as a result of the variation of the dimensional B_F^*. In Cases 2(*a–c*), both the values of B_F and B_{CO} are changed, as a result of the variation of either g (gravity constant) or l (pyrolysis length) or the ratio l/g (see equations (23) and (24) for the definitions of B_F and B_{CO}). In Case 3(*a–c*), E_F is varied when E_F^* is varied.

In the following, the plume profiles as a function of ξ and η will be given first for the reference case. Then the surface heat transfer rate and the combustible flux level will be presented as a function of ξ for Cases 1 to 3.

Figure 2 shows the velocity profiles at different plume heights. Similar to that found in [1], the velocity peak first moves closer to the wall because the stop of the fuel blowing from the wall after $\xi > 1$. Then the velocity boundary layer gradually grows in thickness as can be seen by the profiles at $\xi = 6$ and $\xi = 9$. The thermal boundary layer behaves similarly as shown in Fig. 3. Figure 4 gives the mass fraction distributions of the fuel, oxygen, and carbon monoxide. Initial profiles ($\xi = 1$) indicate a small overlap region between Y_F and Y_O, where significant fuel oxidation reaction occurs. Carbon monoxide is produced there, and it diffuses both toward the free stream and toward the wall. Because of the lack oxygen in the wall region needed for oxidation, the level of CO persists up to the wall. On the other hand, CO is almost completely oxidized as it goes toward the free stream. At $\xi = 3$, the value of Y_F at the wall decreases (compared with that at $\xi = 1$) as a result of the fuel consumption upstream, the reaction zone widens and the peak flame temperature decreases (Fig. 3), and the CO profile looses its peak. Downstream at $\xi = 6$, the flame temperature and the reactivity become so low that large fraction of oxygen reaches the wall. The chemical reactions are in effect frozen and convective-diffusive processes become dominant. This is further illustrated by the profiles at $\xi = 9$.

In Fig. 5, temperature isotherms are plotted in the ξ–η plane. This supplements the information given in Fig. 3. Figure 6 gives the nondimensional fuel reaction rate ($\dot{\omega}_F$) distribution inside the plume. It shows that the fuel reactivity decreases quickly and becomes effectively frozen at $\xi \approx 5$. In [1] the flame tip is located at $\xi = 6.5$ (flame sheet reattachment position). In Fig. 7, two curves on the nondimensional CO

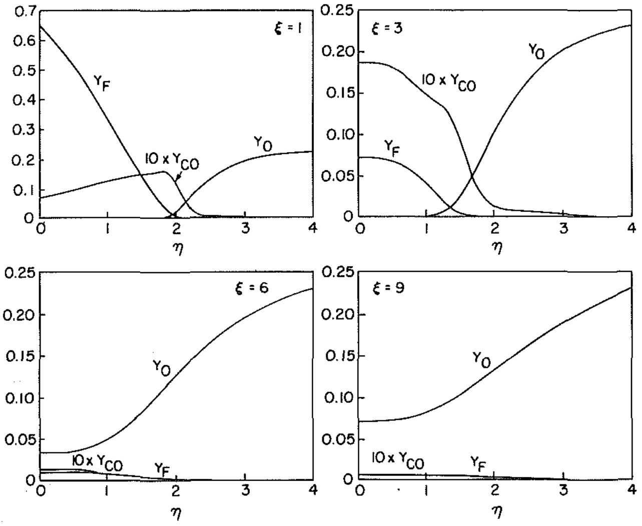

Fig. 4 Mass fraction profiles (reference case)

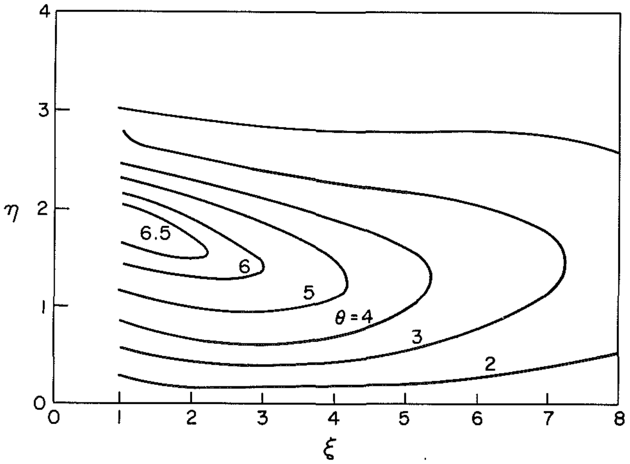

Fig. 5 Temperature isotherms within a wall plume (reference case)

Table 3 Parametric studies

CASE		VARIABLE		B_F	B_{CO}	E_F	E_{CO}
REFERENCE		--		5×10^6	1.762×10^8	51	51
1	1a	B_F^*	$4 \times (B_F^*)_{ref}$	2×10^7	--	--	--
	ref.		$(B_F^*)_{ref}$	5×10^6			
	1b		$1/4 \times (B_F^*)_{ref}$	1.25×10^6			
2	2a	ℓ/g	$4 \times (\ell/g)_{ref}$	10^7	3.524×10^8	--	--
	ref.		$(\ell/g)_{ref}$	5×10^6	1.762×10^8		
	2b		$1/4 \times (\ell/g)_{ref}$	2.5×10^6	0.881×10^8		
	2c		$1/16 \times (\ell/g)_{ref}$	1.25×10^6	0.441×10^8		
3	3a	E_F		--	--	46	--
	ref.					51	
	3b					61	
	3c					71	

"--" values which are the same as that of the reference case.

$(\ell/g)_{ref} = 1.133 \times 10^{-3}$ sec^2

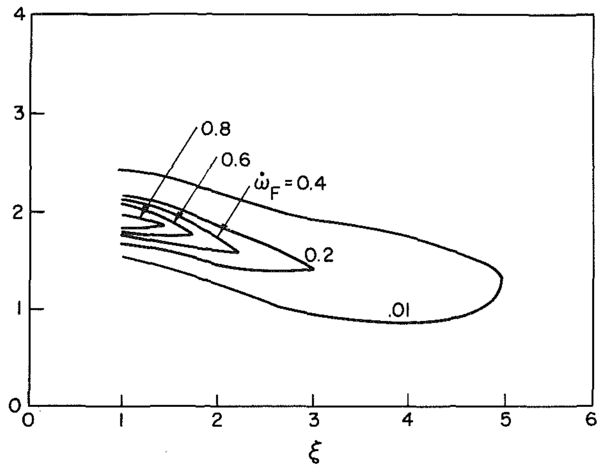

Fig. 6 Nondimensional fuel reaction rate distribution within a wall plume (reference case)

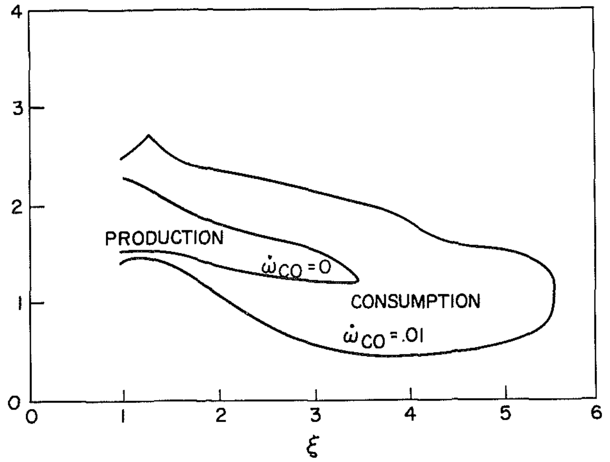

Fig. 7 Production and consumption regions of carbon monoxide within a wall plume (reference case)

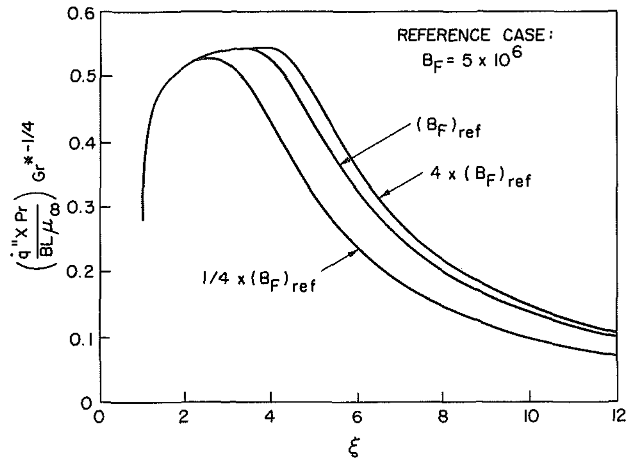

Fig. 8 Nondimensional surface heat transfer versus ξ (cases 1's)

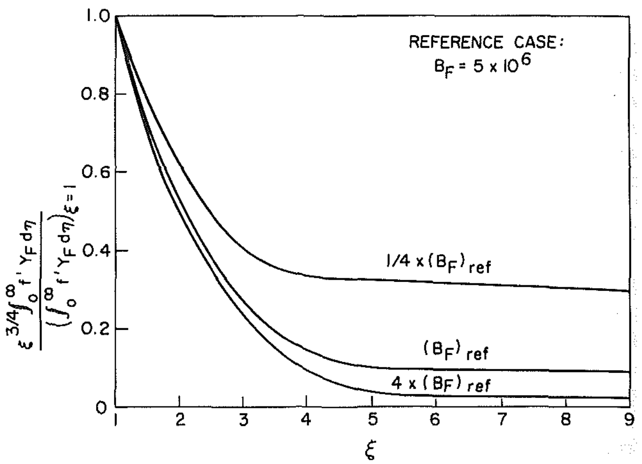

Fig. 9 Fuel mass flux ratio versus ξ (cases 1's)

reaction rates are plotted. As given by equation (22), $\dot{\omega}_{CO}$ can either be negative or positive, depending on whether its production rate is larger or smaller than its oxidation rate. The curve of $\dot{\omega}_{CO} = 0$ in Fig. 7 is the dividing line for the two regions: inside the curve, CO is produced by reaction R.1 faster than that oxidized in reaction R.2; outside this curve, oxidation is faster. The other curve, $\dot{\omega}_{CO} = .01$, serves as a measure of the extent of CO reactions.

So far, we have concentrated on the detailed profiles for the reference plume. In the following, several computed global characteristics will be compared in the parametric study as indicated in Table 3.

Figure 8 shows the dimensionless surface heat transfer rate versus the dimensionless height ξ. In the region between $\xi = 1$ and $\xi = 2$, the heat transfer rates rise sharply from their values in the pyrolysis zone. This is attributed to the suppression of surface fuel pyrolysis for $\xi > 1$ and as a result, the boundary layer shifts closer to the surface (see Figs. 2 and 3). For the three different values of nondimensional fuel frequency factor shown in Fig. 8, the initial rises of heat transfer rate are indistinguishable, indicating that in this region the chemical kinetics are sufficiently fast for all the three cases. However, after the peak is reached, the heat transfer curve with the smallest B_F drops down first, while the one with the biggest B_F drops down the last. It is obvious from Fig. 8 that the nondimensional fuel frequency factor B_F can play an important role in determining the total amount of surface heat transfer in the preheating zone as well as the preheating distances. Physically, B_F is proportional to the ratio of the gas residence time in one pyrolysis length to the fuel chemical reaction time.

Figure 9 gives the ratio of the integrated fuel mass flux to its initial value at $\xi = 1$ as a function of ξ. The fuel flux first decreases quickly at small ξ because of combustion in the plume. However, the mass fluxes level off at larger ξ's and remain essentially constant afterward. This constitutes the "unreacted fuels," which will escape from the flame. Looking at Fig. 9, for the smallest B_F (1.25×10^6), nearly 35 percent of the fuel vapor that enters into the plume remains unreacted and will escape from the flame. Even when $B_F = 2 \times 10^7$ (corresponding to a quite fast kinetics), there is still about 3 percent unreacted fuel. This suggests the important role which the chemical kinetic parameters can play in the analysis of escaped pyrolyzates.

In Fig. 9, the different fuel mass flux curves level off at different values of ξ, which are indicative of the quenching positions for the fuel oxidation process. Figure 10 further illustrates this by plotting the rate of decrease of the fuel mass flux with ξ using equation (27). When the change of flux approaches zero, the reaction is effectively frozen. From Fig. 10, we see that smaller B_F implies a smaller reaction length. Using this figure and Fig. 11 (for CO), it is possible to determine the combustion plume height, which is chemical-kinetic dependent as illustrated by this computation. Figure 11 gives the CO mass flux as a function of ξ.

In the next set of computations (Case 2, see Table 3), both B_F and B_{CO} are varied by a change of the ratio l/g. Figure 12 shows that as l/g decreases, both the preheat length and the peak surface heat flux level decreases. While in the previous case of changing B_F only (B_{CO} fixed), Fig. 8 indicates the

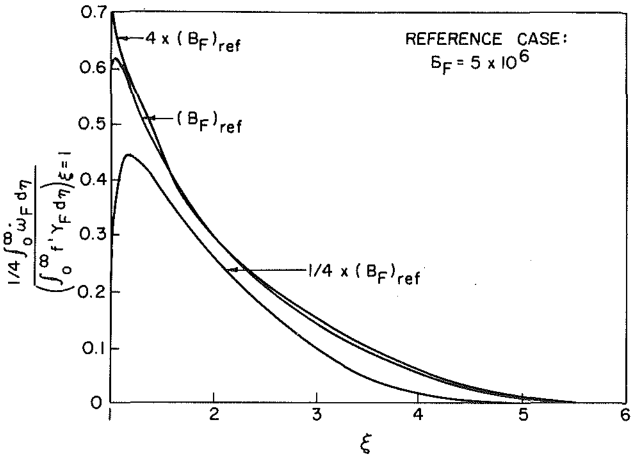

Fig. 10 The rates of change of fuel mass flux ratio w.r.t. ξ as a function of distance (cases 1's)

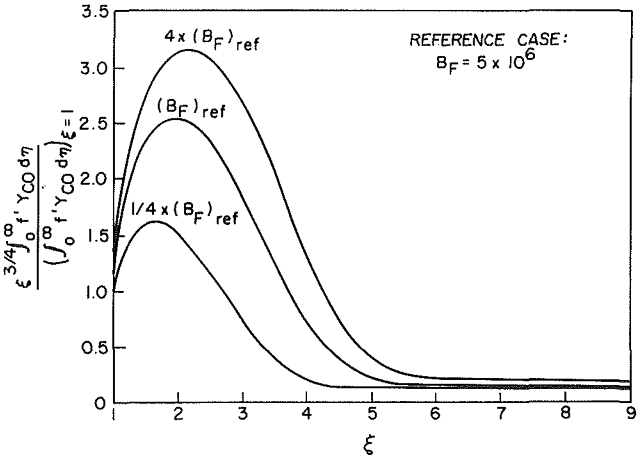

Fig. 11 Carbon monoxide mass flux ratio versus ξ (cases 1's)

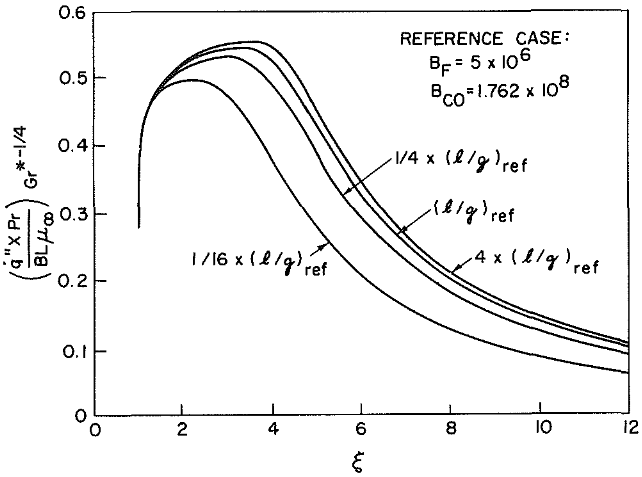

Fig. 12 Nondimensional surface heat transfer rates versus ξ (cases 2's)

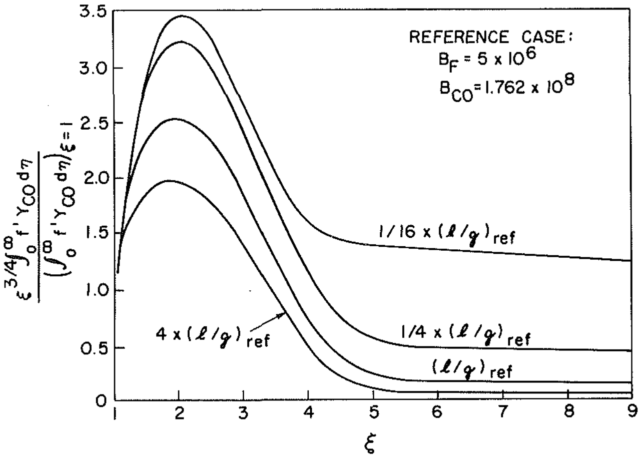

Fig. 13 Carbon Monoxide mass flux ratio versus ξ (cases 2's)

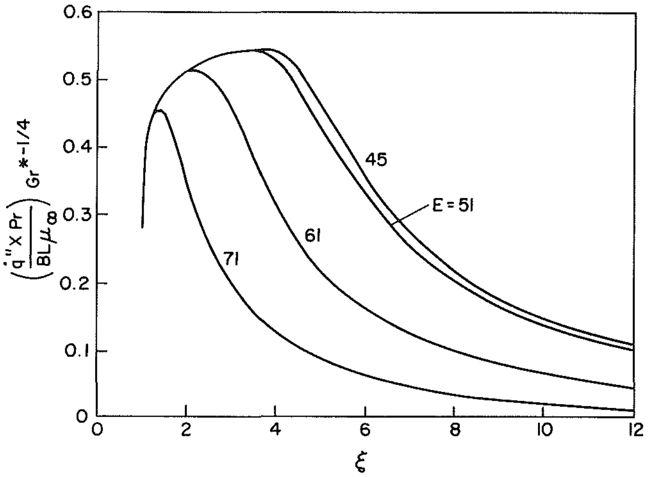

Fig. 14 Nondimensional surface heat transfer rates versus ξ (cases 3's)

predominanat change is in the preheat length only. The effect of varying B_{CO} alone can be found by comparison of Case 1(*b*) with Case 2(*c*); both have the same B_F's but different B_{CO}. Decreasing B_{CO} decreases both the peak heat flux level and the preheat distance.

Comparing Fig. 13 with Fig. 11, also shows that the unreacted CO fraction is much higher when B_{CO} is decreased.

For Case 3, the activation energy of the fuel oxidation reaction is varied. Figure 14 shows that as activation energy is increased, the nondimensional wall heat transfer rate decreases. This is expected, since increasing the value of activation energy slows down the chemical kinetics and as a consequence, facilitates the flame quenching process.

In comparison with the methanol experimental data of [1], the present model, using the reference case parameters, appears to predict the visible flame length and wall heat transfer profile quite well.

Conclusion

An analysis has been presented for a fire plume over a vertical surface using a two-dimensional boundary layer model. Compared with the two previous studies on the same subject [1, 2], the new element in the present work is the inclusion of finite-rate, gas-phase chemical reactions. The gas-phase kinetic model assumes two semiglobal reactions: in the first one, the fuel is oxidized to form carbon monoxide and water vapor, and in the second, carbon monoxide is oxidized to form carbon dioxide. Four nondimensional kinetic parameters are identified: they are B_F and B_{CO}, the nondimensional frequency factors; and E_F and E_{CO}, the nondimensional activation energies.

When the kinetics are slowed by decreasing B_F and/or B_{CO} or by increasing E_F or E_{CO}, the total amount of surface heat transfer in the plume region is decreased. Specifically, slower kinetics shorten the effective preheating distance because of flame tip quenching, and this could be important to upward flame spread or fire growth. Slower kinetics also result in an increase of unreacted combustibles escaping from the plume. In the presence of a cold wall, the escaped combustibles are not negligible even when chemical kinetics are reasonably fast. Thus it suggests that chemical kinetic contribution is fundamental to the study of escaped pyrolyzates.

Although the present work is for natural convection, the corresponding problem for forced convection has been formulated. In such a case, $B_F = (l/U_\infty)\, B_F^*$ and $B_{CO} = (l/U_\infty)\, B_{CO}^*$. Their physical interpretation is the same as that in the natural convective case, i.e., they are proportional to the ratio of flow time over one pyrolysis length to chemical reaction time. Therefore, we expect that qualitatively the forced free-stream velocity U_∞ will play a similar role as the gravitational constant g; e.g., increasing U_∞ decreases B_F and B_{CO} and slows down the kinetics.

One major assumption made in this analysis is that the flow is laminar. Large fire plume normally exhibits turbulent flow characteristics. The interaction of turbulence with chemical kinetics, especially on turbulent flame quenching, is still an unresolved problem. Although more parameters are expected to be added when a mature turbulent flame model emerges in the future, many of the qualitative trends given in the present analysis will probably still remain to be true.

Another assumption made in this study is that both the radiation from the gas phase and the reradiation from the surface are negligible. This may not be true for large size fires and for hot surfaces. With additional radiative heat loss from the flame, the finite-rate chemical kinetic effect should be felt further upstream with flame height further shortened.

The chemical kinetic model used in this analysis is a simple one and serves only as the starting point for more complicated schemes. In the burning of practical fuels, a number of combustion intermediates may be produced on the fuel-rich side of the diffusion flame. This includes soot particles, which are known to have long burnout time. It is interesting also to note that in the experiment by Tewarson [5], where a number of modern plastics are burnt in an overventilated set up, combustion efficiencies of many of these samples are in the 50 or 60 percent range. Although the fuel orientation is not the same as that analyzed in the present work, we believe part of the combustion inefficiency in Tewarson's experiment can be due to the escaped pyrolyzates, as a result of flame tip quenching.

Acknowledgment

This research is supported by the Center for Fire Research, National Bureau of Standards under Grant NB83NADA4002. Dr. James G. Quintiere is the technical monitor.

References

1 Ahmand, T., and Faeth, G. M., "An Investigation of the Laminar Overfire Region Along Upright Surfaces," Vol. 100, ASME JOURNAL OF HEAT TRANSFER, 1978, pp. 112–119.

2 Pagni, P. J., and Shih, T. M., "Excess Pyrolzate," *16th Sym. (Int.) on Combustion Institute*, Pittsburgh, Pa., 1977. pp. 1329–1343.

3 Howard, J. B., Williams, G. C., and Fine, D. C., "Kinetics of Carbon Monoxide Oxidation in Post Flame Gases," *14th Sym. (Int.) on Combustion Institute*, Pittsburgh, Pa., 1973, pp. 975–986.

4 Chen, C. H., "Fire Plume Along Vertical Surfaces: Effect of Finite-Rate Chemical Reactions," M.S. thesis, Department of Mechanical and Aerospace Engineering, Case Western Reserve University, 1983.

5 Tewarson, A., "Physico-Chemical and Combustion/Pyrolysis Properties of Polymeric Materials," Technical Report of National Bureau of Standards, NBS-GCR-80-295, 1980.

6 Sibulkin, M., and Malary, S. F., "Investigation of Completeness of Combustion in A Wall Fire," presented at the 1983 Fall Technical Meeting, Eastern Section/The Combustion Institute, Nov. 8-10, 1983, Providence, RI.

S-M. Jeng

G. M. Faeth
Fellow ASME

Department of Mechanical
Engineering,
The Pennsylvania State
University,
University Park, Pa. 16802

Species Concentrations and Turbulence Properties in Buoyant Methane Diffusion Flames

Past measurements of mean velocities and temperatures in buoyant turbulent, axisymmetric methane diffusion flames burning in still air have been extended to include mean species concentrations (CH_4, N_2, O_2, CO_2, H_2O, CO, and H_2) and turbulence quantities. The new measurements were used to evaluate a Favre-averaged, k-ϵ-g turbulence model of the process – with all empirical constants fixed by measurements in noncombusting flows. Use of the laminar flamelet method to treat scalar properties yielded reasonably good predictions of mean properties. Turbulence predictions were less satisfactory, generally underestimating fluctuation levels and Reynolds stresses in highly buoyant regions of the flows. Measurements indicated significant anisotropy of turbulence properties in the same regions. These findings suggest the need for multistress closure to adequately model turbulence properties in buoyant flames.

Introduction

Buoyant turbulent diffusion flames are a major element in the development of most unwanted fires in structures. The present theoretical and experimental investigation examines the structure of such flames in order to assist efforts to model unwanted fires.

To simplify both measurements and analysis, the investigation was limited to turbulent axisymmetric flames burning in still air. There have been numerous studies of flames under these conditions – Emmons [1] and Brzustowski [2] review early work in the field. Recent measurements of mean temperatures and velocities, using probes, are reported by Becker and Yamazaki [3] for propane flames, and Cox and Chitty [4] and McCaffrey [5] for methane flames. Various scaling laws were used to correlate measurements in these studies, but no attempt was made to model flame structure.

Few detailed models of buoyant flames have been attempted. Tamanini [6] describes a Reynolds (time)-averaged, second-order turbulence closure model allowing for effects of buoyancy on turbulence properties, which was evaluated using measurements of flame shape and radiative heat flux by Markstein [7]. Trends were predicted correctly, but flow widths were underestimated. However, this assessment was not complete, since the measurements only indirectly tested structure predictions, e.g., profiles of flow properties. Furthermore, data were unavailable to properly establish initial conditions and several components of the model.

Pergament and Fishburne [8, 9] use a mixing length model with Arrhenius expressions to prescribe reaction rates in buoyant flames. This model gave reasonable predictions of flame lengths and radiation properties, but flame widths were underestimated – similar to Tamanini [6]. However, the evaluation of structure predictions was again indirect and extension of the Arrhenius expressions to other fuels is uncertain – if not inappropriate for turbulent flames.

You and Faeth [10] have reported earlier structure measurements in buoyant methane flames in this laboratory. The measurements were compared with predictions of a Reynolds-averaged, κ-ϵ-g turbulence model proposed by Lockwood and co-workers [11, 12]. This model had earlier provided good predictions for round flames having negligible buoyancy [11, 13]. However, model performance in this case was poor – attributed to difficulties in defining initial conditions, effects of room disturbances for flames having low momentum, and possible effects of buoyancy and density fluctuations on turbulence properties which were not considered in the model.

A later study in this laboratory, by Jeng et al. [14], achieved more encouraging predictions of mean velocities and temperatures in buoyant methane flames with the same model. This improvement was achieved by carefully controlling room disturbances, as well as measuring initial conditions required by the model. It was found that including effects of buoyancy on turbulence properties had a relatively minor influence on predictions of mean flame structure.

The present investigation extends the work of Jeng et al. [14], providing new measurements of the mean concentration of major species and turbulence quantities in the same buoyant methane flames. Both the existing and new measurements in these flames were used to evaluate a modified version of the κ-ϵ-g model – based on Favre (mass-weighted)-averaging of flow quantities as recommended by Bilger [15]. This approach eliminates a number of terms involving density fluctuations that appear in the governing equations (and are generally ignored) when Reynolds-averaging is used.

In the following section, theoretical and experimental methods are briefly described – concentrating on techniques new to this investigation (see [14] and [16] for further details). This is followed by discussion of results for species concentrations and turbulence quantities.

Experimental Methods

Apparatus. Measurements were completed in three natural gas fueled flames (more than 95 percent methane by volume) considered by Jeng et al. [14]. These flames were injected vertically upward from a water-cooled burner, having an exit diameter of 5 mm, within a screened enclosure to reduce room disturbances. The flames were attached at the burner exit by a small coflow of hydrogen (less than 2 percent of the fuel flow by mass). Injector exit conditions and total radiative heat losses (which were generally less than 20 percent of the heat of reaction) for the flames were measured. Reynolds numbers at the burner exit were 2920, 5850, and 11700 which yielded visible flame heights on the order of 500 mm. Buoyancy dominated most of the visible flame region for the lowest initial Reynolds number, but only became significant near the flame tip for the highest Reynolds

---

Contributed by the Heat Transfer Division for publication in the JOURNAL OF HEAT TRANSFER. Manuscript received by the Heat Transfer Division August 25, 1983.

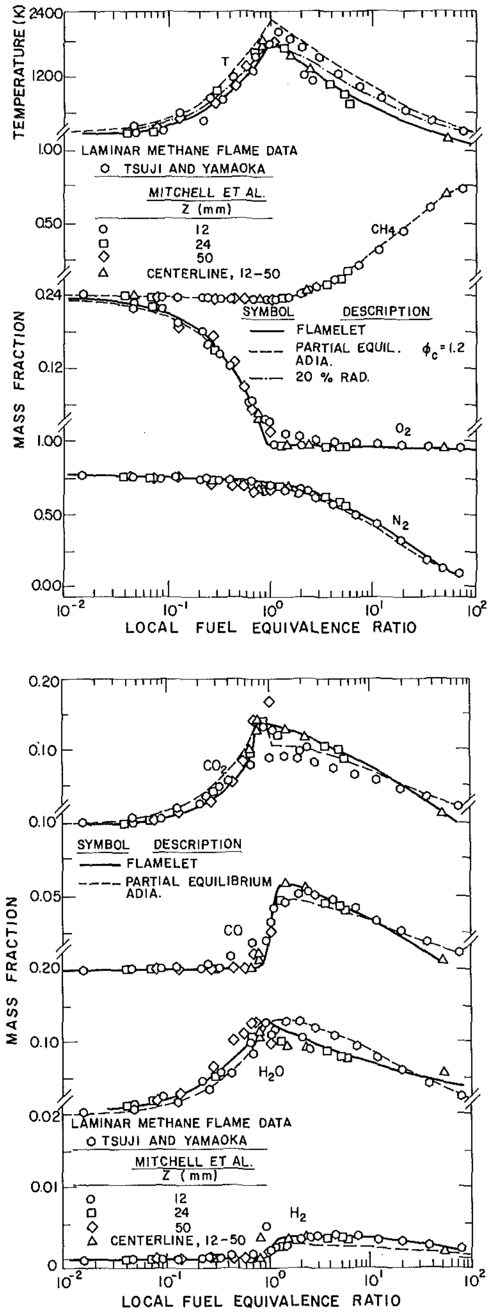

Fig. 1 State relationships for methane diffusion flames burning in air at normal temperature and pressure

number. A complete specification of flame properties and initial conditions appears elsewhere [14, 16].

Instrumentation. Mean and fluctuating velocities were measured with a 50-mW, single-channel, frequency-shifted, helium-neon laser Doppler anemometer (LDA). Major and minor diameters of the measuring volume were 120, 100 μm ($x/d \leq 55$) and 720, 240 ($x/d > 55$). The flow and the surroundings were seeded with 500-nm aluminum oxide particles to avoid concentration biasing and achieve time-averaged quantities – after processing. Combined errors due to gradient broadening, positioning, beam steering, and phase fluctuations were less than 10 percent [16]. Capabilities for repeating measurements over a period of months were within the same limits.

Species concentrations were measured by isokinetic sampling, with a water-cooled probe having an inlet diameter of 2 mm, and analysis was performed with a gas chromatograph [16]. Species found were CH_4, N_2, O_2, CO_2, CO, H_2O, and H_2. Mass ratios of C/H and O/N were checked over the data base yielding mean values and standard deviations as follows: C/H, 2.84 and 0.28; O/N, 0.298 and 0.045. Allowing for hydrogen added at the injector and the actual composition of natural gas yields C/H mass ratios of 2.84-2.96 while the O/N mass ratio of dry air is 0.304. The discrepancies are probably due to effects of ambient water vapor, differential diffusion, and sampling errors. Based on this check, calibration tests and repeatability measurements, we estimate uncertainties of composition measurements to be generally less than 15 percent.

Theoretical Methods

Description. Due to the use of Favre-averaging, the analysis differs somewhat from earlier work [14]; therefore, the new formulation will be presented in the following. It is assumed that the boundary layer approximations apply for a steady, axisymmetric turbulent diffusion flame in an infinite stagnant air environment. Flow velocities are low; therefore, viscous dissipation and kinetic energy are ignored when evaluating energy conservation. Typical of most models of turbulence [10-14], exchange coefficients of all species and heat are assumed to be the same. Radiative heat losses were less than 20 percent in the test flames; therefore, radiation effects are relatively small and are ignored – except as noted later.

Under these assumptions, instantaneous scalar properties such as density, temperature, and species concentrations, are only functions of mixture fraction (the fraction of mass at a point which originated from the burner). Therefore, these functions – termed state relationships – can be found once and for all for each flame condition.

Nomenclature

a = acceleration of gravity
C_i = constants in turbulence model, Table 1
d = burner exit diameter
f = mixture fraction
g = square of mixture fraction fluctuations
k = turbulent kinetic energy
$\tilde{P}(f)$ = Favre probability density function for f
r = radial distance
Re = burner Reynolds number
Sc = laminar Schmidt number
S_ϕ = source term, Table 1
T = temperature
u = axial velocity
v = radial velocity
x = axial distance
Z = height above burner, data of [22]
ϵ = rate of dissipation of turbulence kinetic energy
μ = laminar viscosity
μ_{eff} = effective viscosity
μ_t = turbulent viscosity
ρ = density
σ_i = turbulent Prandtl/Schmidt number
ϕ = generic property, fuel equivalence ratio

Subscripts

c = centerline value, critical value
o = burner exit condition

Superscripts

$(\bar{\ })$ = time-averaged quantity
$(\tilde{\ })$ = Favre-averaged quantity
$(\ )'$ = time-averaged fluctuating quantity
$(\tilde{\ })''$ = Favre-averaged fluctuating quantity

State Relationships. Two methods for constructing state relationships were examined (*i*) the laminar flamelet method of Bilger [17] and Liew et al. [18] and (*ii*) the partial equilibrium method used earlier in this laboratory [10, 14]. The laminar flamelet method is based on observations by Bilger [17] that temperatures and species concentrations in laminar diffusion flames are nearly unique functions of mixture fraction for a wide range of shear rates and positions in the flow. Therefore, measurements in laminar flames are used directly to construct state relationships – viewing observations in turbulent flames as the result of a succession of laminar flamelets sweeping past a given position.

The present flames were assumed to be equivalent to pure methane flames, and the laminar flame measurements of Tsuji and Yamaoka [19-21] and Mitchell et al. [22] were used to construct state relationships. The laminar flamelet correlations used during the investigation are compared to the measurements of [19-22] in Fig. 1. Mixture fraction values used to construct these plots were based on elemental carbon; however, use of both carbon and hydrogen affected mixture fraction values less than 10 percent. It is evident that a nearly universal correlation of the data is found when plotted as a function of mixture fraction (or equivalently, fuel equivalence ratio).

The partial equilibrium method involves assuming local thermodynamic equilibrium – except as noted later. Assuming negligible radiation, under present assumptions, the instantaneous properties at each point in the flow correspond to the thermodynamic equilibrium state reached when burner and ambient gas (at their initial states) are adiabatically mixed with proportions given by the mixture fraction. These computations were also conducted after allowing for a loss of a fixed fraction (20 percent) of the chemical energy released during equilibration—to estimate potential effects of radiative heat losses. Full thermodynamic equilibration was assumed for mixture fractions less than a critical value f_c and frozen mixing (adiabatic mixing of the mixture at f_c and pure fuel) for mixture fractions greater than f_c—since complete equilibration is unlikely at high mixture fractions where reaction rates are low due to low temperatures.

The state relationships found using the partial equilibrium method are also illustrated in Fig. 1. Choosing a critical fuel equivalence ratio for freezing the reaction $\phi_c = 1.2$ yields nearly identical results for both the laminar flamelet and partial equilibrium methods.

Governing Equations. The Favre-averaged forms of the governing equations are

$$\frac{\partial \bar{\rho}\tilde{u}}{\partial x} + \frac{1}{r}\frac{\partial}{\partial r}(r\bar{\rho}\tilde{v}) = 0 \qquad (1)$$

$$\bar{\rho}\tilde{u}\frac{\partial\tilde{\phi}}{\partial x} + \bar{\rho}\tilde{v}\frac{\partial\tilde{\phi}}{\partial r} = \frac{1}{r}\frac{\partial}{\partial r}\left(r\mu_{\text{eff},\phi}\frac{\partial\tilde{\phi}}{\partial r}\right) + S_\phi \qquad (2)$$

where $\tilde{\phi} = \tilde{u}, \tilde{f}, \tilde{k}, \epsilon$, or g; and $\tilde{\phi} = \overline{\rho\phi}/\bar{\rho}$ is a Favre-averaged quantity, while $\bar{\rho}$, etc., are conventional time averages.

The expressions for $\mu_{\text{eff},\phi}$ and S_ϕ, appearing in equation (2), are summarized in Table 1. When written in Favre-averaged form, the governing equations are similar to those found for constant-density flows – without ad hoc deletion of terms involving density fluctuations. However, a velocity pressure gradient term which varies due to buoyancy in the k equation, and an analogous term in the ϵ equation were ignored in order to minimize the number of empirical constants. The justification for this was that earlier work using Reynolds-averaging showed that analogous terms had a relatively small effect for the present flows [14].

The empirical constants needed by the model are also summarized in Table 1. These constants were recalibrated by comparing predictions with recent data from constant and variable density noncombusting jets [16], e.g., isothermal air jets [13, 23-25], heated air jet [26], isothermal SF_6 jet [13], and isothermal CH_4 jet [27]. The constants are generally the same as those proposed in early work with this model [11] – based on constant density boundary layer flows. An exception is $C_{\epsilon 2} = C_{g2}$, where the current value is roughly the average of values used for constant and variable density flows during earlier work [11, 13, 14]. C_μ is taken to be uniform over the flow, since this approach was reasonably satisfactory over the calibration and for the present flows, although others have advocated varying this parameter for axisymmetric flows [17].

The boundary conditions for equations (1) and (2) are

$$r = 0, \frac{\partial\tilde{\phi}}{\partial r} = 0; r \rightarrow \infty, \tilde{\phi} = 0 \qquad (3)$$

where the condition at $r = 0$ is only applied beyond the end of the potential core. Initial conditions were specified at the burner exit, for $2r/d \leq 0.99$, as follows: $f_0 = 1$ and $g_0 = 0$, by definition; $\tilde{u}_0$ and k_0 were measured directly; while ϵ_0 were inferred by matching the decay of k in the potential core. Values used are summarized in [16]. The region $2r/d > 0.99$ was specified by solving the governing equations – assuming linear mean profile and neglecting convection and diffusion terms. The sensitivity of the calculations to uncertainties in initial conditions is examined elsewhere [14, 16]. In general, these effects are less than experimental uncertainties in the following comparison between predictions and measurements. Boundary conditions along the inner edge of the shear layer were found by solving the transport equations within the potential core. The equations were integrated using

Table 1 Summary of turbulence parameters

$\tilde{\phi}$	$\mu_{\text{eff},\phi}$	S_ϕ
$\tilde{u}$	$\mu + \mu_t$	$a(\rho_\infty - \bar{\rho})$
$\tilde{f}$	$(\mu/\text{Sc}) + (\mu_t/\sigma_f)$	0
k	$\mu + (\mu_t/\sigma_k)$	$\mu_t\left(\frac{\partial\tilde{u}}{\partial r}\right)^2 - \bar{\rho}\epsilon$
ϵ	$\mu + (\mu_t/\sigma_t)$	$\left(c_{\epsilon_1}\mu_t\left(\frac{\partial\tilde{u}}{\partial r}\right)^2 - C_{\epsilon_2}\bar{\rho}\epsilon\right)(\epsilon/k)$
g	$(\mu/\text{Sc}) + (\mu_t/\sigma_g)$	$C_{g_1}\mu_t\left(\frac{\partial\tilde{f}}{\partial r}\right)^2 - C_{g_2}\bar{\rho}g\epsilon/k$

C_μ	C_{ϵ_1}	C_{g_1}	$C_{\epsilon_2} = C_{g_2}$	σ_k	σ_ϵ	$\sigma_f = \sigma_g$	Sc
0.09	1.44	2.8	1.87	1.0	1.3	0.7	0.7

$\mu_t = \bar{\rho}\, C_\mu k^2/\epsilon$

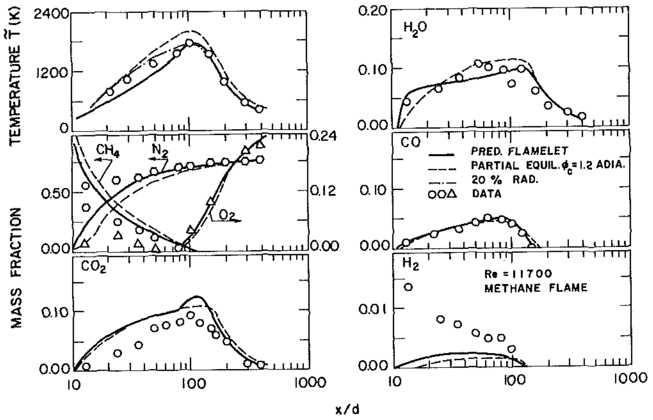

Fig. 2 Mean temperature and species concentrations along the flame axis: Re = 11700

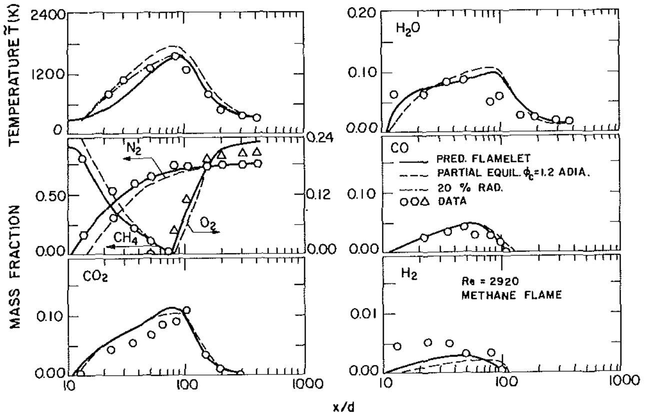

Fig. 3 Mean temperature and species concentrations along the flame axis: Re = 2920

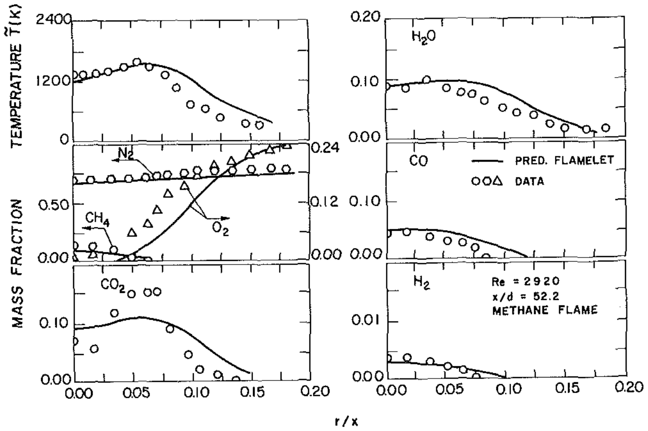

Fig. 4 Radial variation of mean temperature and species concentrations: Re = 2920, *x/d* = 52.2

the GENMIX computer program, with numerical closure and convergence assured similar to past work [11, 13, 14, 16].

Scalar Properties. Scalar properties were found as described by Bilger [15]. Favre-averaged mean quantities were computed from

$$\tilde{\phi} = \int_0^1 \phi(f)\tilde{P}(f)df \tag{4}$$

where $\phi(f)$ is known from the state relationships while $\tilde{P}(f)$ is the Favre probability density function (PDF) of mixture fraction. The Favre PDF was assumed to be a clipped Gaussian function whose mean value and variance can be

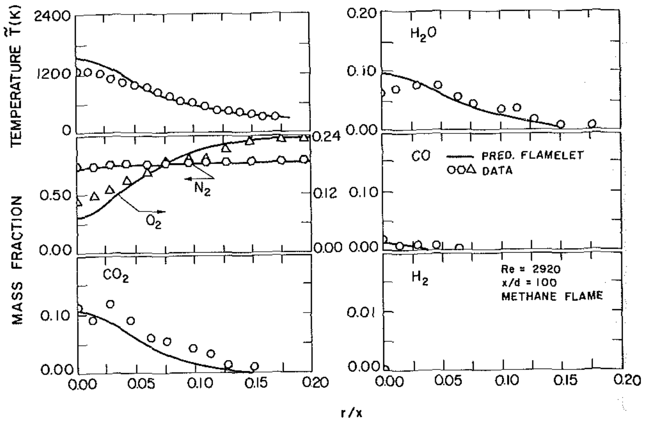

Fig. 5 Radial variation of mean temperature and species concentrations: Re = 2920, *x/d* = 100

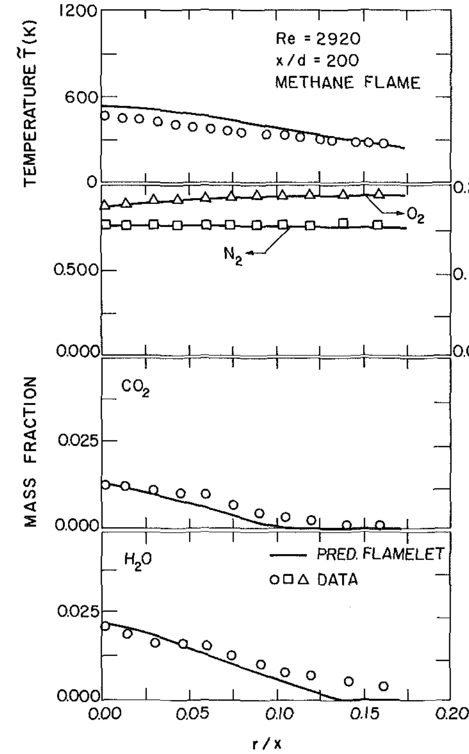

Fig. 6 Radial variation of mean temperature and species concentrations: Re = 2920, *x/d* = 200

computed from known values of $\tilde{f}$ and g as described by Lockwood and Naguib [11]. Time-averaged mean quantities are found from

$$\bar{\phi} = \bar{\rho}\int_0^1 (\phi(f)/\rho(f))\tilde{P}(f)df \tag{5}$$

The expression for $\bar{\rho}$ can be found from equation (5) by setting $\phi(f)$ equal to unity.

Results and Discussion

Mean Structure. Mean velocity predictions with the new model were similar to results reported earlier [14] and will not be repeated here. Due to space limitations, only a portion of the results for flames having Re = 2920 and 11700 are considered in the following – all data and predictions appear in [16].

The maximum difference between predicted Reynolds- and Favre-averaged mean temperatures is less than 200 K at the flame tip, and is generally less than 100 K for the remainder of

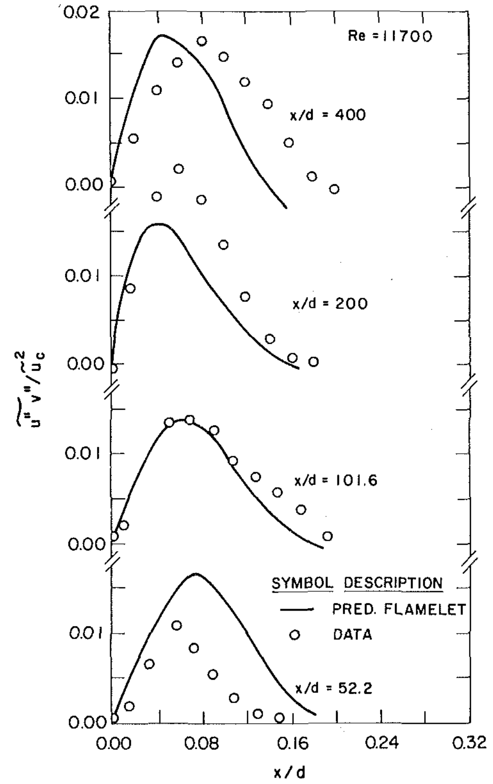

Fig. 7 Radial variation of Reynolds stress: Re = 11700

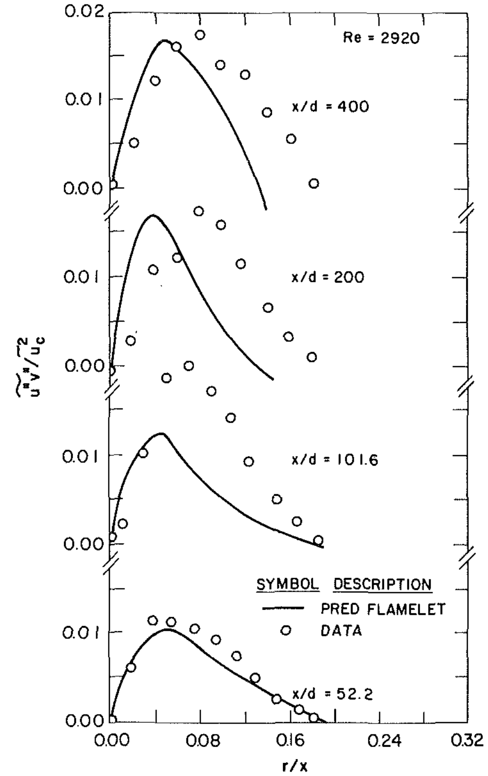

Fig. 8 Radial variation of Reynolds stress: Re = 2920

the flow for present test conditions. Temperatures measured by finite sized thermocouples are generally between the values of these two averaging methods [15]. Recent measurements in jet diffusion flames by Drake et al. [27] suggest that sampling probe measurements of mean concentrations are also between Reynolds- and Favre-averages. Predicted differences between these averages for present flows are smaller than 5 percent; however, which is less than experimental uncertainties. Therefore, to reduce clutter of the figures, the measurements of all scalar properties will be compared with Favre-average predictions in the following.

Predicted and measured axial variation of mean species concentrations and temperatures appear in Figs. 2 and 3. The temperature measurements are corrected for radiation errors [14, 16]. All three methods for constructing state relationships are considered, but as might be expected from the results illustrated in Fig. 1, predictions of all methods are similar. The agreement between predictions and measurements is encouraging – particularly for the laminar flamelet and the partial equilibrium method allowing for radiative heat loss. An exception involves predicted H_2 concentrations near the burner exit, but this is probably due to the presence of the hydrogen coflow used to attach the flames and is not necessarily a defect of the model. The fact that the flame tends to shift toward the burner exit as the initial Reynolds number decreases is predicted by the model – suggesting no major difficulty in representing effects of buoyancy on mean properties over the test range.

The radial variation of mean temperature and species concentrations for Re = 2920 is illustrated in Figs. 4–6. Results are presented for $x/d = 52.2$, 100, and 200, which correspond to positions before, near, and after the maximum temperature (flame tip) is reached along the axis. In this and in the following figures, radial distances are presented as r/x in order to provide a direct indication of flow widths. Fair agreement is observed between predictions and measurements. There is a tendency for the predictions to underestimate the width of the flow. However, based on past experience [10, 14], this could be due to flapping of the flame from low levels of room disturbances – which are difficult to avoid for highly buoyant flows having relatively low levels of momentum. Discrepancies between predicted and measured concentrations of carbon dioxide are also rather large for r/x near 0.05 in Fig. 4. This is felt to be an experimental problem, however, since C/H and O/N mass ratios were near 3.7 and 0.37 in this region, which are significantly above expected values or values measured elsewhere in the flames. Concentration fluctuations cause reductions in mean properties from peak levels seen in the state relationships (near fuel equivalence ratios of unity) as well as overlap of mean fuel and oxygen concentrations. The predictions represent these effects reasonably well.

The results illustrated in Figs. 4–6 are typical of findings for the other two flames – where effects of buoyancy in the luminous flame region are reduced due to higher initial Reynolds numbers. This suggests no particular influence of effects of buoyancy on the comparison between predicted and measured mean properties for the present test range.

Turbulent Structure. Measurements of longitudinal velocity fluctuations are compared with predictions of the Reynolds-averaged κ-ϵ-g model in [14]. The present Favre-averaged model yields similar results for this parameter; therefore, new measurements involving Reynolds stress and all components of velocity fluctuations at $x/d = 52.2$, 101.6, 200, and 400 will be emphasized in the following. Formally, the measurements are time averages while current predictions are Favre averages. The differences between these averages was estimated using measurements of density-velocity correlations in jet diffusion flames and plumes by Driscoll et al. [29] and George et al. [30] after neglecting triple correlations of fluctuating quantities. Favre-averaged velocity fluctuations and peak Reynolds stresses were found to be on the order of 5 and 25 percent less than the comparable Reynolds-averaged quantities. The difference in the case of velocity fluctuations is less than experimental uncertainties; therefore, predictions and measurements will be compared

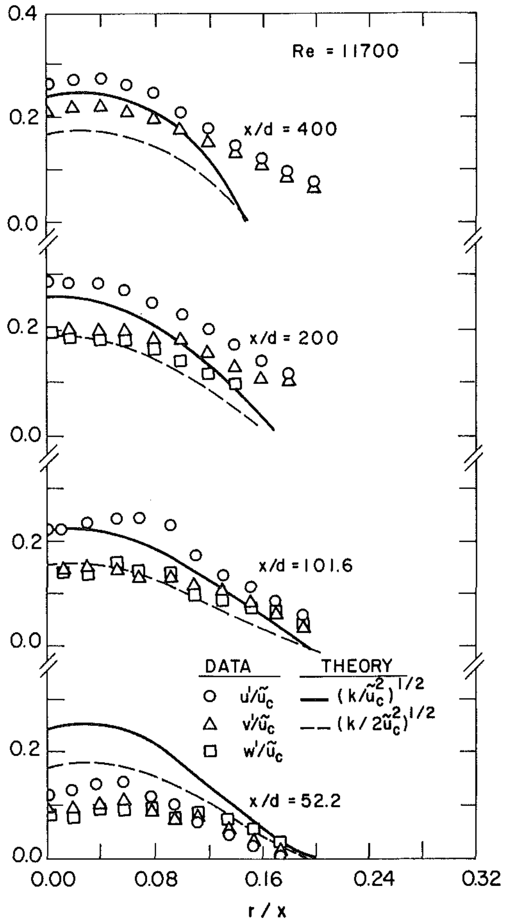

Fig. 9 Radial variation of velocity fluctuations: Re = 11700

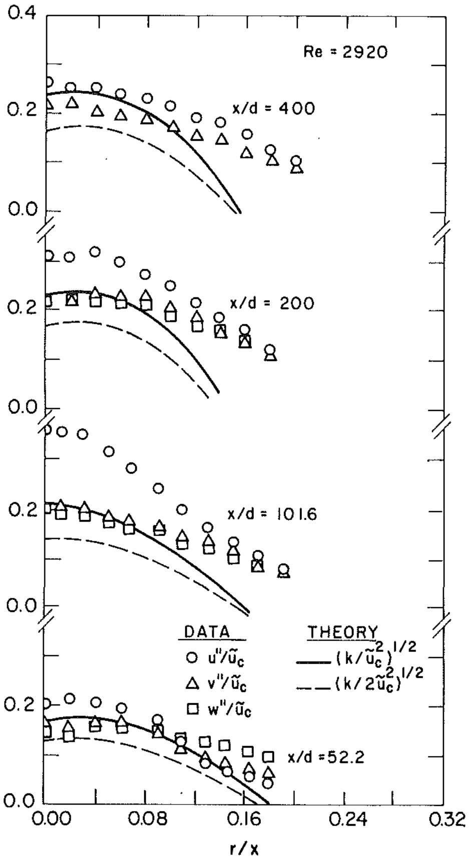

Fig. 10 Radial variation of velocity fluctuations: Re = 2920

directly in order to avoid intrusion of additional empiricism in the evaluation. Predictions using the three methods of finding state relationships were similar; therefore, only flamelet method will be illustrated in the following – to avoid cluttering the figures.

Predicted and measured radial profiles of Reynolds stress in flames having initial Reynolds numbers of 2920 and 11700 are illustrated in Figs. 7 and 8. Only fair agreement is observed between predictions and measurements. Flow widths tend to be underestimated for $x/d > 200$, which may be due to flow disturbances as noted earlier. Peak Reynolds stress levels also tend to be underestimated in highly buoyant regions of the flow, e.g., $x/d = 200$ for Re = 11700 and $x/d = 101.6$ for Re = 2920. The discrepancies are on the order of 25 percent, which is comparable to the estimated differences between Favre- and Reynolds-averaged peak Reynolds stresses discussed earlier = possibly explaining much of the discrepancy.

The radial variation of the three components of velocity fluctuations for the same conditions are illustrated in Figs. 9 and 10. In this case, the anisotropic ratios of components of velocity fluctuations, generally observed in jets [23], are illustrated for the predictions, e.g., $\tilde{u}''^2:\tilde{v}''^2:\tilde{w}''^2 = k:k/2:k/2$. The isotropic prediction, $\tilde{u}''^2:\tilde{v}''^2:\tilde{w}''^2 = 2k/3$, falls between these limits. These predictions agree better with measurements than the Reynolds stress results possibly due to the fact that Favre- and Reynolds-averaged velocity fluctuations are closer in value than Reynolds stresses. However, there is still a tendency to underestimate flow widths far from the burner exit. Levels of anisotropy are also underestimated in strongly buoyant regions – analogous to locations where peak Reynolds stress levels were high in comparison to predictions. This suggests an obvious defect of the current model. Since levels of anisotropy vary throughout the flames, it appears that more complete models, perhaps along the lines of the algebraic stress model of Tamanini [6], will be required for satisfactory predictions of turbulence properties in buoyant flames.

Conclusions

The present Favre-averaged, κ-ϵ-g model has provided predictions of mean velocities and temperatures in turbulent round buoyant flames that are equivalent to earlier findings using Reynolds-averaging [14]. The advantage of the present approach is that this result is accomplished using a single set of empirical constants, found by matching predictions and measurements for constant and variable density noncombusting flows.

The laminar flamelet method for constructing state relationships has provided good predictions of scalar properties in the test flames. This implies that relatively straightforward measurements of the structure of laminar diffusion flames might be used to estimate scalar properties in buoyant turbulent diffusion flames, in agreement with findings of Liew et al. [18] for forced flames. However, additional measurements in turbulent diffusion flames for various fuels will be required to establish the generality of this conclusion. If the approach proves successful, it would provide a practical means of circumventing current difficulties in predicting reaction rates in turbulent diffusion flames – facilitating structure predictions needed to find convective and radiative properties of fires.

The partial equilibrium method for constructing state relationships, using a critical fuel equivalence ratio of 1.2, has yielded results comparable to the laminar flamelet method. To the extent that ϕ_c proves to be constant (recent work with propane and n-heptane flames suggests that this may be roughly true), the method could provide a means of estimating scalar properties in flames where laminar flame data is not available – which is most often the case. Additional measurements are needed, however, to assess this approximation more adequately.

The agreement between predicted and measured turbulence quantities was less satisfactory than for mean quantities – similar to past experience [14]. Underestimation of flow widths far from the burner may be the result of room disturbances, which are very difficult to control for buoyant flows having low momentum. These effects, plus substantial anisotropy in highly buoyant regions of the flow, warrant further theoretical consideration as well – perhaps using a multistress model.

Acknowledgment

This research was supported by the United States Department of Commerce, National Bureau of Standards, Grant No. NB81NADA2044, with H. Baum of the Center for Fire Research serving as Scientific Officer.

References

1 Emmons, H. W., "The Growth of Fire Sciences," *Fire Safety Journal*, Vol. 3, 1980/81, pp. 95–106.

2 Bruzstowski, T. A., "Flaring in the Energy Industry," *Prog. Energy Combust. Sci.*, Vol. 2, 1976, pp. 129–141.

3 Becker, H. A., and Yamazaki, S., "Entrainment, Momentum Flux and Temperature in Vertical Free Turbulent Diffusion Flames," *Combustion and Flame*, Vol. 33, 1976, pp. 123–148.

4 Cox, G., and Chitty, R., "A Study of the Deterministic Properties of Unbounded Fire Plumes," *Combustion and Flame*, Vol. 39, 1980, pp. 191–209.

5 McCaffrey, B. J., "Purely Buoyant Diffusion Flames: Some Experimental Results," NBSIR 79-1910, National Bureau of Standards, Washington, 1979.

6 Tamanini, F., "Reaction Rates, Air Entrainment and Radiation in Turbulent Fire Plumes," *Combustion and Flame*, Vol. 30, 1977, pp. 85–101.

7 Markstein, G. H., "Scaling of Radiative Characteristics of Turbulent Diffusion Flames," *Sixteenth Symposium (International) on Combustion*, Pittsburgh, Pa., 1977, pp. 127–137.

8 Pergament, H. S., and Fishburne, E. S., "Influence of Buoyancy on Turbulent Hydrogen/Air Diffusivity Flames," *Combustion Science and Technology*, Vol. 18, 1978, pp. 127–137.

9 Fishburne, E. S., and Pergament, H. S., "The Dynamics and Radiant Intensity of Large Hydrogen Flames," *Seventeenth Symposium (International) on Combustion*, The Combustion Institute, Pittsburgh, Pa., 1979, pp. 1063–1073.

10 You, H-Z., and Faeth, G. M., "Buoyant Axisymmetric Turbulent Diffusion Flames in Still Air," *Combustion and Flame*, Vol. 44, No. 1-3, 1982, pp. 251–275.

11 Lockwood, F. C., and Naguib, A. S., "The Prediction of the Fluctuations in the Properties of Free, Round-Jet, Turbulent Diffusion Flames," *Combustion and Flame*, Vol. 24, 1975, pp. 109–124.

12 Gosman, A. D., Lockwood, F. C., and Syed, S. A., "Prediction of a Horizontal Free Turbulent Diffusion Flame," *Sixteenth Symposium (International) on Combustion*, The Combustion Institute, Pittsburgh, Pa., 1977, pp. 1543–1555.

13 Mao, C-P., Szekely, G. A., Jr., and Faeth, G. M., "Evaluation of a Locally Homogeneous Flow Model of Spray Combustion," *J. Energy*, Vol. 4, 1980, pp. 78–87.

14 Jeng, S-M., Chen, L-D., and Faeth, G. M., "The Structure of Buoyant Methane and Propane Diffusion Flames," *Nineteenth Symposium (International) on Combustion*, The Combustion Institute, 1982, pp. 349–358.

15 Bilger, R. W., "Turbulent Jet Diffusion Flames," *Prog. Energy Combust. Sci.*, Vol. 1, 1976, pp. 87–109.

16 Jeng, S-M., "An Investigation of the Structure and Radiation Properties of Turbulent Buoyant Diffusion Flames," Ph.D thesis, The Pennsylvania State University, May 1984.

17 Bilger, R. W., "Reaction Rates in Diffusion Flames," *Combustion and Flame*, Vol. 30, 1977, pp. 277–284.

18 Liew, S. K., Bray, K. N. C., and Moss, J. B., "A Flamelet Model of Turbulent Non-Premixed Combustion," *Comb. Science and Technology*, Vol. 27, 1981, pp. 69–73.

19 Tsuji, H., and Yamaoka, I., "Structure Analysis of Counterflow Diffusion Flames in the Forward Stagnation Region of a Porous Cylinder," *Thirteenth Symposium (International) on Combustion*, The Combustion Institute, Pittsburgh, Pa., 1971, pp. 723–731.

20 Tsuji, H., Yamaoka, I., "The Counterflow Diffusion Flames in the Forward Stagnation Region of a Porous Cylinder," *Eleventh Symposium (International) on Combustion*, The Combustion Institute, Pittsburgh, Pa., 1967, pp. 970–984.

21 Tsuji, H., and Yamaoka, I., "The Structure of Counterflow Diffusion Flames in the Forward Stagnation Region of a Porous Cylinder," *Twelfth Symposium (International) on Combustion*, the Combustion Institute, Pittsburgh, Pa., 1969, pp. 997–1005.

22 Mitchell, R. E., Sarofim, A. F., and Clomberg, L. A., "Experimental and Numerical Investigation of Confined Laminar Diffusion Flames," *Combustion and Flame*, Vol. 37, 1980, pp. 227–224.

23 Wygnanski, I., and Fiedler, H. E., "Some Measurements in the Self-Preserving Jet," *J. Fluid Mechanics*, Vol. 38, 1969, pp. 577–612.

24 Becker, H. A., Hottel, H. C., and Williams, G. C., "The Nozzle-Fluid Concentration Field of Round Turbulent, Free Jet," *J. Fluid Mechanics*, Vol. 30, 1967, pp. 285–303.

25 Hetsroni, G., and Sokolov, M., "Distribution of Mass, Velocity, and Intensity of Turbulence in a Two-Phase Turbulent Jet," *J. Appl. Mech.*, Vol. 93, 1971, pp. 315–327.

26 Chevray, R., and Tutu, N. K., "Intermittency and Preferential Transport of Heat in a Round Jet," *J. Fluid Mechanics*, Vol. 88, 1978, pp. 133–160.

27 Birch, A. D., Brown, D. R., Godson, M. G., and Thomas, J. R., "The Turbulent Concentration Field of a Methane Jet," *J. Fluid Mechanics*, Vol. 88, 1978, pp. 431–449.

28 Drake, M. C., Bilger, R. W., and Starner, S. H., "Raman Measurements and Conserved Scalar Modeling in Turbulent Diffusion Flames," *Nineteenth Symposium (International) on Combustion*, The Combustion Institute, Pittsburgh, Pa., 1982, pp. 459–467.

29 Driscoll, W. F., Schefer, R. W., and Dibble, R. W., "Mass Fluxes $\overline{\rho' u'}$ and $\overline{\rho' v'}$ Measured in a Turbulent Nonpremixed Flame," *Nineteenth Symposium (International) on Combustion*, The Combustion Institute, Pittsburgh, 1982, pp. 447–485.

30 George, W. K., Jr., Alpert, R. L., and Tamanini, F., "Turbulence Measurements in an Axisymmetric Buoyant Plume," *Int. J. Heat Mass Transfer*, Vol. 20, 1977, pp. 1145–1154.

M. Bürger

D. S. Kim

W. Schwalbe

H. Unger

Abteilung Reaktorsicherheit und Umwelt,
Institut fur Kernenergetik
und Energiesysteme
(IKE), University of Stuttgart,
7000 Stuttgart 80,
Federal Republic of Germany

H. Hohmann

H. Schins

Joint Research Center,
Ispra Establishment,
21020 Ispra (Varese), Italy

Two-Phase Description of Hydrodynamic Fragmentation Processes Within Thermal Detonation Waves

Large-scale vapor explosions are described by thermal detonation waves, proceeding through a fuel-coolant mixture. A two-phase flow model is used for modeling the processes inside a wave. One phase is formed by the drops of melt and the other by the coolant and the fragments. For the interfacial transfer relations between the phases new descriptions are presented, which extend earlier thermal detonation models. The fragmentation behavior can be calculated from two different models, one based on deformation breakup and Taylor instability and another describing fragmentation by stripping of capillary waves induced by shear flow instabilities. In addition to the time development of the fragmented mass, the models give also the actual sizes of the fragments. Results of the fragmentation models are compared with the experiments on hydrodynamic fragmentation of single drops of gallium in water flows. For vapor explosion experiments with tin-water and salt-water systems the detonation cases are determined using the wave stripping model.

Introduction

Large-scale vapor explosions have been described by use of the detonation model, e.g., [1, 2], which gives an integral concept of the processes. The description of the fragmentation mechanism forms the key part of this analysis, determining the heat release in the detonation wave. The present investigation deals essentially with this part of the modeling.

In the most severe cases of high-pressure waves, hydrodynamic fragmentation mechanisms, which are caused by the relative velocity between melt and coolant induced by the shock front, may dominate. Therefore, an essential task of the modeling is to describe the dynamics inside the detonation wave, that is, the movement of the drops of melt and of the coolant. In steady-state thermal detonation models, e.g., [1, 2], this is done by two-phase descriptions, choosing the drops of melt as one phase and the coolant together with the fragments as another phase. This procedure is based on the assumption of an instantaneous equilibration of velocity and temperature between the fragments and the coolant. Between the two phases mass and heat as well as kinetic energy are transferred by the fragments and these transfer processes together with the hydrodynamic drag of the drops of melt determine the dynamic behavior. The set of equations used for describing these processes inside the detonation wave is given, e.g., in [2]. Modifications presented here refer to this basic modeling.

Within the earlier description of thermal detonation, the movement of the drops of melt was determined by use of a mean drag coefficient for single drops, related to the initial cross section. This value treats effects of deformation and fragmentation in an integral way. For the fragmentation process a correlation was used, based on that of Reinecke and Waldman (see, e.g., in [2]), but modified tentatively to take into account the different velocity development for dense dispersions compared to single drops. Both descriptions are problematic, especially concerning extension to the dispersions which are considered within the detonation theory.

In order to avoid these deficiencies, the interfacial transfer relations, especially the fragmentation process, must be modeled more completely. Thus a theoretical basis will be produced that – after experimental verification – allows extrapolations to different systems and conditions.

Drop Deformation and Hydrodynamic Drag

A first extension of currently available thermal detonation models involves describing the deformation behavior of the drops of melt in the flow field and using actual drag coefficients related to the actual state of the drop in the flow field. This means, that within the exchange terms of the momentum equations (see [2]) the expression $C_{D0} \cdot R_0^2$ is replaced by $C_D \cdot a^2$. Thus the drift and deformation behavior of the drops is calculated as a coupled process, and the drag coefficient is no longer a globally determined input parameter. Instead, a correlation is used that is based on measurements of Wentz and Thodos [3] and takes into account multidrop effects as well as deformation

$$C_D = \frac{4}{3} \beta_F^{-1} \frac{0.396}{\mathrm{Re}^{*0.05} - 1.2} [1 + 1.49(1 - \tilde{a}^{-3})] \qquad (1)$$

The correlation of Wentz and Thodos was determined under steady-state conditions for turbulent flow ($3 \cdot 10^3 < \mathrm{Re}^* < 6.5 \cdot 10^4$) and volume fractions β_F of 0.35–0.88 (or $V_F/V_M = 0.54–7.3$). These regions are of interest in the detonation modeling. The deformation effect, expressed by the term in square brackets, is described according to the single-drop correlation of Hughes and Gilliland [4]. Taking values from steady-state experiments implies a quasi-steady-state approach. The tentative description of the deformation effect by a factor independent of the dispersion and Reynolds number effects is of course limited to a certain parameter range. An improved description, however, needs more empirical knowledge on these relationships.

The deformation behavior of a drop, which is caused by the pressure field of the outside flow, is described on the basis of

---

Contributed by the Heat Transfer Division and presented at the 21st National Heat Transfer Conference, Seattle, Washington, July 24–27, 1983. Manuscript received by the Heat Transfer Division October 3, 1984.

the model of Krauss [5]. It assumes that the flattening drop always has the shape of a planetary ellipsoid (with the semimajor axis perpendicular to the flow direction). The relative motion of the drop masses, induced by the outside pressure field, is then calculated under the further assumptions of incompressible drop fluid and irrotational flow inside the drop. For boundary conditions, only the pressure at the equator and an averaged pressure at the stagnation points are considered. The effect can be represented by a pressure coefficient ΔC_p, which determines the deformation behavior. Using steady-state values for ΔC_p again means a quasi-steady-state approach.

The present modeling uses an extended description taking into account the surface tension and higher flow velocities inside the drop [6]. These extensions are important for drop materials with relatively high surface tensions (such as melts of metals) and for calculating larger deformations. The following equation results, determining the deformation behavior $a(t)$

$$\frac{d^2a}{dt^2} - \frac{1}{a}\left(\frac{da}{dt}\right)^2 = \frac{a}{\frac{a^2}{2} + b^2}\left[\left(\frac{da}{dt}\right)^2\left(2\frac{b^2}{a^2} - \frac{1}{2}\right) + \frac{1}{2}\Delta C_p \frac{\rho_F}{\rho_M} u_r^2 + \frac{\sigma}{\rho_M}\left(\frac{2b}{a^2} - \frac{a}{b^2} - \frac{1}{a}\right)\right] \tag{2}$$

with the initial conditions $a = R$, $da/dt = 0$ for $t = 0$. The first and the last term inside the square brackets of equation (2) result in addition to the solution of Krauss. The first term corresponds to the velocity effect and gives a restraint or enhancement for deformation, depending on the size of the deformation $\tilde{a}$. The last term gives the restraining effect of surface tension.

Hydrodynamic Fragmentation Models

Two hydrodynamic fragmentation models have been developed, providing new descriptions for the decisive interfacial relations within the thermal detonation model. Related to the actual states of the flow field, one of the fragmentation models describes fragmentation by Taylor instability and deformation breakup as a coupled mechanism. The other considers stripping of unstable capillary waves produced by the relative flow of the coolant. Within these models of the fragmentation process, actual fragment sizes and rates of production of fragmented mass – which influence the drift and deformation behavior and vice versa – are calculated.

The two models have been developed with respect to the state of the discussion on hydrodynamic fragmentation processes, which concentrates on stripping processes and the so-called "catastrophic" breakup, attributed to Taylor instabilities. While boundary layer stripping models gave results much too high fragmentation times (more than a factor of ten higher) compared to the experimental results (see, e.g., [6], [7]), Taylor instabilities are usually accepted as determining the fragmentation at higher Weber numbers. The present modeling aids – in addition to provide descriptions for the transfer processes in the detonation model – in a decision on the relevance of the different fragmentation mechanisms.

Fragmentation by Taylor Instability and Deformation Breakup. Taylor instability occurs on the windward side of a drop, which is accelerated by the flow of the surrounding fluid, if the density of the drop material is higher than that of the fluid. In the present model the growth of the waves is calculated from a linearized and nonviscous theory considering the windward drop surface as a plane. An equation of Richtmyer [8] for time-dependent acceleration is used, which is adequate to the time-dependent flow field. The wavelength is determined as the fastest growing one, and for the initial conditions an impulsive perturbation is chosen similar to Cooper and Dienes [9], which is assumed to be determined by the relative velocity of drop and coolant.

In earlier works (e.g., [6, 10]) the fragmentation by Taylor instability was modeled as a sudden breakup of the drop after being completely pierced by the waves. This model seems, however, only to be realistic for large wavelengths, causing "primary" breakup [11] of the drop into several droplets. In fact, also the shadowgraphs as well as the X-ray pictures in [7] only show a breakup into two or several smaller droplets and not a fine fragmentation at the instant which is assigned to

Nomenclature

A = cross section of stripped crest of ring wave
$a;\tilde{a}$ = semimajor axis of planetary ellipsoid; dimensionless: a/R
Bo = Bond number $\rho_M \dot{u}_M R^2/\sigma$
b = semiminor axis of planetary ellipsoid
C_D = drag coefficient
ΔC_p = pressure coefficient, equation (2)
c = phase velocity of a wave
E = degree of fragmented mass, m_{Fr}/m_0
F = flow force on wave crest
F_i^* = functions of geometrical values ϑ, ϵ ($i = 1,2,3$)
f = mass ratio melt/coolant
H = thickness of drop within cylindrical model
k = wave number
$m;m_{Fr}$ = mass of drop without fragments; mass of fragmented parts of the drop
p = pressure
R = radius
r,r^* = radii (see Fig. 2)
Re;Re* = Reynolds number, $\mathrm{Re} = 2 u_r R/\upsilon_F$; $\mathrm{Re}^* = \mathrm{Re} \cdot \beta_F/(1 - \beta_F)$
s = width of wave crest (see Fig. 2)
T = temperature
$t;\tilde{t}$ = time; dimensionless: $0.5\, u_{r0} t . \sqrt{\rho_{F0}/\rho_{M0}}/R_0$
$u;\dot{u}$ = flow velocity in shock front system; acceleration
$u_r;u_r^*$ = relative velocity, $u_M - u_F$; component parallel to drop surface
V = volume
We = Weber number, $\rho_F u_r^2 R/\sigma$
x = coordinate in the direction of the wind
β = volume fraction (of the whole volume)
β^* = sheltering parameter, equation (3)
ϑ, ϑ^* = angles (see Fig. 2)
γ = vapor volume fraction (of the coolant volume)
ϵ = numerical eccentricity of the ellipsoid
λ = wavelength
$\eta;\eta_A$ = wave displacement; wave amplitude
$\eta_S;\eta_B$ = stripping amplitude; basic amplitude of stripping (see Fig. 2)
υ = kinematic viscosity
ρ = density
σ = surface tension

Subscripts

C = coolant
F = fluid (coolant + fragments)
Fr = fragmentation, fragmented
G = air
M = melt
sat = saturation
0 = initial value

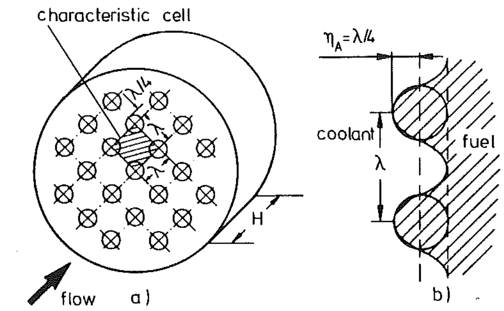

Fig. 1 Sketch of fragmentation by Taylor instability: (*a*) cylindrical model of the drop with wave pattern on the frontal surface; (*b*) detachment of spherical fragments with a radius of λ/4 (side view)

such a "catastrophic" event and interpreted as termination of fragmentation. From the linearized theory, significantly smaller wavelengths are obtained than observed [12]. This could be due to coalescence of the troughs ("bubbles" of coolant) during the later phase of wave growth [13]. On the other hand, the observed breakup in larger droplets, possibly giving the appearance of large waves due to continued stripping, could also be simply caused by the deformation of the drop.

Besides the possible role of Taylor instabilities in primary breakup of the drop, also the efficacy of Taylor instabilities in fine fragmentation at higher Weber numbers cannot be excluded at present. The model presented here investigates essentially the latter possibility. Total penetration of the drop with the relatively small wavelengths, resulting from the linearized theory for higher Weber numbers, cannot be imagined. Instead, two possible processes can be thought of. On one hand, bubbles of coolant could detach and travel into the drop according to the model of Zuber [14] in the case of vapor film boiling, who assumed a vapor bubble radius of λ/4. In the present case, the part of the drop filled by the bubbles should however be assumed as fragmented. Alternatively, break-off of the "spikes" of drop material may be assumed (see, e.g., [15]), which may be favored by the higher growth velocities of the spikes [9]. The latter approach is adapted here, assuming simply break-off of fragments of radius λ/4 according to the inverse model of Zuber. By this, the fragmentation should be overestimated. As an analogy of the present approach, the case of a cooling tube with detaching drops from the liquid film below may be considered. More investigations on the nonlinear stages under given conditions are necessary to determine the real behavior.

For the description, the drop is replaced by a cylindrical model with the windward area πa^2 and the thickness H (Fig. 1(*a*)) also shows the spacing of the Taylor waves on the windward surface, which means break-off of one fragment from a surface area of λ^2. Spherical fragments with radius $\lambda/4$ are assumed to break off, when the amplitudes of the waves reach the same size (Fig. 1(*b*)). After the break-off of the fragments, in the present model, the Taylor waves again start to grow on the remaining drop. Hereby the wavelength and the initial disturbance are again determined according to the aforementioned approach using the actual values of the process. Thus the fragmentation process represents a continued break-off of fragments rather than a sudden breakup.

During this process of Taylor wave growth and break-off, the drop deforms according to the description of the previous chapter. Hereby the cylindrical and the ellipsoidal models of the drop are used simultaneously. The deformation process itself, however, can cause fragmentation. As a criterion, the requirement of minimum surface energy is used, which gives a lower limit of deformation of $\tilde{a}=1.45$ for breakup of the drops into two parts, assuming spherical parts of equal size. After breakup, the deformation process and the Taylor wave growth are assumed to start again with the resulting spherical drops.

Stripping of Waves, Produced by Shear Flow. The shear flow of the fluid parallel to the surface of the drop induces growing waves according to the generation of water waves by wind. The underlying instability of the interface was treated first by Kelvin and Helmholtz (see, e.g., [16] and [17]) for incompressible inviscid fluids with uniform, but different velocities parallel to the interface. However, Jeffreys [16] observed that water waves were initiated by much smaller wind velocities than predicted from this theory. He concluded that irrotational motion in the air flow cannot exist and thus considered the separation of the air flow over the wave crests. This leads to a periodic aerodynamic pressure component in phase with the wave slope, while the Kelvin-Helmholtz mechanism contains an aerodynamic pressure which is in phase with the surface displacement. Based on this hypothesis Jeffreys assumed the aerodynamic pressure to be of the form $\beta^* \rho_G (u_r^* - c)^2 \partial\eta/\partial x$. The Jeffreys approach seems to be appropriate as a first step, although more studies on basic mechanisms seem to be necessary. This is especially true for the conditions of liquid-liquid configurations, high relative velocities, and capillary waves, considered here.

An equation, describing the growth of water waves under the influence of the air flow in a linearized theory, was derived by Jeffreys [16] and Lamb [17]. They considered the motion of the water as approximately irrotational and used an energy balance over one wavelength. Hereby, the dissipation of energy by the viscosity of the water (as a damping effect for wave growth) was also taken into account. For the velocity of waves, the free surface velocity without shear flow was taken, an assumption which needs further examination. Dickerson and Coultas [18] first used these equations to describe the growth and motion of capillary waves on spherical liquid drops in gas streams. The waves were hereby assumed to start from disturbances at the windward stagnation point, forming traveling wave rings around the axis of the drop in the flow direction. The basic equations had to be extended to consider geometrical effects. A further extension to ellipsoidal drops was performed within the present modeling [19]. The equations take the form

$$\frac{1}{\eta_A}\frac{d\eta_A}{dt} = \beta^* \frac{\rho_F}{\rho_M}\frac{(u_r^* - c)^2}{2c} k - 2k^2 \upsilon_M - \frac{1}{2} F_1^*(\vartheta,\epsilon)\frac{d\vartheta}{dt}, \quad (3)$$

$$\frac{d\vartheta}{dt} = \left[\frac{\sigma k}{\rho_M + \rho_F}\right]^{1/2} \frac{1}{bF_3^*(\vartheta,\epsilon)}. \quad (4)$$

Hereby $c = [\sigma k/(\rho_M + \rho_F)]^{1/2}$ is the wave velocity and u_r^* (see Fig. 2) the velocity component parallel to the surface $(u_r^* = u_r F_2^*(\vartheta,\epsilon))$.

While Dickerson and Coultas assume total stripping of the waves when they reach the equator of the drop (which results in nonrealistic amplitudes), the present model uses a more detailed stripping criterion. This is based on the observations of Jeffreys [16], that a wave of given length cannot grow beyond a certain height (called here the "basic amplitude"), which is probably proportional to the wavelength. Furthermore, wind acting on a wave in this critical state will only cause material to be projected from the crests, leaving the height unaltered. In a first approach the basic amplitude is assumed to be half the wavelength. The stripped mass, as well as the radius of the fragments, is determined by a further stripping criterion, which assumes that the work done by the flow force on the crest moving it along its width s must at least be equal to the new surface energy produced by stripping (see Fig. 2)

$$Fs \geq 2\sigma s(2\pi r^* \sin\vartheta^*) \quad (5)$$

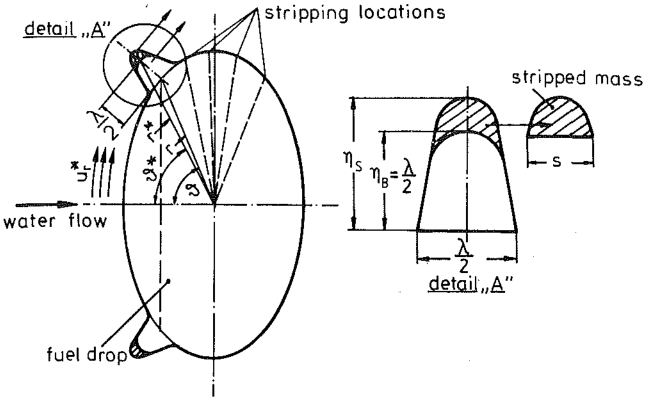

Fig. 2 Sketch of the stripping of the crests of capillary waves on a drop with the shape of a planetary ellipsoid

whereby the flow force F is approximated by

$$F = \beta^*(2\pi r^* \sin\vartheta^*)(\eta_s - \eta_B)\frac{\rho_F}{2}(u_r^* - c)^2 \tag{6}$$

The stripping rate at a certain stripping location on the drop is finally given by

$$\frac{dm_{Fr}}{dt} = \rho_M A (2\pi r^* \sin\vartheta^*)\frac{c}{\lambda} \tag{7}$$

Hereby A denotes the cross section of the stripped crest of a ring wave. The volume of this crest may be regarded as an actual fragment size. A fragment radius can be obtained by considering a corresponding spherical fragment with equal volume. On the other hand the crest of the ring wave should break up itself. This breakup may be given by a requirement of minimum surface energy, as used for deformation breakup.

Thus, when the wave traveling on the drop has reached its first stripping amplitude, the crest is stripped, leaving the basic amplitude, which is allowed to grow and strip again. The result is a pattern of multiple stripping events distributed over the drop with the lowest distance at the drop equator. An additional complication is that the dominant (most rapidly growing) wavelength must change on the drop according to the change of conditions. To take this into account approximately, the wavelength is determined again after certain distances of wave travel.

The pattern given by this model is taken as an approximation for the complex situation, which exists at a certain moment on the drop. Thus the actual stripping rate on the whole drop results, in a quasi-steady-state approach, from the sum over all the local stripping rates (equation (7)) under the given actual conditions. The quasi-steady-state approach assumes that the establishment of a certain pattern corresponding to certain conditions happens quicker than the change of the conditions. In the beginning of the fragmentation process an initiation phase may be possible, e.g., determined by the time for amplitude growth from an initial disturbance to the basic amplitude or alternatively the time for a wave travel over the drop. However, the pattern of stripping may develop rather quickly since small disturbances are existent all over the drop and not only at the forward stagnation point. Therefore, an initial phase is not taken into account at the present state of modeling.

Since intensified stripping occurs at the equator, the mass loss acts against flattening by deformation. Thus, for the calculations presented here, a constant deformation $\bar{a} = 1.2$ was chosen as a first step. Alternatively, a deforming drop – eventually with corrections for the deformation because of stripping – could be considered. The process of fragmentation terminates, according to the model, if capillary wave growth is no longer possible because of velocity equilibration or due to the smallness of the remaining drop.

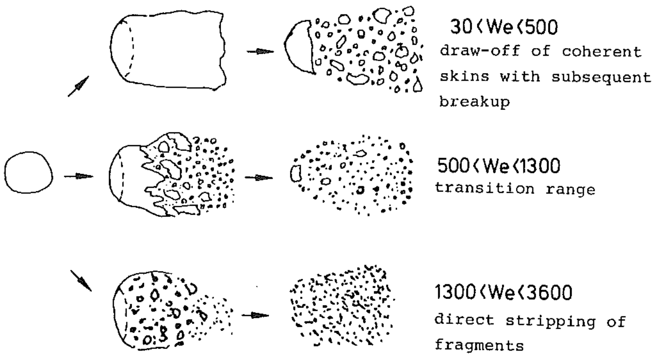

Fig. 3 Sketch of fragmentation phenomena for the studied range of Weber numbers

Comparison With Experimental Results

The comparison of the models with experimental results should be done both globally with detonation experiments of large masses in order to treat integral effects and also in detail, in order to examine the modeling of basic processes. Consequently, both approaches will be considered, starting with a discussion of hydrodynamic fragmentation experiments with single gallium drops in water for examination of the fragmentation modeling, and then making a contribution to the analysis of the vapor explosion experiments of Fry and Robinson [20] and Hohmann et al. [21].

Comparison With Experiments on Hydrodynamic Fragmentation. Experiments with single gallium drops (diameters of 3-5 mm) in streams of water have been performed by Kim et al. [22]. Here a plane and, for the time of observation, a nearly constant flow of water was produced in a channel by a piston, which was driven by the expanding vapor bubble of a wire explosion. The rise time of the flow was in the range 0.1–0.4 ms. Details of the experimental procedure and conditions, as well as a more complete evaluation of the results than performed here, are given in [22].

The experiments covered a range of Weber numbers from 30 to 3600. A significant difference in behavior occurred between low-velocity experiments of, e.g., 5 m/s (We≈70) and high-velocity experiments of, e.g., 20 m/s (We≈1600) water velocity. The low-velocity experiments show a draw-off of an outer shell of the drop, thus giving the appearance of drop enlargement (see Fig. 3 for illustration). Processes like bag or claviform breakup could not be identified. Instead, the process of draw-off may simply be caused by mechanisms like boundary layer stripping, perhaps supported by deformation effects. From the subsequent breakup into small droplets the previous existence of a coherent skin drawn off can clearly be concluded. Breakup occurs probably after further thinning of the skin, due to a requirement of minimum surface energy. A dominance of viscous forces may prevent immediate breakup, then break-off processes combined with wave growth. This low-velocity behavior is not treated by the theoretical descriptions presented here.

In contrast to this behavior, the high-velocity experiments show rapid fragmentation (Fig. 4 for We = 1662), appearing at first sight as a sudden, symmetric blowup, as mentioned, e.g., in [10]. These events occurred in the present experiments as Weber numbers of ~ 10^3, while in [10] much smaller Weber or Bond numbers were given for another liquid–liquid configuration (Hg-H_2O). In experiments with water drops in gas streams such events were observed for We > 10^4 only [12]. In the present experiments, the intermediate velocity region

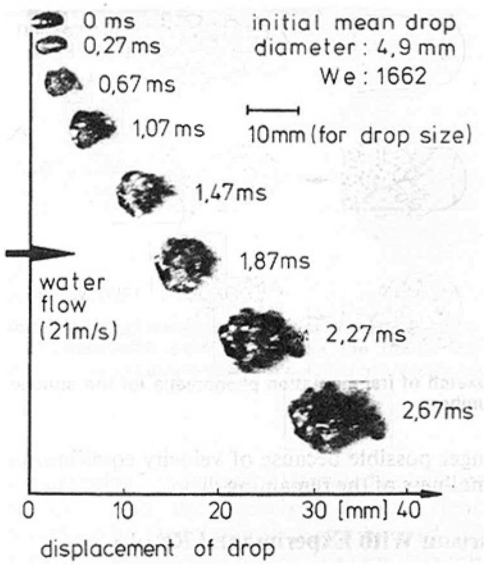

Fig. 4 Time development of the hydrodynamic fragmentation of a gallium drop in a water stream (high-velocity case)

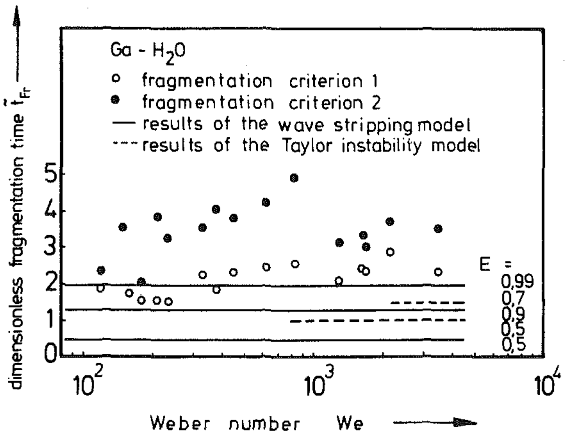

Fig. 5 Comparison of the fragmentation models with experiments on hydrodynamic fragmentation of single gallium drops in water streams

beginning with We≈500 may be considered as a transition region showing progressively more clouds of fragments, thus indicating processes with direct formation of fragments (see Fig. 3). These processes seem to dominate the mechanism of fragmentation at least for We>1000. In the intermediate region also an increase of surface waviness indicating surface instabilities can be observed.

A comparison of the experiments of Kim et al. [22] with the presented fragmentation models is performed here for the fragmentation times. The determination of the fragmentation time is not unique, since a clear distinction between the drop and the fragments is not possible, at least without observation by X-ray methods. Because of this problem, different approximate definitions exist in the literature. Two different criteria have been chosen here. Criterion 1 defines the fragmentation time by the time of doubling of the projected area of the drop and represents a modified version of the criterion used in [10]. Criterion 2 identifies the time of complete fragmentation with the smallness of visible unfragmented parts (observed by the reflection of light) in relation to the existence of large clouds of fragmented mass. The dimensionless times are plotted as a function of the Weber number in Fig. 5.

The results do not confirm the relation $\tilde{t}_{Fr} \sim \mathrm{We}^{-1/4}$ or $\mathrm{Bo}^{-1/4}$, used, e.g., in [10], based on the sudden breakup modeling of Taylor instability. Rather a constant value of $\tilde{t}_{Fr}$ may be deduced, which is usually attributed to stripping processes. Criterion 1 gives a value of $\tilde{t}_{Fr} \approx 2$, while Criterion 2 leads to $\tilde{t}_{Fr} \approx 3.5$. Model calculations, choosing the experimental conditions of the single drop experiments, have been performed for various water velocities and with different Weber numbers by varying the shock front pressure. As an important result, the times needed for a certain degree of fragmentation are obtained. The dimensionless representation in Fig. 5 shows – for both models – nearly constant dimensionless times in a certain range of Weber numbers. The wave stripping model gives a much more rapid and complete fragmentation than the combined Taylor instability and deformation breakup model, for which strong limits of fragmentation occur in addition.

From these results, fine fragmentation by Taylor instabilities seems to be much less important than by stripping of shear flow induced waves. This does not exclude possible effects of primary breakup due to Taylor instabilities, which could however not be observed in the experiment. The appearance of sudden, symmetric blowup needs not to be explained by Taylor instabilities, but may be caused by the combined action of the deformation and the cloud of fragments (see also [10]). Enhanced stripping due to primary breakup could explain a rapid finishing of the fragmentation process [13].

Differing from models on boundary layer stripping, the times given by the present stripping model lie in the range of the experimental findings. This is due to the enhancement of stripping by shear flow instabilities. From Fig. 5, the experimental fragmentation times however seem still to be considerably larger than the predicted ones. In this respect, the uncertainties of the experimental determination of fragmentation times as well as the theoretical idealizations have to be considered (e.g., a delay time has not been taken into account in the calculations). Therefore, the fact that the theory gives smaller times just underlines the capability of the model to explain the observed fragmentation behavior.

In the experiment, fragment sizes of about 10-30 μm in radius were obtained for We = 3520 (u_r = 31 m/s). The theory for Taylor instability yields significantly larger fragments of > 125 μm, while fragments of 33-58 μm, (or 3-20 μm if breakup of the stripped ring is considered) result from the wave stripping model. Again the result may be interpreted as indication for the existence and importance of stripping mechanisms in the experiment. More detailed comparisons, also including drift and deformation behavior, will be done in the future.

Comparison With Vapor Explosion Experiments. Two experiments have been selected for comparison, the tin-water experiment T 107 of Fry and Robinson [20] and the salt-water experiments of Hohmann et al. [21]. In both experiments, detonators were used to trigger the initial mixture of melt and water, but only the latter experiments were performed for different system pressures. Comparisons with theoretical results have already been published for both experiments, e.g., in [2] and [23], but not with a detonation description including the fragmentation and hydrodynamic drag description as presented here. Present calculations with this complete description, without use of input values for $\tilde{t}_{Fr}$ and C_{D0}, were performed with the wave stripping model only.

For determining the stable detonation cases, the Hugoniot tangency condition can be used (see [1, 2]). However, generally the knee point of the Hugoniot curves, designing the onset of saturation, results, while higher pressure cases are doubted to be stable [1]. Therefore, restricting to these cases for the present calculations, a simplified procedure could be chosen. Cases of coincidence of velocity equilibration and saturation were searched and taken as detonation cases, if a tangent could be drawn from the initial point to the

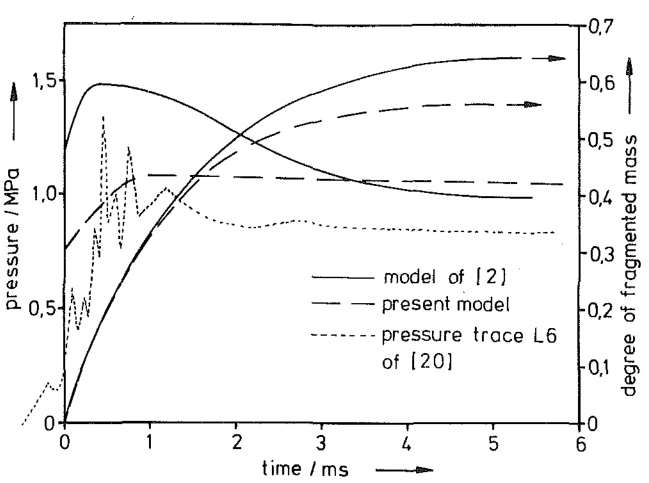

Fig. 6 Theoretical results for the tin-water experiment in comparison with an experimental pressure trace

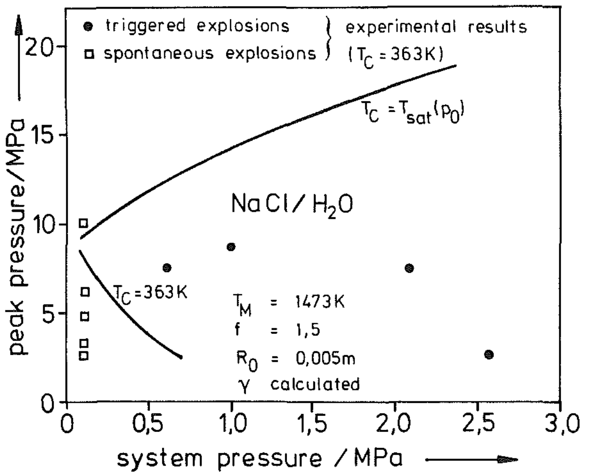

Fig. 7 Peak pressures of the detonation cases calculated with the wave stripping model for the salt-water experiments as a function of the system pressure

saturation-(knee-) point. The mixture parameters have been chosen as in [2] and [23] according to the experimental data, besides calculating the initial vapor volume fraction from a film boiling model for the salt-water case. Inside the wave no vapor is considered, assuming complete collapse of the vapor just at the shock front as in [2].

The comparison with the Fry and Robinson experiment in [2] was essentially based on the pressure trace of the second transducer (L6 in [20]). This choice was somewhat arbitrary; however it was justified by the obvious local effects with strong variations shown by the subsequent pressure transducers. In addition, for these transducers, the reliable part of the traces became shorter and shorter [20]. From the experimental results, it is not quite sure whether a steady-state wave was established. A slow decrease in pressure level can be deduced until at the last two pressure transducers the pressure seems to increase again, although local effects may explain the sharper pressure peaks. On the other hand, the propagation velocity did not vary strongly (78–86 m/s), indicating steady-state behavior.

The value of 80 m/s obtained from the calculation in [2], using the Reinecke and Waldman correlation and adequate input parameters for $\tilde{t}_{Fr}$ and C_{D0}, agrees well with the experimental data. In contrast to this, the detonation wave determined here by use of the wave stripping model has only a velocity of 60 m/s. Correspondingly the shock front and the peak pressures are somewhat smaller, as can be seen from Fig. 6. Therefore, it was concluded in [24] that hydrodynamic fragmentation by stripping of waves could only partly explain the experimental results, although the final pressures at the end of the wave and the degree of fragmented mass are nearly the same in both calculations (see Fig. 6). Inclusion of the experimental pressure trace (L6) in Fig. 6, however, shows that the earlier calculations overestimate the experimental results. The comparison shows that the fragmentation due to the wave stripping model could be enough to explain the experimental result, at least with respect to the pressure level. Then, for explaining the difference in the wave velocity, the conclusion could be that the mixture data were not adequate. To analyse this, further calculations should be performed. Additional experiments with well defined coarse premixtures are also recommended in order to get more assured and reproducible data.

Figure 7 shows the maximum pressures of the detonation cases, calculated for the salt-water system [21], as a function of the system pressure. In addition to a constant water temperature, as used in the experiments, cases for saturated water at the respective system pressure are also considered. For constant water temperature a decrease of peak pressures with increasing system pressures results from the theory. Above 0.7 MPa no further detonation cases could be found; that is, for all these pressures velocity equilibration occurred before saturation of the water could be reached. Experimentally, a maximum of the peak pressures is measured in a range of system pressures between 1–2 MPa, while a sharp decrease was obtained at roughly 3 MPa [21]. (Note: The sharp narrow peaks of width $< 50\ \mu s$ shown in [21] for system pressures of 1 and 2.1 MPa were not considered to be of relevance.) A good agreement exists between the theoretical and experimental propagation velocities for the case with a lower system pressure of 0.6 MPa (theory: 190 m/s, experiment 180 m/s), in spite of the large discrepancy in the peak pressures.

While theory and experiment both give a cutoff for higher system pressures, the differences that remain (e.g., for the detonation pressures) may be due to the restricted relevance of hydrodynamic fragmentation processes within this system because of the low density difference of salt and water. Thus thermally induced fragmentation processes may be dominant, especially for lower pressure levels. Finally, it is noticed that assuming a higher vapor content than resulting from the film boiling calculation for the initial mixture would however favor fragmentation and higher detonation pressures. On the other hand, the propagation velocity belonging to a certain shock front pressure would be reduced (see, e.g., [2]). Theoretical calculations for saturated water show increasing peak pressures in contrast to the result with constant water temperature (Fig. 7). No experiments until now have been available to decide on this result, which would be highly important, e.g., for the analysis of the possibility of vapor explosions within hypothetical high-pressure core melt accidents in nuclear reactors.

Conclusions

An improved description of thermal detonations has been developed by modeling the interphase relations due to the hydrodynamic drag of the drops of melt and the fragmentation processes. For the latter, two models of hydrodynamic fragmentation are presented. Fine fragmentation by Taylor instabilities is described as a continuous process rather than a sudden event. The model, in which deformation breakup also is considered, yields, for an experimental example case with fragmentation of single gallium drops in water streams, a much slower fragmentation and significantly larger fragments than the wave stripping model. Compared to boundary layer stripping, the stripping process is enhanced strongly in the latter model due to the consideration of shear flow instabilities. The results of this model lie in the experimental range. Both, experimentally and theoretically, constant dimensionless fragmentation times are obtained over a wide range of Weber numbers.

The wave stripping model was used within thermal detonation calculations for large scale tin-water and salt-water experiments. The large discrepancies in the latter case indicate that hydrodynamic fragmentation should not be sufficient to explain the experimental results, although the calculated suppression of detonation cases corresponds qualitatively with the experimental findings. Therefore, at least a contribution of thermal fragmentation mechanisms should be considered. In the tin-water case, the discrepancy was smaller, which may be due to the larger difference in the densities for this system.

Acknowledgments

This work was sponsored by and done in cooperation with the Joint Research Center, Ispra, Italy. Part of the work, concerning the detonation description [2], was also sponsored by the German Government (BMFT).

References

1 Sharon, A., and Bankoff, S. G., "On the Existence of Steady Supercritical Plane Thermal Detonations," *International Journal of Heat and Mass Transfer*, Vol. 24, No. 10, 1981, pp. 1561–1572.

2 Schwalbe, W., Bürger, M., and Unger, H., "Investigations on Shock Waves in Large Scale Vapor Explosions," *Proceedings, ASME Winter Annual Meeting*, HTD-Vol. 19, 1981, pp. 89–97.

3 Wentz, C. A., and Thodos, G., "Pressure Drops in the Flow of Gases Through Packed and Distended Beds of Spherical Particles," *AIChE Journal*, Vol. 9, No. 1, 1963, pp. 81–84.

4 Hughes, R. R., and Gilliland, E. R., "The Mechanics of Drops," *Chemical Engineering Progress*, Vol. 48, 1952, pp. 497–500.

5 Krauss, W. E., "Water Drop Deformation and Fragmentation Due to Shock Wave Impact," Ph.D. thesis, University of Florida, 1970.

6 Schriewer, J., "Zur Theorie der hydrodynamischen Fragmentation von Flüssigkeitstropfen in flüssigen Medien durch Stoβwellen mit Anwendungen auf die Systeme Hg/H_2O, Fe/H_2O, Stahl/Na, UO_2/Na," Dissertation, Institut fur Kernenergetic und Energiesysteme, University of Stuttgart, FRG, 1980.

7 Reinecke, W. G., and Waldman, G. D., "An Investigation of Water Drop Disintegration in the Region Behind Strong Shock Waves," *Proc. of Third Int. Conference on Rain Erosion and Related Phenomena*, Hartely Whitney, Hampshire, England, 1970, pp. 629–667.

8 Richtmyer, R. D., "Taylor Instability in Shock Acceleration of Compressible Fluids," *Communications on Pure and Applied Mathematics*, Vol. 13, 1960, pp. 297–319.

9 Cooper, F., and Dienes, J., "The Role of Rayleigh-Taylor Instabilities in Fuel-Coolant Interactions," LA-VR-77-1945, Los Alamos Scientific Lab., 1978.

10 Theofanous, T. G., Saito, M., and Efthimiadis, T., "The Role of Hydrodynamic Fragmentation in Fuel-Coolant Interactions," *Fourth CSNI Specialist Meeting on Fuel-Coolant Interactions*, OECD, CSNI Report No. 37, Vol. 2, 1979, pp, 112–129.

11 Pilch, M., Erdman, C. A., and Reynolds, A. B., "Acceleration Induced Fragmentation of Liquid Drops," NUREG/CR-2247, Department of Nuclear Engineering, University of Virginia, 1981.

12 Reinecke, W. G., and Waldman, G. D., "Shock Layer Shattering of Cloud Drops in Reentry Flight," *AIAA Paper No. 75-152*, 1975.

13 Fishburn, B. D., "Boundary Layer Stripping of Liquid Drops Fragmented by Taylor Instability," *Acta Astronautica*, Vol. 1, 1974, pp. 1267–1284.

14 Zuber, N., "Hydrodynamic Aspects of Boiling Heat Transfer," Ph.D. thesis, University of California, 1959.

15 Chang-Mateu, T., and Bankoff, S. G., "Non-linear Taylor Instability in a Cylindrical Vessel," *Proceedings, 21st National Heat Transfer Conference*, ASME HTD-Vol. 23, 1983, pp. 29–35.

16 Jeffreys, H., "On the Formation of Water Waves by Wind," *Proceedings of the Royal Society*, A, Vol. 107, 1925, pp. 189–206, Vol. 110, 1926, pp. 241–247.

17 Lamb, H., *Hydrodynamics*, 6th ed., Cambridge University Press, London, New York, 1975.

18 Dickerson, R. A., and Coultas, T. A., "Breakup of Droplets in an Accelerating Gas Flow," *AIAA Paper No. 66-661*, 1966.

19 Bürger, M., et al., "Theoretical Investigations on Fragmentation and Thermal Detonation Processes," to be published as EUR-report.

20 Fry, C. J., and Robinson, C. H., "Experimental Observations of Propagating Thermal Interactions in Metal/Water Systems," *Fourth CSNI Specialist Meeting on Fuel-Coolant Interactions*, OECD, CSNI Report No. 37, Vol. 2, 1979, pp. 330–362.

21 Hohmann, H., et al., "Experimental Investigation of Spontaneous and Triggered Vapour Explosions in the Molten Salt/Water System." *Proc. of the Int. Meeting on Thermal Nuclear Reactor Safety*, NUREG/CP-0027, Vol. 2, 1982, pp. 962–971.

22 Kim, D. S., et al., "Experimental Investigation of Hydrodynamic Fragmentation of Galium Drops in Water Flows," *Proc. of ANS/ENS Int. Meeting on Light Water Reactor Severe Accident Evaluation*, Vol. 1, TS-6.4, Cambridge, Mass., 1983.

23 Bürger, M., Schwalbe, W., and Unger, H., "Application of Hydrodynamic and Thermal Fragmentation Models and a Steady State Thermal Detonation Model to Molten Salt-Water Vapor Explosions," *Proc. of the Int. Meeting on Thermal Nuclear Reactor Safety*, NUREG/CP-0027, Vol. 2, 1982, pp. 1378–1387.

24 Bürger, M., et al., "Two Phase Description of Hydrodynamic Fragmentation Processes within Thermal Detonation Waves," *21st National Heat Transfer Conference*, ASME HTD-Vol. 23, 1983, pp. 45–52.

Y. Yamada
M. Akai
Seniors Researchers,
Mechancial Engineering Laboratory,
Tsukuba Science City,
Ibaraki-ken, Japan

Y. Mori
Professor,
Tokyo Institute of Technology,
Oh-okayama, Meguro-ku,
Tokyo, Japan

Shell-and-Tube Side Heat Transfer Augmentation by the Use of Wall Radiation in a Crossflow Shell-and-Tube Heat Exchanger

The heat transfer performance of a crossflow shell-and-tube heat exchanger for high-temperature use in which heat transfer is augmented by the use of wall radiation in both shell and tube sides, is studied. Radiation plates are inserted in the shell side, and twisted cross-tapes in the tube side. Overall heat transfer coefficients are measured to be about a maximum 80 percent larger than those without radiation, where the inlet temperatures of the hot gas range up to 800 °C, while those of the cold gas are about room temperature. Analytical results agree well with experimental results, and an approximate calculation procedure is found to be simple and accurate enough for practical use.

Introduction

Recuperators for heat recovery from high-temperature waste gases, regenerators for high-temperature gas turbine plants, intermediate heat exchangers for high-temperature gas reactor systems, and other high-temperature gas heat exchangers are expected to be used more widely in the near future for the more effective use of heat. In these high-temperature heat exchangers, various methods of heat transfer augmentation are used to aid gas-to-gas heat exchange. These methods are classified roughly into two groups; one uses the extended surfaces of fins, etc., while the other uses improvements in flow patterns through the use of twisted tapes, varied roughness, etc.

However, to provide fins on the tube surface of high-temperature heat exchangers is not practical because superalloys with high creep performance and very low machinability are required. Therefore, heat transfer augmentation by the use of radiation combined with convection is effective because of the high temperature used. Concerning heat transfer augmentation by wall radiation, several fundamental theoretical [1, 2] and experimental investigations [3] have been reported. Mori et al. [4] reported the results of heat transfer augmentation through the use of radiation plates provided in the shell side of a crossflow shell-and-tube heat exchanger. However, in that report the radiation was not very effective, because there was no radiating wall inserted in the tube side, and the emissivity of the heat transfer surfaces was about 0.5. Concerning other augmentation methods, heat transfer augmentation by radiating small particles mixed in working fluid [5, 6], has been studied.

The crossflow shell-and-tube heat exchanger in this report has radiation plates in the shell side and twisted cross-tapes in the tube side. Considerable amount of experimental work has been reported by Bergles et al. [7], and Smith et al. [8], and a successful corrrelation for estimating the augmented heat transfer coefficients by twisted tapes was obtained [7]. In their studies, twisted tapes fit on the inner tube surfaces. However, from the view point of utilizing wall radiation effect inside the tube, twisted tapes do not necessarily fit on the inner tube surfaces. In this report, we used the twisted cross-tapes with a width smaller than the inner tube diameter, which work as both radiating walls and promoters of convective heat transfer. This feature of the twisted cross-tape is considerably different from the idea of conventional twisted tapes. Furthermore, all heat exchanger surfaces have an emissivity higher than 0.9 so that the wall radition effect is as high as possible. Changes in friction factors due to the insertion of the radiating walls are also measured and discussed.

The calculated temperature profiles and heat transfer performance agree well with the measured ones. The analysis of Mori et al. [4] proposed an approximate calculation method which was not adequate to predict the heat transfer performance of heat exchangers with a complicated structure. This report demonstrates a simple approximate calculation procedure that predicts the overall heat transfer coefficient of heat exchangers equipped with radiating walls in both the shell and tube sides.

Experiment

Experimental Apparatus and Procedure. Figure 1 shows roughly the heat exchanger used in this study, and the arrangements of the tubes, radiation plates, and twisted cross-tapes. It is a crossflow shell-and-tube heat exchanger with 35 tubes arranged in line with 5 transverse rows and 7 longitudinal rows. Hot gas flows in the shell side, and cold gas in the tube side. Radiation plates are inserted parallel to the flow direction between the tubes, while the twisted cross-tapes are inserted in the tubes.

Counterflow heat exchangers are considered to have the highest temperature effectiveness among counter, cross, and parallel-flow heat exchangers [9]. However, in high-temperature use, the heat transfer surfaces at the hot end could be exposed to very high temperatures, which could cause structural failure. On the other hand, the temperature effectiveness of parallel-flow heat exchangers is limited, because the outlet temperature of the cold fluid cannot exceed that of the hot fluid. Crossflow heat exchangers have lower temperature effectiveness than counterflow heat exchangers, but save space because of an easier inlet and outlet header design than that of counterflow heat exchangers. Furthermore, multipass crossflow can easily achieve a higher temperature effectiveness than singlepass crossflow. Thus crossflow gas-to-gas heat exchangers are widely used for recuperators operating below 1000°C.

We take out one space between two neighboring radiation plates and divide it into rectangular sections, each of which encloses one tube, and number the surfaces as shown in Fig. 2 for convenience of numerical calculation. The dimensions and the arrangements of the tubes, radiation plates and twisted

---

Contributed by the Heat Transfer Division for publication in the JOURNAL OF HEAT TRANSFER. Manuscript received by the Heat Transfer Division April. 21, 1983.

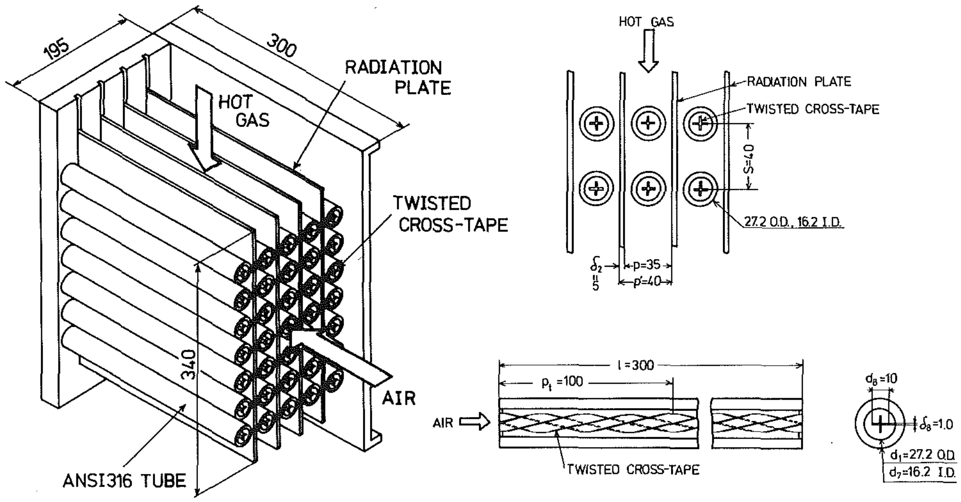

Fig. 1 Augmented heat exchanger assembly with tube, radiation plate, and twisted cross-tape arrangements with all dimensions in mm

cross-tapes are shown in Fig. 1. The tubes and radiation plates are thick enough to embed sheathed thermocouples of 1.0 mm o.d. The material is stainless steel ANSI316 for all the tubes, radiation plates, and twisted cross-tapes.

Conventional twisted tapes are made of single tapes and fitted to the inner surface of the tubes. They provide two functions: as flow swirlers and conducting fins, with rather large pressure drops. Twisted tapes for the purpose of radiating walls do not necessarily fit the inner surfaces, so their width can be less than the inner diameter of the tubes. On the other hand, the smaller width of a single tape brings about a smaller configuration factor between the inner surface and the single tape. Therefore, in this study we have used twisted cross-tapes to increase the configuration factor between the inner surface and the twisted cross-tape, and also to increase the area of the tape. The twisted cross-tapes with smaller width than the inner tube diameter are held coaxially by supports fitted at both ends.

The main working fluid is air in both the shell and tube sides, and in some cases, we used a mixture of air and CO_2 with 10–18 percent volume in the shell side to simulate burned gas and investigate the effect of radiating gas. Hot gas up to 800°C flows into the heat exchanger from the top and the ambient air flows horizontally. The heat exchanger is insulated by a ceramic fiber of about 100 mm thickness.

High-temperature black paint (Tempil Inc., Pyromark) makes higher the emissivity of both the inner and outer tube surfaces as well as the surfaces of both the radiation plates and tapes.

The tubes in the central transverse row, the radiation plates

Nomenclature

A = heat transfer area (m^2)
d_1 = outer tube diameter (m, mm)
d_7 = inner tube diameter (m, mm)
d_8 = twisted cross-tape width (m, mm)
d_e = equivalent hydraulic diameter of a tube (m)
E = heat transfer augmentation coefficient, defined by equation (4)
F_{j-k} = configuration factor between surface j to surface k
f = Fanning friction factor $= 2d\Delta p/\rho u^2 l$
H_{jk} = ratio of (heat tranfser coefficient) × (heat transfer area) of surface k to that of surface $j = h_k A_k/(h_j A_j)$
h = heat transfer coefficient (W/m^2K)
i = number of longitudinal rows
l = tube length (m, mm)
M = radiation-convection parameter $= \epsilon N/\mathrm{Nu}$
m = the number of fins in a twisted tape
N = radiation-conduction parameter $= d\sigma t_{m2,\,\mathrm{in}}{}^3/\lambda$
Nu = Nusselt number $= dh/\lambda$
P = parameters given in equation (11)
Pr = Prandtl number
p = gap between two neighboring radiation plates (m, mm) or pressure (MPa)
p' = transverse tube pitch (m, mm)
p_t = helical pitch defined for 360 deg rotation of the twisted tape (m, mm)
Δp = pressure loss $= f\rho u^2 l/(2d)$ (MPa)
Q = normalized heat flux $= q/ht_{m2,\,\mathrm{in}}$
q = heat flux (W/m^2)
Re = Reynolds number $= ud/\nu$
St = Stanton number = Nu/RePr
s = longitudinal tube pitch (m, mm)
T = normalized temperature $= t/t_{m2,\,\mathrm{in}}$
t = temperature (K, °C)
U = overall heat transfer coefficient (W/m^2K)
U^* = overall heat transfer augmentation coefficient, defined by equation (5)
u = average flow velocity (m/s)
w = mass flow rate (kg/s)

Greek Symbols

δ = thickness of plate or tape (m, mm)
ϵ = emissivity
θ = temperature ratio defined in equation (14)
λ = thermal conductivity (W/mK)
ν = kinematic viscosity (m^2/s)
ρ = density (kg/m^3)
σ = Stefan-Boltzmann constant (W/m^2K^4)

Subscripts

1 to 8 = surfaces shown in Fig. 2
ap = approximate calculation
b = inlet and outlet average
c = convection
exp = experimental result
in = inlet
$m1$ = hot gas or shell-side
$m2$ = cold gas or tube-side
out = outlet
r = combined radiation and convection
th = numerical calculation
w = wall

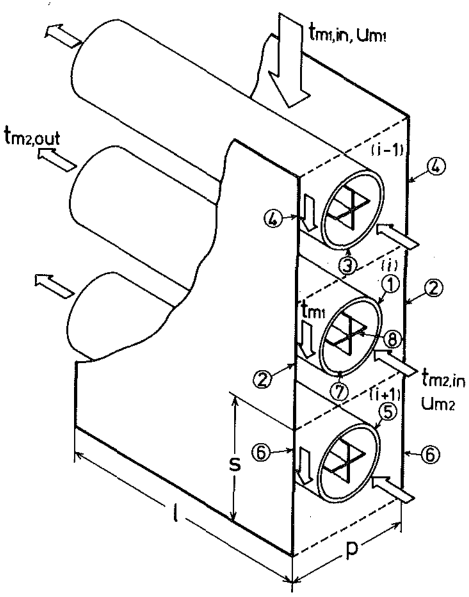

Fig. 2 Idealized model for numerical calculations

around them, and the twisted cross-tapes in them, all have thermocouples. The temperatures of the tubes and twisted cross-tapes are measured only at the central row of the five transverse rows, since the end rows of the five transverse rows might be affected by heat loss in spite of insulation. The thermocouples are installed in the tube walls and on the surfaces of the twisted cross-tapes at the middle position along the flow direction of the cold gas, because the analysis in the later section regards the temperature at these positions as the representative temperatures of the tubes and the twisted cross-tapes. The twisted cross-tapes are too thin to embed the sheathed thermocouples of 1.0 mm o.d. In this study, the thermocouples of 1.0 mm o.d., which have 10-mm-long stainless steel rods with the same diameter as the sheathed thermocouples at the end of the thermocouple junctions, are used. These rods are welded on to the surface of the twisted cross-tapes at the point of middle height of the fins. Therefore, the thermocouple junctions are considered to be placed in a position 0.5 mm above the surface of the twisted cross-tapes. The surface temperatures of the twisted cross-tapes are obtained by correcting the measured temperatures for the fin effect of the rods. The surface temperatures of the tubes are obtained from the measured temperatures by correcting the depth at which the thermocouples are embedded.

The temperatures of the radiation plates are measured only at the two neighboring plates, which face the tubes of the middle row. Sheathed thermocouples are also embedded in the radiation plates, but no correction is needed for surface temperatures because the radiation plates have a uniform temperature profile throughout their thickness. The thermocouples are embedded in positions just facing the tubes. Several thermocouples are also installed in other tubes and radiation plates to check temperature uniformity in the heat exchanger.

The tubeside air temperatures are measured by radiation shielded thermocouples set at the centers of the inlet and outlet of the tubes, while the shellside gas temperatures are measured by a suction pyrometer with a traversing mechanism at five points including the inlet and outlet of the shell side. The suction pyrometer can traverse in the direction perpendicular to the hot and cold gas flows. Therefore, the measured temperature profiles, together with the velocity profiles measured by a Pitot tube, give the bulk temperatures of the hot gas.

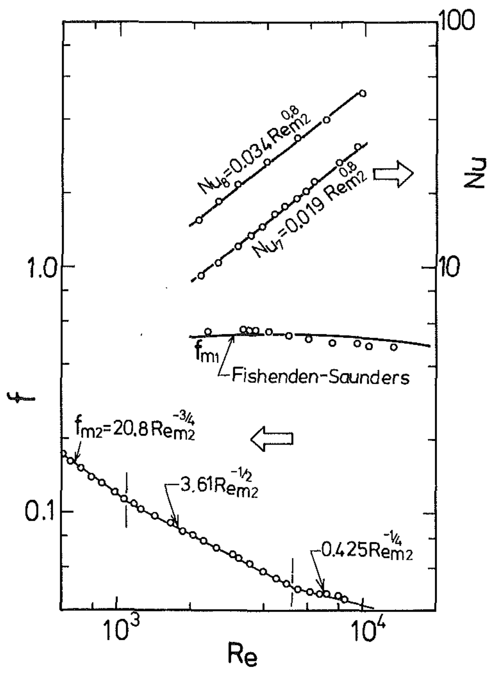

Fig. 3 Nusselt numbers and friction factors in the heat exchanger with radiating walls (no radiation effect)

Experimental Results.

Convection and Pressure Loss Inside Tube Without Radiation Effect. The convective heat transfer coefficients at the inner tube surface, and at the twisted cross-tape surface, and the pressure loss for air flow inside the tube have been measured before by small equipment with only one tube and one twisted cross-tape, in the temperature range without any radiation effect. In that experiment, the tube and the tape were electrically separated from each other, and the tube was heated by an sheathed electric heater wounded tightly around it, while the tape was directly heated by an electric current. They were heated independently with constant heat fluxes. In this case, the thermocouples used for measuring the temperature of the twisted cross-tape were not sheathed, but chromel-alumel wires of 0.2 mm o.d. were spot welded directly onto the surface of the twisted cross-tape. Considering the fin effect of the thermocouple wires, the uncertainty of the measured Nusselt numbers is estimated ±5 percent following after Kline et al. [10]. Figure 3 shows the Nusselt numbers for the inner tube surface Nu_7 and tape surface Nu_8 versus the Reynolds number for the tube inside Re_{m2}, while equation (1) represents the relationship of Nusselt numbers in Fig. 3.

$$Nu_7 = 0.019\,Re_{m2}{}^{0.8},\ Nu_8 = 0.034\,Re_{m2}{}^{0.8};\ Pr = 0.71 \qquad (1)$$

where

$$Nu_7 = \frac{d_e h_7}{\lambda_{m2}},\quad Nu_8 = \frac{d_e h_8}{\lambda_{m2}},\quad Re_{m2} = \frac{d_e u_{m2}}{\nu_{m2}}$$

$$d_e = \frac{\pi d_7{}^2 - 8 d_8 \delta_8 + 4\delta_8{}^2}{\pi d_7 + 4 d_8}$$

Figure 3 also shows the friction factors for the tube inside f_{m2} with the twisted cross-tape inserted, while equation (2) expresses this relationship.

$$f_{m2} = \begin{cases} 0.425\,Re_{m2}{}^{-1/4} & 5200 \leq Re_{m2} \leq 10000 \\ 0.61\,Re_{m2}{}^{-1/2} & 1100 \leq Re_{m2} \leq 5200 \\ 20.8\,Re_{m2}{}^{-3/4} & 100 \leq Re_{m2} \leq 1100 \end{cases} \qquad (2)$$

Convection and Pressure Loss Outside Tube Without Radiation Effect. The Nusselt number Nu_1 for convective heat transfer at the outer tube surface, and Nu_2 at the radiation plate surface in the shell side without any radiation

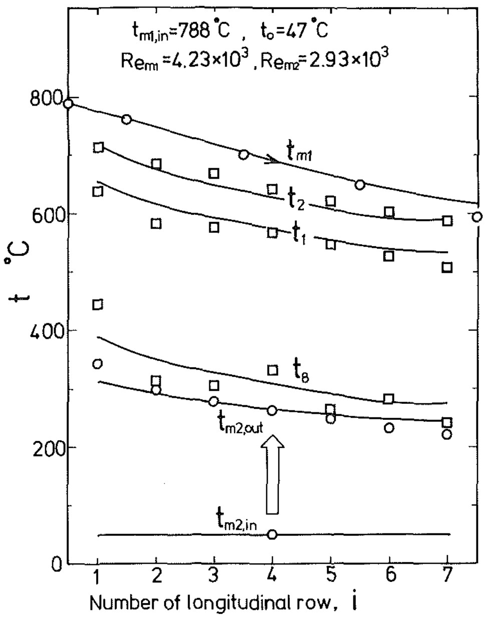

Fig. 4 Temperature profiles in the heat exchanger

effect, have been measured by Mori et al. [4] and given by equation (3).

$$\mathrm{Nu}_1 = 0.334\,\psi\,C_H\,\mathrm{Re}_{m1}^{\,0.6}\mathrm{Pr}^{0.3} \qquad 8\times10^2 < \mathrm{Re}_{m1} < 7\times10^3$$

$$\mathrm{Nu}_2 = c\,\mathrm{Re}_{m1}^{\,0.54}\left(\frac{p}{d_1}-1\right)^{0.47}\left(\frac{s}{d_1}\right)^{0.5} \qquad \mathrm{Pr}=0.71 \qquad (3)$$

$$c=\begin{cases}0.233 & \mathrm{Re}_{m1} < 4\times10^3\\ 0.267 & \mathrm{Re}_{m1} > 5\times10^3\end{cases}$$

ψ, C_H: coefficients determined by tube arrangement presented in [11]

$$\mathrm{Nu}_1 = \frac{d_1 h_1}{\lambda_{m1}}, \quad \mathrm{Nu}_2 = \frac{d_1 h_2}{\lambda_{m1}}, \quad \mathrm{Re}_{m1} = \frac{d_1 u_m}{\nu_{m1}}$$

Nu_1 in equation (3) is identical with the shellside heat transfer coefficient without any radiation plates in an in-line tube bank, given by Fishenden-Saunders [12]. This shows that the radiation plates have little effect on heat transfer coefficients at the outer tube surface for the range covered.

Figure 3 also shows the measured friction factors for the shell side f_{m1} with radiation plates in this study. The uncertainties of f_{m1} and f_{m2} are ±5 percent. The solid line shows Fishenden–Saunders' results [11] with the transverse pitch $p = p' - \delta_2$. Figure 3 indicates that the radiation plates have little effect on shellside friction factors, and this conclusion corroborates the findings of Watanabe [12].

Experiments of Heat Exchanger at High Temperatures. Figure 4 shows typical temperature profiles in the heat exchanger. The abscissa indicates the number of the longitudinal row *i*.

The circles show the hot gas temperatures t_{m1} and the cold air inlet and outlet temperatures $t_{m2,\,\mathrm{in}}$, $t_{m2,\,\mathrm{out}}$, while the squares show the temperatures of the outer tube surfaces t_1, the radiation plates t_2, and the twisted cross-tapes t_8. t_1 and t_8 are measured at the middle positions of the tubes in the cold gas flow direction. The temperatures of the inner tube surfaces t_7 are not shown in Fig. 4, because the temperature differences between the outer and the inner tube surfaces are within 10°C.

The scattering of the measured temperatures of the twisted cross-tapes may have been caused by error in the installation of the thermocouples: i.e., the gaps between the thermocouple junction and the surface of the twisted cross-tape were not necessarily 0.5 mm. An error of 0.1 mm for this gap results in about a 15°C temperature difference. We couldn't locate the thermocouple junctions accurately to within ±0.2 mm, consequently, the uncertainty of the measured temperatures of the twisted cross-tapes comes to ±30°C. The uncertainty of the other measured temperatures is ±10°C, considerably smaller than that of the measured temperatures of the twisted cross-tapes.

The temperatures t_2 lie between t_1 and t_{m1}, and the temperatures t_8 between t_7 ($\fallingdotseq t_1$) and $t_{m2} = (t_{m2,\,\mathrm{in}} + t_{m2,\,\mathrm{out}})/2$, which are considered as the cold gas temperatures at the middle positions of the tubes in the cold gas flow direction. In the shell side, the hot gas heats up not only the tubes, but also the radiation plates, by convection, and the radiation plates heat up the tubes by wall radiatoin. Meanwhile, in the tube side, the tubes heat up not only the cold air by convection but also the twisted tapes by wall radiation, so the twisted tapes heat up the cold air by convection, too. At lower inlet temperatures of the hot gas than that in Fig. 4, the temperatures of the radiation plates t_2, and that of the twisted tapes t_8 approach closer to the hot gas temperatures t_{m1} and the cold gas temperatures t_{m2}, respectively, because radiation effects reduce with lower $t_{m1,\,\mathrm{in}}$.

Heat transfer augmentation coefficients E_{m1} and E_{m2}, which describe the radiation effects quantitatively, are defined in equation (4).

$$E_{m1} = \frac{q_{1r}}{q_{1c}} = \frac{h_{1r}}{h_1} = 1 + \frac{h_2 A_2 (t_{m1} - t_2)}{h_1 A_1 (t_{m1} - t_1)}$$

$$E_{m2} = \frac{q_{7r}}{q_{7c}} = \frac{h_{7r}}{h_7} = 1 + \frac{h_8 A_8 (t_8 - t_{m2})}{h_7 A_7 (t_7 - t_{m2})}$$

$$q_{1c} = h_1 (t_{m1} - t_1)$$

$$q_{1r} = h_1 (t_{m1} - t_1) + h_2 (t_{m1} - t_2) A_2 / A_1 = h_{1r} (t_{m1} - t_1)$$

$$q_{7c} = h_7 (t_7 - t_{m2})$$

$$q_{7r} = h_7 (t_7 - t_{m2}) + h_8 (t_8 - t_{m2}) A_8 / A_7 = h_{7r} (t_7 - t_{m2})$$

$$A_1 = \pi d_1 l,\ A_2 = 2sl,\ A_7 = \pi d_7 l,\ A_8 = 4 d_8 l$$

where the subscript *r* stands for combined radiation and convection whereas the subscript *c* stands for convection alone. h_1, h_2, h_7, and h_8 are the convective heat transfer coefficients determined by equations (3) and (1), and h_{1r} and h_{7r} are the heat transfer coefficients of the outer and inner surfaces including the radiation effects defined in equation (4). q_{1r} and q_{7r} are the heat fluxes at the outer and inner tube surfaces including radiation effects. E_{m1} and E_{m2} show the ratios of the local heat fluxes by combined radiation and convection to their convective components. Therefore, strictly speaking, E_{m1} and E_{m2} do not show the ratios of the heat fluxes with radiating walls to those without radiating walls. However, if we assume that a heat exchanger is consisted of a series of small heat exchangers, E_{m1} and E_{m2} represent locally the ratios of the heat fluxes with radiating walls to those without radiating walls, since the temperature changes by insertion of radiating walls are so small in such small heat exchangers. The amount of heat exchange for each longitudinal row are measured by the temperature differences between the inlet and outlet of cold gas at each row ($t_{m2,\,\mathrm{out}} - t_{m2,\,\mathrm{in}}$), assuming that the cold gas flow is uniformly distributed among the tubes. Thus, local values of q_{1r} and q_{7r} are obtained from the amount of heat exchange for each row divided by the areas of the outer and inner tube surfaces, respectively. Figure 5 shows augmentation coefficients E_{m1}, E_{m2} for the outer and inner tube surfaces and the heat flux q_{1r} at the outet tube surface, from the data of Fig. 4 expressed by circles, squares, and solid black circles, with the estimated uncertainties of ±14, ±10, and ±7 percent, respectively, following the procedure presented by Kline et al. [10]. E_{m1} increases for the tubes of the first row in the flow direction of

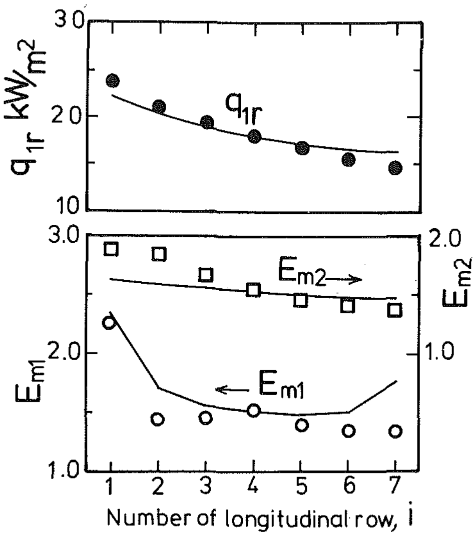

Fig. 5 E_{m1}, E_{m2}, and q_{r1} for Fig. 4

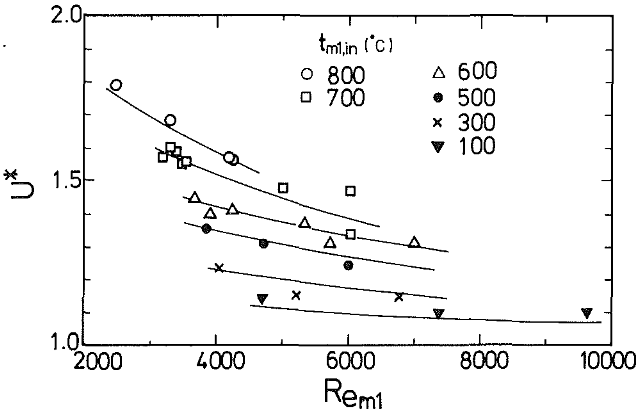

Fig. 6 Overall heat transfer augmentation coefficients U^* versus Reynolds numbers in the shell side R_{em1}

the hot gas, that is, $i = 1$, because the wall radiation from the plenum walls before the first row in the shell side heats the tubes in this row. In principle, the tubes in the last row ($i = 7$) are heated by radiation from the outlet plenum walls in the shell side, so that E_{m1} for the last row increases. However, the experimental results of E_{m1} at the last row did not necessarily increase becasue heat loss to the supports of the entire heat exchanger lowered the temperatures of the outlet plenum walls. The solid lines in Figs. 4 and 5 are the predicted curves given by a theory which will be explained later on.

Overall heat transfer augmentation coefficient U^*, which is defined as the ratio of the overall heat transfer coefficient including radiation effects U_r, to that neglecting radiation effects U_c, is expressed by equation (5).

$$U^* = \frac{U_r}{U_c} \tag{5}$$

where

$$\frac{1}{U_c} = \frac{1}{h_1} + \frac{d_1}{d_7}\frac{1}{h_7} + \frac{d_1}{2\lambda_w}\ln\frac{d_1}{d_7}$$

$$\frac{1}{U_r} = \frac{1}{h_{1r}} + \frac{d_1}{d_7}\frac{1}{h_{7r}} + \frac{d_1}{2\lambda_w}\ln\frac{d_1}{d_7} = \frac{1}{E_{m1}h_1} + \frac{d_1}{d_7}\frac{1}{E_{m2}h_7} + \frac{d_1}{2\lambda_w}\ln\frac{d_1}{d_7}$$

U_c is almost the same as the overall convective heat transfer coefficient without radiating walls, and U_r is the overall heat transfer coefficient with radiating walls. Then, by recalling that the total heat transfer rate is calculated by total heat transfer area, overall heat transfer coefficient, and logarithmic mean temperature difference, we can see that U^* represents the ratios of total heat transfer area without radiating walls to that with radiating walls when the inlet and outlet temperatures and the flow rates of hot and cold gases are fixed. Figure 6 shows the measured U^* versus Re_{m1} with $t_{m1,\mathrm{in}}$ as a parameter with the uncertainty of ±8 percent. Cold air inlet temperatures are nearly 45 °C, and mass flow rates are about the same as those for hot gas. Radiation effects increase with increasing temperature and decreasing flow rate. U^* has a maximum value of about 1.8 at $t_{m1,\mathrm{in}} = 800$°C, $\mathrm{Re}_{m1} \fallingdotseq 2500$, and U^* is less than 1.1 at $t_{m1,\mathrm{in}} = 100$°C, thus showing that radiation effects are negligible in the temperature range below 100°C.

Theoretical Analysis

Numerical Calculation. Figure 2 shows the heat transfer model [4] for analyzing the performance of the heat exchanger in this study. The working fluids are assumed to be nonradiating gases. The temperature of the tube, radiation plate, twisted cross-tape, hot and cold gases are assumed to be uniform in each section in Fig. 2.

Heat balances in the area surrounding the longitudinally ith tube give the following normalized basic equations.

Heat balances give equation (6) for hot gas temperatures (T_{m1}, $-\Delta T_{m1} = T_{m1,i-1} - T_{m1,i}$) and equation (7) for cold gas temperatures (T_{m2})

$$\Delta T_{m1} = P_1\mathrm{St}_1(T_1 - T_{m1}) + P_2\mathrm{St}_2(T_2 - T_{m1}) \tag{6}$$

$$2(T_{m2} - 1) = P_7\mathrm{St}_7(T_7 - T_{m2}) + P_8\mathrm{St}_8(T_8 - T_{m2}) \tag{7}$$

Radiosity analyses [13] give equation (8) for outer tube surface temperatures (T_1) and radiation plate temperatures (T_2), and equation (9) for inner tube surface temperatures (T_7) and twisted tape temperatures (T_8).

$$T_j{}^4 + \frac{1}{M_j}(T_j - T_{m1} - Q_{jr}) = \sum_{k=1}^{6}\left[T_k{}^4 + \frac{1-\epsilon_k}{M_k}(T_k - T_{m1,k} - Q_{kr})\right]F_{j-k} \quad (\mathrm{j}=1,2), \tag{8}$$

$$T_j{}^4 + \frac{1}{M_j}(T_j - T_{m2} - Q_{jr}) = \sum_{k=7}^{8}\left[T_k{}^4 + \frac{1-\epsilon_k}{M_k}(T_k - T_{m2} - Q_{kr})\right]F_{j-k} \quad (\mathrm{j}=7,8), \tag{9}$$

where $T_{m1,k}$ means the temperature of hot gas in the section containing the surface k ($k = 1$ to 6).

Heat conduction in a tube gives equation (10)

$$T_1 - T_7 = P_0 Q_{7r} = -\frac{P_0}{H_{17}}Q_{1r} \tag{10}$$

where the normalized variables are defined in equation (11),

$$T = \frac{t}{t_{m2,\mathrm{in}}},\ Q_r = \frac{q_r}{h t_{m2,\mathrm{in}}}, \mathrm{St} = \frac{\mathrm{Nu}}{\mathrm{RePr}},\ M = \frac{\epsilon\sigma t_{m2,\mathrm{in}}{}'}{h} = \frac{\epsilon N}{\mathrm{Nu}},$$

$$N = \frac{d\sigma t_{m2,\mathrm{in}}{}'}{\lambda},\ A_{m2} = \frac{\pi}{4}d_7{}^2 - 2d_8\delta_8 + \delta_8{}^2,$$

$$P_0 = \frac{d_7 h_7}{2\lambda_w}\ln\frac{d_1}{d_7},\ P_1 = \frac{\pi d_1}{p - d_1},\ P_2 = \frac{2s}{p - d_1},\ P_7 = \frac{\pi d_7 l}{A_{m2}},$$

$$P_8 = \frac{4d_8 l}{A_{m2}},\ H_{17} = \frac{h_7 d_7}{h_1 d_1}, \tag{11}$$

Temperatures are represented by those taken at the middle positions of the tubes in the flow direction of the cold air.

Furthermore, the temperatures of the tubes and radiation plates are evaluated at the position where the flow area in the shell side is the smallest. In equations (8) and (9), $T_{m1,k}$ is the temperature of hot gas in contact with surface k. Configuration factors can be expressed by equation (12) [13].

$$F_{1-1}=0, F_{1-2}=\frac{2s}{\pi d_1}F_{2-1}=\frac{2}{\pi}\tan^{-1}(s/p),$$

$$F_{1-4}=F_{1-6}=\frac{1}{2}(1-F_{1-2}-F_{1-3}-F_{1-5}),$$

$$F_{1-3}=F_{1-5}=\frac{1}{\pi}[\sqrt{(s/d_1)^2-1}+\sin^{-1}(d_1/s)-s/d_1],$$

$$F_{2-3}=F_{2-5}=\frac{\pi d_1}{2s}F_{1-4},$$

$$F_{2-2}\fallingdotseq F_{2-4}=F_{2-6}=\frac{1}{3}(1-F_{2-1}-F_{2-3}-F_{2-5}),$$

$$F_{8-8}\fallingdotseq 1-\frac{1}{2^{1/2}}, F_{8-7}=1-F_{8-8}, F_{7-8}=\frac{4d_s}{\pi d_7},$$

$$F_{7-7}=1-F_{7-8} \tag{12}$$

Equation (12) needs modification for the tubes $i=1$ and $i=7$ because there is no tube either before or after them in the shell side. The effects of the thickness and twist of the twisted cross-tape are neglected in equation (12).

The eight unknowns T_{m1}, T_{m2}, T_1, T_2, T_7, T_8, Q_{1r}, and Q_{7r} in the eight equations, equation (6–10), are numerically calculated under the condition that $t_{m2,\text{in}}$, $t_{m1,\text{in}}$, St, M, ϵ, and the other parameters of heat exchanger sizes, etc., are given. Wall emissivity is given according to Yamada et al. [14]: ϵ_1 to $\epsilon_6 = 0.95$, ϵ_7, $\epsilon_8 = 0.90$.

The numerical calculation method is an iterative one, in which the temperature and heat flux profiles are assumed initially. The profiles are then substituted into the right-hand sides of equations (8) and (9), the fourth-order polynominal equations for T_1, T_2, T_7, and T_8 are solved, and T_{m1}, T_{m2}, Q_{1r}, Q_{7r} are obtained from equatins (6), (7), and (10). Then, newly obtained profiles are compared with the initially assumed ones, and the calculation is repeated until the profiles converge. In the calculation, we had no difficulty in convergence, although equations (8) and (9) are highly nonlinear. Once the temperatures and heat fluxes are obtained, heat transfer augmentation coefficients can be easily calculated using equation (4). Eventually, the overall heat transfer augmentation coefficient U^*_{th} is obtained, according to equation (5), where E_{m1}, E_{m2}, h_1, and h_7 for whole heat exchanger are calculated by averaging those values obtained for each longitudinal row, i = 1 to 7.

Results of Numerical Calculation. The solid lines in Figs. 4 and 5 show the results of the numerical calculation. The calculated results agree well with the experimental results, although the measured temperatures of the twisted cross-tapes scatter for the reason already stated above.

The solid lines in Fig. 6 show the calculated results of U^*_{th} and agree with the experimental results to within ±6 percent.

The numerical results in the case of a mixture of air and CO_2 used as the working fluid agree with the experimental results, thus showing the negligible effect of the radiating gas in this study. The reason for this is that the mean beam lengths of the gas volume in the heat exchanger are considerably smaller, and the temperature levels lower, than those in stack-type recuperators [9].

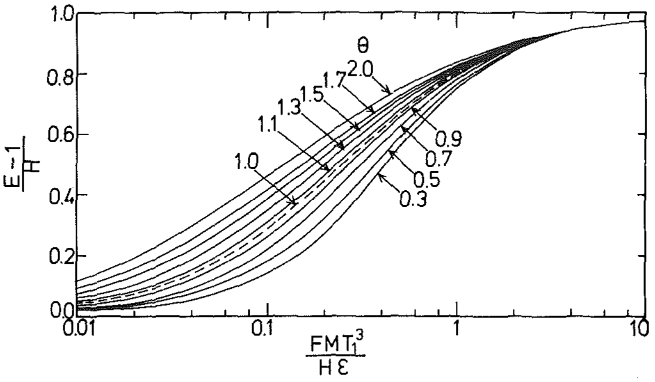

Fig. 7 Diagram of approximate calculation

Approximate Calculation. We apply the approximate calculation method proposed by Mori et al. [4] to estimate the heat transfer performance of heat exchangers without solving equations (6–10) numerically, as follows.

First, equation (13) shows an approximation of configuration factors in the shell side, which means that the radiation plates do not contribute to the radiation heat transfer in the longitudinally neighboring sections at all.

$$F_{1-1}=F_{1-4}=F_{1-6}=F_{2-3}=F_{2-4}=F_{2-5}=F_{2-6}=0,$$

$$F_{2-1}=F_{1-2}\frac{A_1}{A_2}, F_{2-2}=1-F_{2-1}, F_{1-2}=1-2F_{1-3},$$

$$F_{1-3}=F_{1-5}=\frac{1}{\pi}[\sqrt{(s/d_1)^2-1}+\sin^{-1}(d_1/s)-s/d_1] \tag{13}$$

Then, equation (8) ($j=1,2$) and equation (4) combine to reduce to equation (14) for the shell side.

$$\left[\frac{E_{m1}-1}{H_{12}}(1-\theta_1)\right]\Big/\left[1-\left\{\frac{E_{m1}-1}{H_{12}}(1-\theta_1)+\theta_1\right\}^4\right]=\frac{F_1M_1T_1{}^3}{\epsilon_1H_{12}} \tag{14}$$

where

$$\frac{1}{F_1}=\frac{1}{F_{1-2}}+\frac{1}{\epsilon_1}-1+\left(\frac{1}{\epsilon_2}-1\right)\frac{A_1}{A_2}, \theta_1=\frac{T_{m1}}{T_1}, H_{12}=\frac{h_2A_2}{h_1A_1}$$

Equation (9) ($j=7,8$) and equation (4) combine to reduce to equation (15) for the tube side.

$$\left[\frac{E_{m2}-1}{H_{78}}(1-\theta_2)\right]\Big/\left[1-\left\{\frac{E_{m2-1}}{H_{78}}(1-\theta_2)+\theta_2\right\}^4\right]=\frac{F_7M_7T_1{}^3}{\epsilon_7H_{78}} \tag{15}$$

where

$$\frac{1}{F_7}=\frac{1}{F_{7-8}}+\frac{1}{\epsilon_7}-1+\left(\frac{1}{\epsilon_8}-1\right)\frac{A_7}{A_8}, \theta_2=\frac{T_{m2}}{T_1}, H_{78}=\frac{h_8A_8}{h_7A_7}$$

In obtaining equation (15), the temperature difference between the inner and outer tube surfaces is neglected, i.e., $T_7 = T_1$.

Equations (14) and (15) have the same formulation, and E_{m1} and E_{m2} can be obtained if the unknown temperatures T_1, T_{m1}, and T_{m2} are given. Figure 7 shows equations (14) and (15) simultaneously with θ as a parameter. Equation (16) gives U^*, using E_{m1} and F_{m2} obtained from Fig. 7.

$$U^*=\left[1+\frac{1}{H_{17}}\right]\Big/\left[\frac{1}{E_m}+\frac{1}{E_{m2}H_{17}}\right] \tag{16}$$

In practical heat exchanger designs, the inlet and outlet temperatures of hot and cold gases are usually given. For this case, one can obtain the overall heat transfer coefficient U_r, which includes radiation effects, using the following calculation procedure.

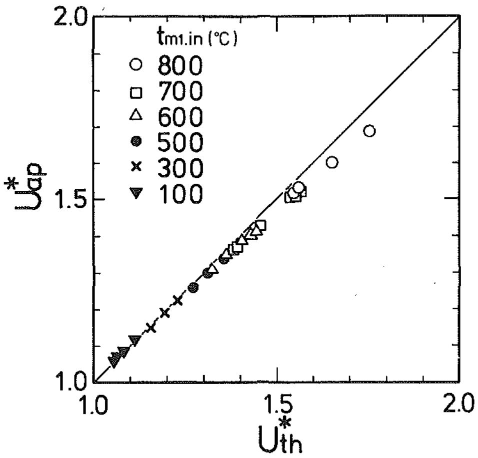

Fig. 8 A comparison of U^*_{ap} using approximate calculations with U^*_{th} using numerical ones

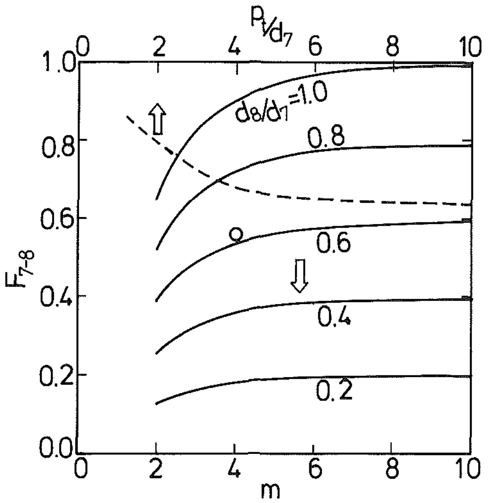

Fig. 9 Configuration factors between inner surfaces and tapes: ____ multifin straight tape ($p_t/d_7 = \infty$); - - - twisted single tape ($m = 2$, ($d_8/d_7 = 1$); 0 twisted cross-tape used in this study

1 Give $t_{m1,\,\mathrm{in}}$, $t_{m1,\,\mathrm{out}}$, $t_{m2,\,\mathrm{in}}$, $t_{m2,\,\mathrm{out}}$, ϵ, w, and other basic sizes of a heat exchanger, etc.

2 Calculate parameters A, h, H, M, F, and U_c.

3 Calculate normalized average temperatures $T_{m1,\,b}$ and $T_{m2,\,b}$, by equation (17)

$$T_{mj,\,b} = \frac{t_{mj,\,\mathrm{in}} + t_{mj,\,\mathrm{out}}}{2t_{m2,\,\mathrm{in}}} \qquad j = 1,2 \tag{17}$$

4 Calculate $T_1 = \dfrac{T_{m1,\,b} + T_{m2,\,b} H_{17}}{1 + H_{17}}$

5 Calculate θ_1, θ_2 and the right-hand sides of equations (14) and (15)

$$\theta_1 = \frac{T_{m1,\,b}}{T_1}, \quad \theta_2 = \frac{T_{m2,\,b}}{T_1}, \quad \frac{F_1 M_1 T_1{}^3}{\epsilon_1 H_{12}}, \frac{F_7 M_7 T_1{}^3}{\epsilon_7 H_{78}}$$

6 Obtain E_{m1}, E_{m2} from Fig. 7.

7 Calculate U^* from equation (16) and obtain $U_r = U^* U_c$.

8 Repeat if the sizes obtained through U_r are different from those given in step 1.

This calculation procedure assumes that representative gas temperatures are the average of inlet and outlet temperatures (step 3), and that tube temperatures are not affected by radiation and can be calculated by pure convection (step 4). The latter assumption is based on the rise in tube temperature caused by the radiation plates; the twisted tapes, on the other hand, reduce the temperature. The radiating walls in the shell and tube sides cancel out their effects on each other. The former assumption leads to error when temperature differences between the inlet and outlet become very large, while the latter leads to error when the difference in heat transfer augmentations between the shell and tube sides becomes significant.

Figure 8 shows a comparison of the approximately calculated U^*_{ap} with the numerically calculated U^*_{th}, and shows that U^*_{ap} is smaller than U^*_{th} by several percent. The reason is that U^*_{th} includes the radiation effects of both the inlet and outlet plenum walls in the shell side as shown in Fig. 4. U^*_{ap} agrees quite well with U^*_{th} for the fourth longitudinal row, when U^*_{th} for each longitudinal row is calculated from E_{m1}, E_{m2}, h_1, and h_7 for each longitudinal row. Thus using the approximate method, we can predict the heat transfer performance of heat exchangers with radiating walls with simplicity and accuracy good enough for practical use.

Evaluation of Augmentation

As for using the twisted cross-tape as an augmentation tool, the configuration factor F_{7-8} increases with the increasing number of fins (m) and the decreasing helical pitch of a tape (p_t) as shown in Fig. 9. Also, the convective heat transfer coefficients of the inner surface h_7 increase with the increasing ratio of d_8/d_7 and decreasing p_t. But both the increased configuration factor and increased convective heat transfer coefficient bring about increased pressure losses.

On the other hand, radiation plates in the shell side scarcely change the convective heat transfer coefficients of the outer tube surfaces h_1, and the pressure losses of the shell side as shown in Fig. 3, while they do show radiation effects. In addition, radiation plates are expected to suppress tube vibration. Therefore, the radiation plate is a highly effective tool for high temperature heat exchangers.

Conclusion

By conducting experiments and analyses on the heat transfer augmentation of a crossflow shell-and-tube heat exchanger, using radiating walls installed separately from heat transfer tubes, we conclude the following:

1 Both the convective heat transfer coefficients and friction factors inside a tube with the twisted cross-tape are well correlated.

2 The overall heat transfer coefficients increase 10–80 percent, compared with those without any radiation effect, under the condition where the inlet temperature of hot gas ranges from 100 to 800 °C, and the Reynolds number of hot gas ranges from 2500 to 8000. Thus the radiating walls are shown to be quite effective for heat transfer augmentation when the inlet temperatures of hot gas are above 100 °C.

3 The analytical results of the temperature profiles and heat transfer performance agree well with the experimental results. The approximate calculation method for estimating the heat transfer performance of heat exchangers is also shown to be accurate and simple enough for practical use.

References

1 Mori, Y., Hijikata, K., and Yamada, Y., "Radiation Effects on Heat Transfer in the Reactor Core and Heat Exchangers of an HTGR," ASME JOURNAL OF HEAT TRANSFER, Vol. 97, No. 3, 1975, pp. 400–405.

2 Mori, Y., Yamada, Y., and Hijikata, K., "Radiation Effects on Performances of Radiative Gas Heat Exchangers at High Temperatures," *International Journal of Heat and Mass Transfer*, Vol. 23, No. 8, 1980, pp. 1079–1089.

3 Yamada, Y., and Mori, Y., "Effects of Radiation Heat Transfer on the

Performance of High Temperature Heat Exchanger (Experimental Results of One Flow Channel)," *Heat Transfer Japanese Research*, Vol. 10, No. 4, 1982, pp. 1-16.

4 Mori, Y., Taira, T., and Watanabe, K., "Heat Exchanger Augmentation by Radiation Plates," ASME Paper No. 76-HT-3, 1976.

5 Modest M. F., Meyer, B. R., and Azad, F. H., "Combined Convection and Radiation in Tube Flow of an Absorbing, Emitting and Anisotropically Scattering Gas-Particulate Suspension," ASME Paper No. 80-HT-27, 1980.

6 Tamehiro, H., Echigo, R., and Hasegawa, S., "Radiative Heat Transfer by Flowing Multiphase Medium—Part 3; An Analysis of Heat Transfer of Turbulent Flow in a Circular Tube," *International Journal of Heat and Mass Transfer*, Vol. 16, No. 6, 1973, pp. 1199-1213.

7 Lopina, R. F., and Bergles, A. E., "Heat Transfer and Pressure Drop in Tape-Generated Swirl Flow of Single-Phase Water," ASME JOURNAL OF HEAT TRANSFER, Vol. 91, No. 3, 1969, pp. 434-442.

8 Smithberg, E., and Landis, F., "Friction and Forced Convection Heat-Transfer Characteristics in Tubes With Twisted Tape Swirl Generators," ASME JOURNAL OF HEAT TRANSFER, Vol. 86, No. 1, 1964, pp. 39-49.

9 Scaccia, D., and Theoclitus G., "Types, Performances and Applications," *Chemical Engineering*, Vol. 87, No. 20, 1980, pp. 121-132.

10 Kline, S. J., and McClintock, F. A., "Describing Uncertainties in Single-sample Experiments," *Mechanical Engineering*, Vol. 75, No. 1, 1953, pp. 3-8.

11 Fishenden, M., and Saunders, O. A., *Introduction to Heat Transfer*, Oxford Clarendon Press, London, 1950.

12 Watanabe, K., "Studies on Heat Transfer Performance of High Temperature Heat Exchanger," Ph.D. dissertation, Tokyo Institute of Technology, 1980.

13 Siegel, R., and Howell, J. R., *Thermal Radiation Heat Transfer*, McGraw-Hill, New York, 1972, p. 239.

14 Yamada, Y., and Akai, M., "Emissivities of Surfaces for High Temperature Heat Transfer" (in Japanese), *J. Mechanical Engineering Laboratory*, Vol. 35, No. 6, 1981, pp. 287-302.

C. Berner[2]

F. Durst[3]

D. M. McEligot[4]
Mem. ASME

Aerospace and Mechanical
Engineering Department,
University of Arizona,
Tucson, Ariz. 85721

Flow Around Baffles[1]

Flow visualization, manometry, and laser-Doppler anemometry have been applied to approximately two-dimensional water flow around segmental baffles with baffle spacing/depth equal to 0.4, window cuts from 10 to 50 percent, and Reynolds numbers ranging from 600–10,500 in order to simulate important aspects relating to shellside flow in shell-and-tube heat exchangers. The main features of the flow (which is eventually periodic in the streamwise direction), development lengths, pressure loss coefficients, and mean and rms velocity distributions are presented.

Introduction

The flow through the shell side of a shell-and-tube heat exchanger is a particularly complicated flow. Since the dominant thermal resistance often occurs on the shellside, baffles are frequently introduced to direct the mainstream approximately perpendicular to the tubes in order to improve the heat transfer coefficient [1]. In practice, important applications cover the gamut from low laminar flow to high Reynolds numbers [2]. Comparable flow patterns could also be found for some hypothesized augmentation surfaces for air-cooled solar collectors, shell-and-plate mixing chambers, some electronic circuit boards, internally cooled turbine blades, and in limiting case, for the flow through some labyrinth shaft seals.

Segmental baffles are treated in this paper; the typical geometry is presented in Fig. 1. After a sequence of baffles, the idealized flow is expected to approach a condition that can be called streamwise periodic. That is, if one considers the region between two successive baffles, the outflow profiles will become nearly the same as the inflow profiles. The situation includes curved shear layers, separation, reattachment and stagnation, recirculaing and boundary layer regions. For numerical prediction of the flow behavior, initial conditions are not known in advance but, instead, are consequences of the solution. Streamwise boundary conditions would be described by periodicity.

In order to concentrate on the difficulties due primarily to the presence of the baffles in general, the present study examined an approximately two-dimensional flow without the interference of tubes. Thus, it must be emphasized that we do not pretend to model a shell-and-tube heat exchanger directly. Objectives included increasing understanding of the general features of the flow, providing data to test turbulence models suggested to predict such flows, and ultimately, guiding improvement.

After summarizing the previous work, the water flow experiment is described along with preliminary flow visualization and pressure drop measurements. The main data – velocity distributions obtained with a laser Doppler anemometer – are presented prior to treating some implications for the parent heat transfer problem. The paper ends with a few major conclusions. Further details and tabulated data are provided by Berner [3].

Previous Work

In the usual terminology, the two-dimensional geometry is determined by the shell depth D (comparable to shell diameter), baffle spacing s, and window cut c or baffle overlap [4]. These terms are defined in Fig. 1, with the exception of the overlap, which is the distance the baffle extends beyond the centerplane, i.e., $D/2-c$. When the Reynolds number is based on the hydraulic diameter of a cross section, it takes the form

$$\mathrm{Re}=2\dot{m}/[W(1+1/\alpha)\,\mu]$$

where W is the width and α is the aspect ratio. Thus the magnitude of the Reynolds number is approximately the same wherever it is defined in the baffle geometry, differing only slightly due to the local aspect ratio.

A general discussion of flow in baffled heat exchangers is presented in the text by Knudsen and Katz [1]. Previous flow visualization for the effects of baffle geometry has been conducted by Gunter, Sennstrom, and Kopp [5] with a test section comparable to a Hele-Shaw cell; the best summary of their photographs still available is apparently the sequence provided by Knudsen and Katz. In a Hele-Shaw cell the streamlines over obstacles are identical in shape with those in a two-dimensional flow of inviscid, irrotational fluid. Hele-Shaw [6] pointed out that the viscous forces are negligible in the plane of interest; therefore, the flow is independent of the Reynolds number. A copy of a motion picture of flow in the shell side of model heat exchangers is also available from the Heat Transfer Research Institute of Alhambra, California, but some copies are old and worn, so it is difficult to see the features.

Tinker [7] considered flow patterns when developing empirical methods to predict pressure drop and heat transfer. Gupta and Katz [8] observed flow patterns in a glass heat exchanger from the movements of foreign particles in a water solution of propylene glycol and used the results to correlate their heat transfer data.

Much of the past work has concentrated on determination of the average shellside coefficients (e.g., Short [9], Gay, Mackley and Jenkins [10]). Palen and Taborek [11] considered the flow in idealized baffled bundles and then extended the model in terms of a network treatment. They suggested that geometries employing medium window cuts and baffle spacing (defined in Fig. 1) would provide the best efficiency. For optimum performance, Taborek [4] suggested that baffle window cuts should remain between the limits of 20–35 percent of the shell diameter, and spacing between 20 percent of the shell diameter and a maximum equal to the shell diameter.

Founti and Whitelaw [12] applied laser-Doppler anemometry to deduce velocity fields in a model of the

---

[1] Supported by National Science Foundation and Max-Planck-Institut für Strömungsforschung.

[2] Also with the French-German Research Institute, F-68301, St. Louis, France.

[3] Also with the Institut für Hydromechanik, Universität Karlsruhe, D-7500 Karlsruhe, West Germany; and Lehrstuhl für Strömungsmechanik, Universität Erlangen, D-8520 Erlangen, West Germany.

[4] Also with the Max-Planck-Institut für Strömungsforschung, D-3400 Göttingen, West Germany, present address: Gould Ocean Systems, P.O. Box 4282, Middletown, R.I. 02840.

Contributed by the Heat Transfer Division and presented at the ASME Winter Annual Meeting, Boston, Massachusetts, November 13–18, 1983. Manuscript received by the Heat Transfer Division June 30, 1983. Paper No. 83-WA/HT-9.

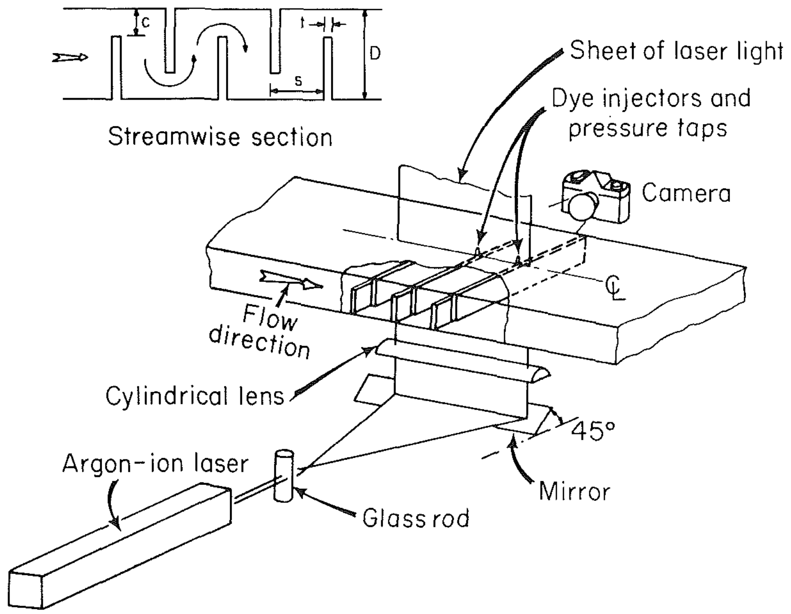

Fig. 1 Nomenclature and schematic diagram of apparatus

shellside of an axisymmetric heat exchanger with disk-doughnut baffles. While not directly applicable to the present work, their observations do provide insight to related problems. For the configurations (diameter and spacing ratios) they investigated, they concluded that similarity of mean and turbulent distributions was achieved after the second set of baffles. Laser-Doppler techniques were also used by Martin, Elphick, and Gollish [13], in a simulated heat exchanger, to examine the flow in an inlet section and an outlet section separated by a single baffle. While their geometry differed significantly from the present work, their general conclusions are related and are mentioned later in the Discussion section.

In work in progress at the University of Arizona, Yu and Heinrich [14] have developed a transient numerical technique for the prediction of streamwise-periodic, laminar flow around segmental baffles. One of their results, pictured in Fig. 2, illustrates typical features to be expected in such flows. For this calculation, the geometrical parameters were $s/D = 0.45$, $c/D = 0.3$, $t/D = 0.05$, and the Reynolds number was 400. The instantaneous streamlines show a large recirculating eddy behind the baffle; this eddy grew as time progressed in the solution. A small corner eddy appears upstream of the baffle. For most of the travel on the upstream side of the baffle, the baffle constrains the mainstream to an approximately parallel flow with boundary layer growth along the baffle countered by slight convergence induced by the growth of the eddy on back of the opposite baffle and the upstream influence of the curved flow region around the tip of the baffle. An unsteady stagnation region appears along the bounding wall; this region resembles an impinging jet in a crosswind. Vorticity contours show an oscillation in the mixing layer downstream of the baffle tip.

A more complete literature review is presented by Gay, Mackley, and Jenkins [10], who obtained local shellside coefficients by an electrochemical mass transfer technique. In general, the existing literature treats this problem in only a qualitative manner and data concerning the quantities of interest in the numerical prediction of baffle flows, such as mean velocities, temperatures, and mean square velocity fluctuations, are not available for series of segmental baffles.

Experiment

The experimental loop was constructed with a 10-cm-dia plastic pipe, which includes a calibrated flow nozzle insert for flow rate measurement, connected to a supply reservoir containing about 400 L of city water. Water flow was induced by an axial propeller driven by a variable speed d-c motor. A line voltage stabilizer and adjustable transformer provided power to the motor and allowed setting the flow rate to a constant value so as to reproduce the same conditions when desired and to give steady flows. A honeycomb and a screen were located upstream of the baffles to obtain a velocity profile as symmetric as possible before entering the baffle test section; the entrance section between the honeycomb and first baffle was about $7D$ in length.

Two types of rectangular test section were employed: (*i*) plexiglass for flow visualization, pressure measurement, and initial laser-Doppler anemometry and (*ii*) Pyrex glass for later use with LDA in an oil solution of the same index-of-refraction (in the results reported here water was the only working fluid). The plexiglass test section (e.g., Fig. 1) had a rectangular cross-section, 30 cm × 6 cm, with an aspect ratio equal to 5, with an opening allowing insertion of baffles of different lengths and spacings. Ten baffles were supported alternately from the top and bottom plates of the test section.

Nomenclature

c = window cut, gap between baffle and shell
D = shell or channel depth
D_h = hydraulic diameter
g_c = unit conversion constant
K = pressure loss coefficient, $2g_c\Delta p/(\rho V_c^2)$
L = length of flow passage
$\dot{m}$ = mass flow rate
Δp = pressure drop between successive baffles on same side
Re = Reynolds number, VD_h/ν; Re_s, based on baffle spacing, $2Vs/\nu$
s = baffle spacing
t = baffle thickness
u,v = velocity components, $\bar{u}$, $\bar{v}$, mean values
V = bulk velocity; V_D, V_c, V_s, based on channel depth, window cut and baffle spacing, respectively
W = channel width
x,y = Cartesian coordinates
α = aspect ratio, e.g., W/c
ρ = fluid density
ν = molecular kinematic viscosity; ν_{eff}, effective kinematic viscosity including turbulent effects

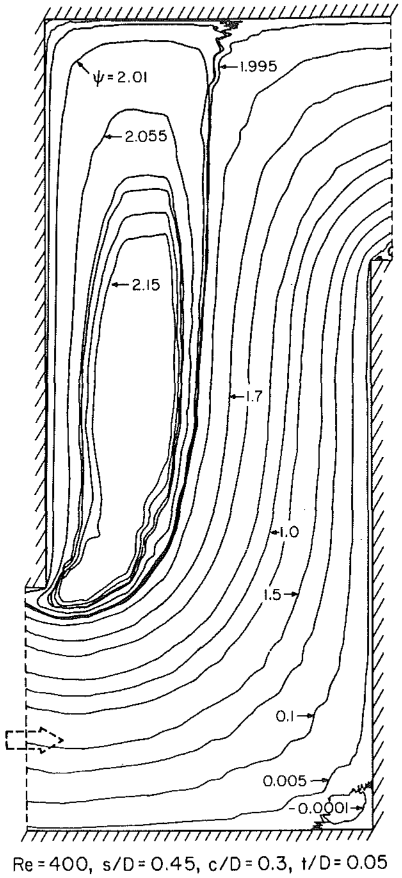

Fig. 2 Numerical prediction of laminar flow via transient technique by Yu and Heinrich, University of Arizona

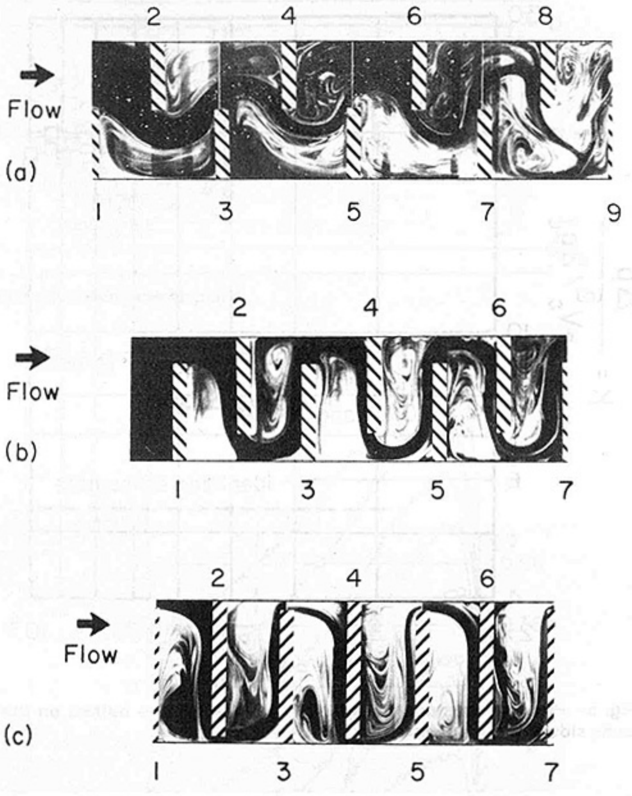

Fig. 3 Flow visualization by dye injection, Re = 600

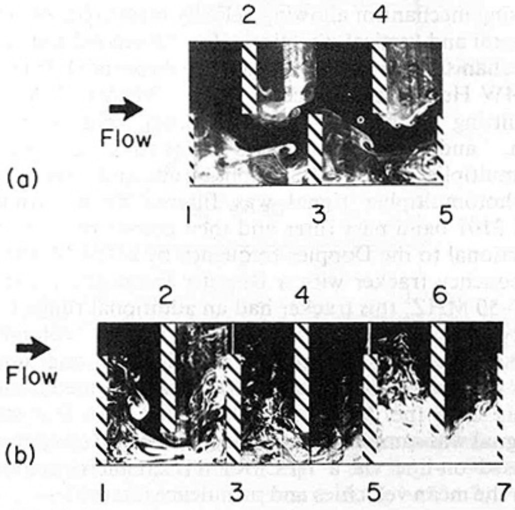

Fig. 4 Flow visualization by dye injection, Re = 1670

Three plexiglass test sections were employed, but this report emphasizes one that is considered as the standard geometry, corresponding to typical dimensions in a commercial heat exchanger. A second involved shorter baffles and a third longer baffles. The nondimensional window cuts, c/D, were 0.3, 0.5, and 0.1, respectively. Baffle spacing was 24 mm (s/D = 0.4) and baffle thickness was 3 mm for all experiments reported. Reynolds numbers, based on the hydraulic diameter between the baffles, ranged from about 600 to 10,000. The pyrex glass section had a cross section of 30 cm by 5 cm and used only the standard baffle geometry. While these cross sections (30 × 6 cms and 30 × 5 cms) may be considered small for a heat exchanger, the geometric ratios – s/D and c/D – were chosen to give geometric similitude with typical commercial heat exchangers although, as indicated earlier, our intent was not to model a shell-and-tube exchanger directly.

Gross flow features have been visualized by injecting fluorescein dye through several 1/2 mm holes and by using aluminum powder as a tracer. For the dye injection method, the holes were located at the centerline of the test section in both the upper and lower walls in the corners downstream of the baffles. After passing sequentially through a rod of glass, a mirror at 45 deg and a cylindrical lens, the beam of a 2 W Argon-Ion laser (Spectra Physics Model 166-1) produced a sheet of light approximately 27 cm wide and 1 mm thick that could be used to illuminate any section of the flow. A 35-mm, single lens reflex camera was focused on the illuminated plane. Photographs of the flow were taken on HP-5 Ilford film with a shutter speed of 1/1000 s.

The same lighting technique was used for the visualization with aluminum powder, but the sheet of light was 4 mm thick instead of 1 mm, in order to provide longer tracks from particles with significant spanwise velocities. In this case, time exposures ranged from 1/8 to 1/2 s.

The holes for the dye injection along the top wall of the test section were also used as pressure taps for static pressure drop measurements with the pressure difference measured between consecutive baffles. For this measurement, due to difficulties in reading the levels in the manometer tubes at low flow rates, the results were limited to flow at Reynolds numbers ranging from about 4000 to 10,000.

Since the flow behind the baffles is a recirculating flow, we chose the laser Doppler anemometer system with frequency shifting by Bragg cells to measure mean and fluctuating velocity components. The principles of the LDA system are reported in the literature (e.g., Durst, Melling, and Whitelaw [15]) and will not be repeated here. For our experiments, we

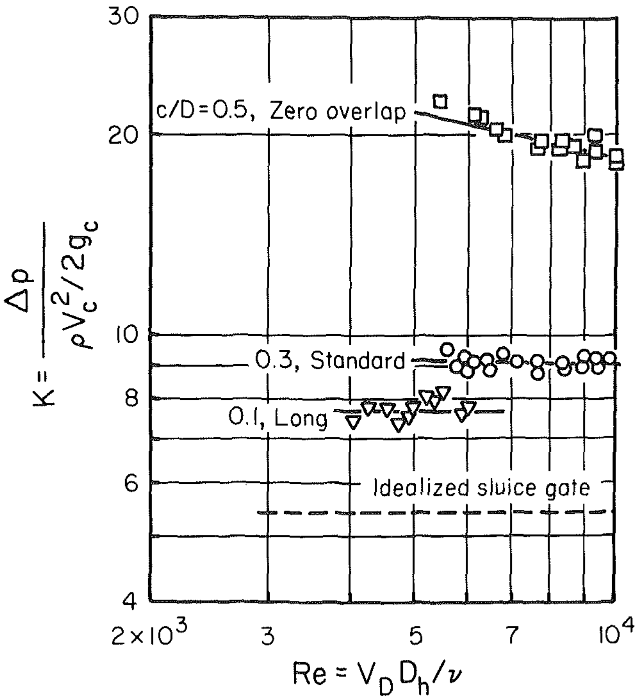

Fig. 5 Pressure loss coefficients between successive baffles on the same side in turbulent flow

used an anemometer working in Doppler differential mode with forward scattering.

The measuring system was set up on a two-dimensional traversing mechanism allowing velocity measurements in both horizontal and vertical directions (for the second test section, the mechanism was adjustable in three directions). It included a 15-MW He-Ne laser (Spectra Physics Model 124A), a TSI transmitting optics with AOM-40 Bragg cells from Intra-Action, and receiving optics consisting of an OEI photomultiplier with EMI S-20 phototube and a set of lenses. The photomultiplier signal was filtered by a Krohn-Hite Model 3101 band pass filter and then converted to a voltage proportional to the Doppler frequency by a TSI Model 1090-1A frequency tracker with a Doppler frequency range from 2 kHZ-50 MHZ, this tracker had an additional range for low velocity measurements. The analog output voltage was processed via a TSI Model 1057 signal conditioner and was finally transmitted to a Disa 55D30 mean voltmeter and to a Phoenix Data Inc. Model No. DAS 6000 A to D converter. The signal was sampled at a frequency of 250 Hz and then was processed on-line via a DEC RT 11/23 microcomputer to obtain the mean velocities and turbulence intensities.

Results

All data presented here were obtained on the vertical centerplane of the test section. Except as noted, they are for plexiglass test sections, so the aspect ratio between the baffles, W/s, was 12 1/2 while in the window cut the aspect ratio W/c ranged from 10 to 50.

Flow Visualization. Before undertaking velocity measurements, flow visualization was conducted (*i*) to deduce the main flow features, (*ii*) to determine the number of baffles necessary to approximate spatially-periodic flow, and (*iii*) to observe the dependence of the flow pattern on the Reynolds number and geometry. Typical photographic sequences are shown in Fig. 3 for a low Reynolds number, Re = 600. In general, the results are comparable to those presented by Gunter, Sennstrom, and Kopp [5] and in the standard geometry (Fig. 3*b*) there is evidence of the features of Fig. 2, which was for slightly different values of the geometrical ratio *s/D*.

Slight differences in the patterns evolve as the flow moves downstream, but the major changes occur from one geometry to another and with Reynolds number. For example, with zero overlap the recirculation eddy ahead of a baffle appears to merge with the larger one downstream of the previous baffle so there is no impingement evident on the common wall.

At Re = 1670, one observes vortices being shed periodically in the curved shear layer from the tip of the baffles as seen in Fig. 4. The flow in the recirculating regions appears more chaotic, with smaller eddies, than at Re = 600. With increasing Reynolds number, the appearance of the recirculating area became very confused and dispersion of the dye was very rapid; however, at Re = 4000 no large eddies were evident being shed from the baffle tips. Comparable observations were made from the flow visualization with aluminum powder.

From the complete collection of photographs, it was seen that in terms of number of baffles, the distance required to reach a flow which is, at least visually, streamwise-periodic is a function of the Reynolds number and geometry. For the standard geometry and at Re = 600, the flow must pass over three to five baffles before it appears periodic, but only over two to three baffles at Re = 1670. For the long baffles with small window cuts the number of baffles required is about two while with zero overlap seven to eight are needed.

Pressure Drop. The pressure drop was measured successively from baffles 2 to 4, 4 to 6, and 6 to 8 for apparently turbulent flow in the three geometries tested. Reynolds numbers based on the cross section of the main channel, ranged from 3600 to 10,500. These sequential measurements also provide a measure of the distance in terms of numbers of baffles required to approach streamwise periodic flow.

For the zero overlap, the pressure drop between baffles 2 and 4 was consistently 10-25 percent higher than between baffles 4 and 6 or 6 and 8. For most runs, this apparent entrance effect was approximately 15 percent, with the lower values at low Reynolds numbers. For the other two geometries, the variation was less than 5 percent. These results are consistent with the observations from the flow visualization.

For the long baffles, or small window cuts, one could characterize the main flow stream crudely as being through a set of wall-slit orifices (comparable to the flow geometry in a variable area flowmeter) connected by 90 deg rectangular elbows to short ducts ($L/s \approx 1.8$). On the other hand, with zero overlap the mainstream organizes itself as through a series of short bends. All three cases can also be considered as a series of contractions and expansions. Therefore, the nondimensional pressure drop is probably best represented as a total loss coefficient *K*, or pressure loss coefficient between successive baffles on the same side of the duct.

For convenience, the total loss coefficient is defined here as $K = 2g_c \Delta p/(\rho V_c^2)$ where V_c is the bulk velocity through the window cut and Δp is measured between successive baffles on the same side. Thus, for a representative unit cell between alternating baffles, the value would be one-half the value presented here. Via continuity and geometrical relationships, these results can be converted to other definitions as desired. The experimental uncertainties, calculated by the technique of Kline and McClintock [16], varied from 7-4 percent for *K* and 4-2 percent for Re as the Reynolds number was increased.

The loss coefficients for turbulent, streamwise periodic flow in the three geometries are presented as Fig. 5. For the two longer baffles, *K* is approximately constant while with zero overlap the data show a tendency to decrease with

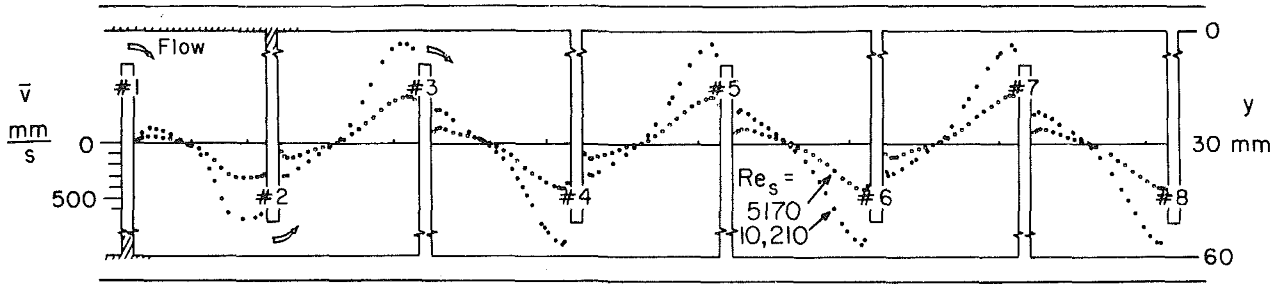

Fig. 6 Evolution of mean velocity profile along centerplane

Reynolds number.[5] The larger value of K for smaller baffles is a consequence of its definition; of course, Δp increases as the baffle length does, for a given flow rate.

The results for the first two geometries appear to be dominated by form or profile drag, while with zero overlap, it is reduced by the larger window so that viscous drag remains significant. These observations can be considered relative to friction data for flow over rough walls. In the terms of Perry, Schofield, and Joubert [17], the shortest baffle acts as a "*d*-type" roughness and the other two act as "*k*-type." A "*d*-type" roughness geometry is one where the friction factor varies with the Reynolds number and therefore, diameter of the duct, while with "*k*-type," the friction factor is primarily dependent on the height of the roughness elements. Alternatively, it can be noted that the two longer baffle geometries resemble sluice gates with submerged outflows [18]. For such gates, our loss coefficient K corresponds to $2/C_q^2$ where C_q is the discharge coefficient of the gate. Rouse [18] notes that $C_q \rightarrow 0.611$ as the gate becomes large relative to the opening, i.e., as $c/D \rightarrow 0$. The data reported here appear to approach this result ($K \rightarrow \sim 5.4$) as the baffles become longer but even at $c/D = 0.1$ show significant additional resistance.

Mean Velocity Distributions. To quantitize flow development and downstream behavior in turbulent flow, velocity measurements were taken for the standard geometry at $\mathrm{Re}_s = 5{,}170$ and 10,200 with the LDA system employing its frequency-shifting capability. The data are tabulated by Berner [3]. The development of the vertical mean velocity component $\bar{v}$ at the centerplane is demonstrated in Fig. 6.

By comparing the profiles between any pair of baffles, one can see that the general profile shapes are approximately the same at both flow rates. For both Reynolds numbers, $\bar{v}(x)$ goes through zero at the same point. One could say the eye of the recirculation region appears to follow the same locus in both cases.

Between the first pair of baffles the mainstream flow is approximately uniform, as in an initial wall jet, which it resembles after the 90° bend from the entrance. The reversed flow region is weak relative to its later magnitude. The two regions accelerate in passing over the next several baffles, approaching profiles with sharper and higher peak values. The location of $\bar{v} = 0$ moves slightly towards the downstream baffle to a position slightly greater than $x/s = 1/3$.

The number of baffles required for $\bar{v}(x)$ to become spatially-periodic within a couple percent was determined by superposing the data between successive baffles from Fig. 6. For $\mathrm{Re}_s = 5170$ flow must pass over four baffles, but only three for $\mathrm{Re}_s = 10{,}200$. These observations are consistent with the pressure drop measurements. In their disk-and-doughnut configuration, Founti and Whitelaw [12] found only two sets (i.e., four baffles) gave full similarity for $2.5 \times 10^4 < \mathrm{Re} < 4.6 \times 10^4$.

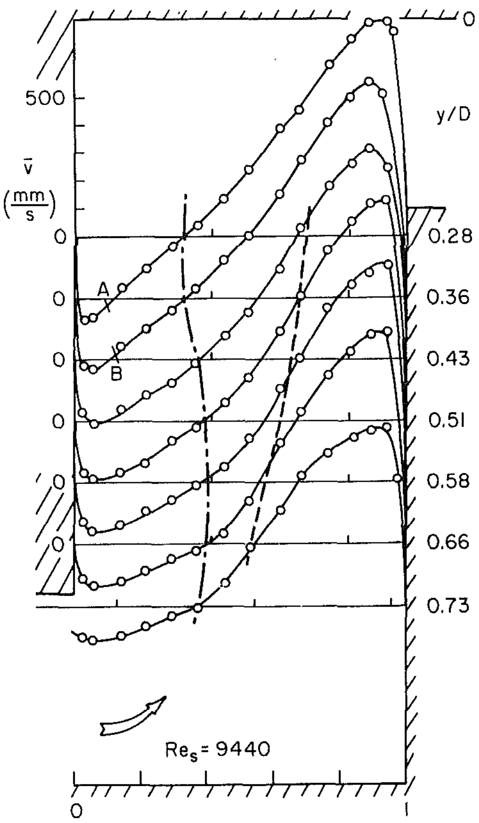

Fig. 7 Streamwise-periodic mean velocity distribution, $\bar{v}(x,y)$

How the flow evolves in the streamwise periodic region downstream is demonstrated in Fig. 7 for $\mathrm{Re}_s = 9440$. The mainstream flow direction is upward along baffle 7. Profile measurements closer to the upper and lower walls were inhibited by interception of one of the laser beams. Light lines connecting points are only drawn for clarity and do not represent analytical predictions.

The velocity peak in the streamwise direction increases and converges towards baffle 7 as the flow proceeds downstream (upwards). Thus the baffle causes the shear layer to converge and accelerate. These features are comparable to the visual observations in Fig. 3(*b*), which, however, shows a laminar flow at Re = 600.

By comparing profiles in the recirculating, downflow region near baffle 6, one can see that the shape changes considerably from top to bottom. The location of zero $\bar{v}$ moves away from the baffle. Possible inflection points appear at the positions marked A and B; these could be an indication of an unstable flow if it were laminar. Alternatively, they might be interpreted as the effect of a second recirculation zone near the wall.

---

[5] Ishigai et al. [23] conducted comparable pressure drop measurements in a model heat exchanger with the tubes removed (and with tubes). Window cut was varied only slightly, $0.19 < c/D < 0.28$, but a wide range of spacing of s/D = 0.13 to 0.95 was covered. In agreement with the data for long baffles in the present experiment, the pressure loss coefficient was found to be approximately independent of Reynolds number. However, the sequence in which their data were correlated obscures the effect of their slight variation in baffle length such that a direct comparison with the present data is not feasible.

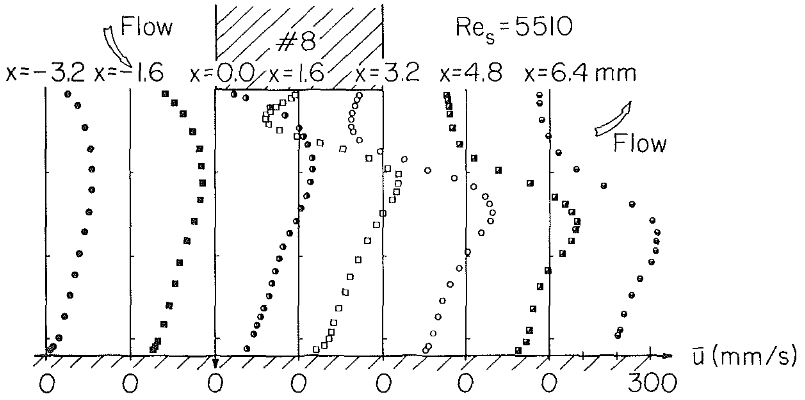

Fig. 8 Mean velocity distribution around tip of a downstream baffle

Inflection points also appear in the profiles of the upward velocities. The dashed line on Fig. 7, constructed by joining points where the second derivative is zero, shows the locus of the curved mixing layer between the recirculating region and the main stream or throughflow. It thus approximates the dividing streamline. This line also implies the possibility of an unstable flow, probably starting at the edge of each baffle. Evidence of the existence of such a flow at Re = 1670 is well illustrated in Fig. 4(*b*) at baffle 1 by three eddies in flight from the top of the baffle toward the bottom wall – but for a laminar flow.

Profiles of the horizontal component $\bar{u}(x,y)$ were measured below the tip of a downstream baffle at $\mathrm{Re}_s = 5510$ in the glass test section. These data are plotted as Fig. 8. They show how the recirculating region behind the baffle merges into the separation bubble generated on its tip.

In the region one thickness ahead of the baffle $\bar{u}(y)$ is positive and small. Extrapolation of the apparent dividing streamline in previous Fig. 7 would intersect the lower wall in the vicinity of $x \approx -3$ or -4mm. Therefore, this region corresponds to the near stagnation region of an impinging jet (two-dimensional) with the jet nozzle very close to the wall. The shape of the peak in $\bar{u}(y)$ with its adjacent inflection point towards the lower wall, as the profiles evolve to the right may not be expected; however, in numerical experiments Huang, Launder, and Leschziner [19] have shown this profile shape to be characteristic in the vicinity of the curved shear layer of an impinging, laminar, two-dimensional jet.

Turbulence Intensity. The root-mean squares of the velocity fluctuation measurements in the vertical direction and between downstream baffles are presented in Fig. 9 for the same locations as the mean velocity profiles of Fig. 7. The mainstream flow between baffles 6 and 7 is upwards, the negative y-direction, i.e., y decreases in the flow direction. The values are normalized by V_s, the bulk velocity between baffles, which is approximately one-quarter of the maximum velocity. The recirculating region behind baffle 6 is on the left and the throughflow on the right.

The intensity profiles increase slightly in the upwards direction. The peak moves from $x/s \approx 0.5$ slightly right to $x/s \approx 0.6$ as the flow proceeds upwards; this shift corresponds to the convergence of the dividing streamline towards baffle 7. The peak is near the dashed line (in Fig. 7) which was taken as representing the locus of the curved mixing layer. The intensity profiles are approximately constant for 1/3 the distance from baffle 6, or roughly across the downward recirculation. The lowest intensities measured were near the location where the maximum mean velocities were found, adjacent to baffle 7. Thus across the mainstream the intensities decrease away from the recirculating region. Spatial resolution was not sufficient to investigate the boundary layer growing on baffle 7, but the higher intensities near the baffle in the upper two profiles may indicate its presence.

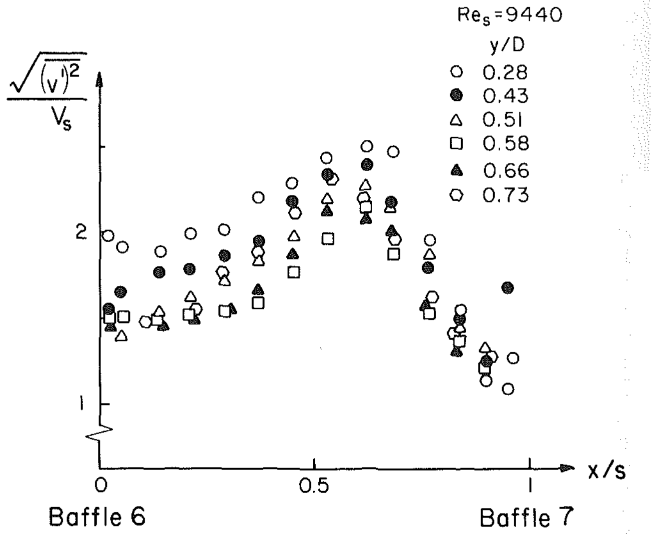

Fig. 9 Turbulence intensity distribution in streamwise-periodic region

Foss [20] has suggested that, for typical mixing layers, turbulence intensities should be approximately 1/6 the difference in mean velocities across the layer. In the flow shown, the difference between the two maxima, upwards and downwards, is about 5 to 6 times V_s, so one might expect $\sqrt{\overline{(v')^2}}/V_s$ to be about 1. Thus the intensities and, consequently, the turbulent mixing appear to be somewhat higher than for a typical plane mixing layer.

Discussion

Implications of this flow study relate to shell-and-tube heat exchangers in two ways; heat transfer paths or resistances and flow-induced oscillations. The effects of the presence of tubes between baffles are not yet clear. One would expect a tube bank to act as the screens in a wind tunnel and improve the large-scale uniformity of the velocity distribution. However, Gunter, Sennstrom, and Kopp [5] reported that, in their preliminary experiments, the insertion of tubes had no apparent effect on the flow pattern. On the other hand, Martin, Elphick, and Gollish [13] demonstrated that, in their inlet/baffle/outlet section, the addition of a densely-packed tube bundle modified the flow, reducing the size of the recirculating regions and causing a more uniform velocity distribution. For the complete range of heat exchanger applications, further experiments are required across a range from no tubes to a densely packed bundle; the present results are expected to be representative of the lower limit of this range, i.e., few or no tubes. For mixing chambers, circuit boards, solar collectors, turbine blade passages, and labyrinth shaft seals, the question of tubes is not pertinent to the application. Further, the tendency away from installing tubes in the window – so that unsupported lengths are shorter – indicates that the information for the vicinity of the baffle tip may be directly useful [21]. And while one usually pictures the shell as being circular, rectangular shell-and-tube configurations are being designed for surface condenser applications [22] and, presumably, low-pressure heat exchangers.

Estimates of heat exchanger performance or design calculations usually treat the shellside flow as being at a uniform velocity V_s perpendicular to the tubes and exchanging energy along their entire outer surface area. For the geometries investigated, about 2/3 or more of the space between the baffles was occupied by a recirculating region (with dense-packed tubes the size of the region would be smaller [13]). One could say that tubes in that region would be "stewing in their own juice" in an approximately isothermal region approaching the local temperature of the fluid inside the tubes. Energy would be transferred to (or from) the mainstream from this region by two paths: (*i*) across the curved mixing layer and (*ii*) across the reversed boundary layer to the baffle, by conduction through the baffle and directly to the mainstream via its boundary layer on the forward side of the baffle (tube/baffle leakage might modify this situation slightly). Therefore, the baffle would participate actively in the heat transfer process and the choice of its material could be significant beyond structural considerations. On the other hand, the velocity of the mainstream is considerably above the bulk velocity so the local heat transfer coefficient would be improved for that section of the tubes.

Flow-induced oscillations are of major concern in the design of tubular heat exchangers [21]. As seen in the laminar flow visualization, one source of periodic disturbances – particularly in the window cut – is the apparent shedding of vortices in the shear layer from the baffle tip. If their frequency is near the natural frequency of the tubes, problems can be expected. An appropriate topic for further study would be to attempt to characterize their average frequency and strength for turbulent flow where they are less obvious. A lower frequency unsteadiness or potential of shedding of the large recirculating eddy behind a baffle may also be expected to scale relative to the baffle length and/or spacing; its characterization is also beyond the scope of the present work but is of potential importance.

The mean velocity distributions and loss coefficients obtained for the standard geometry provide a first test for numerical predictions of turbulent flow around segmental baffles. The resemblance of the laminar and turbulent flow visualization, the velocity distributions, the numerical predictions of Yu and Heinrich [14] for laminar flow, and the results of Gunter, Sennstrom and Kopp [5] indicate that the main features should be predictable via a relatively simple turbulence model (e.g., $\nu_{\text{eff}} = \nu$?). Closer inspection shows differences in detail that will be important in predicting the heat transfer through the baffle and heat loss through the shell wall. Thus apparent agreement between an observed flow pattern and a turbulent calculation may be misleading. Ultimately, the problem of heat exchange with the surfaces will probably require the development of wall treatments accounting for the curvature and acceleration of the flow – hopefully, in conjunction with simple approximations away from the wall.

Concluding Remarks

This study of flow around three sets of segmental baffles in the ranges $600 < \text{Re} < 10{,}500$, $0.1 < c/D < 0.5$ and $s/D = 0.4$ has shown:

1 A streamwise-periodic flow is approximately achieved after sufficient distance for development.

2 The development length necessary is a function of Reynolds number and geometry (c/D).

3 For the standard geometry, $s/D = 0.4$ and $c/D = 0.3$, the main flow features are approximatley the same in laminar and apparently turbulent flows.

Acknowledgments

This material is based upon work supported by the National Science Foundation under Grant MEA-82-07086 and by the Max Planck Institut für Strömungsforschung. We gratefully thank Mssrs. Jordan Reid and Kenneth E. Bauer for constructing the apparatus, Professor F. H. Champagne for providing the data acquisition system, and Mr. A. M. Divrik for the pressure measurements. The United States Government and its representatives have unrestricted right to reproduce and distribute this paper in whole or in part under any copyright secured by the publisher.

References

1 Knudsen, J. G., and Katz, D. L., *Fluid Dynamics and Heat Transfer*, McGraw-Hill, New York, 1958.

2 Chenoweth, J. M., personal communication, Heat Transfer Research, Inc., Alhambra, CA, 1980.

3 Berner, C., "Flow Over Baffles," Tech. report, Aerospace and Mechanical Engineering Department, University of Arizona, 1982.

4 Taborek, J., "Evolution of Heat Exchanger Design Techniques," *Heat Transfer Engineering*, Vol. 1, No. 1, 1979, pp. 15–29.

5 Gunter, A. Y., Sennstrom, H. R., and Kopp, S., "A Study of Flow Patterns in Baffled Heat Exchangers," ASME Paper 47-A-103, 1947.

6 Hele-Shaw, H. J. S., "Flow of Water," *Nature*, Vol. 58, 1898, pp. 34–36.

7 Tinker, T., "Shell Side Characteristics of Shell and Tube Heat Exchangers," *Proceedings, General Discussion on Heat Transfer*, Institution of Mechanical Engineers, 1951, pp. 89–116.

8 Gupta, R. K., and Katz, D. L., "Flow Patterns for Predicting Shell-side Heat Transfer Coefficients for Baffled Shell and Tube Exchangers," *Industrial and Engineering Chemistry*, Vol. 49, 1957, pp. 998–999.

9 Short, B. E., "The Effect of Baffle Height and Clearance on Heat Transfer and Pressure Drop in Heat Exchangers," ASME Paper 47-A-105, 1947.

10 Gay, B., Mackley, N. V., and Jenkins, J. D., "Heat Transfer in Baffled Cylindrical Shell-and-Tube Exchangers—An Electrochemical Transfer Modelling Technique," *International Journal Heat Mass Transfer*, Vol. 19, No. 9, 1976, pp. 995–1002.

11 Palen, J. W., and Taborek, J., "Solution of Shell Side Flow Pressure Drop and Heat Transfer by Stream Analysis Method," *Chemical Engineering Progress Symposium Series*, Vol. 65, No. 92, 1969, pp. 53–63.

12 Founti, M. A., and Whitelaw, J. H., "Shellside Flow in a Model Disc-and-Doughnut Heat Exchanger," Tech. report FS/81/37, Mechanical Engineering Department, Imperial College, London, 1981.

13 Martin, W. W., Elphick, I. G., and Gollish, S., "Flow Distribution Measurement in a Model of a Heat Exchanger," *Engineering Application of Laser Velocimetry*, ASME Winter Annual Meeting, Phoenix, Ariz., 1982.

14 Yu, C.-C., and Heinrich, J. C., personal communication, Aerospace and Mechanical Engineering Department, University of Arizona, Tucson, AZ, 1983.

15 Durst, F., Melling, A., and Whitelaw, J. H., *Principles and Practices of Laser Doppler Anemometry*, Academic Press, London, 1976.

16 Kline, S. J., and McClintock, F. A., "The Description of Uncertainties in Single Sample Experiments," *Mechanical Engineering*, Vol. 75, No. 1, 1953, pp. 3–8.

17 Perry, A. E., Schofield, W. H., and Joubert, P. N., "Rough Wall Turbulent Boundary Layers," *Journal of Fluid Mechanics*, Vol. 37, 1969, pp. 383–413.

18 Rouse, H., *Fluid Mechanics for Hydraulic Engineers*, McGraw-Hill, New York, 1938.

19 Huang, P. G., Launder, B. E., and Leschziner, M. A., "Discretization of Non-linear Convection Processes: A Broad Range Comparison of Four Schemes," Tech. report TFD/83/1, Mechanical Engineering Department, University of Manchester Inst. Sci. Tech., Manchester, U.K., 1983.

20 Foss, J. F., personal communication, Mechanical Engineering Department, Michigan State University, E. Lansing, Mich., 1981.

21 Chenoweth, J. H., "Design of Shell-and-Tube Heat Exchangers to Avoid Flow-induced Vibration," *Heat Transfer 1982*, München, Vol. 6, 1982, pp. 173–178.

22 Marto, P. J., and Nunn, R. H., eds., *Power Condenser Heat Transfer Technology*, Hemisphere, Washington, D.C., 1981.

23 Ishigai, S., Nishikawa, R., Nakayama, Y., Tanaka, S., Saida, I., and Fukuda, Y., "Shell-side Pressure Drop in the Multi-baffled Shell-and-Tube Heat Exchangers," *Bull. Japan Society of Mechanical Engineers*, Vol. 8, No. 32, 1965, pp. 644–651.

Rotary Heat Exchangers With Time Varying or Nonuniform Inlet Temperatures

M. J. Brandemuehl
Research Division,
Carrier Corporation,
Syracuse, N.Y. 13221

P. J. Banks
Division of Energy Technology,
Commonwealth Scientific and
Industrial Research Organization,
Highett, Victoria 3190
Australia

The performance of a counterflow, rotary heat exchanger operating with either transient or nonuniform inlet temperatures is investigated. The effect of transient inlet temperatures is analyzed in terms of the response of the outlet fluid temperatures to a step change in temperature of one of the inlet fluid streams. The effect of temperature nonuniformities is analyzed in terms of the change in steady-state effectiveness due to a circumferential temperature distribution in one of the inlet fluid streams. These temporal and spatial variations are explored using three different methods of analysis. An equilibrium analysis, assuming infinite heat transfer coefficients, is developed from kinematic wave theory. It is used to qualitatively describe the heat transfer process and define the upper limit of performance. A finite difference model of the governing differential equations, using finite transfer coefficients, is employed to obtain a detailed numerical analysis of heat exchanger performance. Results for the complete range of matrix to fluid capacity rate ratio are presented for a balanced and symmetric regenerator. At moderate capacity rate ratios, the numerical analysis predicts unusual temporal periodicity in the transient response. An experimental analysis has also been conducted using a counterflow, parallel passage, rotary heat exchanger made from polyester film. The results are used to substantiate predictions of the numerical model.

Introduction

A rotary heat exchanger, or regenerator, is a regenerative heat exchange device in which a rotating porous matrix of material is alternately exposed to hot and cold fluid streams. A schematic diagram of such a regenerator is shown in Fig. 1, with the fluid streams flowing in countercurrent directions. The counterflow configuration is more common and gives higher performance than the alternative unidirectional flow configuration. Traditionally, these regenerators have been employed in gas turbine engines. Recently, they have assumed importance in solar air-conditioning systems and other air-to-air heat recovery processes requiring a compact high-performance unit.

This paper investigates the performance of a counterflow, rotary regenerator operating with either transient or nonuniform fluid inlet temperatures. A temporal step change and a circumferential nonuniformity are considered. Three different methods of analysis are employed: an equilibrium analysis, a numerical analysis, and an experimental analysis. The equilibrium analysis is used to define the upper limit of performance, while the numerical analysis provides detailed results of use to the designer. The experimental analysis verifies these theoretical models.

While this paper specifically examines rotary regenerator performance, a regenerative heat exchanger may also be of fixed-matrix form in which the hot and cold fluid streams are alternately passed through two or more fixed porous matrices. The performance of a rotary regenerator is based on the circumferential-averaged fluid outlet temperature, while that of a fixed-matrix regenerator is based on the time-averaged fluid outlet temperature during each period. The theoretical analysis is the same for both types of regenerator under steady periodic conditions with uniform inlet temperatures. However, the analysis of the two types of regenerators differs when considering transient or nonuniform inlet temperatures.

In the case of nonuniform inlet temperature, circumferential nonuniformity in inlet fluid temperature to a rotary regenerator corresponds to time variation in inlet fluid temperature during each period in a fixed-matrix regenerator. In the case of transient inlet temperature, the response is presented in terms of the temporal variation of the circumferential-averaged fluid outlet temperature for the rotary regenerator and in terms of the temporal variation of the time-averaged fluid outlet temperature in each successive period for the fixed-matrix regenerator. While the transient response of a rotary regenerator is continuous with time, the response of a fixed matrix regenerator is comprised of a series of discrete points, separated in time by the period duration. While the overall responses of the two types of regenerators are the same, the response of the fixed-matrix regenerator is unable to resolve transient effects on a time scale less than the period duration.

The performance of a regenerator operating under steady periodic conditions with uniform inlet temperatures has been investigated by many authors, and the results are available in the literature [1–4]. However, there have been few theoretical or experimental investigations of rotary regenerators operating with transient inlet temperatures, and none for

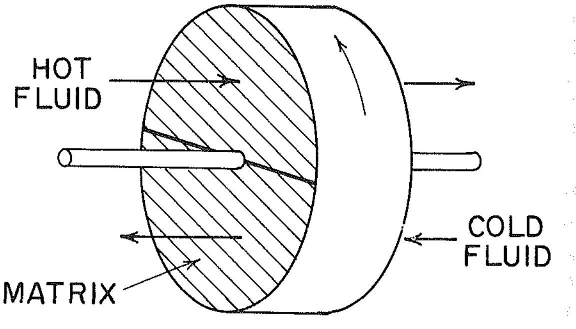

Fig. 1 Schematic diagram of a counterflow rotary heat exchanger

---

Contributed by the Heat Transfer Division and presented at the ASME Winter Annual Meeting, Washington, D.C., November 15–20, 1981. Manuscript received by the Heat Transfer Division September 11, 1981.

nonuniform inlet temperatures to the authors' knowledge. London et al. [5] have examined the transient response of a gas turbine regenerator to a step change in one fluid inlet temperature, using limited computer solutions and an analogy with recuperative heat exchanger theory. Their analysis considered balanced and symmetric regenerators operating at matrix to fluid capacity rate ratios much larger than unity. Chao [6] presents a brief discussion of transients in rotary regenerators using limited theoretical and experimental results.

Willmott and Burns [7, 8] used numerical analysis to predict the transient response of unbalanced and asymmetric fixed-matrix regenerators, considering matrix to fluid capacity rate ratios larger than unity. Shah [9] provides a discussion of transients in recuperative and regenerative heat exchangers, including results from [5, 7, 8].

While the literature generally contains transient results for large matrix to fluid capacity rate ratios, this paper includes results for regenerators operating at small capacity rate ratios. A well-designed regenerator for sensible heat transfer will always be operating at large capacity rate ratios to maximize regenerator efficiency. However, regenerators for heat and mass transfer, such as rotary dehumidifiers or energy recovery units, can be analyzed using an analogy with heat transfer which employs sensible heat regenerator theory [10-12]. This analogy method often requires sensible heat regenerator results for small capacity rate ratios. Recognizing this application, results for the complete range of matrix to fluid capacity rate ratios have been included.

Theoretical Investigation

Governing Equations. The basic equations governing the transfer of heat in regenerators and the measures of performance are defined in this section. Several assumptions have been made in the derivation of these equations. It is assumed that heat transfer between the fluid and matrix is by convection only. As such, heat conduction in the axial and circumferential directions, in both the fluids and matrix, is assumed to be negligible. It is assumed that the temperatures of both the fluids and matrix are uniform in the radial direction. The specific heats of the fluids and matrix are considered constant, as are the heat transfer coefficients between the fluids and matrix. Leakage between the two fluid streams is assumed to be negligible, and the capacity of the matrix in each period is assumed to be much larger than the capacity of the fluid contained in its porous structure.

An energy balance on an element of the matrix yields the following differential equations [10]

$$v_i \frac{\partial t'}{\partial x'} + \mu_i \sigma_i \frac{\partial T'}{\partial \theta'} = 0 \qquad (1)$$

$$i = 1,2$$

$$\mu_i \sigma_i \frac{\partial T'}{\partial \theta'} + J_i (T' - t') = 0 \qquad (2)$$

The subscript i refers to periods 1 or 2. The x'-direction in each period is the direction of fluid flow. Equations (1) and (2) can be rewritten using dimensionless parameters and variables to give the following

$$\frac{\partial t}{\partial x} + \beta_i C_i{}^* \frac{\partial T}{\partial \theta} = 0 \qquad (3)$$

$$i = 1,2$$

$$\beta_i C_i{}^* \frac{\partial T}{\partial \theta} + \mathrm{Ntu}_i (T - t) = 0 \qquad (4)$$

Equations (3) and (4) are constrained by the boundary and initial conditions: $t = t_{i,\mathrm{in}}$ at $x = 0$ and $T(x)$ is known at $\theta = 0$. In periodic steady-state operation, the axial matrix temperature distribution at time θ is equal to that at $\theta + n$, where n is any integer. In these equations, the dimensionless fluid and matrix temperatures are defined as

$$t = \frac{t' - \overline{t'}_{2,\mathrm{in}}}{\overline{t'}_{1,\mathrm{in}} - \overline{t'}_{2,\mathrm{in}}}$$

$$T = \frac{T' - \overline{t'}_{2,\mathrm{in}}}{\overline{t'}_{1,\mathrm{in}} - \overline{t'}_{2,\mathrm{in}}} \qquad (5)$$

where

$$\overline{t'}_{1,\mathrm{in}} = \frac{1}{\beta_1} \int_0^{\beta_1} t'_{1,\mathrm{in}} d\phi$$

$$\overline{t'}_{2,\mathrm{in}} = \frac{1}{\beta_2} \int_{\beta_1}^{1} t'_{2,\mathrm{in}} d\phi \qquad (6)$$

Nomenclature

A_v = heat transfer area per unit volume, m^2/m^3
c_p = specific heat of fluid, J/kg°C
C_i^* = matrix to fluid capacity rate ratio of period i, defined as $(\mu\sigma L/Pv)_i$
e_i = the transient response of period i, defined by equation (10)
h = convective heat transfer coefficient, W/m^2°C
J_i = matrix-fluid convective transfer coefficient per unit capacity of fluid in period i, defined as $J_i = hA_v/\rho c_p \epsilon$, 1/s
L = length of matrix, m
n = an integer defined in Table 2
Ntu_i = number of transfer units in period i, defined as $(JL/v)_i$
P_i = duration of period i, s
t = dimensionless fluid temperature, defined in equation (5)
t' = fluid temperature, °C
T = dimensionless matrix temperature, defined in equation (5)
T' = matrix temperature, °C
v_i = velocity of fluid in matrix passages, m/s
x = dimensionless length variable, defined as x'/L
x' = length variable, m
β_i = dimensionless duration of period i, defined as $P_i/(P_1+P_2)$
β_s = dimensionless azimuthal position of change in nonuniform temperature distribution of Fig. 4
δ = half the magnitude of temperature change in Fig. 4
ϵ = porosity of matrix
η_i = regenerator efficiency defined by equation (7)
θ = dimensionless time variable, defined as $\theta'/(P_1+P_2)$
θ' = time variable, s
μ_i = ratio of mass of matrix to mass of contained fluid in period i
ρ = density of fluid, kg/m^3
σ_i = ratio of specific heat of matrix to specific heat of fluid in period i
ϕ = dimensionless azimuthal angle, defined as $\phi'/2\pi$
ϕ' = azimuthal angle, rad

Subscripts

i = period i, $i = 1, 2$
in = at regenerator inlet
out = at regenerator outlet

Superscripts

= spatial average

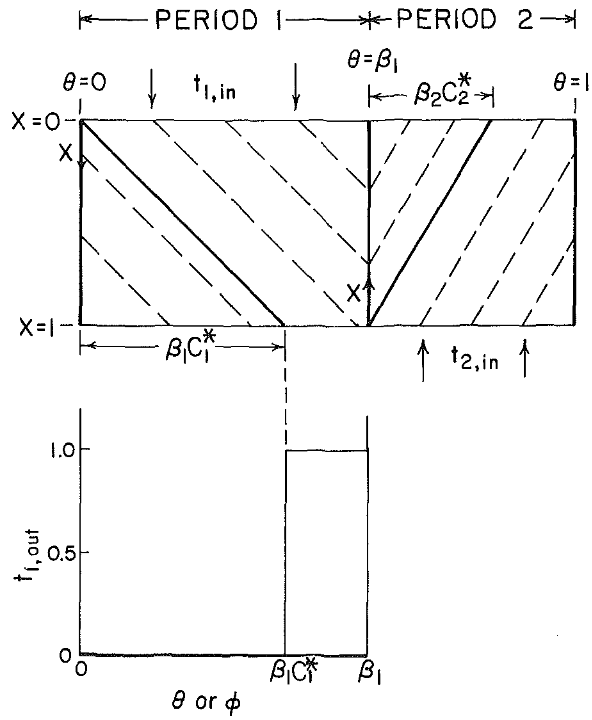

Fig. 2 Wave diagram for regenerator under steady periodic operation with $C_1^* < 1$ and $C_2^* < 1$. Period 1 outlet temperature distribution for constant inlet fluid temperature. The coordinate x increases in the flow direction in each period.

The use of Ntu_i and $C_i{}^*$ as regenerator parameters is based on the nomenclature of Kays and London [3]. (In the nomenclature of Hausen [1], $\text{Ntu}_i = \Lambda_i$ and $C_i{}^* = \Lambda_i/\Pi_i$.) While Kays and London refer to the fluid streams as having either the minimum or maximum capacity rate, such a designation is inappropriate for this paper. Instead, for the analyses of this paper, the fluid stream with variable inlet conditions, in the form of spatial nonuniformities or time variations, will be referred to as period 1. Period 2 refers to the fluid stream with constant inlet temperature.

The performance of the regenerator will be characterized by two separate indicators. Under steady-state conditions, it is characterized by the regenerator efficiency, η_i

$$\eta_i = \frac{\bar{t}_{i,\text{out}} - \bar{t}_{i,\text{in}}}{\bar{t}_{j,\text{in}} - \bar{t}_{i,\text{in}}} \qquad \begin{matrix} i=1,2 \\ j=3-i \end{matrix} \tag{7}$$

By definition of the dimensionless inlet temperatures in equations (5), $\bar{t}_{1,\text{in}} = 1$ and $\bar{t}_{2,\text{in}} = 0$, and equation (7) yields the following

$$\eta_1 = 1 - \bar{t}_{1,\text{out}} \tag{8a}$$

$$\eta_2 = \bar{t}_{2,\text{out}} \tag{8b}$$

For a regenerator operating under steady periodic conditions, conservation of energy requires that the following condition is satisfied.

$$C_2^* \eta_1 = C_1^* \eta_2 \tag{9}$$

For a balanced regenerator, $C_1^* = C_2^*$, $\eta_1 = \eta_2$, and the regenerator efficiency is equal to the regenerator effectiveness of Kays and London [3].

The response of a regenerator to a step change in inlet fluid temperature will be characterized by the transient response, e_i.

$$e_i = \frac{\bar{t}_{i,\text{out}}(\theta) - \bar{t}_{i,\text{out}}(\theta=0)}{\bar{t}_{i,\text{out}}(\theta=\infty) - \bar{t}_{i,\text{out}}(\theta=0)} \qquad i=1,2 \tag{10}$$

The temperatures used in equation (10) are the circumferential average temperatures at the outlet of period i.

Physically, the solution of equations (3) and (4) describes the behavior of a wedge-shaped segment of the matrix, and its associated fluid, as it rotates through the two fluid streams with time. The regenerator efficiency and transient response, however, are defined in terms of spatial average temperatures, averaged over the azimuthal angle, at a particular time.

For regenerators operating under periodic steady-state conditions, the time average outlet temperature of any segment is equal to the spatial average outlet temperature at any time. In effect, the variable θ of equaitons (3) and (4) can simply be replaced by the azimuthal angle variable, ϕ. However, for regenerators operating under transient inlet conditions, the spatial distribution at a particular time must be obtained by solving equations (3) and (4) for segments of the matrix originally at every angular position.

Equilibrium Analysis. The equilibrium analysis assumes infinite heat transfer coefficients between the matrix and the fluid ($\text{Ntu}_i = \infty$) As such, the analysis defines the upper limit of regenerator performance. The assumption also allows the regenerator to be analyzed using kinematic wave theory, a simple yet powerful analytical tool which provides a graphical method for describing the dynamics of the heat transfer process.

Under the conditions $\text{Ntu}_i = \infty$, the matrix and fluid are in thermal equilibrium at every location ($t = T$) and equation (3) can be rewritten as equation (11).

$$\frac{\partial T}{\partial x} + \beta_i C_i^* \frac{\partial T}{\partial \theta} = 0 \tag{11}$$

Equation (11) is of the form of a kinematic wave equation [13, 14]. The solution is such that T is a constant in the (x, θ)-plane in the directions $d\theta/dx = \beta_i C_i^*$. Therefore, T will be constant along lines of constant $\theta - \beta_i C_i^* x$, and since both β_i and C_i^* are constants, these lines will be straight and parallel.

To illustrate this point, consider a regenerator, described by equation (11), operating under steady periodic condition, with $C_1^* < 1$ and $C_2^* < 1$. Figure 2 shows a wave diagram for this situation, which traces the temperature distribution of a segment of the matrix from the time it enters period 1 ($\theta = 0$) until it exits from period 2 ($\theta = 1$). The dashed lines correspond to lines of constant T, and the solid lines correspond to the position of the wavefront between period 1 and period 2 temperatures.

A particular feature of kinematic wave equations of the form of equation (11) is that the temperature at any (x, θ) can be determined from either the initial or boundary conditions. Thus, referring to Fig. 2, the temperature distribution at the outlet of period 1 from $\theta = 0$ to $\theta = \beta_1 C_1^*$ corresponds to the temperature distribution in the matrix at the beginning of the period ($\theta = 0$), which in turn corresponds to the period 2 inlet fluid temperature distribution at its inlet from $\theta = 1 - \beta_2 C_2^*$ to $\theta = 1$. Similarly, the outlet temperature between $\theta = \beta_1 C_1^*$ and $\theta = \beta_1$ is equal to the inlet temperature between $\theta = 0$ and $\theta = 1 - \beta_1 C_1^*$. Figure 2 also shows the period 1 outlet temperature distribution when both the inlet fluid streams have uniform inlet temperatures.

Since the regenerator is operating under steady periodic conditions, Fig. 2 also represents the spatial temperature distribution within the matrix when θ is replaced by ϕ. The regenerator efficiency can then be obtained directly from Fig. 2. Thus, for uniform inlet fluid temperatures, $t_{1,\text{in}} = 1$ and $t_{2,\text{in}} = 0$, the outlet temperature is 0 from $\phi = 0$ to $\phi = \beta_1 C_1^*$ and 1 from $\phi = \beta_1 C_1^*$ to $\phi = \beta_1$. Hence equations (7) give $\eta_1 = C_1^*$ and $\eta_2 = C_2^*$. For nonuniform inlet fluid temperatures, with $t_{1,\text{in}} = f_1(\phi) = f_1(\theta)$ and $t_{2,\text{in}} = f_2(\phi) = f_2(\theta)$, the outlet temperatures must be integrated to obtain the regenerator efficiencies. The results given in Table 1 for regenerator efficiency η_1 can be derived from equations (8) for the cited ranges of C_1^* and C_2^*.

The kinematic wave concept can also be used in the analysis of regenerators operating under transient inlet conditions due to a step change in inlet fluid temperature. At times $\theta < 0$, the matrix is operating under steady periodic conditions at the initial fluid inlet states. At $\theta = 0$, a step change is applied to the period 1 inlet fluid temperature while the period 2 inlet fluid temperature remains unchanged. Because of the linearity of equations (3), (4), and (11), and the definition of the transient response, e_i, the results are independent of the particular choice of initial and final inlet fluid temperatures. Recognizing this fact, the initial inlet temperatures are both set to zero and the period 1 final inlet fluid temperature is set equal to unity. Notice that e_1 is the outlet fluid temperature response of the period in which the step change occurred while e_2 is the response of the opposite period.

In the analysis of regenerators operating under periodic steady state conditions, the solution to equation (11) was applied only to the segment of the matrix which, at $\theta = 0$, was in the position $\phi = 0$. However, for a regenerator operating under transient inlet conditions, the spatial temperature distribution can only be obtained by applying the solution of equation (11) to all segments of the matrix.

To illustrate this technique, consider a balanced symmetric regenerator ($C_1^* = C_2^*$, $\beta_1 = \beta_2 = 0.5$) with $C_1^* = 0.8$. At $\theta = 0$, $t_{1,\mathrm{in}} = t_{2,\mathrm{in}} = 0$ and the matrix is uniformly at $T = 0$. The period 1 inlet fluid temperature is then changed to $t_{1,\mathrm{in}} = 1$. Figure 3 shows the spatial temperature distribution within the matrix at four values of time, $\theta = 0.2$, 0.4, 0.6, 0.8. At $\theta = 0.2$, the temperature change wavefront has begun to propagate through the matrix. The fluid outlet temperature of period 1 remains unchanged with $e_1 = 0$. However, the fluid outlet state of period 2 has already been changed to $e_2 = 0.25$. At $\theta = 0.4$, the temperature wavefront in period 1 has emerged from the matrix causing a step increase in the period 1 response from $e_1 = 0$ to $e_1 = 1$. The fluid outlet temperature of period 2 has continued to increase giving $e_2 = 0.5$. As the temperature wavefront has propagated through the matrix in period 1, the axial temperature distribution of the matrix entering period 2 has continually changed. Since the wavefront has propagated through the matrix in period 1 at $\theta = 0.4$, the axial distribution of the matrix entering period 2 will henceforth remain constant at $T = 1$. At $\theta = 0.6$, the period

Table 1 Period 1 regenerator efficiency for nonuniform inlet temperature from equilibrium analysis. Period 2 efficiency defined as $\eta_2 = (C_2^*/C_1^*)\eta_1$.

$C_1^* \le 1$ $C_2^* \le 1$	$\eta_1 = 1 - \frac{1}{\beta_1}\int_0^{\beta_1(1-C_1^*)} f_1(\phi)d\phi - \frac{C_1^*}{\beta_2 C_2^*}\int_{1-\beta_2 C_2^*}^{1} f_2(\phi)d\phi$
$C_1^* \ge 1$ $C_2^* \le C_1^*$	$\eta_1 = 1 - \frac{C_1^*}{\beta_2 C_2^*}\int_{1-(\beta_2 C_2^*/C_1^*)}^{1} f_2(\phi)d\phi$
$C_2^* \ge 1$ $C_1^* \le C_2^*$	$\eta_1 = 1 - \frac{1}{\beta_1}\int_0^{\beta_1[1-(C_1^*/C_2^*)]} f_1(\phi)d\phi$

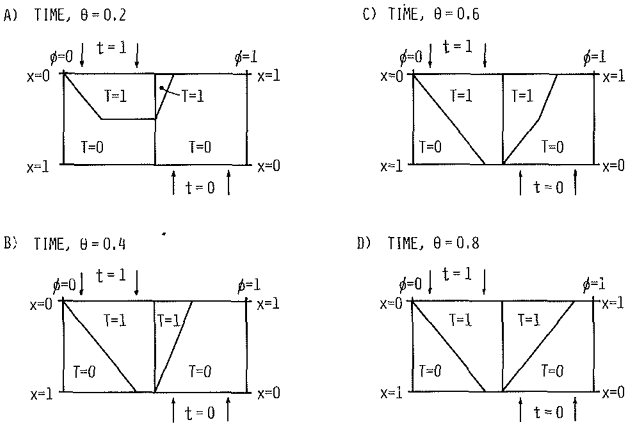

Fig. 3 Spatial temperature distributions for equilibrium analysis of transient response at $\theta = 0.2, 0.4, 0.6, 0.8$ with $C_1^* = C_2^* = 0.8$ and $\beta_1 = \beta_2 = 0.5$. The coordinate x increases in the flow direction in each period.

Table 2 Regenerator transient response for equilibrium analysis

C_1^*	θ range	Response, e_i
$C_1^* \le 1$ $C_2^* \le 1$	$\theta < \beta_1 C_1^*$	$e_1 = 0$
	$\theta \ge \beta_1 C_1^*$	$e_1 = 1$
	$\theta \le \beta_1 C_1^* + \beta_2 C_2^*$	$e_2 = \theta/(\beta_1 C_1^* + \beta_2 C_2^*)$
	$\theta \ge \beta_1 C_1^* + \beta_2 C_2^*$	$e_2 = 1$
$C_1^* \le 1$ $C_2^* \ge 1$	$\theta < \beta_1 C_1^*$	$e_1 = 0$
	$\beta_1 C_1^* \le \theta \le \beta_2 + [\beta_1 C_1^*(1 + C_2^*)/C_2^*]$	$e_1 = \frac{1 - C_1^*}{[1 - (C_1^*/C_2^*)]}$
	$\theta \ge \beta_2 + [\beta_1 C_1^*(1 + C_2^*)/C_2^*]$	$e_1 = 1$
	$\theta \le \beta_2 + (\beta_1 C_1^*/C_2^*)$	$e_2 = C_2^*\theta/(\beta_1 C_1^* + \beta_2 C_2^*)$
	$\theta > \beta_2 + (\beta_1 C_1^*/C_2^*)$	$e_2 = 1$
$C_1^* \ge 1$ $C_2^* \le C_1^*$	all θ	e_1 is undefined
	$\theta \le \beta_1 + (\beta_2 C_2^*/C_1^*)$	$e_2 = C_1^*\theta/(\beta_1 C_1^* + \beta_2 C_2^*)$
	$\theta \ge \beta_1 + (\beta_2 C_2^*/C_1^*)$	$e_2 = 1$
$C_1^* \ge 1$ $C_2^* \ge C_1^*$	$\theta \le \beta_1 C_1^* + n[\beta_2 + (\beta_1 C_1^*/C_2^*)]$	$e_1 = 0^a$
	$\beta_1 C_1^* + n[\beta_2 + (\beta_1 C_1^*/C_2^*)] \le \theta \le \beta_1 C_1^* + (n+1)[\beta_2 + (\beta_1 C_1^*/C_2^*)]$	$e_1 = \frac{C_1^*}{C_2^*}\left(n + \frac{1 - C_1^*}{1 - (C_1^*/C_2^*)}\right)$
	$\theta \ge \beta_1 C_1^* + (n+1)[\beta_2 + (\beta_1 C_1^*/C_2^*)]$	$e_1 = 1$
	$\theta \le \beta_2 + (\beta_1 C_1^*/C_2^*)$	$e_2 = C_2^*\theta/(\beta_1 C_1^* + \beta_2 C_2^*)$
	$\theta \ge \beta_2 + (\beta_1 C_1^*(C_2^*)$	$e_2 = 1$

[a] n is integer such that $n - 1 < \frac{C_1^* - 1}{1 - (C_1^*/C_2^*)} \le n$

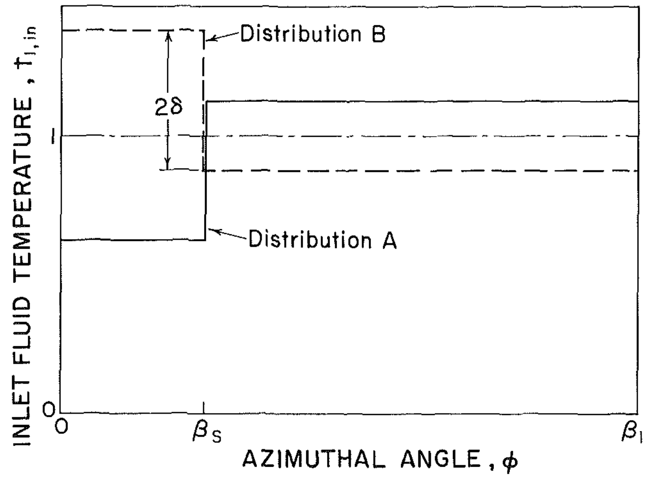

Fig. 4 Temperature distributions of period 1 inlet fluid used in analysis of nonuniform inlet temperatures

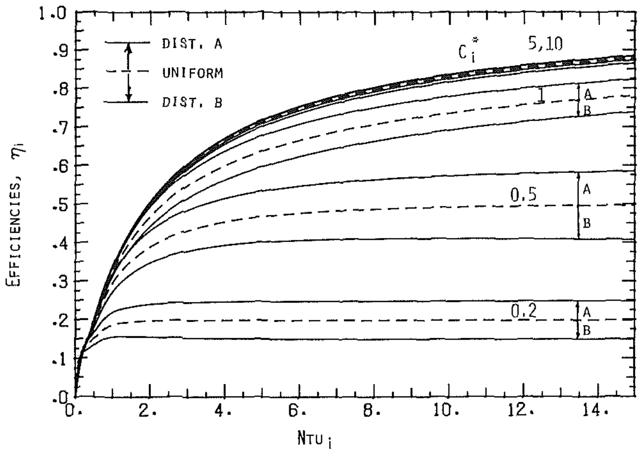

Fig. 5 Regenerator efficiency for nonuniform inlet conditions with $\beta_s = 0.5\beta_1$, $\delta = 0.25$, $\mathrm{Ntu}_1 = \mathrm{Ntu}_2$, $C_1^* = C_2^*$

1 matrix and fluid states are unchanged, while the period 2 transient response has continued its linear increase to $e_2 = 0.75$. The distribution within the matrix in period 2 shows that the equilibrium temperature profile is developing while pushing the lingering transient effects toward the period 2 outlet. At $\theta = 0.8$, all transient effects have been eliminated and the regenerator has reached periodic steady-state operation with $e_1 = 1$ and $e_2 = 1$.

This type of analysis has been performed for the general case of an unbalanced, asymmetric regenerator. The results are presented in Table 2.

The results of these equilibrium analyses define the values of η_i and e_i obtainable from a regenerator operating with infinite heat transfer coefficients. The results of the numerical analysis will show that these limits are approached for large values of Ntu. However, the main value of the analysis lies in the conceptualization of the heat transfer process in terms of a wave of temperature change which propagates through the regenerator with time. The insight gained from this analysis is used to explain the results obtained from the numerical and experimental investigations.

Numerical Analysis. The numerical analysis considers a regenerator with finite heat transfer coefficients as opposed to the infinite transfer coefficients assumed in the equilibrium analysis. The effect of finite transfer coefficients is to broaden, or smear, the equilibrium wavefront as it propagates through the matrix. The sharp wave fronts of Fig. 2 would appear as an expanding fan, with the temperature increasing continuously on both sides of its center.

A regenerator with finite transfer coefficients is described by equations (3) and (4) with their associated boundary and initial conditions. Unfortunately, these equations cannot be solved analytically. Coppage and London [15] review some of the early approximate methods of analysis, most of which apply graphical and analytical techniques to a simplified problem. Lambertson [2] provided the first comprehensive set of solutions using finite difference techniques. Maclaine-cross [11] modified Lambertson's techniques and expanded the range of parameter values. The methods of solution employed in this paper are based on those of Lambertson and Maclaine-cross.

Numerical analysis results have been obtained for steady periodic operation with the inlet fluid temperature distributions shown in Fig. 4, where β_s and δ are parameters describing the distributions. The period 2 inlet fluid temperature has been assumed uniform at zero, and the period 1 inlet fluid temperature is such that $\bar{t}_{1,in} = 1$. For each value of β_s, two distributions, which are reflections of each other about the mean of unity, are used. Distribution A will increase the regenerator efficiency since it exposes the matrix to a higher temperature just before it rotates into the period 2 fluid stream, resulting in a higher period 2 outlet fluid temperature. Similarly, distribution B will reduce the efficiency by exactly the same amount.

Figure 5 gives results as a function of Ntu_i for several values of C_i^*, with $\mathrm{Ntu}_1 = \mathrm{Ntu}_2$, $C_1^* = C_2^*$, $\delta = 0.5$ and $\beta_s = 0.5\beta_1$. These results show that the effect of inlet fluid temperature nonuniformities depends strongly on the matrix to fluid capacity rate ratios. For $C_i^* \geq 10$, nonuniformities have very little effect on regenerator efficiency. However, for $C_i^* \leq 1$, the effect is very pronounced. The difference between the regenerator efficiency with nonuniform inlet temperatures and that with uniform inlet temperatures will increase as δ increases. Table 1 shows that the equilibrium theory predicts $\eta_i = 1.0$ when $C_i^* \geq 1$, $\eta_i = 0.625$ when $C_i^* = 0.5$ and $\eta_i = 0.25$ when $C_i^* = 0.2$, for inlet temperature distribution A of this type. These predictions are seen to be close for small C_i^* values, even at low Ntu_i values.

The numerical analysis of a regenerator operating with a temporal step change in period 1 inlet fluid temperature is similar to that for a regenerator operating under periodic steady-state conditions. The transient response e_i is calculated from equation (10) using the computed time variation of the spatial average outlet fluid temperature. The outlet fluid temperatures for the initial and final steady periodic conditions are predetermined.

Results of the transient numerical analysis are presented in Figs. 6 and 7. Figure 6 shows the period 1 and period 2 transient responses for a balanced and symmetric regenerator with $C_i^* = 0.2$ and $C_i^* = 10$ for a range of values of Ntu_i. When $C_i^* = 0.2$, the results of the numerical analysis approach those of the equilibrium analysis, Table 2, as Ntu_i increases. When $C_i^* = 10$, the period 2 response e_2 also approaches the equilibrium analysis result of Table 2 as Ntu_i increases. While e_1 is undefined for $C_i^* > 1$ in the equilibrium analysis, it appears to approach zero with increasing Ntu_i. The results when $C_i^* = 10$ show good agreement with those of London et al. [5].

Figure 7 shows some unexpected effects of C_i^* on the transient response for a balanced and symmetric regenerator with $\mathrm{Ntu}_i = 16$. From $C_i^* = 0.8$ to $C_i^* = 4$, the transient response, particularly e_1, exhibits a periodicity with time having a wavelength approximately equal to the rotation period. This behavior is in dramatic contrast to both the predictions of the equilibrium theory, which compare well with the numerical results at both small and large values of C_i^* and the results presented in the literature [3, 5–9]. In fact, the periodicity is inherent to the transient operation of a rotary

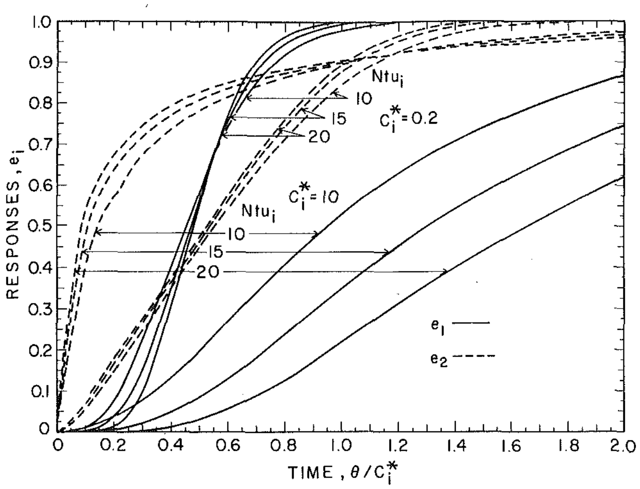

Fig. 6 Transient response of a balanced and symmetric regenerator

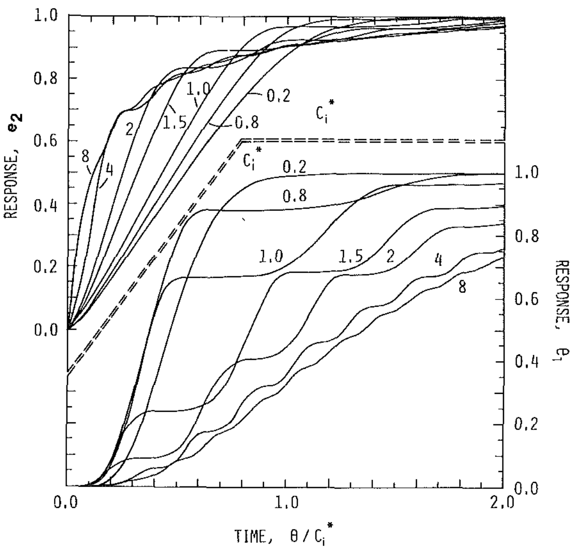

Fig. 7 Effect of C_1^* on regenerator transient response for $\text{Ntu}_1 = \text{Ntu}_2 = 16$ with $C_1^* = C_2^*$

regenerator and is present at all but the smallest values of C_i^*. For large C_i^*, the amplitude and wavelength are small and the response approaches a monotonic increase with time.

The periodic behavior observed in Fig. 7 is due to the effects of finite transfer coefficients and the definition of the transient response as an indicator of the variation in the average fluid outlet temperature with time. Since the transient response represents an instantaneous measure of the outlet fluid temperatures, it reflects not only the changes from one rotation of the matrix to the next, but also the changes due to the propagation of temperature change waves during a single matrix rotation. In the case of infinite transfer coefficients, a balanced regenerator reaches steady-state operation with one rotation of the matrix; and the response is determined by the effects of the change waves on the outlet temperatures during that single matrix rotation. In the case of finite transfer coefficients, several matrix rotations are required to achieve steady-state operation. The overall trend toward steady-state operation is constructed from a series of smaller increases in the response caused by waves of temperature change which emerge at the fluid outlet with each successive rotation of the matrix.

The effects of finite transfer coefficients can be explained in terms of the shape of the temperature change wavefront. When $\text{Ntu}_i = \infty$, temperature changes propagate through the matrix in the form of a sharp wavefront, and the fluid temperature is equal to the matrix temperature at every position. As Ntu_i decreases, the wavefront broadens with time and distance, and the change in matrix temperature lags that of the fluid temperature. Both of these phenomena cause a "trapping" of the wavefront in the matrix, resulting in periodic increases in the transient response. At low values of C_i^*, both the matrix and fluid temperature wavefronts emerge from the matrix during the first period despite being broadened. However, as C_i^* increases, the trailing end of both the fluid and matrix temperature waves are trapped within the regenerator and are exposed to the period 2 fluid. Part of the wavefronts will then emerge with part of them again being exposed to the period 1 fluid. As a result, the transient response does not increase monotonically as for the equilibrium analysis, but increases in steps with each rotation of the matrix.

Figure 8 illustrates this effect using a quasi-equilibrium analysis in which the matrix temperature is assumed to equal

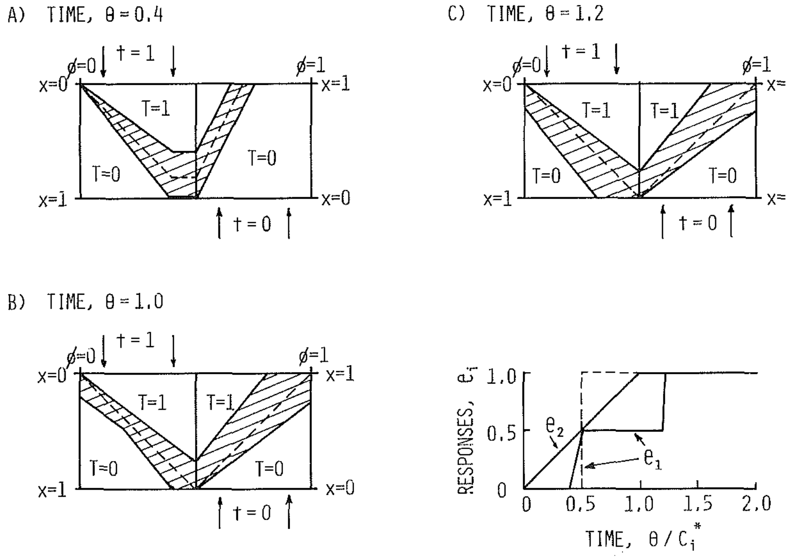

Fig. 8 Quasi-equilibrium analysis of transient response, with equilibrium analysis shown in dashed lines. The coordinate x increases in flow direction in each period. Variation of the transient responses with time is shown.

Table 3 Comparison of numerical and experimental results for nonuniform inlet temperatures

C_2^*/C_1^*	Ntu_1	C_1^*	$\eta_{1,\mathrm{num}}$	$\Delta\eta_{1,\mathrm{num}}$	$\eta_{1,\mathrm{exp}}$	$\Delta\eta_{1,\mathrm{exp}}$	Dist. Fig. 4
0.52	21.8	1.08	0.905	0.037	0.796	0.060	A
						0.046	B
0.52	21.8	5.08	0.996	0.000	0.968	0.004	A
						0.000	B
0.52	21.8	19.08	0.997	0.000	0.976	0.002	A
						0.001	B
0.98	21.0	1.04	0.829	0.049	0.758	0.053	A
						0.050	B
0.98	21.0	5.06	0.916	0.011	0.884	0.011	A
						0.009	B
0.98	21.0	19.01	0.927	0.004	0.898	0.007	A
						0.005	B
1.02	11.6	0.57	0.561	0.113	0.497	0.097	A
						0.099	B
1.02	11.6	3.03	0.831	0.023	0.811	0.031	A
						0.022	B
1.02	11.6	10.05	0.844	0.008	0.825	0.002	A
						0.003	B
2.05	11.4	0.56	0.456	0.098	0.434	0.095	A
						0.097	B
2.05	11.4	3.00	0.475	0.038	0.469	0.033	A
						0.042	B
2.05	11.4	10.03	0.489	0.014	0.472	0.020	A
						0.014	B

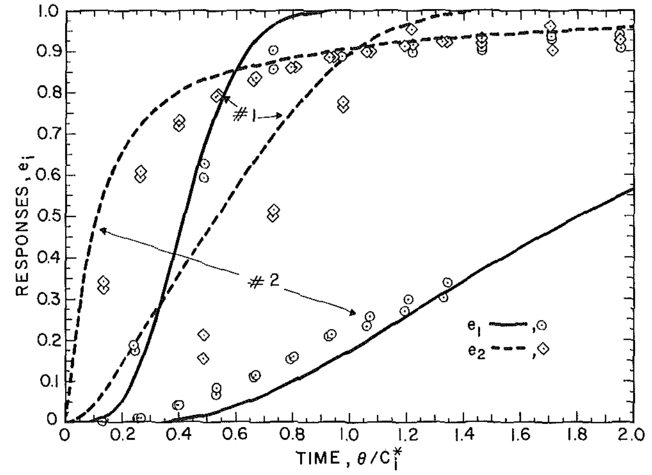

Fig. 9 Comparison of numerical and experimental results for transient inlet conditions. #1: $\mathrm{Ntu}_1 = 12.2$, $C_1^* = 0.59$, $C_2^*/C_1^* = \mathrm{Ntu}_2/\mathrm{Ntu}_1 = 0.89$. #2: $\mathrm{Ntu}_1 = 22.4$, $C_1^* = 20.1$, $C_2^*/C_1^* = \mathrm{Ntu}_2/\mathrm{Ntu}_1 = 0.98$.

the fluid temperature at every position, while the width of the wavefront increases linearly with time and distance about an average matrix to fluid capacity rate ratio of $C_i^* = 1$. At $\theta = 0.4$, the leading edge of the wave has just emerged from period 1, while the remainder is about to enter period 2. At $\theta = 1.0$, part of the wavefront has emerged from period 2, while the distribution in period 1 is already being affected by the trapped wavefront. Notice, though, that the period 1 outlet state remains constant until the effect of this trapped wavefront has propagated through period 1 of the matrix. When $\theta = 1.2$, the trapped part of the wavefront has emerged from period 1 and the regenerator has reached steady state. Under these assumptions, e_2 increases linearly while e_1 increases in two steps. In reality, this periodicity will be accentuated by the fact that the matrix temperature change lags that of the fluid.

Experimenal Analysis

An experimental analysis of a regenerator operating with either nonuniform or transient inlet conditions was undertaken to substantiate the predictions of the theoretical models. The experimental work for this investigation was performed on a regenerator test apparatus located at the CSIRO Division of Mechanical Engineering, now the CSIRO Division of Energy Technology. The apparatus, described in [16] and the Appendix, allows testing of a symmetric regenerator in countercurrent flow conditions.

Experimental tests of the regenerator operating under nonuniform inlet conditions were performed for two values of fluid velocity v_1, two values of v_2, and three different rotation speeds, for both distribution A and distribution B of Fig. 4 with $\beta_s = 0.5\beta_1$. Table 3 shows a comparison of the experimental results with those of the numerical model, for several of these steady state tests. In this table, $\Delta\eta_1$ is defined as the magnitude of the difference between the efficiency with nonuniform inlet conditions and that with uniform inlet conditions. The values of η_1 presented are the efficiencies with uniform inlet conditions. The results justify the main conclusion of the numerical analysis that nonuniform inlet temperatures have little effect on the performance of a regenerator operating with large matrix to fluid capacity rate ratios. As the capacity rate ratio decreases, though, the effect becomes substantially more significant.

Experimental tests of the regenerator exposed to a temporal step change in hot side inlet fluid temperature were also performed for two values of v_1, two values of v_2, and three different rotation speeds. The regenerator was first brought to periodic steady-state conditions and then exposed to a step change in the hot side fluid temperature using a fast-response heater.

Comparisons between the numerical and experimental results for the regenerator exposed to a temporal step change in inlet fluid temperature are shown in Figs. 9 and 10. For these comparisons, the numerical results were calculated using the actual increase in the hot side fluid temperature obtained from the experiment, rather than the step increase assumed in the mathematical model. Use of the actual temperature rise causes a slight delay in the response e_2, particularly at low values of C_i^*. Figure 9 shows comparisons for two different set of parameters: Test 1 corresponds to $\mathrm{Ntu}_1 = 12.2$, $C_1^* = 0.59$, and $C_2^*/C_1^* = \mathrm{Ntu}_2/\mathrm{Ntu}_1 = 0.89$, and Test 2 corresponds to $\mathrm{Ntu}_1 = 22.4$, $C_1^* = 20.1$, and $C_2^*/C_1^* = \mathrm{Ntu}_2/\mathrm{Ntu}_1 = 0.98$. The data points correspond to replicated experimental tests. The

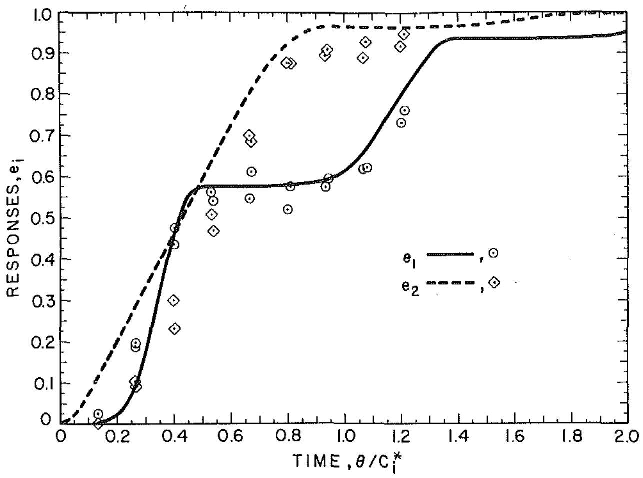

Fig. 10 Comparison of numerical and experimental results for transient inlet conditions with $Ntu_1 = 22.4$, $C_1^* = 1.1$, $C_2^*/C_1^* = Ntu_2/Ntu_1 = 0.98$

differences between the data points of these replicates provide an indication of the precision of the experiment. The results generally show good agreement, although the period 2 response of the experimental tests lags that of the numerical analysis for a short time after the temperature change. This lag in response is attributed to the thermal capacity of the rotor apart from the porous matrix and the transit time of the rotor in the diametral seals. For the small matrix to fluid capacity rate ratio of Test 1, the period 1 response e_1 increases slightly more rapidly than that of period 2, e_2. However for the high capacity rate ratio of Test 2, e_2 responds much more quickly than e_1. Figure 10 presents Test 3 with $Ntu_1 = 22.4$, $C_1^* = 1.1$, and $C_2^*/C_1^* = Ntu_2/Ntu_1 = 0.98$. Both the numerical and experimental results dramatically illustrate the periodic nature of the regenerator response in this regime of matrix to fluid capacity rate ratios.

Conclusions

The investigation of a counterflow, balanced, and symmetric rotary heat exchanger operating under periodic steady-state conditions with circumferentially nonuniform inlet conditions has led to the following major conclusions.

1 At large matrix to fluid capacity rate ratios, associated with high effectiveness heat exchangers, nonuniformities in inlet fluid temperatures have little effect on steady-state regenerator performance. Under these operating conditions, the amount of heat transferred between the two fluid streams depends on the average energy levels of the two streams.

2 At small matrix to fluid capacity rate ratios, which occur in the analysis of heat and mass regenerators, inlet fluid temperature nonuniformities can have a substantial effect on the steady-state performance. This performance can often be predicted by the equilibrium analysis, even at low values of Ntu_i. The regenerator efficiency is increased by nonuniformities of the form of distribution A as shown in Fig. 4 and decreased by nonuniformities of the form of distribution B. Under these operating conditions, the amount of heat transferred between the two fluid streams depends not only on the average energy levels of the two streams, but also on the distribution of that energy within the streams. If this distribution can be varied, it can be optimized to either maximize or minimize the energy transfer. Similarly, by considering the inlet temperature as a design variable, the same level of performance can be achieved by regenerators with considerably different values of Ntu_i and C_i^*.

The investigation of the transient response of a counterflow, balanced, and symmetric regenerator exposed to a transient step change in fluid inlet temperature has produced the following major conclusions.

1 At large matrix to fluid capacity rate ratios, results and conclusions concur with those of London et al. [5] and Willmott and Burns [7]. The period 2 outlet fluid responds much more quickly than the period 1 fluid, and both respond monotonically with time.

2 At small matrix to fluid capacity rate ratios, the results show little sensitivity to Ntu_i and are generally determined by C_i^*. The period 1 outlet fluid responds slightly more rapidly than the period 2 fluid, and both respond monotonically with time. The equilibrium analysis provides a reasonable approximation to regenerator performance, even at low values of Ntu_i.

3 At intermediate values of the matrix to fluid capacity rate ratios, the transient responses exhibit periodicity in time, with the responses increasing in steps with each rotation of the matrix. The effect is most pronounced between $C_i^* = 0.7$ and $C_i^* = 2$, though extending through $C_i^* = 8$. The periodicity is explained by the effects of finite transfer coefficients and the definition of the transient response, and is substantiated by experimental results.

Acknowledgments

The work presented here was sponsored by the U.S. Department of Energy through a contract to the University of Wisconsin for the study of solar desiccant cooling systems (Contract DEAC03-79SF10548), with the experimental work subcontracted to the CSIRO Division of Mechanical Engineering, now the CSIRO Division of Energy Technology.

The authors are very grateful for the assistance of colleagues at the University of Wisconsin Solar Energy Laboratory and the CSIRO Division of Mechanical Engineering. Mr. W. M. J. Ellul at CSIRO was particularly helpful in the experimental work of this paper. Professor J. W. Mitchell of the University of Wisconsin provided much of the initial stimulus for this work and gave valuable advice on the interpretation of the results. The suggestions of Dr. I. L. Maclaine-cross of the University of New South Wales, Australia, were also very helpful.

References

1 Hausen, H., "On The Theory of Heat Exchange in Regenerators," *Zeitschrift fuer Angewandte Mathematik und Mechanik*, Vol. 9, 1929, pp. 173-200.

2 Lambertson, T. J., "Performance Factors of a Periodic-Flow Heat Exchanger," ASME *Transactions*, Vol. 80, 1958, pp. 586-592.

3 Kays, W. M., and London, A. L., *Compact Heat Exchangers*, 2d ed., McGraw Hill, New York, 1964.

4 Shah, R. K., "Thermal Design Theory for Regenerators," *Heat Exchangers: Thermal-Hydraulic Fundamentals and Design*, edited by S. Kakac, A. E. Bergles, and F. Mayinger, Hemisphere/McGraw-Hill, Washington, D.C., 1981, pp. 721-763.

5 London, A. L., Sampsell, D. F., and McGowan, J. G., "The Transient Response of Gas Turbine Plant Heat Exchangers-Additional Solutions for Regenerators of the Periodic-Flow and Direct-Transfer Type," ASME *Journal of Engineering for Power*, Vol. 86, Apr. 1964, pp. 127-135.

6 Chao, W. W., "Research and Development of an Experimental Rotary Regenerator for Automotive Gas Turbines," *Proceedings American Power Conference*, Vol. 17, 1955, pp. 358-374.

7 Willmott, A. J., and Burns, A., "Transient Response of Periodic Flow Regenerators," *International Journal of Heat and Mass Transfer*, Vol. 20, 1977, pp. 753-761.

8 Schmidt, F. W., and Willmott, A. J., *Thermal Energy Storage and Regeneration*, ch. 10, Hemisphere/McGraw-Hill, Washington, D.C., 1981, pp. 219-242.

9 Shah, R. K., "Transient Response of Heat Exchangers," *Heat Exchangers: Thermal-Hydraulic Fundamentals and Design*, edited by S. Kakac, A. E. Bergles, and F. Mayinger, Hemisphere/McGraw-Hill, Washington, D.C., 1981, pp. 915-953.

10 Maclaine-cross, I. L., and Banks, P. J., "Coupled Heat and Mass Transfer in Regenerators-Predictions Using an Analogy with Heat Transfer," *International Journal of Heat and Mass Transfer*, Vol. 15, 1972, pp. 1225-1242.

11 Maclaine-cross, I. L., "A Theory of Combined Heat and Mass Transfer in Regenerators," Ph.D. thesis, Monash University, Melbourne, 1974.

12 Banks, P. J., "Prediction of Heat and Water Vapour Exchanger Performance from that of a Similar Heat Exchanger," *Compact Heat Exchangers-History, Technological Advancement, and Mechanical Design Problems*, edited by R. K. Shah, C. F. McDonald, and C. P. Howard, Book No. G00183, HTD-Vol. 10, ASME, New York, 1980, pp. 57-64.

13 Cassie, A. B. D., "Adsorption of Water Vapor by Wool Fibers. Part II —Theory of Propagation of Temperature Change," *Transactions of the Faraday Society*, Vol. 36, 1940, pp. 453-465.

14 Lighthill, M. J., and Whitham, G. B., "On Kinematic Waves," *Proceedings of the Royal Society of London*, Vol. A229, 1955, pp. 281-345.

15 Coppage, J. E. and London, A. L., "The Periodic-Flow Regenerator—A Summary of Design Theory," ASME *Transactions*, Vol. 75, July 1953, pp. 779-787.

16 Dunkle, R. V., Banks, P. J., and Ellul, W. M. J., "Regenerator Research, Development, and Applications in Australia - 1978 Status," *International Journal of Refrigeration*, Vol. 1, No. 3, Sept. 1978, pp. 143-150

17 Dunkle, R. V. and Maclaine-cross, I. L., "Theory and Design of Rotary Heat Exchangers for Air Conditioning," *Mechanical and Chemical Engineering, Transactions of The Institution of Engineers, Australia*, Vol. MC6, No. 1, May 1970, pp. 1-6.

18 Dunkle, R. V., Banks, P. J., and Maclaine-cross, I. L., "Wound Parallel Plate Exchangers for Air-Conditioning Applications," *Compact Heat Exchangers—History, Technological Advancement and Mechanical Design Problems*, edited by R. K. Shah, C. F. McDonald, and C. P. Howard, Book No. G00183, HTD-Vol. 10, ASME, New York, 1980, pp. 65-71.

APPENDIX

The basic experimental apparatus used for this investigation is described in [16]. Four modifications were made to this apparatus to allow testing for the desired results: a new regenerator was constructed, a fast-response split-duct heater was designed and constructed, the temperature measuring devices were replaced, and the duct configuration was modified.

The regenerator was constructed by spirally winding a polyester film around an aluminum hub [17, 18]. The spirals are separated by aluminum spacers held in spokes to produce parallel flow passages. The polyester film is 0.125 mm thick and the flow passages are 0.914 mm wide giving a matrix porosity to air flow of 88 percent. The regenerator has a length of 160 mm and an effective cross-sectional area of 0.0935 m^2 per period. The properties of the matrix are such that the conductivity assumptions of the theoretical model are justified. The polyester film is thin enough that axial conduction effects are negligible and the resistance to heat transfer into the film at any position is small compared to the matrix-fluid convective transfer resistance. Airflow through the matrix was at a Reynolds number of the order of 100, so that the convective transfer coefficient for the numerical model was predicted assuming laminar flow [3, 17].

A fast-response, split-duct heater was designed to balance the trade-offs between rapid heater response, low heater wire temperature, and high power output. The heater has a response time of approximately 5 s and a power output of up to 3.6 kW. It is constructed to provide spatial nonuniformities as in Fig. 4 with $\beta_s = 0.5\beta_1$.

Thermocouple grids are located immediately upstream and downstream of the regenerator in each flow stream, which allows measurement of both spatial average temperatures and temperature distributions. The error in temperature measurement including radiation effects, is estimated to be 2 percent of the total temperature difference across the regenerator.

The ductwork was modified to allow testing of a regenerator operating under unbalanced flow conditions. The flow rates of the two fluid streams are controlled by separate fans. Flow nozzles are located in each fluid stream, measuring flow rates to within an estimated error tolerance of 1.8 percent. At the regenerator, the two fluid streams are separated by clearance seals, with an average clearance of 1.1 mm. Corrections for the effects of fluid stream mixing due to leakage are made as in [17].

Preliminary tests indicated that the velocity was uniform to within ±10 percent with the regenerator removed. Since the matrix forms the largest flow resistance in each stream, the uniformity of the distributions was expected to improve with the regenerator in place. The temperature distribution with the matrix in position was uniform to within ±3 percent, implying similar uniformity of velocity. Analyses of the regenerator operating under steady periodic conditions showed conservation of energy to within 5 percent.

An Experimental Performance Evaluation of a Disk and Doughnut Type Heat Exchanger

K. P. Goyal[1]

B. K. Gupta

Mechanical Engineering Department,
M.N.R. Engineering College,
Allahabad, India

This paper reports the results of an experimental study in which 158-mm-dia disk and doughnut type 1-2 oil coolers were tested for various combinations of flow rates and clearances between the doughnut baffle and the shell. Oil coolers of 45 L per minute capacity were tested at the diametral clearances of 0.6 mm, 0.87 mm, and 1.25 mm between the doughnut baffle and shell for various flow rates of oil and water. It is found that the decrease in overall heat transfer coefficient with increasing clearance is not significant for most practical purposes. In another series of tests, oil coolers of 90 L per minute capacity with shell surface roughnesses of 4 and 19 microns and diametral clearances of 0.07 mm, 0.33 mm, and 0.59 mm were tested. The experimental results indicate that in this range of low clearances, the overall heat transfer coefficient increases with increasing clearance and surface roughness.

Introduction

A vast variety of installations such as steam power plants, chemical processing plants, space heating, air conditioning, refrigeration systems, and mobile power plants for automotive, marine, and aerospace vehicles use various types of heat exchangers. The design of this equipment can extensively differ on the basis of fluid flow configuration, types of baffles, and application. The shell and tube type heat exchangers are the most widely used heat transfer equipment in process and power industries due to their versatility of varied operating conditions, capability of handling many single and multiphase fluids, and ruggedness. In these heat exchangers hot and cold fluids are not allowed to mix, and their flow directions are continuously changed by baffles if conventional plate baffles are used.

Heat exchangers with various types of plate baffles have been a subject of experimental and theoretical study for a long time. However, there is hardly any published design data that would ensure least cost per unit heat transfer rate. The work, reported in this study, is an effort in that direction where we have tried to find the variation in overall heat transfer coefficient with (*i*) surface roughness of the inside wall of the shell, and (*ii*) the clearance between baffle and shell. These two parameters affect manufacturing cost considerably.

The effect of clearance between segmental baffles and the inside surface of the shell on the performance of a heat exchanger has been reasonably well studied [1-4], but there is hardly any corresponding published literature available for the disk and doughnut type heat exchangers. Available standards [5-7] appear to give recommendations for segmental baffles only. However, the disk and doughnut type heat exchangers have been studied for design considerations [8], shellside pressure drop [9], shellside flow field in the absense of thermal effects [10], and baffle spacing, size of baffle opening, and tube arrangement [11]. It has been reported that for the same pressure drop in shellside fluid, the heat transfer coefficient obtained with disk and doughnut baffles is approximately 15% more than that obtained with segmental baffles [11].

Disk and doughnut type heat exchangers, tested experimentally in this study, are used with steam turbines to cool the lubricating oil. According to the design specifications, heat exchanger shells should have an i.d. of 158 mm, with tolerances of +0.05 to 0.25 mm, and a smooth surface finish of 0.4 to 1 micron. It was found very costly to manufacture shells to these specifications. The effect of relaxation in these specifications on the performance of the oil cooler is the purpose of this paper. This paper reports the results of an experimental study in which 158-mm-dia 1-2 oil coolers were tested for various combinations of oil and water flow rates, surface roughnesses of shell, and clearances between doughnut baffle and shell.

Experimental Setup

A schematic of the experimental setup is shown in Fig. 1. The setup consists of an oil line, water line, and power line. The oil line is a closed loop where hot oil leaves the oil tank at its bottom and returns back at its top after being cooled in the oil cooler. On the other hand, the water line is open. The tap water is first stored in a constant head tank and then supplied to the oil cooler through a centrifugal pump. The water finally leaves to drain after cooling the hot oil. The power line is used to heat oil and to run pumps. The glass thermometers used in the setup were very accurate with 0.1°C divisions. The pressure gauges used in the experiment had least division of 6.9 kPa (1 psi). Besides being less accurate, these gauges were not found very reliable. The capacities of various com-

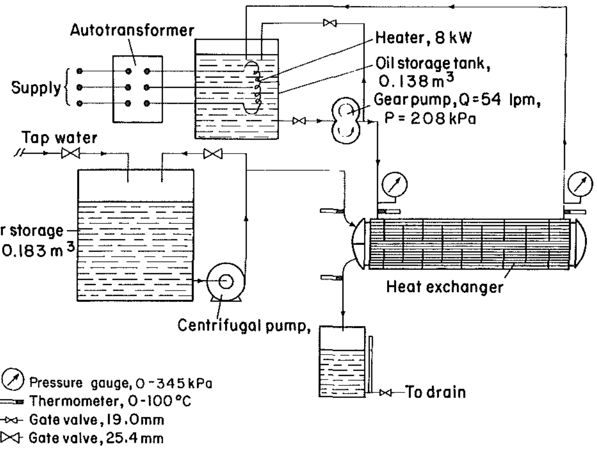

Fig. 1 A schematic diagram of the heat exchanger experimental setup

---

[1] Present address: Phillips Petroleum Company, Salt Lake City, Utah 84107

Contributed by the Heat Transfer Division for publication in the JOURNAL OF HEAT TRANSFER. Manuscript received by the Heat Transfer Division January 21, 1982.

ponents, except the oil cooler, used in the setup, are shown in Fig. 1.

A cross-sectional view of doughnut baffle is shown in Fig. 2. It shows that tubes are arranged hexagonally in this oil cooler. Various dimensions of interest are also given in this figure. The disk baffles used in the tube stack were almost identical to that shown in Fig. 2 except for two major differences: its outside diameter was 146 mm instead of 158 mm used in doughnut baffle, and it did not have any opening at its center as did the latter.

The oil coolers of two different capacities, 45 L per minute and 90 L per minite, were tested. The general specifications of these coolers are given in Table 1. The length of 90 L per minute capacity oil cooler is more than that of 45 L per minute. The spacing between disk and doughnut baffles (p) is 76 mm for the former and 42 mm for the latter. As may be noted from Table 1, both oil coolers are almost identical except their length. The specifications of the oil used in the experiment are given in Table 2.

Experimental Procedure

As shown in Fig. 1, water is supplied to the oil cooler through a centrifugal pump, which in turn is fed by a constant head tank. It may be observed that water enters at the left end of the cooler and exits also at the same end, indicating that there are two passes of water. On the other hand, oil enters at the left end of the cooler and exists at the right end, indicating only one pass for oil. Thus this oil cooler is a 1-2 type heat exchanger. Oil is stored and heated in a tank and the input electrical energy is held constant. A gear pump is used to pump oil to the cooler. As oil passes through the cooler, it loses heat to the surrounding cold water. The cooled oil then returns back to the supply tank.

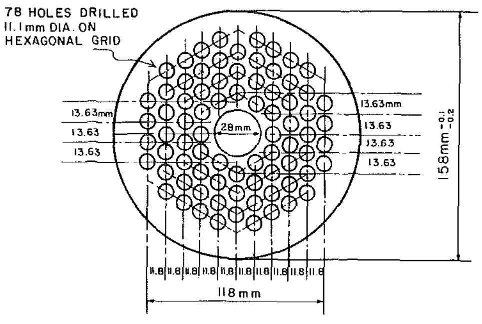

CROSS SECTION
SHOWING TUBE ARRANGEMENT IN DOUGHNUT

Fig. 2 ***Tube arrangement in a disk and doughnut type heat exchanger***

There are four main variables in this investigation: mass flow rate of oil (M_{oil}), mass flow rate of water (M_w), diametral clearance (C_l), and surface roughness of the shell.

Mass flow rates of oil and water through the oil cooler were varied by regulating the bypass valves in the respective flow lines. A measuring tank of known cross-sectional area was used to determine the mass flow rate of water by recording the time to fill the tank to a certain height. The mass flow rate of oil was determined by physically weighing the collected amount of oil in a recorded time. The diametral clearance was varied by turning down the doughnut baffles on a lathe machine. Inside surface roughness of a shell was varied by changing the speed and feed of the boring tool.

Measurements for each set of constant mass flow rate of water, diametral clearance and surface roughness were taken by varying the mass flow rate of oil. Steady-state temperatures of oil at inlet and outlet and those of water at inlet and outlet were then recorded for each mass flow rate of oil. A typical set of measurements, obtained during a test are given in Appendix A. A sample calculation to determine overall heat transfer coefficient U, film heat transfer coef-

Nomenclature

A = heat transfer surface area based on tube o.d., m^2 (defined in equation (B9))
A_c = minimum net crossflow area at a circle equidistant from the baffle openings, m^2 (defined in equation (B12))
A_1 = longitudinal area between shell and disk, m^2
A_u = longitudinal area through doughnut opening, m^2
C = coefficient
C_l = diametral clearance = shell i.d.-doughnut o.d., m
C_p = specific heat, J/Kg K
C_r = clearance ratio = diametral clearance ÷ shell i.d., dimensionless
d = tube outside diameter, m
D = shell diameter, m
F = log mean temperature difference correction factor, dimensionless
G_e = weighted mass velocity of oil, kg/m^{2}s (defined in equation (B11))
h = film heat transfer coefficient, W/m^{2}K
H_1 = heat loss to the surroundings, W
H_{tran} = heat transfer between oil and water, W
k = thermal conductivity, W/mK
L = length of the shell, m
M = mass flow rate, kg/s
n = number of tubes in the stack
Nu = Nusselt number = hd/k, dimensionless
p = distance between two baffles, m
P = oil pressure, Pa
Pr = Prandtl number = $C_p \nu \rho / k$, dimensionless
Q = heat received or supplied, W
r = tube radius, m
Re = Reynolds number = $G_e d / \nu \rho$, dimensionless
s = free circumference at a circle equidistant from alternate baffle openings, m
S = fouling factor, m^{2}K/W
t = time, in Redwood s
T = temperature, °C
U = overall heat transfer coefficient, W/m^{2}K
x = effectiveness $= \dfrac{T_{w,2} - T_{w,1}}{T_{\text{oil},1} - T_{w,1}}$, dimensionless
y = capacity ratio $= \dfrac{T_{\text{oil},1} - T_{\text{oil},2}}{T_{w,2} - T_{w,1}}$, dimensionless

Subscripts

a = ambient
av = average
cb = combined convection and radiation
oil = turbine oil
t = tube
w = water
1 = inside, inlet
2 = outside, outlet

Greek Symbols

Δt_m = log-mean temperature difference, °C
ν = kinematic viscosity, m^2/s
ρ = density, kg/m^3
ρ_0 = density of oil at 15.5°C. kg/m^3

Table 1 Specifications of the oil coolers used in the experiment

Specifications	90 L per minute	45 L per minute
General:		
Type	shell and tube	shell and tube
Oil capacity	90 L per minute	45 L per minute
Water capacity	159 L per minute	67.5 L per minute
Number of oil passes	one	one
Number of water passes	two	two
Shell:		
Material	cast iron	cast iron
Length	1114 mm	757 mm
Outside diameter	178 mm	176.2 mm
Internal diameter and Surface roughness (rms)	158.09 mm and 4 microns 157.83 mm and 19 microns	159.05 mm and 12 microns
Tube stack:		
Material	60/40 brass	60/40 brass
Length	1169 mm	810 mm
Number of tubes	78	78
Tube outside diameter	11.1 mm (7/16 inch)	11.1 mm
Tube thickness	22 BWG = 0.71 mm (.028″)	22 BWG = 0.71 mm
Tube arrangement	hexagonal	hexagonal
Number of doughnuts	7	8
Number of disks	6	7
Spacing between disk and doughnut baffles	76 mm	42 mm
Doughnut hole diameter	28 mm	28 mm
Outer diameters of doughnut	157.76, 157.5 mm	158.45, 158.18, 157.8 mm
Diameter of disk	146 mm	146 mm
Doughnut/disk thickness	1.6 mm	1.6 mm

Table 2 Specifications of turbine oil used in the experiment

Trade name:	DTE heavy medium turbine oil		
Temperatures	21.1°C	60°C	93.3°C
Kinematic viscosity in seconds (t) Redwood No. 1	700	110	52
[Defined in equation (B13)]			
Specific gravity at 15.5°C	= 0.878		
Specific heat at 37.8°C	= 1884 J/kgK		
Thermal conductivity	= 0.137 W/mk		

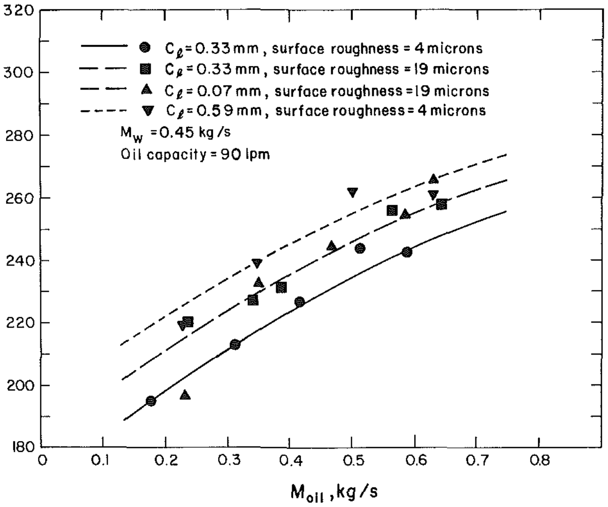

Fig. 3 Overall heat transfer coefficient versus mass flow rate of oil at different diametral clearances and surface roughnesses

ficient h, and various nondimensional numbers of interest is given in the Appendix B. The error analysis of the results is also discussed in the Appendix B.

Results and Discussions

90 L per minute Oil Cooler. This cooler was tested for various mass flow rates of water, mass flow rates of oil, diametral clearances, and shell inside surface roughnesses. Due to limited capacity of the oil pump, this oil cooler could not be tested to its full capacity. Figure 3 shows a plot of overall heat transfer coefficient U_l versus M_{oil} for different diametral clearances and surface roughnesses at a fixed mass flow rate of water 0.45 kg/s. It may be observed that for a surface roughness of 4 microns, overall heat transfer coefficient increases if diametral clearance is increased from 0.33 to 0.59 mm. A possible explanation may be that a low oil velocity gives rise to stagnation zones near the corner of doughnut baffles, which get reduced in magnitude when clearance is increased.

It may also be observed that for a shell of 19 microns surface roughness, the overall heat transfer coefficient U_l is insensitive to the changes in clearance from 0.07 mm to 0.33 mm. No definite conclusions can be drawn till shells with 4 microns surface roughness are also tested with smaller clearances. However, it is felt that for each surface roughness there would be a value of clearance below which the values of U_l will be insensitive to changes in clearance.

A comparison can also be made between shells of two different surface roughnesses. For a diametral clearance of 0.33 mm, values of U_l enhanced with an increase in surface roughness from 4 to 19 microns. The increase may be due to more turbulence imparted to the oil by increased surface roughness. Higher overall heat transfer coefficients were obtained for higher flow rates of water of 0.582 kg/s and 0.711 kg/s as discussed in [12].

Figure 4 shows a plot of mass flow rate of oil versus pressure drop in oil for a fixed mass flow rate of water under conditions similar to that in Fig. 3. As stated earlier, we do not have much confidence in pressure drop values due to less accuracy and reliability of pressure gauges. However, we do

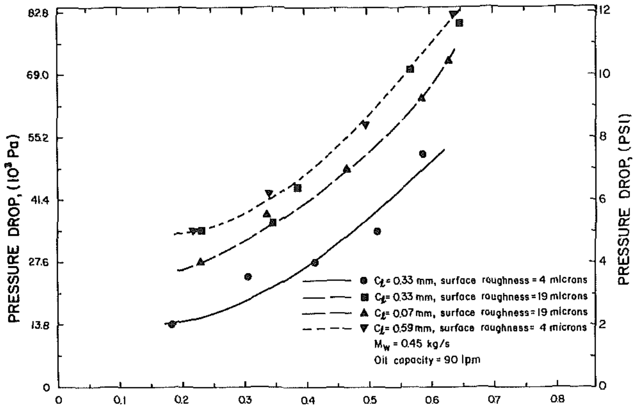

Fig. 4 Oilside pressure drop versus mass flow rate oil under conditions similar to that of Fig. 3

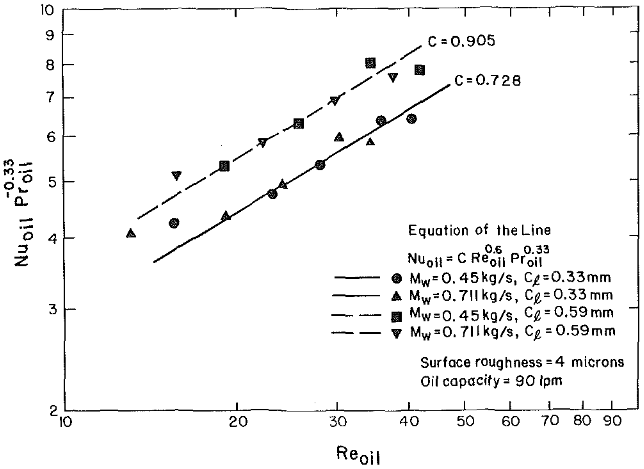

Fig. 5 Nondimensional correlations for 90 L per minute capacity oil cooler

see some trends similar to those in Fig. 3. For a surface roughness of 4 microns, pressure drop in oil did increase with increasing clearance, indicating movement in some stagnation zones. For a surface roughness of 19 microns, pressure drop in oil side appear to be the same or within the accuracy of reading for diametral clearances of 0.07 mm and 0.33 mm. This supports the earlier contention of Fig. 3 that for a given surface roughness, there is a clearance below which overall heat transfer coefficient is insensitive to changes in clearance.

Figure 5 shows a plot of several nondimensional parameters in a form that the oil side film heat transfer coefficients can be determined for the 90-L per minute capacity oil cooler having a surface roughness of 4 microns and diametral clearances of 0.33 mm and 0.59 mm. The following equation correlates these plots:

$$\mathrm{Nu}_{\mathrm{oil}} = C\ \mathrm{Re}_{\mathrm{oil}}^{0.6}\,\mathrm{Pr}_{\mathrm{oil}}^{0.33} \tag{1}$$

where the coefficient C is equal to 0.728 and 0.905 for a diametral clearance of 0.33 mm and 0.59 mm, respectively. As may be seen in Fig. 5, the most of the scattered points lie within 6 percent of the given correlation. For a surface roughness of 19 microns, the coefficient C is calculated to be 0.84 and 0.885 for the diametral clearances of 0.07 mm and 0.33 mm, respectively. The most points lie within 5 percent of the correlation for the former and within 8 percent for the latter. The method of calculation of these non dimensional numbers is discussed in Appendix B.

45 L per minute Oil Cooler. This cooler was also tested for various values of M_w, M_{oil}, and diametral clearances.

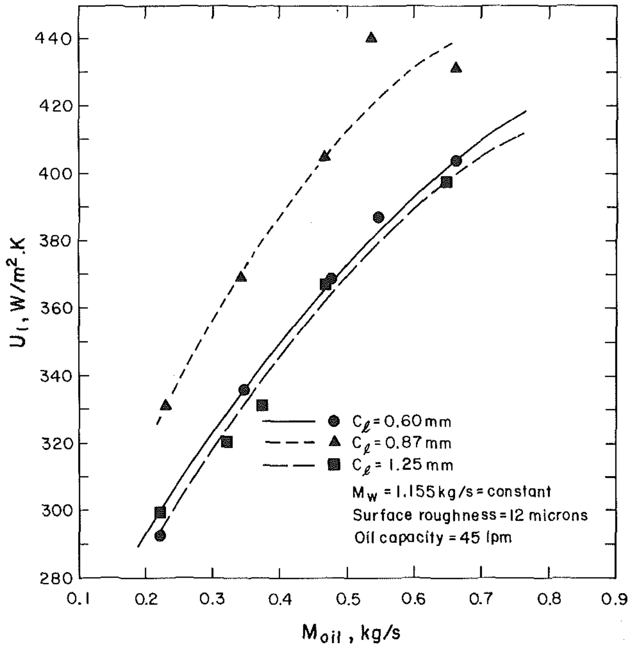

Fig. 6 Overall heat transfer coefficient for different diametral clearances in a 45 L per minute capacity oil cooler

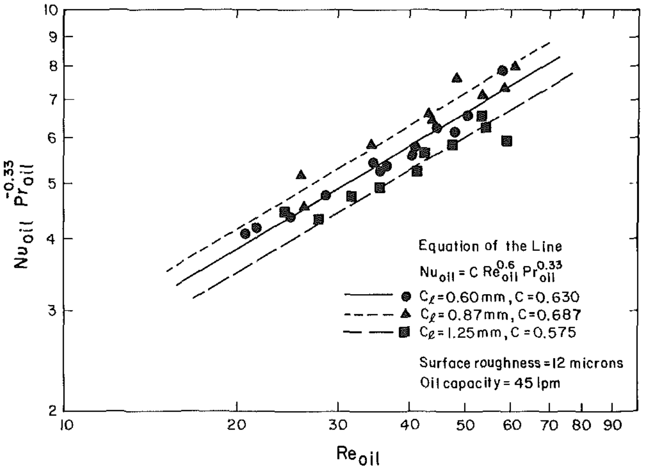

Fig. 7 Nondimensional correlations for different diametral clearances for 45 L per minute capacity oil cooler

Figure 6 shows the variation of overall heat transfer coefficients U_l with various oil flow rates for a fixed water flow rate of 1.155 kg/s and for the diametral clearances of 0.6 mm, 0.87 mm and 1.25 mm. It may be noted that the overall heat transfer coefficient U_l first increases with increasing clearance between doughnut baffle and shell from 0.6 mm to 0.87 mm and then decreases for a diametral clearance of 1.25 mm. An increase in U_l with increasing diametral clearance is also observed in case of 90 lpm oil cooler as shown in Fig. 3 and is thought to be caused by movement of otherwise stagnant oil. The decrease in U_l for 1.25 mm diametral clearance appears to have been caused by direct bypass flow of some fraction of oil through the opening between the doughnut and shell. This leaked oil chose the path of least resistance and flowed straight from one end of the cooler to the other without losing heat to water. This result confirms the findings in [4] for segmental baffles.

The results of the two coolers cannot be compared directly as it was not feasible to have comparable clearances and flow rates. However, a qualitative comparison can still be made. It may be recalled that the values of U_l increased with increasing clearances for both oil coolers and decreased for a diametral clearance of 1.25 mm in 45 1 pm oil cooler (Figs. 3 and 6). There is no convincing explanation for this seemingly opposite trend of results. However, due to the presence of stagnation zones and leaking zones, as discussed earlier, it is felt that the value of U_1 first increases and then decreases with increasing clearances. If so, there would be a zone of clearance which would give optimum heat transfer rate.

Figure 7 shows the plot of several nondimensional parameters in a form that the effect of oil side heat transfer coefficient with different diametral clearances for small oil cooler can be found out. It is clear from the plot that h_{oil} first increases and then decreases with increasing clearance for the ranges shown in Fig. 7. The plots for diametral clearances of 0.6 mm, 0.87 mm, and 1.25 mm produced three straight lines having the values of coefficient C as 0.63, 0.687, and 0.575, respectively. The most scattered points were found to lie within 5, 8, and 3 percent of the correlation given for diametral clearances of 0.6 mm, 0.87 mm, and 1.25 mm, respectively. Each correlation can be expressed by equation (1).

The following quadratic equation was developed to determine the effect of the coefficient C on the clearance ratio.

$$C = 0.09672 + 215.68C_r - 19700C_r^2 \qquad (2)$$

The nondimensional design equation of the 45 L per minute capacity oil cooler, derived from equations (1) and (2) is as follows:

$$\text{Nu}_{\text{oil}} = (0.09672 + 215.68C_r - 19700C_r^2)\text{Re}_{\text{oil}}^{0.6}\,\text{Pr}_{\text{oil}}^{0.33} \qquad (3)$$

It may be noted the unlike other correlations available in literature, equation (3) includes the effect of clearance ratio also.

Conclusions

The oil coolers of 45 and 90 L per minute capacity have been tested for various combinations of flow rates, diametral clearances, and shell inside surface roughnesses. It is found that overall heat transfer coefficient U_1 increases with an increase in the surface roughness of the oil cooler shell under the flow rates studied. An increase in diametral clearance from 0.6 mm to 0.87 mm increases the values of U_1 for the 45 L per minute capacity oil cooler, with a subsequent decrease in U_1 for a diametral clearance of 1.25 mm. Whereas, for the 90 L per minute capacity cooler, an increase in the diametral clearance from 0.07 mm to 0.59 mm increased the value of U_1. This matter needs further investigation as it is perhaps possible to find an optimum range of clearances.

For a surface roughness of 12 microns and a clearance range of 0.6 mm to 1.25 mm, the oil side heat transfer coefficient can be determined from the following correlation

$$\frac{h_{\text{oil}}d}{k_{\text{oil}}} = (0.09672 + 215.68C_r - 19700C_r^2)\text{Re}_{\text{oil}}^{0.6}\text{Pr}_{\text{oil}}^{0.33}$$

Acknowledgment

The authors would like to thank M/s Triveni Engineering Works, Ltd., Naini, Allahabad for supporting this research, and to Dr. Jagdish Lal and Sri I. Saran for encouraging the authors during the course of this investigation.

References

1 Gay, B., Mackley, N. V., and Jenkins, J. D., "Shell Side Heat Transfer Coefficients in Cylindrical Heat Exchangers. The Influence of Geometrical Factors. II - The Leakage Case," *Letters in Heat and Mass Transfer*, Vol. 8, No. 6, 1981, pp. 437-452.

2 Bell, K. J., "Delaware Method for Shell Side Design," *Heat Exchangers: Thermal — Hydraulic Fundamentals and Design*, edited by S. Kakac, A. E. Bergles, and F. Mayinger, Hemisphere Publishing Corporation, Washington, D. C., 1981, pp. 581-618.

3 Tinker, T., "Shell Side Heat Transfer Characteristics of Segmentally Baffled Shell and Tube Heat Exchangers," ASME *Transactions*, Vol. 80, 1958, pp. 36-92.

4 Short, B. E., "The Effect of Baffle Height and Clearance on Heat Transfer and Pressure Drop in Heat Exchangers," ASME Paper No. 47-A-105, 1947.

5 "Specifications for Tubular Heat Exchangers for General Purposes," British Standard 3274, British Standards Institution, London, 1960, p. 48.

6 "Shell and Tube Type Heat Exchangers," Indian Standard 4503, Indian Standards Institution, 9-Bahadur Shah Zafar Marg, New Delhi-1, India, 1967, p. 66.

7 *TEMA Standards*, 6th ed., Tubular Exchanger Manufacturers Association, Inc., 1978, p. 202.

8 Slipcevic, B., "Designing Heat Exchangers with Disk and Ring Baffles," *Sulzer Technical Review*, Vol. 58, No. 3, 1976, pp. 114-120.

9 Slipevic, B., "Shell-Side Pressure Drop in Shell and Tube Heat Exchangers with Disk and Ring Baffles," *Sulzer Technical Review*, Vol. 60, No. 1, 1978, pp. 28-30.

10 Founti, M. A., and Whitelaw, J. H., "Shell-Side Flow in a Model Disc-and-Doughnut Heat Exchanger," AERE-R- 10831, United Kingdom Atomic Energy Authority, Engineering Sciences Division, AERE Harwell, Oxfordshire, England, 1983, p. 13.

11 Short, B. E., "Heat Transfer and Pressure Drop in Heat Exchangers," University of Texas, Pub. No. 4324, 1943, pp. 1-55.

12 Goyal, K. P., and Gupta, B. K., "Improvements in the Design of Oil Coolers used with Steam Turbines," RD/ME-6/1972, Research and Development Center, M.N.R. Engineering College, Allahabad, India, 1972.

13 Batchelor, G. K., *An Introduction to Fluid Dynamics*, Cambridge University Press, Great Britain, 1974, p. 615.

14 Wilcox, D. F., and Booser, E. R., *Bearing Design and Application*, McGraw-Hill, New York, 1st ed., 1957, p. 464.

15 Chapman, A. J., *Heat Transfer*, 3rd ed., Macmillan, New York, 1974, p. 653.

16 Kreith, F., *Principles of Heat Transfer*. 3rd ed., Intext Educational Publishers, New York, 1973, p. 656.

17 Donohue, D. A., "Heat Transfer and Pressure Drop in Heat Exchangers," *Industry and Engineering Chemistry*, Vol. 41, No. 11, Nov. 1949, pp. 2499-2511.

18 Baumeister, T., Avallone, E. A., and Baumeister, T., III, ed., *Marks' Standard Handbook for Mechanical Engineers*, 8th ed., McGraw-Hill, New York, 1978.

19 Holman, J. P., *Heat Transfer*, 5th ed., McGraw-Hill, New York, 1981, p. 570.

20 Wilson, E. E., "A Basis for Rational Design of Heat Transfer Apparatus," ASME *Transactions*, Vol. 37, 1915, pp. 47-82.

21 Kline, S. J., and McClintock, F. A., "Describing Uncertainties in Single-Sample Experiments," *Mechanical Engineering*, Jan. 1953, pp. 3-8.

APPENDIX A

A typical set of measurements is given as follows:

Oil cooler capacity = 45 L per minute
Shell inside surface roughness (rms) = 12 microns
Diametral clearance = 0.6 mm

Exp.	Water side readings			Oil side readings				
No.	t_1 °C	t_2 °C	M_w kg/s	T_1 °C	T_2 °C	M_{oil} kg/s	P_1 psig	P_2 psig
1	29.3	31.7	0.785	58.7	37.0	0.219	2.5	1.5
2	29.3	31.75	0.785	53.1	38.0	0.3225	5.0	2.5
3	29.35	31.75	0.785	49.3	38.2	0.431	8.0	3.5
4	29.25	31.70	0.785	47.8	38.3	0.5055	10.75	4.0
5	29.2	31.6	0.785	45.9	38.1	0.658	15.0	5.5

APPENDIX B

Sample Data Reduction Calculations

As discussed in the test procedure, the temperatures and mass flow rates of oil and water were measured only after the system reached a steady state. The glass thermometers used in the experiment were accurate to within 0.1°C. The average mass flow rates of oil and water were calculated from a set of three readings taken for each liquid. The other variables such as diametral clearance C_l and surface roughness of inside of the shell were measured before the start of the test.

During a typical test run the following measurements were made (Appendix A):

Water inlet temperature, $T_{w,1}$ $=29.2°\text{C}$
Water outlet temperature, $T_{w,2}$ $=31.6°\text{C}$
Oil inlet temperature, $T_{\text{oil},1}$ $=45.9°\text{C}$
Oil outlet temperature, $T_{\text{oil},2}$ $=38.1°\text{C}$
Mass flow rate of water, M_w $=0.785$ kg/s (B1)
Mass flow rate of oil, M_{oil} $=0.658$ kg/s
Average temperature of water, $T_{w,av}$ $=(T_{w,1}+T_{w,2})/2=30.4°\text{C}$
Specific heat of water at 30.4°C, $C_{p,w}$ $=4.178\times10^3$ J/kg K from [13]
Heat received by water, Q_w $=M_w C_{p,w}(T_{w,2}-T_{w,1})=7.871\times10^3$ W
Average temperature of oil, $T_{\text{oil,av}}$ $=(T_{\text{oil},1}+T_{\text{oil},2})/2=42°\text{C}$

The specific heat of oil can be calculated from the following relation [14]:

$$C_{p,\text{oil}}=4.186\times10^3\left[\frac{0.388+0.00045(1.8T_{\text{oil,av}}+32)}{\sqrt{\rho_0\times10^{-3}}}\right] \qquad \text{(B2)}$$

where $\rho_0=$ density of oil at $15.5°\text{C}=878.0\ \text{kg/m}^3$ (Table 2). For an average oil temperature of 42°C, $C_{p,\text{oil}}=1.95\times10^3$ J/kgK Heat supplied by oil is

$$Q_{\text{oil}}=M_{\text{oil}}C_{p,\text{oil}}(T_{\text{oil},1}-T_{\text{oil},2})=10.006\times10^3\ \text{W} \qquad \text{(B3)}$$

It may be noted from equations (B1) and (B3) that the heat supplied by oil is 2135 W more than that received by water. This heat unbalance is believed to be more than the heat loss to the surroundings and is expected to influence the overall heat transfer coefficient between oil and water. Under the circumstances, the heat transfer between oil and water is taken to be the average of the heat supplied by oil and that received by water minus that lost to the surroundings. The heat loss from this uninsulated shell to the surroundings is estimated by determining the overall heat transfer coefficient between oil and ambient.

The calculations show that [15]

$$U_2\simeq h_{cb}=8.45\ \text{W/m}^2\text{K}$$

The heat loss to the surroundings, as calculated from the relation

$$H_1=h_{cb}\pi D_2 L(T_{\text{oil,av}}-T_a) \qquad \text{(B4)}$$

is 60.2 W. Thus, the heat transfer between oil and water is

$$H_{\text{tran}}=\frac{Q_w+Q_{\text{oil}}}{2}-H_1=8879\ \text{W} \qquad \text{(B5)}$$

Overall Heat Transfer Coefficient U_1

The overall heat transfer coefficient between oil and water can be calculated by using the concept of log mean temperature difference (Δt_m) for counterflow in 1-2 oil cooler as discussed in [16].

$$\Delta t_m=\frac{(T_{\text{oil},1}-T_{w,2})-(T_{\text{oil},2}-T_{w,1})}{\ln[(T_{\text{oil},1}-T_{w,2})/(T_{\text{oil},2}-T_{w,1})]}=11.39°\text{C} \qquad \text{(B6)}$$

The heat transfer between oil and water can now be expressed as

$$U_1FA\Delta t_m=H_{\text{tran}}=8879\ \text{W} \qquad \text{(B7)}$$

where F and A are the correction factor and total surface area heat transfer between oil and water, respectively. These quantities are, in turn, calculated from the following relations [15]

$$F=\frac{(y^2+1)^{1/2}}{y-1}\ \frac{\ln\left(\frac{1-x}{1-xy}\right)}{\ln\left(\frac{2-x[y+1-(y^2+1)^{1/2}]}{2-x[y+1+(y^2+1)^{1/2}]}\right)}=0.9752 \qquad \text{(B8)}$$

$$A=\pi dLn=2.06\ \text{m}^2 \ \text{for 45 L per minute oil cooler} \qquad \text{(B9)}$$

The overall heat transfer coefficient, as calculated from (B7) to (B9) is

$$U_1=388\ \text{W/m}^2\text{K}$$

Reynolds Number Re

The Reynolds number for oil side can be expressed as

$$\text{Re}_{\text{oil}}=G_e d/\nu_{\text{oil}}\rho_{\text{oil}} \qquad \text{(B10)}$$

where G_e is calculated on the basis of an area which is the geometric mean of the longitudinal area and crossflow area for oil [17]. However, in this oil cooler the longitudinal area between shell and disk is different than that of the doughnut opening. We, therefore, use an average of these two areas as the longitudinal area for our calculations. Thus

$$G_e=M_{\text{oil}}/\sqrt{A_c(A_u+A_1)/2} \qquad \text{(B11)}$$

where

$$A_1=\frac{\pi}{4}\left[(0.15905)^2-(0.146)^2\right]=31.266\times10^{-4}\ \text{m}^2$$

$$A_u=\frac{\pi}{4}(0.028)^2=6.158\times10^{-4}\ \text{m}^2$$

The crossflow area A_c is the product of p, the distance between the two consecutive baffles and s, the free circumference unoccuplied by tubes at a circle equidistant from alternate baffle openings. The latter is determined by actually measuring the free circumference at a circle of 87 mm diameter by precision digitization in Fig. 2. A value of 123.42 mm was obtained for s which is about 45 percent of the total circumference at 87 mm diameter. Thus

$$A_c=\text{ps}=42\times10^{-3}\times123.42\times10^{-3}$$
$$=51.84\times10^{-4}\text{m}^2 \qquad \text{(B12)}$$

From equation (B11), $G_e=211.27\ \text{kg/m}^2\text{s}$

The kinematic viscosity of oil is calculated from the information given in Table 2 and the following relation [18]

$$\nu_{\text{oil}}=10^{-6}\left(0.26t-\frac{179}{t}\right)\ \text{for}\ 34<t\leq100$$
$$\nu_{\text{oil}}=10^{-6}\left(0.247t-\frac{50}{t}\right)\ \text{for}\ t>100 \qquad \text{(B13)}$$

For an average oil temperature of 42°C, $\nu_{\rm oil} = 54.4 \times 10^{-6}$ m^2/s.

The density of oil is calculated from the following equation [14]

$$\rho_{\rm oil} = \frac{\rho_0}{1 + 7.855 \times 10^{-4}(T_{{\rm oil},av} - 15.5)} \qquad \text{(B14)}$$

For an average oil temperature of 42°C, $\rho_{\rm oil} = 860.1$ kg/m^3
From (B10), ${\rm Re}_{\rm oil} = 50.12$

Prandtl Number Pr

The Prandtl number of oil side can be obtained from the following expression

$$\Pr_{\rm oil} = \frac{C_{p,{\rm oil}}\,\nu_{\rm oil}\,\rho_{\rm oil}}{k_{\rm oil}} \qquad \text{(B15)}$$

using thermal conductivity of oil from Table 2, $\Pr_{\rm oil} = 666.0$

Nusselt Number Nu

The Nusselt number for oil side can be defined as follows [16]

$$\mathrm{Nu}_{\rm oil} = \frac{h_{\rm oil} d}{k_{\rm oil}} \qquad \text{(B16)}$$

where $h_{\rm oil}$ can be determined from the following equation which relates overall heat transfer coefficient to individual film heat transfer coefficients [19]:

$$\frac{1}{U_1} = \frac{1}{h_{\rm oil}} + S_{\rm oil} + \frac{r_2}{r_1}\frac{1}{h_w} + \frac{r_2}{k_t}\ln\left(\frac{r_2}{r_1}\right) + S_w \qquad \text{(B17)}$$

Since oil coolers used in our study were almost new, the fouling factors in equation (B17) can be neglected. It has been shown in [11] and [20] that the heat transfer coefficient for shellside fluid in shell and tube heat exchangers is proportional to 0.6 power of Reynolds number. Thus a plot of the reciprocal of ${\rm Re}^{0.6}$ on the abscissa and the reciprocal of U_l on the ordinate was prepared for a series of tests where $M_{\rm oil}$ was varied and M_w was kept constant. The plot resulted in a straight line as described in [20]. The intercept of this line with the ordinate is equal to the sum of items two through five in the right-hand side of equation (B17). The heat transfer coefficient on oil side ($h_{\rm oil}$) can then be calculated from equation (B17) for various test runs. Once $h_{\rm oil}$ is known, the Nusselt number can be calculated from equation B16).

Error Analysis

The overall heat transfer coefficient is a function of heat transfer between water and oil, correction factor, and the log mean temperature difference as given in equation (B7). The error introduced by the last two items is negligibly small compared to that introduced by the first one.

Heat unbalances of varying amounts were found in almost all runs. The heat unbalance fraction, defined as $(Q_{\rm oil} - H_{\rm tran})/H_{\rm tran}$ was found to vary between +6 percent to +15 percent for 45 L per minute oil cooler −9 percent to +3 percent for 90 L per minute oil cooler. The positive heat unbalance fraction indicates that the heat supplied by oil is more than that received by water and the opposite is true for the negative sign. From the above, a conservative heat unbalance fraction of ±15 percent can be assumed for both oil coolers. This shows that an error of about ±15 percent may be introduced in determining the overall heat transfer coefficient from the experimental data discussed in this paper [21].

E. M. Sparrow
Fellow ASME

A. Chaboki

Department of Mechanical Engineering,
University of Minnesota,
Minneapolis, Minn. 55455

Swirl-Affected Turbulent Fluid Flow and Heat Transfer in a Circular Tube

Experiments were performed to study the fluid flow and heat transfer characteristics for turbulent airflow in a tube in which there is a decaying axisymmetric swirl. Measurements were made of the local swirl angle at the tube wall and of the local Nusselt number and friction factor, all as a function of position along the length of the tube. Supplementary flow visualization experiments were performed to establish the axisymmetry of the swirl and to explore the pattern of fluid flow at the inlet of the tube. The swirl angle was found to decay exponentially along the tube, with the decay being more rapid at lower Reynolds numbers. The swirl gave rise to substantial heat transfer enhancement in the initial portion of the tube. The enhancement prevailed over a greater length of the tube at higher Reynolds numbers than at lower Reynolds numbers. Compared with the enhancements encountered in the conventional thermal entrance region in a nonswirling pipe flow, those associated with swirl are substantially greater and longer lived.

Introduction

This paper describes a multifaceted experimental investigation of the heat transfer and fluid flow characteristics of a turbulent pipe flow in which there is an axially decaying swirl. The work encompassed three distinct but interrelated sets of experiments, each carried out with a separate apparatus. In the first set of experiments, measurements were made to characterize the axial distribution of the swirl strength. The second and third sets of experiments were respectively focused on the effects of the swirl on the local friction factors and heat transfer coefficients along the length of the tube.

The one common feature of the three apparatuses was the swirl generator, the function of which was to provide an axisymmetric swirling flow at the inlet of the test section tube. As described later, the generator induced the swirl by means of 224 holes drilled through the wall of a circular cylinder (i.e., the swirl chamber) so as to be tangential to the inner surface of the wall. Control of the swirl strength at the test section inlet was achieved by varying the distance at which the swirl chamber was situated upstream of the inlet. Flow visualization, documented by photographs, affirmed that the generator delivered nearly perfectly axisymmetric swirl to the inlet of the test section tube.

Air was the working fluid in all of the experiments, and the Reynolds number ranged from 9000 to 43,500. At each Reynolds number, experiments were performed for either two or three swirl strengths at the tube inlet.

The results will be presented in four parts. In the first part, photographs and diagrams documenting the key results of the flow visualization work will be displayed. The swirl decay with axial distance along the tube is presented in the next section. The third and fourth parts, respectively, display the axial distributions of the local friction factor and the local heat transfer coefficient.

A novel approach was used to characterize the local swirl strength. The basis of the characterization was the observation of the track of a small droplet of a tracer fluid introduced locally at the tube wall. The direction of droplet movement along the wall from the point of its introduction is indicative of the relative magnitudes of the axial and tangential wall shear stresses. This direction can be characterized by the angle of the droplet track with respect to the axial direction, so that the angle is a measure of the ratio of the wall shears. The departure of the angle from zero will be used to characterize the strength of the swirl adjacent to the tube wall. The use of a parameter which serves as a measure of the wall-adjacent swirl appears to be particularly apt when the effects of swirl on the wall heat transfer are of major concern, as in the present investigation.

The literature on swirling pipe flows can be subdivided into papers which deal with maintained swirl (e.g., by an inserted twisted tape) or with decaying swirl – the latter being of primary relevance to the present work. A complete survey of the literature on decaying swirl is included in the thesis [1] from which this paper is drawn. Here, owing to space limitations, a somewhat abbreviated survey will be presented.

Two particularly relevant findings from the literature relate to the characterization of the initial swirl (i.e., at the tube inlet) and to the complexity of the flow. In the main, it has been customary to characterize the initial swirl by describing the device that produced the swirl, for instance, a twisted tape upstream of the test section, or the number and orientation of swirl-producing slots and baffles. Less commonly, measurements of the axial and tangential velocity profiles have been made and the cross-sectional integrals of these quantities (i.e., the fluxes of tangential and axial momentum) ratioed to yield the so-called swirl number. In one investigation, the maximum tangential velocity was used to characterize the swirl. Although the aforementioned swirl number includes more detail than the other characterizations used in the literature, it, too, is not definitive because of its integral nature.

With regard to the complexity of the flow, three features are noteworthy. The first is the possibility of backflow adjacent to the tube axis in the presence of strong swirl. Also it has been found that the profile of the axial velocity is markedly affected by the swirl, with the maximum velocity moving from a near-wall location toward the axis as the swirl decays. The maximum tangential velocity also shows a similar movement.

The effect of swirl on pipe-flow heat transfer was investigated in [2–6], while, among these, only [2] included friction factor measurements. Upstream-positioned twisted tapes served both to provide and to characterize the swirl in [2] and [3]. In [4], four square slots were used to inject the gas tangentially into the tube. The angular velocity measurements

---

Contributed by the Heat Transfer Division for publication in the JOURNAL OF HEAT TRANSFER. Manuscript received by the Heat Transfer Division September 12, 1983.

reported there were made in an apparatus whose geometry differed from the heat transfer apparatus. In [5], four flat vanes were used to induce and to characterize the swirl, and only length-averaged Nusselt numbers are reported. Swirl was induced in [6] by a single slot and, in addition, the axis of the swirl-generating tube was not colinear with the axis of the heated test section tube. The resultant swirl was found to be unsymmetric.

Whereas the literature contains interesting and useful information, it also provides the impetus for further work as undertaken here.

Experimental Apparatus

In this section, the three separate apparatuses respectively used in the swirl, pressure drop, and heat transfer experiments will be described along with the swirl generator, which is common to all three. In view of the extensive amount of apparatus involved and with due regard to journal space limitations, the description will deal with the main features of the various apparatuses, with details available in [1].

Swirl Generator. The swirl generator will be described with reference to diagrams (*a*) and (*b*) of Fig. 1. As seen in diagram (*a*), the generator consisted of two parts – the swirl chamber and the plenum chamber – which respectively served to produce the swirl and to control the strength of the swirl at the inlet of the test section. The swirl chamber was a plexiglass cylinder, capped at one end to form a cavity with an internal length of 9.8 cm, i. d. of 7 cm, and wall thickness of 0.635 cm.

Along the portion of the cylinder shown speckled in Fig. 1(*a*), 224 holes, each 0.159 cm in diameter, were drilled through the chamber wall. The deployment of the holes in a typical axial cross section A-A is depicted in Fig. 1(*b*). As seen there, the holes were tangent to the inner surface of the cylinder wall. In each cross section, there were eight such holes separated by a uniform circumferential spacing of 45 deg. At each circumferential station, a total of 28 holes were deployed axially along the cylinder, with a center-to-center distance of 0.191 cm. The front end of the swirl chamber was framed with a 14-cm o.d. annular plexiglass disk.

The swirl chamber and its framing disk formed a closure for one end of a larger plexiglass cylinder (internal diameter and length = 14 cm and 30.5 cm, respectively), i.e., the plenum chamber. The front face of the swirl chamber could be positioned anywhere within the plenum. This enabled adjustment of the distance L between the swirl chamber exit and the inlet of the test section tube, which was situated at the downstream end of the plenum.

The simple aperture shown in the downstream wall of the plenum (Fig. 1(*a*)), suitable for receiving a thin-walled metallic tube of internal diameter D, is one of the three plenum-test section interfaces employed during the experiments. The pictured interface was for the pressure measurement tube. For the swirl measurement tube, a somewhat larger aperture was provided in the plenum wall. In the case of the heat transfer experiments, a portion of the wall was replaced by a thermal isolation barrier designed to minimize extraneous heat losses.

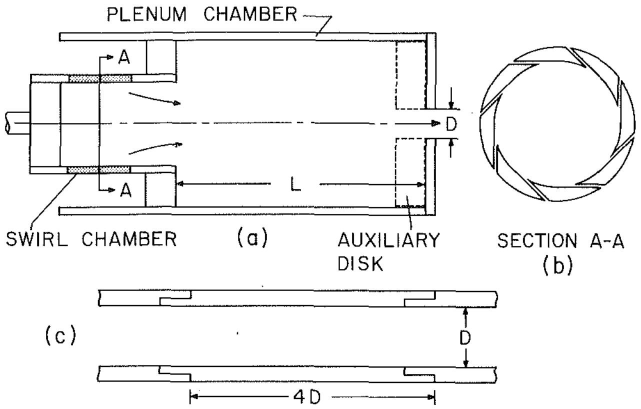

Fig. 1 Diagrams depicting various features of the experimental apparatus

The swirl generator was operated in the suction mode, with air being drawn from the laboratory room through the tangential holes in the wall of the swirl chamber. The swirling flow passed into the plenum chamber where, depending on the active plenum length L, it was attenuated before entering the attached test section tube. A blower positioned at the downstream end of the test section provided the suction which induced the airflow. The flow rate was measured with a calibrated rotameter situated between the test section exit and the blower.

Swirl Measurement Tube. As was noted in the Introduction, the local swirl angle was determined by measuring the direction of the track of a small droplet of tracer fluid introduced at the tube wall. These measurements were performed in a segmented tube, a typical portion of which is pictured in Fig. 1(*c*). As seen there, the tube consisted of a succession of identical modules (21, in total), each of axial length equal to $4D$. The modules were of plexiglass. They were fabricated by cutting appropriate lengths from solid rod stock and precision boring the internal diameter to a finished dimension $D = 2.362$ cm. Protrusions and recesses were machined at the respective ends of each module to achieve the interlocking fit pictured in Fig. 1(*c*).

For the assembled tube, special precautions were employed to achieve straightness. As a further defense against leaks (in addition to the interlocking fits and close machining tolerances), pressure-sensitive tape was placed over all joints on the outside of the tube.

A small radial hole, 0.046 cm in diameter, was drilled through the wall of each module to facilitate the introduction of the tracer fluid. In the assembled tube, the holes were positioned at the low point of the circular cross section (the tube was horizontal).

Prior to a data run, with the tube disassembled, the inside

Nomenclature

D = diameter of test section
f = local apparent friction factor, equation (3)
f_{fd} = fully developed friction factor (nonswirling flow)
h = local heat transfer coefficient, $q/(T_w - T_b)$
k = thermal conductivity
L = active length of plenum chamber
$\dot{m}$ = mass flow rate of air
Nu = local Nusselt number, hD/k
Nu_{fd} = fully developed Nusselt number (nonswirling flow)
p = pressure at tube wall
q = local convective heat transfer rate per unit area
Re = Reynolds number, $4\dot{m}/\mu\pi D$
T_w = local wall temperature
T_b = local bulk temperature
V = mean axial velocity
X = axial coordinate ($X = 0$ at tube inlet)
μ = viscosity
ρ = density
Φ = wall swirl angle

surface of each module was covered with white, self-adhering, plasticized contact paper. The contact paper was then pierced at the points where it covered the aforementioned tracer-fluid injection holes. With the tube assembled and a steady airflow at a preselected Reynolds number in the tube, the tracer fluid was introduced into the respective modules. This was accomplished with a fine-bore injection needle, from which a droplet of the tracer fluid was ejected very slowly into the radial hole. Since the system was operated in the suction mode, the droplet was drawn through the hole and was deposited on the contact paper adjacent to the opening, at which point it moved along the wall under the action of the fluid shear. At the termination of the run, the tube was disassembled, the contact paper removed from the respective modules, and the direction of the droplet path relative to the axial direction was measured.

The tracer fluid was a mixture of lampblack powder and oil.

Pressure Measurement Tube. Axial pressure distributions were measured utilizing a stainless steel tube with a bore diameter of 2.362 cm and an overall length of 84 diameters. The tube was equipped with 14 pressure taps (0.089-cm tap hole) deployed along its length at axial stations, which will be evident from the friction factor results to be presented later. The pressure signals were sensed by a Baratron solid-state, capacitance-type pressure meter which could be operated in three different ranges, 1, 10, and 100 Torr, with respective smallest scale divisions of 10^{-4}, 10^{-3}, and 10^{-2} Torr.

Heat Transfer Apparatus. The heat transfer experiments were performed with a stainless steel tube having an internal diameter of 2.362 cm, a wall thickness of 0.089 cm, and an overall length of 76 diameters. Heating was accomplished by Ohmic dissipation in the tube wall. Thermocouples were spot welded to the outside surface of the tube at 28 axial stations, with a more dense packing in the thermal entrance region (the axial positioning will be evident from the Nusselt number distributions). The thermocouple emfs were sensed and recorded by a Fluke 2240B programmable datalogger.

A number of measures were taken to minimize extraneous heat losses. For one, a portion of the plenum wall at the test section–plenum interface was replaced by a very thin (0.043-cm-thick) annular disk of fiberglass. The low conductance of this disk and its minimal contact with the heated tube virtually eliminated heat losses to the plenum. A second measure was to employ guard heating/cooling to eliminate conduction along the bus bars that delivered electric current to the tube. In addition, the tube was suspended by nylon line rather than by rigid supports. Finally, the entirety of the heat transfer apparatus was housed in an insulation enclosure filled with silica aerogel (thermal conductivity = 80 percent of air).

Flow Visualization

The flow visualization was carried out using the oil-lampblack technique [7]. The purposes of the flow visualization were to establish the symmetry of the swirl, explore the flow separation and reattachment at the tube inlet, and illuminate and clarify the measurement of the wall swirl angle.

To facilitate certain of the visualization studies, it was found convenient to use an auxiliary disk situated at the downstream end of the plenum chamber, as portrayed by the dashed lines in Fig. 1(*a*). The bore diameter of the disk was 2.362 cm, exactly equal to that of the test section tube, and its length was 2.54 cm. Thus, in effect, the disk provided a 2.54 cm upstream extension of the test section tube.

The disk (made of plexiglass) was easily inserted into and withdrawn from the plenum. Thus, with the disk outside the plenum, contact paper could be readily affixed to its upstream face or to its bore, and the oil-lampblack mixture applied to the contact paper. Then, with the disk in place at the downstream end of the plenum and the airflow activated, a visualization pattern was formed. Upon completion of the test, the disk was withdrawn from the plenum and the contact paper removed from the disk and laid flat for measurement and photography.

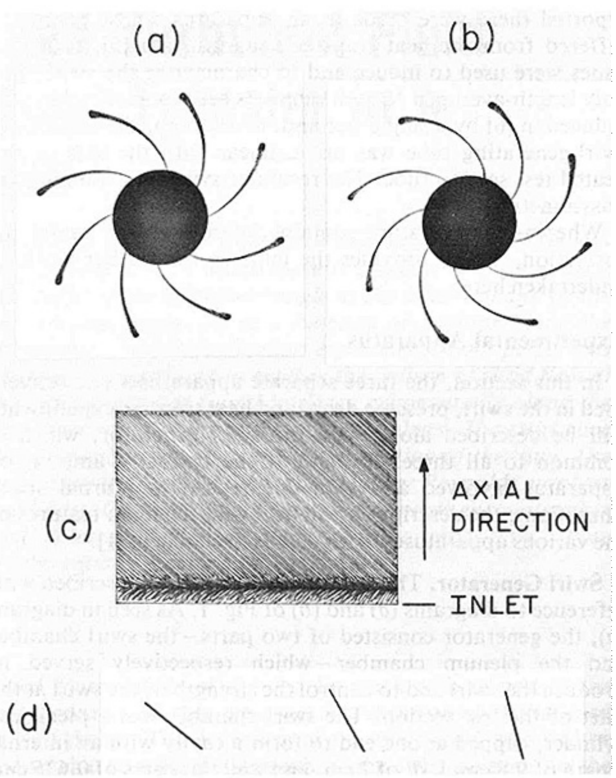

Fig. 2 Flow visualization results

The first experiments to be discussed are those related to the symmetry of the swirl entering the test section tube. For these experiments, prior to the airflow period, dotlike droplets of the oil-lampblack mixture were placed on the contact-paper-covered upstream face of the disk at equal angular intervals around a circle concentric with the tube inlet. In the presence of the airflow, the droplets moved inward toward the tube inlet, and the tracks of their motion are shown in the photographs (*a*) and (*b*) of Fig. 2. Both photographs correspond to the same test section Reynolds number of 43,500 but to different active plenum lengths L, respectively $L/D = 10.75$ for photo (*a*) and $L/D = 0$ for photo (*b*).

In the absence of swirl, the droplet tracks would be radial lines. The spiral paths in evidence in Fig. 2 are, therefore, reflections of a clockwise swirl. Qualitative inspection of the photographs indicates that the swirl is axisymmetric. This observation can be verified quantitatively by drawing rays from the center of the circle to the initial and final points of each droplet track, and then measuring the angle between the rays. For the trajectories of photograph (*a*), the aforementioned angle was 40.3 deg, while that for photograph (*b*) was 53.0 deg. The increase of the angle is indicative of stronger swirl, which is consistent with the fact that when the effective plenum length is zero, there is no opportunity for the swirl to decay in the plenum.

Next, attention will be turned to the flow pattern at the inlet of the test section tube. For these experiments, contact paper was affixed to the bore of the disk and the oil-lampblack mixture brushed on the contact paper to form a uniform film. A typical flow pattern imprinted on the contact paper is pictured in diagram (*c*) of Fig. 2. This pattern corresponds to

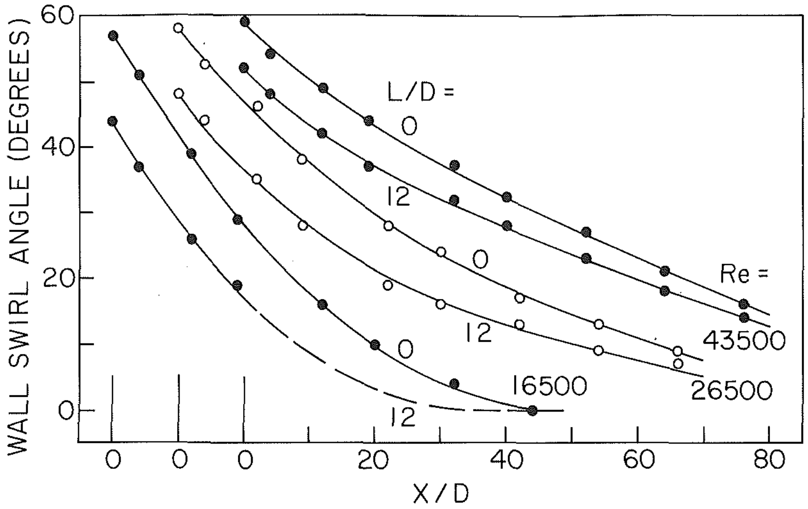

Fig. 3 **Wall swirl angle distributions grouped according to Reynolds number**

a test section Reynolds number of 26,500 and to an effective plenum length L/D = 10.75.

Near the bottom of the diagram is a dark band which corresponds to the zone in which the flow reattaches to the tube wall after having separated at the sharp-edged inlet. This zone is centered at an axial distance of about 0.2*D* from the inlet cross section. The array of finely etched parallel streak lines downstream of the reattachment zone mirror the direction of the wall-adjacent flow in that region. These lines make an angle of 48 deg with the axial direction, indicating a strong swirl component (in a swirl-free flow, the streak lines would be parallel to the axis). The somewhat irregular collection of lines upstream of the reattachment zone corresponds to the backflow leg of the recirculating flow, which fills the separated region.

The final aspect of the flow visualization presentation is an illustration of the tracer droplet tracks from which the wall swirl-angle measurements were made. Figure 2(*d*) is a photograph which shows the actual droplet tracks at X/D = 0, 32, and 64 corresponding to a test section Reynolds number of 43,500 and to an effective plenum length L/D = 12. Had the flow been purely axial, the track would have appeared as a vertical line. Thus Fig. 2(*d*) shows the decay of the swirl along the tube, starting with a wall swirl angle of 52.5 deg at the inlet and decreasing to an angle of 17 deg at X/D = 64.

Swirl Angle Results

Measurements of the wall swirl angle were made at as many as nine axial stations along the length of the test section. The experiments were performed for test section Reynolds numbers Re = 9000, 16,500, 26,500, and 43,500. At each Reynolds number, two initial swirl strengths were employed, respectively corresponding to the shortest and longest active plenum lengths L/D = 0 and L/D = 12.

At the higher Reynolds numbers and larger initial swirls, owing to the high shear forces exerted by the airflow, the droplet tracks were straight and crisp, enabling very accurate determination of the wall swirl angle. However, for lower Reynolds numbers and less vigorous swirls, the track was not as sharp. For these conditions and at downstream measurement stations, the residual swirl was not strong enough to move the droplet upward along the tube wall without gravity-related ambiguities. Swirl angle results are not presented at any axial station where such ambiguities were thought to be significant.

Axial distributions of the wall swirl angle are plotted in Fig. 3 for Reynolds numbers of 16,500, 26,500, and 43,500 (for the reason just cited, the Re = 9000 results are confined to a few axial stations and will be presented in a later figure). The results for all three Reynolds numbers share the same ordinate scale, but the abscissa origins are displaced to avoid overlap of the data. For each Reynolds number, data are presented for the L/D = 0 and 12 plenum lengths. Curves have been faired through the data to provide continuity, and a dashed line has been used to indicate a realistic extrapolation at downstream stations for the Re = 16,500, L/D = 12 case.

Figure 3 shows that the wall swirl angle decreases monotonically toward zero with increasing downstream distance, signalling the decay of the tangential component of the wall shear. Furthermore, the lower the Reynolds number, the more rapid is the decay. This finding is consistent with the stronger viscous forces that are operative in lower Reynolds number flows. At the highest Reynolds number of the experiments (i.e., Re = 43,500), an appreciable swirl remains even after a length of run of 80 diameters.

The swirl strength at the tube inlet corresponding to the zero-L/D plenum is high, as witnessed by the wall swirl angle of approximately 60 deg, which implies a tangential wall shear that is greater than the axial wall shear. The inlet-section swirl corresponding to the L/D = 12 plenum is somewhat lower because of the dissipation that occurs in the plenum. The dissipation is greater at lower Reynolds numbers, and this is reflected in the variation of the initial swirl angle from 52 to 44 deg as Re varies from 43,500 to 16,500.

Another noteworthy feature of the figure is the minimal scatter of the data. This is to be contrasted to the scatter present in the published data for other measures of swirl (e.g., Fig. 5 of [6]).

Another perspective on the swirl angle results is provided by Fig. 4. This is a two-part figure in which the axial distribution of the swirl angle corresponding to the L/D = 0 plenum are plotted in the upper part, while those for the L/D = 12 plenum are plotted in the lower part. The data in each part are parameterized by the Reynolds number, and it is to emphasize the Reynolds number effect that the figure has been prepared. The figure shows that with the same (or nearly the same) swirl at the tube inlet, the decay of the swirl along the tube is much more rapid as the Reynolds number decreases. A similar conclusion about the role of the Reynolds number follows from the experiments of [8] and [9], where different measures of the swirl strength were used.

The analytical work of [10] and [8], respectively for laminar and turbulent flow, suggested that the asymptotic behavior of

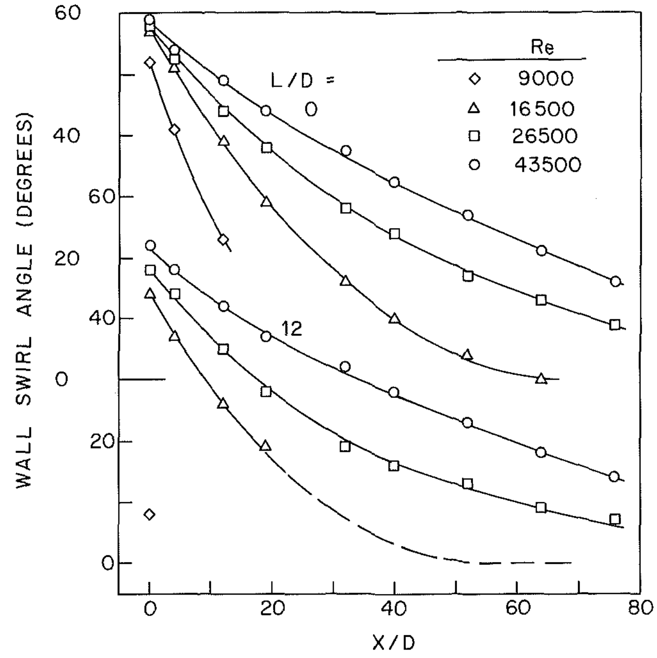

Fig. 4 Wall swirl angle distributions grouped according to plenum length

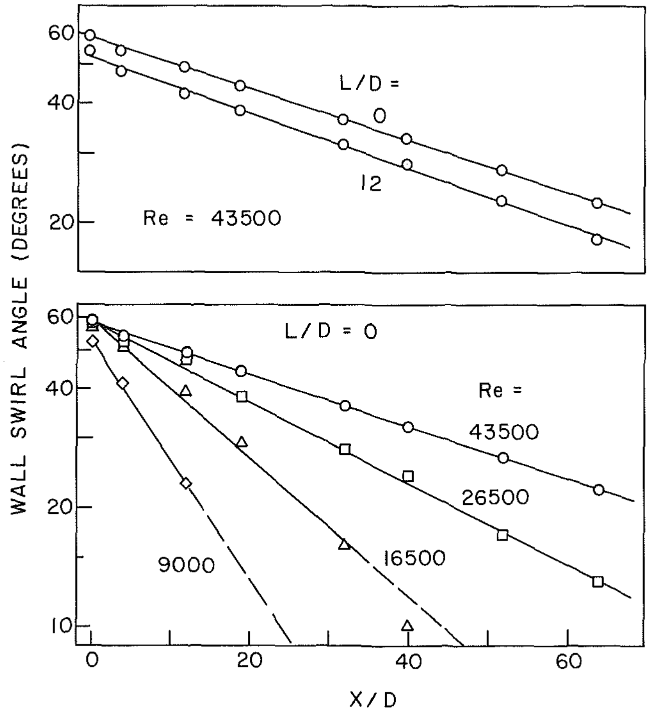

Fig. 5 Demonstration of the exponential axial decay of the wall swirl angle

the decay of swirl is exponential in the flow direction. This prompted the semilogarithmic presentation of swirl angle data in Fig. 5, which is, again, a two-part figure. The axial distributions for a fixed Reynolds number and parametric L/D are plotted in the upper part of the figure, while the results for a fixed L/D and parametric Re are plotted in the lower part.

The two parts of the figure demonstrate that the wall swirl angle follows an exponential law of decay and that, furthermore, the exponential behavior holds all along the tube (the slight data drop-off for Re = 16,500 and $L/D = 0$ is attributable to extraneous gravity effects on the tracer droplet motion). A least-squares fit of all of the semilogarithmic data yielded

$$\text{Swirl Angle (deg)} = C\exp[-\beta(X/D)] \tag{1}$$

where

$$\beta = 483(\text{Re})^{-0.97} \tag{2}$$

and C varies from 52 to 59 as seen in Fig. 5. Equation (2) indicates that the decay-length constant β varies more or less inversely with the Reynolds number. This quantitative finding about the role of the Reynolds number affirms the visual observations of Figs. 3 and 4.

Friction Factor Results

Prior to the swirl flow experiments, fully developed friction factors were evaluated for the same range of Reynolds numbers as were used in the swirl flow experiments. These friction factors were compared with those given by the well-established Blasius formula, with deviations in the 1.7-4 percent range. This excellent agreement served to verify the instrumentation and the measurement technique. Entrance region friction factors were not measured for the no-swirl case.

For the swirling flows, the measured pressure distributions were used to evaluate local apparent friction factors. At each measurement station, the local pressure gradient $(-dp/dX)$ was calculated by fitting a least-squares straight line through the pressures at that point and at the upstream and downstream neighboring points. Then the friction factor was obtained by local application of its equation of definition

$$f = (-dp/dX)D/\tfrac{1}{2}\rho V^2 \tag{3}$$

where $\rho V^2 = (\dot{m}/\tfrac{1}{4}\pi D^2)^2/\rho$, and ρ is the local density at the point of interest.

To provide the fullest perspective for the lcoal swirl-flow friction factors, they are presented in ratio form relative to the fully developed friction factor f_{fd} for the Reynolds number of interest. The values of f_{fd} used in the ratio are those determined in the present nonswirl experiments.

The results for the f/f_{fd} ratio are presented in Figs. 6 and 7, *where they are plotted as a function of the dimensionless axial* position coordinate X/D. Figure 6 consists of two parts which respectively pertain to the upper and lower levels of the initial swirl employed in the experiments (i.e., $L/D = 0$ and 12). In each part of the figure, f/f_{fd} distributions are plotted for Re = 9000, 16,500, 26,500, and 43,500. An overall inspection of Fig. 6 indicates a dramatic difference in the level of the friction factor at small X/D due to differences in the level of the initial swirl. It is also evident that f/f_{fd} drops off more rapidly at high levels of initial swirl, so that at more downstream stations the f/f_{fd} ratio should be less sensitive to the initial swirl. This issue will be explored in a more quantitative manner shortly.

The main message of Fig. 6 relates to the role of the Reynolds number. In this regard, reference may be made to the results for Re = 16,500, 26,500, and 43,500 for $L/D = 0$. As can be seen from either Fig. 4 or Fig. 5, the initial swirl for these cases is virtually the same. Figure 6 shows that the initial values of f/f_{fd} are also nearly the same. However, with increasing downstream distance, the three distributions separate, with a more rapid decline at lower Reynolds numbers. This behavior can be attributed to the more rapid axial decay of the swirl with decreasing Reynolds number that is in evidence in Figs. 4 and 5.

In Fig. 7, the f/f_{fd} distributions for Re = 9000 and L/D = 0, 6, and 12 are brought together in the left-hand part of the figure, and a similar grouping for Re = 43,500 is made in the right-hand portion of the figure. The main point of the figure

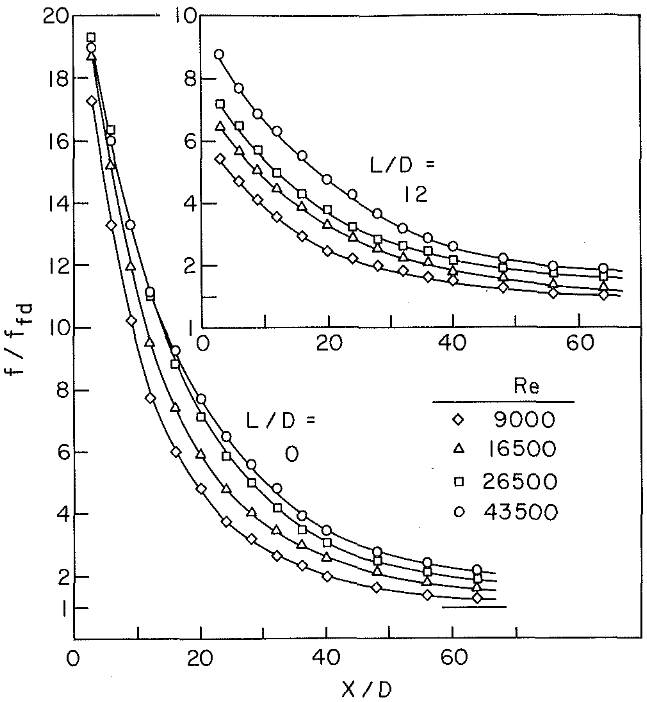

Fig. 6 Friction factor distributions grouped according to plenum length

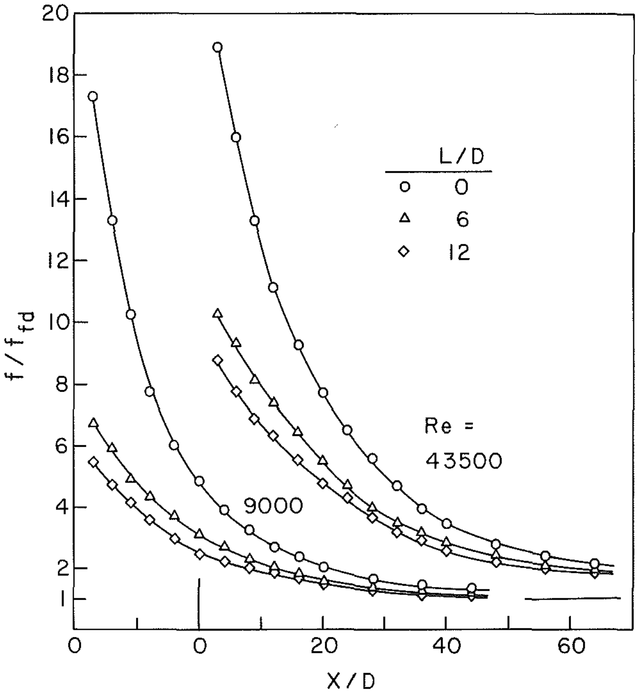

Fig. 7 Friction factor distributions grouped according to Reynolds number

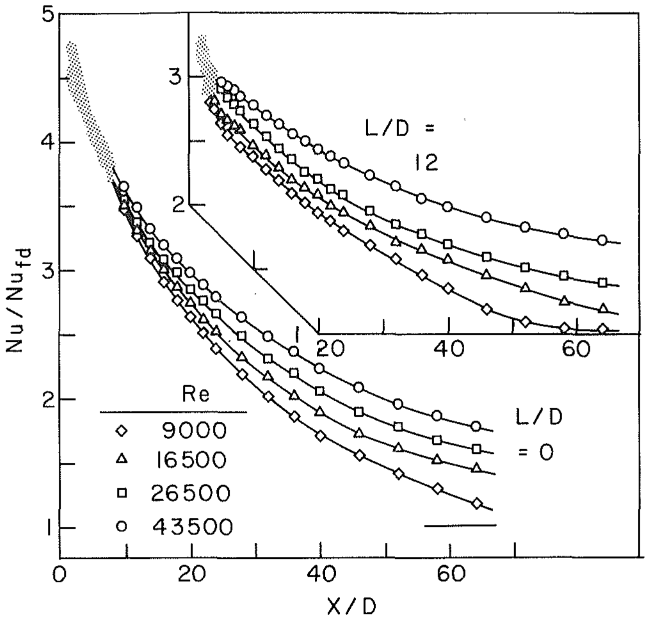

Fig. 8 Nusselt number distributions grouped according to plenum length

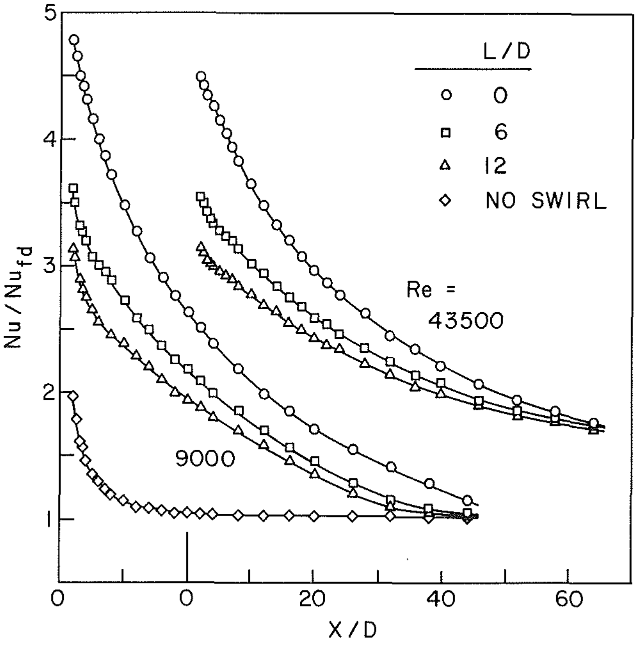

Fig. 9 Nusselt number distributions grouped according to Reynolds number

is the marked differences in the rapidity of the drop-off of f/f_{fd} as a function of the initial swirl. The strongest initial swirl is that associated with $L/D = 0$, and the strength progressively decreases as L/D increases. Figure 7 clearly shows that the stronger the initial swirl, the more rapidly does f/f_{fd} drop off. Thus large differences in the initial values of f/f_{fd} which correspond to different initial swirl strengths die away with increasing downstream distance.

The generally high values of f/f_{fd} that prevail in the upstream portion of the tube are noteworthy. These high values may be attributed to two primary causes. One is the dissipation of the tangential momentum of the swirl. The other is the severe swirl-related distortions of the axial velocity profiles. In particular, the maximum axial velocity may occur near the tube wall, and this gives rise to high wall shear. Also backflow may occur in the central core of the flow, further contributing to the dissipation of momentum.

Heat Transfer Results

Local heat transfer coefficients were evaluated from the basic definition

$$h = q/(T_w - T_b) \tag{4}$$

The local convective heat flux q was determined by correcting the electric power input for axial conduction in the tube wall and for losses through the insulation that surrounds the test section. The value of T_b at any axial station X was found from an energy balance on the fluid, using a control volume which extended from $X = 0$ to $X = X$ and integrating the aforementioned local q values to obtain the heat input to the control volume. Values of the local wall temperature T_w were available from the experimental data.

A dimensionless representation was made in terms of the local Nusselt number

$$\mathrm{Nu} = hD/k \qquad (5)$$

with k at the local bulk temperature. Variable properties were not an issue since the wall-to-bulk temperature differences were kept small (i.e., $< 10°\mathrm{C}$).

Prior to the swirl-flow experiments, heat transfer data were collected for the no-swirl case for Reynolds numbers between 9000 and 43,500. The fully developed Nusselt numbers from these experiments were compared with those from the Petukhov-Popov correlation (equations (8-23) and (8-24) of [11]). The average deviation of the data from the correlation was 5.1 percent, which is within the 6 percent confidence limit of the correlation. This good agreement lends confidence to the heat transfer apparatus and instrumentation.

The local Nusselt numbers for the swirl-flow experiments will be presented in ratio form relative to the fully developed value Nu_{fd} for the same Reynolds number. Owing to its broad acceptance, the Petukhov-Popov correlation will be used for the fully developed Nusselt numbers.

The Nusselt number results, plotted in the form $\mathrm{Nu}/\mathrm{Nu}_{fd}$ versus X/D, are reported in Figs. 8 and 9 in a presentation format that parallels that of Figs. 6 and 7 for the friction factor. In Fig. 8, the results for the upper level of the initial swirl, corresponding to $L/D = 0$, are brought together in the left portion of the figure, while the results for the lower initial swirl level ($L/D = 12$) are brought together at the upper right. For each level of the initial swirl, axial distributions are plotted for Re = 9000, 16,500, 26,500, and 43,500.

From the ordinate of Fig. 8, it is seen that $\mathrm{Nu}/\mathrm{Nu}_{fd}$ is substantially greater than one in the initial portion of the tube. Furthermore, it will be demonstrated shortly that these values of $\mathrm{Nu}/\mathrm{Nu}_{fd}$ are much greater than those which prevail in the thermal entrance region of a pipe with a nonswirling airflow. Thus the swirl is highly enhancing. By comparing the results for $L/D = 0$ and 12, it is also evident that the Nusselt numbers in the initial portion of the tube are quite responsive to the level of the initial swirl, being larger at stronger swirls. The drop-off of $\mathrm{Nu}/\mathrm{Nu}_{fd}$ with X/D also depends on the initial swirl, and this effect will be documented shortly.

The response of the $\mathrm{Nu}/\mathrm{Nu}_{fd}$ distributions to changes in Reynolds number at a fixed initial swirl can be identified by comparing the results in Fig. 8 for Re = 16,500, 26,500, and 43,500 for $L/D = 0$. These cases have almost identical initial swirl (see Figs. 4 and 5). It is seen that the lower the Reynolds number, the more rapidly does $\mathrm{Nu}/\mathrm{Nu}_{fd}$ drop off. Thus swirl is more enhancing with respect to heat transfer at higher Reynolds numbers than at lower Reynolds numbers.

The aforementioned response of $\mathrm{Nu}/\mathrm{Nu}_{fd}$ to the Reynolds number is identical to that already encountered for the friction factor results. The more rapid drop-off of both $\mathrm{Nu}/\mathrm{Nu}_{fd}$ and f/f_{fd} at lower Re is caused by the more rapid decay of the swirl.

In Fig. 9, the $\mathrm{Nu}/\mathrm{Nu}_{fd}$ distributions are grouped according to Reynolds number (for Re = 9000 and 43,500). In each group, results are given for the three swirl levels as characterized by the plenum L/D (=0, 6, and 12). A special feature of the presentation is the inclusion of the $\mathrm{Nu}/\mathrm{Nu}_{fd}$ distribution for the no-swirl case for Re = 9000. No-swirl $\mathrm{Nu}/\mathrm{Nu}_{fd}$ distributions were measured for all the investigated Reynolds numbers, including Re = 43,500. However, due to overlap with other plotted data, the Re = 43,500 no-swirl distribution could not be included in Fig. 9. It is, however, quite similar to that shown for Re = 9000.

Table 1 Relation between $\mathrm{Nu}/\mathrm{Nu}_{fd}$ and the wall swirl angle Φ (deg)

		Re = 26,500		Re = 43,500	
Φ	$L/D=$	0	12	0	12
15		1.65	1.64		
20		1.86	1.83	1.74	1.76
25		2.12	2.05	1.90	1.90
30		2.35	2.27	2.10	2.09
35		2.66	2.53	2.38	2.35
40		2.96	2.83	2.73	2.60
45		3.37	3.23	3.12	2.87

Table 2 Relation between f/f_{fd} and the wall swirl angle Φ (deg)

		Re = 26,500		Re = 43,500	
Φ	$L/D=$	0	12	0	12
15		2.02	2.00		
20		2.55	2.54	2.05	1.92
25		3.35	3.25	2.45	2.26
30		4.60	4.05	3.05	2.95
35		6.15	5.00	4.20	4.15
40		8.25	6.30	6.10	5.65

Inspection of Fig. 9 shows that conventional thermal entrance region effects as occur in nonswirling flows are second order compared with those caused by swirl. For one thing, $\mathrm{Nu}/\mathrm{Nu}_{fd}$ decreases much more rapidly in a conventional entrance region than in a swirling flow. In addition, the magnitudes of $\mathrm{Nu}/\mathrm{Nu}_{fd}$ are substantially smaller for the former.

Figure 9 highlights the effects of the initial swirl on the magnitude of $\mathrm{Nu}/\mathrm{Nu}_{fd}$ and on the rapidity of its drop-off with X/D. It is seen that the initial magnitude of $\mathrm{Nu}/\mathrm{Nu}_{fd}$ is ordered with the initial swirl strength. Furthermore, the greater the initial swirl strength, the more rapidly does $\mathrm{Nu}/\mathrm{Nu}_{fd}$ drom off. Thus the large initial gaps between the $\mathrm{Nu}/\mathrm{Nu}_{fd}$ distributions for the different initial swirls tend to diminish with increasing downstream distance.

It is relevant to seek a correlation between the $\mathrm{Nu}/\mathrm{Nu}_{fd}$ ratio at a given X/D and the wall swirl angle which prevails at that X/D. Such a correlation is presented in Table 1, where $\mathrm{Nu}/\mathrm{Nu}_{fd}$ is listed as a function of the swirl angle (now denoted by Φ) for Re = 26,500 and 43,500. For each Reynolds number, results are presented for both the $L/D = 0$ and 12 initial swirl levels.

The table shows that for a given wall swirl angle Φ, the $\mathrm{Nu}/\mathrm{Nu}_{fd}$ ratio is quite insensitive to the initial swirl level, especially for small and intermediate values of Φ. Also, at a given Φ, $\mathrm{Nu}/\mathrm{Nu}_{fd}$ depends only weakly on Re in the investigated range. The available swirl angle results for Re = 9000 and 16,5000 are not sufficiently complete to enable a listing as extensive as that of Table 1 to be made; however, a limited tabulation for Re = 16,500 indicated a slightly greater sensitivity to the initial swirl level.

A tabulation of f/f_{fd} versus Φ, similar to that for $\mathrm{Nu}/\mathrm{Nu}_{fd}$, is presented in Table 2. At a given Re, the table shows that f/f_{fd} is nearly independent of the initial swirl level when $f/f_{fd} < \sim 4$. In the range of larger f/f_{fd}, the effect of the initial swirl is more pronounced. Furthermore, f/f_{fd} is more sensitive to Re (at a given Φ) than is $\mathrm{Nu}/\mathrm{Nu}_{fd}$.

Concluding Remarks

This investigation of turbulent pipe flow with decaying swirl has encompassed three primary sets of experiments, respectively for the measurement of the local swirl angle at the tube wall, and the local friction factor and Nusselt number. These quantities were determined as a function of axial position along the length of the test section tube. Supplementary flow visualization experiments were also performed to establish the symmetry of the swirl and to examine the flow pattern at the tube inlet.

A special feature of the experiments was the use of a swirl generator which provided a perfectly axisymmetric swirl at the tube inlet. The swirl at any axial station was characterized by the ratio of the tangential and axial shear stresses at the tube wall. This ratio was expressed in terms of the angle between the resultant wall shear stress and the axial direction. The angle was found to decay exponentially along the length of the tube. The rate of decay was more rapid at lower Reynolds numbers.

The swirl gave rise to substantial heat transfer enhancement in the initial portion of the test section tube, the extent of which was ordered according to the initial swirl strength. For a given initial swirl, the ratio Nu/Nu_{fd}, which compares the local and fully developed Nusselt numbers, drops off more rapidly as the Reynolds number decreases. Thus the swirl-related enhancement is longer lived at higher Reynolds numbers than at lower Reynolds numbers. At a given Reynolds number, the Nu/Nu_{fd} ratio drops off somewhat more rapidly for higher initial swirls.

Compared with the Nu/Nu_{fd} ratios encountered in the thermal entrance region of a conventional nonswirling pipe flow, those for the present swirl flows are substantially higher, and these enhanced values persist to greater downstream distances.

The characteristics of the friction factor distributions closely parallel those of the Nusselt number distributions.

The basic data for the Nusselt number and the friction factor that have been presented here can be used as inputs to computations of the enhancement characteristics of swirl-affected pipe flows. Such enhancement evaluations may be performed for a wide variety of constraints (e.g., fixed pumping power, fixed heat duty, fixed mass flow rate, fixed transfer surface area, etc.). The actual execution of the enhancement evaluations is beyond the scope of the paper.

The present heat transfer and friction factor results could not be compared with those of the literature, because it was not possible to find a common ground for the characterization of the swirl.

Acknowledgment

The research reported here was performed under the auspices of the Office of Naval Research.

References

1 Chaboki, A., "Heat Transfer, Pressure Drop, and Flow Visualization for Axially Decaying Swirl in a Turbulent Pipe Flow," M.S. thesis, Department of Mechanical Engineering, University of Minnesota, Minneapolis, Minn., 1983.

2 Blackwelder, R., and Kreith, F., "An Experimental Investigation of Heat Transfer and Pressure Drop in a Decaying Swirl Flow," *Augmentation of Convective Heat and Mass Transfer*, ASME, 1970, pp. 102–108.

3 Narezhnyy, E. G., and Sudarev, A. V., "Local heat Transfer in Air Flowing in Tubes with a Turbulence Promoter at the Inlet," *Heat Transfer—Soviet Research*, Vol. 3, No. 2, 1971, pp. 62–66.

4 Blum, H. A., and Oliver, L. R., "Heat Transfer in a Decaying Vortex System," ASME Paper No. 66-WA/HT-62, 1967.

5 Zaherzadeh, N. H., and Jagadish, B. S., "Heat Transfer in Decaying Swirl Flows," *International Journal of Heat and Mass Transfer*, Vol. 18, 1975, pp. 941–944.

6 Hay, N., and West, P. D., "Heat Transfer in Free Swirling Flow in a Pipe," ASME JOURNAL OF HEAT TRANSFER, Vol. 97, 1975, pp. 411–416.

7 Merzkirch, W., *Flow Visualization*, Academic Press, New York, 1974, pp. 53–56.

8 Kreith, F., and Sonju, O. K., "The Decay of Turbulent Swirl in a Pipe," *Journal of Fluid Mechanics*, Vol. 22, 1965, pp. 257–271.

9 Wolf, L., Jr., Lavan, Z., and Fejer, A. A., "Measurements of the Decay of Swirl in Turbulent Flow," *AIAA Journal*, Vol. 7, 1969, pp. 974–975.

10 Talbot, L., "Laminar Swirling Pipe Flow," *Journal of Applied Mechanics*, Vol. 21, 1954, pp. 1–7.

11 Karlekar, B. V., and Desmond, R. M., *Heat Transfer*, 2d edn., West Publishing, St. Paul, 1982.

J. C. Han
Assistant Professor,
Mechanical Engineering Department,
Texas A&M University,
College Station, Texas 77843
Mem. ASME

Heat Transfer and Friction in Channels With Two Opposite Rib-Roughened Walls

An experimental study of fully developed turbulent air flow in square ducts with two opposite rib-roughened walls was performed to determine the effects of the rib pitch-to-height and rib height-to-equivalent diameter ratios on friction factor and heat transfer coefficients with Reynolds number varied between 7000 and 90,000. Based on the four-sided, smooth-duct correlation and the four-sided, ribbed-duct similarity law, a general prediction method for average friction factor and average Stanton number in rectangular ducts with two smooth and two opposite ribbed walls was developed. There was good agreement between prediction and measurements. The results may be useful for gas turbine blade internal cooling design.

Introduction

One of the well-known methods to enhance the heat transfer from a surface is to roughen the surface by the use of repeated ribs on the surface. However, the increase in heat transfer is accompanied by an increase in the pressure drop of the fluid flow. Many investigations have been directed toward developing predictive correlations for a given rib geometry and establishing a geometry which gives the best heat transfer performance for a given pumping power.

Fully developed turbulent heat transfer and friction in tubes or between parallel plates with repeated-rib rougheners have been studied extensively [1-7]. Considerable data also exist for repeated-rib-roughness in an annular flow geometry, in which the inner annular surface is rough and the outer surface is smooth, to simulate the geometry of fuel bundles in advanced gas-cooled nuclear reactors [8-12]. Based on those previous studies, the effects of rib height-to-equivalent diameter ratio e/D_e, rib pitch-to-height ratio P/e, and rib angle of attack α, on the heat transfer coefficient and friction factor over a wide range of Reynolds number are well established. Semianalytical correlations have been developed for the heat transfer designers. However, in some applications, such as turbine blade internal cooling design, the enhanced heat transfer capability is desired on only two opposite walls of a nominally square duct [13-15]. The heat transfer and friction characteristics in channels of this kind may be different from those of circular tubes, parallel plates, or annuli. The only available data were reported by Burggraf [16], who studied the square duct with two opposite rib-roughened walls with a rib flow-attack angle of 90 deg, rib pitch-to-height ratio of 10, and rib height-to-equivalent diameter ratio of 0.055. Air was the working fluid; constant wall temperature was the boundary condition. Three types of entrance conditions were tested over Reynolds numbers from 1.3×10^4 to 1.3×10^5, namely, downstream of a fully developed hydrodynamic flow (long duct entrance), downstream of a rounded entrance from a plenum (short duct entrance), and downstream of a 180 deg bend, respectively. For the long duct entrance case, Burggraf found the augmentation of the Nusselt number on the ribbed side wall was 2.38 times the fully developed smooth duct flow values when the characteristic dimension was taken as twice the plate spacing. The augmentation of the friction factor was approximately 8.6 times that of the smooth duct results. There was also enhancement of the smooth-side wall heat transfer by 19 percent over the all smooth correlations. He also reported similar trends for the case of a short duct entrance and for the 180 deg bend tests. In this study the emphasis was placed on the effect of entrance conditions on the heat transfer coefficients. Only one particular rib geometry (i.e., $P/e = 10$, $e/D_e = 0.055$) was tested. The effects of the P/e and e/D_e ratios on the heat transfer coefficients and friction factor in the flow channel were not investigated. The friction factor was not clearly reported in all tests.

In view of the foregoing discussion, it is evident that a need exists for a systematic experimental study of turbulent flow in a square duct with two opposite ribbed walls. The emphasis should be placed on the effect of rib geometry on the heat transfer coefficients and friction factor in the fully developed flow region. An experimental study to fulfill this need was recently completed. Air was the working fluid; constant wall heat flux was the boundary condition. The Reynolds number range of this investigation extended from 7000 to 90,000; the P/e ratios varied from 10 to 40; while the e/D_e ratios varied from 0.021 to 0.063. For the results of rib-roughened surfaces to be most useful, general prediction methods are required for both the friction factor and heat transfer coefficient which cover the entire range of significant parameters. Based on the correlation for four sided smooth ducts and the similarity law for four-sided ribbed ducts, a general prediction model for the average friction factor and average heat transfer coefficients was developed for flow in rectangular ducts with two smooth and two opposite rib-roughened walls. This paper will first describe the experimental results. The theoretical analysis will then be presented, and the comparison between the prediction and measurements will be discussed.

The Experimental Apparatus

An experimental facility was constructed to test the agumentation technique and to provide the smooth duct reference data. The test facility was very similar to that of [6]. Figure 1 shows a schematic of the test rig.

A 2-hp blower forced air at room temperature and pressure through a 10.16-cm-dia tube equipped with a 5.08-cm-dia ASME square-edged orifice plate to measure flow rate. A transition section was used between the tube and the unheated entrance duct. At the end of the heated test duct, the air was exhausted into the atmosphere.

The test duct, consisting of four heated parallel aluminum plates, 0.635 cm thick, as shown in Fig. 2(*a*), had cross-sectional dimensions 7.6 cm by 7.6 cm and a heated length of 20 duct diameters. The duct orientation was such that the two opposite rib-roughened walls were vertical. These ribbed walls

---

Contributed by the Heat Transfer Division for publication in the JOURNAL OF HEAT TRANSFER. Manuscript received by the Heat Transfer Division April 11, 1983. Paper No. 83-HT-26.

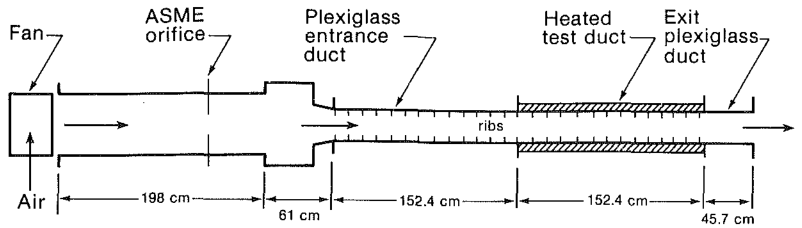

Fig. 1 Top view of the experimental apparatus

were made by gluing square brass ribs to the plate surface in a required distribution as shown in Fig. 2(*b*). For a glue thickness of 0.0127 cm or less, the heat transfer flux to the portion of the plate under the rib is reduced by less than 3 percent; thus the thermal resistance of the glue is negligible. A 0.159-cm-thick asbestos strip was placed along the contact surface between the smooth and the ribbed walls to reduce the possible heat conduction effect. Woven heaters embedded in silicone rubber were adhered uniformly between the aluminum plate and a wood panel to insure good contact. Each aluminum plate had one woven heater; each heater could be independently controlled by a variac transformer and provided a controllable constant heat flux for the entire test plate. The entire heated test duct, including unheated end duct, was mounted centrally in a long horizontal enclosure of cross-sectional dimensions 30.5 cm by 30.5 cm. The enclosure was filled with fiber-glass insulating material. The unheated entrance duct was made of plexiglass plates. This entrance duct served to establish hydrodynamically fully developed flow at the entrance to the heated duct. Additionally, the entrance duct was ribbed over its length on two opposite walls in the same way as the test duct. The test section was instrumented with 36 thermocouples distributed along the length and across the span of the aluminum plates, as shown in Fig. 3. Thermocouples which could be transversed vertically and horizontally were used to measure the bulk mean air temperature entering and leaving the test section. Five pressure taps along the test duct (three on the smooth side and two on the ribbed side) were used for the static pressure drop measurements across the test duct.

Analysis of Data

The pressure drop across the test section was measured by a micromanometer and an inclined manometer. In fully developed duct flow, the friction factor can be determined by measuring the pressure drop across the flow channel and the mass flow rate of the air. The friction factor can be calculated from

$$\bar{f}=\frac{\Delta p}{4(L/D_e)\,(G^2/2\rho g_c)} \qquad (1)$$

During the experiments, it was seen that the magnitude of the pressure drop was about the same when measured from the pressure taps on the smooth side or on the ribbed side. Therefore, the friction factor calculated from equation (1) was an average value (i.e., average friction factor) over the smooth side wall and the ribbed side walls. The average friction factor of the present investigation was based on the adiabatic conditions. The maximum uncertainty in the average friction factor was estimated to be less than 6.6 percent for Reynolds number greater than 10,000 by using the uncertainties estimation method of [20].

For the longitudinally constant heat flux boundary condition of the present investigation, the thermally fully developed region is characterized by wall and fluid temperatures that increase linearly as a function of longitudinal

Nomenclature

A = duct width
A_c = flow channel cross-sectional area, $A_c = AB$
B = duct height
C_p = average specific heat of fluid
D = tube diameter
D_e = equivalent diameter, four times the cross-sectional area divided by the wetted perimeter: $D_e = 2AB/(A + B)$ for rectangular ducts
e = rib height
e^+ = roughness Reynolds number, $(e/D_e)\ \mathrm{Re}(f/2)^{1/2}$
f = friction factor
$\bar{f}$ = average friction factor in a duct with two opposite ribbed-walls
G = mass flux, $\rho\bar{V}$
G_H = heat transfer roughness function
L = test section length
l = the distance between the wall and the position of zero shear stress
P = rib pitch
ΔP = pressure drop across the test section
q'' = heat flux
$\bar{q}''$ = average heat flux in a duct with two opposite ribbed walls
R_{av} = average ray length, $2R_{av}/D_e = (1.156 + B/A - 1)/(B/A)$
Re = Reynolds number, GD/μ
Re_{D_e} = Reynolds number based on equivalent diameter, GD_e/μ
$\mathrm{Re}_{2R_{av}}$ = Reynolds number based on average ray length, $G2R_{av}/\mu$
St = Stanton number
$\overline{\mathrm{St}}$ = average Stanton number in a duct with two opposite ribbed walls
T = temperature
T^+ = dimensionless temperature
$\bar{T}^+$ = average dimensionless temperature
T_b = bulk mean temperature of fluid
T_w = temperature at the wall
$\bar{T}_w$ = average temperature at the wall
u = velocity
u^+ = dimensionless velocity, u/u^*
$\bar{u}^+$ = average dimensionless velocity
u^* = friction velocity, $(\tau/\rho)^{1/2}$
$\bar{V}$ = average velocity of fluid
y = distance from the wall
ρ = average density of fluid
μ = average viscosity of fluid
Pr = Prandtl number
τ = wall shear stress
$\bar{\tau}$ = average wall shear stress in a duct with two opposite ribbed walls

Subscripts

s = four-sided smooth duct
$2s$ = two smooth walls in a duct with two opposite ribbed walls
r = four-sided ribbed duct
$2r$ = two ribbed walls in a duct with two opposite ribbed walls

position. The longitudinal distribution of the fluid bulk mean temperature was represented as a straight line connecting the measured mean values at inlet and exit. Typically, at downstream distances ranging from 10 to 15 hydraulic diameters from the start of heating, as shown in Fig. 4, the wall temperature data paralleled the aforementioned bulk temperature straight line. Consequently, only those data corresponding to the thermally fully developed region were employed for the computation of the heat transfer coefficients. During the tests, it was found that the ribbed surface heat transfer capability was higher than the smooth one. In order to reduce the possible heat conduction effect between the smooth wall and the rough wall, the heat input to the smooth wall was controlled at about 2/3 to 4/5 that of the rough wall. Therefore, the temperature difference between the adjacent walls was maintained between 0.6°C to 1.8°C in all tests, as seen in Fig. 4. Additionally, in order to reduce the thermocouple inaccuracy, which strongly affects the calculated heat transfer coefficient, the temperature rise of air was maintained between 15 and 25°C, and the temperature difference between the wall and fluid was maintained between 20 and 30°C in all tests.

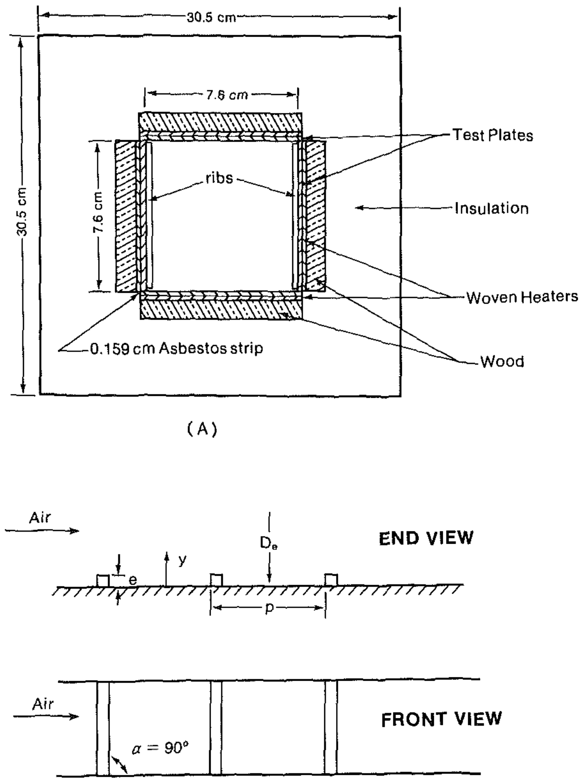

Fig. 2 (*a*) **Cross section of test duct;** (*b*) **rib geometry**

For fully developed turbulent flow in a square duct of the present investigation, the Stanton number on the two smooth walls (St_{2s}) and on the two ribbed walls (St_{2r}) can be calculated from equations (2) and (3), respectively.

$$St_{2s} = \frac{q''_{2s}}{GC_p(\bar{T}_w - T_b)_{2s}} \quad (2)$$

and

$$St_{2r} = \frac{q''_{2r}}{GC_p(\bar{T}_w - T_b)_{2r}} \quad (3)$$

The q''_{2s} and q''_{2r} represent the net heat flux from the smooth and the ribbed walls to the fluid, respectively, whereas $(\bar{T}_w - T_b)_{2s}$ and $(\bar{T}_w - T_b)_{2r}$ are the thermal driving forces averaged over the span of the smooth wall and the ribbed wall, respectively. Notice that the ribbed side heat flux q''_{2r} was based on the projected heat transfer area (not including the increased rib surface area). The maximum uncertainty in the Stanton number was estimated to be less than 6.8 percent for Reynolds number greater than 10,000.

Before initiating experiments with rib-roughened walls, the friction factor and heat transfer coefficient were measured for a four-sided smooth duct and compared with the results given in the literature, as shown in Fig. 5. As seen by the figure there is good agreement between an existing correlation and the experimental results for the present smooth duct with 7.6 cm by 7.6 cm cross section. The friction factor differs by up to 9.0 percent from the modified Karman-Prandtl [21] equation, and the Stanton number differs by up to 9.5 percent from the modified Dittus-Boelter [17] equation.

Experimental Results

In the tests the following ratios were systematically varied: the rib height to equivalent diameter and the rib spacing to rib height. The rib had a square cross section and was glued onto the plate surface at 90 deg to the direction of mainstream flow. The effect of each of these parameters will be discussed separately.

Rib Height-to-Equivalent Diameter. The rib height-to-equivalent diameter ratio was varied from 0.021 to 0.042 to 0.063 by applying three different rib sizes, namely, 0.159 cm, 0.317 cm, and 0.476 cm, on the two opposite walls of the same 7.6 cm square duct. The rib pitch-to-height ratio was kept at a constant value of 10 for this series of tests. The average friction factor and Stanton number calculated from the test results, are shown in Fig. 6. At a given ratio of the rib height to equivalent diameter, the average friction factor approaches

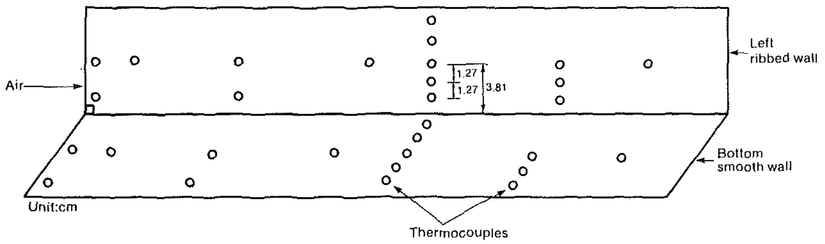

Total = 36 Thermocouples
15 on left ribbed wall
15 on bottom smooth wall
3 on right ribbed wall
3 on top smooth wall

Fig. 3 Detail of thermocouples distributions on test plates

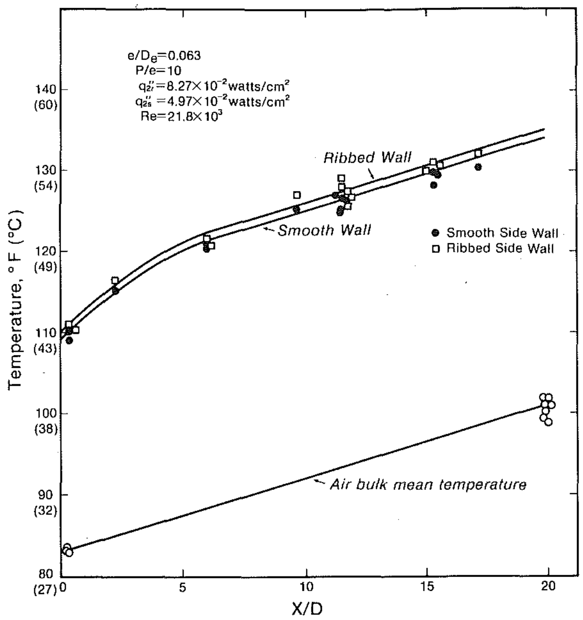

Fig. 4 Air and wall temperature distributions along test duct

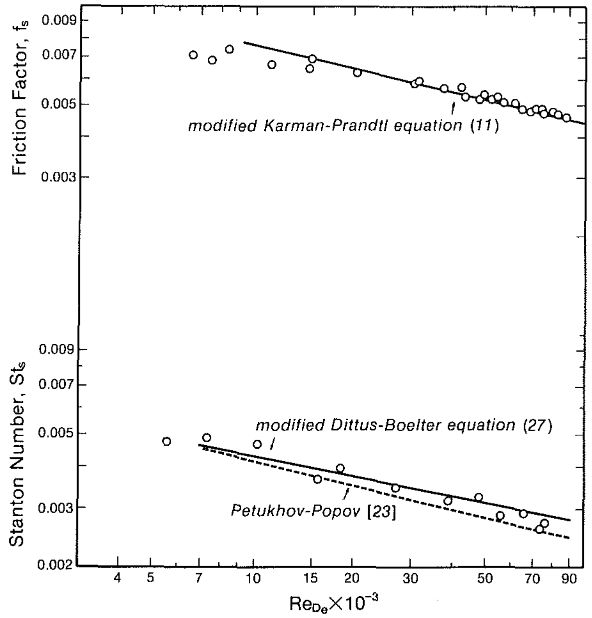

Fig. 5 Test results for smooth surface

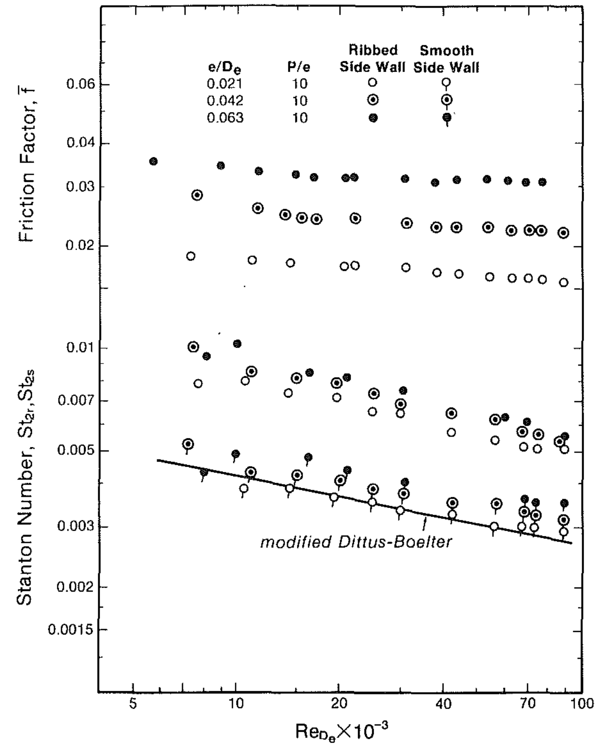

Fig. 6 Test results for different e/D_e ratios

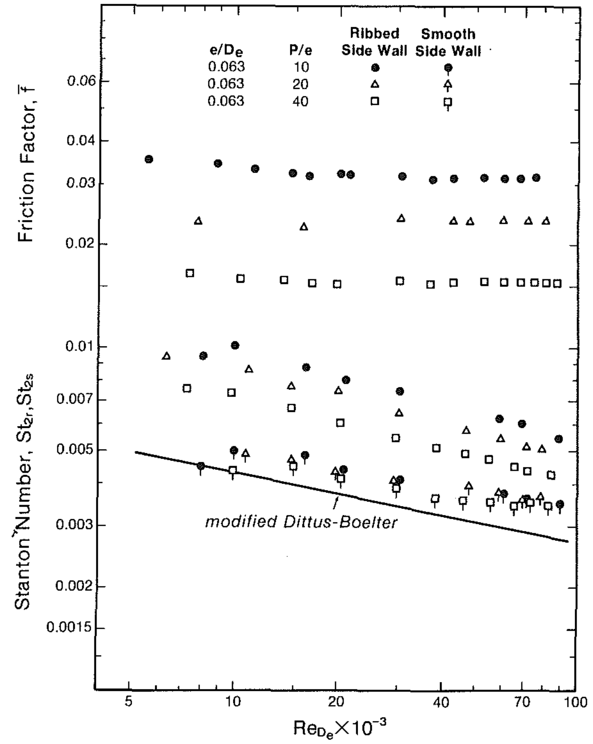

Fig. 7 Test results for different p/e ratios

an approximately constant value as the Reynolds number increases, while the Stanton number continues to decrease with Reynolds number. Both the average friction factor and Stanton number increase with increasing e/D_e. The Stanton number of the ribbed side wall is about 1.8, 2.0, and 2.2 times that of the four-sided smooth duct for an e/D_e ratio of 0.021, 0.042, and 0.063, respectively. The Stanton number of the smooth-side wall is also higher than that of the four-sided smooth duct by up to 25 percent, due to the presence of the ribs on the adjacent walls.

Rib Pitch-to-Height. The rib pitch-to-height ratio was changed from 10 to 20 to 40 by removing the intermediate ribs from the surface before the test. The rib height-to-equivalent diameter ratio was kept at a constant value of 0.063 for this series of tests. Figure 7 shows the average friction factor and Stanton number versus Reynolds number for different P/e ratios. At a given ratio of the rib pitch to height, the friction factor reaches a constant value as the Reynolds number increases, whereas the Stanton number continues to decrease with Reynolds number. Both the average friction factor and Stanton number decrease with increasing P/e. The maximum values of the friction factor and the Stanton number occur at a P/e ratio of 10. The Stanton number of the ribbed side is about 1.5 to 2.2 times that of the four-sided smooth duct when the P/e ratio varies from 40 to 10. The Stanton number of the smooth side is also increased by up to 25 percent.

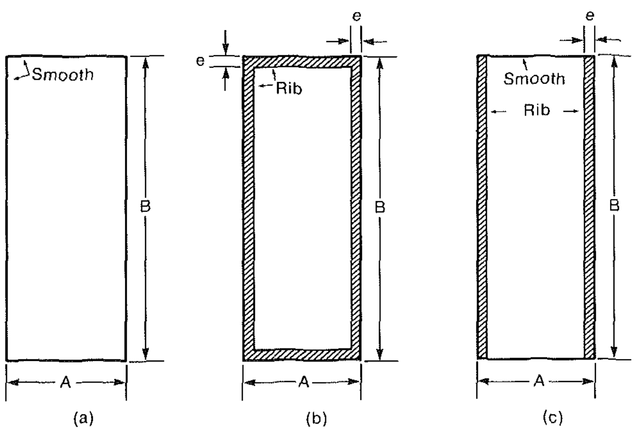

Fig. 8 (*a*) Four-sided smooth duct; (*b*) four-sided ribbed duct; (*c*) two smooth and two opposite ribbed duct

Theoretical Analysis

Prediction Method for Friction Factor. The friction factor for fully developed turbulent flow in a four-sided smooth duct, as shown in Fig. 8(*a*), can be defined by

$$f_s = \frac{\tau_s}{\frac{1}{2}\rho \bar{V}_s^2} \tag{4}$$

Similarly, the friction factor for fully developed turbulent flow in a four-sided ribbed duct, as seen in Fig. 8(*b*), may be defined as

$$f_r = \frac{\tau_r}{\frac{1}{2}\rho \bar{V}_r^2} \tag{5}$$

This analysis concerns fully developed turbulent flow in a rectangular duct with two opposite ribbed walls, as shown in Fig. 8(*c*). The average friction factor for this case may be expressed by the following equation.

$$\bar{f} = \frac{\bar{\tau}}{\frac{1}{2}\rho \bar{V}^2} \tag{6}$$

In equation (6), the average wall shear stress $\bar{\tau}$ can be related to the shear stresses produced by the two smooth and the two ribbed walls by

$$\bar{\tau}(2A+2B)L = (2A\tau_{2s} + 2B\tau_{2r})L \tag{7}$$

In this analysis, it is assumed that the total shear force in a duct with two smooth and two ribbed walls can be approximated by combining the shear force from two smooth walls in a four-sided smooth duct with the shear force from two ribbed walls in a four-sided ribbed duct, i.e.,

$$(2A\tau_{2s} + 2B\tau_{2r})L \cong (2A\tau_s + 2B\tau_r)L \tag{8}$$

It is noted that τ_{2s} is not necessarily equivalent to τ_s and that τ_{2r} is not necessarily equivalent to τ_r. Most likely τ_{2s} would be slightly higher than τ_s due to the adjacent ribbed walls, while τ_{2r} would be slightly lower than τ_r because of its adjacent smooth walls. However, since $\tau_{2s} << \tau_{2r}$ and $A \leq B$ for most of the two opposite rib-roughened ducts in this investigation, the assumption inherent to equation (8) should be reasonable.

Combining equations (4-8), and assuming that the fluid dynamic energy in each duct is about the same, i.e., $\frac{1}{2}\rho\bar{V}^2 \cong \frac{1}{2}\rho\bar{V}_s^2 \cong \frac{1}{2}\rho\bar{V}_r^2$, the average friction factor $\bar{f}$ can be found from

$$\bar{f} = \frac{Af_s + Bf_r}{A+B} \tag{9}$$

Equation (9) gives the average friction factor as a weighted average of the four-sided smooth duct friction factor f_s and the four-sided ribbed duct friction factor f_r. These friction factors are weighted by the smooth wall width A and the ribbed wall height B, respectively.

The friction factor in a four-sided smooth duct can be determined from Karman-Prandtl equation [17] by using an equivalent diameter D_e for Reynolds number calculations

$$\frac{1}{\sqrt{f_s}} = 4.0 \log_{10}(\mathrm{Re}_{D_e}\sqrt{f_s}) - 0.40 \tag{10}$$

Brundrett [21] suggested that equation (10) could be improved by introducing the concept of an average ray length relative to the conventional equivalent diameter, $2R_{av}/D_e$. The friction factor in a four-sided smooth rectangular duct with aspect ratio of B/A would than be written as

$$\frac{1}{\sqrt{f_s}} = 4.0 \log_{10}(\mathrm{Re}_{D_e}\sqrt{f_s}) - 0.40 + 4.0 \log_{10}\left(\frac{2R_{av}}{D_e}\right) \tag{11}$$

Where

$$\begin{aligned} \frac{2R_{av}}{D_e} &= \frac{1.156 + (B/A - 1)}{B/A} \qquad (12) \\ &= 1.156 \text{ for square ducts} \end{aligned}$$

It is noted that equations (10) and (11) give values of f_s that differ by no more than 4 percent in a square duct with $B = A$. The differences in f_s are even less for rectangular ducts with $B > A$.

The friction factor in a four-sided ribbed duct can be deduced from the so-called friction similarity law. Nikuradse [18] first proposed the law of the wall and developed the friction similarity law to correlate the friction data for fully developed turbulent flow in tubes with rough (sand coated) walls. This same method has been successfully extended to correlate friction data for turbulent flow in tubes with repeated-rib roughness [2]. Assuming that the same method can be applied to flow in a four-sided ribbed duct, as shown in Fig. 8(*b*), the law of the wall can be expressed by the dimensionless velocity profile normal to the wall

$$u^+ = 2.5 \ln \frac{y}{e} + R_M(e^+) \tag{13}$$

The momentum transfer roughness function R_M is a boundary condition which represents the dimensionless velocity u^+ at a distance e (rib height) from the wall. Integration of equation (13) across the cross-sectional area of a flow channel gives

$$\begin{aligned} \bar{u}^+ &= \frac{1}{A_c}\int_0^l \left[2.5 \ln \frac{y}{e} + R_M(e^+)\right] dA_c \\ &= \frac{1}{A_c}\int_0^l 2.5 \ln \frac{y}{l}\, dA_c + 2.5 \ln \frac{l}{e} + R_M(e^+) \\ &= -2.5 + 2.5 \ln \frac{l}{e} + R_M(e^+) \qquad (14) \end{aligned}$$

Where l is the distance between the ribbed wall and the position of zero shear stress, and y is the distance from the ribbed wall. The dimensionless average velocity across the channel in a four-sided ribbed duct can be written in terms of the friction factor f_r as:

$$\bar{u}^+ = \sqrt{\frac{2}{f_r}} \tag{15}$$

Substituting equation (15) into equation (14), the friction similarity law for flow in a four-sided ribbed duct yields

$$R_M(e^+) = \sqrt{\frac{2}{f_r}} + 2.5 \ln \frac{e}{l} + 2.5 \tag{16}$$

The length l can be related to duct dimension by

$$l = \tfrac{1}{2}A = \frac{A+B}{4B} D_e \tag{17}$$

Inserting the expression for l from equation (17) into equation (16), we obtain

$$R_M(e^+) = \sqrt{\frac{2}{f_r}} + 2.5 \ln \frac{2e}{D_e} + 2.5 \ln \frac{2B}{A+B} + 2.5 \tag{18}$$

As pointed out by Dalle Donne and Meyer [11], the parameter $R_M(e^+)$ is independent of the macroscopic geometry (tube or duct), and it is only dependent on type of roughness present on the surface (microscopic geometry). Therefore, values of $R_M(e^+)$ measured in a four-sided ribbed tube can be applied to a four-sided ribbed duct with the same type of rib geometry. A well-known correlation for $R_M(e^+)$ for flow in ribbed tubes with $0.01 \leq e/D_e \leq 0.04$ was obtained by Webb et al. [2], given by

$$R_M(e^+) = 0.95(P/e)^{0.53}; \; P/e \geq 10, \; e^+ \geq 35 \tag{19}$$

The friction factor in a four-sided ribbed duct can be predicted by combining equations (18) and (19)

$$f_r = \frac{2}{\left[0.95(P/e)^{0.53} - 2.5 \ln \dfrac{2e}{D_e} - 2.5 - 2.5 \ln \dfrac{2B}{A+B}\right]^2} \tag{20}$$

Applying equations (11) and (20) to predict f_s and f_r, the average friction factor in a duct with two smooth and two ribbed walls can then be found using equation (9).

Prediction Method for Heat Transfer. The prediction method for heat transfer will be very similar to that for friction factor as described earlier if the heat and momentum transfer analogy is applied. For fully developed turbulent flow in four-sided smooth ducts and four-sided ribbed ducts, the corresponding Stanton numbers can be defined by equation (21) and equation (22).

$$\mathrm{St}_s = \frac{q_s''}{GC_p(\bar{T}_w - T_b)_s} \tag{21}$$

$$\mathrm{St}_r = \frac{q_r''}{GC_p(\bar{T}_w - T_b)_r} \tag{22}$$

The average Stanton number for fully developed turbulent flow in a rectangular duct with two smooth and two opposite ribbed walls may be expressed as

$$\overline{\mathrm{St}} = \frac{\bar{q}''}{GC_p(\bar{T}_w - T_b)} \tag{23}$$

where

$$\bar{q}''(2A+2B)L = (2Aq_{2s}'' + 2Bq_{2r}'')L \tag{24}$$

If the analogous assumption for heat transfer follows the same form as was made for friction factor, then

$$(2Aq_{2s}'' + 2Bq_{2r}'')L \cong (2Aq_s'' + 2Bq_r'')L \tag{25}$$

By combining equations (21–25) assuming that the temperature gradient in each case is about the same, i.e., $(\bar{T}_w - T_b) \cong (\bar{T}_w - T_b)_s \cong (\bar{T}_w - T_b)_r$, the average Stanton number can be written as

$$\overline{\mathrm{St}} = \frac{A\mathrm{St}_s + B\mathrm{St}_r}{A+B} \tag{26}$$

The Stanton number in a four-sided smooth duct can be determined from Dittus–Boelter correlation [17] by using an average ray length for Reynolds number calculations

$$\mathrm{St}_s = \frac{0.023}{\mathrm{Re}_{D_e}^{0.2} \mathrm{Pr}^{0.6} (2R_{av}/D_e)^{0.2}} \tag{27}$$

The Stanton number in a four-sided ribbed duct can be deduced from the heat transfer similarity law. Dipprey and Sabersky [19] developed the so-called heat transfer similarity law to correlate heat transfer data for fully developed turbulent flow in tubes with rough (sand coated) walls. This similarity method has been extended to correlate heat transfer data for tubulent flow in rib-roughened tubes [2]. It is assumed that the same method can be applied for flow in a four-sided ribbed duct using the heat and momentum transfer analogy, giving a dimensionless temperature profile normal to the ribbed wall as

$$T^+ = 2.5 \ln \frac{y}{e} + G_H(e^+, \mathrm{Pr}) \tag{28}$$

where, by definition

$$T^+ = \frac{(T_w - T)_r \rho C_p u^*}{q_r''} \tag{29}$$

T_w is the temperature of the ribbed wall, T is the temperature of the fluid at a distance y from the ribbed wall, and q_r'' is the heat flux from the ribbed wall to the fluid. Integrating equation (28) over the flow channel cross section and combining with equations (14) and (15), produces

$$\bar{T}^+ = \sqrt{2/f_r} - R_M(e^+) + G_H(e^+, \mathrm{Pr}) \tag{30}$$

where the dimensionless average temperature profile can be expressed by

$$\bar{T}^+ = \frac{\sqrt{f_r/2}}{\mathrm{St}_r} \tag{31}$$

Substituting equation (31) into equation (30), the heat transfer similarity law for flow in a four-sided ribbed duct yields

$$G_H(e^+, \mathrm{Pr}) = R_M(e^+) + \frac{f_r/2\mathrm{St}_r - 1}{\sqrt{f_r/2}} \tag{32}$$

Assuming that the heat transfer roughness function $G_H(e^+, \mathrm{Pr})$ is independent of the flow channel cross-sectional area and is only dependent on rib geometry, the $G_H(e^+, \mathrm{Pr})$ measured in tube flow [2] can be employed for duct flow for similar rib geometries, i.e.,

$$G_H(e^+, \mathrm{Pr}) = 4.5(e^+)^{0.28} \mathrm{Pr}^{0.57}; \; e^+ \geq 25 \tag{33}$$

The Stanton number in a four-sided ribbed duct can be predicted by combining equations (32) and (33), to give

$$\mathrm{St}_r = \frac{f_r/2}{1 + \sqrt{f_r/2}\,[G_H(e^+, \mathrm{Pr}) - R_M(e^+)]} \tag{34}$$

The average Stanton number in a duct with two smooth and two ribbed walls can be predicted by using equations (27) and (34) to find St_s and St_r, and inserting these values into equation (26).

Results Comparison and Discussion

Figure 9 shows the comparison of average friction factor from equation (9) with measurements taken in a square duct ($A = B$) having two opposite ribbed walls. The agreement between theory and measurements is quite acceptable over the entire range of e/D_e for a p/e ratio of 10. However, the predicted friction factor is up to 10 percent lower than the measured data for p/e ratios of 20 and 40 with high Reynolds numbers. In order to demonstrate the applicability of the prediction method, Fig. 10 gives a comparison of the average friction factor predicted by equation (9) with measurements in a rectangular duct ($B = 11.6\,A$ and $B = 18.4\,A$) having two opposite ribbed walls [6, 22]. Again, the agreement is acceptable except that the prediction is up to 12 percent higher than measurements made in a duct having $B/A = 11.6$, $e/D_e = 0.102$, and $p/e = 10$. The acceptable agreement confirms that equations (11) and (20) can be combined with equation

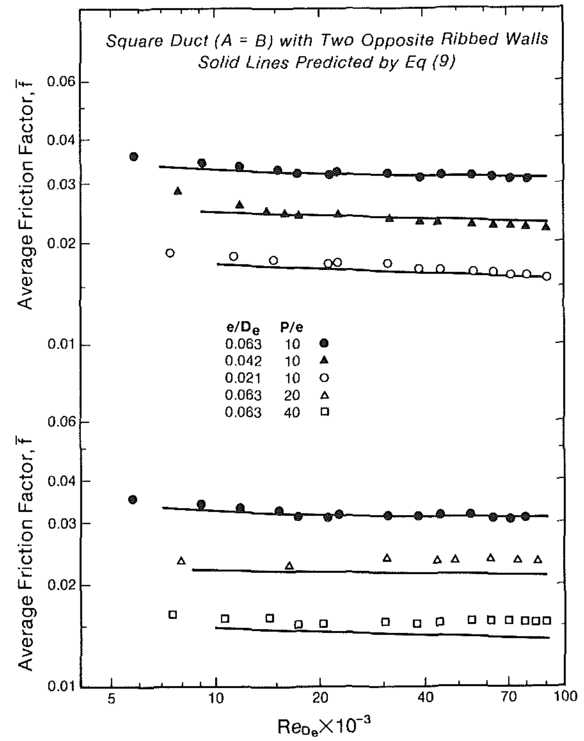

Fig. 9 Comparison of prediction with the present friction data in square duct with two opposite ribbed walls

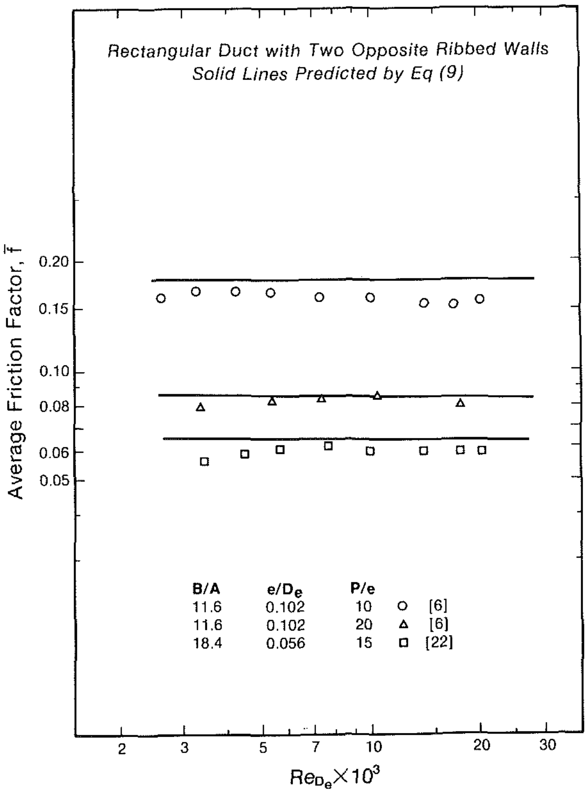

Fig. 10 Comparison of prediction with the previous friction data in rectangular duct with two opposite ribbed walls

(9) to predict the average friction factor in rectangular ducts with different aspect ratios ($B \geq A$), and having two opposite rib-roughened walls.

Figure 11 indicates the comparison of average Stanton number predicted by equations (26) with the present measured data. The data were calculated from that in Figs. 6 and 7, i.e., $\overline{St} = 1/2\ (St_{2s} + St_{2r})$. The predicted average Stanton numbers are very close to those measured at various e/D_e ratios with a p/e of 10. However, the prediction can be off as much as 10 percent for a p/e ratio of 40. The acceptable agreement confirms that equations (27) and (34) can be combined with equation (26) to predict the average Stanton number in duct flow with two opposite ribbed walls.

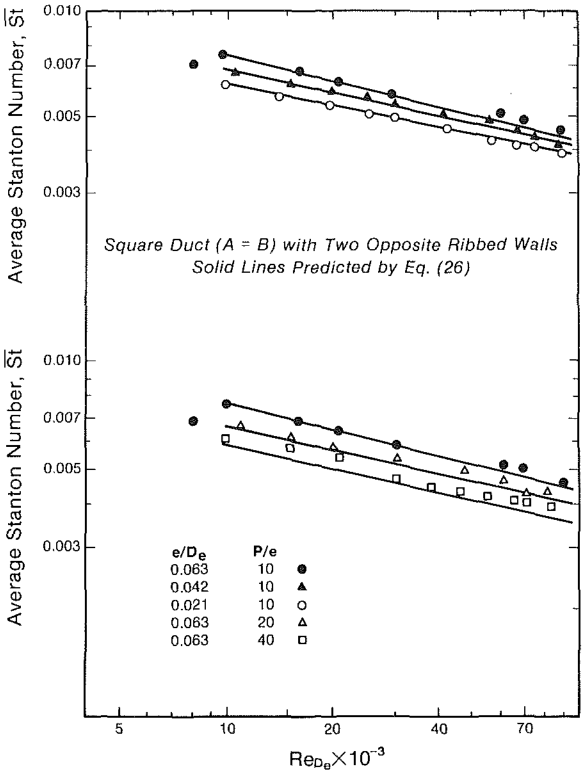

Fig. 11 Comparison of prediction with the present heat transfer data in square duct with two opposite ribbed walls

It is interesting to note that the friction factor and heat transfer coefficients of the ribbed wall is influenced by the adjacent smooth side wall in the two-sided, ribbed-wall duct, as shown in Figs. 12 and 13. The solid lines represent the friction factor and Stanton number in a square duct with four-sided ribbed walls predicted by equation (20) and equation (34), respectively. The results show that the friction factor can be reduced by 30 ~ 45 percent over the range of e/D_e and p/e ratios due to the presence of the adjacent smooth walls. It is noted that the ribbed side Stanton number is decreased up to 10 percent over the range of the investigation due to the presence of the adjacent smooth walls, whereas the smooth side Stanton number is increased up to 25 percent due to the influence of the adjacent ribbed walls.

Conclusions

An experimental study of fully developed turbulent air flow in square ducts with two opposite rib-roughened walls has been performed. The effects of the rib height-to-equivalent diameter and rib pitch-to-height ratios on the heat transfer coefficients and friction factor have been investigated. Based on the four-sided smooth ducts correlation and the four sided ribbed ducts similarity law, a general prediction method for flow in rectangular ducts with two smooth and two opposite ribbed walls has been developed. The following conclusions can be drawn:

1 The Stanton number of the ribbed side wall is about 1.5 to 2.2 times that of the four-sided smooth duct for the range of the test data. However, these values are up to 10 percent lower than that for the four-sided ribbed duct because the influence of the smooth walls.

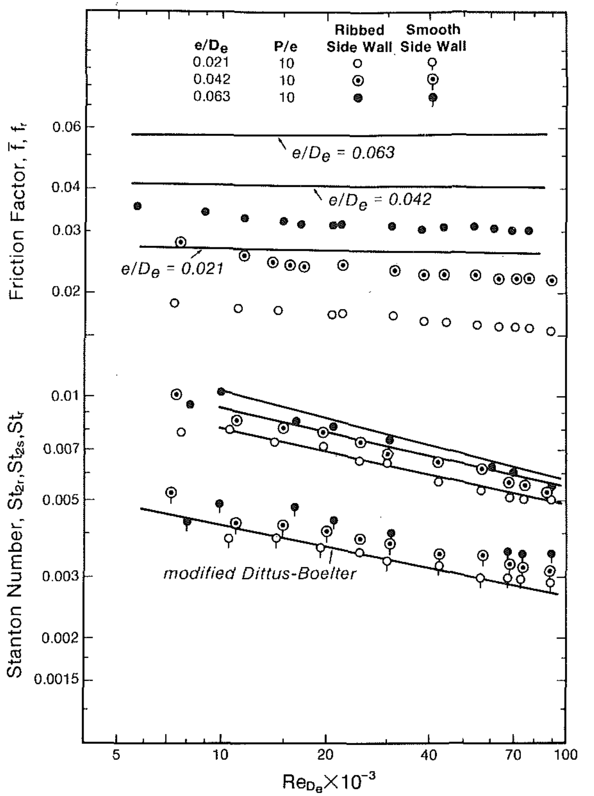

Fig. 12 Comparison between prediction in four-sided ribbed duct and the present data for different e/D_e ratios

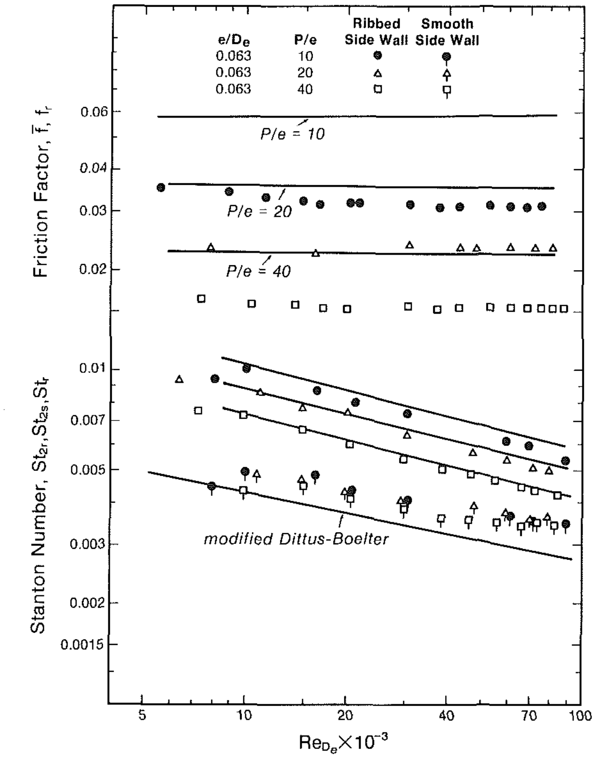

Fig. 13 Comparison between prediction in four-sided ribbed duct and the present data for different p/e ratios

2 The Stanton number of the smooth side wall is also enhanced by up to 25 percent due to the presence of the ribs on the adjacent walls.

3 The average friction factor is about 2.1 to 6.0 times that of the four-sided smooth duct for the range of the test data. However, these values are about 30–45 percent lower than that for the four-sided ribbed duct because the presence of the adjacent smooth walls.

4 The average friction factor can be determined by a weighted average of the four-sided smooth duct friction factor, and the four-sided ribbed duct friction factor, as indicated in equation (9). Similarly, the average Stanton number can be predicted by a weighted average of the four-sided smooth duct Stanton number and the four-sided ribbed duct Stanton number, as noted in equation (26). There is good agreement between prediction and measurements. The prediction method and experimental data may be applied to the design of gas turbine blade internal cooling passages.

Acknowledgment

This work was sponsored by the National Science Foundation under Grant MEA-8205234. Their support is gratefully acknowledged.

References

1 Nunner, W., "Heat Transfer and Pressure Drop in Rough Tubes," AERE lib/Trans. 786, 1958.

2 Webb, R. L., Eckert, E. R. G., and Goldstein, R. J., "Heat Transfer and Friction in Tubes with Repeated-rib Roughness," *International Journal of Heat and Mass Transfer*, Vol. 14, 1971, pp. 601–617.

3 Lewis, M. J., "An Elementary Analysis for Predicting the Momentum and Heat Transfer Characteristics of a Hydraulically Rough Surface," ASME JOURNAL OF HEAT TRANSFER, Vol. 97, 1975, pp. 249–254.

4 Lewis, M. J., "Optimizing the Thermohydraulic Performance of Rough Surfaces," *International Journal of Heat and Mass Transfer*, Vol. 18, 1975, pp. 1243–1248.

5 Kader, B. A., and Yaglom, A. M., "Turbulent Heat and Mass Transfer from a Wall with Parallel Roughness Ridges," *International Journal of Heat and Mass Transfer*, Vol. 20, 1977, pp. 354–357.

6 Han, J. C., Glicksman, L. R., and Rohsenow, W. M., "An Investigation of Heat Transfer and Friction for Rib-Roughened Surfaces," *International Journal of Heat and Mass Transfer*, Vol. 21, 1978, pp. 1143–1156.

7 Gee, D. L., and Webb, R. L., "Forced Convection Heat Transfer in Helically Rib-Roughened Tubes," *International Journal of Heat and Mass Transfer*, Vol. 23, 1980, pp. 1127–1136.

8 Hall, W. B., "Heat Transfer in Channels Having Rough and Smooth Surface," *J. Mech. Enging Sci.*, Vol. 4, 1962, pp. 287–291.

9 Wilkie, D., "Forced Convection Heat Transfer From Surfaces Roughened by Transverse Ribs," *Proceedings of the 2nd Int. Heat Transfer Conference*, Vol. 1, AICHE, New York, 1966.

10 White, L., and Wilkie, D., "The Heat Transfer and Pressure Loss Characteristics of Some Multi-start Ribbed Surfaces," *Augmentation of Convective Heat and Mass Transfer*, edited by A. E. Bergles and R. L. Webb, ASME, New York, 1970.

11 Dalle Donne, M., and Meyer, L., "Turbulent Convective Heat Transfer from Rough Surfaces with Two-Dimensional Rectangular Ribs," *International Journal of Heat and Mass Transfer*, Vol. 20, 1977, pp. 582–620.

12 Meyer, L., "Thermohydraulic Characteristics of Single Rods with Three-Dimensional Roughness," *International Journal of Heat and Mass Transfer*, Vol. 25, 1982, pp. 1043–1058.

13 Suo, M., "Turbine Cooling," *Aerothermodynamics of Aircraft Gas Turbine Engines*, edited by Oates, G., Air Force Aero Propulsion Lab., AFAPL TR 78-52, 1978.

14 Hennecke, D. K., "Turbine Blade Cooling in Aero Engines—Some New Results, Future Trends, and Research Requirements," *Study in Heat Transfer*, edited by Hartnett et al., Hemisphere Corp., New York, 1979.

15 Taylor, J. R., "Heat Transfer Phenomena in Gas Turbine," ASME Paper No. 80-GT-172, 1980.

16 Burggraf, F., "Experimental Heat Transfer and Pressure Drop with Two-Dimensional Turbulence Promoter Applied to Two Opposite Walls of a Square Tube," *Augmentation of Convective Heat and Mass Transfer*, edited by A. E. Bergles and R. L. Webb, ASME, New York, 1970, pp. 70–79.

17 Rohsenow, W. M., and Hartnett, J. P., *Handbook of Heat Transfer*, McGraw-Hill, New York, 1973, pp. 7–122.

18 Nikuradse, J., "Laws for Flow in Rough Pipes," NACA TM 1292, 1950.

19 Dipprey, D. F., and Sabersky, R. H., "Heat and Momentum Transfer in Smooth and Rough Tubes in Various Prandtl Number," *International Journal of Heat and Mass Transfer*, Vol. 6, 1963, pp. 329–353.

20 Kline, S. J., and McClintock, F. A., "Describing Uncertainties in Single-Sample Experiments," *Mechanical Engineering*, Vol. 75, Jan. 1953, pp. 3–8.

21 Kakac, S., and Spalding, D. B., *Turbulent Forced Convection in Channels and Bundles*, Vol. I, Hemisphere Publishing, New York, 1979, pp. 361–367.

22 Han, J. C., "Convective Heat Transfer Augmentation in Channels Using Repeated-Rib Roughness," Sc.D. thesis, Department of Mechanical Engineering, Massachusetts Institute of Technology, Sept. 1976, p. 222.

23 Karlekar, B. V., and Desmond, R. M., *Heat Transfer* (2d ed.), West Publishing, New York, 1982, pp. 496–498.

Analysis of Low-Peclet Heat Transfer During Slug Flow in Tubes With Axial Wall Conduction

H. M. Soliman
Associate Professor,
Department of Mechanical Engineering,
University of Manitoba,
Winnipeg, Manitoba,
Canada R3T 2N2
Mem. ASME

An exact solution is presented for the temperature distribution during slug flow inside an infinitely long tube with a finite heated length. The solution takes into consideration axial conduction in the fluid and tube wall, which are characterized by Peclet number and a wall conduction parameter, respectively. Results of bulk and wall temperatures, convective heat flux and Nusselt number are presented for low and high Peclet numbers using a range of values for the wall conduction parameter. It is concluded that wall conduction can have substantial effects on the heat transfer characteristics in the areas surrounding the beginning and end of direct heating. These effects can be much more pronounced than the effects of fluid conduction.

Introduction

Heat transfer in the entrance region of ducts has received considerable attention due to its relevance to many engineering applications. An important extension of the original work of Graetz involved the inclusion of axial conduction in the fluid. This was found to have a significant influence on the heat transfer characteristics of flows with low Peclet number ($\mathrm{Pe} < 100$) [1]. Analytical solutions were reported for different configurations and boundary conditions using both numerical and exact methods. An excellent review of these investigations was compiled by Shah and London [2].

Recent research efforts were directed towards the more realistic situation in which axial conduction in the tube wall was considered along with axial fluid conduction. Faghri and Sparrow [3] analyzed the situation of fully developed laminar flow in an infinite tube with a semi-infinite heated section. Later, Zariffeh et al. [4] extended the analysis to situations where a finite heated length exists in a very long tube. It was concluded in both investigations that axial wall conduction can have significant effects on the heat transfer characteristics due to the conduction of substantial amounts of heat away from the directly heated section.

Inclusion of tube-wall conduction complicates the analysis since the heat transfer problem becomes a conjugated one. Exact solutions become difficult to obtain, and probably this was the reason for adopting a numerical approach in the previous investigations [3, 4]. The purpose of this investigation is to develop an exact solution for the heat transfer problem considered earlier by Zariffeh et al. [4] with only one simplification; that is the assumption of slug flow rather than laminar flow throughout the flow channel. The assumption of slug flow makes the present results applicable to turbulent flow of liquid metals with negligible eddy diffusion of heat.

Analysis

Consider the slug flow of an incompressible, constant property fluid in an infinitely long tube ($-\infty < x < \infty$) with inside radius r_i and small wall thickness t. The tube is directly heated over a finite length $0 \le x \le l$ with a uniform heat flux q_w'' and is externally insulated both upstream ($-\infty < x < 0$) and downstream ($l < x < \infty$) of the heated section. The fluid enters the tube with a uniform temperature T_i in the far upstream region and leaves the tube with a uniform temperature T_0 in the far downstream region. This arrangement simulates the heat transfer passage of many engineering devices and experimental setups.

Governing Equations. The energy equation and boundary conditions governing the temperature distribution within the whole flow domain ($-\infty < \eta < \infty$ and $0 \le R \le 1$) can be written in the following dimensionless form

$$\frac{1}{2}\frac{\partial \theta}{\partial \eta} = \frac{\partial^2 \theta}{\partial R^2} + \frac{1}{R}\frac{\partial \theta}{\partial R} + \frac{1}{\mathrm{Pe}^2}\frac{\partial^2 \theta}{\partial \eta^2} \tag{1}$$

$$\theta(0,\eta) \text{ is finite}, \qquad -\infty < \eta < \infty \tag{2a}$$

$$\theta(R,-\infty) = 0, \qquad 0 \le R \le 1 \tag{2b}$$

$$\theta(R,\infty) = 1, \qquad 0 \le R \le 1 \tag{2c}$$

and

$$\frac{\partial \theta}{\partial R} = \frac{F}{4L} + \frac{K}{\mathrm{Pe}^2}\frac{\partial^2 \theta}{\partial \eta^2} \qquad \text{at } R = 1 \tag{2d}$$

It is clear from energy equation (1) that the influence of fluid axial conduction on the temperature distribution within the flow domain is strongly dependent on the magnitude of Peclet number. For large values of Pe, the last term in the right-hand side of equation (1) becomes insignificant and the energy equation reduces to the standard Graetz problem. The influence of wall conduction is characterized by the single dimensionless group K (appearing in equation (2*d*)), which will be referred to as the wall conduction parameter.

Temperature Distribution. The approach followed here is to divide the flow domain into three different regions and to seek an independent solution for each region. Upstream from the directly heated section ($\eta < 0$) is region 1, the directly heated section ($0 \le \eta \le L$) is called region 2, and downstream from the directly heated section is region 3. It is expected that each of the three solutions will contain unknown constants that can be evaluated by matching the temperature and heat flux at the two interfaces $\eta = 0$ and $\eta = L$.

Following the method of separation of variables, the temperature distribution within region 1 can be developed as

$$\theta_1 = A_0 I_0(\lambda_0 R) e^{\alpha_0 \eta} + \sum_{j=1}^{\infty} A_j J_0(\lambda_j R) e^{\alpha_j \eta} \tag{3}$$

where A_0 and A_j are arbitrary constants to be determined later

$$\alpha_0 = (\mathrm{Pe}^2/4)[1 \pm \sqrt{1 - (4\lambda_0/\mathrm{Pe})^2}] \tag{4a}$$

and

Contributed by the Heat Transfer Division for publication in the JOURNAL OF HEAT TRANSFER. Manuscript received by the Heat Transfer Division August 4, 1984.

$$\alpha_j = (\mathrm{Pe}^2/4)[1+\sqrt{1+(4\lambda_j/\mathrm{Pe})^2}] \tag{4b}$$

Equation (3) satisfies energy equation (1) and boundary conditions (2*a*) and (2*b*). The eigen values λ_0 and λ_j can be determined by substituting the first and second terms of equation (3), respectively, into boundary condition (2*d*), keeping in mind that $F=0$ in region 1. Starting with the first term, we get

$$8\lambda_0 I_1(\lambda_0) - K\mathrm{Pe}^2 I_0(\lambda_0)[1 \pm \sqrt{1-(4\lambda_0/\mathrm{Pe})^2} - 8\lambda_0^2/\mathrm{Pe}^2] = 0 \tag{5a}$$

where the positive sign for the square root in equation (5*a*), and of course in equation (4*a*) also, correspond to $K \leq I_1(\mathrm{Pe}/4)/[(\mathrm{Pe}/4)I_0(\mathrm{Pe}/4)]$, while the negative sign correspond to higher values of K. For any combination of K and Pe, equation (5*a*) can be solved by any suitable iterative method for the corresponding value of λ_0. Four-decimal-place accuracy was imposed in the present computations. We should note that for any value of Pe, the value of λ_0 follows this pattern: $\lambda_0=0$ at $K=0$, increases to $\lambda_0=\mathrm{Pe}/4$ as K increases to $K=I_1(\mathrm{Pe}/4)/[(\mathrm{Pe}/4)I_0(\mathrm{Pe}/4)]$, and then decreases with further increase in K down to $\lambda_0=0$ at $K=\infty$.

Substituting now the second term of (3) into (2*d*) results in

$$8\lambda_j J_1(\lambda_j) + K\mathrm{Pe}^2 J_0(\lambda_j)[1+\sqrt{1+(4\lambda_j/\mathrm{Pe})^2} + 8\lambda_j^2/\mathrm{Pe}^2] = 0 \tag{5b}$$

Again for any combination of K and Pe the transcedental equation (5*b*) can be solved for as many eigenvalues λ_j as desired. It must be noted, however, that the eigenfunctions $J_0(\lambda_j)$ do not form an orthogonal set due to the form of boundary condition (2*d*). This fact will be given special consideration later, since it has a strong relevance to the evaluation of the arbitrary constants A_0 and A_j.

Similarly, in region 3 the temperature distribution which satisfies equations (1), (2*a*), and (2*c*) can be developed as follows, using the method of separation of variables

$$\theta_3 = 1 + \sum_{j=1}^{\infty} D_j J_0(\mu_j R) e^{\beta_j(\eta-L)} \tag{6}$$

where D_j is a set of arbitrary constants and

$$\beta_j = (\mathrm{Pe}^2/4)[1-\sqrt{1+(4\mu_j/\mathrm{Pe}^2}] \tag{7}$$

A shift in the η-coordinate was introduced in equation (6) since θ_3 deviates from unity only in the neighborhood of $\eta=L$. Thus this shift is necessary in order to keep the values of D_j within reasonable bounds. Substituting equation (6) into equation (2*d*) results in the following transcedental equation for the evaluation of eigenvalues μ_j

$$8\mu_j J_1(\mu_j) + K\mathrm{Pe}^2 J_0(\mu_j)[1-\sqrt{1+(4\mu_j/\mathrm{Pe})^2} + 8\mu_j^2/\mathrm{Pe}^2] = 0 \tag{8}$$

The root $\mu=0$ is a possible solution of equation (8) for all values of Pe and K. However, this root was ignored since the corresponding eigenfunction ($J_0(\mu)=1$), when included in solution (6), would place this solution in violation of boundary conditions (2*c*). Similar to region 1, the eigenfunctions $J_0(\mu_j)$ do not form an orthogonal set. While producing the present results, four-decimal-place accuracy was imposed on the values of λ_j and μ_j.

In region 2 the standard method of separation of variables could be used successfully for the development of a solution for the temperature distribution; however, it would be necessary to use a numerical method for the evaluation of the corresponding eigenvalues. Consequently, this approach was abandoned, and using superposition instead, a solution consisting of three parts was obtained as follows

$$\theta_2 = \left[\frac{\eta}{L} + \frac{R^2}{8L} - \frac{1}{16L} + \frac{2}{\mathrm{Pe}^2 L} + \frac{4K}{\mathrm{Pe}^2 L}\right] + \left[\sum_{j=1}^{\infty} C_j J_0(\mu_j R) e^{\beta_j \eta}\right]$$
$$+ \left[B_0 I_0(\lambda_0 R) e^{\alpha_0(\eta-L)} + \sum_{j=1}^{\infty} B_j J_0(\lambda_j R) e^{\alpha_j(\eta-L)}\right] \tag{9}$$

where B_0, B_j, and C_j are arbitrary constants. Each of the three parts of this solution (contained between two brackets in equation (9)) would separately satisfy energy equation (1) and boundary condition (2*a*). The whole solution satisfies boundary condition (2*d*) with $F=1$, keeping in mind that $\lambda_0, \lambda_j, \mu_j, \alpha_0, \alpha_j$, and β_j all have the same values developed earlier in regions 1 and 3. The first part of solution (9) represents the solution in the fully developed segment of region 2, while the second and third parts account for the influences of fluid and wall axial conduction near the beginning and end of the directly heated section, respectively.

Evaluation of the Coefficients. In order to complete the solution, the series expansion coefficients in equations (3), (6), and (9) must be determined. This can be done by matching the temperature and heat flux at the two interfaces $\eta=0$ and $\eta=L$. Imposing the condition $\theta_1(R,0)=\theta_2(R,0)$, we get

Nomenclature

c_p = specific heat of fluid
h = heat transfer coefficient
K = $\frac{tk_w}{r_i k}$ = wall conduction parameter
k = thermal conductivity of fluid
k_w = thermal conductivity of tube wall
L = $\frac{l/r_i}{\mathrm{Pe}}$ = dimensionless heated length
l = heated length
Nu = Nusselt number defined by equation (32)
Pe = $2r_i\rho U c_p/k$ = Peclet number
q_f'' = convective heat flux
q_w'' = input heat flux to tube wall
R = r/r_i = dimensionless radial coordinate
r = radial coordinate
r_i = tube radius
T = temperature
T_b = bulk temperature
T_i = upstream inlet temperature
T_0 = downstream exit temperature
T_w = wall temperature
t = wall thickness
U = fluid velocity
x = axial coordinate
$\alpha_0, \alpha_j, \beta_j$ = exponents given by equations (4*a*), (4*b*) and (7), respectively
η = $\frac{x/r_i}{\mathrm{Pe}}$ = dimensionless axial coordinate
θ = $(T-T_i)/(T_0-T_i)$ = dimensionless temperature
θ_b = $(T_b-T_i)/(T_0-T_i)$ = dimensionless bulk temperature
θ_w = $(T_w-T_i)/(T_0-T_i)$ = dimensionless wall temperature
$\lambda_0, \lambda_j, \mu_j$ = eigen values
ρ = fluid density
Ψ_j, ω_j = sets of orthonormal functions given by equation (14)

$$A_0I_0(\lambda_0R)+\sum_{k=1}^{\infty}A_kJ_0(\lambda_kR)=\frac{R^2}{8L}-\frac{1}{16L}+\frac{2}{\mathrm{Pe}^2L}+\frac{4K}{\mathrm{Pe}^2L}$$
$$+\sum_{k=1}^{\infty}C_kJ_0(\mu_kR)+B_0I_0(\lambda_0R)e^{-\alpha_0L}$$
$$+\sum_{k=1}^{\infty}B_kJ_0(\lambda_kR)e^{-\alpha_kL}\tag{10}$$

Continuity of heat flux at $\eta=0$, $\partial\theta_1/\partial\eta(R,0)=\partial\theta_2/\partial\eta(R,0)$ results in

$$\alpha_0A_0I_0(\lambda_0R)+\sum_{k=1}^{\infty}\alpha_kA_kJ_0(\lambda_kR)=\frac{1}{L}+\alpha_0B_0I_0(\lambda_0R)e^{-\alpha_0L}$$
$$+\sum_{k=1}^{\infty}\beta_kC_kJ_0(\mu_kR)+\sum_{k=1}^{\infty}\alpha_kB_kJ_0(\lambda_kR)e^{-\alpha_kL}\tag{11}$$

Similarly, the continuity of temperature and heat flux at $\eta=L$ produce the following two conditions, respectively

$$\sum_{k=1}^{\infty}D_kJ_0(\mu_kR)=\frac{R^2}{8L}-\frac{1}{16L}+\frac{2}{\mathrm{Pe}^2L}+\frac{4K}{\mathrm{Pe}^2L}+B_0I_0(\lambda_0R)$$
$$+\sum_{k=1}^{\infty}C_kJ_0(\mu_kR)e^{\beta_kL}+\sum_{k=1}^{\infty}B_kJ_0(\lambda_kR)\tag{12}$$

and

$$\sum_{k=1}^{\infty}\beta_kD_kJ_0(\mu_kR)=\frac{1}{L}+\sum_{k=1}^{\infty}\beta_kC_kJ_0(\mu_kR)e^{\beta_kL}$$
$$+\alpha_0B_0I_0(\lambda_0R)+\sum_{k=1}^{\infty}\alpha_kB_kJ_0(\lambda_kR)\tag{13}$$

The major difficulty remaining is that neither $J_0\,(\lambda_kR)$ nor $J_0\,(\mu_kR)$ form an orthogonal set of eigenfunctions. This was resolved by employing the well-known theory of functions of a real variable [5]. Accordingly, two orthonormal sets of functions ω and Ψ were constructed such that ω_n is a linear combination of the first n functions of the $J_0(\lambda_kR)$ set, and similarly Ψ_n is a linear combination of the first n functions of the $J_0(\mu_kR)$ set, i.e.,

$$\omega_n=\sum_{k=1}^{n}a_{n,k}J_0(\lambda_kR)\tag{14a}$$

and

$$\Psi_n=\sum_{k=1}^{n}b_{n,k}J_0(\mu_kR)\tag{14b}$$

Orthonormality of ω and also of Ψ implies that

$$\int_0^1\omega_i\omega_jdR=0\text{ for }i\neq j\tag{15a}$$
$$=1\text{ for }i=j$$

and

$$\int_0^1\Psi_i\Psi_jdR=0\text{ for }i\neq j\tag{15b}$$
$$=1\text{ for }i=j$$

The method of evaluating the coefficients $a_{i,j}$ and $b_{i,j}$ in equation (14) is described clearly in [5] and hence will not be given here. In order to use the new orthonormal sets ω and Ψ in equations (10) to (13), we must express equation (14) in the following form

$$J_0(\lambda_nR)=\sum_{k=1}^{n}P_{n,k}\omega_k\tag{16a}$$

and

$$J_0(\mu_nR)=\sum_{k=1}^{n}S_{n,k}\Psi_k\tag{16b}$$

where the coefficients $P_{i,j}$ and $S_{i,j}$ are obtainable by inverting the matrices containing $a_{i,j}$ and $b_{i,j}$, respectively. Substituting equation (16) into equations (10-13), we get the following relations

$$A_0I_0(\lambda_0R)+\sum_{k=1}^{\infty}\sum_{j=1}^{k}A_kP_{k,j}\omega_j=\frac{R^2}{8L}-\frac{1}{16L}+\frac{2}{\mathrm{Pe}^2L}+\frac{4K}{\mathrm{Pe}^2L}$$
$$+\sum_{k=1}^{\infty}\sum_{j=1}^{k}C_kS_{k,j}\Psi_j+\sum_{k=1}^{\infty}\sum_{j=1}^{k}$$
$$B_kP_{k,j}\omega_je^{-\alpha_kL}+B_0I_0(\lambda_0R)e^{-\alpha_0L}\tag{17}$$

$$\alpha_0A_0I_0(\lambda_0R)+\sum_{k=1}^{\infty}\sum_{j=1}^{k}\alpha_kA_kP_{k,j}\omega_j=\frac{1}{L}$$
$$+\sum_{k=1}^{\infty}\sum_{j=1}^{k}\alpha_kB_kP_{k,j}\omega_je^{-\alpha_kL}$$
$$+\alpha_0B_0I_0(\lambda_0R)e^{-\alpha_0L}+\sum_{k=1}^{\infty}\sum_{j=1}^{k}\beta_kC_kS_{k,j}\Psi_j\tag{18}$$

$$\sum_{k=1}^{\infty}\sum_{j=1}^{k}D_kS_{k,j}\Psi_j=\frac{R^2}{8L}-\frac{1}{16L}+\frac{2}{\mathrm{Pe}^2L}+\frac{4K}{\mathrm{Pe}^2L}+B_0I_0(\lambda_0R)$$
$$+\sum_{k=1}^{\infty}\sum_{j=1}^{k}C_kS_{k,j}\Psi_je^{\beta_kL}+\sum_{k=1}^{\infty}\sum_{j=1}^{k}B_kP_{k,j}\omega_j\tag{19}$$

and

$$\sum_{k=1}^{\infty}\sum_{j=1}^{k}\beta_kD_kS_{k,j}\Psi_j=\frac{1}{L}+\sum_{k=1}^{\infty}\sum_{j=1}^{k}\beta_kC_kS_{k,j}\Psi_je^{\beta_kL}$$
$$+\alpha_0B_0I_0(\lambda_0R)+\sum_{k=1}^{\infty}\sum_{j=1}^{k}\alpha_kB_kP_{k,j}\omega_j\tag{20}$$

It is possible now to take advantage of orthonormality relations (15). Multiplying equations (17) and (19) by Ψ_m and equations (18) and (20) by ω_m, then integrating with respect to R from 0 to 1, these new relations between the coefficients can be easily obtained

$$\sum_{k=m}^{\infty}C_kS_{k,m}=-\int_0^1\left(\frac{R^2}{8L}-\frac{1}{16L}+\frac{2}{\mathrm{Pe}^2L}+\frac{4K}{\mathrm{Pe}^2L}\right)\Psi_mdR$$
$$+(A_0-B_0e^{-\alpha_0L})\int_0^1I_0(\lambda_0R)\Psi_mdR$$
$$+\sum_{k=1}^{\infty}\sum_{j=1}^{k}(A_k-B_ke^{-\alpha_kL})P_{k,j}\int_0^1\omega_j\Psi_mdR\tag{21}$$

$$-\sum_{k=m}^{\infty}\alpha_k(A_k-B_ke^{-\alpha_kL})P_{k,m}=-\frac{1}{L}\int_0^1\omega_mdR$$
$$+\alpha_0(A_0-B_0e^{-\alpha_0L})\int_0^1I_0(\lambda_0R)\omega_mdR$$
$$-\sum_{k=1}^{\infty}\sum_{j=1}^{k}\beta_kC_kS_{k,j}\int_0^1\Psi_j\omega_mdR\tag{22}$$

$$-\sum_{k=m}^{\infty}(D_k - C_k e^{\beta_k L})S_{k,m} =$$

$$-\int_0^1\left(\frac{R^2}{8L}-\frac{1}{16L}+\frac{2}{\mathrm{Pe}^2L}+\frac{4K}{\mathrm{Pe}^2L}\right)\Psi_m dR$$

$$-B_0\int_0^1 I_0(\lambda_0 R)\Psi_m dR - \sum_{k=1}^{\infty}\sum_{j=1}^{k} B_k P_{k,j}\int_0^1 \omega_j \Psi_m dR \qquad (23)$$

and

$$\sum_{k=m}^{\infty}\alpha_k B_k P_{k,m} = -\frac{1}{L}\int_0^1 \omega_m dR - \alpha_0 B_0\int_0^1 I_0(\lambda_0 R)\omega_m dR$$

$$+\sum_{k=1}^{\infty}\sum_{j=1}^{k}\beta_k(D_k - C_k e^{\beta_k L})S_{k,j}\int_0^1 \Psi_j\omega_m dR \qquad (24)$$

Examining the foregoing system of equations, we observe similarities between equations (21) and (23) and between equations (22) and (24) that can be used in reducing the system. Actually, equations (21) and (23) will become identical if we adopt the following relations

$$A_0 = -B_0(1-e^{-\alpha_0 L}), \qquad (25a)$$

$$A_k = -B_k(1-e^{-\alpha_k L}), 1\le k\le\infty \qquad (25b)$$

and

$$D_k = -C_k(1-e^{\beta_k L}), 1\le k\le\infty \qquad (25c)$$

The form to which both equations (21) and (23) reduce is

$$\sum_{k=m}^{\infty}C_k S_{k,m} = -\int_0^1\left(\frac{R^2}{8L}-\frac{1}{16L}+\frac{2}{\mathrm{Pe}^2L}+\frac{4K}{\mathrm{Pe}^2L}\right)\Psi_m dR$$

$$-B_0\int_0^1 I_0(\lambda_0 R)\Psi_m dR - \sum_{k=1}^{\infty}\sum_{j=1}^{k} B_k P_{kj}\int_0^1 \omega_j\Psi_m dR \qquad (26)$$

Also, with conditions (25), equations (22) and (24) reduce identically to

$$\sum_{k=m}^{\infty}\alpha_k B_k P_{k,m} = -\frac{1}{L}\int_0^1 \omega_m dR - \alpha_0 B_0\int_0^1 I_0(\lambda_0 R)\omega_m dR$$

$$-\sum_{k=1}^{\infty}\sum_{j=1}^{k}\beta_k C_k S_{k,j}\int_0^1 \Psi_j\omega_m dR \qquad (27)$$

In effect, the system of equations (21) to (24) has been replaced by the equivalent, but simpler, system of (25) to (27). Satisfying one system will definitely satisfy the other.

Each of equations (26) and (27) represents a set of N equations, where N is the number of eigenvalues λ_j or μ_j. On the other hand, equations (26) and (27) contain $(2N+1)$ unknowns; these are B_0, B_j $(1\le j\le N)$ and C_j $(1\le j\le N)$. Hence an additional relation is required, and this can be obtained by equating the average temperature in regions 1 and 2 at the interface $\eta=0$. Multiplying both sides of equation (10) by R and integrating with respect to R from $R=0$ to $R=1$, taking into consideration relation (25a), we get

$$B_0 I_1(\lambda_0)/\lambda_0 = \sum_{k=1}^{\infty}A_k J_1(\lambda_k)/\lambda_k - \sum_{k=1}^{\infty}B_k J_1(\lambda_k)e^{-\alpha_k L}/\lambda_k$$

$$-\left(\frac{2K+1}{\mathrm{Pe}^2L}\right) - \sum_{k=1}^{\infty}C_k J_1(\mu_k)/\mu_k \qquad (28)$$

Equations (25–28) provide a complete set of linear algebraic relations for the evaluation of all series expansion coefficients introduced in equations (3), (6), and (9). Several standard methods of solution can be used for this set. In the present computations, a simple iterative method was employed, in which iteration was continued until the relative change in all coefficients came with ±0.01 percent. Once these coefficients are determined, the temperature becomes completely defined everywhere in the flow domain.

The Special Case K = 0. The assumption of negligible axial conduction in the wall constitutes a simple limiting case of the present analysis. Major sources of simplification include: (a) $\lambda_j=\mu_j$ for all j with both sets being the roots of $J_1(\lambda_j)=0$, and (b) $J_0(\lambda_j)$ constitute an orthogonal set of functions, as well as $J_0(\mu_j)$ of course. Capitalizing on these features, the following values can be obtained for the relevant parameters appearing in the analysis

$$\lambda_0 = 0, \alpha_0 = \mathrm{Pe}^2/2 \qquad (29a)$$

$$B_0 = -\frac{2}{\mathrm{Pe}^2 L} \qquad (29b)$$

$$B_j = \frac{\beta_j\int_0^1 R^3 J_0(\lambda_j R)dR}{4L(\alpha_j-\beta_j)J_0^2(\lambda_j)}, 1\le j\le\infty \qquad (29c)$$

$$C_j = -\alpha_j B_j/\beta_j, \qquad 1\le j\le\infty \qquad (29d)$$

and values of A_0, A_j, and D_j are easily calculable from equation (25). Results for this special case will be presented along with those corresponding to finite K-values in order to illustrate the effect of wall conduction.

Results and Discussion

The foregoing analysis indicates that all the relevant heat transfer parameters at any point in the flow domain can be determined given the values of Peclet number Pe, the wall conduction parameter K, and the dimensionless length of the directly heated length L. While computations based on the foregoing analysis can be performed for any combination of Pe, K, and L, the objective here is to present a sample of the results that would be indicative of the effects of fluid and wall axial conduction on the heat transfer characteristics. Accordingly, two values of Peclet numbers were selected; a small value (Pe = 5) for which fluid conduction is known to be significant and a large value (Pe = 50) for which fluid conduction is negligible. A range of K values was used for each value of Pe. To facilitate comparisons, the actual length of the directly heated section was fixed at $l/r_i=200$ (i.e. $L=40$ at Pe = 5 and $L=4$ at Pe = 50). This length was large enough to allow for a fully developed region within the directly heated section for all the cases considered.

Before generating the results, trials were performed in order to determine the proper value of N. It was found that the value of N (necessary for good accuracy) increases as Pe decreases. On the other hand, K had almost no influence on the value of N. For all the cases presented here, very good convergence in the values of temperature, heat flux, and Nusselt number throughout the flow domain as well as excellent matching at $\eta=0$ and $\eta=L$ were found to be achievable with $N=30$.

Convective Heat Flux. The heat flux at the fluid-wall interface, given by $q_f''=kT/r$ at $r=r_i$, can be expressed in dimensionless form as

$$\frac{q_f''}{q_w''} = 4L\frac{\partial\theta}{\partial R} \qquad \text{at } R=1 \qquad (30)$$

Equations (3), (6), and (9) were substituted in (30) resulting in an expression for each region from which q_f''/q_w'' was computed.

Results for Pe = 5 and 50 are shown in Figs. 1(a) and 1(b), respectively. In both figures, the axial distribution of the

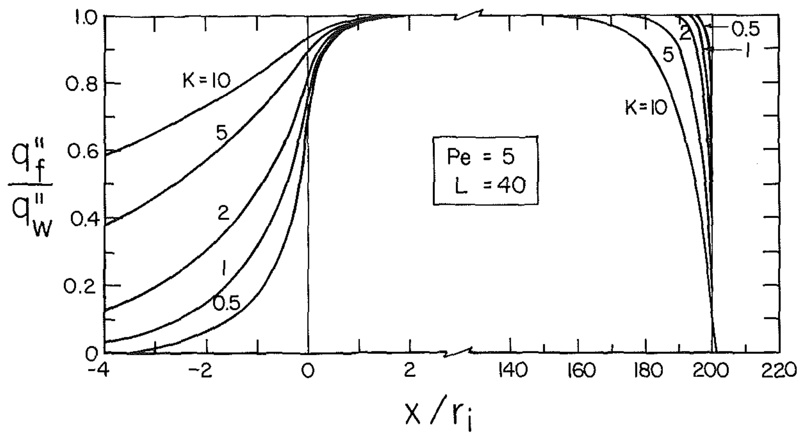

Fig. 1(*a*) Effects of wall conduction on the convective heat flux at low Peclet number

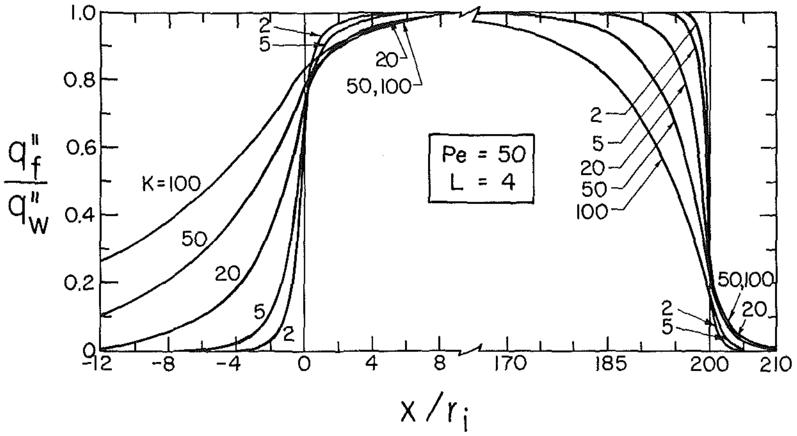

Fig. 1(*b*) Effects of wall conduction on the convective heat flux at high Peclet number

convective heat flux is presented in the neighbourhood of the beginning and end of direct heating using different values of K. Attention must be directed towards the change of scale in the x-axis in these figures and all the future figures as well.

In interpreting the results in Figs. 1(*a*) and 1(*b*), it must be pointed out that for the case $K=0$ the dimensionless quantity q_f''/q_w'' is equal to zero in the upstream ($x/r_i<0$) and downstream ($x/r_i>200$) regions and is uniformly equal to one in the directly heated region ($0 \leq x/r_i \leq 200$). The present results show that axial wall conduction caused substantial deviations from this behavior with significant amounts of heat carried away from the directly heated region. Upstream heating is seen to be more pronounced in magnitude and extent than downstream heating for all values of K, especially at low Peclet numbers. On the other hand, in the directly heated section, the deviation of q_f''/q_w'' from unity is larger in magnitude and extent near the end of heating than near the beginning of heating. These deviations are quite substantial and must be taken into consideration particularly in interpreting experimental results.

The influence of K on the value of q_f''/q_w'' is shown in Figs. (1*a*) and 1(*b*) to be monotonic in the upstream region and the portion of the directly heated region near the end of heating. In both areas the deviation of q_f''/q_w'' from the value corresponding to $K=0$ increases in magnitude and extent as K increases. Downstream from the directly heated region, the starting value of q_f''/q_w'' at $x/r_i=200$ increases as K decreases, but the subsequent rate of decrease along x increases as K decreases. This causes curve crossing in the close vicinity of $x/r_i=200$ which may not be clear in Figs. 1(*a*) and 1(*b*). In the segment of the directly heated region near the beginning of the heating the behavior can be summarized as follows:

(*a*) at $x=0$, the value of q_f''/q_w'' first decreases as K increases and then reverves trend with further increase in K.

(*b*) Some distance away from $x=0$, the trend conforms to a monotonic decrease in q_f''/q_w'' with increase in K.

(*c*) Between these two locations, curves of q_f''/q_w' cross and overlap as shown in Figs. 1(*a*) and 1(*b*).

The magnitude of the convective heat flux is shown by the present results to be dependent on both K and Pe. In the vicinity of the beginning of direct heating, the present results agree in trend with the results of Faghri and Sparrow [3].

Bulk and Wall Temperatures. For the present slug flow condition, the dimensionless bulk temperature can be expressed as,

$$\theta_b = 2\int_0^1 \theta R \; dR \tag{31}$$

Results based on equation (31) are shown in Fig. 2(*a*) for Pe = 5 and Fig. 2(*b*) for Pe = 50 with special emphasis on the areas around the beginning and end of direct heating.

In order to explain the influences of fluid and wall conduction, we will start with the basic behavior which would result when ignoring both mechanisms. This standard behavior is closely represented by the lines of $K=0$ in Fig. 2(*b*). The dimensionless bulk temperature for this case is very close to zero in the upstream region, increases almost linearly

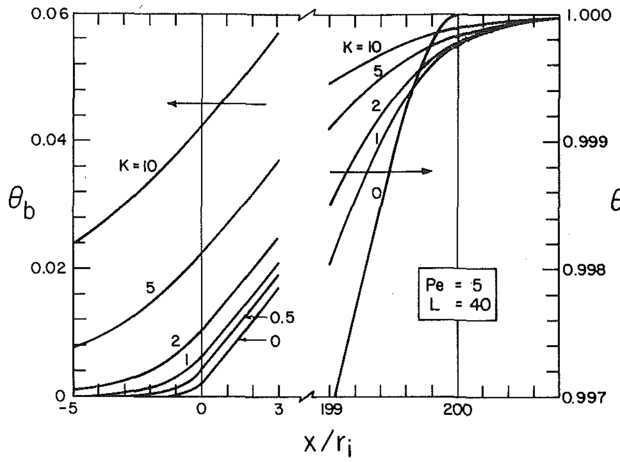

Fig. 2(*a*) **Effects of wall conduction on the dimensionless bulk temperature at low Peclet number**

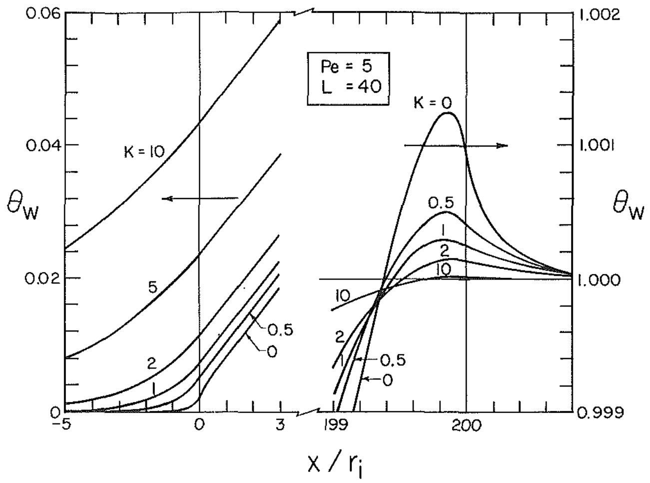

Fig. 3(*a*) **Effects of wall conduction on the dimensionless wall temperature at low Pecelt number**

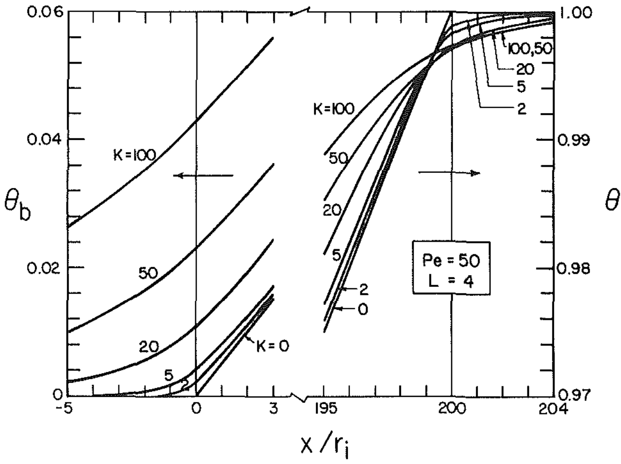

Fig. 2(*b*) **Effects of wall conduction on the dimensionless bulk temperature at high Peclet number**

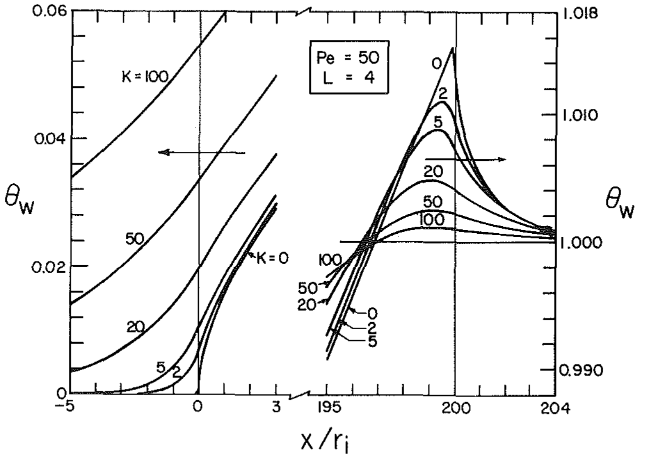

Fig. 3(*b*) **Effects of wall conduction on the dimensionless wall temperature at high Peclet number**

in the directly heated region up to $\theta_b = 1$ at $x = l$, and remains at $\theta_b = 1$ throughout the downstream region. Introducing fluid conduction only (e.g., the lines of $K = 0$ in Fig. 2(*a*)) changes some aspects of this basic behavior with back heating extending for some distance in the upstream region, nonzero temperature at $x = 0$, and deviations from the linear distribtuion of θ_b near the beginning and end of direct heating. Adding wall conduction ($K \neq 0$) causes more increase in θ_b at $x = 0$ with back heating extending further into the upstream region. In addition, the bulk temperature at $x = 1$ starts deviating from one and the region of nonlinear increase in θ_b within the directly heated section becomes larger. Figures 2(*a*) and 2(*b*) clearly indicate that wall conduction can have much more profound effects than fluid conduction.

The value of θ_b at $x = 0$ represents the fraction of the total heat added which is conducted upstream and $(1 - \theta_b)$ at $x = l$ represents the fraction which is conducted downstream. Figures 2(*a*) and 2(*b*) clearly show that the fraction conducted upstream is always higher than the fraction conducted downstream. This can be attributed to the fact that the mechanisms of fluid and wall conduction aid each other in moving heat upstream, but oppose each other in moving heat downsteram. The value of θ_b at $x = 0$ might appear small, thus indicating that only a minor amount of heat is conducted upstream; however, it must not be forgotten that all this heat is extracted from a small portion of the directly heated region near $x = 0$, causing significant effects there. As a matter of fact, θ_b at $x = 0$ is strongly dependent on L, and higher values of θ_b would result for smaller values of L.

The distribution of dimensionless wall temperature is shown in Figs. 3(*a*) and 3(*b*) for Pe = 5 and 50, respectively. Near the beginning of direct heating, wall and fluid conduction are shown to cause monotonic increases in the value of θ_w with wall conduction being the more effective mechanism. In addition, the rate of change in the slope of θ_w at $x = 0$ is shown to decrease with an increae in the value of K. Near $x = l$, the dimensionless wall temperature reaches a maximum before dropping gradually to 1 in the downstream region. Both fluid and wall conduction cause a decrease in the magnitude of the maximum wall temperature. Figures 3(*a*) and 3(*b*) also show that the axial increase in wall temperature upstream from this maximum value deviates more and more from the normal linear form ($K = 0$, Pe = 50) with an increase in K and/or a decrease in Pe.

Nusselt Number. The local Nusselt number is normally defined as $\mathrm{Nu} = 2r_i h/k$, where the heat transfer coefficient is given by $h = q_f''(T_w - T_b)$. In dimensionless form we get,

$$\mathrm{Nu} = \frac{q_f''/q_w''}{2L(\theta_w - \theta_b)} \tag{32}$$

While Nusselt number is one of the most important heat transfer parameters used in engineering design, equation (32)

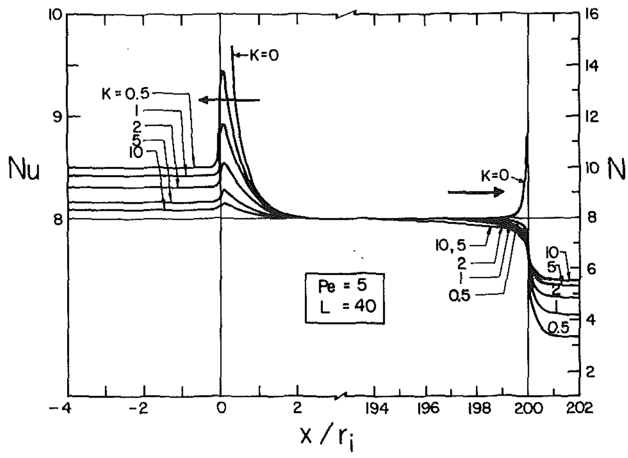

Fig. 4(*a*) Effects of wall conduction on Nusselt number at low Peclet number

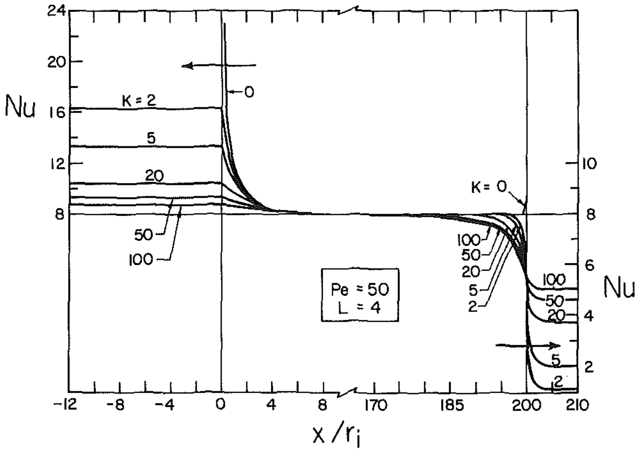

Fig. 4(*b*) Effects of wall conduction on Nusselt number at high Peclet number

illustrates the strong tie between Nu and the quantities q_f''/q_w'', θ_b, and θ_w. All the previously discussed effects of fluid and wall conduction on the convective heat flux, bulk, and wall temperatures will reflect in a combined way on the value of Nusselt number.

Figures 4(*a*) and 4(*b*) show the effect of K on the axial distribution of Nu for low and high Peclet numbers, respectively. The basic distribution at negligible fluid and walk conduction (approximated by $K=0$ and $\mathrm{Pe}=50$) is that of zero Nusselt number in the upstream region, infinite value at $x=0$, decreasing axially to the fully developed value of $\mathrm{Nu}=8$, and remaining constant until the end of direct heating is approached where the value of Nu starts increasing to some finite value at $x=l$. Comparing the lines of $K=0$ in Figs. 4(*a*) and 4(*b*), we conclude that axial fluid conduction strongly influences the value of Nu but does not change the form of the distribution. At any value of x we find that Nu decreases as Pe decreases. As well, the axial distance x required to reach the fully developed value of Nu decreases as Pe decreases.

On the other hand, the wall conduction parameter K is seen to have very strong influences on the magnitude of Nu and its form of distribution along the tube. Generally speaking, at any nonzero value of K, Nusselt number starts at zero in the far upstream region, increases to an almost uniform value (in a plateau) as the directly heated section is approached, reaches a maximum in the directly heated section near $x=0$ before dropping to the fully developed value. As the end of direct heating is approached, the value of Nu starts decreasing down to a uniform value in the downstream region near $x=l$ before dropping further to zero in the far downstream region. The extent of the segment over which Nu has a uniform value is larger in the upstream than the downstream region and both increase as K increases. Also the deviation of Nu from its fully developed value near the end of direct heating increases in magnitude and extent as K increases. In the meantime, the difference between the peak Nusselt number near $x=0$ and the uniform value in the upstream region is shown to decrease with increases in K and/or Pe.

In conclusion, axial wall conduction is shown to be a very important factor in determining the heat transfer characteristics of flows in circular tubes. Its influences can be much more substantial than the influences of axial fluid conduction. All these influences exist in areas surrounding the beginning and end of direct heating, while the fully developed portion of the directly heated region does not experience any changes. It is hoped that the present analysis and results would be useful in the design of heat transfer passages and interpretation of experimental results where applicable.

Acknowledgment

Development of the computer program used in executing the present computations was done in part by Mr. D Austen. Financial assistance provided by the Natural Sciences and Engineering Research Council of Canada is gratefully acknowledged. Thanks are also due to Mrs. Violet M. Lee for her efforts in preparing the typed manuscript.

References

1 Vick, B., and Ozisik, M. N., "Effects of Axial Conduction and Convective Boundary Conditions in Slug Flow Inside A Circular Tube," ASME Journal of Heat Transfer, Vol. 103, 1981, pp. 436–440.

2 Shah, R. K., and London, A. L., *Laminar Flow Forced Convection in Ducts*, Academic Press, New York, 1978.

3 Faghri, M., and Sparrow, E. M., "Simultaneous Wall and Fluid Axial Conduction in Laminar Pipe-Flow Heat Transfer," ASME Journal of Heat Transfer, Vol. 102, 1980, pp. 58–63.

4 Zariffeh, E. K., Soliman, H. M., and Trupp, A. C., "The Combined Effects of Wall and Fluid Axial Conduction on Laminar Heat Transfer in Circular Tubes," *Proceedings of the Seventh International Heat Transfer Conference*, Vol. 3, 1982, pp. 131–136.

5 Natanson, I. P., *Theory of Functions of a Real Variable*, Frederick Ungar Publishing Co., New York, 1961.

J. W. Baughn
Professor.
Mem. ASME

M. A. Hoffman
Professor.

R. K. Takahashi
Postgraduate Research Engineer.

University of California
Davis, Calif. 95616

B. E. Launder
Professor,
University of Manchester Institute
of Science and Technology,
Manchester, England
Mem. ASME

Local Heat Transfer Downstream of an Abrupt Expansion in a Circular Channel With Constant Wall Heat Flux

Measurements have been made of the local heat transfer coefficients to an air flow downstream of an axisymmetric abrupt expansion in a circular pipe with a constant wall heat flux. The experimental technique uses an electrically heated thin gold film on a plastic substrate. The flow upstream of the expansion was unheated and fully developed. Runs were made with small diameter to large diameter ratios of 0.267 to 0.800 and over the Reynolds numbers range of 5,300 to 87,000 (based on downstream diameter). The results include measurements near the expansion corner region where no previous measurements have been reported. These provide clear evidence of a secondary recirculation. Comparisons are also made with previous experimental results in the region of reattachment.

Introduction

The aim of the experimental studies described here was to provide new accurate data on the local heat transfer coefficient in the vicinity of an axisymmetric pipe expansion with steady turbulent flow upstream. This flow is particularly interesting in that peak heat transfer coefficients downstream of the abrupt expansion may be up to 11 or more times the fully developed heat transfer coefficient for the same Reynolds number. These high heat transfer coefficients occur in the region of the reattachment of the shear layer to the tube wall, typically a distance of 5–15 step heights downstream of the abrupt expansion.

Just downstream of the expansion, the fluid recirculates near the wall and is gradually reentrained by the jet. Although mean velocities in the recirculating region are only a few percent of the jet discharge velocity, turbulence levels are high. Flow measurements in this region are thus difficult and, consequently, data are few. Numerical predictions, for example those reported in Chieng and Launder [1], indicate that mean flow parameters in the main flow are "only weakly dependent on the model of turbulent transport in the immediate wall vicinity." However, computed levels of the local heat transfer coefficient are "especially sensitive to the near-wall model." By comparing measured and calculated wall-to-flow mean heat transfer coefficients, inferences may be drawn about turbulence models for near-wall regions of separated flows.

A few investigators have studied turbulent axisymmetric abrupt expansion flows [2–5] and their results, though agreeing fairly well on the magnitude and location of the maximum local Nusselt number, are ambiguous in the corner region (0–3 step heights downstream). The main reason for their high uncertainties in this region is attributed to the high axial thermal conduction in their metal pipe walls in this region and, consequently, to the uncertainties in the large conduction corrections required to determine the wall heat flux.

At the University of California at Davis a technique has been developed in which the tube wall can be heated in such a way as to give a precisely known and virtually uniform heat flux [6, 7]. This technique involves using a thin gold coating vacuum deposited on a pliable polyester sheet as the electrical resistance heating element. The sheet is glued to the inner surface of a thin-walled, cast acrylic tube. Thermocouples glued to the back (i.e., the wall side) of the sheet then measure precise inner wall temperatures. This method results in very low rates of both axial and circumferential heat conduction in the wall. Using this method of wall heating, accurate data were obtained in the corner region of the abrupt expansion.

Review of Previous Experimental Research

Experimental research on the heat transfer in regions of separated and reattached flows inside of pipes and ducts goes back at least to the work of Boelter, Young, and Iversen [2] in 1948. They measured the heat transfer coefficients to air flowing in a circular pipe in the separated and reattachment regions downstream of an orifice at Reynolds numbers of 17,000, 22,900, and 26,400. By using a steam jacket around the downstream portion of the pipe, they achieved essentially isothermal wall surface conditions. They reported maximum heat transfer coefficients near the point of reattachment about four times the fully developed flow values.

Proceeding chronologically, the next studies on axisymmetric abrupt expansions were those of Ede, Hislop, and Morris [3] in 1956. (Ede and co-workers wrote several other relevant reports in this area, but unfortunately none of these seems to have been published in the technical journals.) They ran an extensive series of experiments on heat transfer to flowing water downstream of an abrupt expansion in a circular brass pipe with electrical resistance heating both upstream and downstream of the expansion. The experiments covered a wide range of Reynolds numbers from about 3,700 to 45,000 (based on the downstream pipe diameter). The maximum Nusselt numbers were somewhat lower than those reported by Boelter et al., being roughly three times the fully developed Nusselt number. These lower values may be due at least in part to the fact that they heated the upstream pipe as well as the downstream one; the average heat flux upstream was twice that downstream. They used sets of five copper-constantan thermocouples around the circumference at a series of axial locations to make their outer pipe-wall temperature measurements. These data were then corrected for the temperature drop through the wall. They admitted that this correction resulted in a significant degree of uncertainty in the Nusselt numbers, especially at the higher heat fluxes, since small errors in the wall temperature drop could lead to

---

Contributed by the Heat Transfer Division for publication in the JOURNAL OF HEAT TRANSFER. Manuscript received by the Heat Transfer Division December 7, 1983.

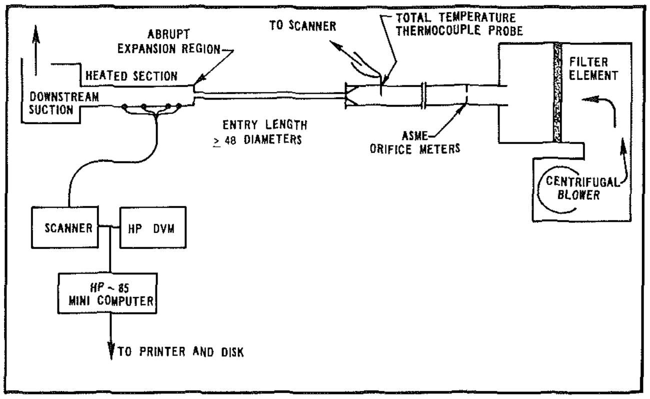

Fig. 1(*a*) Diagram of the experimental apparatus

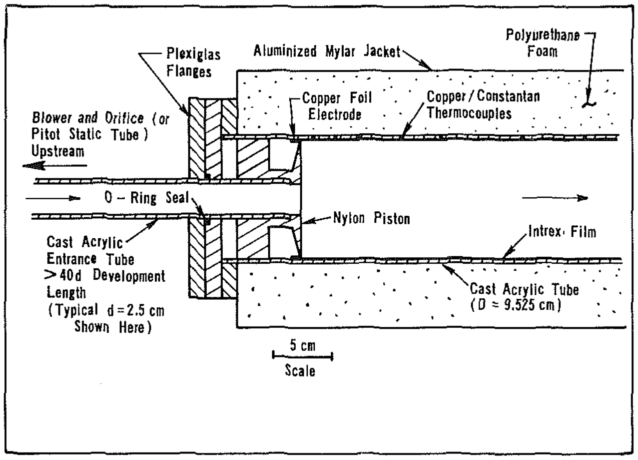

Fig. 1(*b*) Cross section of the heated tube in the abrupt expansion region

large uncertainties in the film temperature drops (which were often less than 1°C).

In 1966, Krall and Sparrow [4] published results of an experimental study of turbulent heat transfer downstream of an orifice in a circular tube. Unlike the earlier work of Boelter et al. [2], they used an electrically heated stainless steel tube downstream of the orifice, giving them an essentially constant wall heat flux boundary condition. Also water was used as the coolant instead of air. They used 32 iron-constantan thermocouples mounted on the top half of the tube at various axial lcoations (and three thermocouples on the bottom of the tube to check for symmetry). They ran four different orifices with diameters of 0.25, 0.33, 0.50, and 0.67 tube diameters over a range of Reynolds numbers from 10,000 to 130,000 at two different Prandtl numbers of 3 and 6. Their extensive results revealed a strong dependence of the maximum heat transfer coefficient on Reynolds number (also implied by Ede's results) varying approximately as $\mathrm{Re}^{2/3}$. They also found that the smaller the orifice diameter (and hence the greater the distance travelled by the jet in terms of small jet diameters before reattachment), the larger was the value of the maximum heat transfer coefficient at a given flow rate. Values of the maximum Nusselt number ranged from three to nine times the fully-developed values at distances of 1.25 to 2.5 pipe diameters downstream of the orifice.

In 1970, Zemanick and Dougall [5] published results of detailed experiments on the turbulent heat transfer downstream of an abrupt expansion in a circular pipe. As in the early work of Boelter et al. [2] they used air as the working fluid. They imposed a nearly constant heat flux boundary condition downstream of the abrupt expansion by using an electrically heated pipe. The primary instrumentation consisted of thermocouples mounted on the outer surface of the downstream tube. Zemanick and Dougall's results agree quite well with those of the earlier researchers insofar as the axial variation of the local Nusselt number is concerned. Their peak Nusselt number, however, increased approximately as the 0.8 power of Reynolds number and appeared to have significant compressibility effects in some runs. Their carefully documented experimental results have been compared in [1] with numerical results based on a two-layer model of the near-wall zone.

The present experiments improve upon the work of Zemanick and Dougall [5] in two important ways. First, the effect of wall conduction, for which a large correction was often required in the earlier work, is almost entirely eliminated. Second, compressibility effects are reduced by using a larger apparatus, resulting in smaller velocities for the same Reynolds numbers.

Experimental Apparatus

At the upstream end of the experiment, a 1 hp squirrel cage blower delivered ambient air into either a 6.35 cm (2-1/2 in.) i.d. or 9.53 cm (3-3/4 in.) i.d. cast acrylic tube (see Fig. 1(*a*)). The tube contained either an ASME orifice plate or a pitot-static probe, depending upon the flow rate being used. These flow-measuring devices were connected via tygon tubing to a micromanometer capable of measuring pressure differences to within ±0.03 mm of water. Also located in the tube, through feed-through holes in the tube wall, were two calibrated 0.08 mm (3 mils) diameter copper-constantan thermocouples, each glued to the outside of two 3-mm-dia ceramic rods. These thermocouples measured the total temperature of the upstream air flow at the tube axis.

On the downstream end of the entry tube was a smooth transition into a smaller cast acrylic tube of inner diameter *d*. This latter, unheated tube led directly into the abrupt expansion and was at least 48 *d* in length to ensure an effectively fully developed velocity profile just before the abrupt expansion. A detailed drawing of the abrupt expansion region is

Nomenclature

c_p = heat capacity
d = upstream tube diameter
D = heated tube (downstream) diameter
h = heat transfer coefficient
H = step height $(D-d)/2$
$\dot{m}$ = mass flow rate
Nu = Nusselt number
$\mathrm{Nu}_{\mathrm{DB}}$ = Nusselt number determined by Dittus-Boelter Equation
$\mathrm{Nu}_{\max}$ = maximum Nusselt number
Pr = Prandtl number
q_e'' = local electrical heat flux
q_1'' = local conduction heat loss
R = electrical resistance
Re = $4\dot{m}/\pi\mu D$
Re_d = $4\dot{m}/\pi\mu d$
T = local wall temperature
$\bar{T}$ = average tube wall temperature
T_B = local bulk temperature
T_f = film temperature
T_{ref} = temperature at which R_{ref} was measured
V = voltage across heated tube
w = width of gold film
x = axial position
$x_{\max}$ = position of maximum Nusselt number
α = temperature coefficient of resistivity of the gold film
δ_g = thickness of gold film
ρ_e = electrical resistivity

shown in Fig. 1(*b*). On the downstream end of each of the small diameter tubes was a nylon "piston" which defined the abrupt expansion into the heated tube which had a fixed diameter of $D = 9.525$ cm. Five different values of d (2.54, 3.81, 5.08, 6.35, and 7.62 cm) were used to obtain a range of d/D values between 0.267 and 0.800.

The heated tube had a heated length of 171 cm (18 dia) and a wall thickness of 3.2 mm (1/8 in.). The tube material, cast acrylic, was chosen for its low thermal conductivity, which ensured minimal axial conduction in the wall. It was round within 0.1 mm, and the diameter varied by less than 0.3 mm. To the inner surface of the tube was glued a sheet of Intrex,[1] a thin transparent gold-film vacuum-deposited on a 0.13 mm (0.005 in.) polyester sheet substrate. By passing an alternating current through the gold film on the Intrex sheet, an essentially uniform heat flux was provided. The Intrex was glued to the tube while being tightly pressed against the tube inner surface by an inflated rubber tube. A capillary cement was injected with a hypodermic syringe through small holes in the tube wall to ensure a permanent bond between the Intrex and the tube wall.

Copper foil strip "electrodes" glued with silver-loaded paint to the surface of the Intrex at each end of the heated tube were the means by which electrical contact was made with the gold film. The copper electrodes were connected to a variable transformer in series with a 120V a-c regulator, allowing an adjustable, but stable, a-c voltage to be dialed into the electrodes. Voltages used in the experiments ranged from 42 to 125V a-c, providing a total power to the heated tube of 42 to 380 W. This, in turn, gave heat fluxes of 0.008 to 0.072 W/cm^2. These low heat fluxes and the corresponding low wall temperatures (typically 5-20°C above the bulk temperature) result in negligible buoyancy effects.

To minimize axial conduction in the area near the corner of the abrupt expansion, the copper foil electrode was located about 5 cm upstream of the large tube entrance, away from the tube flanges. The conduction from the power leads was negligible. To further reduce axial conduction, the abrupt expansion piston was designed of low thermal conductivity nylon and with minimal contact area with the Intrex/tube wall (Fig. 1(*b*)). To minimize radial conduction losses to the ambient air,the tube was covered with 5.1 cm of polyurethane foam and, to minimize radiation losses to the room, the foam was wrapped in an aluminized mylar jacket.

The local tube wall temperatures were measured with thermocouples (0.08 mm copper-constantan) epoxied to the back side of the Intrex through small holes in the tube wall. A conduction analysis showed that the temperature drop through the sheet and conduction losses by the leads were negligible. There were 35 calibrated thermocouples located at different axial positions along the tube. The nonuniform axial thermocouple spacing ranged from 5 mm near the abrupt expansion corner to 150 mm near the exit of the large diameter, heated tube. Most of the axially distributed thermocouples were at the top of the tube. However, six additional thermocouples placed at other angular locations were used to check the symmetry of the heat transfer to the flow. The thermocouple leads tied into a reference temperature junction box in an HP 3495A multiplex scanner. The thermocouple EMF's were measured with an HP 3455A digital multimeter to an accuracy of ± 5 μV ($\pm$0.12°C). This multimeter was also used for the measurement of the gold coating voltage. The scanner and multimeter were controlled by software in an HP-85 micro-computer through an HP interface bus. The raw data were then stored on tape and later transferred to a disk on a minicomputer, where the final data reduction was made.

Measurements and Data Reduction

Two considerations determined the amount of electrical power used to heat the downstream tube. The first was that the heat flux should be small enough to allow the properties of the air to be regarded as constant and uniform. The second was that the difference between the wall and bulk temperatures should be high enough that measurement uncertainties of temperature differences (wall to bulk fluid) would be small. The power chosen was that which gave a maximum temperature difference of about 20°C. At the location on the tube wall where the maximum heat transfer rates occurred, the temperature difference was only about 4-5°C, since Nusselt numbers in this region were typically 4-5 times the fully developed values. With the uncertainties in our temperature measurements (about $\pm$0.1°C) the corresponding uncertainties in the maximum Nusselt numbers due to temperature measurements were about $\pm$3 percent.

With the flow rate and electrical power set, the system was allowed to reach steady-state conditions as determined when the temperature difference between a given thermocouple in the heated tube wall, and the total temperature inlet probes became constant. The total time for data acquisition after steady-state conditions were reached was less than 1 min. Although the ambient temperature changed by as much as 1°C per hour, this did not affect the measurements since the thermal response of the system and data acquisition time were much shorter than this.

A total of 54 runs were made with different values of expansion ratios d/D and Reynolds numbers. Runs made from the first set of data to the last set over a period of three months gave repeatability within 5 percent, and usually within 3 percent. Two runs were made with $d/D = 1.0$ (i.e., a straight pipe) and with the heated tube rotated 180 deg end-to-end, such that the thermocouples ordinarily in the corner area of the abrupt expansion were now at the tube exit. The $d/D = 1.0$ runs were compared with the well-documented studies of heated tube entrance regions in order to verify that the present experimental apparatus was indeed operating correctly. The results of these runs are discussed later.

The first step in the data reduction was the calculation of the local electrical heat flux generated in the Intrex film, $q_e''(x)$. Three factors cause $q_e''(x)$ to vary with location x: variations in the local thickness of the gold film, $\delta_g(x)$, the variation of the width of the Intrex sheet w and the local temperature effect on the electrical resistivity of the Intrex. The first two factors were assumed negligible after examining the results of the runs with $d/D = 1.0$ (discussed later). The effect of the local temperature on the gold film resistivity is given by the film temperature coefficient of resistivity α. This was measured in separate tests with sample strips of the Intrex placed in a constant temperature calibration bath where it was found that $\alpha = 0.00116\,°\mathrm{C}^{-1}$. With a known value for α and the gold film temperatures measured by thermocouples, the temperature effect on $q_e''(x)$ could be included in the data reduction.

The local heat flux was calculated as

$$q_e''(x) = \frac{I^2}{w}\frac{d}{dx}[R(x)] \tag{1}$$

where I is the electrical current, and $R(x)$ is the electrical resistance between one electrode and the position x. Introducing the gold film resistivity, $\rho_e(T)$, then

$$\frac{d}{dx}[R(x)] = \frac{1}{w}\frac{\rho_e(T)}{\delta_g(x)} \tag{2}$$

Also $I = V/R(\bar{T})$, where V is the voltage across the Intrex and $R(\bar{T}) = R(T_{\mathrm{ref}})\,\{1 + \alpha[\bar{T} - T_{\mathrm{ref}}]\}$ is the resistance across the entire Intrex sheet of average temperature $\bar{T}$. T_{ref} is the temperature at which $R(T_{\mathrm{ref}})$ was measured.

---

[1] Intrex is a product of Sierracin/Sylmar Co., Sylmar, Calif.

The local temperature affects the local resistivity as

$$\frac{\rho_e(T)}{\delta_g(x)} = \frac{w}{L}\{1+\alpha[T-T_{\mathrm{ref}}]\}R(T_{\mathrm{ref}}) \tag{3}$$

where L is the length of the Intrex sheet. Equation (1) finally becomes

$$q_e''(x) = \frac{V^2}{wLR(T_{\mathrm{ref}})}\,\frac{\{1+\alpha[T-T_{\mathrm{ref}}]\}}{\{1+\alpha[\bar{T}-T_{\mathrm{ref}}]\}^2} \tag{4}$$

with $w = \pi D$ for our circular tube geometry. Equation (4) can be used with the measured voltage, dimensions, reference resistance, and local temperature to obtain the local heat flux.

The local bulk temperature was determined as

$$T_B(x) = \frac{\pi D}{\dot{m}c_p}\int_0^x [q_e''(x) - q_l''(x)]dx + T_{B_i} \tag{5}$$

where T_{B_i} is the inlet bulk temperature at the abrupt expansion, $q_l''(x)$ is the local conduction heat flux through the Intrex to the insulation.

The local conduction heat fluxes were determined using a two-dimensional conduction analysis. The boundary conditions for this analysis were the measured inside temperatures of the Intrex and a free-convection heat transfer coefficient on the outside of the insulation. The results are insensitive to the outside boundary conditions because of the thickness of the insulation. The local conduction heat loss in all cases was less than 2 percent of the local electrical heating q_e'' for all positions more than 5 cm from the expansion. At 1 cm from the expansion, it was always less than 10 percent of q_e''. After evaluation of q_e'', equation (5) was then numerically integrated using the standard trapezoidal rule.

The local heat transfer coefficient was then calculated from

$$h(x) = \frac{q_e''(x) - q_l''(x)}{T(x) - T_B(x)} \tag{6}$$

Finally, the local Nusselt number was calculated as

$$\mathrm{Nu}(x) = \frac{h(x)D}{k(T_f)} \tag{7}$$

where T_f is the local film temperature $T_f = 0.5\,[T(x) + T_B(x)]$. Since the difference in wall temperature and the bulk temperature is small, there is no significant effect of using the film temperature for evaluating the fluid properties compared to using the bulk temperature.

The uncertainties in the reported results, estimated with odds of 20:1 and using the method of [8], are as follows: the uncertainties in the Reynolds numbers are about ±2.3 percent at all Reynolds numbers; the uncertainties in the Nusselt numbers range from about ±6.6 percent at the peak Nusselt numbers to about ±2 percent at the lowest Nusselt numbers. Details on the method of estimating the uncertainties for this experimental technique are given in [9, 10].

Experimental Results

Symmetry Check. The six thermocouples located circumferentially around the heated pipe showed a maximum temperature difference from each other of 0.4°C. The average temperature difference was typically < 0.1°C, corresponding to a variation of Nusselt number around the pipe of about 1 percent. This verifies that the average flow and heat transfer were axisymmetric and that buoyancy effects are negligible in the Reynolds number range of this study.

Results for d/D = 1.0. The results for an expansion ratio of d/D = 1.0 (i.e., a straight pipe) run are shown in Fig. 2. Also shown for comparison is the Nusselt number distribution recommended by Kays and Crawford (i.e., equation (8-38) and Table 13-7 (Re = 50,000) in [11]). The present results show good agreement with this equation with a maximum deviation of 4 percent. It may be noticed that the data points do not show a random scatter of 4 percent, but more of an axially dependent "slow" variation about the prediction curve. This variation is probably due to the variation of gold film thickness, and thus the electrical resistance, on the Intrex. Similar 4 percent variations in the gold film thickness have been observed by the authors in other experiments using the Intrex film [6, 7].

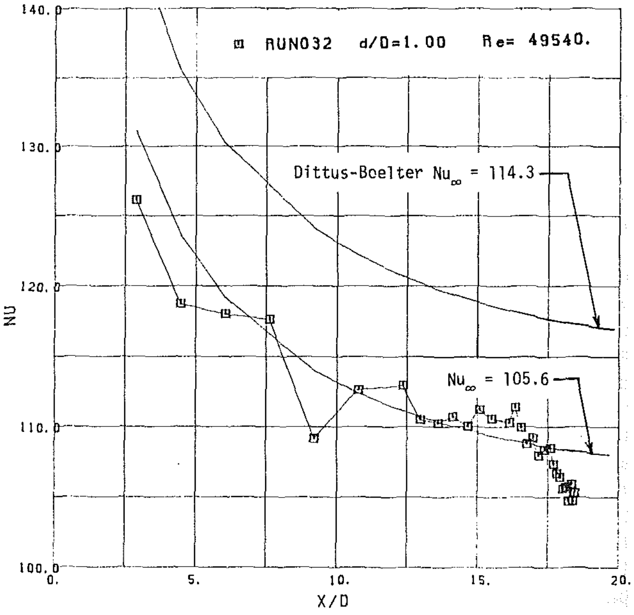

Fig. 2 Experimental results for the thermal development in the straight tube compared to the analytical equation in Kays and Crawford [11] for two values of the fully developed Nusselt number Nu

Also shown on Fig. 2 is a scaling of the Kays and Crawford variation of the Nusselt number in the inlet region [11], but now using the classic Dittus-Boelter relation for the fully developed Nusselt number instead of the Kays and Crawford value of 105.6.

$$\mathrm{Nu}_{\mathrm{DB}} = 0.023\mathrm{Re}^{0.8}\mathrm{Pr}^{0.4} = 114.3$$

(i.e., the Kays and Crawford curve has been multiplied by 114.3/105.6 to obtain the DB curve). As expected, the present results lie about 10 percent below the extrapolated Dittus-Boelter relation, in general agreement with the experimental results of [12] at a Reynolds number of about 50,000.

The good agreement of our d/D = 1.0 run with documented results is a verification that the apparatus gives results consistent with published results, and hence gives confidence in the abrupt expansion results described next.

Results of Abrupt Expansion Runs. The measured variation of the Nusselt number with distance downstream of the expansion is shown for the five expansion ratios over a range of Reynolds numbers in Figs. 3-7. The symbols on these figures are the calculated points from the experimental data and have been connected with straight lines by the computer graphics program. Following convention, streamwise distance is normalized by the step height $H(H = 0.5(D-d))$, and the Nusselt number is normalized by the value for fully developed pipe flow given by the Dittus-Boelter formula. Generally, the results display a similar character to earlier studies with a peak level of heat transfer coefficient occurring at about ten step heights downstream, followed by a gradual reversion toward the value associated with fully developed pipe flow. Because the present measurement technique effectively eliminates axial conduction, the data give not only more details of the Nusselt number variation, but also significant

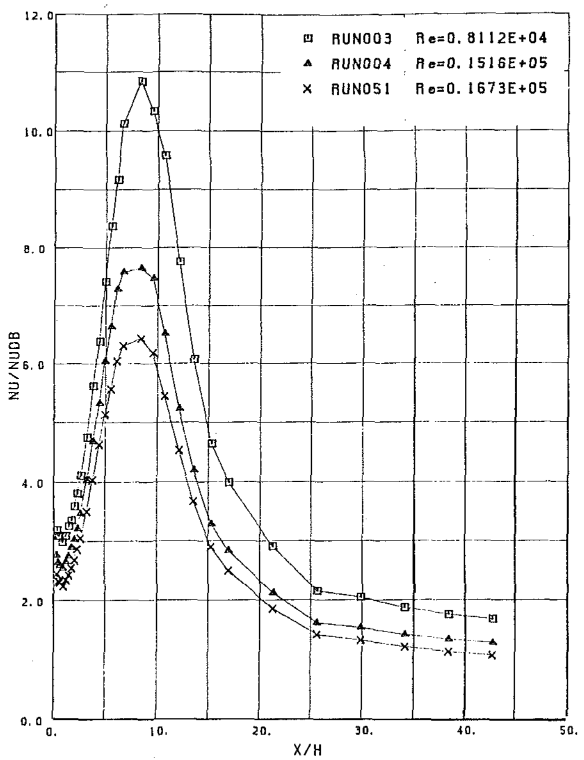

Fig. 3 Heat transfer downstream of the abrupt expansion for *d*/*D* = 0.266 and various Reynolds numbers

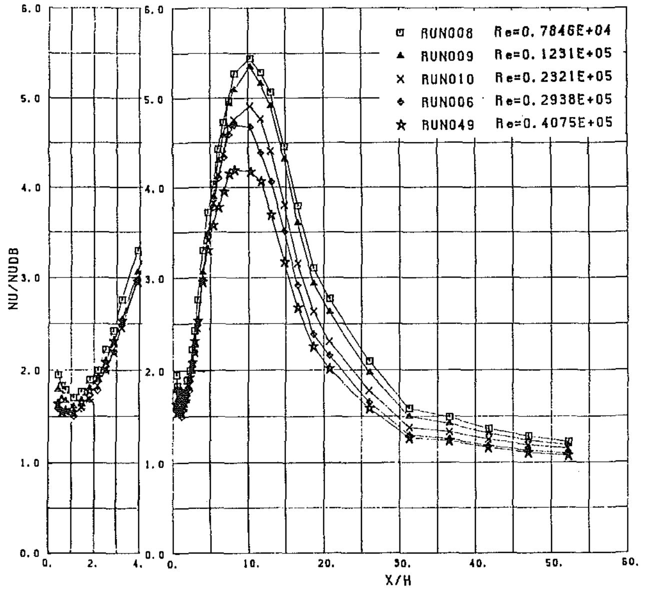

Fig. 4 (*a*) Heat transfer downstream of the abrupt expansion for *d*/*D* = 0.400 and various Reynolds numbers, and (*b*) with adjusted scales to clarify corner region results

quantitative *differences* in behavior from that hitherto reported.

For all expansion ratios, one sees that as the Reynolds number is progressively raised, the value of $\mathrm{Nu}/\mathrm{Nu}_{\mathrm{DB}}$ falls monotonically. This behavior is qualitatively in accord with the water tests of [3] but disagrees with the air study by Zemanick and Dougall [5] where, for downstream Reynolds numbers above about 30,000, the ratio of peak to fully developed Nusselt numbers was reported as independent of Re. The maximum Nusselt number from the present tests is plotted in Fig. 8 as a function of *upstream* Reynolds number, Re_d; this choice of Reynolds number (in place of Re_D) greatly

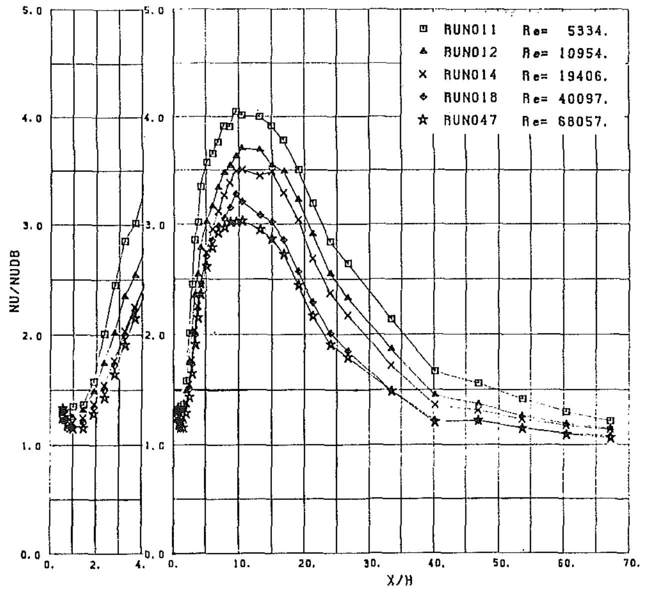

Fig. 5 (*a*) Heat transfer downstream of the abrupt expansion for *d*/*D* = 0.533 and various Reynolds numbers, and (*b*) with adjusted scales to clarify corner region results

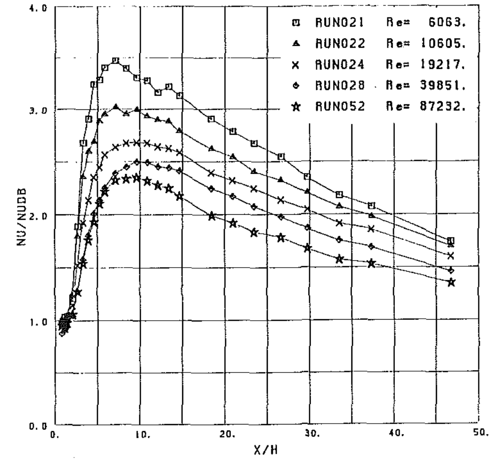

Fig. 6 Heat transfer downstream of the abrupt expansion for *d*/*D* = 0.666 and various Reynolds numbers

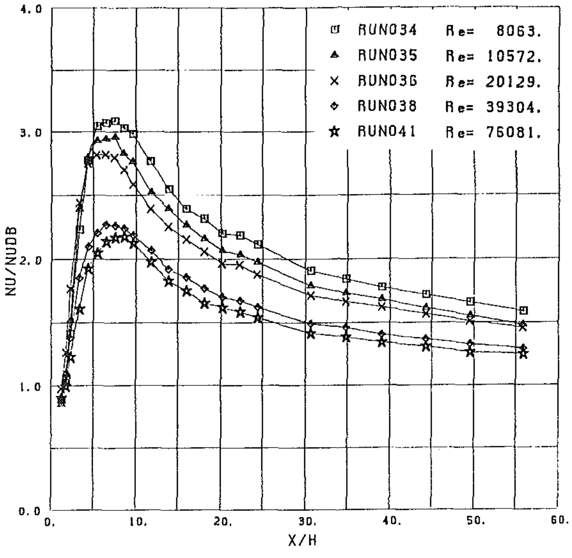

Fig. 7 Heat transfer downstream of the abrupt expansion for *d*/*D* = 0.800 and various Reynolds numbers

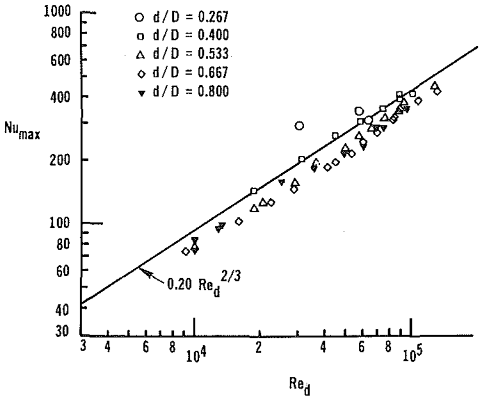

Fig. 8 Reynolds number dependency of the maximum Nusselt number compared to an equation suggested by Zemanick and Dougall [5]

reduces the effect of expansion ratio on the maximum Nusselt number, Nu_{max}. The data indicate an exponent of approximately 2/3, although there is some suggestion that the slope increases as the Reynolds number is raised.

There is a weak suggestion in the data that the Reynolds number affects the distance (x/H) to the position of Nu_{max} (see Figs. 3–7). However, although the uncertainties in the results are small, they are still large enough to make this suggestion speculative.

Figure 9 shows for Re ≈ 19,000 the variation in the position of maximum Nusselt number for various expansion ratios. Increasing the expansion ratio (i.e., decreasing d/D) initially raises the distance to the position of maximum heat transfer, a behavior consistent with the variation in the reattachment point observed in the plane, single backward-facing step [13]. For axisymmetric expansions greater than 2, however, ($d/D < 0.5$), the distance to maximum heat transfer decreases as the expansion ratio, d/D is decreased. So far as we know, this latter behavior has not been reported hitherto, but it does seem consistent with the limit of a small axisymmetric jet discharged into a large plenum. The outer edge of such a free jet advances at an angle such that, *if it* were not influenced by the presence of the wall, it would attach to the wall at approximately six step heights.

The present measurements succeed in resolving the variation of Nusselt number very near the corner region. As discussed earlier, previous experiments have been unable to obtain accurate data in this zone due to conduction in the tube wall. The results of Emerson [14] do seem to indicate a minimum in the Nusselt number; however, he attributes this to wall conduction. The data here show a mutually consistent decrease as x/H approaches low values. For the three largest step heights (d/D = 0.266, 0.400, and 0.533) a minimum value of Nu occurs at approximately one step height from the step, a feature that very strongly suggests the presence of a counterrotating eddy trapped in the corner beneath the larger and more active recirculating flow region. Notice that the minimum level of Nu is larger, the greater the expansion ratio. This reflects, at least in part, that the relevant length scale for convective heat removal is that of the recirculating zone itself. The fact that the Nusselt numbers are greater than in fully developed pipe flow indicates that the level of the turbulent transport is high even though the recirculating velocities will be only a few percent of the bulk mean velocity. This feature agrees at least qualitatively with what is known about turbulent transport processes in recirculating flows. For the two smallest expansions (d/D = 0.667 and 0.80), no distinct minimum in the Nusselt number can be discerned.

A direct comparison with the measurements of Zemanick and Dougall [5] is provided in Figs. 10–14. Zemanick and Dougall [5] point out that at a Reynolds number of 40,754 their Mach number was 0.66 and speculate that compressibility effects may be affecting their data. It is appropriate to comment, however, that an increase in Mach number reduces the spreading rate of the mixing layer and this would tend to shift the reattachment point (and, we may suppose, the positioning of the Nusselt number peak) *downstream* rather than upstream relative to the incompressible limit. The data for an expansion ratio of 0.533 (0.54 for Zemanick and Dougall [5]) exhibit a rather similar discrepancy for a nominal Reynolds number of 10,000, while those at Re = 47,000 display more serious differences. Although it is not possible to be certain of the cause of the differences between the two sets of measurements, the need to apply, in the case of Zemanick and Dougall's [5] experiments, large corrections for the effects of axial conduction seems the most probable source of error.

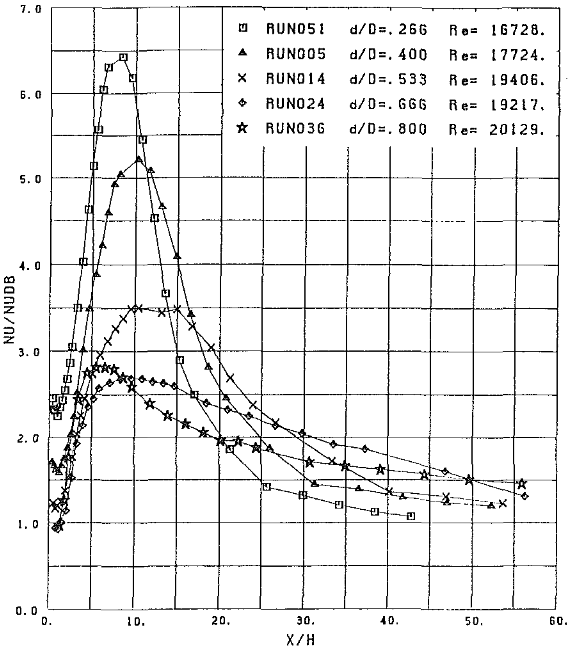

Fig. 9 Effect of changing step heights at approximately the same Reynolds number

Conclusions

1 The electrical heating of a gold-coated plastic sheet has been found to provide an ideal means of measuring heat transfer coefficients in separated gas flows. Despite the rapid variation of surface temperatures that may occur (due to the variations in heat transfer coefficient), the effects of conduction in the film and substrate are of minor significance even near the corner region. This has permitted a detailed mapping of the Nusselt number in the vicinity of the expansion, a region that has hitherto not been resolved by experiments.

2 For a given expansion ratio, the ratio of peak to fully developed Nusselt number falls as the Reynolds number is raised, although the rate of decrease becomes small at the upper end of the Reynolds number range covered in these experiments.

3 The peak level of Nusselt number is correlated fairly well by the Reynolds number in the upstream pipe irrespective of expansion ratio. Over the present range of Reynolds numbers, the Nusselt number varies approximately as $Re_d^{2/3}$, although there is some indication that the exponent increases for $Re_d > 50{,}000$.

4 For expansion ratios of 2:1 or greater, the Nusselt number reaches a minimum value at about one step height downstream of the expansion, a feature that suggests the

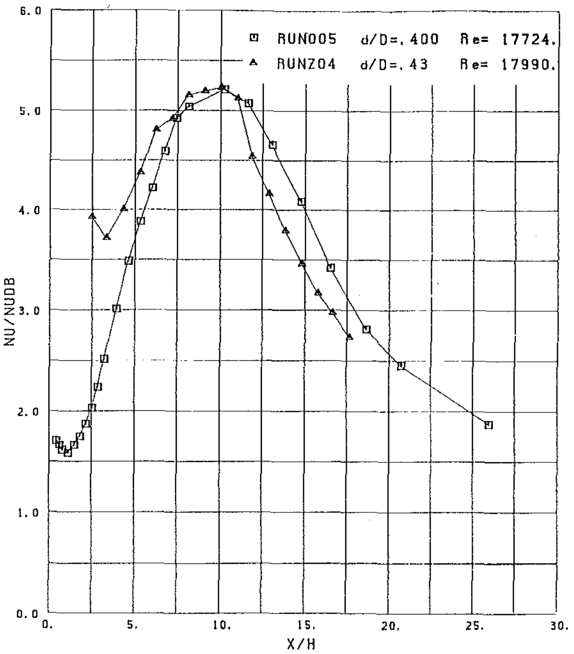

Fig. 10 Comparison of the present *d*/*D* = 0.400, Re ~ 18,000 results with those of Zemanick and Dougall (run Z04) [5]

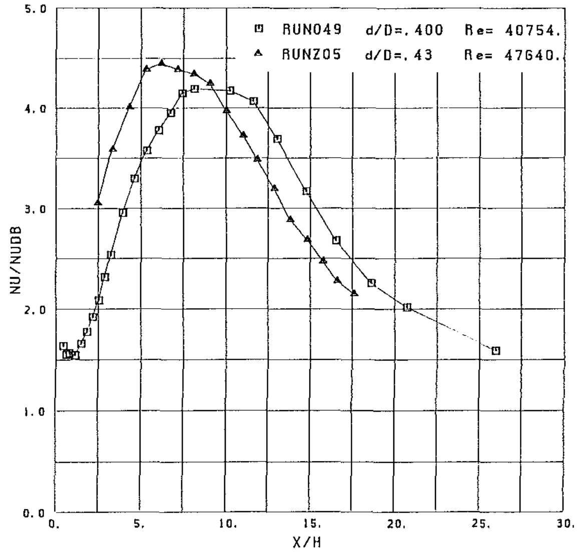

Fig. 11 Comparison of the present *d*/*D* = 0.400, Re ~ 41,000 results with those of Zemanick and Dougall (run Z05) [5]

existence of a counterrotating secondary vortex in the corner region.

Acknowledgment

The authors gratefully acknowledge the support of the National Science Foundation for this research under grant no. MEA-8103657.

References

1 Chieng, C. C., and Launder, B. E., "On the Calculation of Turbulent Heat Transport Downstream From an Abrupt Pipe Expansion," *Numerical Heat Transfer*, Vol. 3, 1980, pp. 189-207; (discussion in Vol. 5, 1982, pp. 493-496.)

2 Boelter, L. M. K., Young, G., and Iversen, H. W., "An Investigation of Aircraft Heaters XXVII—Distribution of Heat Transfer Rate in the Entrance Section of a Circular Tube," NACA-TN-1451, 1948.

3 Ede, A. J., Hislop, C. I., and Morris, R., "Effect on the Local Heat-Transfer Coefficient in a Pipe of an Abrupt Disturbance of the Fluid Flow:

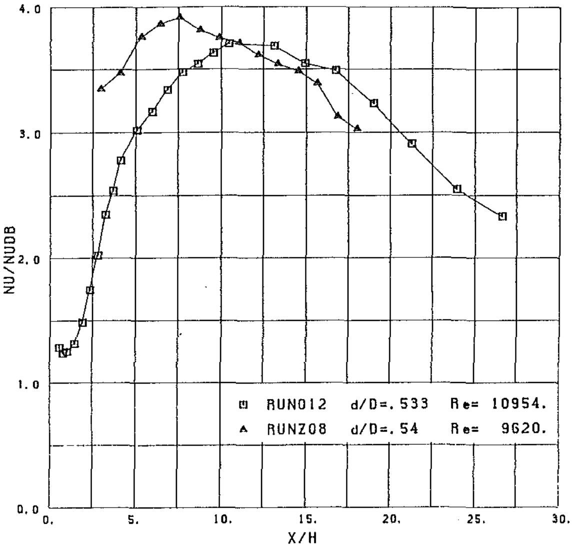

Fig. 12 Comparison of the present *d*/*D* = 0.533, Re ~ 11,008 results with those of Zemanick and Dougall (run Z08) [5]

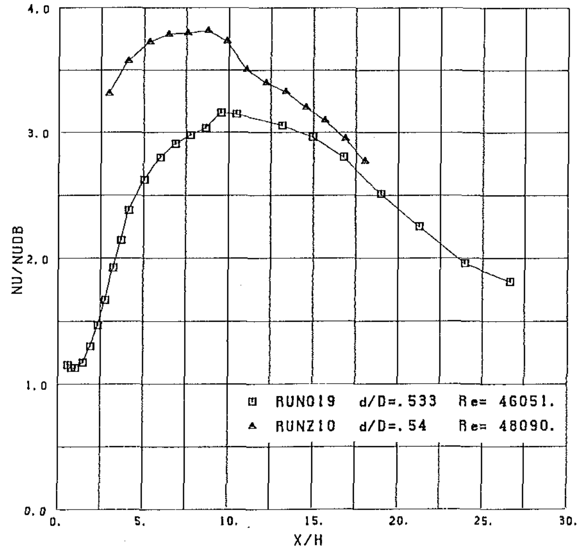

Fig. 13 Comparison of the present *d*/*D* = 0.533, Re ~ 46,000 results with those of Zemanick and Dougall (run Z10) [5]

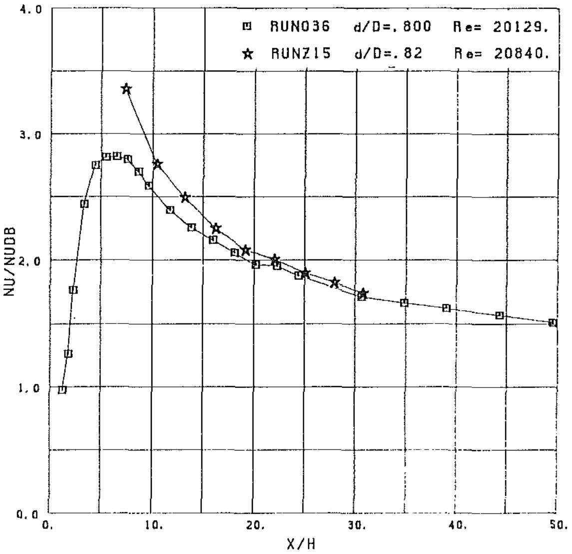

Fig. 14 Comparison of the present *d*/*D* = 0.800, Re ~ 20,000 results with those of Zemanick and Dougall (run Z15) [5]

Abrupt Convergence and Divergence of Diameter Ratio 2:1," *Proc. Inst. Mech. Engrs. London*, Vol. 170, 1956, p. 1113.

4 Krall, K. M., and Sparrow, E. M., "Turbulent Heat Transfer in the Separated, Reattached and Redevelopment Regions of a Circular Tube," ASME JOURNAL OF HEAT TRANSFER, Vol. 83, 1961, p. 131.

5 Zemanick, P. P., and Dougall, R. S., "Local Heat Transfer Downstream of Abrupt Circular Channel Expansion," ASME JOURNAL OF HEAT TRANSFER, Vol. 92, 1970, p. 53.

6 Baughn, J. W., Hoffman, M. A., Launder, B. E., and Takahashi, R., "Turbulent Heat Transport in Circular Ducts with Circumferentially-Varying Heat Flux," ASME JOURNAL OF HEAT TRANSFER, Vol. 106, 1984, pp. 64–70.

7 Baughn, J. W., Takahashi, R. K., Hoffman, M. A., and McKillop, A. A., "Local Heat Transfer Measurements Using an Electrically-Heated Thin Gold-Coated Plastic Sheet," *Proceedings HTD*, Vol. 31, 22nd National Heat Transfer Conference, Aug. 1984.

8 Kline, S. J., and McKlintock, F. A., "Describing Uncertainties in Single Sample Experiments," *Mechanical Engineering*, Vol. 75, No. 1, 1953, pp. 3–8.

9 Kaul, S., "An Experimental Study of the Local Heat Transfer From a Cylinder to Air in a Channel with Blockage," M.S. thesis, University of California, Davis, 1984.

10 Lee, D., "Measurement of the Turbulent Heat Transport Downstream of an Abrupt Expansion in a Circular Duct with a Constant Wall Temperature," M.S. thesis, University of California, Davis, 1984.

11 Kays, W. M., and Crawford, M. E., *Convective Heat and Mass Transfer*, 2d ed., McGraw-Hill, 1980.

12 Black, A. W., and Sparrow, E. M., "Experiments on Turbulent Heat Transfer in a Tube with Circumferentially Varying Thermal Boundary Conditions," ASME JOURNAL OF HEAT TRANSFER, Vol. 89, 1967, pp. 258–268.

13 "The Backward Facing Step," *Proceedings of the 1980-1981 AFOSR-HTTM-Stanford Conference on Complex Turbulent Flows*, Test Case 0421, Stanford University, 1981.

14 Emerson, W. H., "Heat Transfer in a Duct in Regions of Separated Flow," *Proceedings of the Third International Heat Transfer Conference*, Chicago, AIChE, Vol. 1, Aug. 1966, pp. 267–275.

Entrainment Effects on Impingement Heat Transfer: Part I—Measurements of Heated Jet Velocity and Temperature Distributions and Recovery Temperatures on Target Surface

B. R. Hollworth
Associate Professor.
Mem. ASME

S. I. Wilson
Research Assistant.

Mechanical and Industrial
Engineering Department,
Clarkson College of Technology,
Potsdam, N.Y. 13676

Experiments were conducted to characterize a heated turbulent air jet discharged from a square-edged orifice having length to diameter equal to unity. Reported are measurements of mean axial velocity and total temperature in the jet as well as recovery temperatures on a flat surface normal to the jet axis. A simple theoretical model, which predicts distributions of recovery temperature consistent with the test data, is given.

Introduction

Arrays of impinging fluid jets have found a number of applications where high rates of convective heat or mass transfer are required. Uses range from the drying of paper stock and films to the cooling of gas turbine engine components. A number of experimental studies (such as [1-3]) have been conducted to obtain convective heat transfer data for such arrays; these data are then used in the design of impingement systems. The objectives of such work have been to determine how convective heat transfer rates are affected by such parameters as fluid flow rate, fluid properties, and system geometry. Martin [4] has recently compiled a comprehensive review of the related literature.

For most impingement cooling configurations, jets are discharged into a confined space in which also circulates the heated spent fluid. It is well known that the performance of these systems is adversely affected by the entrainment of such fluid into the jets; it is likely that this causes the heat transfer "degradation" observed [5-7] in impingement-with-crossflow situations. Heat transfer coefficients have traditionally been defined in terms of the difference between the jet plenum temperature (T_p) and the target temperature (T_s), so that the effect has simply been buried in the reported values of h. Recently Striegl and Diller [8] examined the effect of thermal entrainment upon the heat transfer to an impinging slot jet. Little work has been done, however, to isolate and measure this effect for axisymmetric jets. Thus a study was initiated here with that ultimate objective.

The entrainment process which occurs within a typical array of impinging jets is quite complex, owing to the nonuniform distributions of velocity and temperature in the fluid circulating between the jets. It was felt appropriate, therefore, to begin with the simplest possible case: a single heated turbulent air jet, submerged in quiescent room temperature air, and impinging normal to a flat surface. This study is divided into two tasks described below:

Task 1: Design and assemble a test rig for local heat transfer measurements and conduct tests to characterize the jet itself. These include making measurements of mean velocity and total temperature within the jet, and of recovery temperatures over the surface on which the jets impinge. Also develop an analytical model to predict the distribution of such recovery temperatures.

Task 2: Measurement of local heat fluxes on the target surface. These measurements are used to develop a heat transfer correlation that specifically accounts for the temperature difference between the jet and the surrounding fluid.

This paper presents the methods and results for Task 1; and Task 2 will be the subject of a subsequent paper. The independent test variables and their ranges for this study are given in Table 1. These ranges correspond to those for which heat transfer measurements will be made for Task 2. In all cases, the entrained fluid is atmospheric air, available at the prevailing room temperature and local barometric pressure. Jets are always turbulent, but exit velocities are low enough so that compressibility effects are small.

For these tests, jets are discharged from square-edged orifices with aspect ratio equal to unity. This orifice design corresponds to those employed for a number of practical applications and is essentially the same geometry used for earlier impingement studies [3] at Clarkson. Both orifices were calibrated and found to have discharge coefficients in the range 0.75–0.77 for the range of exit velocities (see Table 1) used.

It is worth noting that, while the literature contains abundant data on velocity and temperature distributions in free jets originating from nozzles or long tubes, the data for jets issuing from orifices such as considered here are scanty.

Test Apparatus and Methods

The test apparatus for this study is shown in Fig. 1. It consists of an air delivery loop, a jet plenum with interchangeable orifice plates, and a large flat surface (oriented normal to the jet axis) on which the jet impinges. The water

Table 1 Test variables

Variable	Symbol[a]	Range
Orifice diameter	d	2.5 mm, 10 mm
Ambient temperature	T_a	20–25°C
Jet plenum temperature	T_p	$T_a{}^a$, $T_a + 30°\mathrm{C}$, $T_a + 60°\mathrm{C}$
Jet exit velocity	U_o	50–125 m/s
Jet Reynolds Number	Re	7×10^3–70×10^3
Standoff	z	d–$30d$

[a] Only velocities were measured for $T_p = T_a$

Contributed by the Heat Transfer Division for publication in the JOURNAL OF HEAT TRANSFER. Manuscript received by the Heat Transfer Division August 17, 1983.

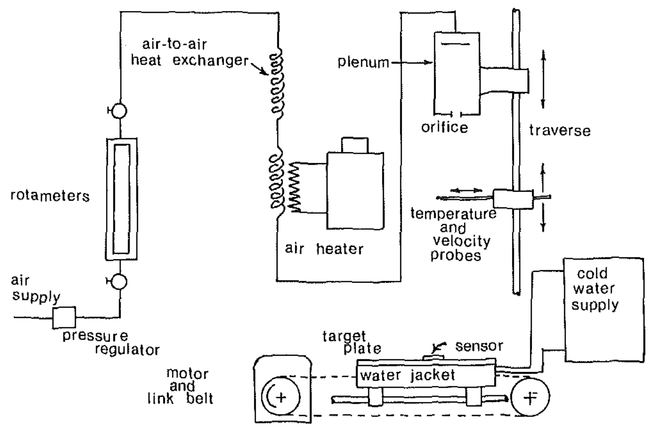

Fig. 1 Test system

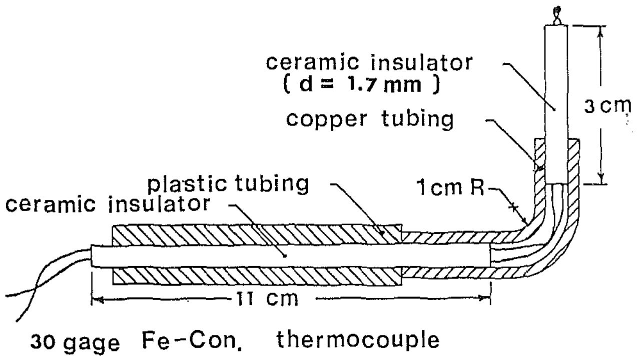

Fig. 2 Total temperature probe

jacket shown in Fig. 1 will be used to provide an isothermal target for the heat transfer measurements of Task 2. For the current work, it is used simply as a moveable platform to support an adiabatic plate on which recovery temperatures are measured. The apparatus includes, also, velocity and total temperature probes with suitable traversing mechanisms. The rig and test methods are described briefly below, and in more detail in [9].

The test fluid is filtered and dried air delivered by a compressor at a discharge pressure of appoximately 6 bars absolute. Air flow to the test rig is controlled with hand-operated valves and measured with precision (±1 percent) rotameters. The constant supply pressure produced by a regulator in the line, along with the constant back pressure (atmospheric pressure), insure constant mass flow rate during each test or series of tests. The experiment included making measurements for both isothermal ($T_p = T_a$) and heated ($T_p > T_a$) jets. It was necessary, in both cases, to precisely control the jet plenum temperature by appropriately heating or cooling the supply air. For those tests requiring an isothermal jet, a large (approx. 20 m^2 of heat transfer surface) finned tube crossflow heat exchanger was used to bring the jet air into thermal equilibrium with ambient air. In some instances, the temperature of compressed air reaching the laboratory differed from the ambient temperature by as much as 3°C; by using the heat exchanger described above, it was always possible to bring T_p to within $\pm 0.5^\circ$C of T_a. A 6-kW circulation heater with feedback temperature controller supplied the plenum with heated air whenever tests were to be conducted with nonisothermal jets. With this closed-loop system, T_p could be set and held to within 0.2°C of the desired value.

The jet plenum is an airtight box with square cross section, fabricated from 9-mm aluminum plate. Outside dimensions are 102 mm × 102 mm × 216 mm parallel to the jet orifice axis. One endwall is the orifice plate, at whose center is located the jet orifice. There are two such interchangeable plates – one for each ($d = 10$ mm, $d = 2.5$ mm) of the orifices tested. Air enters at the opposite end of the chamber and a baffle is located immediately beneath the inlet to diffuse the entering flow. The plenum also contains two screens to mix the jet air. Instrumentation includes two taps and two iron-constantan TC's (thermocouples) for measurement of stagnation pressure and temperature; all are installed downstream of the second screen. As Table 1 indicates, the maximum temperature difference ($T_p - T_a$) for these tests was not large. It was thus necessary to measure all fluid temperatures as precisely as possible to avoid large percentage uncertainties in the data. Preliminary tests indicated that, while the air temperature T_p was quite uniform in the plenum, it was subject to measurement errors sometimes approaching 3-4°C, about half of which was due to conduction along the stainless steel sheath which carried the TC leads. It was found [9], that this error was virtually eliminated if the probe was inserted until the junction was at least midway into the plenum. Errors due to radiation between the warm exposed TC junctions and the relatively cool plenum walls were eliminated by enclosing each junction within a polished cylindrical shroud and by lining the plenum with thermal insulation to raise the inside surface temperature.

Nomenclature

C_D = discharge coefficient
C_p = specific heat at constant pressure, J/kg-K
C_1-C_5 = numerical constants
d = jet orifice diameter, m
h = convective heat transfer coefficient, W/m^2-K
$\dot{m}$ = mass flow rate, kg/s
M = blowing parameter, $\rho_j U_o / \rho_\infty U_\infty$
P_a = ambient pressure, Pa
r = recovery factor; radial distance, m
$r_{1/2}$ = jet half-width, m
Re = jet Reynolds number, $4\dot{m}/\pi\mu d$
s = axial distance from pole of jet, m
$\bar{s}$ = s/d
s_o = distance between jet pole and orifice exit plane, m
T_a = ambient temperature, K
T_o = local total temperature in jet, K
T_{om} = total temperature on jet centerline, K
T_p = jet plenum temperature, K
T_r = recovery temperature, K
T_s = surface temperature, K
U = jet axial velocity, m/s
U_m = jet centerline velocity, m/s
U_o = jet exit velocity, m/s
U_∞ = crossflow velocity, m/s
v = radial velocity in wall jet, m/s
V = maximum radial velocity in wall jet, m/s
x = axial distance from orifice exit plane, m
$\bar{x}$ = x/d
y = distance normal to target surface, m
Y = thickness of wall jet, m
z = standoff; normal distance between orifice and target surface, m
$\bar{z}$ = z/d
α = exponent, see equation (1) and (2)
ΔP = pressure difference, Pa
ΔT = temperature difference, K
μ = dynamic viscosity, Pa-s
ρ_∞ = crossflow density, kg/m^3
ρ_j = jet exit plane density, kg/m^3
θ = $(T_r - T_a)/(T_p - T_a)$

Distributions of axial velocity U and total temperature T_o within the jet were measured by manually traversing with suitable probes mounted on the three-axis Unislide mechanism. Velocities were measured using a conventional pitot-static probe (dia = 1.7 mm) connected to suitable manometers. The probe was sufficiently small to resolve velocity profiles in most regions of the jet(s), except near the exit plane of the smallest ($d = 2.5$ mm) orifice. Measurements of total temperature were made using a special probe (Fig. 2) designed to minimize conduction error. It was configured with a 90 deg bend so that the sheath material nearest the junction was aligned with the jet axis, along which there was a relatively small temperature gradient. Moreover, the probe sheath segment nearest the junction was made from low conductivity magnesium oxide of small diameter to further reduce conduction losses. This design was found to be quite satisfactory. Procedures for measuring velocities and total temperatures in the jet were essentially the same – except that, of course, different probes and readout devices were used in each case. Ambient temperature T_a was measured with two thermocouples located at the same elevation as the jet orifice. One was placed 15 cm off the jet axis and the second at $r = 30$ cm. The average of the two readings was taken to be T_a; and they differed, in the worst case, by 0.8°C.

Techniques used to align the probe with the jet axis are discussed in [9]. For each test run, the plenum pressure corresponding to the desired jet velocity was set using the pressure regulator and control valves in the air supply line, and the desired plenum temperature was obtained by appropriately setting the heater controller. For tests requiring an isothermal jet, the heat exchanger replaced the heater. After plenum conditions has reached steady state, centerline velocities (or temperatures) were measured for $0 \leq \bar{x} \leq 30$ at intervals of approximately $d/2$. Finally, radial profiles were established by moving the probe to the appropriate $\bar{x}$ and traversing radially outward until essentially zero velocity or excess temperature was found. This procedure was repeated for each test condition indicated in Table 1. All such measurements were made in the absence of a target surface.

The adiabatic impingement surface, with detail of sensing element, is shown in Fig. 3. The surface is a laminated assembly of styrofoam and balsa wood, with dimensions given in the figure. Radial profiles of recovery temperature T_r were obtained by traversing the surface slowly past the jet. The sensing element is a small (3.2-mm-dia) polished copper disk to whose back surface is soldered a copper-constantan TC. The disk is imbedded flush with the surface, at the center of the target. Heat leak from the sensor was minimized by making it as thin as possible (to reduce edge losses) and by providing a dead air space behind it. All surfaces of the air space were lined with aluminum foil to eliminate radiation, and TC wires were kept small (dia = 0.13 mm) to minimize lead losses. For a given test run, the exit velocity U_o and the plenum temperature T_p were set exactly as described. A pitot tube was used to locate the jet axis, and the target plate was positioned so that the jet stagnation point was at the center of the temperature-sensing disk. The plate was oriented in a horizontal plane so that the jet would always impinge on its long axis as the plate was traversed past the jet. Values of T_r at the stagnation point were first measured at various $\bar{z}$ by moving the plenum parallel to the jet axis. Radial profiles, T_r versus r, were then obtained by traversing the plate past the stationary jet plenum for several $\bar{z}$.

An error analysis [9] was conducted to estimate the uncertainty in the data obtained. Typical uncertainty for velocity measurements is ±1 percent. No special effort was made to measure *absolute* temperatures precisely, as data were correlated in terms of temperature differences. However, all thermocouples were calibrated together and found to agree to within ±0.2°C over the temperature range of this experiment.

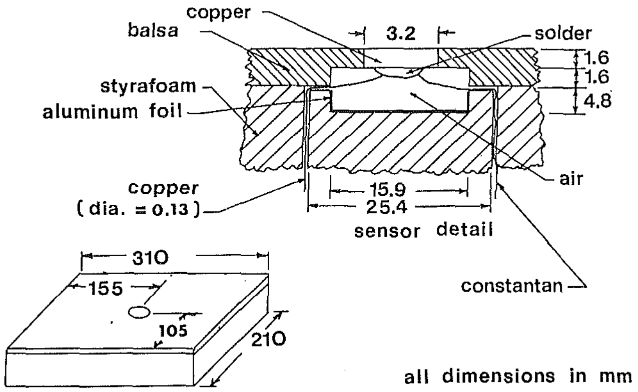

Fig. 3 Adiabatic plate, with sensor

The uncertainty in excess total temperature $(T_o - T_a)$ was estimated to be ±0.7°C, while the uncertainty in excess recovery temperature varied from ±0.5°C near the stagnation point to ±0.7°C at larger r-values of interest.

Analytical Model

The surface flow associated with an impinging jet is divided into two regions. In the region nearest the stagnation point (usually termed the deflection zone) flow is turned from the axial to the radial direction, and there is a significant favorable pressure gradient on the surface. Tani and Komatsu [10] indicate that this zone extends to $r \cong 2.5 r_{1/2}$ where $r_{1/2}$ is the jet halfwidth at the distance $\bar{z}$ from the orifice in the absence of the target surface. In the region outboard of the deflection zone (termed the wall jet zone) flow is essentially radial and the surface pressure is everywhere equal to the prevailing ambient pressure. Proposed is a simple analysis which gives an approximate, but useful, prediction of the distribution of recovery temperature on that part of the surface washed by the wall jet.

Glauert [11] first analyzed the wall jet by treating it as inner layer, behaving as a conventional turbulent boundary layer, joined to an outer layer, which behaves essentially as a radial free jet. Subsequent experiments [12, 13] verified his predictions of velocity distributions and rate of growth. These investigators determined that velocity profiles in the wall jet are "experimentally" similar, and that the maximum radial velocity V (which occurs at the juncture of the inner and outer layers) decays according to

$$V/U_o = C_1/(r/d)^{\alpha} \tag{1}$$

where C_1 is a constant. The exponent α was found to be in the neighborhood of 1.1; a value of $\alpha = 1$ is obtained for a free jet spreading on a frictionless surface. Moreover, the wall jet spreads such that its thickness Y, measured normal to the surface, increases almost linearly with r. Poreh et al. [14] found that, for sufficiently large $\bar{z}$, V does not depend explicitly upon U_o or d. Instead, it depends only upon $\bar{z}$ and the jet's kinematic momentum flux, $K = C_D(\pi/4)d^2 U_o^{\,2}$. The relationship eventually established from their measurements is

$$Vz/\sqrt{K} \simeq 1.32(r/z)^{-\alpha} \tag{2}$$

In terms of the variables used in this paper, it becomes

$$V/U_o = 1.32\sqrt{C_D}(\pi/4)\bar{z}^{\alpha-1}(r/d)^{-\alpha} \tag{3}$$

where their data indicate that $\alpha = 1.1$. Thus equation (3) implies that V/U_o is a weak function of $\bar{z}$.

The heat content of a jet impinging on an adiabatic surface remains constant and may be determined from the initial jet flow ($\dot{m}$) and jet temperature (T_p). This is expressed as

$$\int_o^Y \rho v \Delta T 2\pi r dy = \dot{m}(T_p - T_a), \tag{4}$$

where ΔT is excess total temperature $(T_o - T_a)$ and v is radial velocity. Equation (4) may be rewritten as

$$rY\Delta T_m V \int_o^1 \frac{\Delta T}{\Delta T_m} \frac{v}{V} \frac{dy}{Y} = \frac{\dot{m}(T_p - T_a)}{2\pi\rho} \tag{5}$$

where $\Delta T_m(r)$ is maximum excess total temperature. This value occurs, in this situation, near the wall and may be taken as an estimate of the excess recovery temperature $(T_r - T_a)$. It has been assumed above that both density and specific heat are constant, which is reasonable for relatively low velocities and moderate jet heating such as considered here. If one assumes, also, that both velocity and temperature profiles are self-similar, the integral that appears in equation (5) is a constant whose value is determined by the shapes of these nondimensional profiles. The assumptions of similarity are approximations. As previously noted, velocity profiles are not, in the rigorous sense, similar. While there are a number of references that contain temperature data for wall jets, none correspond exactly to the case (radial flow on an adiabatic surface) considered here.

The variation of recovery temperature may be determined (to within a multiplicative constant) from equation (5) using suitable expressions for $\dot{m}$, V, and Y. The initial flow rate is given by

$$\dot{m} = C_D \frac{\pi}{4} d^2 \rho U_o \tag{6}$$

where C_D is the discharge coefficient of the jet aperature. The maximum radial velocity V is given by equation (1), where we assume $\alpha = 1.0$ and use $Y = C_2 r$ where C_2 is a numerical constant. If these are substituted into equation (5) the following simple expression for the local recovery temperature results

$$\theta \equiv (T_r - T_a)/(T_p - T_a) = C_3 \left(\frac{r}{d}\right)^{-1} \tag{7}$$

The value of the numerical constant C_3 may be determined (see the Results section) from our test data. If, on the other hand, one uses equation (3) for V, equation (5) gives

$$\theta = C_4 \bar{x}^{-0.1} (r/d)^{-0.9} \tag{8}$$

where C_4 is a numerical constant. Finally, the work of Cooper [15], related to buoyant plumes impinging upon a ceiling, suggests a correlation involving the enthalpy flux $Q = \dot{m}c_p(T_p - T_a)$ and kinematic momentum flux of the jet. For the case considered here (Q and K both constant for the entire jet flow), one obtains a relationship whose form is identical to that of equation (8).

Results and Discussion

Mean axial velocities were determined from differential pressure (ΔP) measurements from the pitot probe using

$$U = \left[2C_p T_o \left\{1 - \left(\frac{P_a}{P_a + \Delta P}\right)^n\right\}\right]^{1/2} \tag{9}$$

where P_a is a barometric pressure, T_o is local total temperature, and $n = (\gamma - 1)/\gamma$. It is well known that jets entrain considerable amounts of the fluid through which they pass, which causes the jet's mass flux to increase with $\bar{x}$ though the total momentum flux (in the absence of buoyant forces) remains constant. Thus the profiles become wider and "flatter" as low momentum ambient fluid is incorporated into the jet. Figure 4 shows the variation of centerline velocity U_m for jets heated to 30°C and 60°C above T_a. Velocity distributions in nonisothermal jets are not, in general, the same as those in isothermal jets. For example, the centerline velocity of a heated jet (which is less dense than the surrounding fluid) drops off more rapidly than that of an isothermal jet, and its width grows at a greater rate with $\bar{x}$. For our tests, however, the degree of heating is small enough, in both cases, so that its effect on U_m is insignificant. In fact, our data [9] for an isothermal jet give virtually the same decay curve as shown in Fig. 4. The initial region of a free jet contains a potential core in which the centerline velocity remains equal to the exit velocity U_o. The length of the core depends upon aperture geometry and is ordinarily in the neighborhood 6-8d for jets discharged from conventional nozzles. For the orifices tested here, the length is 2-3d, which agrees well with those reported by Obot [16] for orifices of similar design. Moreover, there is a good agreement with his measurements of U_m/U_o versus $\bar{x}$.

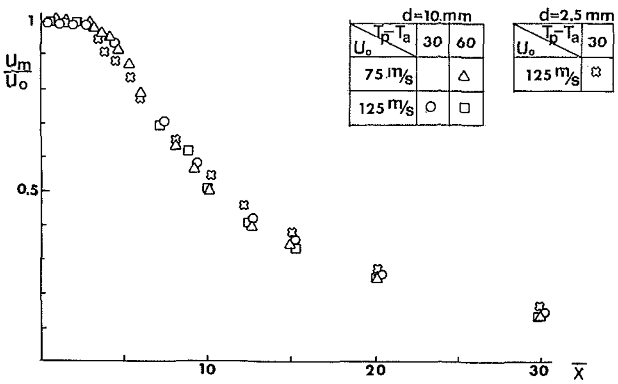

Fig. 4 Decay of centerline velocity, heated jet

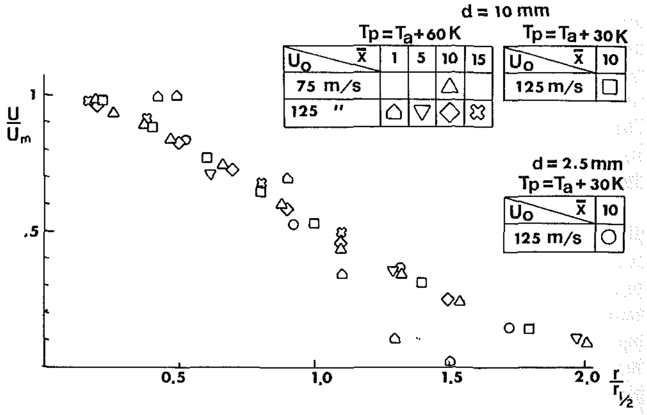

Fig. 5 Velocity profiles, heated jet

The main region of a free jet is characterized by the existence of similar velocity profiles; this is true [17] for both isothermal and nonisothermal jets. Figure 5 shows profiles for heated jets measured at several axial stations. If velocity U is normalized by dividing by local centerline velocity U_m, and radial position r by dividing by local half-width $r_{1/2}$ (the local value of r at which $U = U_m/2$), then these may all be collapsed onto a universal profile, as the figure shows. Included also is one profile taken at $\bar{x} = 1$, which shows the uniform velocity within the potential core of the jet's initial region. Data for an isothermal jet [9] exhibits the same behavior, and agreement between our profiles and data in the literature [13, 17] is quite satisfactory.

The main region of an isothermal free jet is bounded by a cone. To further characterize its behavior one must specify the location of the cone's vertex (the so-called pole of the jet) and the rate at which the jet diverges. Centerline velocity in this region decays according to

$$U_m/U_o = C_5/(\bar{x} + s_o/d) \tag{10}$$

where C_5 is a constant, and s_o is the distance between the pole and the exit plane. Equation (10) was linearized and the least-

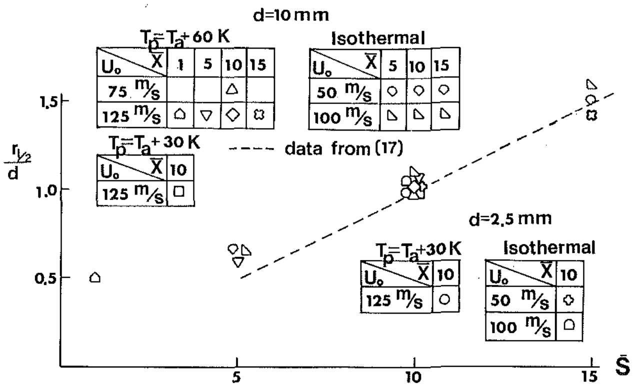

Fig. 6 Spreading of jet

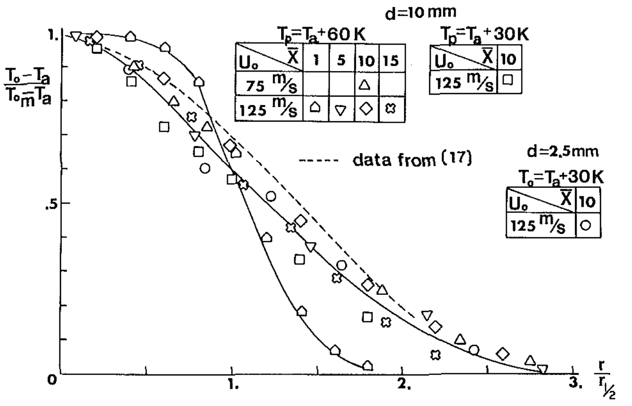

Fig. 7 Total temperature profiles

squares method used to fit a line to our data for $\bar{x} \geq 8$. In this fashion, the pole was found to be about $0.05d$ downstream of the exit plane. Abramovich [17] indicates that, as a point of reference, $s_o \cong 2d$ for a conventional nozzle. Figure 6 shows the rate at which the jets spread. Values of $r_{1/2}$ were read directly from radial velocity profiles, and $\bar{s}$ is axial distance measured from the pole. For our case the pole is virtually in the exit plane, so that $\bar{x}$ and $\bar{s}$ are essentially equal. The dashed line, whose equation is

$$r_{1/2}/d=0.097\bar{s} \tag{11}$$

represents experimental data reported by Abramovitch [17] for a nozzle of unspecified geometry, while Hrycak et al. [13] find a slope of 0.093 for an orifice design close to ours. It is important to note that such linear behavior is exhibited only in the main region of the jet. A best fit to our data for $\bar{x} \geq 10$ gives the line

$$r_{1/2}/d=0.097\bar{s}+0.05 \tag{12}$$

which is essentially in agreement with the results previously cited. It should be pointed out, also, that jet boundaries are actually somewhat curved for nonisothermal jets. While data points for heated jets should not, therefore, have been included in determination of the line, we felt it to be permissible because the degree of heating is, for this experiment, quite moderate.

Temperatures within the jet were measured using the probe shown in Fig. 2, which actually measures a recovery temperature T_r related to the local total temperature by

$$T_o=T_r+(1-r)\,U^2/2C_p \tag{13}$$

Values of total temperature were calculated from equation (13) using a recovery factor (r) of 0.75, a value reported [18] for a probe of similar design. The largest "correction" that had to be made was 2°C. Figure 7 shows temperature profiles obtained in this fashion; radial position is nondimensionalized in the manner used when showing radial distributions of velocity. The profiles of Fig. 7 are similar in the main part of the jet, and are somewhat broader than velocity profiles. This is consistent with behavior observed by other investigators, as reported by Abramovitch [17]; in fact the dashed line in the figure is a typical temperature profile taken from this reference. Total temperature on the jet axis should vary according to

$$(T_{om}-T_a)/(T_p-T_a)=f(\bar{x}) \tag{14}$$

where $f=1$ in the initial part of the jet and f decays as $\bar{x}^{-1}$ in the main part. Our own data [9] (not shown here) shows this behavior, and agrees well with results given by Abramovitch for the main part of the jet. For smaller $\bar{x}$ such a direct comparison could not be made, as our jets had considerably shorter potential core regions.

The next phase of this study will involve measurement of local heat flux (q) for a heated jet impinging on a flat plate with uniform surface temperature T_s. Local heat transfer coefficients are defined by

$$q=h(T_\infty-T_s) \tag{15}$$

where T_∞ is a suitable fluid temperature. Florschuetz and Metzger [19] rightfully refer to this as a "three-temperature" problem, and it has similarities to film cooling in which a coolant (with temperature T_2) is introduced onto a solid surface to form a blanket which thermally isolates the surface from an ambient fluid with temperature T_1. The performance of such a scheme is characterized by a film effectiveness (η) defined by

$$\eta=(T_1-T_r)/(T_1-T_2) \tag{16}$$

where local recovery temperatures (T_r) are usually measured on an adiabatic surface. For subsequent calculations of heat transfer on the same surface, the effective fluid temperature is taken to be T_r as calculated from equation (16). While there is no rigorous basis for this procedure, it has proven to give satisfactory results except in regions quite near the holes or slots through which coolant is injected. This procedure has also been used to correlate heat transfer from an impinging plume in a study [15] previously cited.

It is felt that a similar approach might prove useful for the problem at hand. To explore this possibility, measurements of local T_r were made on the adiabatic plate of Fig. 3 at the same test conditions for which heat flux measurements are to be made. Figures 8 and 9 show the resulting distributions of T_r on a flat surface normal to the heated jet axis. No tests were run for the case $T_p=T_a$ because several investigators, including ourselves, have already made such measurements. It was found [2, 3, 20] that, for this condition, recovery temperatures may exceed T_p due to entrainment; this effect is discussed in [2]. Values of the dimensionless recovery temperature at the stagnation point decay with $\bar{z}$ as shown by Fig. 8. The element (see Fig. 3) used to measure T_r is somewhat larger than our smallest orifice, so that (for $d=2.5$ mm) it actually indicates a recovery temperature averaged over a circle of diameter $1.3d$. For small $\bar{z}$, T_r drops off rapidly with r/d near the stagnation point. Hence the data for $d=2.5$ mm falls slightly below that for $d=10$ mm for $\bar{z} \leq 5$.

Figure 9 shows radial profiles of dimensionless T_r, which are essentially similar for large $\bar{z}$ ($\bar{z} \geq 5$) when r is normalized by dividing by $r_{1/2}$ at $\bar{x}=\bar{z}$. It is apparent, from comparing Figs. 7 and 9, that profiles of dimensionless T_r are considerably broader than those of dimensionless T_o. This occurs because the relatively hot fluid near the impinging jet's axis becomes the fluid layer nearest the solid surface as the jet spreads over the target plate. It is again worth examining the similarity between this impingement problem and a film cooling situation. For the latter, effectiveness is usually high

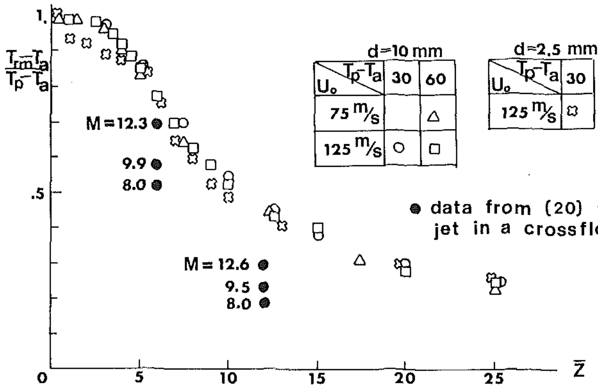

Fig. 8 Stagnation point recovery temperatures

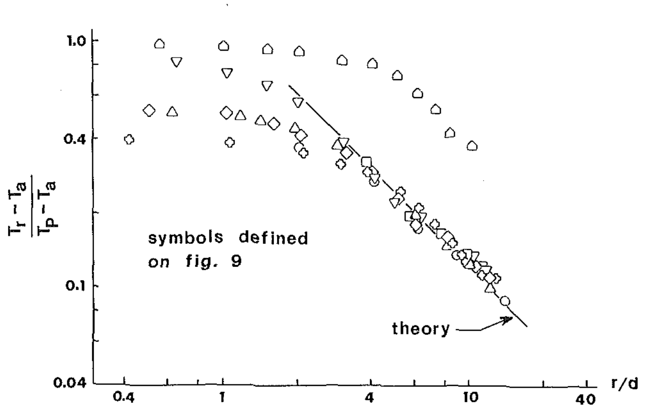

Fig. 10 Wall jet recovery temperatures

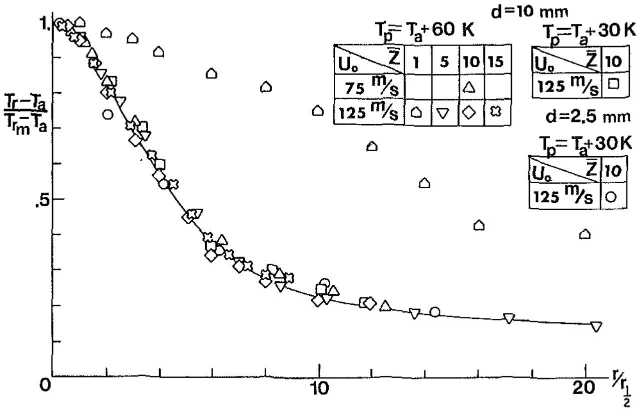

Fig. 9 Radial profiles of recovery temperature

(~ 100 percent) near the coolant injection site and decays, due to entrainment of undesirable ambient fluid into the film, with increasing distance from the site. For the problem considered here, the injection site corresponds, more or less, to the jet stagnation point. If one takes T_a to be the ambient fluid temperature and T_{rm} to be the effective "coolant" temperature, Fig. 9 becomes, in fact, a map of local η on the impingement surface. Also shown on this figure are recovery temperatures for $\bar{z}=1$, whose profiles are apparently influenced by confinement of the flow due to the nearby orifice plate. Obot et al. [21] recently measured the effects of confinement for an air jet issuing from a nozzle at the center of a circular plate of radius R, oriented parallel to the impingement surface. Tests were run at $R/d=8.7$, $R/d=17.4$, and without the plate. His data indicates that, between these limits, the effect of confinement is small for $8 \leq \bar{z} \leq 12$ and negligible for $\bar{z} \geq 12$. For our work, the jets were confined by a square 10.2 cm × 10.2 cm orifice plate whose effective radius R (taken to be $\pi R^2 = (10.2\ \text{cm})^2$) is 5.75 cm. Our intention was not to make a comprehensive determination of the effects of confinement; however, our measurements do correspond to two values of the confinement ratio ($R/d=5.75$ for $d=10$ mm and $R/d=23.0$ for $d=2.5$ mm) that are in the range of practical interest and that overlap Obot's range. Our data (compare ○ 's and □ 's on Fig. 9) indicate that R/d does not affect T_r at $\bar{z} \simeq 10$; this is undoubtedly true also for $\bar{z} \geq 10$. In fact, the T_r profile for $\bar{z}=5$ (run only for $d=10$ mm) is virtually identical to those for larger $\bar{z}$.

Bouchez and Goldstein [20] measured T_r for a heated jet impinging on an adiabatic plate in the presence of a crossflow. Tests were conducted at $\bar{z}=6$ and 12 for various values of the blowing parameter M. Our distributions of T_r on the target surface cannot be readily compared to theirs, as the latter were quite skewed even at the largest M (~ 12) they used. It is worthwhile, however, to compare values of stagnation point T_r. Figure 8 includes several points deduced from the data in [20] that clearly show that the recovery temperature is sensitive to even a very modest crossflow. For their largest M the recovery temperature is considerably lower than those we observed (for $M=\infty$) at $\bar{z}=6$ and 12. At larger $\bar{z}$, the behavior is most pronounced due to the increased mixing and lengthening of the jet as it is deflected by the crosswind.

An approximate theoretical model was previously developed to predict local T_r on the impingement surface. To check the model, the data of Figs. 8 and 9 were used to generate a plot of the dimensionless recovery temperature θ versus r/d, and the result is shown as Fig. 10. The data for $\bar{z} \geq 5$ collapse onto a single curve for r/d large enough to fall within the wall jet region and begin to depart from this curve at values of r/d corresponding to $r \cong 3r_{1/2}$ for each $\bar{z}$. The experimental uncertainty in θ tends to be largest when $(T_r - T_a)$ is small. For $(T_p - T_a) = 60°\text{C}$, it varies typically between ±4 percent at smaller r/d and ±10 percent at the largest r/d on Fig. 10. For $(T_p - T_a) = 30°\text{C}$, these values increase to ±6 percent at small r/d and ±19 percent (our worst case) at large r/d. A multiple regression routine was used to fit a best curve to all data for $r \geq 3r_{1/2}$, and the result was

$$\theta = a(r/d)^b \bar{z}^c \tag{17}$$

with $a=1.10$, $b=-0.95$, and $c=0.01$. The value of b falls midway between those predicted by equations (7) and (8); the very small value of c indicates that θ is virtually independent of $\bar{z}$, consistent with the behavior predicted by equation (7). If one uses the least-squares method to force a curve with $b=-1.0$ and $c=0.0$ to best fit the data for $r > 3r_{1/2}$, the resulting curve has $a=1.24$. This curve is shown as a solid line on the figure and appears to fit the data quite satisfactorally: the mean deviation between the curve and the data points is ±6 percent. Also shown as ⬠ -symbols on the figure are the data for $\bar{z}=1$. For small $\bar{z}$, the flow is essentially a radial confined one, and the wall jet analysis cannot be expected to predict its behavior.

Measurements of jet velocity and temperature were made with the jet discharging vertically downward. It was presumed that buoyancy effects would be negligible; and tests were conducted (at $U_o = 75$ m/s, $d=10$ mm, $T_p = T_a + 60°\text{C}$) with the jet aimed upward to verify this assumption. The effects of body forces were relatively insignificant: at $\bar{x}=15$, the centerline velocity was about 2 percent higher for the heated jet directed upward. A complete characterization of such a flow should include some indication of turbulence levels. While none were given in this paper, we anticipate that the next phase of this study will include these measurements.

Conclusions

Measurements were made to characterize heated and isothermal turbulent air jets issuing into quiescent room air from square-edged orifices with unity aspect ratio. Significant conclusions are the following:

1 Profiles of mean axial velocity and total temperature are similar in the main part of the jet, and the decay rates of these quantities on the jet axis are generally consistent with data in the literature. The length of the potential core is three orifice diameters, which is about half the length generally reported for jets formed by conventional nozzles.

2 Profiles of dimensionless recovery temperature were measured on a flat plate normal to the jet axis. For $\bar{z} \geq 5$, these profiles were similar and could be collapsed onto a universal profile if radial position is normalized by dividing by the "arrival" value of the jet half-width. A simple theoretical model, which assumed self-similar velocity and temperature profiles, was used to predict (to within a multiplicative constant) the variation of recovery temperature associated with the fully developed wall jet. The constant was determined from our experimental data.

Acknowledgments

The authors wish to thank a reviewer who pointed out the mutual relevance between the present work and heat transfer studies for fire plumes impinging upon a ceiling and suggested possible improvements to the theoretical model.

References

1 Friedman, S. J., and Mueller, A. C., "Heat Transfer to Flat Surfaces," *Proceedings, General Discussion on Heat Transfer*, The Institute of Mechanical Engineers, London, England, 1951, pp. 130-142.

2 Gardon, R., and Cobonpue, J., "Heat Transfer Between a Flat Plate and Jets of Air Impinging On It," *International Developments in Heat Transfer, Proc. of 2nd International Heat Transfer Conference*, ASME, New York, N.Y., 1962, pp. 454-460.

3 Hollworth, B. R., and Berry, R. D., "Heat Transfer From Arrays of Impinging Jets With Large Jet-to-Jet Spacing," ASME JOURNAL OF HEAT TRANSFER, Vol. 100, No. 2, 1978, pp. 352-357.

4 Martin, H., "Heat and Mass Transfer Between Impinging Gas Jets and Solid Surface," *Advances in Heat Transfer*, Vol. 13, Academic Press, 1977, pp. 1-59.

5 Kercher, D. M., and Tabakoff, W., "Heat Transfer by a Square Array of Round Air Jets Impinging Perpendicular to a Flat Surface Including the Effect of Spent Air," ASME *Journal of Engineering for Power*, Vol. 92, No. 1, 1970, pp. 73-82.

6 Chance, J. L., "Experimental Investigation of Air Impingement Heat Transfer Under an Array of Round Jets," *Tappi*, Vol. 57, No. 6, 1974, pp. 108-112.

7 Metzger, D. E., Florschuetz, L. W., Takeuchi, D. I., Behee, R. D., and Berry, R. A., "Heat Transfer Characteristics for Inline and Staggered Arrays of Circular Jets With Cross Flow of Spent Air," ASME JOURNAL OF HEAT TRANSFER, Vol. 101, 1979, pp. 526-531.

8 Striegl, S. A., and Diller, T. E., "An Analysis of The Thermal Entrainment Effect on Jet Impingement Heat Transfer," ASME Paper No. 82-WA/HT-54, 1982.

9 Wilson, S., "Entrainment Effects on Impingement Heat Transfer, Part I: Measurements of Heated Jet Velocity and Temperature Distributions and Recovery Temperatures on Target Surface," M.S. thesis, MIE Dept., Clarkson College of Technology, December 1982.

10 Tani, I., and Komatsu, Y., "Impingement of a Round Jet on a Flat Surface," *11th International Conference on Applied Mechanics*, 1966, pp. 672-676.

11 Glauert, M. B., "The Wall Jet," *Journal of Fluid Mechanics*, Vol. 1, pt. 6, Dec. 1956, pp. 625-643.

12 Gauntner, J. W., Livingood, J. N. B., and Hrycak, P., "Survey of Literature on Flow Characteristics of a Single Turbulent Jet Impinging on a Flat Plate," NASA TN D-5652, Feb. 1970.

13 Hrycak, P., Lee, D. T., Gauntner, J. W., and Livingood, J. N. B., "Experimental Flow Characteristics of a Single Turbulent Jet Impinging on a Flat Plate," NASA TN D-5690, Mar. 1970.

14 Poreh, M., Tsuei, Y. G., and Cermak, J. E., "Investigation of a Turbulent Radial Wall Jet," *Journal of Applied Mechanics*, June 1967, pp. 457-463.

15 Cooper, L. Y., "Heat Transfer From a Buoyant Plume to An Unconfined Ceiling," ASME JOURNAL OF HEAT TRANSFER, Vol. 104, 1982, pp. 446-451.

16 Obot, N. T., Mujumdar, A. S., and Douglas, W. J. M., "The Effect of Nozzle Geometry on Impingement Heat Transfer Under a Round Turbulent Jet," Paper No. 79-WA/HT-53, presented at ASME Winter Annual Meeting, New York, N.Y., 1979.

17 Abramovitch, G. N., *The Theory of Turbulent Jets*, trans. by Scripta Technica, M.I.T. Press, Cambridge, Mass., 1963.

18 Moffat, R. J., "Gas Temperature Measurement," *Temperature: Its Measurement and Control in Science and Industry*, Vol. III, pt. 2, No. 52.

19 Florschuetz, L. W., and Metzger, D. E., "Effects of Initial Crossflow Temperature on Turbine Cooling With Jet Arrays," paper presented at the Heat and Mass Transfer in Rotating Machinery XIV International Centre for Mass Transfer Symposium, Dubrovnik, Yugoslavia, Aug. 30-Sept. 3, 1982.

20 Bouchez, J. P., and Goldstein, R. J., "Impingement Cooling from a Circular Jet in a Cross Flow," *International Journal of Heat and Mass Transfer*, Vol. 13, 1975, pp. 719-730.

21 Obot, N. T., Douglas, W. J. M., and Mujumdar, A. S., "Effect of Semi-Confinement on Impingement Heat Transfer," *Proceedings of 7th International Heat Transfer Conference*, Munich, Sept. 1982.

An Analysis of the Effect of Entrainment Temperature on Jet Impingement Heat Transfer

S. A. Striegl
Westinghouse Electric Corporation,
Idaho Falls, Idaho 83401
Assoc. Mem. ASME

T. E. Diller
Department of Mechanical Engineering,
Virginia Polytechnic Institute and
State University,
Blacksburg, Va. 24061
Mem. ASME

An analytical model is developed to determine the effect of the temperature of entrained fluid (entrainment temperature) on the local heat transfer to a single, plane, turbulent impinging jet. Solutions of the momentum and energy equations for a single impinging jet are accomplished using similarity and series analyses. Solutions of the energy equation are obtained for the two limiting cases of entrainment temperatures equal to the plate temperature and the initial jet temperature. The analytical solutions are superposed to obtain the solution for all intermediate entrainment temperatures. The constants in the turbulence model are determined by comparing the analytical solutions to experimentally determined local heat transfer rates for single impinging jets issuing into an environment with a controlled entrainment temperature. When the single jet model is applied to jet arrays it predicts that the entrainment in the recirculation region between the jets can significantly affect the heat transfer. Comparison of the model to heat transfer measurements performed for jet arrays shows that the model successfully predicts the local heat transfer in jet arrays.

Introduction

When an impinging jet issues into an environment that is at a temperature different from that of the jet, entrainment of the surrounding fluid will affect the heat transfer from the surface to the impinging jet. Little work has been done on the surface heat transfer for impinging jets that includes this thermal entrainment effect. Schauer and Eustis [1] used integral solutions to analyze the effect of thermal entrainment on a single impinging jet. They presented experimental results limited to jets issuing into (*a*) an environment at the jet temperature, and (*b*) an environment at the impingement plate temperature. Vlachopoulos et al. [2] studied the heat transfer from a single, hot, axisymmetric impinging jet issuing into a cool environment. They obtained the velocity and temperature profiles for a compressible wall jet numerically, but relied on empirical expressions for the heat transfer. The anlaysis presented here is directed at analytically predicting the heat transfer.

In many practical heat transfer applications, arrays of impinging jets are used. Thermal entrainment is important in jet arrays because entrainment of air in the recirculating flow region between the jets can significantly affect the heat transfer. Several investigators have noted differences in the local heat and mass transfer rates to single and multiple jets [3, 4]. This discrepancy is attributed to jet interaction between the adjacent jets in jet arrays; however, it is not clear how much of the discrepancy between single and multiple jet heat transfer may have been due to entrainment, since the temperatures and mass concentrations in the recirculation region were not reported. Thermal entrainment will be important in any situation where the temperature of the environment surrounding the jet differs from the initial temperature of the jet. With multiple jets, spent air will be entrained and will therefore affect the heat transfer. As the spent air exits the flow feld, the additional effect of the fluid crossflow may be important [5]. In the present study the effects of crossflow were minimized to assure that thermal entrainment is the predominant effect.

A simple analytical model is developed to account for the effect of thermal entrainment on the local heat transfer to a single impinging jet. The thermal analysis uses similarity and series solutions, some of which have been presented in the literature. Additional solutions are given to account for thermal entrainment by using boundary conditions which have not previously been applied to the analyses. The single-jet model is then applied to multiple jets to account for the entrainment of the fluid in the recirculation region.

The analysis is limited to impingement heights that produce bell-shaped heat transfer distributions ($h/b_o > 6$). The model presented is for a two-dimensional air jet; however, the model can be easily extended to submerged two-dimensional jets of any fluid. The same type of model could also be extended to handle axisymmetric jets.

Analysis

The impinging jet is divided into three distinct flow regions as shown in Fig. 1: the free jet, the impingement region, and the wall jet. The equations of motion and energy are solved in each of these regions.

The boundary conditions for the solution of the energy equations will depend on the relationship between the initial temperature of the jet T_i, the temperature of the environment surrounding the jet T_∞, and the temperature of the impingement plate T_w. These three temperatures are used to form a dimensionless entrainment factor

$$\bar{F}=\frac{T_i-T_\infty}{T_i-T_w} \tag{1}$$

In terms of the entrainment factor, two limiting cases of boundary conditions for the energy equation can be specified. For a jet issuing into an environment at the same temperature, $T_i = T_\infty$, $\bar{F} = 0$, and thermal entrainment will not affect the heat transfer. When the jet issues into an environment which is at the plate temperature, $T_\infty = T_w$, $\bar{F} = 1$, and thermal entrainment will have the greatest effect on the heat transfer.

The energy equation in the impingement and wall jet regions is solved for the two limiting cases of boundary conditions corresponding to $\bar{F} = 0$ and $\bar{F} = 1$. To obtain the solution for intermediate values of $\bar{F}$, the solutions for $\bar{F} = 0$

Contributed by the Heat Transfer Division and presented at the ASME Winter Annual Meeting, Phoenix, Arizona, November 14-19, 1982. Manuscript received by the Heat Transfer Division April 27, 1983. Paper No. 82-WA/HT-54.

and $\bar{F} = 1$ are linearly superposed. The superposition is valid because the energy equation and the boundary conditions are linear. Thus, the temperature distributions and the resulting heat transfer correlations contain the entrainment factor as a parameter.

The Free Jet. As the free jet enters the impingement region, the velocity and temperature profiles of the free jet provide the upper boundary conditions for the impingement region. Thus the free jet is analyzed to determine these boundary conditions for the impingement region. The velocity and temperature profiles of the free jet can be assumed to be similar in the fully developed region beyond the potential core [6-8]. The potential core extends about six slot widths from the slot opening. Thus a similarity solution is valid only for impingement heights greater than six slot widths. This is not a severe limitation, since many practical heat transfer applications involve fully developed impinging jets.

Rajaratnam [9] presents a similarity solution for the two-dimensional free jet velocity that was originally done by Goertler. The velocity profiles are scaled by the centerline velocity decay

$$\frac{V_m}{V_o} = C_8\sqrt{\frac{b_o}{Y_1}} \tag{2}$$

where C_8 is the velocity decay rate, and a profile spreading rate

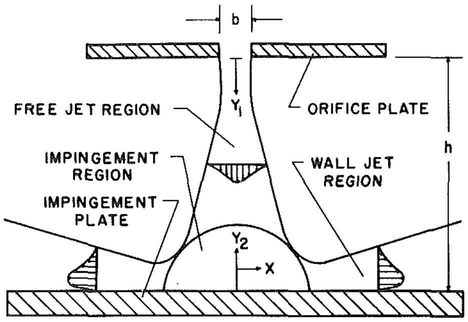

Fig. 1 The impinging jet

$$\delta_{0.5} = C_9 Y_1 \tag{3}$$

where C_9 is the spreading rate. An average value of 0.114 is used for C_9 [9]. The value for C_8 does not directly enter into the impingement region solution that follows.

Goertler's solution is applicable to both the velocity and temperature fields if the temperature profiles are properly scaled. Defining a dimensionless temperature in the free jet

$$\bar{T}_1 = \frac{T_1 - T_\infty}{T_m - T_\infty} \tag{4}$$

the centerline temperature is

Nomenclature

b = actual slot width
b_o = effective slot width, equation (38)
B_A, B_B, B_1, B_2 = temperature coefficients for impingement region, equations (10) and (13)
C_1, C_2 = free jet temperature parameters, equations (5) and (6)
C_3, C_4 = wall jet velocity parameters, equations (22) and (23)
C_5, C_6 = wall jet temperature parameters, equations (27) and (28)
C_7 = turbulence parameter for impingement region, equation (33)
C_8, C_9 = free jet velocity parameters, equations (2) and (3)
C_D = discharge coefficient
C_p = specific heat
f_1, f_3 = velocity similarity functions in impingement region
$\bar{F}$ = entrainment factor, equation (1)
F_A, F_B, F_0, F_2 = temperature functions for impingement region, equations (10) and (13)
G_2 = wall jet temperature function ($\bar{F} = 0$)
h = impingement height
h_s = stagnation region heat transfer coefficient, equation (33)
h_{wj} = wall jet region heat transfer coefficient, equation (36)
H = wall jet velocity and temperature function, ($\bar{F} = 1$)
K = thermal conductivity
K_w = turbulence parameter for wall jet, equation (24)
Nu_s = stagnation region Nusselt number, equation (34)
Nu_{wj} = wall jet region Nusselt number, equation (37)
Pr = Prandtl number
T_i = initial temperature of jet
T_m = centerline temperature of free jet
T_{mw} = maximum temperature in wall jet
T_w = plate temperature
T_∞ = temperature of the environment surrounding the jet
T_S, T_{S_1}, T_{S_2} = temperatures in impingement region, equations (32), (10), and (13)
T_{wj}, T_{w1}, T_{w2} = temperatures in wall jet region, equations (35), (30), and (29)
$\bar{T}_1$ = temperature in free jet, equation (4)
$\bar{T}$ = dimensionless temperature
U = velocity parallel to the plate
U_m = maximum velocity in the wall jet, equation (22)
V_m = maximum velocity in the free jet, equation (2)
V_o = initial velocity of jet
X = coordinate parallel to plate, Fig. 1
X^* = width of stagnation region, equation (8)
X_T^* = width of temperature profile, equation (17)
Y_1, Y_2 = coordinates perpendicular to plate, Fig. 1

Greek Letters

$\delta_{w\,0.5}$ = half-width of wall jet velocity profile
$\delta_{wT\,0.5}$ = half-width of wall jet temperature profile
$\delta_{T\,0.5}$ = half-width of free jet temperature profile
δ_{TS} = thermal boundary layer thickness in impingement region
$\delta_{0.99}$ = width of free jet velocity profile
ϵ_m = eddy diffusivity, equation (24)
γ = similarity variable, equation (7)
η = similarity variable, equation (26)
μ = mean value of data
ν = kinematic viscosity
ρ = density
σ = standard deviation of data

$$\frac{T_m - T_\infty}{T_i - T_\infty} = C_1 \sqrt{\frac{b_o}{Y_1}} \tag{5}$$

and the temperature profile width is

$$\delta_{T\,0.5} = C_2 Y_1 \tag{6}$$

where C_1 is the temperature decay rate, and C_2 is the temperature profile spreading rate. Several investigators have determined the temperature profile spreading rate from measured temperature distributions [7, 8, 10]. An average value of $C_2 = 0.15$ is used hereafter. The temperature decay rate C_1 appears in the stagnation region heat transfer correlation, and values are determined by matching the measured heat transfer to the correlation. The average value of C_1 thus determined is then checked against values of the temperature decay rate presented in the literature.

The Impingement Region. Because of the strong favorable pressure gradient in the impingement region where the flow is turning sharply, the flow in the impingement region can be analyzed as a laminar boundary layer. Andreyev et al. [11] used the Blasius series to obtain a solution to the laminar momentum equation in the impingement region. They used the first two terms of the series to describe the impingement region velocity parallel to the plate as

$$U = B_1 f_1'(\gamma) X + 4B_2 f_3'(\gamma) X^3 \tag{7}$$

where $\gamma = Y_2 \sqrt{B_1/\nu}$, and B_1 and B_2 are constants. To provide the upper boundary condition, Andreyev obtained the velocity distribution at the edge of the boundary layer by measuring the pressure distribution on the impingement plate.

At the end of the impingement region, the velocity at the edge of the boundary layer will reach a maximum, after which the flow will decelerate as the boundary layer continues to spread out along the plate. Andreyev et al. [11] determined the width of the impingement region X^* from measurements of the velocity distribution at the edge of the boundary layer. It is approximately equal to the width of the free jet at the impingement plane, $\delta_{0.99}$ at $Y_1 = h$. From Goertler's solution with a velocity profile spreading rate of 0.114, the value is

$$X^* = \delta_{0.99} = 0.34\,h \tag{8}$$

Details of the momentum boundary layer solution for $f_1'(\gamma)$ and $f_3'(\gamma)$ are given by Andreyev et al. [11].

With the introduction of a dimensionless temperature $\bar{T}(\gamma)$ the laminar energy boundary layer equation is

$$U \frac{\partial \bar{T}}{\partial \gamma} + \frac{1}{\mathrm{Pr}} \frac{\partial^2 \bar{T}}{\partial \gamma^2} = 0 \tag{9}$$

Series representations of the dimensionless temperature are used to obtain the solution of equation (9) with boundary conditions corresponding to $\bar{F} = 0$ and $\bar{F} = 1$.

When $\bar{F} = 0$, the temperature of the free jet is constant because thermal entrainment does not affect the temperature distribution. Thus the free-stream temperature for the thermal boundary layer in the stagnation region is constant. The series solution to the energy equation for this case has been performed by Andreyev et al. [11]. The series representation of the temperature in the boundary layer is

$$\bar{T}_{S1} = \frac{T_{S1} - T_w}{T_\infty - T_w} = F_0(\gamma) + \frac{B_2}{B_1} F_2(\gamma) X^2 \tag{10}$$

where B_1 and B_2 are constants defined as in Andreyev's solution. The boundary conditions are

at

$$Y_2 = 0, \bar{T}_{S1} = 0 \tag{11}$$

or

$$F_0(0) = F_2(0) = 0$$

at

$$Y_2 = \delta_{TS}, \bar{T}_{S1} = 1 \tag{12}$$

or

$$F_0(\delta_{TS}) = 1, \text{ and } F_2(\delta_{TS}) = 0$$

When $\bar{F} = 1$, the free jet temperature will no longer be constant because entrainment of the surrounding fluid affects the temperature distribution in the free jet. Thus the free-stream temperature for the thermal boundary layer in the impingement region is not constant. The solution to the energy equation for this case is an extension of the Blasius series used in the previous solution. Since it has not been previously published, the analysis is given in some detail. Further details are given in [12].

The solution for $\bar{F} = 1$ begins with the assumption of a series relation for the dimensionless temperature profile similar to equation (10).

$$\bar{T}_{S2} = \frac{T_{S2} - T_\infty}{T_i - T_\infty} = B_A F_A(\gamma) + B_B F_B(\gamma) X^2 \tag{13}$$

The free jet temperature distribution at the impingement plane ($Y_1 = h$) is used as the boundary condition at the edge of the thermal boundary layer in the impingement region. This is done by approximating the free jet temperature distribution with a parabolic relation $\bar{T}_{S2} = B_A + B_B X^2$. Thus the boundary conditions are

at

$$Y_2 = 0, \quad \bar{T}_{S2} = 0 \tag{14}$$

or

$$F_A(0) = F_B(0) = 0$$

at

$$Y_2 = \delta_{TS}, \quad \bar{T}_{S2} = B_A + B_B X^2 \tag{15}$$

or

$$F_A(\delta_{TS}) = F_B(\delta_{TS}) = 1$$

Now the coefficients in equation (13) can be determined. From equation (15), the freestream temperature at the stagnation point ($X = 0$) is taken as the centerline temperature of the free jet at the impingement plane (equation (5)).

$$\bar{T}_{S2} = \frac{T_m - T_\infty}{T_i - T_\infty} = C_1 \sqrt{\frac{b_o}{h}} = B_A \tag{16}$$

The width of the temperature profile at the impingement plane can be expressed in terms of the width of the velocity profile using the ratio of the temperature and velocity profile spreading rates of the free jet.

$$X_T^* = \frac{0.15}{0.114} X^* = 0.45\,h \tag{17}$$

Since $\bar{T}_{S2}$ must equal zero at the edge of the boundary layer with $X = X_T^*$, equation (15) gives

$$B_B = \frac{-B_A}{X_T^{*2}} \tag{18}$$

Using the series representations of the velocity and temperature distributions and collecting like powers of X, the series representation of the laminar energy boundary layer equation, equation (9), becomes

$$F_A'(\gamma) f_1'(\gamma) + \frac{1}{\mathrm{Pr}} F_A''(\gamma) = 0 \tag{19}$$

$$2 f_1(\gamma) F_B(\gamma) - F_B'(\gamma) f_1(\gamma) - \tag{20}$$

$$12 \frac{B_2 B_A}{B_1 B_B} f_3(\gamma) F_A'(\gamma) - \frac{1}{\mathrm{Pr}} F_B''(\gamma) = 0$$

where $f_1(\gamma)$ and $f_3(\gamma)$ are functions which describe the velocity distribution in the impingement region and are defined in Andreyev's solution of the momentum equation [11]. Using Andreyev's values for B_2 and B_1 and the values of B_A and B_B determined here

$$\frac{B_2 B_A}{B_1 B_B} = 0.38\left(\frac{X_T^*}{X^*}\right)^2 = 0.66 \tag{21}$$

Equations (20) and (21), along with similar equations describing the velocity distribution given by Andreyev, are solved simultaneously to obtain the temperature distribution.

The Wall Jet. At the end of the impingement region, the free-stream velocity begins to decrease. The boundary layer undergoes a transition from laminar to turbulent flow and after some distance becomes a fully developed wall jet. The velocity profiles of a fully developed wall jet are nearly similar, although there is some debate as to whether the profiles are actually similar and at what point downstream the wall jet is sufficiently fully developed [6, 13, 14, 15]. The similarity solution that follows is assumed to be valid beginning at the end of the stagnation region. The validity of this assumption is tested when the wall jet heat transfer correlation is compared with the experimental data.

Rao [15] has performed a similarity solution for the two-dimensional wall jet. The maximum velocity in the wall jet and the velocity profile width are scaled by the following relations

$$\frac{U_m}{V_o} = C_3\sqrt{\frac{b_o}{X}} \tag{22}$$

$$\delta_{w\,0.5} = C_4 X \tag{23}$$

where C_3 is the velocity decay rate, and C_4 is the velocity profile spreading rate. Rao employed Prandtl's second hypothesis to model the eddy diffusivity for momentum

$$\epsilon_m = K_w U_m \delta_{w\,0.5} \tag{24}$$

where K_w is a constant. Because the wall jet behaves as a flat plate boundary layer near the wall and as a free shear layer further out, a single value of K_w will not produce a good fit to the velocity profiles. Thus a different value of K_w was used by Rao in the inner and outer layers. The inner and outer layers are joined at the point of maximum velocity. Values of K_w that are different from those Rao used are determined in the present study. Using average values of the velocity decay rate and velocity profile spreading rate presented by Rajaratnam [9], $C_3 = 3.5$ and $C_4 = 0.068$, the values of K_w that best fit the velocity decay are: inner region $K_w = 0.0041$, and outer region $K_w = 0.014$. Using the relations for the maximum velocity and velocity profile width in the wall jet, the turbulent momentum boundary layer equation is transformed into a ordinary differential equation

$$H'(\eta)^2 + H''(\eta)H(\eta) + \frac{2K_w}{C_4}H'''(\eta) = 0 \tag{25}$$

where

$$H'(\eta) = \frac{U}{U_m} \text{ and } \eta = \frac{Y_2}{\delta_{w0.5}} \tag{26}$$

The boundary conditions are $H'(0) = H(0) = 0$ and $H'(\infty) = 0$. The solution of the resulting similarity form of the momentum equation using the above values of K_w and C_4 was obtained numerically with a Runge Kutta method and is presented in [12].

As in the stagnation region, the energy equation in the wall jet region must be solved for the two limiting cases of boundary conditions corresponding to $\bar{F} = 0$ and $\bar{F} = 1$. When $\bar{F} = 1$, the temperature profiles are similar to the velocity profiles. The maximum temperature decay is

$$\frac{T_{mw} - T_\infty}{T_i - T_\infty} = C_5\sqrt{\frac{b_o}{X}} \tag{27}$$

where C_5 is the temperature decay rate. The temperature profile width is

$$\delta_{wT\,0.5} = C_6 X \tag{28}$$

where C_6 is the temperature profile spreading rate. Cadek [16] found the ratio of the velocity profile spreading rate to the temperature profile spreading rate to be

$$\frac{C_4}{C_6} = 0.67$$

Thus the analytical solutions for the temperature profiles will be identical to the velocity profiles if η is scaled by C_4/C_6 and if the profile is scaled using the maximum temperature decay, equation (27). Therefore, the dimensionless temperature in the wall jet region when $\bar{F} = 1$ is

$$\bar{T}_{w2} = \frac{T_{w2} - T_\infty}{T_i - T_\infty} = C_5\sqrt{\frac{b_o}{X}}\,H'\left(\eta\frac{C_4}{C_6}\right) \tag{29}$$

Like the temperature decay rate in the free jet C_1, the temperature decay rate in the wall jet C_5 is left as a parameter to be determined by matching the measured heat transfer to the correlation.

When $\bar{F} = 0$ a new solution to the energy equation is required because of the different boundary conditions than the $\bar{F} = 1$ case. Using the same similarity variable as in the solution to the energy equation when $\bar{F} = 1$, a dimensionless temperature for the $\bar{F} = 0$ case is defined equal to the function G_2

$$\bar{T}_{w1} = \frac{T_{w1} - T_w}{T_\infty - T_w} = G_2\left(\eta\frac{C_4}{C_6}\right) \tag{30}$$

An ordinary differential equation for the turbulent energy boundary layer equation similar to that for the momentum equation is again obtained

$$H\left(\eta\frac{C_4}{C_6}\right)G_2'\left(\eta\frac{C_4}{C_6}\right) + \frac{2K_w}{C_6}G_2''\left(\eta\frac{C_4}{C_6}\right) = 0 \tag{31}$$

with boundary conditions, $G_2'(0) = 0$ and $G_2(\infty) = 1$. The solution to the equation for this case is also obtained numerically and is tabulated in [12]. Because of the form assumed for the velocity and temperature decay (equations (23) and (27)), the wall jet solution is independent of the free jet and impingement region solutions. That is, it is assumed that the decay and spreading rates of the wall jet are not a function of the impingement height or decay rates of the free jet.

Heat Transfer. Analytical correlations for the local heat transfer coefficients in the stagnation and wall jet regions are determined as follows. First the dimensionless temperature profiles for the $\bar{F} = 0$ and $\bar{F} = 1$ cases are transformed to the common denominator $T_i - T_w$ using the entrainment factor $\bar{F}$. The temperature profiles are then superposed to form a dimensionless temperature profile which is valid for any value of $\bar{F}$. The local heat transfer coefficient based on $T_i - T_w$ is determined using the temperature gradient at the plate surface. Finally, a Nusselt number correlation is obtained for the stagnation and wall jet regions.

Stagnation Region Heat Transfer. The temperature distribution in the stagnation region can be expressed in terms of the $\bar{F} = 0$ and $\bar{F} = 1$ temperature solutions as

$$\bar{T}_S = \frac{T_S - T_w}{T_i - T_w} = \bar{T}_{S1}(1 - \bar{F}) + \bar{T}_{S2}\bar{F} \tag{32}$$

The local heat transfer coefficient is

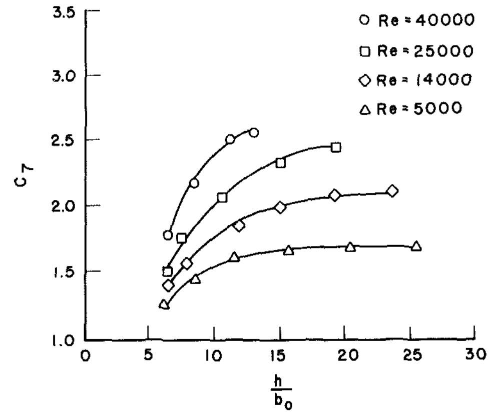

Fig. 2 The effect of turbulence on heat transfer in the impingement region

$$h_s = \frac{KC_7 \left.\dfrac{\partial T_S}{\partial Y_2}\right|_{Y_2=0}}{T_w - T_i} \qquad (33)$$

where K is the molecular thermal conductivity of air and C_7 is a parameter which accounts for the effect of turbulence on the stagnation region heat transfer. The parameter C_7 is needed because turbulence in the free jet is carried into the stagnation region and increases the heat transfer over that predicted by the laminar analysis. Several investigators have examined the effect of turbulence on the stagnation region heat transfer [17, 18, 19, 20]. Hoogendoorn [20] developed a stagnation region Nusselt number correlation that uses the measured free jet turbulence as a parameter. However, attempts to develop an anayltical correlation for C_7 have been largely unsuccessful. Therefore, C_7 must be determined experimentally.

From the computed temperature distributions, the nondimensional gradients at the plate are: $F_0'(0) = 0.496$, $F_2'(0) = 0.448$, $F_A'(0) = 0.496$, and $F_B'(0) = 0.400$. The resulting Nusselt number, which is valid throughout the impingement region, is

$$\mathrm{Nu}_s = \frac{h_s b_o}{K} = 1.64\, C_7 \sqrt{\mathrm{Re}} \left(\frac{b_o}{h}\right)^{3/4} \left[1 - 2.89\left(\frac{X}{h}\right)^2\right] \qquad (34)$$

$$(1-\bar{F}) + C_1 \sqrt{\frac{b_o}{h}} \left[1 - 3.86\left(\frac{X}{h}\right)^2\right] \bar{F}$$

where $\mathrm{Re} = V_o b_o/\nu$. Equation (34) is prescribed for $X/h < 0.34$.

Wall Jet Region Heat Transfer. The temperature distribution in the wall jet region can be expressed in terms of the $\bar{F} = 0$ and $\bar{F} = 1$ temperature solutions as

$$\bar{T}_{wj} = \frac{T_{wj} - T_w}{T_i - T_w} = \bar{T}_{w1}(1-\bar{F}) + \bar{T}_{w2}\bar{F} \qquad (35)$$

The local heat transfer coefficient must be defined using the eddy diffusivity as

$$h_{wj} = \frac{\epsilon_m \rho C_p \left.\dfrac{\partial T_{wj}}{\partial Y_2}\right|_{Y_2=0}}{T_i - T_w} \qquad (36)$$

The nondimensional gradients at the plate are: $H''(0) = 6.60$, $G_2{}'(0) = 0.911$. The resulting Nusselt number correlation in the wall jet region is

$$\mathrm{Nu}_{wj} = \frac{h_{wj} b_o}{K} = 0.00174\, C_3 \mathrm{Re} \sqrt{\frac{b_o}{X}} \qquad (37)$$

$$\left[(1-\bar{F}) + 4.85\, C_5 \sqrt{\frac{b_o}{X}}\, \bar{F}\right]$$

where equation (37) is prescribed for $X/h > 0.34$.

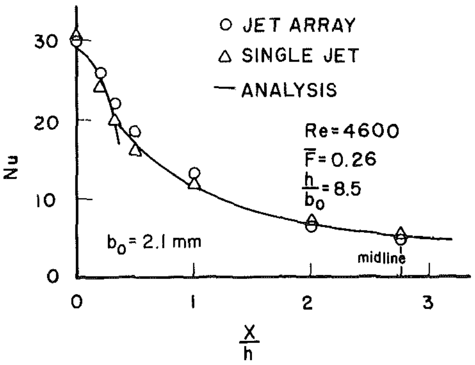

Fig. 3 Comparison of single and multiple impinging jet Nusselt number distributions

Note that the wall jet velocity decay C_3 is left as a free parameter. Although the eddy diffusivity model in the wall jet region solution was adjusted to produce a reasonable value of C_3, the actual value of C_3 differed slightly for tests run with different slot widths. Because the wall jet region solutions are independent of the free jet and impingement region solutions, the wall jet parameters C_3 and C_5 are independent of the impingement region parameters C_1 and C_7. All of these parameters, C_7, C_1, C_3, and C_5, arise from coefficients used in the turbulence models. The parameters are arranged so that they can easily be related to the velocity or temperature decay.

Results

Local heat flux data were obtained for single and multiple impinging jets issuing from slot orifices of various widths as reported in [21]. The apparatus was enclosed to allow control of the jet entrainment temperature $\bar{F}$. Effective values of the slot width were used, b_o, based on the measured discharge coefficients

$$b_o = C_D b \qquad (38)$$

Heat transfer data were first analyzed for single jets to determine the values of the parameters in the Nusselt number correlations. The effect of turbulence on the stagnation region heat transfer, C_7 was determined by matching the stagnation region Nusselt number correlation to the heat transfer data at the stagnation point for $\bar{F} = 0$. C_7 is shown in Fig. 2 as a function of the dimensionless impingement height for several values of the Reynolds number. The values of C_7 also exhibit a dependence on slot width which is not shown in Fig. 2. The data for each slot width do not cover a sufficiently broad range of Reynolds numbers to allow a complete evaluation of the effect of slot width on C_7; however, the value of C_7 increases by approximately 10 percent for a 50 percent increase in slot width at a constant Reynolds number.

Values of the free jet temperature decay rate C_1 were obtained by matching the stagnation region Nusselt number correlation to the stagnation point heat transfer data for $\bar{F} > 0$ using values of C_7 interpolated from Fig. 2. A mean value of $C_1 = 2.13$ ($\sigma = 0.60$) was determined from a sample of 10 tests for each slot width.

Values of the wall jet velocity decay C_3 were obtained by matching the wall jet Nusselt number correlation to the heat transfer data for $\bar{F} = 0$ at several values of X/b_o. In the analysis, the wall jet eddy diffusivity model was adjusted so that the mean value of C_3, using data from all slot widths, would equal 3.5. The values of C_3 show a dependence on slot width, Reynolds number, and X/b_o, with the primary

Table 1 Values of the wall jet velocity and temperature decay

Slot width, $b(b_o)$		15mm(11.0 mm)	10mm(6.9 mm)	5mm(3.5 mm)	3mm(2.1 mm)
C_3	μ	3.78	3.24	3.83	4.03
	σ	0.248	0.304	0.536	0.659
C_5	μ	0.236	0.294	0.346	0.581
	σ	0.0902	0.117	0.126	0.128

dependence on slot width. The mean values of C_3 determined for each slot width are presented in Table 1 along with the standard deviations of the data.

Values of the wall jet temperature decay C_5 were obtained by matching the wall jet Nusselt number correlation to the data for $\bar{F} > 0$ using the mean values of C_3 for each slot width. The values of C_5 are also primarily a function of slot width. The values of C_5 are presented in Table 1 along with the standard deviations of the data. The means and standard deviations of C_3 and C_5 presented were determined from data at three values of X/h from seven separate tests for each slot width.

Local heat transfer data for multiple jets were analyzed for the center jet of the three jet array. This was compared with single jet data from the same nozzle at the same Reynolds number and impingement height. Figure 3 shows the Nusselt number distribution for a multiple jet along with the Nusselt number distribution for a single jet. The analytical curve is plotted using equations (34) and (37) with the appropriate turbulence constants. The agreement between the single and multiple jet results holds out to the midpoint between the jets of the jet array ($X/h = 2.75$). For the conditions of Fig. 3 the analysis predicts a maximum transfer effect due to thermal entrainment of 11 percent at $X/h = 2.75$. Larger effects are seen for larger values of $\bar{F}$ and X/b_o. When the entrainment effect is taken into account, no significant differences between single and multiple jet heat transfer can be seen.

Discussion

The value of the free jet temperature decay, $C_1 = 2.13$, compares well with the values of 2.14 to 2.31 obtained by Sfeir [8] from his measurements of the temperature distributions in free jets. Moreover, the values of the turbulence correction in the impingement region C_7 are within the same range as those determined from measurements of the stagnation point heat transfer presented in the literature [4, 16, 22]. As seen in Fig. 2, the values increase with increasing jet Reynolds number and larger dimensionless impingement height.

The analytical model for the wall jet was adjusted to produce reasonable values of the wall jet velocity decay C_3 (Rajaratnam [9] suggests $C_3 = 3.5$). The values obtained, however, are dependent on the slot width. Sakipov et al. [23] found a similar dependency of the wall jet velocity decay on slot width from measurements of the shear stress at the wall.

The values of the wall jet temperature decay C_5 appear to be low. No values of the temperature decay for a plane wall jet were found in the literature. It is reasonable, however, to assume that the ratio of the wall jet velocity and temperature decays is approximately equal to the ratio of the velocity and temperature profile width. Sfeir [8] found that this was true for the free jet. Thus the values of the wall jet temperature decay would be expected to be about 2.3. As seen in Table 1 the values of C_5 determined are much smaller.

The apparently low values of C_5 obtained and the dependence of C_3 and C_5 on the slot width are indications that the simple one-constant turbulence model and the similarity solution used for the wall jet are not sufficient. Rao [15] determined values of the constants in the turbulence model to best fit the measured velocity profiles. In the present study, values of K_w that best fit the velocity decays presented in the literature were determined. Launder [24] explains the difficulty of using a simple algebraic turbulence model to predict both the velocity decay and the velocity profiles in wall jets. A more complex model is therefore needed in the wall jet region.

Using the uncertainties in the values of C_3 and C_5 from Table 1, the wall jet region Nusselt number correlation fits the data from each slot to within 25 percent when $\bar{F} = 0$ and 45 percent when $\bar{F} = 1$ for $5 < X/b_o < 40$ at a confidence level of 90 percent. The impingement region Nusselt number correlation fits the data from all the slots to within 15 percent with $\bar{F} = 0$ and 50 percent when $\bar{F} = 1$ over the entire impingement region at a confidence level of 90 percent.

Because the constants for the $\bar{F} = 1$ solution (C_1 and C_5) depend on the experimentally determined constants for the $\bar{F} = 0$ solution (C_7 and C_3), the deviations in the values are larger for C_1 and C_5 and the agreement between the data and the correlations is the worst for the $\bar{F} = 1$ case. Schauer and Eustis [1] obtained better agreement between their data and correlations for $\bar{F} = 1$ than that obtained here; however, they presented data for only one slot width and a very limited range of impingement heights and Reynolds numbers. The agreement obtained here when $\bar{F} = 0$ is about as good as that obtained by other investigators [4, 22] using empirical correlations.

For the jet array experiments, heaters were used to control the air temperature outside the ends of the jet array and minimize end effects. The additional heat input increased the value of the entrainment factor over that which would have occurred naturally. For the multple jet case in Fig. 3, $\bar{F} \approx 0.16$ would have resulted naturally.

The heat transfer distributions were measured along a line perpendicular to the slot which passes through the midpoint of the slot length. Because the flow will exit the flow field symmetrically about this line, the crossflow parallel to the slot was minimized. Moreover, because the heat transfer in jet arrays was measured for the center jet of a three-jet array, crossflow perpendicular to the slot was also minimized.

Conclusion

An analytical correlation which accounts for thermal entrainment in single jets was developed. Thermal entrainment can significantly affect the heat transfer from the surface to a single impinging jet. In any multiple jet situation, fluid from the recirculation region between the jets will be entrained by the jets. Therefore, thermal entrainment will be important in any multiple impinging jet situation. When the thermal entrainment is included, the single-jet model successfully predicts the heat transfer for widely spaced multiple jets.

References

1 Schauer, J. J., and Eustis, R. H., "The Flow Development and Heat Transfer Characteristics of Plane Turbulent Impinging Jets," Stanford University, Department of Mechanical Engineering, Technical Report No. 3, 1963.

2 Vlachopoulos, J., and Tomich, J. F., "Heat Transfer from a Turbulent

Hot Air Jet Impinging Normally on a Flat Plate," *Canadian Journal of Chemical Engineering*, Vol. 49, 1971, pp. 462-466.

3 Korger, M., and Krizek, F., "Mass-Transfer Coefficient in Impingement Flow from Slotted Nozzles," *International Journal of Heat and Mass Transfer*, Vol. 9, 1966, pp. 337-344.

4 Gardon, R., and Akfirat, J. C., "Heat Transfer Characteristics of Impinging Two-Dimensional Air Jets," ASME JOURNAL OF HEAT TRANSFER, Vol. 88, 1966, pp. 101-108.

5 Florschuetz, L. W., Truman, C. R., and Metzger, D. E., "Streamwise Flow and Heat Transfer Distributions for Jet Array Impingement with Crossflow," ASME JOURNAL OF HEAT TRANSFER, Vol. 103, 1981, pp. 337-342.

6 Forthmann, E., "Turbulent Jet Expansion," NACA TM 789, 1934.

7 O'Callaghan, P. W., Probert, S. D., and Newbert, G. J., "Velocity and Temperature Distributions for Cold Air Jets Issuing from Linear Slot Vents into Relatively Warm Air," *Journal of Mechanical Engineering Science*, Vol. 17, No. 3, 1975, pp. 139-149.

8 Sfeir, A. A., "The Velocity and Temperature Fields of Rectangular Jets," *International Journal of Heat and Mass Transfer*, Vol. 19, 1976, pp. 1289-1297.

9 Rajaratnam, N., *Turbulent Jets*, Elsevier Scientific Publishing Co., New York, 1976.

10 Hegge Zijnen, B. G. van der, "Measurements of the Distribution of Heat and Matter in a Plane Turbulent Jet of Air," *Applied Scientific Research*, Sect. A., Vol. 7, 1958, pp. 277-292.

11 Andreyev, A. A., Dakhno, V. N., Savin, V. K., and Yudaev, B. N., "Investigation of Heat Transfer in a Gradient Flow Region for Plane Turbulent Jet Impinging on a Plate Situated Normal to the Flow," NASA TTF-14195, 1972.

12 Striegl, S. A., "The Effect of Entrainment on Jet Impingement Heat Transfer," M.Sc. thesis, Virginia Polytechnic Institute and State University, Blacksburg, Va., 1982.

13 Bakke, P., "An Experimental Investigation of a Wall Jet," *Journal of Fluid Mechanics*, Vol. 2, 1957, pp. 467-472.

14 Schwarz, W. H., and Cosart, W. P., "The Two-Dimensional Turbulent Wall Jet," *Journal of Fluid Mechanics*, Vol. 10, 1960, pp. 481-495.

15 Rao, V. K., "A Note on Mass Transfer in Turbulent Wall Jets," *International Journal of Heat and Mass Transfer*, Vol. 23, 1980, pp. 1690-1693.

16 Cadek, F. F., and Zerkle, R. D., "Local Heat Transfer Characteristics of Two-Dimensional Impinging Air Jets—Theory and Experiment," *Heat Transfer 1974*, Vol. II, Japan Society of Mech. Engrs., 1974, pp. 15-19.

17 Gardon, R., and Akfirat, J. C., "The Role of Turbulence in Determining the Heat Transfer Characteristics of Impinging Jets," *International Journal of Heat and Mass Transfer*, Vol. 8, 1965, pp. 1261-1272.

18 Yokobori, S., et al., "Role of Large Scale Eddy Structure on Enhancement of Heat Transfer in Stagnation Region of Two-Dimensional, Submerged, Impinging Jet," *Sixth International Heat Transfer Conference*, Vol. 5, Hemisphere Pub., Washington, D.C., 1973, pp. 305-310.

19 Kataoka, K., and Mizushina, T., "Local Enhancement of the Rate of Heat Transfer in an Impinging Round Jet by Free-Stream Turbulence," *Proceedings of the 5th International Heat Transfer Conference*, Vol. 2, 1974, pp. 305-309.

20 Hoogendoorn, C. J., "The Effect of Turbulence on Heat Transfer at a Stagnation Point," *International Journal of Heat and Mass Transfer*, Vol. 20, 1977, pp. 1333-1338.

21 Striegl, S. A., and Diller, T. E., "The Effect of Entrainment Temperature on Jet Impingement Heat Transfer," ASME JOURNAL OF HEAT TRANSFER, Vol. 106, 1984, pp. 27-33.

22 Martin, H., "Heat and Mass Transfer Between Impinging Gas Jets and Solids Surfaces," *Advances in Heat Transfer*, Vol. 13, 1977, pp. 1-60.

23 Sakipov, Z. B., Kozhakhmetov, D. B., and Zubareva, L. I., et al., "Analysis of Turbulent Jets Flowing over Smooth and Rough Flat Surfaces," *Heat Transfer—Soviet Research*, Vol. 7, No. 4, 1975, pp. 125-133.

24 Launder, B. E., and Spalding, D. B., *Lectures in Mathematical Models of Turbulence*, Academic Press, New York, 1972.

S. Ramadhyani[1]
Assoc. Mem. ASME

M. Zenouzi

K. N. Astill
Mem. ASME

Department of Mechanical Engineering,
Tufts University,
Medford, Mass.

Combined Natural and Forced Convective Heat Transfer In Spherical Annuli

This paper presents numerical finite difference solutions of combined natural and forced convective heat transfer in spherical annuli. The flow is assumed to enter the annulus through a port in the bottom of the outer sphere and exit through a diametrically opposite port. The spheres are isothermal and at different temperatures. The governing conservation equations are reduced to dimensionless form and the nondimensional parameters of the problem are identified. The influence of these parameters of the problem are identified. The influence of these parameters on the solution is studied. Details of the flow field and temperature field are presented by means of velocity vector and isotherm maps. Circumferential average and local Nusselt numbers are presented and compared with earlier numerical work in which the effects of natural convection were ignored. It is shown that the buoyancy effects can have a very significant impact on the heat transfer and fluid flow, particularly at low Reynolds numbers.

1 Introduction

In a recent publication, Ramadhyani et al. [1] presented the results of numerical finite difference computations of forced convection heat transfer in spherical annuli. There a study was made of the thermal and hydrodynamic phenomena occurring when a fluid is pumped into the annulus between two concentric isothermal spheres through a port in the outer sphere and is allowed to flow out through a diametrically opposite port. In that analysis the variation of density with temperature was assumed to be zero, and consequently, the effect of buoyancy forces on the heat transfer and fluid flow was not taken into account. In the present paper it is shown that natural convection effects may have a significant influence on the flow pattern and on the magnitudes of the heat transfer coefficients at the two spherical surfaces.

Convective heat transfer in spherical annuli is encountered in several practical instances. These include the temperature control of gyroscope gimbals, the cooling of spherical fuel elements in homogeneous nuclear reactors, and the guard-cooling of cryogenic liquids in spherical containers. Although the cited applications encompass wide ranges of the governing parameters, viz., the Reynolds and Rayleigh numbers and the radius ratio, the present investigation is restricted to a range of Reynolds and Rayleigh numbers in which the flow is believed to be laminar. The range of radius ratios explored in this work is expected to encompass most practical instances.

Previous analytical investigations of this problem are described in [1-4] and have all been directed at the case of purely forced convection. The few experimental studies of this problem reported in the literature [3], [5-7] also implicitly ignore the possibility of superposed natural convection and offer correlations for the Nusselt number in terms of the Reynolds number and geometric parameters. The present authors believe that this is the first analysis of combined natural and forced convection in a spherical annulus.

In this study, two concentric isothermal spheres at different temperatures are considered. Fluid is pumped into the annulus through a port in the bottom of the outer sphere and is allowed to flow out through a port at the top. The temperature of the fluid at the inlet port is equal to the temperature of the outer sphere, while the inner sphere is at a higher temperature. Thus buoyancy effects assist the flow at the inner sphere surface and are opposed to the main flow near the surface of the outer sphere. The resulting flow patterns are highly complex and preclude an anaytical solution; consequently, a finite difference solution procedure described by Patankar [8] was employed. In view of the large number of governing parameters, an exhaustive study of the problem would have been prohibitively expensive, and solutions have been obtained only for judiciously selected values of each parameter. The results obtained from these computations include local and circumferentially averaged Nusselt numbers, and detailed descriptions of the temperature and velocity distributions in the annulus.

2 Analysis and Solutions

2.1 The Governing Conservation Equations. As shown in Fig. 1, the calculation domain is bounded by concentric spheres of radii r_1 and r_2, and the flow enters and leaves the annulus through diametrically opposite circular ports, the angular apertures of which are α_i and α_o, respectively. The spherical coordinate system depicted in the figure is employed in the solution of the problem. It is assumed that the flow is radial and uniform over the inlet port and that it is laminar, axisymmetric, and steady throughout the calculation domain.

The analysis begins with the equations of conservation of mass, momentum, and energy, all expressed in spherical coordinates. In these equations, terms pertaining to the variation of the dependent variables in the ϕ-direction are omitted under the assumption of axisymmetry, and terms corresponding to viscous dissipation and flow work are omitted from the energy equation. In addition, all fluid properties are treated as constants with the exception of the density appearing in the body force terms in the momentum equations. In these terms a linear variation of density with temperautre is assumed, according to the equation

$$\rho = \rho_o [1 - \beta (T - T_o)] \tag{1}$$

where ρ_o and T_o are the reference density and temperature, and β is the coefficient of thermal expansion. Some simplification of the resulting body force terms is effected by defining an effective pressure

$$p^* = p - \rho_o g \, r \cos \theta \tag{2}$$

The conservation equations may then be expressed in

---

[1] Presently at School of Mechanical Engineering, Purdue University, West Lafayette, Ind. 47907

Contributed by the Heat Transfer Division for publication in the JOURNAL OF HEAT TRANSFER. Manuscript received by the Heat Transfer Division April 29, 1984.

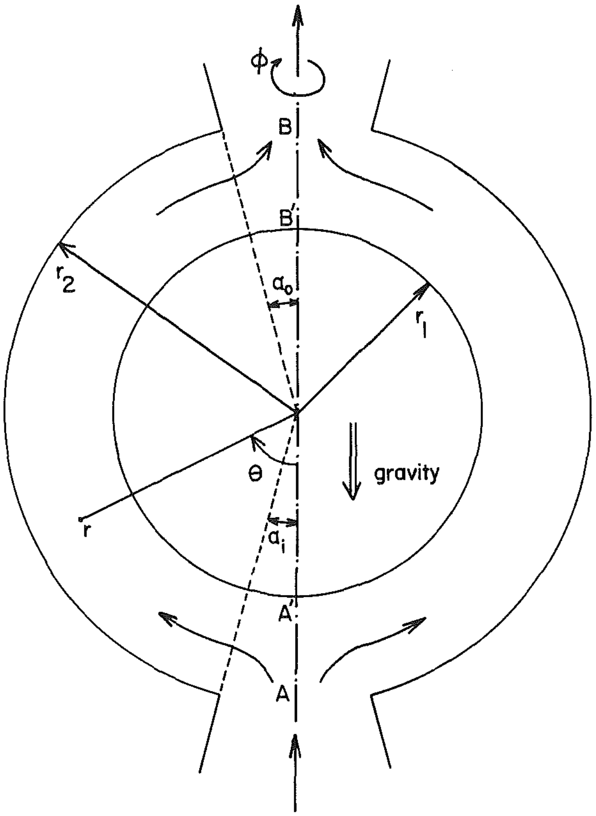

Fig. 1 Schematic depiction of the flow domain and the spherical coordinate system

dimensionless form through the introduction of a reference velocity $\bar{v}$, a reference length r_1, and a reference temperature difference $(T_1 - T_2)$. $\bar{v}$ is the average velocity at the equator ($\theta = 90$ deg) in the main flow direction and is obtained from the equation

$$\bar{v}=\dot{m}/[\rho\Pi(r_2^2-r_1^2] \tag{3}$$

Dimensionless variables are then formed as follows

$$U=v_\theta/\bar{v}, V=v_r/\bar{v}, R=r/r_1$$

$$P=p^*/\rho\bar{v}^2, \Phi=(T-T_2)/(T_1-T_2) \tag{4}$$

The dimensionless differential equations expressing conservation of mass, of r and θ momentum, and of energy may be written as

$$(1/R^2)\partial(R^2V)/\partial R+(1/R\sin\theta)\partial(U\sin\theta)/\partial\theta=0 \tag{5}$$

$$V\partial V/\partial R+(U/R)\partial V/\partial\theta-U^2/R=-\partial P/\partial R$$
$$-(\mathrm{Ra}/\mathrm{Re}^2\mathrm{Pr})\Phi\cos\theta/(R_o-1)$$
$$+[\nabla^2V-2V/R^2-(2/R^2\sin\theta)\partial(U\sin\theta)/\partial\theta](R_o-1)/\mathrm{Re} \tag{6}$$

$$V\partial U/\partial R+(U/R)\partial U/\partial\theta+UV/R=-(1/R)\partial P/\partial\theta$$
$$+(\mathrm{Ra}/\mathrm{Re}^2\mathrm{Pr})\Phi\sin\theta/(R_o-1)$$
$$+[\nabla^2U+(2/R^2)\partial V/\partial\theta-U/(R^2\sin^2\theta)](R_o-1)/\mathrm{Re} \tag{7}$$

$$V\partial\Phi/\partial R+(U/R)\partial\Phi/\partial\theta=\nabla^2\Phi(R_o-1)/(\mathrm{RePr}) \tag{8}$$

where ∇^2 is the two-dimensional Laplacian expressed in spherical coordinates as

$$\nabla^2=(1/R^2)\partial(R\partial/\partial R)/\partial R+(1/R^2\sin\theta)\partial(\sin\theta\partial/\partial\theta)/\partial\theta \tag{9}$$

and the dimensionless groups R_0, Re, Pr, and Ra are defined as

$$R_0=r_2/r_1, \mathrm{Re}=\rho\bar{v}(r_2-r_1)/\mu, \mathrm{Pr}=\mu C_p/k \tag{10}$$
$$\mathrm{Ra}=g\beta(r_2-r_1)^3(T_1-T_2)/(\nu\alpha)$$

The boundary conditions employed in the solution of the problem will now be described. The problem is assumed to be axisymmetric; i.e., the θ derivatives of temperature and radial velocity are zero along the line segments AA′ and BB′ in Fig. 1, and the tangential velocity is itself zero along these segments. Along the two solid spherical surfaces the conditions of no-slip and zero normal velocity are applicable. The two surfaces are assumed to be isothermal and at different temperatures. Over the cross section of the inlet port, the fluid velocity is assumed to be radial and uniform, and the inlet

Nomenclature

A = surface area of either inner or outer sphere
C_p = specific heat at constant pressure
g = acceleration due to gravity
$h,\bar{h}$ = local and circumferential average heat transfer coefficients
k = thermal conductivity of the fluid
$\dot{m}$ = mass flow rate through the annulus
$\mathrm{Nu}_I,\mathrm{Nu}_O$ = local Nusselt numbers at inner and outer spherical surfaces (equation (21))
$\overline{\mathrm{Nu}}_I,\overline{\mathrm{Nu}}_O$ = circumferential average Nusselt numbers (equation (18))
$\overline{\mathrm{Nu}}_{I,\mathrm{f.c.}},\overline{\mathrm{Nu}}_{O,\mathrm{f.c.}}$ = circumferential average Nusselt numbers in the limit of pure forced convection
p,p^* = dimensional static pressure and effective pressure (equation (2))
P = dimensionless effective pressure $p^*/\rho\bar{v}^2$
Pr = Prandtl number $\mu C_p/k$
Q = magnitude of the rate of heat transfer at the surface of either sphere
r = radial coordinate
r_1,r_2 = radii of inner and outer spheres
R = dimensionless radius r/r_1
R_O = radius ratio r_2/r_1
Ra = Rayleigh number $g\beta(r_2-r_1)^3(T_1-T_2)/(\nu\alpha)$
Re = Reynolds number $\rho\bar{v}(r_2-r_1)/\mu$
T_1,T_2 = temperatures of the inner and the outer sphere
U,V = dimensionless tangential and radial velocities (equation (4))
v_θ,v_r = dimensional velocities in the tangential and radial directions
$\bar{v}$ = mean velocity at $\theta = 90$ deg in the main flow direction
V_i = ratio of inlet velocity to mean velocity
α = thermal diffusivity of the fluid
α_i,α_o = angular apertures of inlet and outlet ports
β = coefficient of thermal expansion
θ = tangential coordinate
μ = dynamic viscosity of the fluid
ν = kinematic viscosity
ρ = density of the fluid
ϕ = azimuthal coordinate
Φ = dimensionless temperature $(T-T_2)/(T_1-T_2)$
Φ_i = dimensionless temperature of the inflow

temperature is taken to be equal to that of the outer sphere. The inlet temperature is one of the parameters of the problem, and a complete exploration of the situation would require that several different values be assigned to it. However, in the interests of economy, computations were restricted to a single value of inlet temperature, the present choice being deemed to be the case of greatest interest.

At the outlet port, an a priori specification of the boundary conditions is not possible, because the conditions prevailing there are strongly dependent on the conditions upstream in the calculation domain. However, the fluid velocity at the outlet port is expected to be predominantly in the outward radial direction and the influence of the boundary values at the outlet port on the computed solution is expected to be weak. Indeed, at sufficiently high flow velocities, the outlet boundary values are expected to be governed almost totally by the downstream convection of upstream values, i.e., the conservation equations may be viewed as being locally parabolic. In view of this expectation, the strategy adopted at the downstream boundary, in the case of U and Φ, is to isolate the computational domain from the downstream boundary value by setting the diffusion fluxes corresponding to these quantities to zero. Since the flow is convection dominated at the outlet port, the error incurred by this strategy is small. The actual implementation of the idea may be accomplished either by setting the second derivatives of U and Φ in the radial direction to zero, or by setting the diffusion coefficients at the outflow boundary to zero. The latter procedure, being convenient to implement in the computer program, was employed in the present calculations. As a post-processing step, the values of U and Φ at the outlet port were set equal to the values at the nearest upstream neighboring locations, after converged solutions had been obtained.

In the case of the radial component of velocity V, mass conservation requires a diminution of the radial velocity with increasing radius. Hence setting the radial second derivative to zero would be inappropriate. However, any reasonable velocity distribution over the outlet port that guaranteed global conservation of mass would be acceptable. The procedure adopted in the present work in specifying the radial outflow boundary velocity is intimately linked to the finite difference scheme employed in the solution of the problem. The procedure is identical to that described in considerable detail in [1], and, in view of this, a description of it will not be repeated in the present paper.

With the exception of the outlet cross section, the boundary conditions may be expressed as follows:

$$\partial V/\partial\theta = U = \partial\Phi/\partial\theta = 0 \text{ along } \theta = 0, \theta = \Pi \qquad (11)$$

$$U = V = 0, \Phi = 1, \text{ at } R = 1 \qquad (12)$$

$$U = V = \Phi = 0 \text{ at } R = R_0 \text{ and } \alpha_i \leq \theta \leq \Pi - \alpha_o \qquad (13)$$

$$U = 0, V = V_i, \Phi = 0 \text{ at } R = R_0 \text{ and } 0 \leq \theta \leq \alpha_i \qquad (14)$$

The quantity V_i appearing in equation (14) is the dimensionless inlet velocity, a purely geometric quantity given by the expression

$$V_i = (R_0^2 - 1)/[2R_0^2(1 - \cos\alpha_i)] \qquad (15)$$

In the present investigation, the port apertures α_i and α_o were fixed at 0.2 radian, and the influence of varying these parameters was not studied. The Prandtl number was fixed at 0.7 (approximately that for air), and two different radius ratios, 1.2 and 2.0, were examined. In each case, the Reynolds number was successively assigned the values 5, 50, and 100, while the Rayleigh number was varied between 10^2 and 10^7. A more complete exploration of the problem would have been prohibitively expensive.

2.2 The Finite Difference Solutions. As mentioned earlier, the finite difference solution procedure employed in this work is an adaptation of the method described in detail in [8]. An abbreviated description of the method may also be found in [1]. As discussed in [1], the finite difference equations were derived by integrating the governing partial differential equations over each of the control volumes in the discretized domain. The resulting finite difference coefficients were computed using the power-law scheme described in [8]. Staggered grids were used for the momentum equation, and the SIMPLER solution algorithm [8] was employed to solve the coupled hydrodynamic equations. However, an important difference between the procedure followed in [1] and in the present work is that, in the present work, the hydrodynamic solutions were obtained simultaneously with the thermal solutions because of the coupling between the energy and the momentum equations. Thus the solution of the energy equation constituted an additional step in the algorithm.

In order to determine a grid distribution that would produce acceptable accuracy, initial computations were carried out at three different mesh sizes: 35 × 18 nonuniform, 35 × 24 uniform, and 35 × 24 nonuniform. The numbers denote, respectively, the number of grid points in the circumferential and the radial directions. In the nonuniform grid cases, the grid points were closely packed near each sphere surface in order to improve the resolution. The solutions from the three grid sizes showed very little variation between each other. The grid fineness checks are presented in detail in [9]. For the final computations, a nonuniform grid of 35 × 24 points was employed. In the final computations, the maximum solution error in the velocities computed at any nodal point in the domain is less than 5 percent; most of the nodal points have errors well below this limit. In particular, the calculated velocities near the spherical surfaces are highly accurate, and only a few nodal points in the interior of the flow field approach the cited error limit. With regard to the temperature field, the solution error at any nodal point is less than 2 percent.

In addition to the grid fineness checks, the computer program was tested in the limiting situations of pure natural convection and pure forced convection. In the former situation, the analytical solutions of Mach and Hardee [10], and the numerical solutions of Astill et al. [11], were used for comparison. Excellent agreement was obtained in the calculated velocity field and in the local Nusselt number distribution. In the limit of pure forced convection, the present computations are in agreement with those presented in [1]. As a final check on the calculations energy balances were computed from the converged solutions for velocity and temperature. These energy balances confirmed that the net heat transferred at the spherical surfaces was equal to the enthalpy change of the fluid, between inlet and outlet, multiplied by the mass flow rate of the fluid.

In view of the complex nature of the flow and the coupling between the momentum equations and the energy equation, the iterative solution process converged slowly. In order to expedite the convergence, solutions obtained at lower Rayleigh numbers were supplied as initial guesses for solutions at higher Rayleigh numbers. In addition, underrelaxation of the momentum and energy equations was found to be necessary. Typically, between 120 and 150 iterations were required to obtain an acceptable level of convergence. On the Tufts University DEC-10 computer system, CPU times of the order of 20 minutes were necessary for each solution run.

3 Results and Discussion

The computations were performed for radius ratios of 1.2 and 2 at a Prandtl number of 0.7. The Reynolds number was assigned values of 5, 50, and 100 and the Rayleigh number was varied between 10^2 and 10^7. All calculations were carried out for a dimensionless inlet temperature of zero, a dimen-

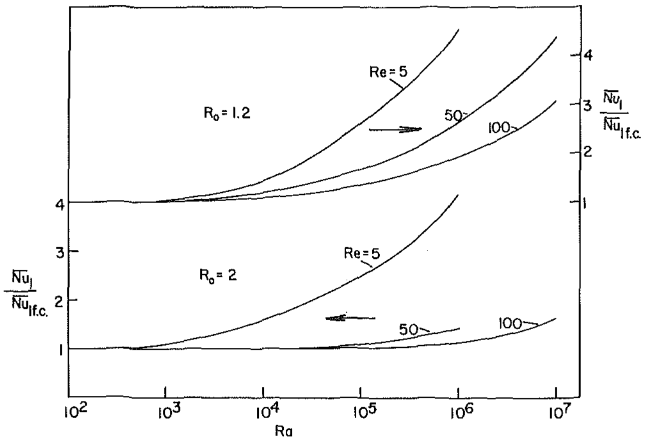

Fig. 2 Variation of normalized average Nusselt number at inner sphere surface, Pr = 0.7

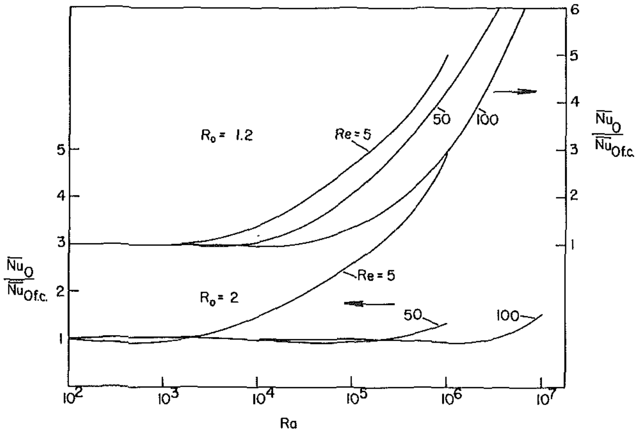

Fig. 3 Variation of normalized average Nusselt number at outer sphere surface, Pr = 0.7

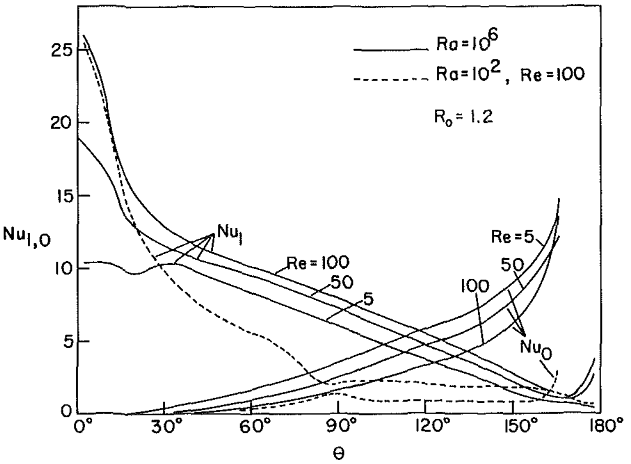

Fig. 4 Variation of local Nusselt numbers at inner and outer sphere surface, Pr = 0.7

sionless inner sphere temperature of 1, and a dimensionless outer sphere temperature of 0. The only exception was a single case in which the inner sphere temperature was prescribed to be 0 and the outer sphere temperature was 1.

3.1 Heat Transfer. The circumferential average Nusselt numbers at the two spherical surfaces are defined by the equation

$$\overline{\mathrm{Nu}} = \bar{h}(r_2 - r_1)/k \tag{16}$$

where $\bar{h}$ is the average heat transfer coefficient calculated as

$$\bar{h} = Q/A(T_2 - T_1) \tag{17}$$

Q is the magnitude of the rate of heat transfer at the surface of either sphere, and A is the corresponding surface area. Since the local heat flux per unit area is given by $q = -k\, \partial T/\partial r$, the circumferential average Nusselt numbers at the two surfaces may be written in terms of the dimensionless variables as

$$\mathrm{Nu}_{I,O} = \frac{\left[\int_0^{\Pi} |\partial\Phi/\partial R| \sin\theta\, d\theta\right](R_2 - R_1)}{2(\Phi_1 - \Phi_2)} \tag{18}$$

The subscripts I and O denote the inner and outer spheres and $|\partial\Phi/\partial R|$ is evaluated at the corresponding surface.

In Figs. 2 and 3, normalized inner and outer sphere average Nusselt numbers are plotted against the Rayleigh number for the three different Reynolds numbers and two radius ratios studied in this work. In each figure, the ordinate is normalized by the value of the Nusselt number in pure forced convection. These normalizing values were obtained from [1]. In both figures it is seen that the curves for Re = 5 lie above those for Re = 50 which, in turn, lie above the curves for Re = 100. As is to be expected, this indicates that, at a given Rayleigh number, the natural convection effects are more significant at lower values of Reynolds number. Furthermore, the figures show that at high Rayleigh numbers ($\approx 10^6 - 10^7$) there is a significant augmentation of the Nusselt number by the superimposed natural convection. The augmentation is more pronounced for the smaller radius ratio, $R_O = 1.2$, and for the outer sphere average Nusselt number. An interesting feature of Fig. 3 is the slight downward slope of the $\overline{\mathrm{Nu}}_O$ curves corresponding to $R_O = 2$ and low to medium Rayleigh numbers.

Figure 4 shows the variation of local Nusselt numbers at the inner and outer spheres with angular position θ. The local Nusselt number is defined by the equations

$$\mathrm{Nu} = h(r_2 - r_1)/k \tag{19}$$

and

$$h = |k\partial T/\partial r| / (T_1 - T_2) \tag{20}$$

In terms of dimensionless variables, the local Nusselt number may be expressed as

$$\mathrm{Nu}_{I,O} = |\partial\Phi/\partial R|(R_2 - R_1) \tag{21}$$

Where I and O stand for the inner and the outer sphere, respectively, and $|\partial\Phi/\partial R|$ is evaluated at the corresponding surface. The curves in Fig. 4 are for the case of $R_O = 1.2$ and Ra = 10^6. Qualitatively similar curves are obtained for $R_O = 2$ but are not presented here. In order to show the effect of the superimposed natural convection on the variation of local Nusselt numbers, the curves corresponding to Re = 100 and Ra = 100 are also drawn on the figure for comparison.

Attention is first directed to the curves for Nu_I at Re = 100 corresponding to the two cases Ra = 10^2 and Ra = 10^6. The former is a forced convection dominated situation while the latter is a case of combined convection. A comparison of the two curves shows that while the heat transfer in the inlet region ($\theta \leq 15$ deg) is virtually unaffected by natural convection effects, there is a very substantial augmentation of Nu_I for 15 deg < θ < 150 deg in the case of Ra = 10^6. The buoyancy assistance received by the flow at the surface of the inner sphere is responsible for higher velocities and correspondingly greater heat transfer rates. In the case of Nu_O, strong enhancement of the heat transfer rate is found for $\theta > 90$ deg. Again this effect may be interpreted in terms of the details of the fluid flow field. The presentation of the computed fluid velocity vectors later in this paper will shed additional light on this phenomenon.

Attention is now drawn to the trend in the Nu_I curves corresponding to Re = 5, 50, and 100, and Ra = 10^6. As may be expected, the curve for Re = 100 is the highest while the

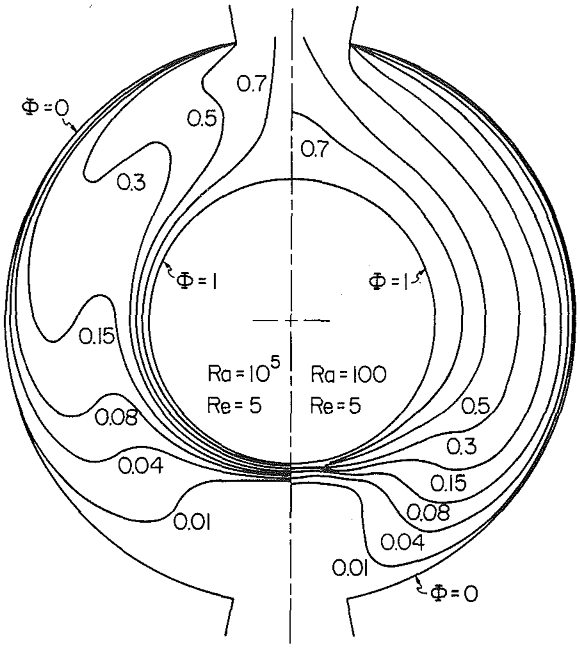

Fig. 5(*a*) Computed isotherms, Pr = 0.7 and Re = 5

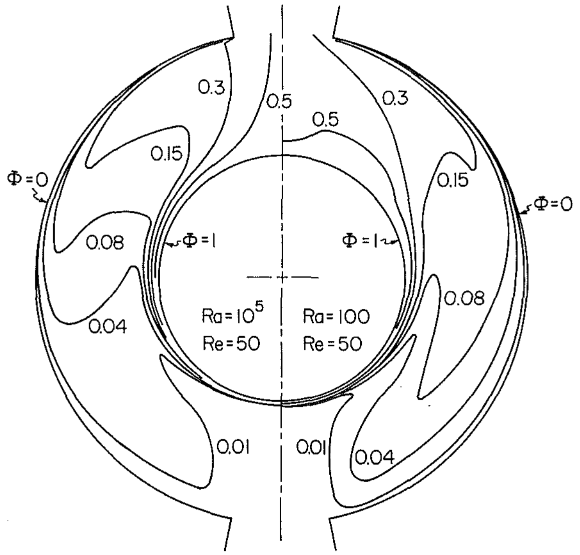

Fig. 5(*b*) Computed isotherms, Pr = 0.7 and Re = 50

curve for Re = 5 is the lowest. In the case of Nu_O, however, the opposite trend is observed; Re = 100 is the lowest curve while Re = 5 is the highest. This difference between Nu_I and Nu_O is due to the fact that natural convection and forced convection combine to reinforce the heat transfer at the inner sphere whereas they produce opposing effects at the outer sphere. In particular, at the outer sphere, the forced convective flow tends to diminish the heat transfer while the natural convection enhances the heat transfer. The isotherms and fluid velocity vectors to be presented in the ensuing paragraphs will further illustrate this point.

In Figs. 5(*a*) and 5(*b*), isotherm plots are furnished for several combinations of Rayleigh and Reynolds numbers for the case of $R_o = 2$. Figure 5(*a*) depicts isotherms for Re = 5 and two Rayleigh numbers, 10^5 and 10^2; the two halves of the figure depict the two different cases. For Ra = 10^5, the flow and heat transfer are influenced by both forced convection and natural convection, i.e., the situation is in the regime of mixed convection. For Ra = 10^2, the flow and heat transfer are completely dominated by forced convection. As may be seen from the isotherms, the temperature distributions in the annulus are very different in the two cases. The close spacing of the isotherms near the inner sphere surface in the case of Ra = 10^5 indicates large temperature gradients and high heat fluxes. Near the outer surface, the isotherms are observed to be closely spaced in the upper portion of the spherical surface for Ra = 10^5. Thus, natural convection effects tend to augment the heat transfer from the entire inner spherical surface and from the upper portion of the outer spherical surface.

Similar remarks apply to Fig. 5(*b*) in which isotherms are depicted for Re = 50 and Ra = 10^5 and 10^2. In this figure, however, the differences between the two halves are not as dramatic as in Fig. 5(*a*), because the superimposed natural convection effects at Ra = 10^5 do not influence the situation as strongly as at Re = 5. The peculiar shape of the isotherm labeled 0.5 for Ra = 10^2 and Re = 50 is due to the presence of a separation bubble in the upper part of the flow field. The flow separates from the inner sphere surface in this region. Finally, on comparing the isotherms in the left halves of Fig. 5(*a*) and 5(*b*), it is observed that if the Reynolds number is increased from 5 to 50 while keeping Ra fixed at 10^5, the heat transfer rate at the inner sphere is increased and the rate at the outer sphere is decreased.

To round out this discussion, Figs. 6, 7, and 8 depict velocity vectors in the flow field for three different conditions. The foot of each vector is at the location corresponding to the fluid velocity it represents. In Fig. 6, the flow depicted is one at low Reynolds and Rayleigh numbers, Re = 5 and Ra = 10^2. The toroidal recirculation region formed near the inlet port is caused by fluid entrainment and inertia effects. Figure 7 depicts velocity vectors for Re = 5 and Ra = 10^5. In this flow field, the size and location of the recirculation region are different, because the eddy is being driven partly by buoyancy forces. The acceleration of the flow near the inner sphere due to buoyancy forces is clearly seen. Figure 8, a depiction of the case in which the inner and outer sphere temperatures are interchanged, is intended to give a qualitative appreciation of the significant effects of buoyancy forces. In this situation, the dimensionless temperatures of the inner and outer spheres are 0 and 1, respectively, and the inlet fluid temperature is 0. Buoyancy assists the main flow near the outer sphere and opposes it near the inner sphere. The result of this is the complicated flow pattern shown in the figure.

The flow field depicted in Fig. 8 is useful in interpreting certain results presented in [3]. In that work, an experimental investigation, supplemented by numerical solutions, was conducted for an annulus of $R_o = 1.2$ with water as the annulus fluid. The inner sphere was cooled to 0°C, while the outer sphere was adiabatic. The water inlet temperature was 53°C. The numerical solutions were obtained for Reynolds numbers from 4.4 to 440, while the experimental investigation spanned the Reynolds number range from 41 to 1086. Buoyancy effects were neglected in the numerical solutions. The Rayleigh number computed on the basis of the temperature difference between inflow and the inner sphere was 3×10^7.

In comparing the experimental and numerical results in [3], it was observed that, in the experiments, flow separation from the inner sphere occurred at a smaller value of θ than was predicted by the numerical solutions. Examination of Fig. 8 in the present paper reveals flow separation from the inner sphere due to a buoyancy-driven downflow at the inner sphere surface. Based on this observation, it is suggested that the discrepancies in separtion angles reported in [3] were due to the neglect of buoyancy effects in the numerical solution. Unfortunately, a quantitative comparison between [3] and the present work is not possible because of differences in the thermal boundary conditions.

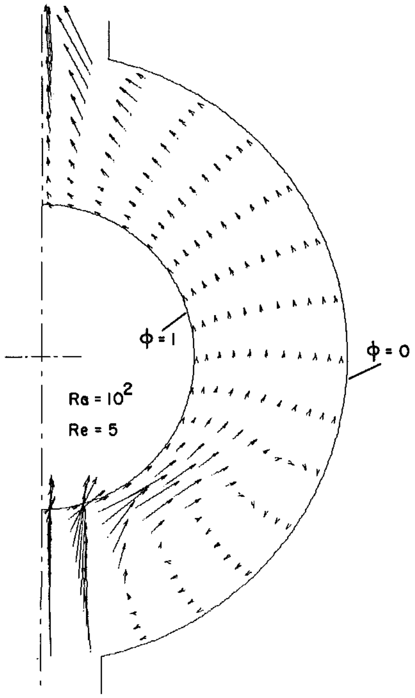

Fig. 6 Computed velocity vectors

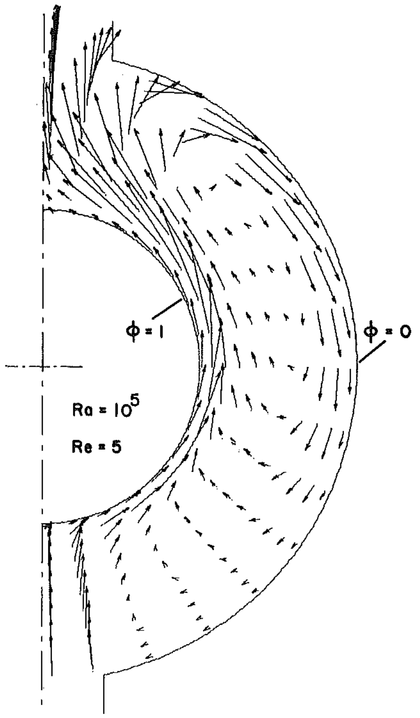

Fig. 7 Computed velocity vectors

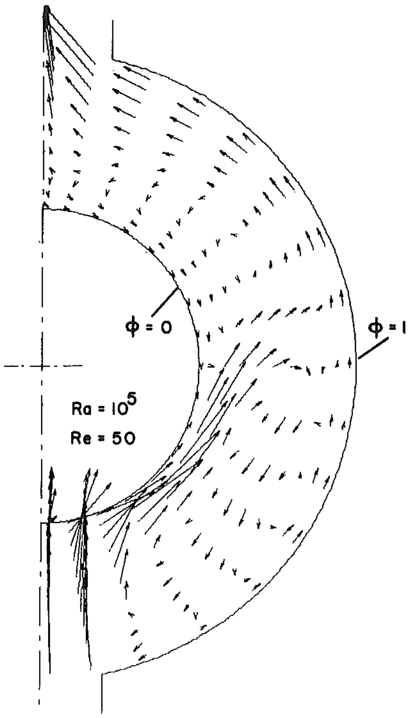

Fig. 8 Computed velocity vectors

4 Conclusions

In the present paper, laminar mixed convection heat transfer between concentric isothermal spheres has been studied. This work is a supplement to an earlier study that dealt with the case of pure forced convection in the same situation. The main outcome of the present work is a demonstration of the great impact of buoyancy effects on the heat transfer rates at the two spherical surfaces. The various heat transfer and fluid flow phenomena occurring in this situation have been studied for several values of Reynolds number and Rayleigh number. The results have been presented in the form of graphs for overall Nusselt numbers, local Nusselt numbers, isotherm maps, and velocity vector plots.

References

1 Ramadhyani, S., Torbaty, M., and Astill, K. N., "Laminar Forced Convection Heat Transfer in Sperhical Annuli," ASME JOURNAL OF HEAT TRANSFER, Vol. 105, May 1983, pp. 341–349.

2 Astill, K. N., "An Analysis of Laminar Forced Convection Between Concentric Spheres," ASME JOURNAL OF HEAT TRANSFER, Vol. 98, Nov. 1976, pp. 601–608.

3 Tuft, D. B., and Brandt, H., "Forced Convection Heat Transfer in a Spherical Annulus Heat Exchanger," ASME JOURNAL OF HEAT TRANSFER, Vol. 104, Nov. 1982, pp. 670–677.

4 Cobble, M. H., "Spherical Shell Heat Exchanger—Dirichlet Problem," *Journal of the Franklin Institute*, Sept. 1963, pp. 197–206.

5 Rundell, H. A., Ward, E. G., and Cox, J. E., "Forced Convection in Concentric-Sphere Heat Exchangers, ASME JOURNAL OF HEAT TRANSFER, Vol. 90, Feb. 1968, pp. 125–129.

6 Cox, J. E., and Sahni, B. K., "The Concentric Sphere Heat Exchanger," ASME JOURNAL OF HEAT TRANSFER, Vol. 93, Nov. 1971, pp. 468–469.

7 Newton, R. L., "An Experimental Investigation of Forced Convection Between Concentric Spheres," M.S. thesis, Department of Mechanical Engineering, Tufts University, 1977.

8 Patankar, S. V., *Numerical Heat Transfer and Fluid Flow*, Hemisphere-McGraw-Hill, 1980.

9 Zenouzi, M., "Combined Natural and Forced Convective Heat Transfer in Spherical Annuli," M.S. thesis, Department of Mechanical Engineering, Tufts University, 1981.

10 Mack, L. R., and Hardee, H. C., "Natural Convection Between Concentric Spheres at Low Rayleigh Numbers," *International Journal of Heat and Mass Transfer*, Vol. 11, Mar. 1968, pp. 387–396.

11 Astill, K. N., Leong, H., and Martorana, R., "A Numerical Solution for Natural Convection in Concentric Spherical Annuli," CSDL Report P-1034, The Charles Stark Draper Laboratory, Inc., Cambridge, Mass., 1980.

Onset of Thermal Convection in a Fluid Layer Subjected to Transient Heating From Below

M. Kaviany
Department of Mechanical Engineering,
University of Wisconsin—Milwaukee,
Milwaukee, Wis. 53201
Mem. ASME

The onset of convection in a horizontal layer of fluid subject to time-dependent heating from below is studied both experimentally and analytically. The fluid layer is confined by a rigid boundary at the bottom and a shear-free surface at the top. The fluid, which is initially quiescent, is heated by increasing the temperature of the lower surface at a constant time-rate. The experimental observation of the time of the onset of convection is made through the sudden change in variation of the temperature of the lower surface with respect to time. The onset is also observed through the sudden change in the fringe pattern created by holographic interferometry. Various layer depths are considered in order to observe the influence of this variable on the onset time. The analytical prediction is made by application of the linear amplification theory subject to boundary conditions similar to those of the experiment. Good agreement is found between the experimental and analytical results. Comparisons are also made with the experimental and analytical results available in the literature.

1 Introduction

The stability of a horizontal fluid layer subject to time-independent temperature distribution has been studied extensively [1]. However, most of the situations in which the criteria for the onset of convection are required involve time-dependent temperature fields. In some instances, these situations can be approximated or reduced to time-independent problems [2, 3]. Theoretical treatment of the time-dependent temperature field through the application of the linear amplification theory was initiated by Foster [4, 5] and continued by others [6-8]. Although this initial value approach does not completely describe the physics of the system, good agreement has been found between its predictions and available experimental results [6, 8-10]. Two empirical aspects of this dynamic linear stability analysis that have been subjects of refinement are: (*i*) the initial condition for the disturbances, and (*ii*) the criterion for the determination of the onset of convection time. Among the various causes for the disturbances are thermodynamic fluctuations, nonuniformity in the temperature of the layer, and environmental vibrations. A general description of the disturbances is not presently feasible. The results obtained to data [6, 11] suggest that if the temperature changes taking place at the boundaries are rather smooth, the initial conditions have a less significant effect on the magnitude of onset time. Regarding the criterion for marking the onset time, an empirical determination suggested by Foster [4] seems to be satisfactory. He suggested that the onset time be marked as the time at which the magnitude of the disturbance grows by one thousand times its initial value. This assumes that even at the time of the onset the disturbances are small enough to justify the linearization approximation.

The lower bounds for the time of the onset is determined via the method of energy [12], which results in the time interval over which the generalized energy of the fluid layer is guaranteed to decay. This time interval is lower bound of the onset time.

The prediction of the time of the onset is also approached via the nonlinear amplitude equation using a forcing function [13-15]. The solutions to the nonlinear amplitude equation [16], which are valid only for low heating rates, lead to the determination of the time of the onset as well as the later stages of the growth. Random as well as deterministic descriptions of this forcing function are made by using the experimental data. The results [15] show that a deterministic model can predict the time of the onset of both step change and ramp-type change in the surface temperature, while the stochastic model is only appropriate for a ramp-type change.

The time-dependent problem has also been investigated experimentally [9-10, 17-22] where evaporative heating, gas absorption, and heating from below are the causes of instability. General agreement between the experimental results and theoretical predictions has been reported [9-10, 18, 21].

The problem considered here is that of a horizontal layer of water heated from below by increasing the temperature of the lower surface at a constant temporal rate. This is similar to the experiment in [10], except that the heating rates used are smaller, and shallow as well as deep layers are considered. Figure 1 gives a schematic of the system considered. The lower surface is rigid and the upper surface, which is exposed to air, is approximated as a shear-free surface. The effect of the side walls is not considered. The time of the onset of convection is predicted by applying the amplification theory (similar to [5]

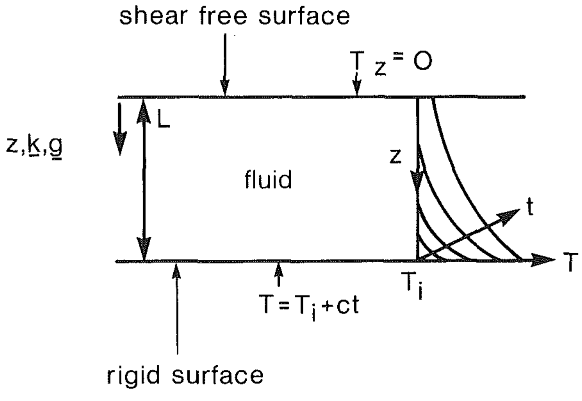

Fig. 1 A schematic of the problem considered

Contributed by the Heat Transfer Division for publication in the JOURNAL OF HEAT TRANSFER. Manuscript received by the Heat Transfer Division July 22, 1983.

except for a finite layer thickness). The experimental determination of the time of the onset is made by examination of the temporal variation of the lower surface temperature and also by holographic interferometry. The effect of the layer thickness and the heating rate on the time of the onset is examined. The experimental and analytical results obtained here are compared with the results available in the literature.

2 Governing Equations and Solution

The linearized governing equations which are based on the principles of conservation of mass, momentum, and energy, for a fluid layer of infinite horizontal extension and subject to the Boussinesq approximation and a linear equation of state, can be found in [1, 4, 6]. By separating the temperature field into mean component T and perturbation component θ, and in the absence of any mean motion, these equations (after proper manipulation) become

$$(\mathrm{Pr}^{-1}\partial_t - \partial_{zz} + a^2)(\partial_{zz} - a^2)w = a^2\theta \tag{1}$$

$$(\partial_t - \partial_{zz} + a^2)\theta = -\mathrm{Ra}\,wT_z \tag{2}$$

$$(\partial_t - \partial_{zz})T = 0 \tag{3}$$

where $\mathbf{u} = \mathbf{i}u + \mathbf{j}v + \mathbf{k}w$, and a is the horizontal wave number. The variables are nondimensionalized using $L^2\alpha^{-1}$, L, $cL^2\alpha^{-1}$, $\alpha\nu g^{-1}\ \beta^{-1}\ L^{-3}$, and αL^{-1} to scale the time, length, mean temperature, perturbation temperature, and perturbation velocity, respectively.

2.1 Mean Temperature Distribution. The temperature of the lower surface is allowed to increase linearly with time. The upper surface is assumed to be adiabatic which, for some systems is more realistic than a constant temperature surface. Note that if the conduction mode persists, due to molecular diffusion, the upper surface temperature will eventually change (unlike the situations studied in [4, 5, 12-15, 19]). Therefore, the initial and boundary conditions for equation (3) are

$$\begin{aligned} T(z,t=0) &= 0 \\ T_z(z=0,t) &= 0 \\ T(z=1,t) &= t. \end{aligned}$$

The solution to equation (3) subject to the foregoing condition is given by Ozisik [22] and is

$$T = t + 2^{-1}(z^2-1) + 2\sum_{l=1}^{\infty}(l-2^{-1})^{-3}\pi^{-3}(-1)^{l-1}$$
$$\exp[-(l-2^{-1})^2\pi^2 t]\cos(l-2^{-1})\pi z \tag{4}$$

2.2 Perturbation Component of Temperature. Equation (2) is subject to the following boundary and initial conditions

$$\begin{aligned} \theta(z,t=0) &= \theta_i(z) \\ \theta_z(z=0,t) &= 0 \\ \theta(z=1,t) &= 0 \end{aligned}$$

The abiabatic upper surface condition is the same as that applied to the mean temperature and the lower surface boundary condition corresponds to a perfectly conducting surface.

The method of solution is that of inner Galerkin as described in [24]. In this method, a set of trial functions is chosen such that they satisfy the boundary conditions. By properly choosing these functions, their orthogonality property can be used such that after proper manipulations the spatial dependence can be eliminated. The perturbation component of temperature can be written as

$$\theta = \sum_{m=1}^{\infty} B_m(t)\cos(m-2^{-1})\pi z \tag{5}$$

2.3 Velocity Distribution. Equation (1) is subject to the following boundary and initial conditions

$$\begin{aligned} w(z,t=0) &= w_i(z) \\ w_{zz}(z=0,t) &= w(z=0,t)=0 \\ w_z(z=1,t) &= w(z=1,t)=0 \end{aligned}$$

The boundary conditions are for shear free upper and rigid lower surfaces.

Due to the spatial orthogonality property required [6], the following trial function is used

$$w = \sum_{k=1}^{\infty} A_k(t)\eta_k(z) = \sum_{k=1}^{\infty} A_k(t)[(\sinh\lambda_k)^{-1}\sinh(\lambda_k z)$$
$$-(\sin\tau_k)^{-1}\sin(\tau_k z)] \tag{6}$$

where λ_k and τ_k are given in the Appendix.

2.4 Characteristic Equations. By substituting equation (5) into equation (2) and multiplying the resulting equation by $\cos(j-1/2)\pi z$ and integrating over the range of z between zero and unity, one obtains

$$(B_j)_t = -[(j-2^{-1})^2\pi^2 + a^2]B_j$$
$$-2\mathrm{Ra}\sum_{k=1}^{\infty} A_k\left\{I_{koj} + \sum_{l=1}^{\infty} I_{klj}\exp[(l-2^{-1})^2\pi^2 t]\right\}$$
$$j = 1,2,3\ \ldots \tag{7}$$

Similarly, by substituting equation (6) into equation (1) and after performing the proper manipulations [21], one obtains

Nomenclature

A_k, B_m = coefficients in the Fourier series
a = horizontal wave number
c = rate of change of the increase in the temperature of the lower surface
g = gravitational constant
$I_{kj}, I_{nj}, I_{koj}, I_{kli}, N_j$ = integrals defined in the Appendix
$\mathbf{i},\mathbf{j},\mathbf{k}$ = unit vectors
L = layer thickness
Pr = Prandtl number, $\nu\alpha^{-1}$
Ra = Rayleigh number, $g\beta cL^5\nu^{-1}\alpha^{-2}$
t = time
T = mean temperature
u,v,w = perturbation components of velocity
$\mathbf{u}$ = velocity vector
$\bar{w}$ = amplification factor, defined by equation (9)
x,y,z = cartesian coordinate axes

Greek

α = thermal diffusivity
β = coefficient of volumetric expansion
γ = eigenvalue
λ_k, τ_k = defined in the Appendix
θ = perturbation component of temperature
ν = kinematic viscosity

Subscripts

c = critical
i = initial
o = reference
t,z = t-, z-derivative

$$(A_j)_t = -\Pr(\gamma_j + a^2)A_j + N_j^{-1}\Pr a^2 \sum_{k=1}^{\infty} A_k I_{kj}$$

$$-N_j^{-1}\Pr a^2 \sum_{m=1}^{\infty} B_m I_{mj} \quad j=1,2,3\ldots \tag{8}$$

where the eigenvalue γ_j and quantities N_j, I_{kj}, I_{mj}, I_{koj}, and I_{klj} are given in the Appendix.

2.5 Initial Condition for the Disturbances. Among the sources of disturbances are the thermodynamic fluctuations, temperature nonuniformity within the fluid, and environmental vibrations. The numerical solutions are sensitive to the initial conditions and the specification of these conditions is done empirically. The sensitivity of the results on the initial condition has been discussed in [11] and also in [4, 6]. Here we assume identical initial magnitudes for all wavelengths and for all modes in the series representing the disturbances (i.e., equations (5) and (6)), but these magnitudes are not the same for w and θ. As will be shown, this results in magnitudes for the time of the onset of convection (the critical time) that is in agreement with the experimental results. The initial conditions chosen are

$$A_k(t=0) = 5 \times 10^{-5}$$
$$B_m(t=0) = 3.5 \times 10^{-5}$$

Other choices for these quantities did not alter the time of the onset of convection as long as the magnitudes for all modes are the same.

The linear amplification theory does not describe the physics of the problem completely. For example, the description of the disturbances that are actually generated continuously by this initial value method is not physically correct. A discussion of the advantages and disadvantages of the linear amplification theory is given in [6]. A more realistic description based on a forcing function is given in [15].

The time of the onset of convection is defined [4] as when

$$\bar{w} = \left[\int_0^1 w^2(z,t)\,dz \Big/ \int_0^1 w^2(z,t=0)\,dz\right]^{1/2} \tag{9}$$

reaches a magnitude of 1000. The experimental results of [19] show that this criterion should depend on the Prandtl number, i.e., as the Prandtl number increases, this amplification factor should decrease. The empirical specification of this dependency is not pursued here. However, as will be shown, the experimental results of this study nearly follow the trend found in [19].

Equations (7) and (8) subject to the above initial conditions are solved numerically using the Runge-Kutta-Gill method [25]. The series was truncated by using fifteen terms for each k and l and m [21].

3 Experiment

An experiment was devised so that the time of the onset of convection could be measured for selected and controlled heating rates.

3.1 Apparatus. The inside of the test cell has a width of 13 cm, a depth of 7.5 cm, and a height of 16 cm. The top is covered by an adjustable urethane foam block. The sides of the cell are made of plexiglass and glass. The base is made of a lead block. This lead block and the four copper tubes that pass through it constitute a heat exchanger. The copper tubes are imbedded into the lead block by casting of molten lead. The four counterflow passages are 1.9 cm from the top surface of this lead block. The top surface of the block is in contact with the water layer. This arrangement results in a near uniform lower surface temperature for the water layer. The fluid used in the heat exchanger is distilled water, and its temperature is controlled by an adjustable-temperature circulator. The cell is insulated by several layers of fiber glass wrappings. The test cell rests on a 1.2 × 2.4 m^2 vibration isolation table. Thermocouples are placed in the fluid layer, in the lead block near its upper surface, in the small gap above the water layer, inside the insulations in the circulator, and along the lines from the circulator to the heat exchanger. The output of the thermocouples is monitored and stored at a preselected rate in a digital voltmeter (HP 3456A) capable of reading voltages as low as 10^{-7} V. The aforementioned system allows for control of the lower surface of the cell to as low as 0.020 C/min.

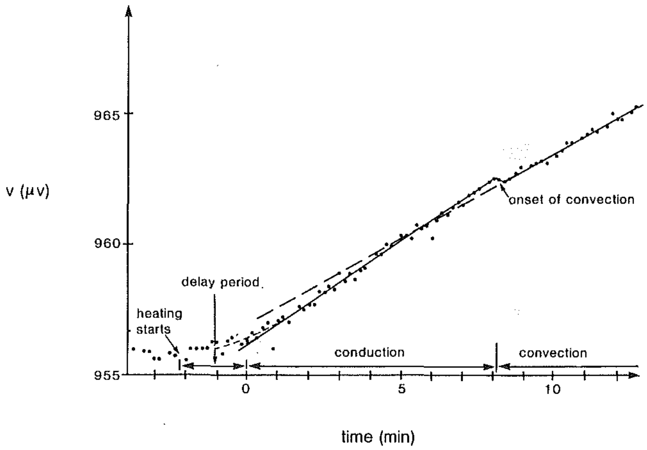

Fig. 2 Variation of the lower surface temperature with time. The symbols show the recorded results, and the solid curve is a curve fit to the recorded results. There are 41 (μv) per 1°C in this temperature range.

3.2 Determination of Onset Time. This is done by two means. The first one is by monitoring the temperature of the lower surface of the cell. When convection starts, an abrupt change in the rate of heat transfer from the base will occur. This change can readily be observed in the curve showing the variation of the lower surface temperature with time. Prior to the onset of convection, the slope of this curve is kept constant; by properly varying the temperature of the circulator, at the time of the onset the slope changes and becomes smaller in magnitude. Figure 2 gives an example of this phenomenon. The straight lines are curve fit to the recorded output from the thermocouple.

Due to the particular response time associated with the heater-heat exchange-test cell system, it is not possible to start with an exactly linear increase in the temperature of the lower surface. The initial portion of the heating process deviates from the desired constant rate, as shown in Fig. 2. In determining the onset time, the time at which the heating begins was taken to be the intercept of the constant c line (solid line) and the initial temperature. However, since the initial nonlinear portion of the curve must also be accounted for, by approximating the nonlinear portion with another straight line and by making the appropriate correction[1] the onset time is then given in a range instead of a single value. As the dimensional onset time increases the contribution of this nonlinear portion becomes smaller. Therefore, for the larger dimensional onset times, only single values are given. It should be noted that although the absolute accuracy of the thermocouples is not very high, for results that are presented here the change in the slope of the lower surface temperature was always clear.

The second method of determining the onset time is by passing a monochromatic and collimated beam of light through the fluid layer and observing any sudden changes in

---

[1] If c was the heating rate over Δt and c' was over $\Delta t'$, then it was assumed that c was applied through $\Delta t + \Delta t' c'/c$.

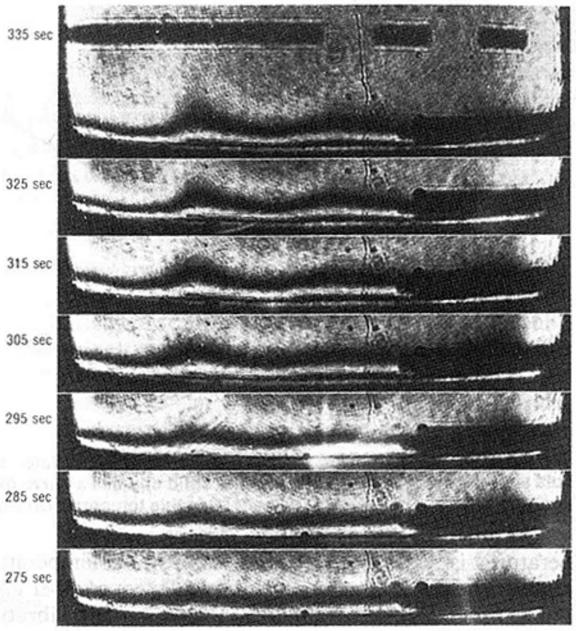

Fig. 3 The onset of convection and the consequent changes in the fringe pattern created by holographic interferometry. The time of the onset of convection is taken to be at 280 s.

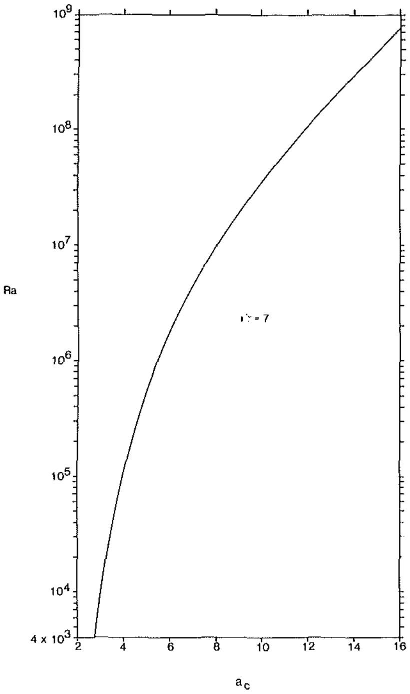

Fig. 4 Variation of the critical wave number with the Rayleigh number for Pr = 7

the fringe pattern created by holographic interferometry. The principle of this method is given by Vest [26] and has been used very successfully by many investigators, e.g., [27]. A 15-mW He-Ne laser was used as the source. The holographic plate was processed in-situ to allow for real time observations. For the test cell used here, using water as the fluid, the temperature difference corresponding to one fringe shift is 0.085°C. The heating rate c required for the onset of convection to take place in 3 to 20 min is in the range of 0.020 to 0.30°C/min. Therefore, the number of fringes that are observed are not more than 4. Longer durations of heating were avoided because of the changes in the ambient temperature and also because of complications with evaporative cooling, especially for a layer thickness of less than 3 cm. Figure 3 shows the evolving fringes. The start of convection is demonstrated by the deviation of the fringes from horizontal straight lines.

In all the cases reported, the onset times determined independently by these methods were in good agreement with a maximum difference of 8 percent. When the contribution of the nonlinear portion of the heating curve was significant, it was found that the onset time determined by interferometry was within the range found from the heating curve.

3.3 Procedure. Pure water and 30 percent by weight glycerin-water solution were used as the fluid. The fluid was poured into the tank to selected depths. Then the temperature of the lower surface was matched to the uniform water layer temperature verified using thermocouples and interferometry.

It was not possible to obtain a complete and continuous adiabatic condition at the upper surface. However, for each experiment with water, before the heating began, this condition was obtained in the following manner. The small air gap above the water layer was never completely saturated. In order to avoid the cooling effect of evaporation (which accelerates the onset), the water layer temperature was varied (throughout) in order to balance the heat loss due to evaporation by equal heat gain from the air gap. The dry- and wet-bulb air temperatures were measured; and, through the use of the available formulas for partial pressure of water in air and correlations for coefficients of convective heat and mass transfer [28], the desired water layer temperature was determined. However, for a large onset time (associated with small fluid depths), the upper surface temperature increased during the experiment and this balance was upset. This process was not as practical when a glycerin-water solution was used; consequently, no thickness layer less than 2.15 cm was attempted for this fluid.

Once the conditions of uniform layer temperature, negligible evaporative heating and near steady state were satisfied, the heating processes were commenced. The temperature of the circulator was increased by a constant amount and at equal time intervals. The proper mass flow rate for the circulating water was determined a priori and was kept constant through the experiment.

4 Predicted Results

Application of the dynamic linear stability theory results in determination of the time of the onset of convection with the Rayleigh number and the Prandtl number as the independent parameters. It will also result in the distributions of the perturbation temperature and velocity, as well as variation of the onset time with the wave number. The wave number that corresponds to the smallest onset time (for a given Ra and Pr) is called the critical wave number. The predicted onset times reported hereafter correspond to the critical wave numbers.

4.1 Critical Wave Number. For a given Prandtl number, as Rayleigh number increases, the critical wave number also increases. This is shown in Fig. 3 for Pr = 7. The trend is similar to those predicted for different boundary conditions [4, 5] and also measured [9].

4.2 Effect of Prandtl Number. Under the Boussinesq approximation, the thermophysical properties are assumed to remain constant, except for density in the body force. In the experimental results that follow, due to the heating process, the Prandtl number changes slightly. Figure 5 shows the variation of the critical time with Prandtl number. The results are for $Ra = 10^8$. As the Rayleigh number decreases, this Prandtl number dependency becomes less pronounced. The results show that the critical time is only slightly sensitive to

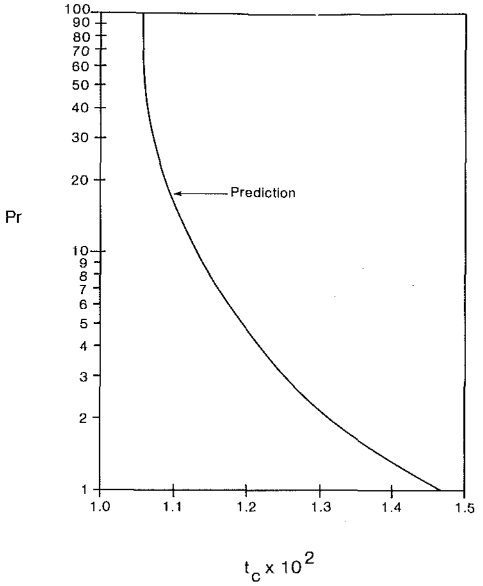

Fig. 5 Variation of the time of the onset with Prandtl number, Ra = 10^8

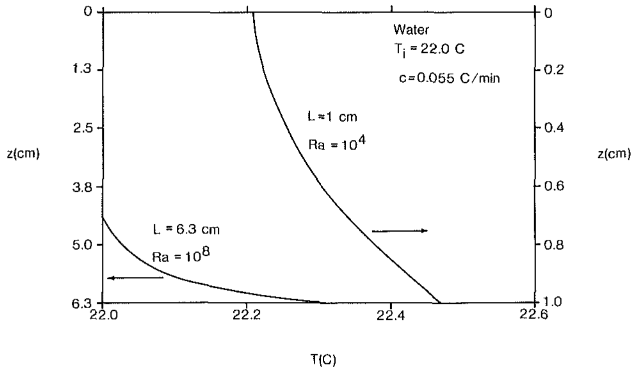

Fig. 6 Comparison between the predicted temperature distributions for two different fluid layer thicknesses. Other parameters are kept the same.

the changes in Prandtl number for water at and around room temperature.

4.3 Effect of Layer Thickness. Due to the adiabatic condition imposed on the upper surface, its temperature will increase if the effect of the lower surface heating penetrates up to this surface. For a given fluid and heating rate c, this requires L to be small. Figure 6 shows that for c = 0.055°C/min, with water as the fluid at the time of onset, the upper surface is substantially increased for $L = 1$ cm (Ra = 10^4, $t_c = 0.751$), while it is unchanged for $L = 6.3$ cm (Ra = 10^8, $t_c = 0.0117$).

4.4 Comparison With Other Predictions. Variations in the onset time with respect to the Rayleigh number are shown in Fig. 7. The results are for this study and several other studies. Here, due to excessive computational requirements, the results are not extended below Ra = 4×10^3. The approximate relationship between t_c and Ra, which is valid for Ra > 10^5, is also given. The results found in [4] for two shear-free surfaces are also shown. In [4], the adiabatic surface considered here was replaced by a constant temperature surface. The lower limit as predicted by the energy method [12] for two shear-free surfaces, using thermal boundary conditions identical to those of [4] are also shown. The predictions made using the finite-amplitude method [15] for liquid Helium (Pr = 0.78), two rigid surfaces, and thermal boundary conditions identical to [4] are also given. These results are based on a forcing function that is determined from the experimental results. It has been suggested in [12] that for long time scales, when the temperature profile is nearly linear (when one surface is heated and the other kept at constant temperature), that for this quasi-steady situation the results of marginally stable states may be applicable. The critical Rayleigh numbers for marginally stable states for the case of rigid-rigid (1707.76), rigid-free (1100.65), and free-free (657.51) are also shown. According to [12], since for the linear profile the dimensional temperature difference is $ct_cL^2\alpha^{-1}$, then $\text{Ra}_c = g\beta L^5 c\nu^{-1}\alpha^{-2}t_c = \text{Ra}\ t_c$ or $\text{Ra} = \text{Ra}_c t_c^{-1}$. Moreover, the experimental results of [19] (Fig. 3 in [19], not shown here) and also the results of the energy method show that this quasi-steady behavior begins at approximately $t_c = 1$. However, this is not the case for the results of amplification theory, which show this to happen approximately at $t_c = 3$, i.e., $\text{Ra} \simeq 3\ \text{Ra}_c t_c^{-1}$ or $t_c \simeq 3\ \text{Ra}_c \text{Ra}^{-1}$. This overprediction for large t_c by the amplification method was also pointed out in [19]. The adiabatic boundary condition applied here allows for the upper surface temperature to increase, and therefore, for large time scales, the effective temperature difference is smaller than that given above. Thus no direct comparison can be made. The results of finite amplitude method show an asymptotic trend for Ra < 1000, with a slope that is larger than that expected for quasi-steady behavior.

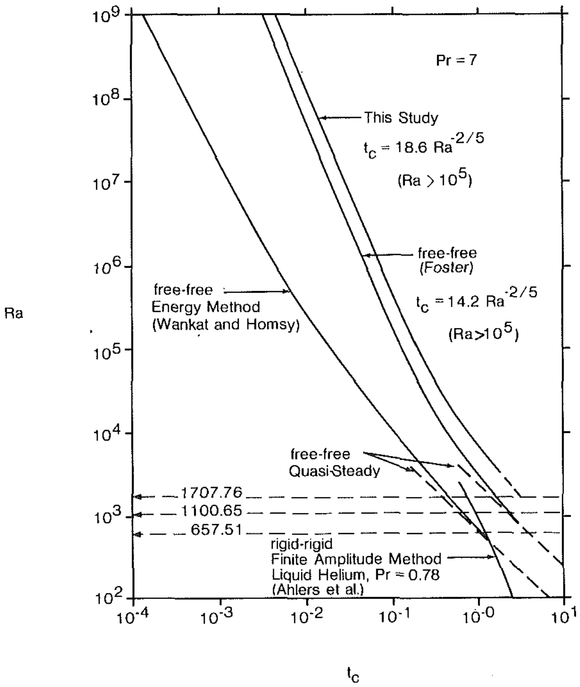

Fig. 7 The results of several predictions for the variations of the onset time with the Rayleigh numbers. Also shown are the critical Rayleigh numbers associated with the marginally stable states.

From Fig. 7, it can be seen that the predicted results of this study, which are an extension of [4], are in general agreement with the available results.

5 Experimental Results and Comparison

The experimental results of this study and those of others are given in Fig. 8 in terms of nondimensionalized variables. For clarity, only the predictions of this study are shown. A few typical data points from the results of [9] (where the cause of instability is evaporative cooling) and [10] (which is due to heating from below) are shown. Some of the experimental results of [15] for liquid Helium subject to rigid-rigid boundary conditions are also shown. As mentioned earlier, the error bars are only present for those data points with

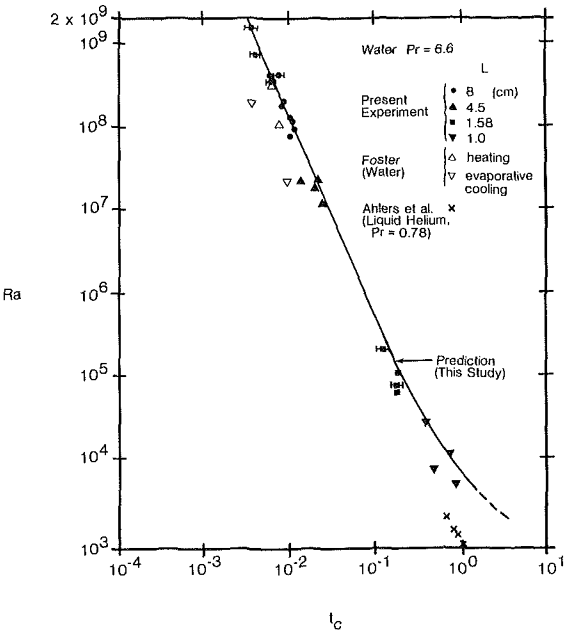

Fig. 8 Variation of the time of the onset with Rayleigh number, Pr = 6.6. The symbols show the experimental results and the solid curve shows the predicted results.

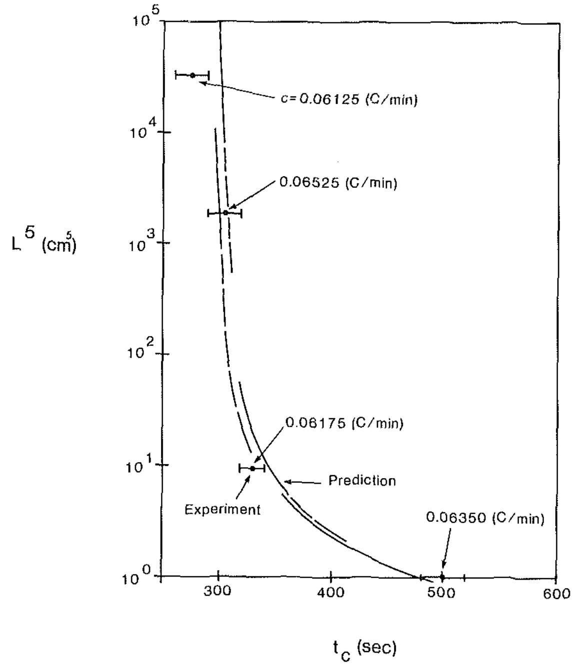

Fig. 10 Variation of the time of the onset of convection with the layer thickness for the heating rate of about 0.0625 C/min, Pr = 6.6

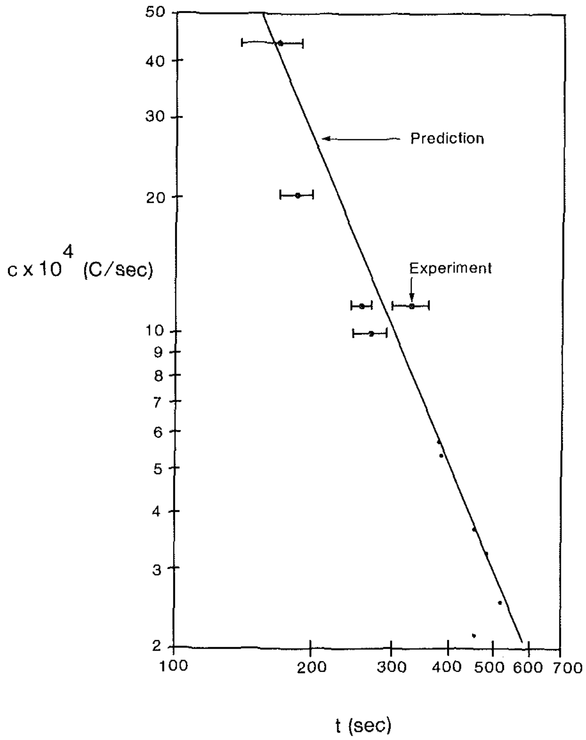

Fig. 9 Variation of the time of the onset of convection with the heating rate Pr = 6.6. Symbols show the experimental results and the solid curve shows the predicted results.

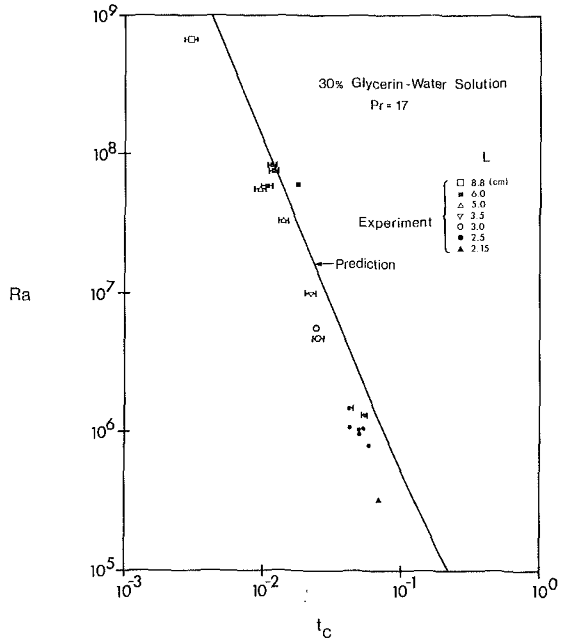

Fig. 11 Variation of the time of the onset with Rayleigh number, Pr = 17. The symbols show the experimental results and the solid curve shows the predicted results.

relatively short dimensional time[2], where the contribution of the nonlinear portion of the heating curve is relatively significant (Fig. 2). For small fluid layer depths the evaporation from the top was difficult to control. Therefore, at low Rayleigh numbers, the agreement between the experimental and predicted results is not as good as it is for large Rayleigh numbers. The results of [15] seem to follow the trend that is found in this study for low Rayleigh number. However, note that the presence of the second rigid boundary and also the smaller Prandtl number both result in an increase of the nondimensional onset time.

Figure 9 shows the dimensional results (for water) for the variation of the critical time with the heating rate for a layer thickness of 8 cm. The predicted results are shown with the solid curve and the experimental results are shown with symbols. For a smaller layer thickness the agreement is not as good as seen in Fig. 8.

Figure 10 shows the dimensional results (for water) of the variation of the critical time with the layer thickness for heating rates of about 0.0625°C/min. The measured results for a layer thickness of 1 cm are not typical for small layer thicknesses. As previously mentioned, evaporative cooling

---

[2] Note that the nondimensional onset time is scaled with αL^{-2}.

causes added instability and accelerates the onset of convection.

Figure 11 shows the variation of nondimensionalized critical time with the Rayleigh number for 30 percent by weight Glycerin-water solution. The agreement between the predicted and measured results is not as good as that for water but a general and fair agreement is apparent. This trend was also observed in [19] (Fig. 1 in [19], not shown here), where a large range of Prandtl numbers were considered. As mentioned in [19], this suggests that the amplification factor used as the criterion for marking the onset time must depend on the Prandtl number.

An attempt was made to measure the critical wavelength via the distorted isothermal lines. However, since in the interferometry method used here the change in the index of refraction is integrated over the path length of the beam, any such measurement will not be associated with a single wave and therefore is not meaningful. Ahlers et al. [15] have discussed the structure of the cellular motion at the onset.

6 Summary

Predicted and experimental results of the time of the onset of thermal convection for a horizontal fluid layer heated from below have been presented. The dynamic linear stability theory predicts the dependency of the time of the onset on the Rayleigh and Prandtl numbers. The experimental results obtained here apply the sudden changes in the heat transfer rate from the lower surface, and also the sudden changes in the fringes created by holographic interferometry, as indicators of the time of the onset. Heating rates of 0.020 to 0.30°C/min and layer thicknesses of 1-8 cm are considered. Good agreement is found between the experimental and predicted results, but it is better for water than for the glycerin-water solution. For the smaller layer thicknesses, evaporative cooling from the top surface becomes more difficult to control, which results in the acceleration of the onset of convection. Comparison of the results obtained here with the available predicted and experimental results also show a general agreement.

Acknowledgment

The support of the National Science Foundation through Initiation Grant MEA 82-04837 is greatly appreciated. The author would also like to thank Messrs T. Vuong and J. Roesler, both students at the University of Wisconsin–Milwaukee, for their assistance with the experiments.

References

1 Chandrasekhar, S., *Hydrodynamic and Hydromagnetic Stability*, Dover, 1981.

2 Lick, W., "The Instability of a Fluid Layer with Time-Dependent Heating," *J. Fluid Mech.*, Vol. 21, 1965, pp. 565-576.

3 Currie, I. G., "The Effect of Heating Rate on the Stability of Stationary Fluids," *J. Fluid Mech.*, Vol. 29, 1967, pp. 337-347.

4 Foster, T. D., "Stability of Homogeneous Fluid Cooled Uniformly from Above," *Physics of Fluids*, Vol. 8, 1965, pp. 1249-1257.

5 Foster, T. D., "Effect of Boundary Conditions on the Onset of Convection," *Physics of Fluids*, Vol. 11, 1968, pp. 1257-1262.

6 Mahler, E. G., Schechter, R. S., and Wissler, E. H., "Stability of a Fluid Layer with Time-Dependent Density Gradients," *Physics of Fluids*, Vol. 11, 1968, pp. 1901-1912.

7 Gresho, P. M., and Sani, R. L., "The Stability of a Fluid Layer Subjected to a Step Change in Temperature Transient vs. Frozen Time Analysis," *International Journal of Heat and Mass Transfer*, Vol. 14, 1971, pp. 207-221.

8 Davis, E. J., and Choi, C. K., "Cellular Convection with Liquid-Film Flow," *J. Fluid Mech.*, Vol. 81, 1977, pp. 565-592.

9 Foster, T. D., "Onset of Convection in a Layer of Fluid Cooled from Above," *Physics of Fluids*, Vol. 8, 1965, pp. 1770-1774.

10 Foster, T. D., "Onset of Manifest Convection in a Layer of Fluid with a Time-Dependent Surface Temperature," *Physics of Fluids*, Vol. 12, 1969, pp. 2482-2487.

11 Jhaveri, B. S., "Rayleigh-Benard Convection from Thermodynamic Fluctuations," Ph.D. dissertation, Stanford University, 1979.

12 Wankat, P. C., and Homsy, G. M., "Lower Bounds for the Onset of Instability in Heated Layers," *Physics of Fluids*, Vol. 20, 1977, pp. 1200-1201.

13 Jhaveri, B., and Homsy, G. M., "Randomly Forced Rayleigh-Benard Convection," *J. Fluid Mech.*, Vol. 18, 1980, pp. 329-348.

14 Jhaveri, B., and Homsy, G. M., "The Onset of Convection in Fluid Layers Heated Rapidly in a Time-Dependent Manner," *J. Fluid Mech.*, Vol. 114, 1982, pp. 251-260.

15 Ahlers, G., Cross, M. C., Hohenberg, P. C., and Safran, S., "The Amplitude Equation Near the Convective Threshold: Application to Time-Dependent Heating Experiments," *J. Fluid Mech.*, Vol. 110, 1981, pp. 297-334.

16 Newel, A. C., and Whitehead, J. A., "Finite Bandwidth, Finite Amplitude Convection," *J. Fluid Mech.*, Vol. 38, 1969, pp. 279-303.

17 Soberman, R. K., "Onset of Convection in Liquids Subjected to Transient Heating from Below," *Physics of Fluids*, Vol. 2, 1959, pp. 131-138.

18 Blair, L. M., and Quinn, J. A., "The Onset of Cellular Convection in a Fluid Layer with Time-Dependent Density Gradients," *J. Fluid Mech.*, Vol. 36, 1969, pp. 385-400.

19 Davenport, I. F., and King, C. J., "The Onset of Natural Convection from Time-Dependent Profiles," *International J. of Heat and Mass Transfer*, Vol. 17, 1974, pp. 69-76.

20 Spagenberg, W. G., and Rowland, W. R., "Convective Circulation in Water Induced by Evaporative Cooling," *Physics of Fluids*, Vol. 4, 1961, pp. 743-750.

21 Mahler, E. G., "The Stability of Fluids Subjected to Adverse Nonlinear Time-Dependent Density Gradients," Ph.D. dissertation, The University of Texas at Austin, 1969.

22 Onat, K., and Grigull, V., "Des Einsetzen der Konvektion in Flussigkeiten Über Einer beheizten Waagerechten Platte," *Würme und Stoffübertragung*, Vol. 3, 1970, pp. 103-113.

23 Ozisik, M. N., *Heat Conduction*, John Wiley & Sons, 1980.

24 Snyder, L. J., Spriggs, T. W., and Stewart, W. E., "Solution of the Equation of Change by Galerkin's Method," *AIChE Journal*, Vol. 10, 1964, pp. 535-540.

25 Romanelli, M. J., *Mathematical Methods for Digital Computers*, edited by Ralston and Wilf, John Wiley & Sons, 1960.

26 Vest, C. M., *Holographic Interferometry*, John Wiley & Sons, 1979.

27 Aung, W., Fletcher, L. S., and Sernas, V., "Developing Laminar Free Convection Between Vertical Flat Plates with Asymmetric Heating," *International J. of Heat and Mass Transfer*, Vol. 15, 1972, pp. 2293-2308.

28 Kreith, F., *Principles of Heat Transfer*, Intext Educational Publishers, 1976.

APPENDIX

The following trial differential equation is chosen [6]

$$\eta_{zzzz} + \gamma_k (\eta_{zz} - a^2 \eta) = 0$$

with the boundary conditions

$$\eta_{zz}(0) = \eta(0) = \eta_z(1) = \eta(1) = 0$$

The solution is that given in equation (12), where

$$\lambda_k = [-\gamma_k + (\gamma_k^2 + 4\gamma_k a^2)^{1/2}]^{1/2} 2^{-1/2}$$

$$\tau_k = [+\gamma_k + (\gamma_k^2 + 4\gamma_k a^2)^{1/2}]^{1/2} 2^{-1/2}$$

The eigenvalues γ_k are obtained from the following transcendental equation

$$\lambda_k^{-1} \tanh\lambda_k - \tau_k{}^{-1} \tan\tau_k = 0$$

The integrals which are evaluated analytically, but are not given here, are

$$N_j = -\int_0^1 [\eta_j (\eta_j)_{zz} - a^2 \eta_j^2] dz$$

$$I_{kj} = \int_0^1 (\eta_k)_{zz} \eta_j dz$$

$$I_{nj} = \int_0^1 \eta_j \cos(m - 1/2)\pi z \, dz$$

$$I_{koj} = \int_0^1 z\eta_k \cos(j - 1/2)\pi z \, dz$$

$$I_{klj} = \int_0^1 \eta_k \sin(l - 1/2)\pi z \cos(j - 1/2)\pi z \, dz$$

Natural Convection Heat Transfer Through Inclined Longitudinal Slots

J. G. Symons

M. K. Peck

Division of Energy Technology,
Commonwealth Scientific and
Industrial Research Organization,
Highett, Victoria, Australia

The convective rates of heat transfer through inclined longitudinal slots is studied for the case where heat is transferred from a lower heated isothermal surface, through the slots, to an upper cooled isothermal surface. Experimental data are given for longitudinal slots having aspect ratios from 6-12, slot heights of 25-60 mm, inclinations from horizontal to vertical, and Ra $< 10^7$. *Data are also given for a transverse slot of aspect ratio 6, for inclinations from horizontal to vertical, and Ra* $< 10^7$. *It is shown that convective heat transfer rates are essentially independent of slot orientation for inclinations up to 15 deg from the horizontal, but longitudinal slots are more effective in suppressing natural convection than transverse slots with the same aspect ratio, for inclinations from 24 to 75 deg from the horizontal. The difference in heat transfer rates for longitudinal and transverse slots inclined between 24 and 75 deg from the horizontal are shown to be due to different convective flows occurring in each slot. The heat flow measurements are supported by convective flow visualization experiments which demonstrate the modes of convective flow within slots.*

Introduction

Natural convection heat transfer across inclined rectangular cavities is of interest in many engineering systems. In particular, convection heat loss is experienced from the absorber panel to the cover in flat-plate solar collectors. This convective flow can be suppressed with closely spaced partitions extending from the absorber to the cover, which form long rectangular cavities or slots. The convective rates of heat transfer through long inclined slots has been the subject of several studies for the case where the long axis of the slot is oriented across the inclined plane. However, the case with the long axis oriented up the slope has been largely ignored, even though this configuration is of particular interest for solar collectors.

The generalized problem being considered is that of natural convection heat transfer from a lower heated isothermal surface to an upper cooled isothermal surface through a rectangular cavity of dimensions and incliation as indicated in Fig. 1.

There have been many natural convection heat transfer studies for the case of inclined parallel isothermal surfaces when H is much smaller than either L or D (see, for example, summaries of previous works in [1-3]). Convective heat transfer can be suppressed if either H/L or H/D is large. This can be done by using either honeycombs (where $L \cong D$), or slots (where $L >> D$ for transverse slots or $L << D$ for longitudinal slots). Natural convection heat transfer through inclined honeycombs has been extensively studied for a variety of honeycomb sections including square, rectangular, circular, hexagonal, and sinusoidal; and in a variety of honeycomb wall materials; see for example [4-9].

The suppression of natural convection using parallel partitions to form slots has also been considered. Edwards [10] reported an analysis and experiments on convection using lateral partitions between horizontal isothermal surfaces, ($\theta = 0$). McCormack et al. provided an analysis [11, 12] and Imberger provided experimental data [13] for the case with vertical isothermal surfaces bounding transverse slots. Catton et al. [14] analysed the general problem of inclined transverse slots for 60 deg $\leq \theta \leq$ 165 deg, while Ozoe et al. reported an analysis and experiments on inclined square [15] and rectangular [16] transverse slots for 0 deg $\leq \theta \leq$ 90 deg and 0 deg $\leq \theta \leq$ 180 deg, respectively. Further experimental data are available from Edwards et al. [17], Smart et al. [9], and from the interferometric study of Myer et al. [18].

In all of these cases only transverse slots have been studied, while the problem of suppressing natural convection in inclined longitudinal slots has not been reported. It is the objective of this paper to provide experimental data on natural convection heat transfer rates through inclined longitudinal slots and to relate the influence of Rayleigh number Ra, H, A, and θ on the Nusselt number Nu. Comparisons are also made between the convection heat transfer results and the observed flow patterns in inclined longitudinal and transverse slots of the same geometry.

Throughout this work, the term aspect ratio A is used to indicate the slenderness of the slots. For longitudinal slots the

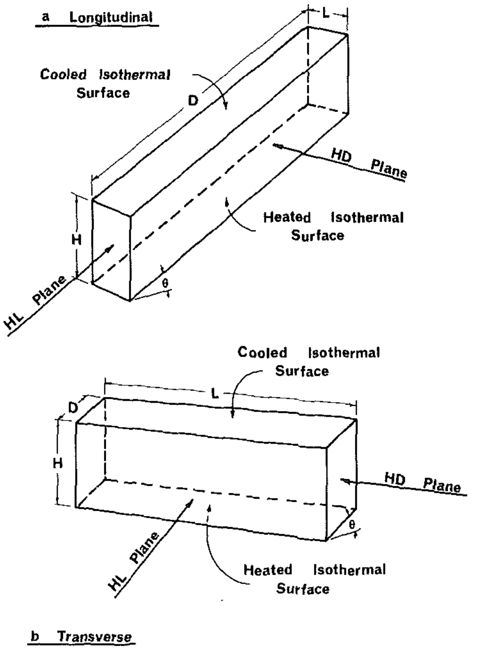

Fig. 1 Description of the inclined slots

Contributed by the Heat Transfer Division for publication in the JOURNAL OF HEAT TRANSFER. Manuscript received by the Heat Transfer Division June 22, 1983.

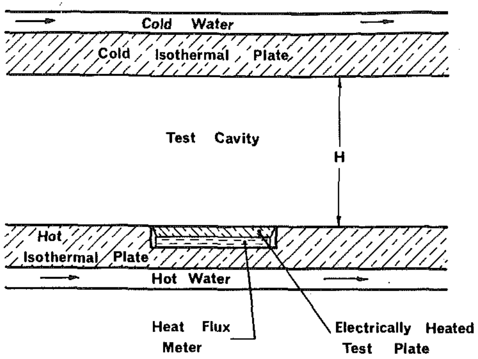

Fig. 2 Schematic of experimental equipment for measurement of convective heat transfer rates

aspect ratio A is H/L, and for transverse slots the aspect ratio is H/D.

Measurement of Convective Heat Transfer Rates

A natural convection heat transfer apparatus has been developed to measure rates of convective heat transfer between two isothermal parallel plates. The apparatus is described in detail by Peck [19] and shown schematically in Fig. 2. It comprises hot and cold copper plates (each measuring 450 × 450 mm), maintained at set operating temperatures via water circulating through tubes attached to the back of each plate. The heated (lower) plate has a 125 × 125 mm electrically heated test plate and heat flux meter inserted into its center. This guarded heat flux meter assembly enables the total heat flux to be measured over a representative central area of the isothermal surfaces, avoiding edge effects. Electrical power to the small test plate is adjusted until the heat flux meter voltage approaches zero. Under these conditions, the temperature of the small test plate is almost identical to the temperature of the hot isothermal plate. The rate of electric power supplied to the test plate is equal to the rate of heat transfer from the test plate into the test cavity provided the heat flux meter voltage is zero. In practice, a small imbalance is accepted on the heat flux meter and a calibration constant is used to correct this small error in heat transfer measurement.

The isothermal plates were polished, to give an emittance of approximately 0.05, and the slot partitions installed between them. Laminated aluminum foil on paper was attached to the periphery of the plates to establish a linear temperature profile between the hot and cold surfaces. The whole assembly was then thermally insulated and mounted in a pressure vessel filled with dry air. After setting the required pressure, a settling period of typically 40 min was allowed for steady-state conditions to be obtained, and then all data were recorded over a test period of about 1 hr. The rate of convectively induced heat transfer from the hot to the cold isothermal surface was determined as the measured rate of heat transfer minus the heat transferred by combined radiation and slot wall conduction. The latter was initially estimated by measuring the rate of heat transfer at low Ra, where Nu = 1, and then subtracting the calculated heat transfer rate due to air conduction. This experimental procedure is similar to that used previously, [2, 7–9]. A detailed account of the equipment, calibration, experimental procedures and accuracies, is reported in [19], together with an account of experiments performed to check the data from this apparatus with that previously reported in the literature.

Table 1 Details of the longitudinal and transverse slots

Longitudinal slots

Slot no.	H (mm)	$A = H/L$	D (mm)	C	N
1	25	6	450	547	6.58
2	37	6	450	876	10.5
3	60	6	450	1313	15.8
4	60	8.4	450	1313	15.8
5	60	12	450	1313	15.8

Transverse slot

Slot no.	H (mm)	$A = H/D$	L (mm)	C	N
6	60	6	450	1313	15.8

To obtain the data reported in this paper, the hot and cold isothermal plate temperatures were held constant at approximately 60 and 30°C, respectively, and measured with calibrated type-T thermocouples. The air pressure inside the pressure vessel was variable up to 700 kPa, to achieve Ra up to 10^7. The Rayleigh Number was calculated for dry air properties at the arithmetic mean temperature of the hot and cold plates. The inclination of the slots was varied by rotating the pressure vessel and its contents. The experimental instrumentation was controlled and monitored by microprocessor, and the overall system uncertainy was less than 5 percent in Ra and 7 percent in Nu [19].

The slot wall material was Teflon FEP[1] type 50A, having a wall thickness of 13 μm and thermal emittance of 0.31. This plastic film material is of particular interest for suppressing convection in flat-plate solar collectors due to its high thermal, chemical, and weathering stability, low thermal conductance, and high solar transmittance. The endwalls of slots, i.e., the HL planes for the longitudinal slots, and the HD planes for the transverse slot, were made from the laminated aluminum foil on paper to provide a linear temperature profile. The dimensions of the longitudinal and transverse slots tested are listed in Table 1.

The measured convective heat transfer results are shown in

---

[1] Teflon FEP is manufactured by DuPont de Nemours, Inc

Nomenclature

A = aspect ratio
C = slot wall conduction group, = $k_f H/k_w \delta$
C_p = specific heat of air, (J kg^{-1} K^{-1})
D = length of slot, Fig. 1, (m)
g = gravitational constant, (m s^{-2})
h_c = convective heat transfer coefficient, (W m^{-2} K^{-1})
K = constant, equation (1)
k_f = thermal conductivity of air, (W m^{-1} K^{-1})
k_w = thermal conductivity of slot wall, (W m^{-1} K^{-1})
H = height of slot, Fig. 1, (m)
L = width of slot, Fig. 1, (m)
N = radiation group, = $4\ \sigma\ T^3\ H/k_f$
Nu = Nusselt number, = $h_c\ H/k_f$
Nu_0 = Nusselt number for $\theta = 0$ deg
Ra = Rayleigh number, = $g\beta\ (T_h - T_c)\ H^3\ \rho^2\ C_p/\mu\ k_f$
T = mean temperature, = $(T_h + T_c)/2$, (K)
T_c = temperature of cooled isothermal surface, (K)
T_h = temperature of heated isothermal surface, (K)
β = volumetric thermal expansion coefficient for air, (K^{-1})
δ = semithickness of slot wall, (m)
ϵ = emittance of slot wall
θ = slot inclination, Fig. 1, (deg)
μ = dynamic viscosity of air, (kg m^{-1} s^{-1})
ρ = density of air, (kg m^{-3})
σ = Stefan-Boltzmann constant

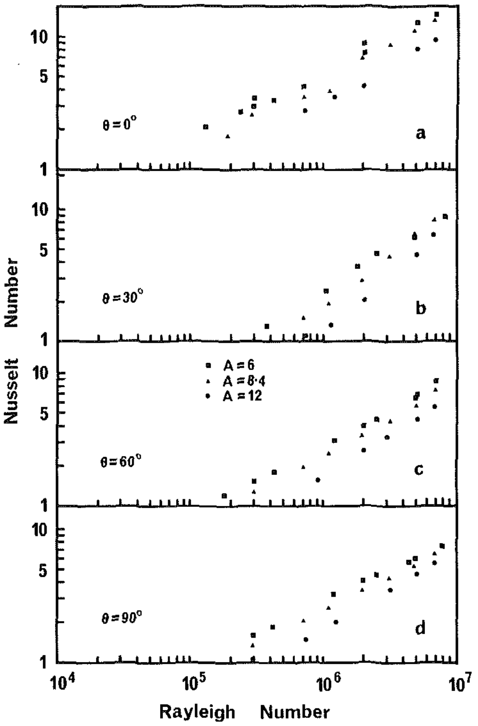

Fig. 3 Experimental results for the longitudinal slots with H = 60 mm, and various A

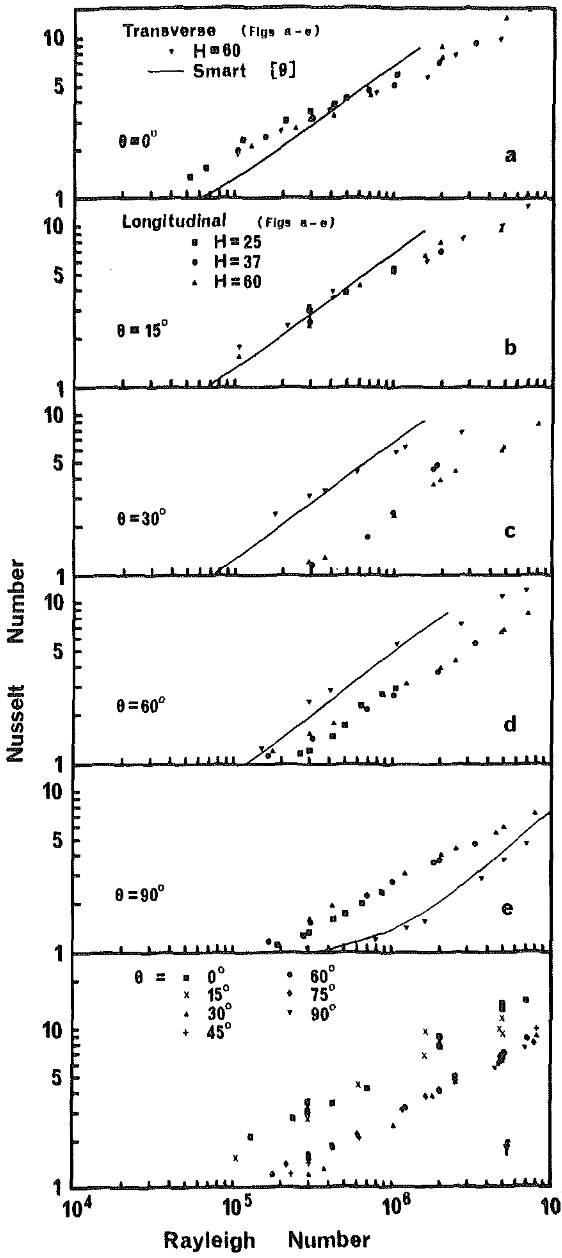

Fig. 4 Experimental results for the longitudinal and transverse slots with A = 6:

(a–e) Transverse slot results:
▽ H = 60 mm
——— smart [9]
Longitudinal slot results:
■ H = 25 mm
◆ H = 37 mm
▲ H = 60 mm
and θ as shown

(f) Longitudinal slot results for H = 60 mm and θ as shown

Figs. 3, 4, and 5. The results are presented in terms of the Nusselt number and the Rayleigh number, both of which are defined in the Nomenclature.

Figure 3 shows the results for longitudinal slots with H = 60 mm. As expected, if the aspect ratio is increased, convection is negligible for progressively higher values of Ra. Alternatively, for a given Ra, increasing A tends to reduce Nu. Also from Fig. 3, Nu is generally larger for $\theta = 0$ deg, than for 30 deg $\leq \theta \leq$ 90 deg.

The results for both longitudinal and transverse slots with $A = 6$ are plotted in Figs. 4(a-e) for angles of inclination of 0, 15, 30, 60, and 90 deg. For $\theta = 0$ and 15 deg no significant difference between the longitudinal and transverse slots exists. Clearly for $\theta \cong 0$ deg, the orientation of the slots is irrelevant. For $\theta = 30$ and 60 deg, the transverse slot data lies to the left of that for the longitudinal slots. This indicates that the longitudinal slots suppress convection to a higher Ra than for the transverse slots and have lower Nu over the range of Ra considered. For $\theta = 90$ deg, the opposite effect occurs, that is, the transverse slot suppresses convection to a higher Ra than that for the longitudinal slot.

For the longitudinal slots in Fig. 4(a-e), the results are in close agreement for all values of H.

Figure 4(f) shows the effect of varying θ for longitudinal slot number 3 of Table 1. The results fall into two groups; those for 0 deg $\leq \theta \leq$ 15 deg and those for 30 deg $\leq \theta \leq$ 90 deg.

This trend is further illustrated in Fig. 5, where transverse and longitudinal slots of similar geometry are compared. For the longitudinal slot, Nu is seen there to be almost independent of θ for 0 deg $\leq \theta \leq$ 15 deg, and a weak function of θ for 25 deg $\leq \theta \leq$ 90 deg. The minimum Nu appears to correspond to $\theta \cong 24$ deg.

In his study of inclined transverse slots, Smart et al. [19] presented experimental data and two empirical correlation equations to predict Nu as a function of Ra, θ, A, ϵ and the dimensionless groups C (for slot wall conduction), and N (for radiation). The results from the correlation equations from [9] are plotted in Figs. 4(a-e) and Fig. 5 and are in approximate agreement with the transverse slot data. In Fig. 4, the correlation for $\theta < 60$ deg underpredicts Nu for low Ra, and overpredicts Nu for high Ra, while the correlation for $\theta = 90$ deg only slightly overpredicts Nu for all Ra. Similarly in Fig. 5, the correlation from [9] underpredicts Nu for all θ. The values of θ, A, ϵ, and N used in these experiments were all within the ranges covered in [9], but the value of C is 1313 (from Table 1), compared with 42 to 332 in [9]. A comparison of the predicted and measured values of critical Rayleigh number for $\theta = 0$ deg in [9] indicates that the correlation

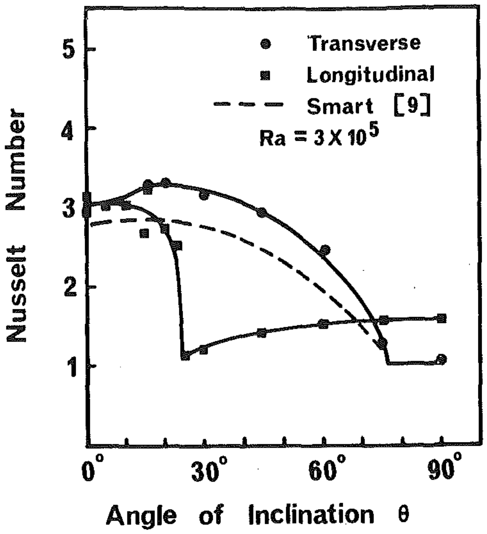

Fig. 5 Experimental results for the transverse and longitudinal slots with H = 60 mm, and A = 6

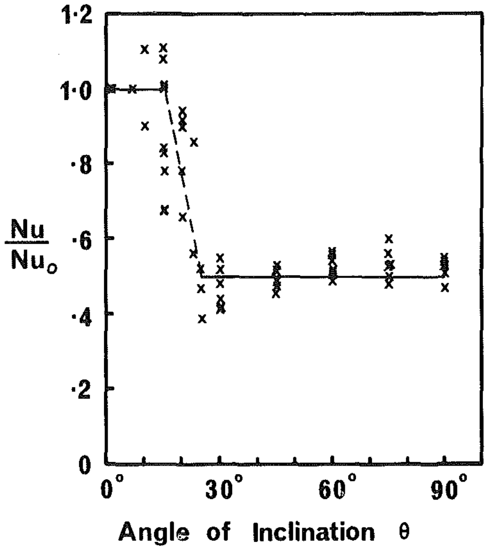

Fig. 6 Normalized heat transfer results for the longitudinal slot with various A, Ra, and θ

tended to overpredict the critical Rayleigh number in that study, a trend consistent with these findings.

The correlation equations in [9] can be used (with the foregoing reservations) to estimate Nu for transverse slots, and for longitudinal slots when 0 deg $\leq \theta \leq$ 15 deg. However, these equations are in serious error when predicting Nu for longitudinal slots when $\theta >$ 20 deg, and so a new empirical correlation is required.

Figure 6 shows the heat transfer results for longitudinal slots with H = 60 mm, $6 \leq A \leq 12$, and $3 \times 10^5 \leq \mathrm{Ra} \leq 5 \times 10^6$. The results have been normalized by estimating $(\mathrm{Nu}/\mathrm{Nu}_0)$ where Nu_0 is the corresponding Nusselt number for θ = 0 deg. It can be seen that the ratio $(\mathrm{Nu}/\mathrm{Nu}_0)$ is nearly constant over the ranges 0 deg $\leq \theta \leq$ 15 deg, and 25 deg $\leq \theta \leq$ 90 deg. This suggests a simple empirical heat transfer correlation

$$\frac{\mathrm{Nu}}{\mathrm{Nu}_0}=K$$

where $K = 1$ for 0 deg $\leq \theta \leq$ 15 deg

$= 0.5$ for 25 deg $\leq \theta \leq$ 90 deg but Nu $\not< 1$.

The standard deviation of the experimental results about K = 1 is 0.118, and about K = 0.5 is 0.045. Over the range 15 deg $< \theta <$ 25 deg, K can be linearly interpolated between K = 1 for θ = 15 deg, and K = 0.5 for θ = 25 deg, with a standard deviation of 0.154. This empirical equation can be used to estimate Nu for longitudinal slots when $6 \leq A \leq 12$, 0 deg $\leq \theta \leq$ 90 deg, and $\mathrm{Ra} \leq 5 \times 10^6$.

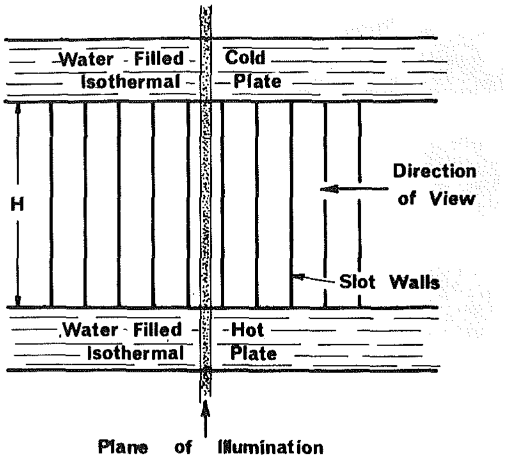

Fig. 7 Schematic of experimental equipment for convective flow visualization

These Nu trends for longitudinal slots are contrary to previous findings on inclined rectangular cavities and inclined transverse slots where Nu is frequently correlated against Ra cosθ [20, 9]. Similarly, the method of Kurzweg [21] (which states that for inclined channels the critical Ra $\propto$ secθ) cannot be used for longitudinal slots. The critical Ra is taken here to be the Rayleigh number at which Nu departs significantly from Nu = 1.

Throughout the experiments, it was found that for $\theta >$ 30 deg, all convective heat transfer rates were very stable and highly repeatable for both longitudinal and transverse slots. However for $\theta \leq$ 30 deg, the rates were found to be consistently unstable as shown by the heat flux meter output voltage. The standard deviation on the correlating equation is larger for $\theta \leq$ 25 deg due to this instability. This problem was very severe in those experiments conducted at high Ra. It is for this reason that no data are given for slot No. 1 at θ = 30 deg, because in that experiment the Nu measurements could not be consistently reproduced. This instability will be discussed further.

Convection Flow Visualization

A visualization experiment was conducted to study the convective flows in longitudinal and transverse slots. The apparatus is described in detail by Peck and Scott [22] and is shown schematically in Fig. 7. The hot and cold isothermal plate temperatures were set at the required levels by passing temperature controlled water through each plate. The surface temperatures were uniform to within 0.25°C. Ten transparent parallel walls were located between the transparent isothermal plates to thermally isolate the central test slot from the environment and thus minimize heat losses and boundary effects. The slot wall material was 1-mm-thick polycarbonate, providing a flat rigid wall with minimal optical distortion. The center slot was illuminated with collimated light from a 1-kW halogen tube to provide a sheet of light parallel to the slot walls and illuminating the full length of the slot. The whole assembly was mounted in bearings so that the inclination could be varied from horizontal to vertical.

The experimental procedure comprised setting the temperatures to give the required value of Ra, allowing the flow to stabilize for at least 40 min, introducing cigar smoke to the test slot with minimal disturbance to the flow, again waiting for the flow to stabilize, then photographing the convective flow at the required angle of inclination. The slot dimensions

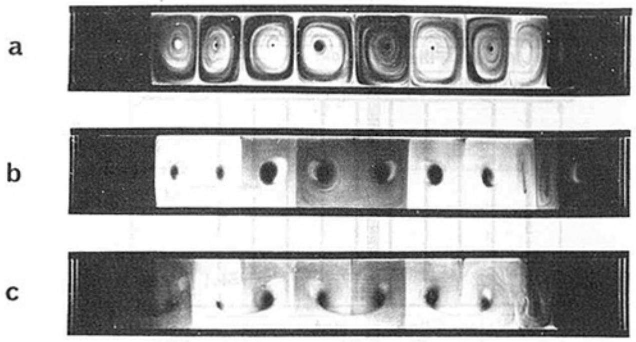

Fig. 8 Convective flow photographs for the transverse slot, Ra = 3×10^5, $A = 6$, $H = 60$ mm.

(a) $\theta = 0$ deg
(b) $\theta = 30$ deg
(c) $\theta = 60$ deg

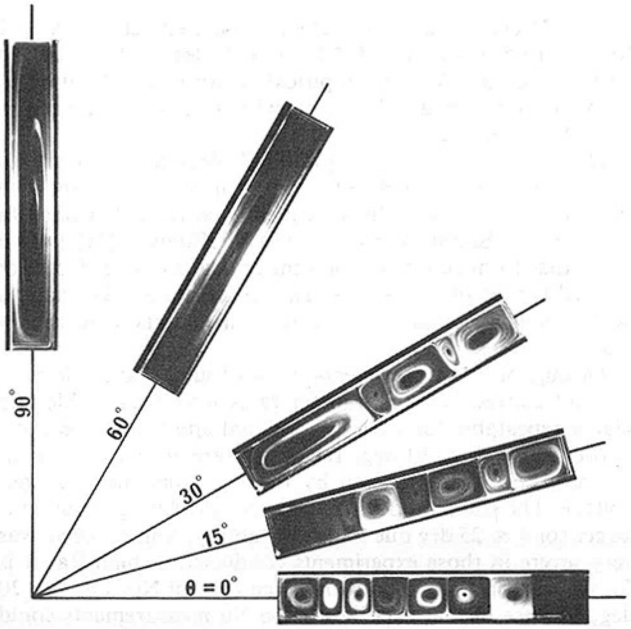

Fig. 9 Convective flow photographs for the longitudinal slot, for Ra = 3×10^5, $A = 6$, $H = 60$ mm, and θ as shown

corresponded to those for slot numbers 3 and 6, and a Rayleigh number of 3×10^5 was chosen to reproduce the conditions for the heat transfer experiments depicted in Fig. 5.

Figure 8 shows a sample of photographs for the transverse slot as viewed through the *HL* plane. For 0 deg $\leq \theta \leq$ 70 deg the convective flow comprised multiple cells, rotating in alternate directions. When $\theta >$ 70 deg, a single roll circulation was established with a transverse axis, a flow which is not easily photographed when viewed through the *HL*-plane.

Photographs for the longitudinal slot as viewed through the *HD*-plane are shown in Fig. 9. These apply for θ increasing from 0 to 90 deg. For $\theta = 0$ deg, the same multicell flow exists as for the transverse slot, Fig. 8. As θ was increased, every second cell (those flowing down the hot surface and up the cold surface), became narrower, while the remaining cells became wider. As θ was increased further, the narrow cells were progressively displaced leaving the wide cells to coalesce. When θ was increased beyond 35 deg, all the small cells disappeared leaving one long unicell flowing up the hot surface and down the cold, a flow pattern that existed for 35 deg $\leq \theta \leq$ 90 deg.

It was found with the longitudinal slot that when multiple cells were established at $\theta = 0$ deg and θ was then increased, the multiple cell pattern existed for θ up to about 35 deg. However, when θ was greater than about 20 deg, small disturbances to the flow caused some or all of the narrow cells to disappear, tending towards single cell flow. Alternatively, if unicell circulation was established at large θ, this pattern persisted for θ as low as 10 deg provided the system was not disturbed.

Figure 8 shows 12 cells for the transverse slot at $\theta = 0$ deg, while Fig. 9 shows only 8 for the longitudinal slot $\theta = 0$ deg for the same Ra, H, and A. In repeated experiments under the same conditions, the number of cells initially formed in the multicellular flow was either 6, 8, 10, 12, or 14 for both longitudinal and transverse slots.

Discussion

The difference in convective heat transfer through longitudinal and transverse slots, as indicated in Fig. 5, can now be explained from the visualization studies. Over the range 0 deg $\leq \theta \leq$ 15 deg the convective flow in both the transverse and longitudinal slots comprises multiple counter rotating cells, and providing the slots have the same aspect ratio and H, then Nu is similar for each orientation. While this flow pattern persists in transverse slots for $\theta <$ 70 deg, there is a transition from multiple cells to a unicell circulation in the longitudinal slot at $\theta \cong$ 24 deg. The unicell flow reduces the rate of convective heat transfer to half of that achieved with multiple cell flow.

A transition from multiple cells to unicell circulation was reported by Ozoe et al. [15, 16] for transverse cavities, with $0 < H/D \leq 1$. In those cases, as θ increased, the transition at $\theta \cong$ 10 deg was to unicell circulation with a transverse axis. For the transverse slots studied here with $H/D = 6$, this transition did not occur until $\theta \cong$ 70 deg, supporting the Ozoe et al. claim that the transition angle is a function of aspect ratio. Ozoe et al. also noted that a local maximum in Nusselt Number occurred at $\theta \cong$ 55 deg, a substantially steeper angle than the 20 deg noted here for the transverse slot as in Fig. 5. This lack of agreement is not surprising, because a unicell flow was reported by Ozoe et al. at $\theta = 55$ deg, whereas multiple cells were observed here for transverse slots. Arnold et al. [1] noted flow transitions in transverse cavities at inclinations of 65 deg for $H/L = 1/12$, and 25 deg for $H/L = 1$, as did Graham and Mallinson [23] at $\theta = 60$ deg to 70 deg for $H/L = H/D = 1/5$. It is apparent that while unicellular flow with a transverse axis was established in the transverse slot studies of [1, 15, 16, 23], the larger aspect ratio used in this study has suppressed that flow until $\theta \simeq$ 70 deg.

There are no prior publications to compare flow transition in longitudinal slots. However, the large drop in Nu for unicellular flow, as in Fig. 5, was not found in the transverse slot studies cited here. This is probably due to the very long unicellular flow path lengths experienced in the longitudinal slot, where D/H is large, as compared with that for the transverse slots where D/H is small. The inclination corresponding to minimum Nu in longitudinal slots was $\theta \cong$ 24 deg for the range of Rayleigh considered.

The variability in measurement of Nu for $\theta \leq$ 30 deg can be explained qualitatively from the flow visualization experiments. For θ up to about 15 deg, the number of convection cells for both the transverse and longitudinal slots varied from 6 to 14, sometimes changing during an experiment, but always with an even number. Ozoe's numerical study [3], also demonstrated variations in the Nu for transverse slots close to horizontal caused by the number of rolls present. At around $\theta = 30$ deg, narrow cells were sometimes observed in these longitudinal slot flow visualization experiments. If narrow cells are sometimes located over the test plate of the natural convection apparatus where the heat flux measurements are made, then Nu will vary. For $\theta \geq 35$ deg, the longitudinal slot always had unicell circulation, thus giving a stable and repeatable Nu.

Conclusions

For inclined slots with aspect ratio of 6, two convective flow patterns exist depending on the angle of inclination. For transverse slots, multiple cells with longitudinal axes exist for $\theta \leq 70$ deg, and a single cell with transverse axis occurs for $\theta > 70$ deg. For longitudinal slots, multicellular flow with transverse axes occur for $\theta \leq 24$ deg, changing to unicellular flow with transverse axis if $\theta > 24$ deg. For both slot orientations, unicellular flow has lower values of Nu associated with it than experienced for multicellular convective flow. For convection suppression, longitudinal slots are therefore more effective than transverse slots of the same aspect ratio, when $24 \text{ deg} < \theta < 75$ deg.

As similar convective flows occur in both longitudinal and transverse slots for $\theta \leq 15$ deg, the rates of convective heat transfer are similar. Consequently, existing empirical equations for predicting Nu in transverse slots can also be used for longitudinal slots for small angles of inclination. While for transverse slots Nu can be correlated against Ra Cos θ, this is not the case for longitudinal slots. For longitudinal slots, the heat transfer rates can be correlated in the form Nu/Nu_0 is equal to 1.0 for $0 \text{ deg} \leq \theta \leq 15$ deg, and equal to 0.5 for $25 \text{ deg} \leq \theta \leq 90$ deg.

For transverse slots, the critical Ra is usually taken to be proportional to Sec θ. This relation does not hold for longitudinal slots, where the critical Ra is insensitive to θ over the range $0 \text{ deg} \leq \theta \leq 15$ deg, and over the range $25 \text{ deg} \leq \theta \leq 90$ deg. As expected from previous natural convection studies, if the aspect ratio is increased, the critical Ra also increases and thus reduces Nu for any given Ra.

Acknowledgment

Support was provided under the (Australian) National Energy Research Development and Demonstration Program administered by the Department of National Development and Energy. The authors wish to thank Mr. R. Gani for his valuable comments on the manuscript.

References

1 Arnold, J. N., Catton, I., and Edwards, D. K., "Experimental Investigation of Natural Convection in Inclined Rectangular Regions of Differing Aspect Ratios," ASME Journal of Heat Transfer, Vol. 98, 1976, pp. 67-71.

2 Hollands, K. G. T., et al., "Free Convective Heat Transfer Across Inclined Air Layers," ASME Journal of Heat Transfer, Vol. 98, 1976, pp. 189-193.

3 Ozoe, H., "Natural Convection in a Confined Regime," Doctor of Engineering thesis, Okayama University, 1976.

4 Edwards, D. K., and Catton, I., "Prediction of Heat Transfer by Natural Convection in Closed Cylinders Heated from Below," *International Journal of Heat and Mass Transfer*, Vol. 12, 1969, pp. 23-30.

5 Charters, W. W. S., and Peterson, L. F., "Free Convection Suppression Using Honeycomb Cellular Materials," *Solar Energy*, Vol. 13, 1972, pp. 353-361.

6 Edwards, D. K., and Sun, W. M., "Effect of Wall Radiation on Thermal Instability in a Vertical Cylinder," *International Journal of Heat and Mass Transfer*, Vol. 14, 1971, pp. 15-18.

7 Hollands, K. G. T., "Natural Convection in Horizontal Thin Walled Honeycomb Panels," ASME Journal of Heat Transfer, Vol. 95, 1973, pp. 439-444.

8 Cane, R. L. D., et al., "Free Convective Heat Transfer Across Inclined Honeycomb Panels," ASME Journal of Heat Transfer, Vol. 99, 1977, pp. 86-91.

9 Smart, D. R., Hollands, K. G. T., and Raithby, G. D., "Free Convection Heat Transfer Across Rectangular-Celled Diathermanous Honeycombs," ASME Journal of Heat Transfer, Vol. 102, 1980, pp. 75-80.

10 Edwards, D. K., "Suppression of Cellular Convection by Lateral Walls," ASME Journal of Heat Transfer, Vol. 91, 1969, pp. 145-150.

11 McCormack, D. E., Leal, L. G., and Imbergr, J., "Natural Convection in a Shallow Cavity With Differentially Heated End Walls. Part 1: Asymptotic Theory," *Journal of Fluid Mechanics*, Vol. 65, 1974, pp. 209-229.

12 McCormack, D. E., Leal, L. G., and Imberger, J., "Natural Convection in a Shallow Cavity With Differentially Heated Endwalls. Part 2: Numerical Solutions," *Journal of Fluid Mechanics*, Vol. 65, 1974, pp. 231-246.

13 Imberger, J., "Natural Convection in a Shallow Cavity With Differentially Heated Endwalls. Part 3: Experimental Results," *Journal of Fluid Mechanics*, Vol. 65, 1974, pp. 247-260.

14 Catton, I., Ayyaswamy, P. S., and Clever, R. M., "Natural Convection Flow in a Finite, Rectangular Slot Arbitrarily Oriented With Respect to the Gravity Vector," *International Journal of Heat and Mass Transfer*, Vol. 17, 1974, pp. 173-184.

15 Ozoe, H., Sayama, H., and Churchill, S. W., "Natural Convection in an Inclined Square Channel," *International Journal of Heat and Mass Transfer*, Vol. 17, 1974, pp. 401-406.

16 Ozoe, H., et al., "Natural Convection in an Inclined Rectangular Channel Heated on One Side and Cooled on the Opposing Side," *International Journal of Heat and Mass Transfer*, Vol. 17, 1974, pp. 1209-1217.

17 Edwards, D. K., Arnold, J. N., and Wu, P. S., "Correlations for Natural Convection through high L/D Rectangular Cells," ASME Journal of Heat Transfer, Vol. 101, 1979, pp. 741-743.

18 Meyer, B. A., Mitchell, J. W., and El-Wakil, M. M., "Natural Convection Heat Transfer in Moderate Aspect Ratio Enclosures," ASME Journal of Heat Transfer, Vol. 101, 1979, pp. 655-659.

19 Peck, M. K., "An Apparatus for the Measurement of Natural Convection Heat Transfer in Enclosures," CSIRO Division of Energy Technology Technical Report TR4. Commonwealth Scientific and Industrial Research Organization, Melbourne, 1984; in press.

20 Clever, R. M., "Finite Amplitude Horizontal Convection Rolls in an Inclined Layer," ASME Journal of Heat Transfer, Vol. 95, 1973, pp. 407-408.

21 Kurzweg, V. H., "Stability of Natural Convection Within an Inclined Channel," ASME Journal of Heat Transfer, Vol. 92, 1970, pp. 190-191.

22 Peck, M. K., and Scott, L. H., "Flow Visualization Apparatus for Natural Convection," *J. Physics E: Scientific Instruments*, Vol. 16, No. 4, 1983, pp. 251-252.

23 Graham, A. D., and Mallinson, G. D., "Three-Dimensional Convection in an Inclined Differentially Heated Box," 6th Australasian Hydraulics and Fluid Mechanics Conference, Adelaide, Australia, Dec. 5-9, 1977.

Effect of a Protuberance on Thermal Convection in a Square Cavity

M. Kaviany
Department of Mechanical Engineering,
University of Wisconsin—Milwaukee,
Milwaukee, Wis. 53201
Assoc. Mem. ASME

Thermal convection resulting from a temperature difference between two vertical surfaces of a square cavity is considered. The effects of a semicylindrically shaped protuberance, located at the bottom of the cavity, on total and local heat transfer rates are examined numerically. The numerical results are for a Prandtl number of 0.71 and for Rayleigh numbers up to 10^4. The results show that the presence of the protuberance leads to a decrease in heat transfer rates in the lower part of the cavity. This relative decrease initially becomes more pronounced as the Rayleigh number increases, but is less significant as the Rayleigh number increases past a critical value. This critical Rayleigh number depends on the radius of the protuberances and its value increases as the radius increases. These results are in general agreement with those found in other investigations dealing with the effects of partitions.

1 Introduction

The problem of thermal convection in cavities has been studied experimentally, e.g., [1, 2], and analytically, e.g., [2–17]. For a square cavity with no internal heat generation and where the driving force is the temperature difference between the two vertical surfaces, the results obtained by Batchelor [3] and Elder [4], among others, have shown that the conduction regime persists roughly up to a Rayleigh number of 500. They have also shown that beyond a Rayleigh number of about 1000 the boundary layer regime sets in and that for Rayleigh numbers greater than 10^9 the flow is turbulent. It is expected that for low Rayleigh numbers the transport of energy and momentum in the cavity is significantly affected by the geometry of the boundary. Therefore, the presence of a protuberance that significantly alters the geometry of the cavity can alter the transport process in the cavity, especially at low Rayleigh numbers (cf. [13]).

As a result of this boundary nonuniformity, the velocity and temperature fields and the local and average Nusselt numbers will be different than those associated with no protuberance. The extent of these changes and their dependency on the Rayleigh number is the subject of the following analysis.

In this study the effect of a semicylindrically shaped protuberance located at the lower surface of a long square cavity is studied numerically. The finite difference techniques that have proven to be successful for the study of cavities with no protuberances, e.g., [2–7], are applied along with the coordinate transformation that allows handling of curved surfaces [18–20]. Steady-state solutions to the time-dependent governing equations are sought. The conclusion of Spradley and Churchill [10], that the Boussinesq approximation is valid for steady-state flow in cavities, is followed. The study is limited to a Prandtl number of 0.71 and Rayleigh numbers up to 10^4.

2 Analysis

The problem considered is the two-dimensional flow in a square cavity with a protuberance in the shape of a semicircle located symmetrically at the bottom surface. A Cartesian coordinate system is adopted with the z-axis in the direction opposite to the gravity vector and the origin at the left bottom corner of the cavity. The side walls are parallel to the gravity vector and are kept at constant temperatures with the left-side wall at a higher temperature than the one on the right side. The upper and lower surfaces are insulated.

2.1 Governing Equations. The governing equations that are expressions of conservation of mass, momentum and thermal energy are nondimensionalized using H, $T_h - T_c$, $H^2\alpha^{-1}$, $\rho_0\alpha^2 H^{-2}$, αH^{-1} for length, temperature, time, pressure and velocity, respectively. Following Batchelor [3] and Elder [4], the velocity and the stream function are used to eliminate pressure as a variable and to eliminate the need for the direct inclusion of the continuity equation in the analysis. The resulting governing equations are

$$\nabla^2\psi = \omega \qquad (1a)$$

$$\frac{D\omega}{Dt} = \mathrm{Pr}\,\nabla^2\omega + \mathrm{Ra}\,\mathrm{Pr}\,\theta_x \qquad (2a)$$

$$\frac{D\theta}{Dt} = \nabla^2\theta \qquad (3a)$$

where subscript x indicates partial differentiation with respect to x. The velocities are defined as $u = -\psi_z$ and $w = \psi_x$. The initial and boundary conditions are

at $t = 0$.

$$\psi = \omega = \theta = 0 \qquad (4a)$$

for $t > 0$;

upper surface $\psi = 0, \quad \omega = \psi_{zz}, \ \theta_z = 0$ (4b)

lower surface $\psi = 0, \quad \omega = \psi_{nn}, \ \theta_n = 0$ (4c)

left surface $\psi = 0, \quad \omega = \psi_{xx}, \ \theta = 1$ (4d)

right surface $\psi = 0, \quad \omega = \psi_{xx}, \ \theta = 0$ (4e)

where n indicates normal derivative. Equations (1a–4e) completely specify the temperature and the flow fields in the enclosure.

2.2 Coordinate Transformation. The velocity and thermal energy equations are nonlinear and coupled. Therefore, exact solutions to these are not obtainable. However, approximate solutions via finite difference forms of these equations are obtainable. Application of rectangular grids to the domains, such as the one considered here where the boundaries are

---

Contributed by the Heat Transfer Division for publication in the JOURNAL OF HEAT TRANSFER. Manuscript received by the Heat Transfer Division May 13, 1983.

curved, requires a large number of grid points and requires further interpolations within the grids that contain the curved boundaries.

As an alternative to the rectangular grids in the physical plane, the technique of a boundary-fitted coordinate system is used here. The method for the automatic numerical generation of general curvilinear coordinate systems is described by Thompson, Thomas, and Mastin [18] and Thompson [19]. The boundary-fitted physical coordinate system is created by numerically solving the following system of elliptic equations

$$ax_{\xi\xi}-2bx_{\xi\eta}+cx_{\eta\eta}=0 \qquad (5a)$$

$$az_{\xi\xi}-2bz_{\xi\eta}+cz_{\eta\eta}=0, \qquad (5b)$$

where

$$a=x_{\eta}{}^{2}+z_{\eta}{}^{2}, \quad b=x_{\xi}x_{\eta}+z_{\xi}z_{\eta}, \quad c=x_{\xi}{}^{2}+z_{\xi}{}^{2} \qquad (5c)$$

which are subject to the Dirichlet boundary conditions relating the boundary points in the physical domain to those in the transformed domain. The distribution of the grid points can be controlled by introducing the appropriate terms [19] into equations (5*a*) and (5*b*).

The transformed plane is covered with a net of square grids; and when Equations (5*a*) and (5*b*), together with the proper boundary conditions, are solved, the corresponding grid points and grid net in the physical plane will be established. The transformed plane is bounded by $\xi = 0$, $\xi = 1$ and $\eta = 0$, $\eta = 1$, corresponding to the two side walls and the lower and upper surfaces, respectively.

2.3 Transformed Governing Equations. In order to use the square uniform mesh in the $\xi-\eta$ plane, the governing equations and the corresponding boundary and initial conditions must be transformed. The results are

$$a\psi_{\xi\xi}-2b\psi_{\xi\eta}+c\psi_{\eta\eta}=J^{2}\omega \qquad (1b)$$

$$J^{2}\omega_{t}+J(\psi_{\eta}\omega)_{\xi}-J(\psi_{\xi}\omega)_{\eta}=\mathrm{Pr}(a\omega_{\xi\xi}-2b\omega_{\xi\eta}+c\omega_{\eta\eta})$$
$$+J\,\mathrm{Ra}\,\mathrm{Pr}(z_{\eta}\theta_{\xi}-z_{\xi}\theta_{\eta}) \qquad (2b)$$

$$J^{2}\theta_{t}+J(\psi_{\eta}\theta)_{\xi}-J(\psi_{\xi}\theta)_{\eta}=(a\theta_{\xi\xi}-2b\,\theta_{\xi\eta}+c\theta_{\eta\eta}) \qquad (3b)$$

where J is the Jacobian of transformation and is equal to $x_{\xi}z_{\eta}-x_{\eta}z_{\xi}$. The transformed initial and boundary conditions are:

at $t=0$:
$$\psi=\omega=\theta=0 \qquad (6a)$$

for $t>0$

$$\eta=1: \quad \psi=0, \quad \omega=\frac{c}{J^{2}}\psi_{\eta\eta}, \quad c\theta_{\eta}-b\theta_{\xi}=0 \qquad (6b)$$

$$\eta=0: \quad \psi=0, \quad \omega=\frac{c}{J^{2}}\psi_{\eta\eta}, \quad c\theta_{\eta}-b\theta_{\xi}=0 \qquad (6c)$$

$$\xi=0 \quad \psi=0, \quad \omega=\frac{a}{J^{2}}\psi_{\xi\xi}, \quad \theta=1 \qquad (6d)$$

$$\xi=1 \quad \psi=0, \quad \omega=\frac{a}{J^{2}}\psi_{\xi\xi}, \quad \theta=0 \qquad (6e)$$

The heat flux through the vertical walls is one of the quantities of interest; the corresponding transformation for this quantity is

$$\xi=0,1 \quad , \quad \theta_{n}=\frac{a\theta_{\xi}-b\theta_{\eta}}{\mathrm{Ja}^{1/2}} \qquad (7)$$

which is the local Nusselt number along the vertical walls.

3 Solution

The solution procedure consists of solving the finite difference form of the transformation equation, i.e., equations (5*a*) and (5) subject to the Dirichlet boundary conditions, and then calculating and storing all the required transformation derivatives. Next, the finite difference forms of the governing equations, i.e., equations (1*a*-3*a*) and (6*a*-6*e*), are solved using the derivatives obtained before.

3.1 Transformation Equations. The derivatives in equations (5*a*) and (5*b*) are approximated by second-order central finite difference expressions. Uniform grid spacings of $\Delta\xi = \Delta\eta$ are applied. The resulting equations are solved for x and z at each internal grid point using the Gauss-Seidel method described by Lapidus [21]. The relaxation factor was increased after a number of iterations. Convergence was assumed whenever the maximum change in the values of x or z between two consecutive iterations was less than 10^{-6}. Once the solutions to equations (5*a*) and (5*b*) are found, then the required derivatives are calculated using second-order central finite difference forms for the interior points and first-order backward difference forms for the boundary points.

3.2 Governing Equations. The vorticity and the thermal energy equations are solved in their time-dependent forms and the steady-state solutions to them are found. It is assumed that the values of ψ, ω, θ, u, and w at each grid point are the average values over a small volume of fluid surrounding the point. The procedure is that described by Torrance [5] and applied successfully by MacGregor and Emery [7] and Emara [2] and others (e.g., [12]). The method developed by Torrance [5] preserves the conservative and transportative properties of vorticity and energy. The calculation procedure is as follows.

1 The time step is limited by the stability requirement, which is determined by the grid spacing, maximum velocities, and the Prandtal number. The field of grid points is searched in order to find the maximum velocities. Then the time step is determined for the next time advancement.

Nomenclature

a,b,c = defined in equation (5*c*)
H = the height of the cavity which is equal to its width
J = Jacobian of transformation
Nu = Nusselt number
Pr = Prandtl number
R = radius of the protuberance divided by the height
Ra = Rayleigh number
t = time
T = temperature
u = horizontal component of velocity
w = vertical component of velocity
x,z = horizontal and vertical axes, in the physical plane
α = thermal diffusivity
η,ξ = the coordinates in the transformed plane
ρ = density
θ = dimensionless temperature $= \dfrac{T-T_c}{T_h-T_c}$
ψ = stream function
ω = vorticity

Superscript

$\bar{\ }$ = average

Subscripts

c = cold
h = hot
n = normal
max = maximum value
0 = reference
x,z,η,ξ = derivative with respect to x, z, η, ξ
∞ = zero grid size

Table 1 Comparison between the results obtained in this study and those reported in [12]. The results are for Ra = 10^6, Pr = 0.71 with no protuberance.

	Grid net	$\bar{Nu}$	ψ_{mid}	ψ_{max}
Present study	31×31	9.929	18.684	19.067
	41×41	9.757	17.793	18.560
	61×61	9.372	17.177	17.555
	81×81	9.160	16.947	17.334
	∞(extrapolated)	8.888	16.653	17.050
de Vahl Davis & Jones	∞(extrapolated)	8.903	16.350	16.772

2 Temperature at all the interior grid points is advanced with an explicit difference form that uses the second-order upwind finite difference form for the convective terms, the second-order central finite difference form for the diffusive terms and the first-order forward finite difference form for the time derivative.

3 Vorticity at all interior grid points is similarly advanced with the buoyancy term written in a second-order central finite difference form using the updated temperature field.

4 Stream function at all interior grid points is updated with the updated vorticity field. The second-order central finite difference form is used and the method of successive overrelaxation is employed to obtain the new stream function at each grid point. Convergence is assumed whenever the maximum normalized change in the value of ψ between any two successive iterations is less than 10^{-4}.

5 Temperatures at the upper and lower surfaces are calculated using the second-order backward finite difference form.

6 Vorticity at boundary grid points is calculated using the second order backward finite difference form.

7 Velocities and their mean values, which are needed for determining the time step and the convective terms in the next iteration, are calculated.

8 The integrated heat fluxes through the left and right walls are calculated using equation (7) for the local Nusselt number and applying a trapezoidal approximation in order to obtain the average Nusselt number. Equation (7) is approximated by the second-order backward and central finite difference forms.

Steps 1-8 are repeated until the difference between the integrated heat flux through the left wall and that through the right wall is less than 10^{-4}.

3.3 Validation. The result for the case of no protuberance was compared with those available in the literature [12-16]. Since most of computational difficulties arise at higher Rayleigh numbers, even though for the sake of computational economy this study is limited to Ra ≤ 10^4, the validation was extended up to Ra = 10^6. The Richardson-Gaunt extrapolation [17] is used to determine the approximate asymptotic values of the Nusselt numbers for an infinitely large number of grid nodes. The extrapolation formula for halfing the spacing by changing the grid net from a 41 × 41 net to an 81 × 81 net is [17]

$$\bar{Nu}_\infty = \frac{\bar{Nu}_{81\times 81} - 0.25\bar{Nu}_{41\times 41}}{0.75}$$

Table 1 shows the results for the Nusselt number at a Rayleigh number of 10^6 and Prandtl number of 0.71. The results reported by de Vahl Davis and Jones [12], which also used grid nets of up to 81 × 81 along with the Richardson-Gaunt extrapolation, are also shown. The values of the average Nusselt number obtained in this study are nearly identical to those reported by them. The values of the stream functions found in this study are slightly larger than theirs. Considering the errors associated with the various approximations made in the numerical integrations, the results obtained here and those reported in [12] are in relatively good agreement.

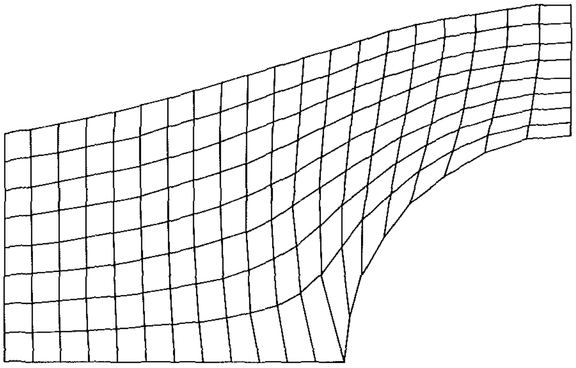

Fig. 1 Part of the grid net generated numerically for R = 0.2

With this validation of the approximation methods and computational algorithm, the results for the cases where the protuberance is present now follow.

4 Results and Discussion

In all, three geometries are considered. The first one is a square cavity without any protuberance and this is used for validation of the computations and as a reference. The other two are for square cavities with protuberances of radii of one-fifth and two-fifths of the height, i.e., R = 0.2 and R = 0.4. For the sake of computational economy, a grid net of 41 × 41 is chosen. Figure 1 shows a portion of the grid net around the proturberance for R = 0.2. In the vicinity of the intersection of the protuberance and the bottom surface, the grid sizes are larger than those elsewhere. This is not expected to create a problem as long as the velocities are low and no flow reversal takes place in the regions with a coarse grid size. Since for the cases where the protuberance is present the computation is limited to Ra ≤ 10^4, it is expected that a 41 × 41 grid net will suffice. Note that along the boundary of the cavity the flow is subjected to the no slip condition. Therefore, when the fluid passes over the semicylinder, this no-slip boundary condition tends to suppress the formation of vortices.

The presence of the protuberance, in general, results in lower velocities near the bottom corners. Furthermore, due to the asymmetry associated with the passage of a viscous fluid over a semicylinder, the presence of the protuberance enhances the asymmetry that is inherent in thermal convection in square cavities.

Figure 2 shows the lines of constant stream function for R = 0.2, Ra = 10^4, and Pr = 0.71. The presence of the protuberance reduces the flow in the lower corner next to the cold vertical surface and in the areas near the intersection of the protuberance and the bottom surface. Figure 2 shows that there is only one cell in the cavity (the same as that observed in the absence of the protuberance). However, the center of the cell, i.e., the point of maximum value for the stream function, is moved upward. Similar results are obtained for R = 0.4, i.e., a single cell with the center still closer to the upper surface.

Figure 3 shows the lines of constant temperature for R = 0.2, Ra = 10^4, and Pr = 0.71. The requirement of zero

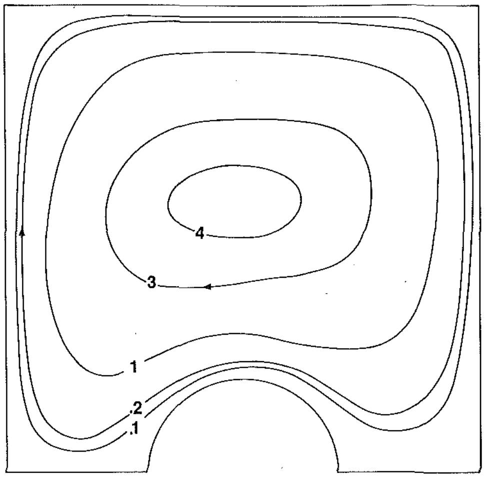

Fig. 2 Lines of constant stream function, $R = 0.2$, $Ra = 10^4$, and $Pr = 0.71$

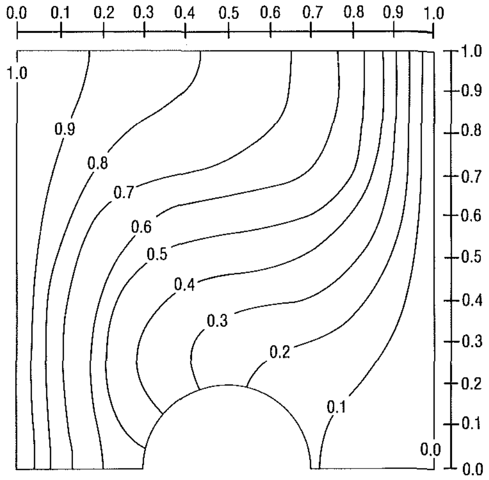

Fig. 3 Lines of constant temperature, $R = 0.2$, $Ra = 10^4$, and $Pr = 0.71$

gradient on the protuberance makes the isothermal lines even closer to horizontal than they were without the protuberance. The local heat transfer rate in the bottom right corner has decreased due to the presence of the protuberance. Note that this area (and also the upper left corner) is subject to low heat transfer rates even when no protuberance is present. Similar results are found for $R = 0.4$, but the extent of reduction in the local heat transfer rate in the lower portion of the cavity is even more pronounced.

Figure 4 shows the variation of the local Nusselt number with height at both the hot (left) and the cold walls. Normalization is done with respect to the average Nusselt number. The results are for $Ra = 10^4$ and $Pr = 0.71$. The results show that as R increases, the normalized local Nusselt number decreases near the lower surface and increases near the upper surface. Note that the magnitude of the average Nusselt number which is used for normalization decreases with an increase in R, as will be further discussed later. Note that the location of the maximum local Nusselt number moves upward, for both hot and cold surfaces, as a result of the presence of the protuberance. But the location of maximum local Nusselt number is still below the $z = 0.5$ plane, even for $R = 0.4$. The results also show a significant difference in heat transfer from the lower left corner when R is increased for 0.2 to 0.4.

Figure 5 shows the change in the average Nusselt number as

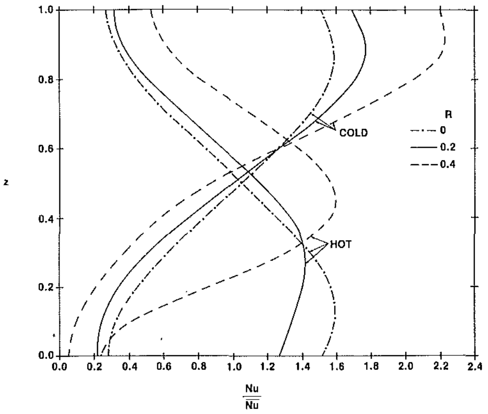

Fig. 4 Variations in the distribution of the normalized local Nusselt number with respect to the radius of the protuberance. The results are for $Ra = 10^4$ and $Pr = 0.71$.

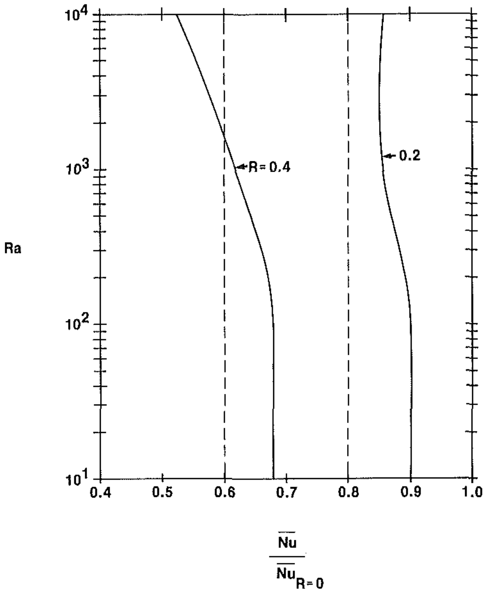

Fig. 5 Variation in the ratio of average Nusselt number in the presence of a protuberance to that when no protuberance is present, with respect to Rayleigh number. The results are for $Pr = 0.71$, $R = 0.2$ and 0.4.

a result of the presence of the protuberance. The average Nusselt numbers are normalized with respect to their values for no protuberance. The dashed lines are drawn for reference and represent 60 and 80 percent reductions in the average Nusselt number. These hypothetical limits are based on the idea that the effect of the presence of the protuberance on the average Nusselt number may be demonstrated using an "effective" heat transfer area, which is taken to be $1 - R$. The results show that the fluid dynamics of the system defies such a simple description and that the relative reduction in the average Nusselt number depends on the Rayleigh number. The numerical results are also represented in Table 2. The slight outward turn shown in Fig. 5 for $R = 0.2$ is an indication that as the velocities become larger and larger the effect of the protuberance will be less significant, but this will not start until a critical Rayleigh number is reached. In the case of $R = 0.2$ this critical Rayleigh number is approximately 5×10^3. The results for $R = 0.4$ show that this critical Rayleigh number is larger than 10^4. Since accurate results for $Ra > 10^4$ require a finer grid net than the one used here, the results for higher Rayleigh numbers are not reported, but they show that this critical Rayleigh number is

Table 2 The Nusselt number and the maximum value for the stream function as computed with a 41 × 41 grid net, Pr = 0.71. The quantities in the parentheses are for the case of no protuberance and are found by extrapolation to an infinitely large number of nodes.

R	Ra	10^1	10^2	10^3	10^4		10^3	10^4
0	$\overline{Nu}$	1.002	1.003	1.129	2.275	ψ_{max}	1.158	5.115
		(1.002)	(1.003)	(1.118)	(2.238)		(1.174)	(5.079)
0.2		0.904	0.906	0.972	1.950		0.805	4.203
0.4		0.679	0.679	0.691	1.194		0.359	2.514

reached for $R = 0.4$ at around 5×10^4. Therefore, it is expected that for a given R, as the Rayleigh number increases the normalized average Nusselt number will first decrease and then after reaching a minimum will begin to increase and will reach the value of unity for very large values of Rayleigh number. This trend is also observed in [13] when the protuberance was a thin, but finite thickness rectangular partition. In [13] the cases involving more than one partition (where the location of the partitions were allowed to vary) were also considered.

5 Summary

Laminar steady-state, two-dimensional thermal convection in a square cavity and in the presence of a protuberance located symmetrically at the bottom surface is studied by obtaining approximate numerical solutions to the governing equations. The effects of the protuberance on the velocity and temperature fields and the local and average Nusselt numbers are determined and the extent of these effects and their dependency on Rayleigh number are examined.

Local Nusselt Number. The results show that for the smaller protuberance radius the flow access to the lower corners is only slightly blocked and that the position of maximum local Nusselt number on the hot vertical surface is in the lower portion of this surface, which is similar to the results for the case of no protuberance. This is independent of the Rayleigh number. However, the results for the larger protuberance radius show that at relatively low Rayleigh numbers the flow access to the lower corners is significantly blocked; and, therefore, the position of maximum local Nusselt number on the hot vertical surface is in the central region of this surface. But, as the Rayleigh number increases, the flow access to the lower corners becomes sufficient such that for sufficiently large Rayleigh numbers the distribution of the local Nusselt number becomes similar to that for the case of no protuberance.

Average Nusselt Number. In the presence of a protuberance of radius R, the average Nusselt number is always smaller than that for no protuberance. As the Rayleigh number increases, initially this reduction becomes worse, but after reaching a maximum the reduction becomes less significant. The results suggest that as the Rayleigh number becomes very large, the average Nusselt number will asympotically reach its value for no protuberance. This trend is also found in other investigations dealing with rectangular partitions.

References

1 Eckert, E. R. G., and Carlson, W. O., "Natural Convection in an Air Layer Enclosed between Two Vertical Plates with Different Temperatures," *International Journal of Heat and Mass Transfer*, Vol. 2, 1961, pp. 106-120.

2 Emara, A. A., "On Thermal Convection with Internal Heating in Fluid Layers," Ph.D. dissertation, The Ohio State University, 1977.

3 Batchelor, G. K., "Heat Transfer by Free Convection Across a Closed Cavity between Vertical Boundaries at Different Temperatures," *Quarterly of Applied Mathematics*, Vol. XII, No. 3, 1954, pp. 209-233.

4 Elder, J. W., "Numerical Experiments with Free Convection in a Vertical Slot," *Journal of Fluid Mechanics*, Vol. 24, pt. 4, 1960, pp. 823-843.

5 Torrance, K. E., "Comparison of Finite-Difference Computations of Natural Convection," *Journal of Research of the National Bureau of Standard—B. Mathematical Sciences*, Vol. 72B, No. 4, 1968, pp. 281-301.

6 Rubel, A., and Landis, F., "Numerical Study of Natural Convection in a Vertical Rectangular Enclosure, High Speed Computing in Fluid Dynamics, *The Physics of Fluids Supplement II*, 1969, pp. 208-213.

7 MacGregor, R. K., and Emery, A. F., "Free Convection Through Vertical Plane Layers—Moderate and High Prandtl Number Fluids," ASME JOURNAL OF HEAT TRANSFER, Vol. 91, 1969, pp. 391-403.

8 MacGregor, R. K., "The Natural Convection of Fluids in Rectangular Vertical Enclosures," Ph.D. dissertation, University of Washington, 1967.

9 Le Quere, P., Humphrey, J. A. C., and Sherman, F. S., "Numerical Calculation of Thermally Driven Two-Dimensional Unsteady Laminar Flow in Cavities of Rectangular Cross Section," *Numerical Heat Transfer*, Vol. 4, 1981, pp. 249-283.

10 Spradley, L. W., and Churchill, S. W., "Pressure and Buoyancy-Driven Thermal Convection in a Rectangular Enclosure," *Journal of Fluid Mechanics*, Vol. 70, pt. 4, 1975, pp. 705-720.

11 Strada, M., and Heinrich, J. C., "Heat Transfer Rate in Natural Convection at High Rayleigh Numbers in Rectangular Enclosures in Numerical Study," *Numerical Heat Transfer*, Vol. 5, 1982, pp. 81-93.

12 de Vahl Davis, G., and Jones, F. P., "Natural Convection in Square Cavity, A Comparison Exercise," *Proceedings of the Second International Conference on Numerical Methods in Thermal Problems*, edited by Lewis, Morgan, and Schnefler, July 7-10, 1981, Venice, Italy.

13 Chang, L. C., Lloyd, J. R., and Yang, K. T., "A Finite Difference Study of Natural Convection Complex Enclosures," *Proceedings of the Seventh International Heat Transfer Conference*, Munich, Vol. 2, 1982, pp. 183-188.

14 de Vahl Davis, G., "Laminar Natural Convection in an enclosed Rectangular Cavity," *International Journal of Heat and Mass Transfer*, Vol. 11, 1968, pp. 1675-1693.

15 Lauriat, G., "Accurate Solutions of Natural Convection Flows in Square Cavities at High Rayleigh Numbers with a Cubic Spline Approximation," ASME Paper No. 82-WA/HT-71, 1982.

16 Markatos, M. C., and Pericleous, C. A., "A Laminar and Turbulent Natural Convection in an Enclosed Cavity," *Natural Convection in Enclosures*, ASME 4TD-Vol. 26, 1983, pp. 59-68.

17 Churchill, S. W., Chao, P., and Ozoe, H., "Extrapolation of Finite-Difference Calculating of Laminar Natural Convection in Enclosures to Zero Grid Size," *Numerical Heat Transfer*, Vol. 4, 1981, pp. 39-51.

18 Thompson, J. F., Thomas, F. C., and Mastin, C. W., "Automatic Numerical Generation of Body-Filtered Curvilinear Coordinate System for Field Containing Any Number of Arbitrary Two-Dimensional Bodies," *The Physics of Fluids Supplement II*, 1969, pp. 208-213.

19 Thompson, J. F., "Numerical Solution of Flow Problems Using Body-Filled Coordinate Systems," *Computational Fluid Dynamics*, edited by W. Kollmann, Hemisphere, 1980, pp. 1-98.

20 Projahn, V., Rieger, H., and Beer, H., "Numerical Analysis of Laminar Natural Convection between Concentric and Eccentric Cylinders," *Numerical Heat Transfer*, Vol. 4, 1981, pp. 131-146.

21 Lapidus, L., *Digital Computation for Chemical Engineers*, McGraw-Hill, 1962.

R. W. Bjorge
Medium Steam Turbine Department,
General Electric Company,
Lynn, Mass. 01910
Assoc. Mem. ASME

P. Griffith
Professor,
Department of Mechanical Engineering,
Massachusetts Institute of Technology,
Cambridge, Mass. 02139
Fellow Mem. ASME

Initiation of Waterhammer in Horizontal and Nearly Horizontal Pipes Containing Steam and Subcooled Water

Localized slug formation from a stratified flow of steam and subcooled water in a pipe traps a steam bubble, which collapses rapidly and causes a waterhammer. This phenomenon was studied experimentally at low pressures. Several tests, including measurement of the critical conditions for waterhammer initiation, were performed. An analytical model was developed that can predict whether waterhammer initiation will occur for given flow conditions. Predictions of this model agree well with experimental results. The use of the model in evaluating the susceptibility of a piping system to condensation waterhammer is described.

Introduction

Since the damaging waterhammer event in the steam generator feedwater line of Indian Point No. 2 [1], researchers have sought to better understand condensation waterhammer in horizontal and nearly-horizontal pipes containing steam and subcooled water. Roidt [2] showed that this phenomenon results from the collapse of a steam bubble formed by a water slug in an initially stratified flow. As part of a comprehensive study of the problem, Block et al. [3] outlined an approach to the theoretical prediction of waterhammer initiation, but concluded that advances in the understanding of interfacial transport phenomena were required to permit such a prediction. Considerable work has since been done in this area, notably by Bankoff et al. [6]

The work reported here (and in greater depth by Bjorge [4]) was aimed at quantifying the initiating mechanism of steam bubble collapse-induced waterhammer in a horizontal or nearly horizontal pipe which supplies subcooled water to a steam-filled chamber. Several experiments were performed in a low-pressure laboratory apparatus, including measurements of the critical inlet water flow rate for waterhammer initiation. A one-dimensional stratified flow model is presented here that predicts liquid depths and steam flow rates along a pipe. A criterion for localized water slug formation is applied to this calculated result to predict waterhammer initiation. Good agreement is seen between experimental and analytical results.

Experiments

A schematic diagram of the experimental apparatus is shown in Fig. 1. The test section includes 1.22 m of transparent Lexan pipe and 0.78 m of brass pipe. Brass pipe 0.40 m in length was removed from the end of the test section nearest the steam tank for one series of tests.

Film of steam–water interactions in the test section were taken at a speed of 100 frames per s. This film shows a side view of the end of the transparent part of the test section nearest the steam tank. The water slug formation process is shown in Fig. 2. After the resulting steam bubble collapse, the pipe is filled with liquid on the left and nearly empty on the right. Gravity waves originate from this discontinuity, seeking to reestablish a stratified flow. In a few seconds, another water slug forms. This periodic waterhammer continues indefinitely.

To provide a useful check on the liquid wall friction computation and the numerical solution approach, liquid depth measurements were made in an air–water system for a range of water flow rates and pipe inclinations.

To verify the condensation heat transfer coefficient computation (for the steam–water system), liquid temperatures near the pipe exit were measured for a range of water flow rates and inlet subcoolings, using thermocouple T.C. #2 in Fig. 1.

As the inlet water flow rate is increased, liquid depths along the pipe increase, increasing the steam velocities. Eventually, a water slug forms and causes a condensation waterhammer. This critical inlet water flow rate was measured. Decreasing the inlet water temperature, increasing the pipe length, and increasing the pipe inclination were each seen to reduce the critical inlet water flow rate for waterhammer initiation.

All of these data were for the initiation of waterhammer with a slowly increasing inlet water flow. However, if the inlet water flow rate was increased rapidly, it was possible to initiate waterhammer at a lower inlet water flow rate. Also, once periodic waterhammers are started, reducing the inlet water flow rate below that required for waterhammer initiation does not stop them. In fact, even if the inlet water flow is shut off, up to several minutes elapse before waterhammers cease.

The Analytical Model

The flow geometry analyzed is shown in Fig. 3. Though not present in the experiments reported here, the vented steam flow, $\dot{m}_{SO}$, is included for the sake of generality. The analytical method follows that of Linehan et al. [5], and solution of the resulting equations yields the liquid depth, liquid temperature, and steam mass flow rate at all locations along the pipe. A stratified-slug flow regime transition criterion can then be applied to determine the location, if any, where a water slug will form.

To simplify the analysis, the flow is assumed to be steady and one-dimensional. The steam is assumed to be saturated at a constant temperature along the pipe, and the ratio of steam to liquid density is assumed to be small. The liquid depth is taken to be critical at the pipe discharge and to vary gradually over the pipe length. The gradually varied flow assumption will give inaccurate results within 2 to 3 hydraulic depths of the exit. However, well upstream, where water slug formation occurs, the error will be small.

Define dimensionless variables as follows:

Contributed by the Heat Transfer Division for publication in the JOURNAL OF HEAT TRANSFER. Manuscript received by the Heat Transfer Division March 29, 1983.

$$
\begin{aligned}
d_L^* &= d_L/D & T_L^* &= (T_L - T_{LO})/(T_S - T_{LO}) \\
x^* &= x/D & \mathrm{Nu} &= h_c D_{h,L}/k_L \\
\alpha &= A_S/(\pi D^2/4) & q^* &= h_c A_L (T_S - T_L)/(\dot{m}_L i_{fg}) \\
\dot{m}_L^* &= \dot{m}_L/\dot{m}_{LO} & \phi &= \frac{(1-\alpha)}{\alpha}\,\frac{\rho_S V_S^2}{\rho_L V_L^2} \\
\dot{m}_S^* &= \dot{m}_S/\dot{m}_{LO} & \psi &= \frac{(1-\alpha)}{\alpha}\,\frac{V_S}{V_L} \\
\tau_L^* &= \tau_L S_L/(\rho_L g A_L) & \omega_0 &= \frac{i_S - i_{LO}}{i_{fg}} \\
\tau_S^* &= \tau_S S_g/(\rho_S g A_S) & \zeta &= 1 - \mathrm{Fr}^2(1+\phi) \\
\tau_i^* &= \tau_i S_i/(\alpha \rho_L g A_L) & \bar{\omega}_1 &= 1 + \frac{i_S - i_L}{i_{fg}} \\
\mathrm{Fr}^2 &= \dot{m}_L^2 S_i/(\rho_L^2 g A_L^3) & \bar{\omega}_2 &= \frac{i_L - i_{LO}}{i_{fg}}
\end{aligned}
\qquad (1)
$$

Using three definitions, the dimensionless governing equations are:

$$\zeta \frac{dd_L^*}{dx^*} = -\tau_L^* - \tau_i^* - \tau_S^* - \theta + 2\mathrm{Fr}^2 q^*(\psi - 1) \qquad (2)$$

$$\frac{dT_L^*}{dx^*} = q^* \left(\frac{S_i D}{A_L}\right)\left(\frac{\bar{\omega}_1}{\omega_0}\right) \qquad (3)$$

$$\dot{m}_S^* = \frac{\dot{m}_{SO}}{\dot{m}_{LO}} + \frac{\bar{\omega}_2}{\bar{\omega}_1} \qquad (4)$$

Equation (2) reduces to the equation of gradually varied open channel flow when no steam flow is present. In the work of Linehan et al. [5], $V_I = 1.14\ V_L$ was used. Trial calculations using $V_I = V_L$ showed that the contribution of terms involving V_I was small, so they have been omitted from equation (2).

The boundary conditions at $x^* = 0$ are $T_L^* = 0$ and $\dot{m}_S^* = \dot{m}_{SO}/\dot{m}_{LO}$ (0 for the experiments reported here). The boundary condition at $x^* = L/D$ is $\zeta = 0$, this being the condition that the depth of an open-channel flow is critical at a free overfall. The quantities τ_L, τ_I, τ_S and h_c remain to be specified to permit the solution of equations (2-4).

The wall shear stresses, τ_L and τ_S, are calculated from the turbulent pipe flow shear stress equation

$$\tau = \frac{f}{8} \rho V^2 \qquad (5)$$

where

$$f = 0.3164\ \mathrm{Re}^{-0.25} \qquad (6)$$

In equation (6)

$$\mathrm{Re}_L = \frac{\rho_L V_L D_{h,L}}{\mu_L} \qquad \mathrm{Re}_S = \frac{\rho_S V_S D_{h,S}}{\mu_S} \qquad (7)$$

and

Nomenclature

A_L = liquid flow area (m^2)
A_S = steam flow area (m^2)
c_1 = heat transfer coefficient multiplier, equations (11) and (12)
c_{PL} = liquid specific heat (J•kg^{-1} •K^{-1})
d_L = liquid depth (m)
d_L^* = dimensionless liquid depth, d_L/D
D = pipe diameter (m)
$D_{h,L}$ = liquid hydraulic diameter, equation (8) (m)
$D_{h,S}$ = steam hydraulic diameter, equation (8) (m)
f = friction factor, equation (6)
f_A = friction factor, equation (10)
Fr = Froude number, equation (1)
g = gravitational acceleration, 9.80665 m • s^{-2}
h_c = condensation heat transfer coefficient, (W • m^{-2} • K^{-1})
i_{fg} = enthalpy of vaporization (J • kg^{-1})
i_L = liquid enthalpy (J • kg^{-1})
i_{LO} = inlet liquid enthalpy (J • kg^{-1})
i_S = steam enthalpy (J • kg^{-1})
$\dot{m}_L$ = liquid mass flow rate (kg • s^{-1})
$\dot{m}_{LO}$ = inlet liquid mass flow rate (kg • s^{-1})
$\dot{m}_S$ = steam mass flow rate (kg • s^{-1})
$\dot{m}_{SO}$ = vented steam mass flow rate (kg • s^{-1})
$\dot{m}_L^*$ = dimensionless liquid mass flow rate, equation (1)
$\dot{m}_S^*$ = dimensionless steam mass flow rate, equation (1)
N_{TD} = Taitel-Dukler stability parameter, equation (13)
Nu = Nusselt number for condensation, equation (1)
p = pressure (Pa)
Pr_L = liquid Prandtl number
q^* = dimensionless condensation rate, equation (1)
Re_L = liquid Reynolds number, equation (7)
Re_S = steam Reynolds number, equation (7)
S_I = steam-liquid interface perimeter (m)
S_L = liquid wall perimeter (m)
S_S = steam wall perimeter (m)
T_L = liquid temperature (K)
T_{LO} = inlet liquid temperature (K)
T_S = steam temperature (K)
T_L^* = dimensionless liquid temperature, equation (1)
V_I = interface velocity (m • s^{-1})
V_L = liquid velocity (m • s^{-1})
V_S = steam velocity (m • s^{-1})
x = axial position (m)
x^* = dimensionless axial position, x/D
α = void fraction, $A_S/(\pi D^2/4)$
ζ = dimensionless group, equation (1)
θ = pipe inclination (radians)
μ_L = liquid viscosity (kg • s^{-1} • m^{-1})
μ_S = steam viscosity (kg • s^{-1} • m^{-1})
ρ_L = liquid density (kg • m^{-3})
ρ_S = steam density (kg • m^{-3})
τ_i = interfacial shear stress (N • m^{-2})
τ_i^* = dimensionless interfacial shear stress, equation (1)
τ_L = liquid wall shear stress (N • m^{-2})
τ_L^* = dimensionless liquid wall shear stress, equation (1)
τ_S = steam wall shear stress (N • m^{-2})
τ_S^* = dimensionless steam wall shear stress, equation (1)
ϕ = dimensionless group, equation (1)
ψ = dimensionless group, equation (1)
ω_0 = dimensionless temperature difference, equation (1)
$\bar{\omega}_1$ = dimensionless temperature difference, equation (1)
$\bar{\omega}_2$ = dimensionless temperature difference, equation (1)

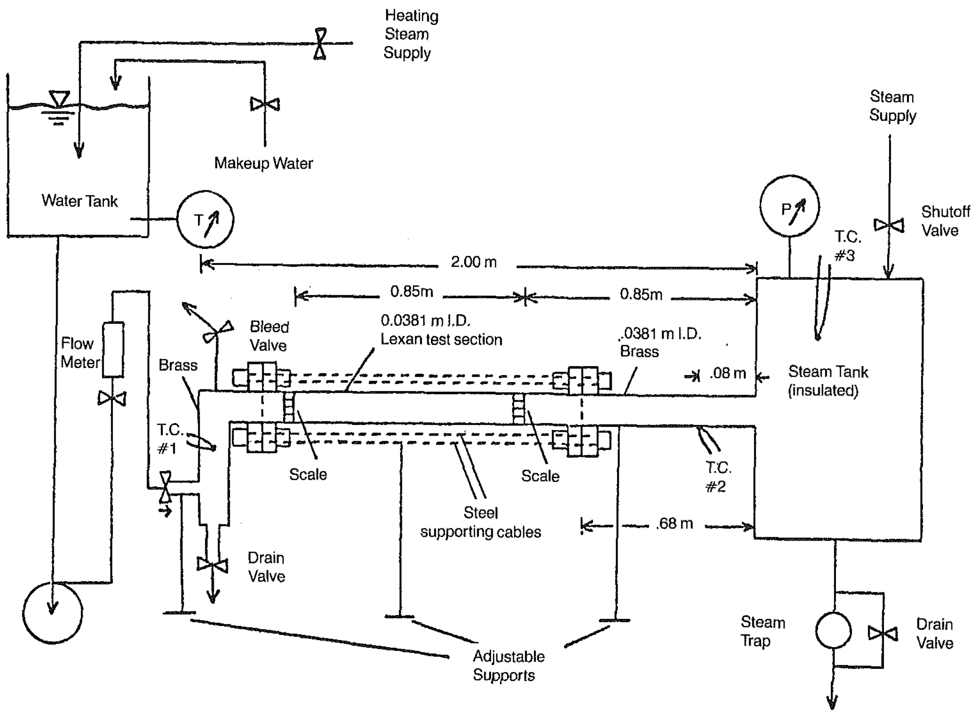

Fig. 1 Schematic of test apparatus

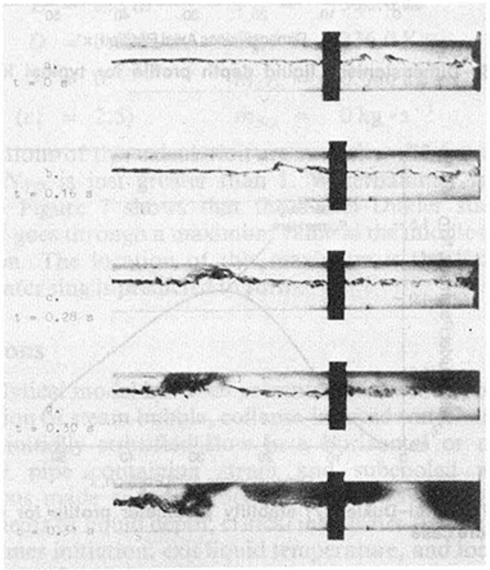

Fig. 2 Details of water slug formation

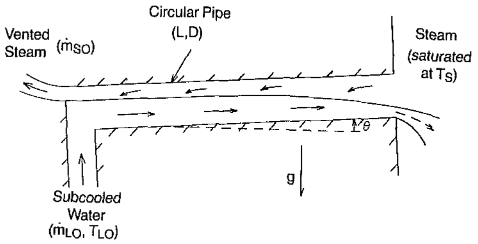

Fig. 3 Flow geometry selected for analysis

$$D_{h,L}=\frac{4A_L}{S_L+S_I}\qquad D_{h,S}=\frac{4A_S}{S_S+S_I}\tag{8}$$

are used as an approximation.

Linehan et al. [5] suggested that the interfacial shear stress could be calculated as a linear superposition of the non-condensing interfacial shear stress and the suction parameter

$$\tau_i=\frac{f_A}{8}\rho_S V_S{}^2+\frac{V_S}{S_I}\frac{d\dot{m}_L}{dx}\tag{9}$$

Linehan et al. [5] used data from a rectangular channel with a 10 to 1 aspect ratio to obtain a correlation for f_A. Using the definitions of equations (7) and (8), an approximation to this correlation for a pipe of arbitrary cross-section is

$$f_A=4.86\times 10^{-6}\ \mathrm{Re}_L+0.0524\tag{10}$$

The interfacial condensation heat transfer coefficient correlation of Bankoff et al. [6] for a rectangular channel with a 10 to 1 aspect ratio is used as the basis for calculating the interfacial condensation rate. Two correlations were made by Bankoff et al. [6]: one for a smooth interface and one for a rough interface. From the point of view of water slug formation prediction, a conservative calculation method is to take the heat transfer coefficient to be the larger of the values calculated from the two correlations. In a partially filled circular pipe, secondary flows are present which are unimportant in a wide rectangular channel. Thus condensation rates should be higher than in a rectangular channel. This effect is accounted for here by multiplying the Bankoff et al. [6] correlation by a constant c_1, determined from experimental data. Using the definitions of equations (7) and (8), an approximation to the Bankoff et al. [6] correlation for a pipe of arbitrary cross section is

Smooth interface

$$\mathrm{Nu}=0.236c_1\mathrm{Re}_S{}^{0.027}\mathrm{Re}_L{}^{0.49}\mathrm{Pr}_L{}^{0.42}\tag{11}$$

Rough interface

$$\mathrm{Nu}=1.17\times 10^{-10}c_1\mathrm{Re}_S{}^{2.1}\mathrm{Re}_L{}^{0.55}\mathrm{Pr}_L{}^{1.16}\tag{12}$$

From a comparison with waterhammer initiation and liquid temperature rise data discussed later, the value of 2.5 was found to give the best agreement of theoretical predictions with the experimental results of this study.

Though most often applied to small void fraction conditions, the stratified-slug flow transition criterion of Taitel and Dukler [7] was found to predict well whether a water slug would form at any location along the pipe. This criterion gave better agreement with the waterhammer initiation data than

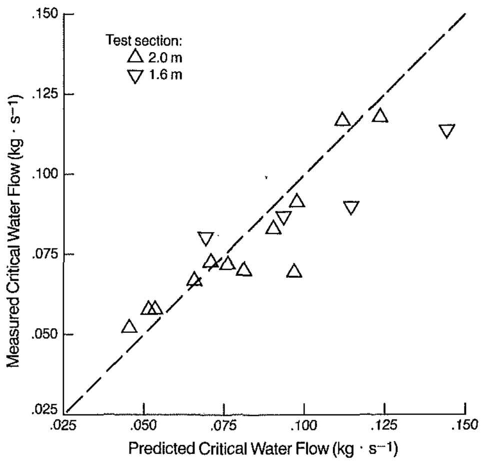

Fig. 4 Comparison of measured with predicted critical inlet water flow rates for waterhammer initiation

did that of Mishima and Ishii [8]. The boundary of Taitel and Dukler [7] between stratified and slug flow is

$$N_{TD}=\frac{\phi \mathrm{Fr}^2}{(1-d_L{}^*)^2}=1.0 \tag{13}$$

for a horizontal or nearly horizontal circular pipe. (The reader should note that in Taitel and Dukler [7] the final form of this equation is misprinted and in error by a factor of α).

One way to prevent condensation waterhammer is to ensure that the pipe runs full. The criterion of Wallis et al. [9] for the minimum water flow rate necessary to run the pipe full was expressed by Block et al. [3] as

$$\frac{16\dot{m}_{LO}{}^2}{\pi^2\rho_L{}^2gD^5}=0.25 \tag{14}$$

The region where waterhammer is predicted to occur is thus bounded by the stratified flow instability limit of equation (13) and the pipe-full limit of equation (14).

The Numerical Solution

The system of equations (2-4) and boundary conditions (with τ_L, τ_1, τ_S, and h_c calculated as has been described) was solved numerically.

When a solution for the flow field has been obtained, the Taitel and Dukler [7] stability parameter N_{TD} in equation (13), is calculated for each node. Localized water slug formation, leading to a steam bubble collapse-induced waterhammer, is predicted when the Taitel-Dukler parameter exceeds 1.0 at any node. Define the critical value of any one of the input parameters as that which separates the waterhammer region from the stable region when the other input parameters are held constant. This value may be found by varying the input parameter until the computed maximum Taitel-Dukler parameter is just greater than 1.0. The inlet water flow rate is of particular significance because it is a parameter that can be readily controlled in an existing piping system. However, at the design stage, the piping geometry and the inlet water temperature may also be amenable to modification.

If the inlet water flow rate was increased rapidly, waterhammer initiation was seen to occur at lower inlet water flow rates than in the quasi-steady case examined here. Although it does not consider these transient effects, a simple approach can be used to provide a bound on the waterhammer region which may be sufficiently conservative. If the inlet water flow is assumed to be immediately heated to saturation, a known constant steam flow will exist along the pipe. The liquid depths can be computed in one "leftward sweep" and the location of the maximum Taitel-Dukler parameter will be at the water inlet, where the liquid depth is greatest. Water slug formation at the water inlet is of no real significance. However, if a water slug cannot form even with these assumptions, it is plausible that waterhammer initiation will not occur even under transient conditions. The result of this calculation is termed the "absolute stability limit."

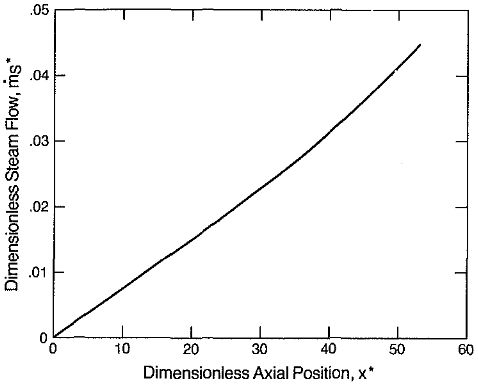

Fig. 5 Dimensionless steam flow rate profile for typical low-pressure case

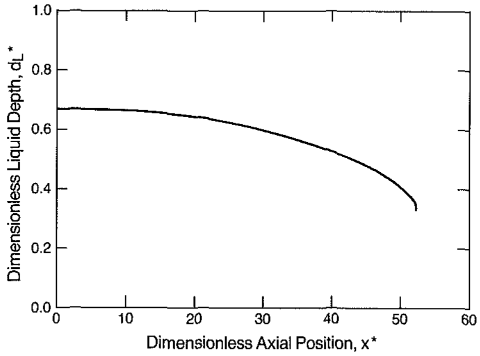

Fig. 6 Dimensionless liquid depth profile for typical low-pressure case

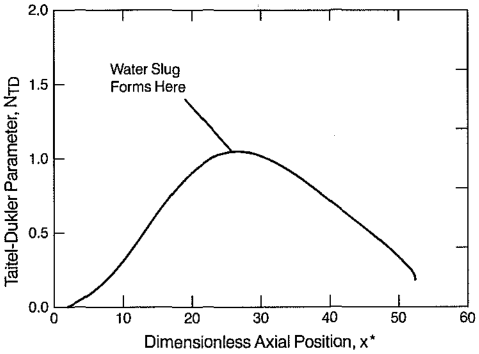

Fig. 7 Taitel-Dukler [7] stability parameter profile for typical low-pressure case

Numerical Results

The numerical model described here can be used to predict the liquid depth profile in an air-water test. These predictions agree well with the air-water liquid depth data, thus verifying the liquid wall shear stress relation and the computational method.

The numerical model was used to predict the critical inlet water flow rates for waterhammer initiation for the conditions tested. Use of $c_1=1.0$ in equations (11) and (12) overpredicted the measured critical inlet water flow rates. It was decided to find the value of c_1 that minimized the rms percentage deviation between the predictions and the data. This was found to be $c_1 = 2.5$. A comparison of measured with predicted critical inlet water flow rates for waterhammer initiation is shown in Fig. 4, for $c_1 = 2.5$. Good agreement is seen (the rms deviation is 13.6 percent).

Thus multiplying the arbitrary cross section equivalent of the Bankoff et al. [6] heat transfer coefficient by the factor $c_1 = 2.5$ provides the best agreement between prediction and data on waterhammer initiation. To check that this correction is appropriate, the numerical solution was carried out with $c_1 = 2.5$ for the exit liquid temperature test conditions. The predicted values of condensation efficiency (T_L^* at exit) agreed well (0.10 rms deviation) with measured values, which ranged from 0.36 to 0.56. This provides experimental justification for the heat transfer coefficient adjustment needed to predict waterhammer initiation data. Consequently, the validity of the Taitel-Dukler stability criterion is verified.

Two sets of photographs were taken of water slug formation in, respectively, the 1.6-m and 2.0-m test sections. For the conditions of these photographed tests, the numerical model was applied to determine the locations where water slug formation was first predicted to occur as the inlet water flow rate was increased. Calculated locations were seen to agree well with those observed.

Computed results are shown in Figs. 5, 6, and 7 for a typical set of conditions seen in the experimental apparatus of this study:

$$\begin{array}{rclrcl} L &=& 2.0\,\mathrm{m} & T_S &=& 396.0\,\mathrm{K} \\ D &=& 0.0381\,\mathrm{m} & T_{LO} &=& 336.0\,\mathrm{K} \\ \theta &=& 0 & \dot{m}_{LO} &=& 0.086\,\mathrm{kg}\cdot\mathrm{s}^{-1} \\ (c_1 &=& 2.5) & \dot{m}_{SO} &=& 0\,\mathrm{kg}\cdot\mathrm{s}^{-1} \end{array}$$

The conditions of this calculation are such that the maximum value of N_{TD} is just greater than 1. Waterhammer is thus predicted. Figure 7 shows that the Taitel-Dukler stability parameter goes through a maximum value in the middle of the test section. The location of this maximum is the location where a water slug is predicted to form.

Conclusions

An analytical model has been presented here which predicts the initiation of steam bubble, collapse-induced waterhammer from an initially stratified flow in a horizontal or nearly horizontal pipe containing steam and subcooled water. Calculations made with this model compare favorably with measurements of liquid depth, critical inlet water flow rate for waterhammer initiation, exit liquid temperature, and location of water slug formation taken in a low-pressure laboratory apparatus with a circular pipe. A design procedure for use in studying the susceptibility of a steam-water system to waterhammer events of the type studied here is described in Appendix A.

Expressions for the wall and interfacial shear stresses, condensation heat transfer coefficient, and stratified-slug flow regime transition from the literature were incorporated into the model presented here. Other than multiplying the heat transfer coefficient correlation (which had been obtained from rectangular channel data) by a factor of 2.5, no empiricism needed to be introduced into the model. This one correction is justified by experimental measurements of exit liquid temperatures. The model should therefore well approximate the phenomena involved. However, further experimental work on the condensation heat transfer coefficient in countercurrent flow of steam and subcooled water in pipes with circular and other cross sections (including large and small pipes over a range of operating pressures) would be useful. A correlation of this heat transfer data could then be incorporated into the model presented here and should improve the reliability of waterhammer initiation predictions. Other areas which warrant investigation include the effects of rapid increases in inlet water flow rate and the presence of noncondensible gases on waterhammer initiation.

Acknowledgments

This project was sponsored by Boston Edison Company and Northeast Utilities, Inc. Dr. Bjorge acknowledges the support of the National Science Foundation in the form of a Graduate Fellowship. Mr. Bill Finley constructed the test apparatus.

References

1 Cahill, W. J., "Feedwater Line Incident Report - Indian Point Unit No. 2," Consolidated Edison Co., AEC Docket No. 50-247, 1974.

2 Roidt, R. M., "Steam-Water Slugging in Steam Generator Feedwater Lines," Westinghouse Research Memo No. 74-7E9-FLINE-M1, Pittsburgh, Pa., 1975.

3 Block, J. A., et al., "An Evaluation of PWR Steam Generator Waterhammer," NRC Report NUREG-0291, 1977.

4 Bjorge, R. W., "Initiation of Waterhammer in Horizontal or Nearly-Horizontal Pipes Containing Steam and Subcooled Water," Ph.D thesis, Massachusetts Institute of Technology, 1982.

5 Linehan, J. H., Petrick, M., and El-Wakil, M. M., "The Condensation of a Saturated Vapor on a Subcooled Film During Stratified Flow," *Chem. Eng. Prog.*, Vol. 66, 1970, pp. 11-20.

6 Bankoff, S. G., et al., "Countercurrent Steam-Water Flow in a Flat Plate Geometry," NRC Report NUREG/ CR-2783, 1982.

7 Taitel, Y., and Dukler, A. E., "A Model for Predicting Flow Regime Transitions in Horizontal and Near Horizontal Gas-Liquid Flow," *AIChE Journal*, Vol. 22, 1976, pp. 47-55.

8 Mishima, K., and Ishll, M., "Theoretical Prediction of Onset of Horizontal Slug Flow," ASME *Journal of Fluids Engineering*, Vol. 102, 1980, pp. 441-445.

9 Wallis, G. B., Crowley, C. J., and Hagi, Y., "Conditions for a Pipe to Run Full When Discharging Liquid into a Space Filled With Gas," ASME *Journal of Fluids Engineering*, Vol. 99, 1977, pp. 405-413.

APPENDIX A

Design Procedure for Waterhammer Avoidance

The procedure described here is appropriate for use in the flow geometry of Fig. 3. For many practical cases it is possible to simplify the actual system to this form and obtain significant, though less accurate, results.

The following steps may be followed to determine if a piping system has the potential to produce a waterhammer event of the type studied here:

1 Determine if there are any horizontal or nearly horizontal pipe runs in which steam and subcooled water may both be present. Abnormal operating conditions and equipment characteristics (e.g., leaky valves) should be considered. If there are no such pipe runs, the condensation waterhammer studied here cannot occur.

2 Use equation (14) to determine if the pipe will run full for all flow rates and system conditions possible. If it will, the condensation waterhammer studied here will not occur.

3 Use the "absolute stability limit" model for the worst flow rates and system conditions possible. If the Taitel-Dukler stability parameter, equation (13), cannot be made to exceed 1.0, the condensation waterhammer studied here is not expected to occur.

4 Use the best-estimate model ($c_1 = 2.5$) for the worst flow rates and system conditions possible. If the Taitel-Dukler stability parameter cannot be made to exceed 1.0, condensation waterhammer is unlikely, though possible. The

proximity of operating conditions to the best-estimate limit compared with the "absolute stability limit" should be considered in assessing the risk of waterhammer. If the Taitel-Dukler parameter does exceed 1.0, waterhammer problems are to be expected.

If a waterhammer problem seems likely, the following actions may be considered in an attempt to eliminate the problem:

1 Reduce the inlet water subcooling

2 Reduce the pipe length

3 Increase the pipe diameter, thereby raising the critical inlet water flow rate

4 Decrease the pipe diameter to ensure the pipe always runs full

5 Modify other system operational characteristics to keep the system in the safe operating region

6 Add valves or other devices to prevent the establishment of a stratified flow

The effect of each of these modifications can be found by applying the analytical method presented here.

Two other actions may also be considered, though their effect cannot be predicted using the method presented here:

1 Add noncondensible gas to the system, reducing the condensation rate and also reducing the effect of steam bubble collapse, should it occur

2 Tilt the pipe upward, reducing the steam-water interfacial area

H. Honda
Professor,
Department of Mechanical Engineering,
Okayama University,
Okayama, Japan 700

T. Fujii
Professor,
Research Institute of
Industrial Science,
Kyushu University,
Kasuga, Japan 816

Condensation of Flowing Vapor on a Horizontal Tube—Numerical Analysis as a Conjugate Heat Transfer Problem

Condensation of flowing vapor on a horizontal tube is numerically analyzed under given conditions of vapor and coolant. Besides the usual boundary layer concept, some approximations are introduced for the determination of shear stress at the vapor-liquid interface. The conjugation of the two-phase boundary layer equations and the heat conduction equation within the tube wall is achieved by using an iterative scheme at the outer surface of the tube wall. The solution thus obtained reveals the effects of vapor velocity, tube material, heat transfer of coolant side, etc., upon circumferential distributions of temperature, heat flux density, and Nusselt number at the outer tube surface. Also the solution compared well with available experimental results for the wall temperature distribution and average Nusselt number. The heat transfer characteristics of steam and refrigerant vapors resemble those of the tubes with uniform wall heat flux density and uniform wall temperature, respectively.

Introduction

The present analysis concerns laminar film condensation on a horizontal tube under the influence of vapor velocity. Gaddis [1] presented a rigorous treatment of the two-phase boundary layer equations of vapor and condensate for the front part of a tube with uniform wall temperature. Fujii et al. [2] proposed an approximate method to solve the two-phase boundary layer equations for the tube surfaces with uniform wall temperature and uniform wall heat flux density. The numerical results show that the average heat transfer coefficient for the latter is smaller than that for the former, with their difference increasing with the increase in vapor velocity; the numerical results agree reasonably well with their own experimental results for steam. However, it is apparent that neither of these boundary conditions apply accurately to the actual situation.

Recently, Nicol and Wallace [3] took account of two-dimensional wall conduction in their analysis, where the effect of vapor suction upon the interfacial shear stress was neglected. Nobbs and Mayhew [4] used various models of interfacial shear stress for downward vapor flow, and Nicol et al. [5] applied a dry friction factor to the interface for horizontal vapor flow. In these analyses the circumferential wall conduction was assumed to be negligible in comparison with the radial one.

The foregoing literature survey shows the problem to be studied exists in the assumptions used for the vapor boundary layer and the thermal boundary condition at the tube wall. In this paper this problem is treated as that of conjugate heat transfer, and the numerical results are compared with available experimental ones.

Analysis

Formulation of the Problem. The physical model and coordinate system are shown in Fig. 1. A saturated vapor with temperature T_s and oncoming velocity U_∞ flows across a horizontal tube making an angle φ_0 from the vertical axis. The vapor condenses on the tube, which is cooled internally by a coolant with temperature T_c and velocity v_c to form a smooth liquid film. The liquid flows separately around the tube and meets at φ_f. The separation of vapor boundary layer takes place at angles ψ and ψ' measured clockwise and counterclockwise from φ_o, respectively.

The assumptions employed in the formulation of the present problem are: (*i*) the liquid film and vapor boundary layer are laminar. (*ii*) The thickness of the liquid film δ and the vapor boundary layer Δ are much smaller than the tube radius r_o. (*iii*) The inertia and pressure terms in the momentum equation and the convection terms in the energy equation for the liquid film can be neglected. (*iv*) The shear stress τ_i acting at the liquid–vapor interface is negligible in the downstream region of the separation points. (*v*) The circumferential velocity at the liquid–vapor interface is much smaller than the mainstream velocity U_φ around the tube. (*vi*) All physical properties are constant. (*vii*) The heat transfer coefficient at the inner tube surface α_c is uniform. (*viii*) Surface tension effect is negligible.

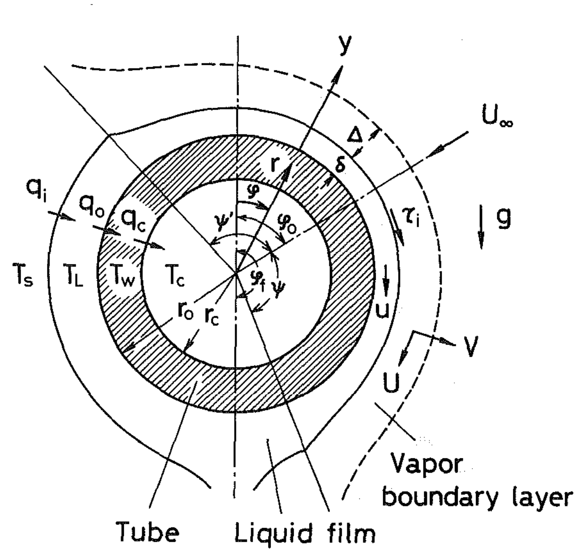

Fig. 1 Physical model and coordinate system

Contributed by the Heat Transfer Division for publication in the JOURNAL OF HEAT TRANSFER. Manuscript received by the Heat Transfer Division June 22, 1983.

Based on these assumptions, the conservation equations are written as:

for the vapor boundary layer

$$\frac{1}{r_0}\frac{\partial U}{\partial \varphi}+\frac{\partial V}{\partial y}=0 \tag{1}$$

$$U\frac{1}{r_o}\frac{\partial U}{\partial \varphi}+V\frac{\partial U}{\partial y}=U_\varphi\frac{1}{r_o}\frac{dU_\varphi}{d\varphi}+\nu_v\frac{\partial^2 U}{\partial y^2} \tag{2}$$

for the liquid film

$$\nu_L\frac{d^2u}{Ldy^2}+g\sin\varphi=0 \tag{3}$$

$$\frac{d^2T_L}{dy^2}=0 \tag{4}$$

for the tube wall

$$\frac{\partial^2 T_w}{\partial r^2}+\frac{1}{r}\frac{\partial T_w}{\partial r}+\frac{1}{r^2}\frac{\partial^2 T_w}{\partial \varphi^2}=0 \tag{5a}$$

The boundary and compatibility conditions are

$$U_{\delta+\Delta}=U_\varphi,\ \left(\frac{\partial U}{\partial y}\right)_{\delta+\Delta}=0 \quad \text{at} \quad y=\delta+\Delta \tag{6}$$

$$\left.\begin{aligned}&\mu_L\left(\frac{\partial u}{\partial y}\right)_i=\mu_V\left(\frac{\partial U}{\partial y}\right)_i=\tau_i, \quad U_i=0, \quad T_i=T_s &(7)\\ &\rho_L\frac{1}{r_0}\frac{d}{d\varphi}\int_0^\delta udy=-\rho_V V_i=\frac{q_i}{h_{fg}} &(8)\end{aligned}\right\}\text{at } y=\delta$$

$$\left.\begin{aligned}&u=0, \quad T_L=T_{wo} &(9)\\ &\lambda_w(\partial T_w/\partial r)_0=\lambda_L(\partial T_L/\partial y)_o=q_o &(10a)\end{aligned}\right\}\ \text{at } y=0\ (r=r_o)$$

$$\lambda_w(\partial T_w/\partial r)_c=\alpha_c(T_{wc}-T_c)=q_c \quad \text{at} \quad r=r_o \tag{11a}$$

Method of Numerical Analysis. By using the method of Truckenbrodt [6] as modified by Fujii et al. [2] equations (1) and (2) are transformed to

$$\frac{dz}{d\varphi}=\frac{1}{\bar{U}_\varphi}\left\{0.441(1-\bar{V}_i\sqrt{2z})-5.4z\frac{d\bar{U}_\varphi}{d\varphi}\right\} \tag{12}$$

with the boundary condition

$$\text{for } \varphi_o=0, \quad dz/d\varphi=0 \quad \text{at} \quad \varphi=0 \tag{13a}$$

$$\text{for } \varphi_o\neq 0, \quad dz/d\varphi=\text{finite} \quad \text{at} \quad \varphi=\varphi_o \tag{13b}$$

where z is a function of the momentum thickness as

$$z=\frac{2\mathrm{Re}_V}{d0^2}\left\{\int_\delta^{\delta+\Delta}\frac{U}{U_\varphi}\left(1-\frac{U}{U_\varphi}\right)dy\right\}^2 \tag{14}$$

Then, the dimensionless shear stress at the liquid–vapor interface $\bar{\tau}_i$ is obtained as

$$\bar{\tau}_i=\pm 9.11\kappa_a{}^{0.4}(\kappa+\kappa_a)^{0.6}\bar{U}_\varphi/\sqrt{z} \quad \text{for} \quad \varphi\gtreqless\varphi_o \tag{15}$$

where

$$\kappa_a=0.0682+0.123\bar{V}_i\sqrt{z}, \quad \kappa=zd\bar{U}_\varphi/d\varphi \tag{16}$$

Thus the problem of solving the vapor boundary layer equations is reduced to that of directly obtaining the interfacial shear stress from the solution of equation (12).

Equation (12) is solved from φ_o to the angles where the values of $\bar{\tau}_i$ take their extremums. The distributions of $\bar{\tau}_i$, in the region after the extremums, are represented by parabolic

Nomenclature

A = $\mathrm{Pr}_L/\mathrm{Fr}H$
A_{ov} = $\mathrm{Pr}_L/\mathrm{Fr}H_{ov}$
B = Pr_L/RH
B_{ov} = Pr_L/RH_{ov}
c_p = specific heat at constant pressure
d = tube diameter
$\bar{d}_c$ = d_c/d_o
Fr = Froude number, $U_\infty{}^2/gd_o$
Ga = Galileo number, $gd_o{}^3/\nu_L{}^2$
g = gravitational acceleration
H = phase change number, $c_{pL}(T_s-T_{wo})/h_{fg}$
H_{ov} = $c_{pL}(T_s-T_c)/h_{fg}$
h_{fg} = latent heat of condensation
Nu = Nusselt number, $\alpha d_o/\lambda_L$
Nu_c = Nusselt number at inner tube surface, $\alpha_c d_c/\lambda_c$
Pr = Prandtl number
q = heat flux density
$\bar{q}$ = $qd_o/\lambda_L(T_s-T_c)$
R = $\rho\mu$ ratio, $(\rho_L\mu_L/\rho_V\mu_V)^{1/2}$
Re_V = vapor Reynolds number, $U_\infty d_o/\nu_V$
Re_L = two-phase Reynolds number, $U_\infty d_o/\nu_L$
Re_c = coolant Reynolds number
r = radial coordinate
$\bar{r}$ = r/d_0
T = temperature
$\bar{T}$ = $(T-T_c)/(T_s-T_c)$
t = tube thickness
U,V = vapor velocity components in φ- and y-directions
U_∞ = oncoming velocity
U_φ = mainstream velocity around tube
$\bar{U}_\varphi$ = U_φ/U_∞
$\bar{U}_{\varphi p}$ = value of $\bar{U}_\varphi$ defined in equation (23*a*)
$\bar{U}_{\varphi R}$ = value of $\bar{U}_\varphi$ defined in equation (23*b*)
$\bar{V}_i$ = suction parameter, $-V_i\sqrt{\mathrm{Re}_V}/U_\infty$
u = liquid velocity component in φ-direction
v_c = coolant velocity
X = $\bar{\delta}\sqrt{\mathrm{Re}_L}$
y = radial outward distance from outer tube surface
z = defined in equation (14)
α = heat transfer coefficient
Δ = vapor boundary layer thickness
δ = liquid film thickness
$\bar{\delta}$ = δ/d_o
κ,κ_a = defined in equation (16)
λ = thermal conductivity
μ = dynamic viscosity
ν = kinematic viscosity
ρ = density
τ_i = shear stress at liquid-vapor interface
$\bar{\tau}_i$ = $\tau_i\sqrt{\mathrm{Re}_V}/(\rho_V U_\infty{}^2/2)$
φ = angular coordinate, see Fig. 1.
φ_b = singular point of equation (21)
φ_f = confluence point of liquid flows
φ_o = forward stagnation point of vapor flow
ψ,ψ' = separation angles measured from φ_o

Subscripts

c = inner tube surface; also coolant
i = liquid-vapor interface
L = liquid
m = average value
o = outer tube surface
s = saturation
V = vapor
w = tube wall

Superscript

* = values defined in equations (35), (36), (38), and (40)

curves that are continuous with the upstream solution up to the second derivatives, and the intersections of these curves with $\bar{\tau}_i = 0$ are assumed to be the separation points. By this modification of Truckenbrodt's method, the value of $\bar{\tau}_i$ more closely agrees with the accurate numerical solution by Terril [7] for single-phase flows with and without uniform suction.

Integration of equation (4) from $y = 0$ to $y = \delta$ subject to relevant boundary conditions yields an expression of q_i, and its substitution into equation (8) yields

$$\rho_L h_{fg} \frac{1}{\ } \frac{d}{\ } \int^{\delta} u dy = \frac{\lambda_L}{\ } (T_s - T_{wo}) \qquad (17)$$

The potential flow $\bar{U}_{\varphi p}$ and $\bar{U}_{\varphi R}$, which corresponds to the pressure distribution measured by Roshko [8], represent almost the highest and the lowest values among the previous measurements with and without suction, respectively [2, 9]. The value of Nu_c is given by

$$\mathrm{Nu}_c = 0.023\mathrm{Re}_c^{0.8}\mathrm{Pr}_c^{0.4}$$

while measured values of α_c are used when the numerical solutions are compared with corresponding experimental results.

Corrections to "Condensation of Flowing Vapor on a Horizontal Tube—Numerical Analysis as a Conjugate Heat Transfer Problem," by H. Honda and T. Fujii, published in the November 1984 issue of the ASME JOURNAL OF HEAT TRANSFER, pp. 841-848.

	Error	Correction
Equation (2)	$U\frac{1}{r_o}\frac{\partial U}{\partial \varphi} + V\frac{\partial U}{\partial y} = U_\varphi \frac{1}{r_o}\frac{dU_\varphi}{d\varphi} + \nu_v \frac{\partial^2 U}{\partial y^2}$	$U\frac{1}{r_o}\frac{\partial U}{\partial \varphi} + V\frac{\partial U}{\partial y} = U_\varphi \frac{1}{r_o}\frac{dU_\varphi}{d\varphi} + \nu_V \frac{\partial^2 U}{\partial y^2}$
Equation (3)	$\nu_L \frac{d^2u}{Ldy^2} + g\sin\varphi = 0$	$\nu_L \frac{d^2u}{dy^2} + g\sin\varphi = 0$
Equation (14)	$z = \frac{2\mathrm{Re}_V}{d0^2}\left\{\int_\delta^{\delta+\Delta} \frac{U}{U_\varphi}\left(1 - \frac{U}{U_\varphi}\right)dy\right\}^2$	$z = \frac{2\mathrm{Re}_V}{d_0^2}\left\{\int_\delta^{\delta+\Delta} \frac{U}{U_\varphi}\left(1 - \frac{U}{U_\varphi}\right)dy\right\}^2$
Equation (21)	$\frac{dX}{d\varphi} = \frac{1 - \bar{T}_{wo} - \frac{2}{3}A_{ov}X^4\cos\varphi - \frac{1}{2}B_{ov}\frac{d\bar{\tau}_i}{d\varphi}X^3}{2A_{ov}X^3\sin\varphi + B_{ov}\bar{\tau}_i x^2}$	$\frac{dX}{d\varphi} = \frac{1 - \bar{T}_{wo} - \frac{2}{3}A_{ov}X^4\cos\varphi - \frac{1}{2}B_{ov}\frac{d\bar{\tau}_i}{d\varphi}X^3}{2A_{ov}X^3\sin\varphi + B_{ov}\bar{\tau}_i X^2}$

In Table 1, $_o$ should read ϕ_o.

On p. 846, the lower half of the figure in column 1 should be exchanged with the figure in column 2.

where φ_b is determined so that the denominator at the right-hand side of equation (21) becomes zero in the region $0 < \varphi < \varphi_o$.

Equations (12) and (21), which constitute simultaneous ordinary differential equations for X and z as functions of φ, can be solved numerically with given distributions of $\bar{U}_\varphi$ and $\bar{T}_{wo}$.

Equations (5*a*), (10*a*), and (11*a*) are written in terms of dimensionless variables as

$$\frac{\partial \bar{T}_w}{\partial \bar{r}^2} + \frac{1}{\bar{r}}\frac{\partial \bar{T}_w}{\partial \bar{r}} + \frac{1}{\bar{r}^2}\frac{\partial^2 \bar{T}_w}{\partial \varphi^2} = 0 \qquad (5b)$$

$$\frac{\lambda_w}{\lambda_L}\left(\frac{\partial \bar{T}_w}{\partial \bar{r}}\right)_o = \left(\frac{\partial \bar{T}_L}{\partial \bar{y}}\right)_o = \frac{1 - \bar{T}_{wo}}{\bar{\delta}} = \bar{q}_o \quad \text{at} \quad \bar{r} = \bar{r}_o \qquad (10b)$$

$$\frac{\lambda_w}{\lambda_L}\left(\frac{\partial \bar{T}_w}{\partial \bar{r}}\right)_c = \mathrm{Nu}_c \frac{\lambda_c}{\lambda_L}\frac{\bar{T}_{wc}}{\bar{d}_c} = \bar{q}_c \quad \text{at} \quad \bar{r} = \bar{r}_c \qquad (11b)$$

Equation (5*b*) and simultaneous equations (12) and (21) are coupled so that the values of $\bar{T}_{wo}$ and $\bar{q}_o$ are continuous. The solution of these equations depends on the following nine parameters.

$\varphi_0, \bar{U}_\varphi, \mathrm{Re}_L,\ A_{ov}, B_{ov}, \bar{d}_c, \lambda_w/\lambda_L, \lambda_c/\lambda_L$ and Nu_c.

In the numerical analysis two kinds of distributions of mainstream velocity are used in the region $\bar{\tau}_i > 0$ as

$$\bar{U}_\varphi = \bar{U}_{\varphi p} = 2\sin(\varphi - \varphi_o) \qquad (23a)$$

$$\bar{U}_\varphi = \bar{U}_{\varphi R} = 1.762(\varphi - \varphi_o) - 0.314(\varphi - \varphi_o)^3 - 0.0338(\varphi - \varphi_o)^5 \qquad (23b)$$

In the case of $\varphi_o \neq 0$, z and X are expanded to the power series of $(\varphi - \varphi_o)$ subject to boundary condition (13*b*) as

$$z = z_o + a(\varphi - \varphi_o) + \ldots \qquad (28)$$

$$X = X_o + b(\varphi - \varphi_o) + \ldots \qquad (29)$$

When X_o at $\varphi_o = 0$ is taken as the first approximation, z_o, a and b are obtained by substituting equations (28) and (29) into equations (12) and (21), and numerical calculation of these two equations is carried out for $\varphi \leq \varphi_o$. The numerator at the right-hand side of equation (21) is required to be zero at $\varphi = \varphi_b$ from boundary condition (22*b*). Until this condition is satisfied, trial guesses of X_o and the foregoing calculation are repeated. The convergence criterion was taken as

$$|X_o^{j+1} - X_o^j| / X_o^{j+1} \leq 10^{-5}$$

where X_o^j and X_o^{j+1} denote the jth and $(j+1)$th initial values. The solution of X has the following characteristics.

$$(dX^j/d\varphi) \to \pm\infty \quad \text{at} \quad \varphi \to \varphi_b^j$$

and

$$(dX^{j+1}/d\varphi) \to \mp\infty \quad \text{at} \quad \varphi \to \varphi_b^{j+1}$$

Therefore, values of X and z in the region $\varphi_b - \Delta\varphi \leq \varphi \leq \varphi_b + \Delta\varphi$ were extrapolated from the solution in the region $\varphi_b + \Delta\varphi \leq \varphi < \varphi_o$, where $\Delta\varphi = \pi/100$. Thereafter, the calculation of equations (12) and (21) was continued up to $-\pi$ for $\varphi \leq \varphi_o$. The solution of X for $\varphi \geq \varphi_o$ tends to infinity at the point $\varphi = \varphi_f\ (\geq \pi)$, which is regarded as the confluence point of the liquid flow around the tube.

Step (2): Solve equation (5*b*) subject to boundary conditions (10*b*) and (11*b*), where the value of $\bar{\delta}$ obtained in Step

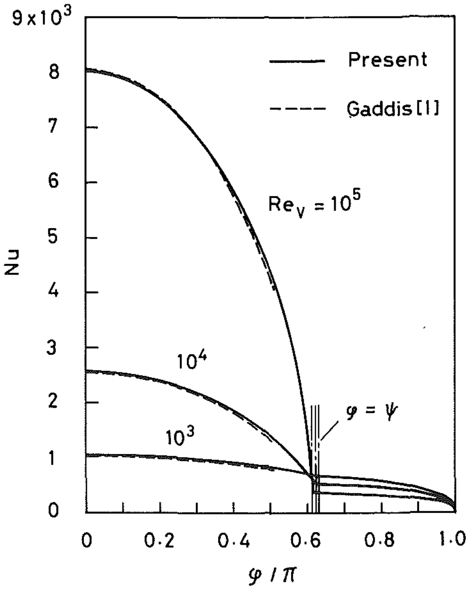

Fig. 2 Comparison of the present result with Gaddis's [1] for Nu for uniform wall temperature: steam, $\varphi_o = 0$, $\bar U_\varphi = \bar U_{\varphi p}$, Ga = 1.02×10^9, $Pr_L = 1.74$, $H = 2 \times 10^{-3}$, $\rho_L/\rho_V = 1600$ and $\nu_L/\nu_V = 0.014$

(1) is used. The calculation was carried out by the successive overrelaxation method with 101 grid points in the region $0 \leq \varphi \leq \pi$ in the case of $\varphi_o = 0$, and 200 grid points in the region $0 \leq \varphi \leq 2\pi$ in the case of $\varphi_o \neq 0$, and 6 to 11 grid points in the region $\bar r_c \leq \bar r \leq 0.5$. The convergence criterion was taken as

$$|\bar T^{k+1}_{w,ij} - \bar T^{k}_{w,ij}| < 10^{-5} \sim 10^{-4}$$

where $\bar T^{k}_{w,ij}$ and $\bar T^{k+1}_{w,ij}$ denote the kth and $(k+1)$th solutions.

Step (3): Return to Step (1) with the value of $\bar T_{wo}$ obtained in Step (2), and repeat the process until the values of $\bar T_w$ and $\bar q_o$ converge. The convergence criteria were taken as

$$|T^{n+1}_{w,ij} - T^{n}_{w,ij}| < 10^{-3}$$

and

$$|q^{n+1}_{o,j} - q^{n}_{o,j}| / q^{n+1}_{o,j} < 10^{-3}$$

where n denotes the number of iterations.

Numerical Results

The local heat transfer coefficient α and the local Nusselt number Nu are defined by

$$\alpha = q_o / (T_s - T_{wo}) \tag{30}$$

and

$$\mathrm{Nu} = \alpha d_o / \lambda_L \tag{31}$$

Two kinds of definition are introduced for the average heat transfer coefficient and the representative temperature of the outer tube surface such that (i) α_m is based on area-average temperature T_{wom} and (ii) α^*_m and T^*_{wom} are consistent with the definition of the overall heat transfer coefficient.

For case (1);

$$\alpha_m = q_{om} / (T_s - T_{wom}) \tag{32}$$

where

$$q_{om} = \frac{1}{2\pi} \int_0^{2\pi} q_o d\varphi \tag{33}$$

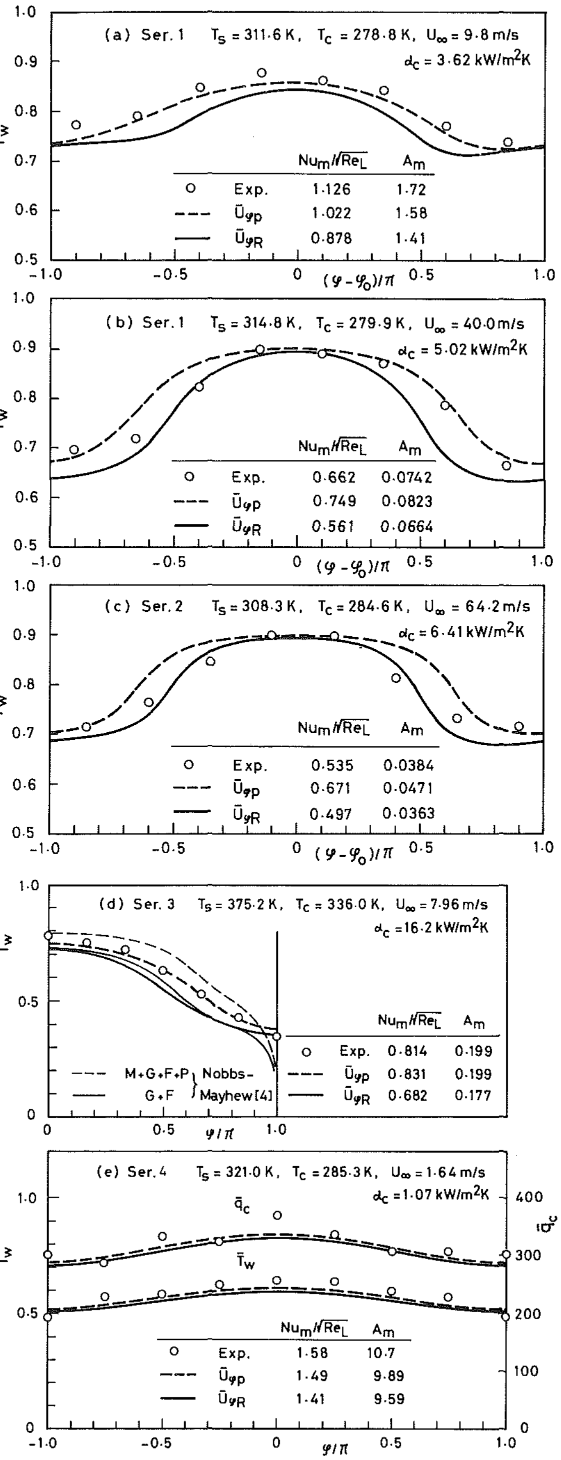

Fig. 3 Comparison between the present and experimental results for $\bar T_w$

and

$$T_{wom} = \frac{1}{2\pi} \int_0^{2\pi} T_{wo} d\varphi \tag{34}$$

For case 2; α^*_m and T^*_{wom} are determined as the solutions of the following equations

$$q_{om} = \alpha^*_m (T_s - T^*_{wom}) \tag{35}$$

$$q_{om} = \left\{ \frac{1}{\alpha^*_m} - \frac{d_o}{2\lambda_w} \ln \bar d_c + \frac{1}{\alpha_c \bar d_c} \right\}^{-1} (T_s - T_c) \tag{36}$$

Table 1 Summary of experimental data used for comparison with the present analysis

Series	Fluid	Tube material	d_o mm	t mm	T_s °C	$T_s - T_c$ °C	α_c kW/m^{2}K	o rad	Reference
1	steam	copper	37.2	3.5	~38	~31	2.9~5.0	1.52	[2]
2	steam	brass	18.6	3.0	~30	~24	6.4~12.2	1.52	[2]
3	steam	copper	19.1	1.63	~100	~39, ~78	8.5~16.6	0	[4]
4	R-113	copper	37.1	3.5	~47	~35	1.0~1.7	0	[10]
5	R-113	copper	8.0	1.5	~47	~11	3.8~5.7	0	[10]

It is mentioned here that the values of α_m and α_m^* agree precisely when there is no circumferential wall conduction. The average Nusselt numbers for α_m and α_m^* are defined by

$$\mathrm{Nu}_m = \alpha_m d_o / \lambda_L \tag{37}$$

and

$$\mathrm{Nu}_m^* = \alpha_m^* d_o / \lambda_L \tag{38}$$

In a similar manner the dimensionless parameters A_m and $A^*{}_m$ are defined as

$$A_m = \mathrm{Pr}_L / \mathrm{Fr} H_m \tag{39}$$

and

$$A_m^* = \mathrm{Pr}_L / \mathrm{Fr} H_m^* \tag{40}$$

where

$$H_m = c_{pL}(T_s - T_{wom})/h_{fg}$$

and

$$H_m^* = c_{pL}(T_s - T_{wom}^*)/h_{fg}.$$

Comparison between the Present and Previous Results. Figure 2 compares the present result for the circumferential variation of Nu for condensation of steam on a tube of uniform temperature with that of Gaddis [1], which is one of the most rigorous solutions for the two-phase boundary layer equations of vapor and condensate in the front part of a tube. In the applicable range of $0 \le \varphi \le 1.6$ both results agree within 3.7 percent.

Figures 3(*a-e*) are the comparison on the circumferential distribution of $\bar{T}_w$ between the present and previous experimental results [2, 4, 10], which were obtained under the conditions as shown in Table 1. In each figure the calculated value of $\bar{T}_w$ for $\bar{U}_{\varphi p}$ (thick dotted line) is higher than that for $\bar{U}_{\varphi R}$ (thick solid line), and the experimental data for steam are close to the former when U_∞ is small and to the latter when U_∞ is large. The values of the average heat transfer parameters $\mathrm{Nu}_m/\sqrt{\mathrm{Re}_L}$ and A_m are also shown in the figures. These parameters were adopted for presentation with reference to the uniform wall temperature solution [2, 10], in which $\mathrm{Nu}_m/\sqrt{\mathrm{Re}_L}$ can be expressed as a function of $A = \mathrm{Pr}_L/\mathrm{Fr}H$ and $B = \mathrm{Pr}_L/RH$. The tendencies of these values are consistent with those of T_{wo}. The theoretical results by Nobbs and Mayhew [4] are also shown by thin solid and dotted lines in Fig. 3(*d*). The former and the latter corresponds to the solutions with the terms of momentum (M), gravity (G), friction (F) and pressure (*P*), and with only (G) and (F) terms, respectively. The experimental data lie between these two lines, except near $\varphi = \pi$. In Fig. 3(*e*) for R-113, where comparisons of local heat flux density at the inner surface $\bar{q}_c$ are also made, the experimental data are a little higher than the numerical results for both $\bar{T}_w$ and $\bar{q}_c$.

Figure 4 shows the comparison between the present and previous experimental results for the average Nusselt number on the coordinates of $\mathrm{Nu}_m/\sqrt{\mathrm{Re}_L}$ versus A_m. Each measured value and corresponding calculated values for $\bar{U}_{\varphi p}$ and $\bar{U}_{\varphi R}$ are connected by a solid line. The result by Nusselt [11] for condensation in quiescent vapor

$$\mathrm{Nu}_m = 0.73(\mathrm{Ga}\mathrm{Pr}_L/H_m)^{0.25} = 0.73 A_m{}^{0.25}\sqrt{\mathrm{Re}_L} \tag{41}$$

is also shown by a chain line. The difference between this line and the data shows the effect of U_∞. For the data of steam in series 1 and 2, the measured values are a little higher than the calculated values in the region $A_m \gtrsim 1$, and lie between the latters in the region $A_m \lesssim 1$. For the data of Nobbs and Mayhew [4] in series 3 the measured values are a little higher than both calculated ones when $(T_s - T_c)$ is high in the region $A_m \lesssim 1$. For the data of R-113, there is a tendency for the measured values to become higher than the calculated ones as A_m decreases in each series of 4 and 5. This tendency is marked for greater values of d_o, $(T_s - T_c)$, and U_∞ as shown elsewhere [10] and is accompanied by the appearance of ripples on the surface of the liquid film.

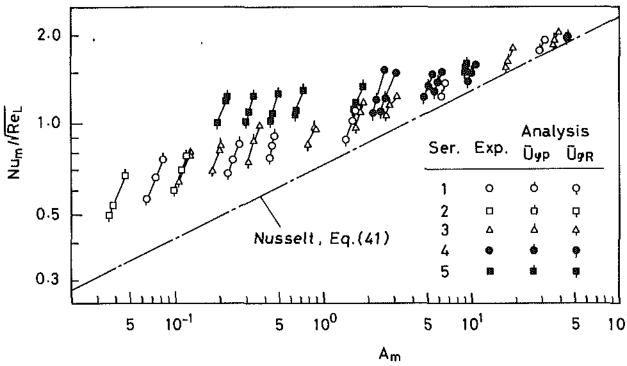

Fig. 4 Comparison between the present and experimental results for Nu_m

Characteristics of Local and Average Heat Transfers. Figures 5(*a*) and 5(*b*) compare the present result with the results for uniform wall temperature and uniform wall heat flux density, which were obtained using the present computer program, on the circumferential distributions of $\bar{q}_o$, $\bar{T}_{wo}$, and Nu for copper and titanium tubes and $\mathrm{Re}_L = 10^5$ and 3×10^6 for steam condensation. The latter solutions to be compared are those satisfying equations (35) and (36). The effect of conduction within the tube wall on $\bar{q}_o$ becomes marked as Re_L increases, particularly for the copper tube. The effect on $\bar{T}_{wo}$ appears markedly near $\varphi = \pi$ and the variations of $\bar{T}_{wo}$ and $\bar{q}_c$ are monotonic for all cases in contrast to that of $\bar{q}_o$. However, the shape of distribution of Nu is scarcely affected by the tube materials, Re_L and the thermal boundary conditions at the tube wall. The difference between the solutions of uniform wall temperature and uniform wall heat flux density in the magnitude of Nu becomes large as Re_L increases and the present result lies between them for the copper tube and is closer to the latter solution for the titanium tube. It is natural that the difference between $\bar{T}_{wo}$ and $\bar{T}_{wc}$ for the titanium tube is larger than that for the copper tube.

Figures 6(*a*) and 6(*b*) show the similar comparison for R-114 condensation on a copper tube. The effect of wall conduction is somewhat different from that of steam condensation, particularly on the distribution of $\bar{q}_o$, and the value of Nu for the present solution agrees well with that for uniform wall temperature. This fact is due to a much larger

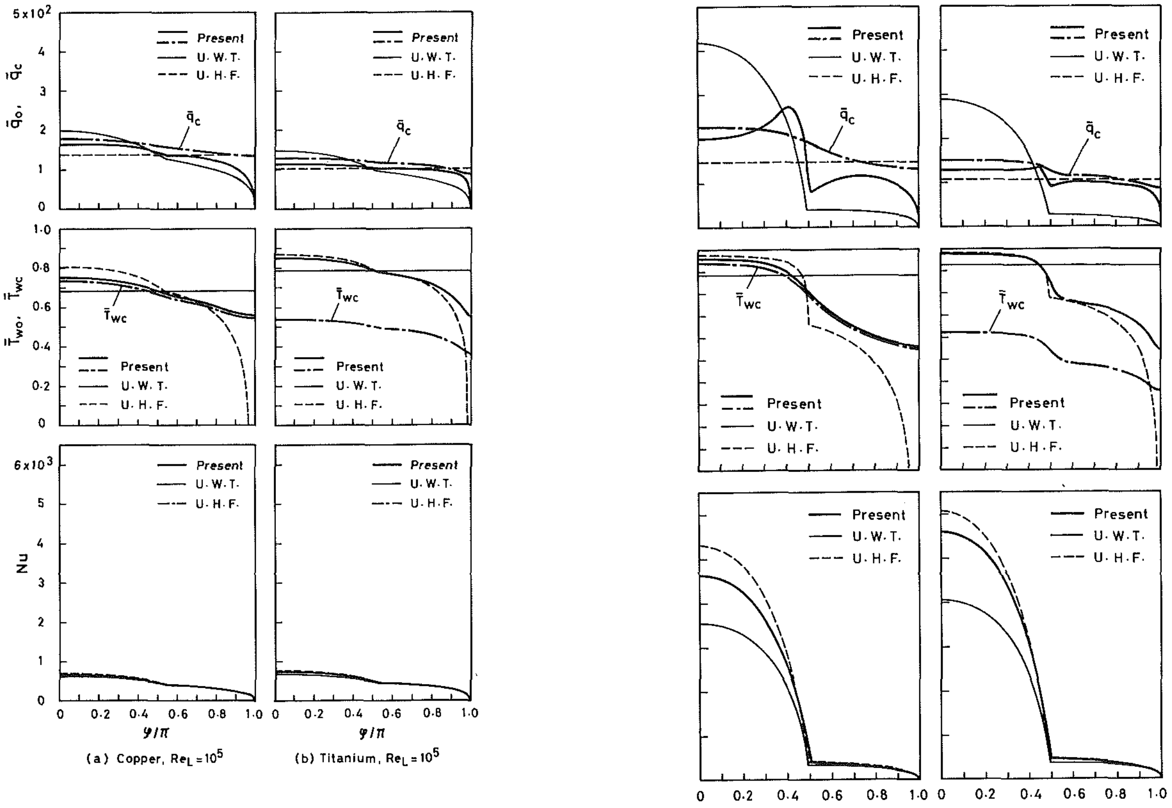

(a) Copper, $Re_L = 10^5$ (b) Titanium, $Re_L = 10^5$

(c) Copper, $Re_L = 3\times10^6$ (d) Titanium, $Re_L = 3\times10^6$

Fig. 6 Comparison of the present result with the results for uniform wall temperature and uniform wall heat flux density for $\bar{q}_o$, $\bar{T}_{wo}$, and Nu. R = 114, d_o = 19.05 mm, t = 1.245 mm, φ_o = 0, $\bar{U}_\varphi$ = $\bar{U}_{\varphi R}$, T_s = 33°C, T_c = 21°C and v_c = 2 m/s.

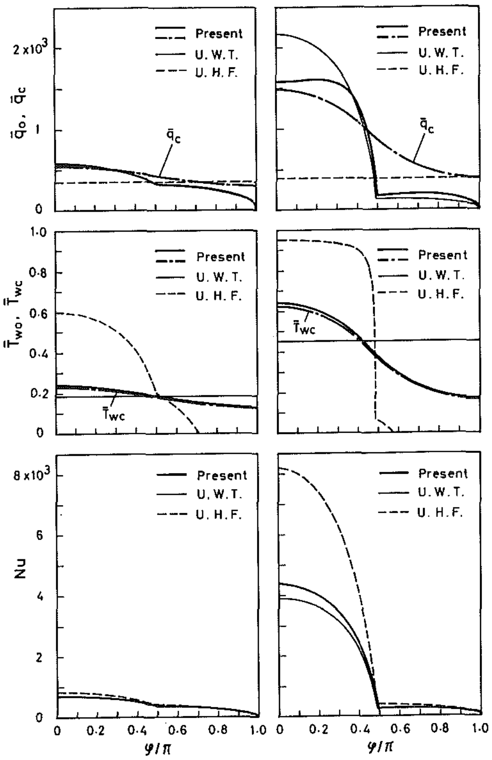

(a) Copper, $Re_L = 10^5$ (b) Copper, $Re_L = 3\times10^6$

Fig. 5 Comparison of the present result with the results for uniform wall temperature and uniform wall heat flux density for $\bar{q}_o$, $\bar{T}_{wo}$, and Nu. Steam, d_o = 19.05 mm, t = 1.245 mm, φ_o = 0, $\bar{U}_\varphi$ = $\bar{U}_{\varphi R}$, T_s = 33°C, T_c = 21°C and v_c = 2 m/s.

value in the dimensionless temperature drop across the condensate film $(1-\bar{T}_{wo})$ for R-114 in comparison with that for steam.

Figures 7(a) and 7(b) show a comparison between the downward and horizontal vapor flows on the local heat transfer characteristics for steam condensation on an aluminum brass tube. The values of Nu_m, Nu_m^*, A_m, and A_m^* are also described in the figures. It is seen that the heat transfer is not affected by the body force in the front part of the tube but only in the rear part after the separation points, and the differences between the two cases in the values of Nu_m, Nu_m^*, A_m, and A_m^* are only a few percent. However, the difference in the values of Nu_m and Nu_m^* becomes 12 percent at $A_m = A_m^* = 0.005$ when $\bar{U}_{\varphi p}$ is used for $\bar{U}_\varphi$, though they are not shown in the figures.

Figures 8(a) and 8(b) show a comparison between steam and R-114 condensation on an aluminum brass tube for the relation between $\mathrm{Nu}_m/\sqrt{\mathrm{Re}_L}$ and A_m. The thick solid and dotted lines correspond to the solutions for $\bar{U}_{\varphi R}$ and $\bar{U}_{\varphi p}$, respectively, and the chain line shows equation (41) for the Nusselt's solution. The solutions for uniform wall temperature and uniform wall heat flux density are also shown by thin lines in the figures. The value of $\mathrm{Nu}_m/\sqrt{\mathrm{Re}_L}$ for steam becomes smaller than that for R-114 with the decrease of A_m. The present solution for conjugate heat transfer agrees fairly well with the solution for uniform wall temperature for R-114 and with that for uniform wall heat flux density for steam. However, contrary to the local value of Nu shown in Figs. 5 and 6, the magnitude of $\mathrm{Nu}_m/\sqrt{\mathrm{Re}_L}$ is in the order of the solutions for uniform wall temperature, conjugate heat transfer and uniform wall heat flux density, depending on the values of T_{wom}. It is also seen that the value of $\mathrm{Nu}_m/\sqrt{\mathrm{Re}_L}$ for uniform wall temperature increases with the decrease of A_m for $A_m < 0.1$, which is due to the decrease of $(T_s - T_{wo})$ with the decrease of A_m.

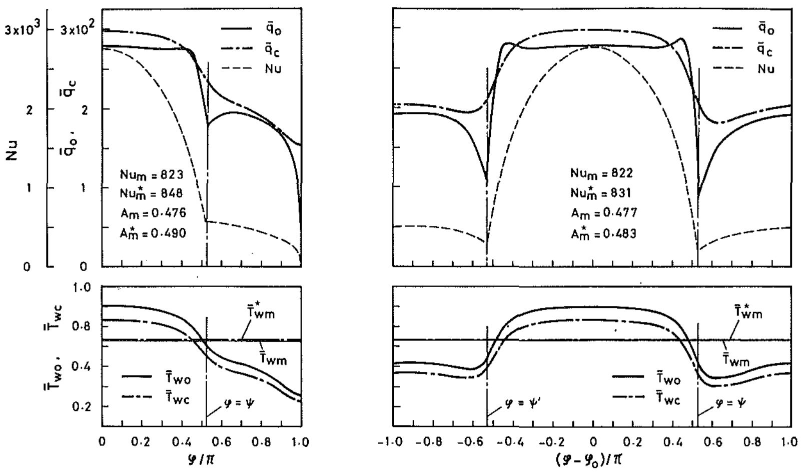

(a) $\varphi_o = 0$ (b) $\varphi_o = \pi/2$

Fig. 7 Comparison between downward and horizontal vapor flows for $\bar{q}_o$, $\bar{q}_c$, Nu, $\bar{T}_{wo}$, and $\bar{T}_{wc}$. Steam, aluminum brass, d_o = 31.75 mm, t = 1.245 mm, $Re_L = 10^6$, $\bar{U}_\varphi = \bar{U}_{\varphi R}$, T_s = 33°C, T_c = 21°C and v_c = 2 m/s.

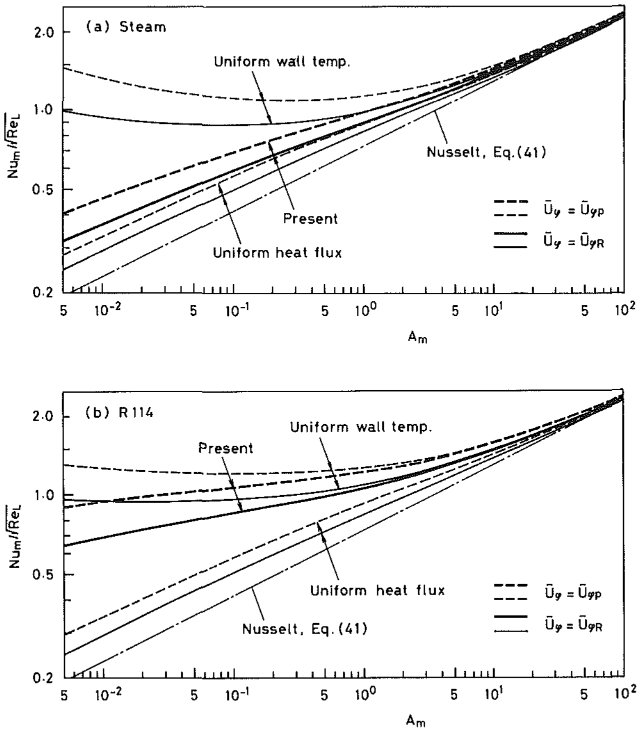

Fig. 8 Comparison between steam and R = 114 condensation for the relation of $Nu_m/\sqrt{Re_L}$ versus A_m. Aluminum brass, φ_o = 0, d_o = 19.05 mm, t = 1.245 mm, T_s = 33°C, T_c = 21 °C, and v_c = 2 m/s.

Figure 9 shows the effect of tube material on the average Nusselt number for steam and R-114 condensation. The values of $Nu_m^*/\sqrt{Re_L}$ increase with the ascending order of the thermal conductivity of tube material, i.e., titanium, aluminum brass and copper, due to the circumferential wall conduction. The difference of the value of $Nu_m/\sqrt{Re_L}$ between the copper and titanium tubes increases with the decrease of A_m^* and reaches 24 and 27 percent at $A_m^* = 0.005$ for steam and R-114, respectively. Comparison of the present solution for $\bar{U}_{\varphi R}$ in Fig. 8 and for the aluminum brass tube in Fig. 9 shows that the value of Nu_m is a few percent smaller than Nu_m^*. The order of difference is almost the same for the other cases.

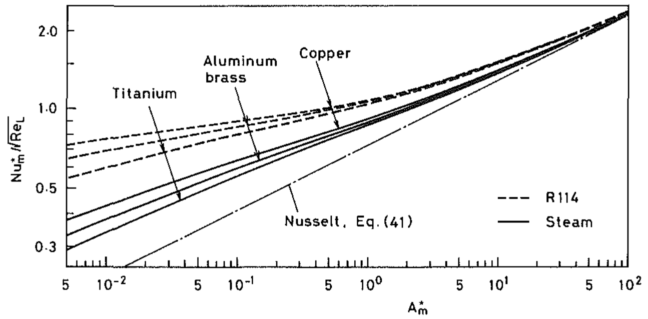

Fig. 9 Effect of tube material on average Nusselt number. d_o = 19.05 mm, t = 1.245 mm, φ_o = 0, $\bar{U}_\varphi = \bar{U}_{\varphi R}$, T_s = 33°C, T_c = 21°C, and v_c = 2 m/s.

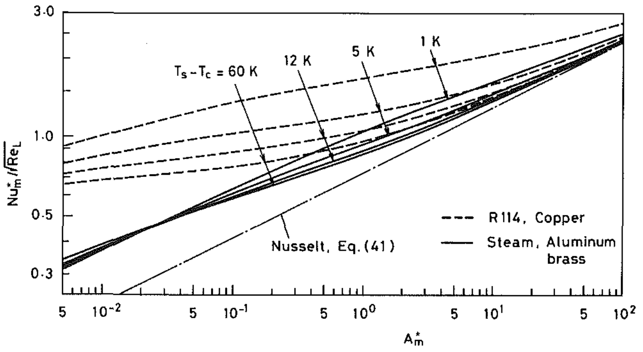

Fig. 10 Effect of overall temperature difference on average Nusselt number. d_o = 31.75 mm for aluminum brass tube and d_o = 19.05 mm for copper tube, t = 1.245 mm, φ_o = 0, $\bar{U}_\varphi = \bar{U}_{\varphi R}$, T_c = 21°C, and v_c = 2 m/s.

Figure 10 shows the effect of overall temperature difference $(T_s - T_c)$ on the average Nusselt number for steam condensation on an aluminum brass tube and for R-114 condensation on a copper tube. The effect is significant particularly for R-114, which suggests the necessity of another dimensionless parameter to correlate these data.

Conclusion

The problem of conjugate heat transfer during condensation of flowing vapor on an internally cooled horizontal tube has been numerically solved by using an iterative scheme that deals alternately with the two phase boundary layer equations and the wall conduction equation. The conclusions are as follows:

1 The comparison of the present result with the previous theoretical and experimental results shows that the present analysis is satisfactory for predicting condensation characteristics for steam and refrigerants insofar as the assumption of smooth liquid film is valid.

2 The local and average heat transfers are considerably affected by the oncoming velocity of the vapor, its mainstream velocity distribution around the tube, the physical properties of the fluid and tube, and the overall temperature difference. However, the difference between the downward and horizontal vapor flows is small for the average heat transfer.

3 The average Nusselt number Nu_m for refrigerant condensation on a tube with large thermal conductivity is a little lower than that for uniform wall temperature, while that for steam condensation on a tube with small thermal conductivity is a little higher than that for uniform wall heat flux density. The value of Nu_m is smaller than that of Nu_m^*, but the difference is not appreciable.

References

1 Gaddis, E. S., "Solution of the Two Phase Boundary-Layer Equations for Laminar Film Condensation of Vapour Flowing Perpendicular to a Horizontal Cylinder," *International Journal of Heat Mass Transfer*, Vol. 22, 1979, pp. 371-382.

2 Fujii, T., Honda, H., and Oda, K., "Condensation of Steam on a Horizontal Tube—The Influence of Oncoming Velocity and Thermal Condition at the Tube Wall," *Condensation Heat Transfer*, ASME New York, 1979, pp. 35-43.

3 Nicol, A. A., and Wallace, D. J., "Condensation with Appreciable Vapour Velocity and Variable Wall Temperature," NEL Report No. 619, 1976, pp. 27-38.

4 Nobbs, D. W., and Mayhew, Y. R., "Effect of Downward Vapour Velocity and Inundation on Condensation Rates on Horizontal Tube Banks," NEL Report No. 619, 1976, pp. 39-52; also Nobbs, D. W., "The Effect of Downward Vapour Velocity and Inundation on the Condensation Rates on Horizontal Tubes and Tube Banks," Ph.D. thesis, University of Bristol, Bristol, England, 1975.

5 Nicol, A. A., Bryce, A., and Ahmed, A. S., "Condensation of Horizontally Flowing Vapour on a Horizontal Cylinder Normal to the Vapour Stream," *Proc. 6th Int. Heat Transfer Conference*, Toronto, Vol. 2, 1978, pp. 401-406.

6 Truckenbrodt, E., "Ein einfaches Näherungsverfahren zum Berechnen der laminaren Reibungsschicht mit Absaugung," *Forschung*, Vol. 22, 1956, pp. 147-157.

7 Terril, R. M., "Laminar Boundary-Layer Flow Near Separation with and without Suction," *Trans. Roy. Soc. London*, Ser. A, Vol. 253, 1960, pp. 55-100.

8 Roshko, A., "A New Hodograph for Free-Streamline Theory," NACA TN3168, 1954.

9 Morsy, M. G., "Skin Friction and Form Pressure Loss in Tube Bank Condensers," Ph.D. thesis, University of Glasgow, Scotland, 1973.

10 Honda, H., Nozu, S., and Fujii, T., "Vapour to Coolant Heat Transfer during Condensation of Flowing Vapour on a Horizontal Tube," *Proc. 7th Int. Heat Transfer Conf.*, München, Vol. 5, 1982, pp. 77-82.

11 Nusselt, W., "Die Oberflächenkondensation des Wasserdampfes," *Zeit. Ver. Deut. Ing.*, Vol. 60, 1916, pp. 541-546; 569-575.

Boiling Heat Transfer From a Horizontal Tube in an Upward Flowing Two-Phase Crossflow

M. E. Wege
Graduate Student.

M. K. Jensen
Assistant Professor.
Member ASME

Department of Mechanical Engineering,
University of Wisconsin—Milwaukee,
Milwaukee, Wis. 53201

An experimental investigation has been performed to determine the effects of a low-quality (≤ 20 percent) upward flowing mixture on the nucleate boiling on a single horizontal tube. An electrically heated, 12.7-mm-dia tube was centered in a plane wall vertical channel, the width of which resulted in channel width-to-tube diameter ratios (w/d) of 1.16 and 1.95. The working fluid was R-113. The two-phase heat transfer data showed a variety of effects. For a fixed w/d, pressure (P), and quality (x), the average heat transfer coefficients ($\bar{h}$) increased with increasing mass velocity (G), but the effect of G decreased as the wall superheat (ΔT) increased. For a fixed w/d, G and x, $\bar{h}$ increased as the pressure increased except at low ΔT's where the reverse was found. For fixed w/d, P and G, $\bar{h}$ increased with increasing quality with the effect appearing to be more pronounced at the lower pressure. At a fixed P, G and x, $\bar{h}$ was at larger w/d ratios at small ΔT's, but as the wall superheat increased an inversion occured and $\bar{h}$ became smaller at the larger w/d ratio. The behavior exhibited in this experiment can be explained in terms of the velocity of the fluid flowing past the test section. The data were successfully predicted to within an average deviation of ±11.6 percent using a Chen-type correlation. Data from the literature also were predicted well.

Introduction

To develop more efficient heat exchanger designs and design methods for the case of boiling in the shell without resorting to extensive testing of multitube bundles of various geometries for each fluid/surface combination, detailed knowledge of the separate effects of many parameters is required. These separate effects then could be combined into a general design technique. A logical beginning to this process would be to study the building block of a multitube heat exchanger – a single tube – which is subjected to conditions that could be found in heat exchangers with boiling in their shells; i.e., a two-phase crossflow over a single horizontal tube.

Various pool boiling and forced convective boiling heat transfer studies indicate that the flow of a single-phase or a two-phase mixture over a horizontal tube or a horizontal array of tubes will produce a significantly higher heat transfer coefficient than that obtained during saturated pool boiling at the same wall superheat. In several pool boiling studies, e.g., [1-4], with limited numbers of tubes in arrays, vapor rising from the lower tubes induced circulation and turbulence around the upper tubes, which resulted in higher heat transfer coefficients, with the effect being most pronounced at lower wall superheats. The effect decreased with increasing heat flux.

In studies on large, multitube kettle reboiler bundles [5-9], the more recent work on both average and local heat transfer characteristics indicates that there is a substantial recirculatory flow in the shell resulting in a forced convective flow over much of the tube bundle. This flow of a vapor-liquid mixture causes a large increase in the heat transfer coefficient compared to pool boiling. The coefficients increased with increasing height in the bundle. However, the effect of geometry and the effect of the forced convection are not separable, nor are the local conditions accurately known.

Straight-through forced convective flow through arrays of tubes also have been studied [10, 11] and have indicated that they have basically the same characteristics as found in the kettle reboilers. Nakajima [10] concluded that vaporization of the thin film on the outside of the tube is an important factor in the increase in the heat transfer coefficient in the upper sections of a bundle.

Cornwell et al. [8, 9] suggest that a correlation [12] developed for low quality flow boiling is applicable to flow in geometries such as tube bundles. However, there appears to be a quite large overprediction using this method when applied to reboiler data. Brisbane et al. [13], in attempting to develop a prediction method for a kettle reboiler, conclude that a method of calculating the local heat transfer coefficient is essential to understanding the heat transfer behavior.

Various investigations, e.g., [14-16], have examined the effect of a crossflow of a subcooled or saturated liquid over a single horizontal tube. From the most recent investigation [16], at a given wall superheat, the heat flux in the nucleate, transition, and film boiling regions was shown to increase with increasing velocity. The only study [17] with a two-phase mixture (x < 5 percent) in crossflow over a single tube indicates a significant increase in the heat transfer coefficient with increasing quality at a constant mass velocity. A 15-mm tube was centered in a 25-mm channel and vapor was injected 100 mm below the tube centerline. It is possible that because of the manner and location of the vapor injection, the data are not truly representative of two-phase crossflow boiling. No correlation of the data was presented.

Because of the lack of data and of a prediction method for a single horizontal tube in a two-phase crossflow, which could be used to help predict the heat transfer behavior in kettle reboilers or in straight-through heat exchangers, the present experimental investigation was undertaken.

Experimental Apparatus

To accomplish the objective set forth in the preceding section, a test section was designed for insertion into a closed flow loop that uses refrigerant R-113 as the working fluid. The fluid flow rate to the test section was controlled by a combination of changing the pump speed and bypassing fluid around the test section. Inlet fluid conditions were set by adjusting the steam flow to a steam/R-113 heat exchanger and

---

Contributed by the Heat Transfer Division for publication in the JOURNAL OF HEAT TRANSFER. Manuscript received by the Heat Transfer Division June 2, 1983.

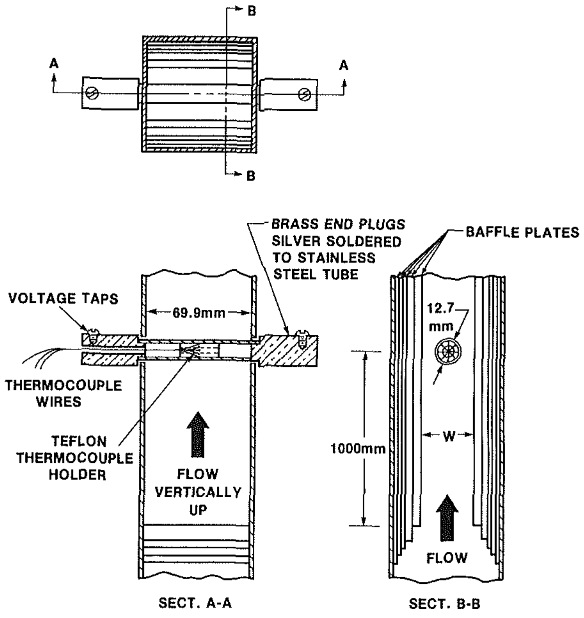

Fig. 1 Test section schematic

by adjusting the power to variable-power electric preheaters. Test-section pressure was controlled with valves located just downstream of the test section. Valves just upstream of the test section were used to keep a high pressure in the preheaters so that when a large pressure drop was taken across those valves the liquid would flash into a liquid/vapor mixture. A four-thermocouple thermopile was located just upstream of these flashing valves to measure the liquid temperature prior to flashing. After passing through the test section, the two-phase mixture passes through pressure control valves and a water-cooled condenser; the liquid R-113 then flows through one of three calibrated rotameters.

The test section was comprised of two main components: the heated tube and the duct in which it was positioned (see Fig. 1). The heated portion of the 321 stainless steel tube was 12.7 mm in diameter and 69.9 mm long; the wall thickness was 0.254 mm. Brass end-plugs, silver-soldered to the tube, conducted electrical power to the test section and served both as supports for positioning the tube in the duct and as a hydraulic sealing surface. Voltage taps were located on the end-plugs. Through one end-plug, a hole was drilled to allow access for the copper-constantan thermocouples on the inner wall.

Eight thermocouples were located circumferentially at 45 deg intervals around the inside of the tube at the midpoint of the heated length. They were held tightly against the inside of the tube wall by a cylindrical Teflon holder; the thermocouple beads were electrically insulated from the test section itself with a thin coating of epoxy.

The tube was centered horizontally in a 70-mm-sq duct and held there securely with electrically insulating packing glands. The flow channel width was varied by the addition or removal of baffle plates, which were secured to the duct wall such that the test section was always centered in the rectangular flow channel. The channel length, from a somewhat contoured entrance to the test-section centerline, was approximately 1000 mm. The channel width was varied such that channel width-to-tube diameter ratios of 1.16 and 1.95 were obtained. A pressure tap was located about 150 mm above the test section.

A high accuracy (± 0.69 kPa) pressure gauge was used to measure the test-section pressure. A thermocouple located near the pressure tap was used to measure the fluid temperature at that point and served as a check on the saturation temperature obtained from the pressure measurement. Direct-current power was supplied by a low ripple ($<$ 1 percent) power supply. Test-section current was obtained from a calibrated shunt. Test section voltage drop, shunt voltage, and all thermocouple voltages were measured using a high accuracy ($\pm$ 1 μv) digital voltmeter.

Experimental Procedure

To ensure the accuracy of the data, the R-113 was thoroughly degassed prior to any testing. This degassing was accomplished by boiling the refrigerant in a storage/degassing tank for several hours after any refrigerant was added to the system. The R-113 vapor was condensed in a water-cooled condenser and returned to the tank while liberated gases were vented to the atmosphere. After degassing, the tank was sealed to prevent any air from going back into solution. At this point the experiment was ready to begin.

The flow rate to the test-section was set at predetermined levels by adjusting the pump speed and the bypass valves. The back pressure held on the preheaters was fixed by setting the flashing valves, and the test-section pressure was then maintained by adjusting the valves downstream of the test section. Both the test-section flow rate and pressure were steady. The test-section quality was determined by an enthalpy balance across the flashing valves. The temperature of the liquid R-113 upstream of these valves was changed by varying power and/or steam to the preheaters. This temperature was fixed such that a specified test-section quality would be obtained when the pressure of the liquid R-113 was reduced to the test-section pressure. Specified heat fluxes were set by adjusting the voltage drop across the test section.

Before any data were taken once the flow conditions were set, the flow loop was allowed to come to steady state; this took approximately 1 hr. The heat flux was then set, the test section (which has a much smaller thermal capacitance than

Nomenclature

d = tube diameter (mm)
F = effective two-phase Reynolds number factor
g = gravitational acceleration (m/s^2)
G = mass velocity based on minimum flow area (kg/m^{2}s)
h = local heat transfer coefficient (W/m^{2}K)
$\bar{h}$ = average heat transfer coefficient (W/m^{2}K)
h_{conv} = heat transfer coefficient from convective flow only, $h_l F$ (W/m^{2}K)
h_{fg} = enthalpy of vaporization (J/kg)
k = thermal conductivity (W/mK)
n = Reynolds number exponent
P = pressure (kPa)
Pr = Prandtl number
q'' = heat flux (W/m^2)
S = suppression factor (equation (2))
ΔT = wall superheat (K)
V = velocity (m/s)
w = pitch or channel width (mm)
X = Martinelli parameter (equation (4))
X_0 = bubble growth region (equation (3))
x = quality
ρ = density (kg/m^3)
μ = dynamic viscosity (kg/ms)
σ = surface tension (N/m)

Subscripts

l = liquid
nb = nucleate pool boiling
v = vapor

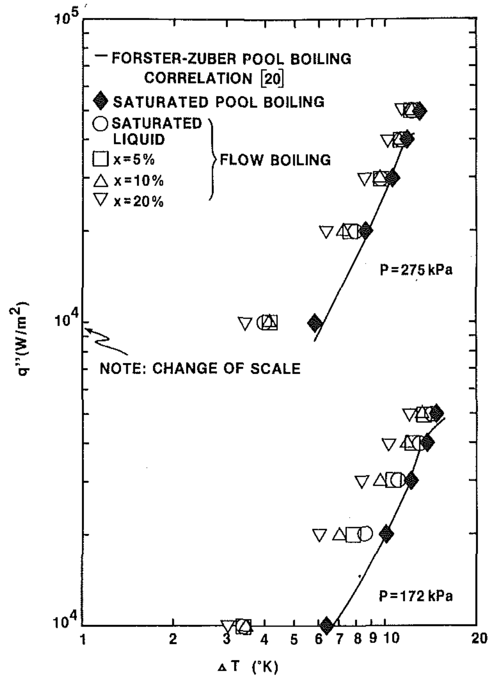

Fig. 2 Effect of quality on the boiling curve

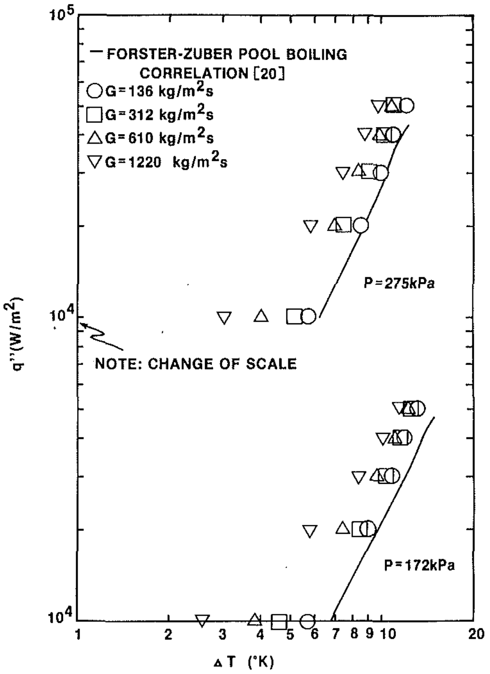

Fig. 3 Effect of mass velocity on boiling curve

the loop) allowed to come to thermal equilibrium (about 5 min), and all data were then taken; this procedure continued until data at all heat fluxes were obtained. Flow conditions were then changed to the next desired set point, and the complete procedure was repeated. In order to prevent boiling hysteresis, the test section power initially was increased slowly to the highest heat flux. Then all data were taken at decreasing heat flux levels. Local heat transfer coefficients were calculated by using an average heat flux over the heated surface area, the R-113 saturation temperature, and the local outside wall temperatures. Average heat transfer coefficients were obtained by averaging the local heat transfer coefficients. The outside wall temperatures were obtained by solving the cylindrical heat conduction equation assuming constant thermophysical properties and using the measured inside wall temperature and heat generation rate. Circumferential conduction was assumed to be negligible because of the thin tube wall, low metal thermal conductivity, and high heat transfer coefficient.

The nominal ranges of experimental conditions covered in this study are as follows:

heat flux	10,000 to 50,000 W/m^2
quality	0–20 percent
pressure	172 and 275 kPa
mass velocity	70–1200 kg/m^{2}s
pitch-to-diameter ratio	1.16 and 1.95
single-phase Reynolds Numbers	2900–39,000

The maximum test section quality obtainable decreased as mass velocity, the w/d ratio, and pressure increased. Thus, limited data were obtained at the highest w/d ratio and mass velocities. In addition, single-phase forced convection data and pool boiling data were taken. In all, approximately 290 two-phase forced convective average heat transfer coefficients were obtained. Uncertainties in the experimental data, as estimated through a propagation-of-error analysis, are estimated to be: P, ± 1.5 kPa; G, ±2 percent; x, ±6 percent; q'', ±1 percent; h, ±6 percent. Only typical data are presented in the figures. Details of the experimental apparatus and procedure and complete data tables can be found in [18].

Results and Discussion

Single-phase heat transfer coefficients were obtained at the two w/d ratios over a range of Reynolds numbers (based on gap mass velocity and tube diameter) from about 2900 to 39,000. At low mass velocity there was a tendency for the data to deviate from a linear behavior, perhaps due to a transition from laminar to turbulent flow in the duct. Various single-phase heat transfer correlations are available for single tubes in essentially infinite flow fields. However, because of significant duct blockage caused by the heated tube, it was felt that a correlation which describes the heat transfer from a tube in a multitube bundle would be a better model of the present geometry. Thus, using a correlation for the first tube row in an inline tube bundle (as presented in [19]), the present data could be predicted with an average deviation of ±14.0 percent. This is relatively good agreement considering the different geometry, in particular, the solid walls enclosing the tube in this experiment.

Pool boiling data (shown on Fig. 2) at 172 and 275 kPa were obtained in the duct with all baffles removed and a slightly subcooled ($<$ 1 K) flow velocity of less than 1 cm/s ($G < 10$kg/m^{2}s). For prediction of the heat transfer coefficient for a variety of conditions, a correlating equation is required. Therefore, two correlations from the literature (Forster-Zuber [20] and Stephen-Abdelsalam [21]) were used to predict the pool boiling data. The best fit of the test data from the present surface-fluid combination was achieved using the Forster-Zuber [20] correlation. This correlation (evaluated at the experimental wall superheats) predicted all of the nucleate pool boiling heat transfer coefficient data with an average deviation of ±7.2 percent.

Although the flow regimes in the duct were not observed, they can be predicted approximately by the flow regime maps of Taitel and Dukler [22]. (Hosler [23] has reported that the flow patterns in rectangular and circular channels are similar.) From these flow regime maps, it was determined that the flow was in the bubbly/slug transition regime for the lowest mass velocity/lowest quality combination and shifted toward the churn regime as the mass velocity and quality increased. The majority of the conditions were in the slug flow regime.

As shown in Figs. 2-6, the two-phase flow heat transfer data show a variety of effects, depending upon the combination of mass velocity, quality, pressure, and w/d ratio. All of the average two-phase heat transfer data appear to be

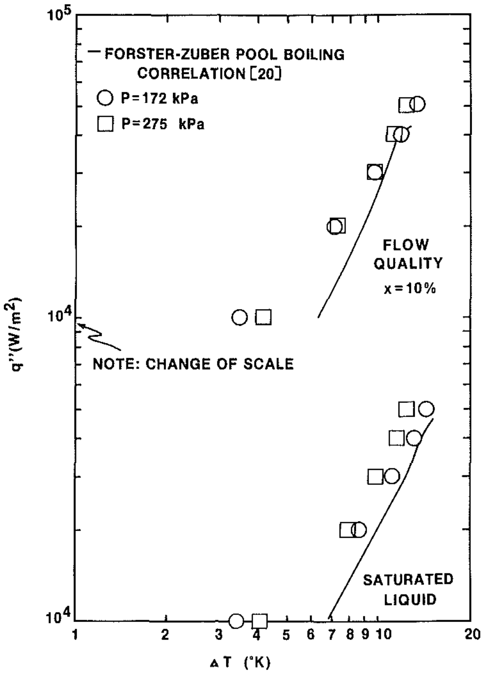

Fig. 4 Effect of pressure on boiling curve

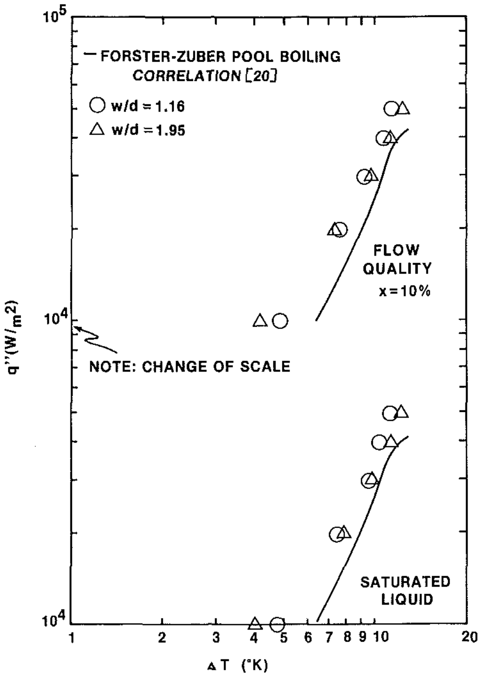

Fig. 5 Effect of *w/d* ratio on the boiling curve

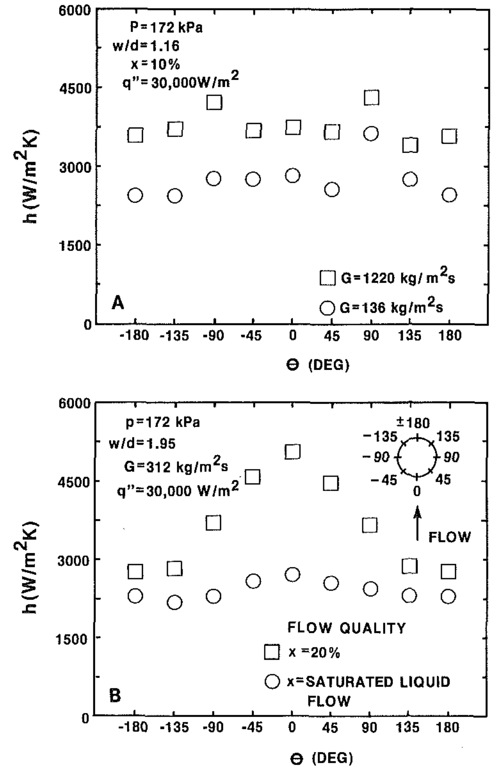

Fig. 6 Circumferential distribution of heat transfer coefficients: (a) variation with mass velocity; (b) variation with quality

consistent with crossflow single-phase and saturated liquid flow boiling experience in that the convective heat transfer coefficient increases with increasing velocity. In addition, the behavior is similar to forced convective boiling in straight tubes with h increasing with increasing quality at fixed other conditions. In the discussion to follow, the effect of the five main parameters (P, w/d, G, x, q'', or ΔT) on the average heat transfer coefficient, $\bar{h}$ qualitatively will be related to the fluid velocity flowing past the tube. (The fluid velocity can be obtained from $V=G/\rho$, where ρ is the effective two-phase density. At fixed G, a decreasing pressure or an increasing quality will cause the fluid velocity to increase.) Unless otherwise stated, *the effect of one or two parameters on* $\bar{h}$ *will* be discussed assuming that all the other parameters remain fixed.

An increasing quality increases the average heat transfer coefficient $\bar{h}$; this parameter seems to have more effect at lower pressures (see Fig. 2). For fixed flow conditions, increasing the quality decreases the mixture density; thus, to maintain a constant G, the fluid velocity must increase. Decreasing the pressure lowers the density even more, necessitating a corresponding increase in velocity with a result increase in $\bar{h}$.

The average heat transfer coefficient also increases with increasing G (see Fig. 3). The effect of mass velocity decreases as the wall superheat increases. Thus, at high wall superheats, all of the curves tend to approach the fully developed nucleate boiling curve. This is consistent with in-tube forced convective boiling. For fixed flow conditions, changes in G are directly proportional to an increased fluid velocity.

As opposed to the monotonic effects of G and x exhibited on Figs. 2 and 3, the effects of pressure and w/d ratio on the boiling curve exhibit reversals as shown in Figs. 4 and 5. This reversal was present in the other data sets. The crossover point of these curves shifts downward to lower wall superheats as quality decreases. At moderate to high wall superheats, an increasing pressure increases $\bar{h}$, which is consistent with pool boiling (see Fig. 4). However, at low wall superheats, an increase in pressure decreases $\bar{h}$. Thus, comparing this behavior to the data on Fig. 3, there appears to be a trade-off between an increase in $\bar{h}$ due to increasing pressure (as in pool boiling) and a decrease in $\bar{h}$ due to the decreased flow velocity caused by the increased fluid density which accompanies the increase in pressure. It seems that the pressure effects dominate at higher wall superheats, while the velocity effects dominate at the lower wall superheats. An explanation as to what occurs with the two-phase and saturated liquid flows will be given below.

The w/d ratio exhibits a similar behavior with respect to wall superheat (see Fig. 5). As w/d increases at small wall superheats, $\bar{h}$ increases; but at higher wall superheats, $\bar{h}$ decreases as w/d increases. The interaction among pressure, quality, w/d ratio, and wall superheat, as shown by the trends of the data in Figs. 4 and 5, can be explained in terms of the approach velocity of the fluid and the thickness of an assumed "bubble boundary layer" around the heated tube.

Although the exact flow behavior is unknown, suppose that a "bubble boundary layer" grows on the heated tube and that the thickness of this boundary layer is proportional to the amount of vapor generated. Also assume that this boundary layer effectively decreases the flow area in the gap, thus causing an "effective velocity" in the gap to be larger than the mean velocity. At a fixed pressure, the boundary layer would thicken with increasing wall superheat because of more vapor generation; at a fixed wall superheat, the boundary layer would thicken with decreasing pressure because of decreased vapor density. At a fixed mass velocity (based on minimum flow area), $\bar{h}$ increases as w/d increases at low wall superheats because the approach velocity in the duct increases. However, at higher wall superheats, $\bar{h}$ decreases as w/d increases. This behavior can be explained in the following way. As w/d becomes small and the wall superheat becomes large, the thickness of the bubble boundary layer would begin to have more and more effect on increasing the fluid velocity in the gap whether it was a saturated liquid or a two-phase flow. (Note that at $w/d = 1.16$, the distance between the duct wall and the tube wall is 1.08 mm; for $w/d = 1.95$, the distance is 6.03 mm.) Thus there could be a strong geometry-vaporization rate interaction that would affect the heat transfer coefficient.

The trends in the circumferential heat transfer coefficient distribution depend greatly on the combination of flow conditions (see Fig. 6). While there was some scatter in the data, there was some generally consistent behavior. Three definite patterns in the data were observed: the heat transfer coefficient either was highest at the ±90 deg locations, highest at 0 deg, or was relatively constant over the complete circumference. The channel width-to-tube diameter ratio also affected the heat transfer coefficients. It appears that as the fluid velocity in the gap increases, the peak heat transfer coefficients shifts from 0 deg to ±90 deg, with some combination of conditions resulting in a relatively constant heat transfer coefficient between these two other conditions.

Two other observations should be noted. For some combinations of conditions, the tube wall temperatures at 0 deg and ±45 deg fluctuated approximately 1-2K with a period in the order of 0.25 to 0.50 s. This may be caused by alternating slugs of liquid and vapor washing over the tube, thus affecting the heat transfer. This behavior would be consistent with the fluid being in the slug flow regime as stated above. The second observation concerns a burnout point. An attempt was made to obtain heat transfer data at higher heat fluxes. However, the accidential burnout of a test section as the loop was coming to steady state indicated that the critical heat flux (CHF) condition is significantly below the pool boiling value. Thus only heat fluxes less than or equal to 50,000 W/m^2 were tested thereafter. The conditions at this one burnout point were approximately: $P \simeq 275$ kPa; $G \simeq 312$ kg/m^{2}s; $x \simeq 10$ percent; $w/d = 1.16$; and $q'' \simeq 80{,}000$ W/m^2. The Zuber correlation [24], as modified by Lienhard and Dhir [25], for saturated pool boiling predicts a critical heat flux of about 240,000 W/m^2. The CHF in subcooled and saturated crossflow is greater than the pool boiling value (e.g., [26]). Why the present datum point was so low is unknown, but it may have been caused by the small gap.

Correlation of Data

The actual mechanism controlling the magnitude of the heat transfer coefficients has been suggested to be the evaporation of a thin film covering the heater surface beneath the growing bubble (see, for instance, [10, 11, 27, 28]). For engineering purposes, the proposed methods are not suitable. Using the Chen correlation [29], as developed for in-tube forced convective boiling, with the suppression factor developed by Bennett et al. [30], Chen's empirically determined F-factor as presented in correlation form in [31], and Grimison's [19] single-phase heat transfer correlation for crossflow (with the Reynolds Number evaluated as if the liquid only was flowing across the tube) the convective boiling data could be predicted with an average deviation of ±18.3 percent. The Chen correlation should not be expected to fit the data well, since the effective two-phase Reynolds number factor F is based on the ratio of the two-phase pressure gradient to the liquid-only pressure gradient in a straight tube. The present geometry with flow over a bluff body is considerably different than in-tube with different characteristics. However, the form of the Chen correlation (equation (1))

$$h = h_l F + h_{nb} S \tag{1}$$

used to predict two-phase heat transfer coefficients is entirely appropriate if the F-factor is developed for the specific geometry.

The S-factor represents the suppression of the nucleate boiling contribution. This is dependent on the convective heat transfer coefficient, the liquid thermal conductivity, and the size of the bubble growth region [30]. The expression for S developed by Bennett et al. (equation (2)) for both in-tube and shell side thin-film (crossflow) forced convective boiling takes into account the geometry influence implicitly in the convective coefficient.

$$S = \frac{k_l}{h_{\text{conv}} X_o}\left[1 - e^{-\left(\frac{h_{\text{conv}} X_o}{k_l}\right)}\right] \tag{2}$$

where

$$X_o = 0.041\left[\frac{\sigma}{g(\rho_l - \rho_v)}\right]^{1/2} \tag{3}$$

Thus, for the present geometry, only an appropriate F-factor needs to be developed.

Bennett and Chen [32] developed an expression for the F-factor for in-tube boiling and also applied it to thin-film evaporation [30]. This factor, obtained by applying the Reynolds' analogy to two-phase flow, is composed of a Prandtl number expression multiplied times a pressure gradient ratio. Both terms are taken to the power $n/(n+1)$, where the exponent n represents the Reynolds number exponent in an in-tube, single-phase heat transfer coefficient correlation, its value being 0.8. For single-phase flow across the tube banks $n \simeq 0.6$; this value will be used in the present correlation. By analogy to the in-tube experience, the pressure gradient ratio was fit to a function involving the Martinelli parameter

$$X = \left(\frac{1-x}{x}\right)^{0.9}\left(\frac{\rho_v}{\rho_l}\right)^{0.5}\left(\frac{\mu_l}{\mu_v}\right)^{0.1} \tag{4}$$

An additional term to account for the geometry-vaporization rate interaction will be included in the F-factor, since it affects the velocity as discussed above. A dimensionless group that seems appropriate to describe the geometry effect is the channel width-to-tube diameter ratio w/d. Following a procedure similar to that used by Chen to develop the empirical F-factor for in-tube boiling, empirical F-factors for crossflow boiling were calculated and then fitted, using a nonlinear regression program, to the following equation

$$F = [1 + (0.0684 + 0.384w/d)(1/X)^{-0.419+0.519w/d}]\left[\frac{\text{Pr}_l + 1}{2}\right]^{0.375} \tag{5}$$

For the data obtained, the Martinelli parameter covered the range $0.25 < X < 5$. Using this F-factor (equation (5)), the S-factor described by equation (2), the Forster-Zuber correlation [20] for the pool boiling, and the single-phase heat

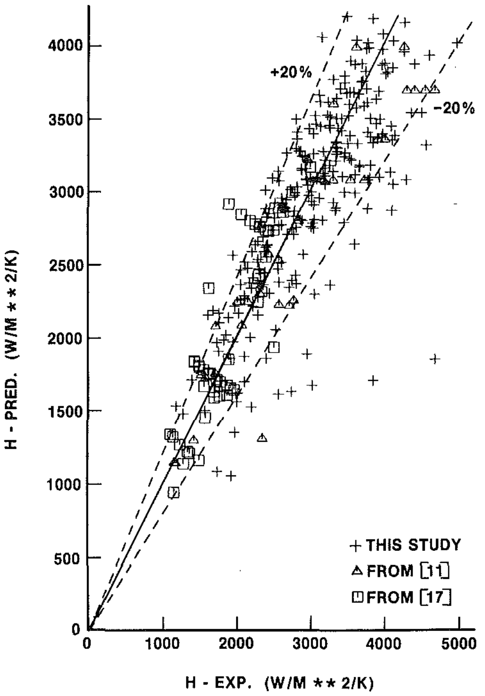

Fig. 7 Comparison of the present data to predictions using equations (1), (2), and (5)

transfer tube bundle correlation [19] by Grimison, the average heat transfer coefficients were predicted at the same wall superheat as the experimental data using equation (1) with an average deviation of ±11.6 percent; 85 percent of the data were predicted to within ±20 percent, and 96 percent were within ±30 percent (see Fig. 7). The data, which are shown to be considerably underpredicted on Fig. 7, generally are for saturated flows at the lowest heat flux.

Data from two other papers [11, 17] were also predicted. The data from [11] were for R-113 at one bar and were taken in the sixth row of a tube bundle with $w/d = 1.24$. Fluid conditions ranged from saturated liquid to a quality of about 2 percent and mass velocity ranged from 95 kg/m^2s to 440 kg/m^2s. A correlation [33] that can predict the single-phase heat transfer coefficient in the sixth row of a tube bundle was used in place of the one used above. The 33 data points were predicted with an average deviation of ±21.2 percent. However, when the pool boiling correlation given in their paper is used in place of the Forster-Zuber correlation, the data are predicted with an average deviation of ±11.1 percent.

Bitter's [17] data were for R-11 at about one atmosphere and were taken on a single tube in a plane wall channel with $w/d = 1.67$. Fluid conditions ranged from saturated liquid to a quality of about 5 percent. Mass velocities from 55.5 to 1360 kg/m^2s were used. The 57 data points were predicted with an average deviation of ±19.2 percent. Eleven points were predicted with a deviation greater than ±30 percent. However, eight of these points were from the same data set (55.5 kg/m^2s, 2600 W/m^2, various qualities) and all were consistently underpredicted by over 35 percent; if these data are eliminated then the average deviation on the remaining 49 points is ±14.0 percent. Further improvement in this prediction might also have been made if Bitter would have presented some pool boiling data so that the best pool boiling correlation to fit the data from his fluid/surface combination could have been used in the prediction.

For all 372 points from the three studies, the average deviation between the prediction and the experimental data is ±11.9 percent, with 84.1 percent of the data predicted to within ±20 percent and 95.4 percent within ±30 percent.

Conclusions

An experimental investigation has been performed on two-phase crossflow boiling heat transfer on a single horizontal tube. Data on the behavior of local and average heat transfer coefficients have been reported for a variety of fluid conditions and geometries. The following conclusions can be drawn from this study:

1 A flow of a two-phase mixture over a horizontal tube can significantly increase the heat transfer coefficient compared to saturated pool boiling or to saturated flow boiling.

2 The heat transfer behavior for various combinations of geometry and fluid flow conditions can be explained in terms of the fluid velocity past the test section.

3 The standard Chen *F*-factor correlation developed for axial flow appears not to be applicable to crossflow over a horizontal tube.

4 A Chen-type correlation has been modified so that it describes well the trends of the data from three studies that cover two fluids, four *w/d* ratios, single tubes, and a tube located in a multitube bundle. However, additional work must be done to confirm the accuracy of the proposed correlation, especially with regard to multitube heat exchangers, over a wider range of pressures, flow conditions, and fluids.

Acknowledgments

This work as supported in part by the Graduate School at the University of Wisconsin – Milwaukee.

References

1 Robinson, D. B., and Katz, D. L., "Effect of Vapor Agitation on Boiling Coefficients," *Chemical Engineering Progress*, Vol. 47, 1951, pp. 317-324.

2 Myers, J. E., and Katz, D. L., "Boiling Coefficients Outside Horizontal Tubes," *Chemical Engineering Progress Symposium Series*, Vol. 49, No. 5, 1953, pp. 107-114.

3 Wall, K. W., and Park, E. L., Jr., "Nucleate Boiling of N-Pentane, N-Hexane and Several Mixtures of the Two From Various Tube Arrays," *International Journal of Heat and Mass Transfer*, Vol. 21, 1978, pp. 73-75.

4 Wallner, R., "Boiling Heat Transfer in Flooded Shell and Tube Evaporators," *Proceedings of the 13th International Congress of Refrigeration*, 1971, Paper 2.19, pp. 185-191.

5 Palen, J. W., and Taborek, J. J., "Refinery Kettle Reboilers—Proposed Method for Design and Optimization," Vol. 58, No. 7, 1962, pp. 37-46.

6 Palen, J. W., and Small, W. M., "New Way to Design Kettle and Internal Reboilers," *Hydrocarbon Processing*, Vol. 43, No. 11, 1963, pp. 199-208.

7 Palen, J. W., Yarden, A., and Taborek, J., "Characteristics of Boiling Outside Large-Scale Horizontal Multitube Bundles," *AIChE Symposium Series*, Vol. 68, No. 118, 1972, pp. 50-61.

8 Leong, L. S., and Cornwell, K., "Heat Transfer Coefficients in a Reboiler Tube Bundle," *Chemical Engineer*, No. 343, 1979, pp. 219-221.

9 Cornwell, K., Duffin, N. W., and Schuller, R. B., "An Experimental Study of the Effects of Fluid Flow on Boiling Within a Kettle Reboiler Tube Bundle," ASME Paper No. 80-HT-45, 1980.

10 Nakajima, K. I., "Boiling Heat Transfer Outside Horizontal Multitube Bundles," *Heat Transfer—Japanese Research*, Vol. 7, No. 2, 1979, pp. 1-24.

11 Polley, G. T., Ralston, T., and Grant, I. D. R., "Forced Crossflow Boiling in an Ideal In-Line Tube Bundle," ASME Paper No. 80-HT-46, 1980.

12 Cornwell, K., and Leong, L. S., "On the Analysis of Low Quality Flow Boiling," *International Journal of Heat and Fluid Flow*, Vol. 1, No. 1, 1979, pp. 63-69.

13 Brisbane, T. W. C., and Grant, I. D. R., "A Prediction Method for Kettle Reboiler Performance," ASME paper No. 80-HT-42, 1980.

14 Vliet, G. C., and Leppart, G., "Critical Heat Flux for Nearly Saturated Water Flowing Normal to a Cylinder," ASME JOURNAL OF HEAT TRANSFER, Vol. 86, 1964, pp. 59-67.

15 Fand, R. M., Keswani, K. K., Jotwani, M. M., and Ho, R. C. C., "Simultaneous Boiling and Forced Convection Heat Transfer From a Horizontal Cylinder to Water," ASME JOURNAL OF HEAT TRANSFER, Vol. 98, 1976, pp. 395-400.

16 Yilmaz, S., and Westwater, J. W., "Effect of Velocity on Heat Transfer to Boiling Freon-113," ASME paper No. 79-WA/HT-35, 1979.

17 Bitter, R. C., "Heat Transfer from a Horizontal Tube with Transverse Flow of Evaporating Saturated R-11," *International Institute of Refrigeration Bulletin*, Annexe 1972, pp. 97-107.

18 Wege, M. E., "Boiling Heat Transfer from a Horizontal Tube in an

Upward Flowing Two-Phase Crossflow," M.S. thesis, Department of Mechanical Engineering, University of Wisconsin – Milwaukee, 1983.

19 Incropera, F. P., and DeWitt, D. P., *Fundamentals of Heat Transfer*, John Wiley and Sons, New York, 1981, p. 355.

20 Forster, H. K., and Zuber, N., "Dynamics of Vapor Bubbles and Boiling Heat Transfer," *AIChE Journal*, Vol. 1, 1955, pp. 531–535.

21 Stephan, K., and Abdelsalam, M., "Heat Transfer Correlations for Natural Convection Boiling," *International Journal of Heat and Mass Transfer*, Vol. 23, 1980, pp. 73–87.

22 Bergles, A. E., Collier, J. G., Delhaye, J. M., Hewitt, G. F., and Mayinger, F., *Two-Phase Flow and Heat Transfer in the Power and Process Industries*, Hemisphere Publishing Corporation, Washington, D.C., 1981, pp. 14–15.

23 Hosler, E. R., "Flow Patterns in High Pressure Two-Phase (Steam-Water) Flow with Heat Addition," Paper presented at 9th Nat. U.S. Heat Transfer Conference, Seattle, AIChE preprint, No. 22, Aug. 1967.

24 Zuber, N., "On Stability of Boiling Heat Transfer," *Transaction ASME*, Vol. 80, 1958, pp. 711–720.

25 Lienhard, J. H., and Dhir, V. K., "Hydrodynamic Prediction of Peak Pool Boiling Heat Fluxes from Finite Bodies," ASME JOURNAL OF HEAT TRANSFER. Vol. 95, pp. 152–158, 1973.

26 Hasan, M. Z., Hasan, M. M., Eichhorn, R., and Lienhard, J. H., "Boiling Burnout During Crossflow Over Cylinders, Beyond the Influence of Gravity," ASME JOURNAL OF HEAT TRANSFER, Vol. 103, 1981, pp. 478–484.

27 Cornwell, K., and Schuller, R. B., "A Study of Boiling Outside a Tube Bundle Using High Speed Photography," *International Journal of Heat and Mass Transfer*, Vol. 25, 1982, pp. 683–690.

28 Niels, G. H., "Some Boiling Aspects in Kettle Evaporators," *Boiling Phenomena*, edited by S. Van Stralen and R. Cole, Hemisphere Publishing Corporation, Washington D.C., 1979, pp. 937–945.

29 Chen, J. C., "Correlation for Boiling Heat Transfer to Saturated Fluids in Convective Flow," *I and EC Process Design and Development*, Vol. 5, 1966, pp. 322–329.

30 Bennett, D. L., Davis, M. W., and Hertzler, B. L., "The Suppression of Saturated Nucleate Boiling by Forced Convective Flow," *AIChE Symposium Series, No. 199*, Vol. 76, 1980, pp. 91–103.

31 Bergles, A. E., et al., *Two-Phase Flow and Heat Transfer in the Power and Process Industries*, Op Cit., p. 250.

32 Bennett, D. L., and Chen, J. C., "Forced Convective Boiling in Vertical Tubes for Saturated Pure Components and Binary Mixtures," *AIChE Journal*, Vol. 23, 1980, pp. 454–461.

33 ESDU, "Convective Heat Transfer During Crossflow of Fluids Over Plain Tube Banks," Item No. 73031, 1973, Engineering Sciences Data Unit, London.

ERRATA

Corrections to Author's Closure to a Discussion of "Design and Optimization of Air-Cooled Heat Exchangers," by C. P. Hedderich, M. D. Kelleher, and G. N. Vanderploats published in the February 1984 issue of the JOURNAL OF HEAT TRANSFER, p. 256.

Authors' Closure

In any attempt to move forward in the field of Heat Transfer, the comments and viewpoints of a practioner are always appreciated. It appears though, that some unfortunate and unwarranted implications have been drawn by Mr. Rubin. Our goal in the paper was to demonstrate the usefulness to the heat transfer design of the optimization techniques that have been used for over a decade in structural design. Our goal is not to replace the designer with the computer—it would be foolish to try.

The following replies are offered to Mr. Rubin's specific comments:

The method proposed is *applicable* to the design of commercial air-cooled heat exhangers. It is a tool, one of many, it is hoped, that the designer will use.

Not all air-cooled heat exchangers utilize circular fans. There are many applications in the transportation industry where ram air is utilized.

Mr. Rubin's comments on the discrete sizes of components available to the designer only point out the need to extend the techniques of heat exchanger design optimization to include more advanced optimization algorithms. More to the point, the use of continuous variables is common practice early in the design process, rapidly providing a near optimum from which to discritize the actual parameters.

To reiterate: our purpose was not to eliminate the designer but to provide tools that will make the design process more efficient. As is stated in the paper's abstract, the method we have proposed "is shown to be a useful tool for heat exchanger design."

M. I. Drucker[2]

V. K. Dhir
Mem. ASME

R. B. Duffey[3]

School of Engineering &
Applied Science,
University of California
at Los Angeles,
Los Angeles, Calif. 90024

Two-Phase Heat Transfer for Flow in Tubes and Over Rod Bundles With Blockages[1]

A study of single- and two-component, two-phase heat transfer mechanisms for vertical flow inside of tubes and over rod bundles with blockages has been made. Existing heat transfer data for air–water flow in tubes with a liquid Reynolds number range of 2000 to 150,000 and void fractions up to 0.40 have been correlated as a function of $\alpha Gr/Re^2$. *The correlation has also been found to compare well with limited high Prandtl number data obtained with liquids other than water and for flow over rod bundles when an empirical constant is modified. Correlations have also been developed for the heat transfer coefficient in the vicinity of flow blockages in rod bundles. The heat transfer data have been obtained on a four rod bundle with sleeve-type blockages for a Reynolds number range of 230 to 6900 and void fractions up to 0.15. Significant enhancement of the heat transfer coefficient has been observed downstream of the blockages.*

1 Introduction

During the blowdown phase of a hypothetical loss of coolant accident in a PWR, the overheated cladding may swell locally as a result of high pressure in the fuel pin. The swollen cladding can block the flow channels between the fuel pins and the resultant flow redistribution will in turn affect the local heat transfer rates. Knowledge of heat transfer mechanisms in the vicinity of blockages in rod bundles is essential to describe the thermal-hydraulic response of the core during the reflood phase of the accident.

Several reviews of experimental studies of two-phase, gas–liquid heat transfer mechanisms have been made. In his review, Collier [1] concluded that one reason that two-phase heat transfer coefficients are higher than single-phase heat transfer coefficients is that the introduction of a gas phase tends to increase the liquid-phase velocity. Collier stated that the enhancement in low liquid Reynolds number flow is due to the presence of bubbles, which greatly enhance the local turbulence. In his review, Michiyoshi [2] concurred with Collier's conclusion and found that the ratio of the two-phase to single-phase heat transfer coefficients for bubbly and slug flow increased with the cross-sectionally averaged void fraction. The enhancement in heat transfer coefficient however decreased with an increase in the liquid Reynolds number. Shah [3] has assembled and correlated the published data and has proposed a functional form of the ratio of the two phase to single phase heat transfer coefficient as

$$\psi \equiv \frac{\mathrm{Nu}_{00}}{\mathrm{Nu}_o} = \frac{h_{tp}}{h_{sp}} = f(j_d/j_c, \mathrm{Fr}_c) \qquad (1)$$

However, a working correlation is proposed only for data with a liquid Reynolds number less than 170. In rationalizing the use of liquid Froude number, Shah maintains that it will implicitly account for flow pattern effects.

Two phase heat transfer is largely dominated by its turbulent nature. Serizawa, Kataoka, and Michiyoshi [4, 5] have made a detailed study of the structure of turbulence in air-water bubbly flow. They concluded that in the turbulent transport process it is the turbulent velocity components of the liquid phase that are the most important. Contrary to this observation, Theofanous and Sullivan [6] have found that there is a strong dependence of the turbulent intensity on the flow rate of the discontinuous phase. Theofanous et al. have experimentally studied turbulent intensity in two-phase bubbly flow in pipes, and have modeled the effect of turbulence on wall shear stress.

Studies of single-phase heat transfer in the vicinity of flow blockages in tubes and rod bundles have been made by Hall and Duffey [7], Koram and Sparrow [8], and Murakami, Kikuchi, and Michiyoshi [9]. Hall and Duffey have suggested a method for calculating flow split between blocked and unblocked regions of a rod bundle. Koram and Sparrow have made a detailed investigation of the turbulent single-phase heat transfer downstream of an asymmetric blockage in a tube. Their results show a significant enhancement of the heat transfer downstream of the blockage with two identifiable maxima. The maximum occurring on the unblocked side of the tube has been attributed to the impingement of flow deflected by the blockage, while the maximum found on the blocked side was attributed to the flow's reattachment to the wall. The heat transfer coefficient downstream of the blockage was found to vary both in azimuthal and axial directions. The results of Murakami et al. for heat transfer downstream of a blockage in a rectangular channel are quite similar to those of Koram and Sparrow. Murakami et al. conclude that downstream enhancement is a function of the ratio of blocked to unblocked flow area in the channel. The enhancement in heat transfer is attributed to the higher liquid velocities brought about by eddies and mixing in the separation and reattachment zones. Consistent with the results of Koram and Sparrow, the maximum heat transfer coefficient is found to occur near the flow reattachment location.

At present no quantitative study exists in the literature for single- and two-phase heat transfer in the vicinity of blockages in rod bundles. Knowledge of heat transfer mechanism in the vicinity of a blockage is essential to develop models to describe reflood behavior of ballooned rod bundles. The purpose of this experimental study is threefold:

(*i*) To correlate existing two phase bubbly and bubbly slug flow heat transfer data for flow inside of tubes and to extend the correlation to unblocked rod bundles.

(*ii*) To study both single- and two-phase (without phase

---

[1] Work supported by EPRI, Palo Alto, Calif.

[2] *Currently at Bechtel Power Corp., Los Angeles, Calif.*

[3] Nuclear Safety and Analysis Department, EPRI, Palo Alto, Calif.

Contributed by the Heat Transfer Division and presented at the ASME Winter Meeting, Phoenix, Arizona, November 14–19, 1982. Manuscript received by the Heat Transfer Division January 3, 1983. Paper No. 84-WA/HT-47.

change) heat transfer in the vicinity of blockages in a rod bundle.

(*iii*) To correlate data for local and maximum enhancement in heat transfer downstream of flow blockages in a rod bundle.

By expressing the heat transfer coefficients in a ratio form similar to equation (1), the results can be extended to dispersed flows. In these flows the wall heat transfer is increased by turbulence induced by the presence of a discontinuous phase in the continuous vapor phase. For this reason, the experimental setup used in this work is very similar to that used in film boiling and quenching studies [10, 11] performed at UCLA.

2 Two-Phase Heat Transfer in Tubes

Momentum and Heat Transfer Considerations. Previous experimental investigations unequivocally show that the presence of gas bubbles in a flowing liquid enhance the heat transfer coefficient. The functional form of the two-phase heat transfer coefficient has been the subject of many studies yet uncertainty still remains as to the role of various flow parameters [5, 6]. Despite this uncertainty, it is nevertheless conceivable that the presence of the discontinuous gas phase leads to agitation or turbulence which increases the wall shear stress. If it is assumed that the wall shear stress in the presence of the discontinuous phase is equal to the sum of the single-phase wall shear stress and a shear stress directly attributable to the interaction of the phases, the two-phase wall shear stress can be written as

$$\tau_{tp} = \tau_{sp} + \tau_i \tag{2}$$

In writing the above equation no distinction between the wall surface area and the interfacial surface area leading to τ_i at the wall has been made. This simplification is of little consequence since the constants will be determined empirically. By expressing the shear stresses in terms of skin friction coefficients, equation (2) can be expressed as

$$(C_f)_{tp}\rho_c j_c^2 = (C_f)_{sp}\rho_c j_c^2 + (C_f)_i \bar{\rho}\, u_i^2 \tag{3}$$

In equation (3), the two-phase wall shear stress has been written in terms of the density and velocity of the continuous phase rather than the mean density and the mean velocity of the mixture. The last term in equation (3), representing the shear stress resulting from interaction of the two phases has been expressed in terms of an effective density and the square of a velocity characterizing interaction between the two phases. By assuming that the velocity u_i is proportional to the relative velocity between the two phases, the term $\bar{\rho} u_i^2$, can be expressed as a product of the density difference between the two phases, the gravitational acceleration and a characteristic length. The characteristic length would best be expressed as an average bubble diameter, but the presence of many bubbles of different sizes precludes this. For this reason the hydraulic diameter of the tube is taken as the characteristic length. After replacing $\bar{\rho} u_i^2$ by $(\rho_c - \rho_d) g D_h$ in equation (3) and dividing throughout by $\rho_c j_c^2$, it is found that

$$(C_f)_{tp} = (C_f)_{sp} + \frac{(C_f)_i (\rho_c - \rho_d) g\, D_h}{\rho_c j_c^2} \tag{4}$$

or

$$\frac{(C_f)_{tp}}{(C_f)_{sp}} = 1 + \frac{(C_f)_i}{(C_f)_{sp}}\,\frac{(\rho_c - \rho_d) g\, D_h}{\rho_c j_c^2} \tag{5}$$

If it is accepted that the Reynolds analogy can be applied to two-phase flows as is true for single-phase flows [13], equation (5) can be written as

$$\psi \equiv \frac{\mathrm{Nu}_{00}}{\mathrm{Nu}_o} = 1 + \frac{l(C_f)_i}{(C_f)_{sp}}\,\frac{\mathrm{Gr}}{\mathrm{Re}^2} \tag{6}$$

In equation (6) the ratio $\mathrm{Re}^2/\mathrm{Gr}$ represents a modified Froude number. Although the use of the Froude number is attractive in the sense that it can reduce two dimensionless groups into one, explicitly written Reynolds and Grashof numbers allow one to determine the relative importance of single-phase turbulence and of buoyancy-driven turbulence resulting from the presence of the second phase. As derived, equation (6) is applicable only to flow in vertical tubes.

The ratio $(C_f)_i/(C_f)_{sp}$ will depend on the void fraction representing the flow regime of the two-phase flow, i.e., the Grashof number characterizing the turbulence created by the discontinuous phase and the single-phase Reynolds number. Thus, in general, the ratio of the skin friction coefficients can be written as

$$\frac{(C_f)_i}{(C_f)_{sp}} = f_1(\alpha, \mathrm{Gr}, \mathrm{Re}) \tag{7}$$

Nomenclature

A_F = cross-sectional flow area
c_f = skin friction coefficient
c_p = specific heat of the tube wall material
D_h = hydraulic diameter
D_i, D_o = inner and outer tube wall diameters, respectively
D_s = outer diameter of the central portion of the sleeve-type blockage
Fr_c = Froude number, $[\rho_c j_c{}^2/(\rho_c - \rho_d) g D_h]$
g = gravitational acceleration constant
Gr = Grashof number, $[(\rho_c - \rho_d) g D_h{}^3]/\rho_c \nu_c{}^2$
h = heat transfer coefficient
j_c, j_d = superficial velocity of the continuous and discontinuous phases respectively
k_c = thermal conductivity of the continuous phase
k_w = thermal conductivity of the tube wall material
L_{in}, L_t = length of the entrance and test section portions of the rod bundle, respectively
Nu = Nusselt number, hD_h/k_c
Nu = Nusselt number corresponding to the maximum heat transfer coefficient downstream of the blockage
$\mathrm{Nu}_o, \mathrm{Nu}_{00}$ = Nusselt number corresponding to the undisturbed and thermally fully developed single- and two-phase flows, respectively
Nu_o^* = Nusselt number corresponding to thermally fully developed single phase flow based on the local Reynolds number Re* after flow split
p = pitch of the rod bundle
P_{in}, P_t = energy dissipation rate in the entrance and test sections of the rod bundle, respectively
Re = Reynolds number, $j_c D_h/\nu_c$
Re* = local Reynolds number after flow split in the inner channel of the blocked four rod bundle
T_i, T_o = inner and outer tube wall temperatures, respectively

and equation (6) for ψ can be rewritten as

$$\psi = 1 + f_2(\alpha,\mathrm{Gr},\mathrm{Re}) \qquad (8)$$

The functional form of f_2 is to be determined by correlation of available data.

Theofanous and Sullivan [6] used a momentum balance of a control volume containing both continuous and discontinuous phases to derive an equation for the buoyancy driven turbulent kinetic energy. For a highly turbulent continuous phase flow, the ratio of the two phase turbulent energy to the single phase kinetic energy was derived to be

$$\left(\frac{u'}{j_c}\right)^2 = \frac{(C_f)_{sp}}{2}(1 \pm \alpha)(1-\alpha) + \delta\alpha(1-\alpha)\left|\frac{\rho_c-\rho_d}{\rho_c}\right|\frac{g\,D_h}{4j_c^2} \qquad (9)$$

where the plus sign is used for upflow and the minus sign for downflow.

If the foregoing analysis is extended by defining the two phase wall shear stress as

$$\tau_{tp} = \rho_c(u')^2 = \frac{(C_f)_{tp}}{2}\rho_c j_c^2 \qquad (10)$$

Equation (9) can be rewritten as

$$(C_f)_{tp} = (C_f)_{sp}(1 \pm \alpha)(1-\alpha) + \delta\alpha(1-\alpha)\left|\frac{\rho_c-\rho_d}{\rho_c}\right|\frac{g\,D_h}{2j_c^2} \qquad (11)$$

Through the application of Reynolds analogy to equation (11), as was done earlier in conjunction with equation (5), an expression for the ratio of the two-phase Nusselt number to the single-phase Nusselt number for upflow is found to be

$$\psi = (1-\alpha^2) + \frac{\delta\alpha(1-\alpha)}{2(C_f)_{sp}}\frac{\mathrm{Gr}}{\mathrm{Re}^2} \qquad (12)$$

If δ is assigned its mean empirical value of 3 and $(C_f)_{sp}$ a value of 0.005 corresponding to that for fully developed turbulent flow in a smooth pipe, equation (12) reduces to

$$\psi = (1-\alpha^2) + 300(1-\alpha)\frac{\alpha Gr}{\mathrm{Re}^2} \qquad (13)$$

This final equation represents an extension of Theofanous and Sullivan's [6] model based on momentum considerations of a control volume in two-phase flow and will be compared with available data.

Correlation of Tube Data. Several investigators [13-18] have studied two-phase heat transfer for gas-water upflow in tubes. The relative enhancement $\psi - 1$ in heat transfer observed in these studies is plotted in Fig. 1. The discontinuous phase for these studies was air and the continuous phase was water. The data cover a liquid Reynolds number range of 2000 to 150,000 and void fractions from 0.01 to 0.40. Tabulation of the data can be found in [19].

The void fractions have been evaluated using superficial gas and liquid velocities and the correlations of Harmathy [20] for bubbly flow $\alpha < 0.20$ as

$$\alpha = \left[\frac{j_d + j_c}{j_d} + 1.53\frac{(1-\alpha)^2}{j_d}\left(\frac{\sigma g(\rho_c-\rho_d)}{\rho_c^2}\right)^{0.25}\right]^{-1} \qquad (14)$$

and of Zuber and Findlay [20] for bubbly-slug flow $0.20 < \alpha < 0.40$ as

$$\alpha = \left[\frac{j_d + j_c}{j_d} + \frac{1.41}{j_d}\left(\frac{\sigma g(\rho_c-\rho_d)}{\rho_c^2}\right)^{0.25}\right]^{-1} \qquad (15)$$

From Fig. 1, it is clearly seen that the relative enhancement, $\psi - 1$, is adequately described as a function of the dimensionless group $\alpha\mathrm{Gr}/\mathrm{Re}^2$ when plotted on a log-log scale. A best fit line shows that most of the data are correlated within ±35 percent by the expression

$$\psi = 1 + 2.5(\alpha\mathrm{Gr}/\mathrm{Re}^2)^{0.50} \qquad (16)$$

The available data, as well as equation (16), both show that for $\alpha\mathrm{Gr}/\mathrm{Re}^2 \leq 10^{-3}$ little enhancement in heat transfer is obtained with the addition of a discontinuous phase. From this observation it can be reasoned that for a fixed α and Gr, as the Reynolds number is increased, the turbulence of the base flow tends to dominate any agitation or turbulence created by the discontinuous phase.

Equation (13), also plotted in Fig. 1, shows a much stronger dependence of $\psi - 1$ on $\alpha\mathrm{Gr}/\mathrm{Re}^2$ than that shown by the data or equation (16). Much of the experimental work done by Theofanous and Sullivan is for very small void fractions. For $\alpha = 10^{-3}$ and $\alpha\mathrm{Gr}/\mathrm{Re}^2 \simeq 10^{-3}$, extension of Theofanous and Sullivan's model yields an enhancement of about 30 percent in the two-phase heat transfer coefficient. The available data,

Nomenclature (cont.)

$T_l(z)$ = local bulk fluid temperature at an axial position z
u_i = velocity characterizing interaction between the continuous and discontinuous phases
X = distance from the midplane of the sleeve-type blockage
$X_{\max}$ = distance between the midplane of the sleeve-type blockage and the location of the maximum heat transfer coefficient downstream of the blockage
X_s = one-half of the sleeve length
z = distance from the bottom of the rod bundle

Greek Letters

α = void fraction
δ = distribution parameter of Theofanous and Sullivan [6]
θ = $\mathrm{Nu}(X/D_s)_{tp}/\mathrm{Nu}_{00}$
$\theta_{\max}$ = $\mathrm{Nu}_{\max,tp}/\mathrm{Nu}_{00}$
ν_c = kinematic viscosity of the continuous phase
ρ_c, ρ_d = density of the continuous and discontinuous phases, respectively
$\bar{\rho}$ = effective density of a two-phase mixture
σ = surface tension
ϕ = $\mathrm{Nu}(X/D_s)_{sp}/\mathrm{Nu}_o$
ϕ^* = $\mathrm{Nu}(X/D_s)_{sp}/\mathrm{Nu}_o^*$
$\chi_{\max}$ = $\mathrm{Nu}_{\max,tp}/\mathrm{Nu}_o$
ψ = $\mathrm{Nu}_{00}/\mathrm{Nu}_0$

Subscripts

c = property of the continuous phase
d = property of the discontinuous phase
0 = single-phase undisturbed and thermally fully developed flow conditions
00 = two-phase undisturbed and thermally fully developed flow conditions
sp = single phase
tp = two phase

Superscript

$*$ = local property of the inner channel after flow split

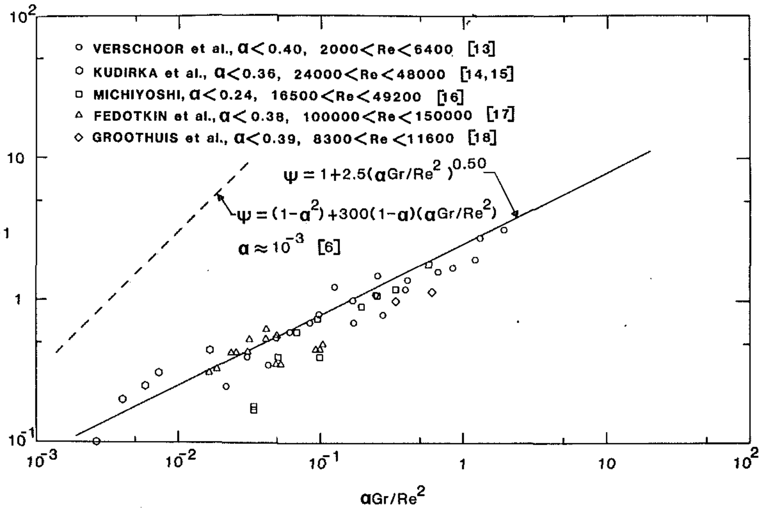

Fig. 1 Correlation of the two-component, two-phase heat transfer enhancement, ψ-1, for flow in tubes; 1.77 < Pr < 6.70

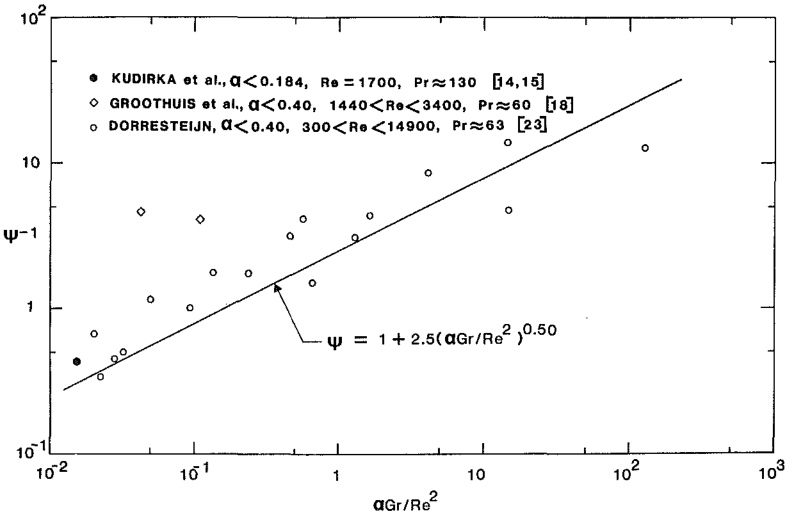

Fig. 2 Correlation of the two-component, two-phase heat transfer enhancement, ψ-1, for flow in tubes; 60 < Pr < 130

which are quite sparse in that range, show little if any enhancement. It is possible that uncertainty in measurements in this range of parameters has about the same magnitude as the enhancement in heat transfer expected from equation (9). More two-phase flow heat transfer data at high Reynolds numbers is needed to resolve some of these differences.

The relative enhancement $\psi-1$ observed in studies with liquids other than water is plotted in Fig. 2. The data cover a liquid Reynolds number range of 300 to 14,900 and void fractions from 0.03 to 0.40. Figure 2 shows that the enhancement in heat transfer is correlated well with the dimensionless group $\alpha\mathrm{Gr}/\mathrm{Re}^2$. The high Prandtl number data ($\mathrm{Pr} \geq 60$) are seen to be faithful to equation (16) developed from water data ($1.77 \leq \mathrm{Pr} \leq 6.70$). This suggests that within the uncertainty of the available data ψ is independent of Prandtl number.

Although the correlation presented as equation (16) is based on data in which liquid was the continuous phase and gas the discontinuous phase, its functional form should be applicable to entrained flows where gas is the continuous phase and liquid droplets are the discontinuous phase. For this situation it is necessary to replace α with $(1-\alpha)$ and to evaluate both the Reynolds and Grashof numbers for the gas or vapor properties. In addition, the empirical constants will need to be ascertained by comparing the correlation with the data.

3 Blocked Four-Rod Bundle Experimental Apparatus and Procedures

The experiments for the determination of two-phase heat transfer coefficients without phase change were conducted on an ohmically heated four-rod bundle. Demineralized water was utilized as the continuous phase and nitrogen gas as the discontinuous phase. As shown in Fig. 3, the two-phase mixture moved vertically up over four stainless steel rods that were arranged in a square grid of same pitch as fuel elements in a PWR. The rod bundle was enclosed in a plexiglass tube situated upon an inlet header which through a series of screens acted as a water-nitrogen mixing chamber.

Sleeve-type blockages were positioned at the midplane of the test section. To each end of the blockage a 26.7 cm segment of stainless steel tube was attached thereby forming the test section. Two of the four rods were instrumented with twenty chromel-alumel thermocouples. The thermocouples were spot-welded along the same side of the tube. The attachment of separate entrance and exit sections to the test section increased the total length of the rod bundle to 146 cm.

As shown in Fig. 4, each blockage was constructed of three separate pieces machined such that a constant material cross-sectional area of approximately 0.23 cm² was always

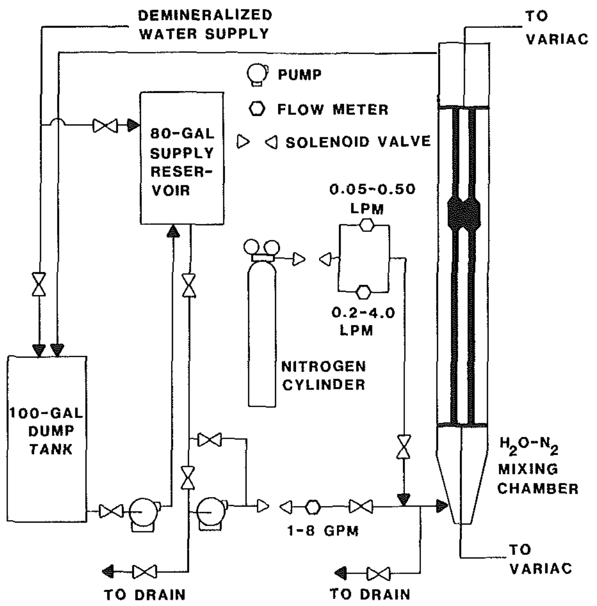

Fig. 3 Schematic diagram of the experimental setup for four-rod bundle

maintained. The maximum diameter of the blockage assembly was such that when assembled the adjacent rods would touch each other. This configuration resulted in a 60 percent flow blockage of the inner flow channel while providing a nearly infinite flow bypass in the outer channel.

The thermocouples on the instrumented rods were biased against the output of a thermocouple placed in the mixing chamber. This arrangement allowed for the direct measurement of the difference in temperature between the inner test section wall and the inlet water temperature. After amplification by a factor of 100, the thermocouple output was recorded on a multichannel recorder.

With assumption of negligible circumferential conduction in the tube wall, solution of the one-dimensional conduction equation in the radial direction yielded the temperature difference across the tube wall as

$$T_o - T_i = \frac{P_t}{2k_w L_t}\left[\frac{\left(\dfrac{D_i^2 - D_0^2}{2} + D_i^2 \ln(D_o/D_i)\right)}{D_o^2 - D_i^2}\right] \qquad (17)$$

The local bulk fluid temperature was calculated from the enthalpy rise as

$$T_l(z) - T_l(0) = \frac{P_{\rm in}}{\rho c_p j_c A_f} + \frac{z - L_{\rm in}}{L_t}\left(\frac{P_t}{\rho c_p j_c A_f}\right) \qquad (18)$$

Generally, the difference between T_o and $T_l(z)$ was much larger (1-5°C) than the difference between T_o and T_i (≈ 0.1°C). Knowing the temperature difference between the rod surface and the fluid, it was possible to evaluate the local heat transfer coefficient by making a simple energy balance for the test section as

$$h = \frac{P_t}{4\pi D_o L_t [T_o - T_l(z)]} \qquad (19)$$

Generally, three to six runs were made for each velocity combination studied. The maximum uncertainty in the single-phase heat transfer coefficient is ±15.3 percent. The maximum uncertainty in the two-phase case is found to be ±28.2 percent.

The cross-sectionally averaged void fraction was calculated in the same manner as done earlier for the tube data.

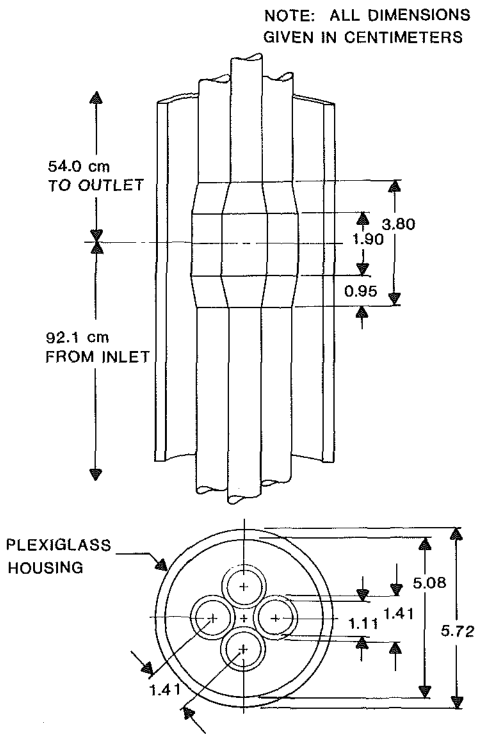

Fig. 4 Side and top views of the sleeve-type blockages used in the four-rod bundle

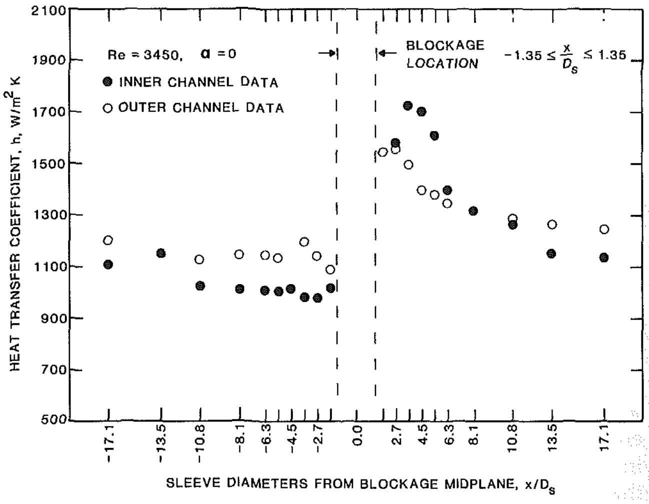

Fig. 5 Variation of the single-phase heat transfer coefficient in the vicinity of the blockage for both the inner and outer flow channels, Re = 3450

4 Discussion of Results for Rod Bundle

Single-Phase Heat Transfer. The single-phase heat transfer data were analyzed for 13 superficial liquid velocities ranging from 1-30 cm/s. Based on a hydraulic diameter of 0.0223 m, these velocities correspond to a Reynolds number range of 230-6900.

Typical heat transfer coefficient profiles in the region bounding 17 sleeve diameters upstream and downstream of the blockage midplane are plotted in Fig. 5 for a flow with a Reynolds number of 3450. Far upstream of the blockage the inner channel heat transfer coefficient values are nearly constant, though near the blockage a gradual depression is noted. The heat transfer rate reaches a minimum value at approximately $X/D_s = -3$, or 1.5 sleeve diameters upstream of the blockage. For turbulent flows (Re > 2000), the

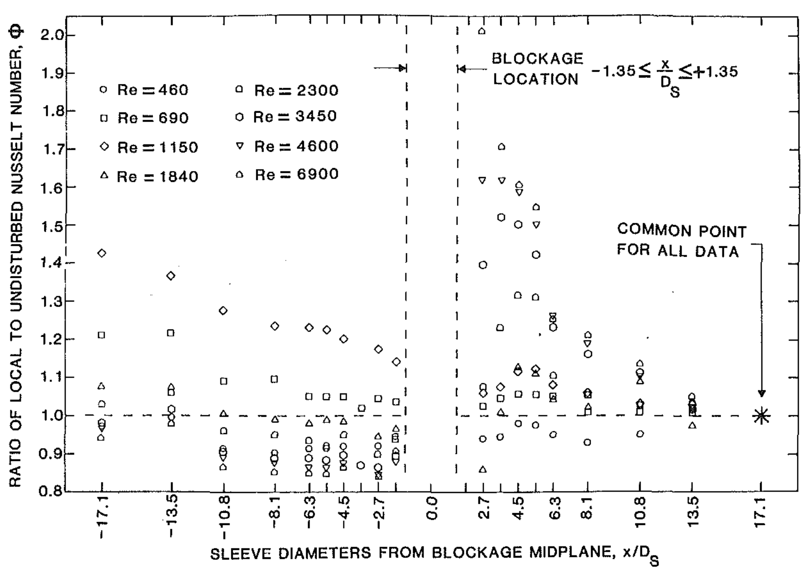

Fig. 6 Variation of ϕ in the vicinity of the blockage

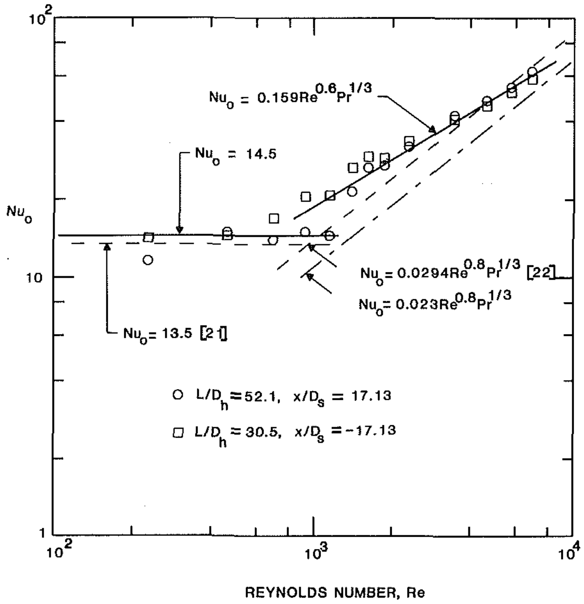

Fig. 7 Dependence of Nusselt number on the Reynolds number for undisturbed and thermally fully developed single-phase flow

reduction in heat transfer coefficient ranges from 10–16 percent. The reduction in the heat transfer coefficient is caused by flow diversion from the inner channel to the outer channel as the fluid tries to avoid the high resistance region created by the blockage. Downstream of the blockage, a significant enhancement in the heat transfer coefficient is found. Koram and Sparrow [8] have explained that this enhancement is attributable to the turbulence in the separation and reattachment regions in the downstream wake of the blockage. It is possible to identify these regions in Fig. 5. Immediately downstream of the blockage is the separation region featuring high turbulence which greatly enhances the heat transfer rate. The heat transfer coefficient reaches a maximum value when the flow reattaches to the tube wall. Following the peak, an exponential decay of the heat transfer coefficient characterizes the flow redevelopment region. The undisturbed heat transfer coefficient value is usually attained within fifteen sleeve diameters from the blockage midplane.

The effect of the blockage on the outer channel heat transfer coefficient profile upstream of the blockage is not as pronounced as in the inner channel. Due to the large bypass flow area, the increase in the heat transfer coefficient in the outer channel caused by flow diversion upstream of the blockage is small. At $X/D_s = -3.6$, the heat transfer coefficient attains the maximum upstream value at virtually the same axial position at which the inner channel data is at its minimum. Downstream of the blockage there is a significant enhancement of the heat transfer rate followed by an exponential decay back to nearly an undisturbed and fully developed value.

The ratio ϕ of the local Nusselt number to the Nusselt number, corresponding to the heat transfer coefficient for the undisturbed and fully developed flow, is plotted in Fig. 6 for various Reynolds numbers. The data plotted in Fig. 6 are for the inner channel. The single-phase flow is assumed to attain undisturbed and fully developed flow conditions 17.1 sleeve diameters downstream of the blockage midplane and the value of the heat transfer coefficient at that location is used to define Nu_0. At very low Reynolds number the flow appears to be fully developed far upstream, with $\phi = 1$, however as the Reynolds number increases the length of the entrance region increases and at $X/D_s = -17.1$ the value of ϕ tends to be greater than 1. For Re = 1150, where ϕ at $X/D_s = -17.1$ is 1.43, the variation of the Nusselt number closely resembles that of a thermally developing flow. Further increase in the Reynolds number shows a decrease in the far upstream values of ϕ, and for Re ≥ 2300 it is found that $\phi \simeq 1$.

Downstream of the blockage the distribution of ϕ shows the regions of flow separation, reattachment, and redevelopment. For Re ≥ 920, a downstream maximum is clearly seen with each data set. As the velocity is increased the location of maximum, which is originally found to be at 5.5 sleeve diameters downstream, tends to shift closer to the blockage. For Reynolds numbers less than 690, no separation or reattachment of the flow downstream of the blockage is indicated by the data.

Correlation of Undisturbed and Fully Developed, Single-Phase Heat Transfer Data. The two thermocouples placed farthest upstream and downstream of the blockage midplane are sufficiently away from the blockage that their output is deemed to represent the undisturbed flow conditions. The single-phase Nusselt number Nu_o for these locations is plotted in Fig. 7 as a function of Reynolds number. Two separate regions are quickly noted, a laminar flow region in which Nu_o

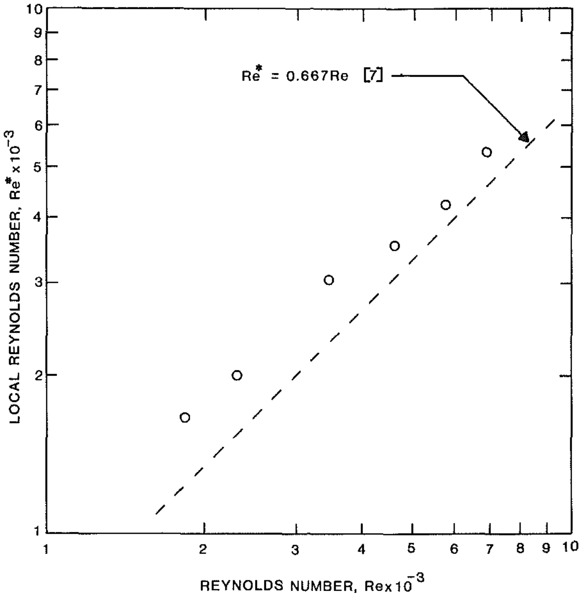

Fig. 8 Correlation of the local Reynolds number Re* after flow split with the Reynolds number Re based on the average flow rate over the rod bundle

is constant (Re ≤ 1150) and a turbulent flow region in which Nu_o varies with Re (Re ≥ 1610).

The undisturbed and fully developed laminar flow data are best correlated as

$$Nu_o = 14.5 \quad (20)$$

The value given by equation (20) is about 7.5 percent higher than that predicted by Kim [21] for a square lattice.

The turbulent flow data of Fig. 7 lying in the Reynolds number range of 1610 to 6900 are correlated within ±10 percent as

$$Nu_o = 0.159\, Re^{0.6} Pr^{1/3} \quad (21)$$

Also plotted in Fig. 7 are two other correlations for turbulent flow: the Dittus-Boelter correlation for flow in tubes and the Weisman [22] correlation for flow over rod bundles. The present data generally tend to be about 17 percent higher than the Weisman correlation and 35 percent higher than the Dittus-Boelter correlation. Equation (21) also correlates the data far upstream of the blockage for 1150 < Re < 1840. Since the flow at this location and for these Reynolds numbers was still developing thermally, this occurrence is purely coincidental and has no significance attributed to it.

Correlation of Single-Phase Heat Transfer Data Downstream of the Blockage. The reduction in the inner channel heat transfer coefficient immediately upstream of the blockage has been attributed to a reduced flow rate brought about by flow diversion to the outer channel where the flow resistance is less. By assuming that the flow remaining in the inner channel is thermally fully developed it is possible to calculate a local Reynolds number Re* based on the minimum heat transfer coefficient measured immediately upstream of the blockage and use of equation (21). Figure 8 is a plot of Re*, as a function of the bundle averaged undisturbed Reynolds number Re. For low flow rates, Re < 1840, the data do not show any measurable reduction in the heat transfer coefficient upstream of the blockage. This implies that probably little or no flow diversion occurred and that Re* is equal to Re. However, with increasing flow rates Re* tends to be smaller than Re, approximately 23 to 26 percent lower for Re 3450. Figure 8 also shows a prediction of a 33 percent reduction based on a model proposed by Hall and Duffey [7].

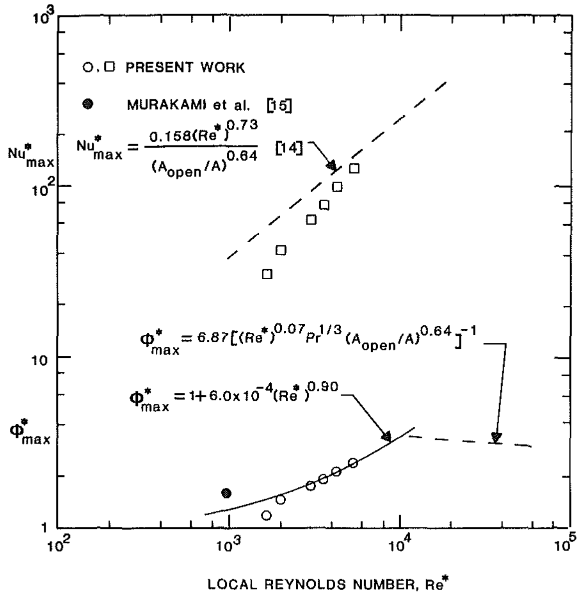

Fig. 9 Dependence of Nu_{max}* and ϕ_{max}* on Re*

Downstream of the blockage the maximum heat transfer coefficient occurs at the point of reattachment. By assuming that the reduced flow rate that was established upstream of the blockage is not altered immediately downstream of the blockage, it is possible to correlate the maximum heat transfer coefficient with the local Reynolds number. The upper portion of Fig. 9 is a plot of Nu^*_{max} as a function of Re*. Alongside this data, the Nusselt number based on a correlation of Koram and Sparrow [8] is plotted. Since in the present geometry $A_{blocked}/A \simeq 0.60$, the Koram and Sparrow correlation is plotted with $A_{open}/A = 0.40$. The correlation was developed for Re > 11,000, yet the present data, for 1600 < Re* < 5400, show a very similar dependence on the Reynolds number. For low Re* the present data are about 50 percent lower, however for higher Re* the deviation is only 20 percent. One explanation for the lower heat transfer coefficient values is that, unlike the impervious blockage of Koram and Sparrow, the open geometry in the present experiment allows for the flow in the outer channel downstream of the blockage to divert back into the inner channel thereby impairing the effectiveness of the recirculating flow. Murakami et al. [9] made a comparison of heat transfer coefficients observed behind both impervious and permeable blockages in a rectangular channel. Their results show that a secondary flow through the permeable blockage does indeed tend to reduce the maximum heat transfer coefficient by about 20 percent in comparison to that for the impervious blockage. The present geometry provides an effectively infinite flow bypass at the blockage while a tube as used in the study by Koram and Sparrow will have no flow bypass whatsoever. Therefore, the Nusselt number based on the maximum heat transfer coefficient for a rod bundle containing a large number of rods and having only a finite flow bypass will be bounded by the present data and the values predicted from the correlation of Koram and Sparrow.

The lower portion of Fig. 9 shows a plot of ϕ^*_{max} as a function of Re*. In this figure the data of Murakami et al. [9] for the case of 60 percent flow blockage is also plotted. The present data and one data point of Murakami et al. are correlated as

$$\phi^*_{max} \equiv \frac{Nu_{max,sp}}{Nu_o} = 1 + 6.0 \times 10^{-4} (Re^*)^{0.90} \quad (22)$$

The ϕ^*_{max}, as determined by taking the ratio of Koram and Sparrow's correlation for Nu_{max},sp to the Nusselt number predicted by the Dittus–Boelter correlation for turbulent flow in a tube, is also plotted for $A_{\text{open}}/A = 0.40$ and Pr = 6.7 (water at 295 K). From the behavior of $\phi^*_{\max}$ as seen in the lower half of Fig. 9, it can be concluded that the single-phase heat transfer enhancement downstream of a blockage will first increase with Reynolds number, reach a maximum value, and will then decrease.

The location of the maximum heat transfer coefficient downstream of the blockage has been found to shift towards the midplane of the blockage with an increasing Reynolds number as

$$\frac{X_{\max}-X}{D_s} = 6.0\exp(-3.4\times10^{-4}\text{Re}^*) \tag{23}$$

The distribution of ϕ in the flow redevelopment region downstream of the location of flow reattachment is correlated as

$$\phi = 1+(\phi_{\max}-1)\exp\left[-0.21\left(\frac{X-X_{\max}}{D_s}\right)\right] \tag{24}$$

In the flow redevelopment region, flow from the outer channel diverts back into the inner channel. For this reason equation (24) is written in terms of ϕ rather than ϕ^*.

Two-Phase Heat Transfer. Two-phase heat transfer data have been obtained in a Reynolds number range of 1150 to 3450. The various combinations of water and Nitrogen gas velocities have yielded average void fractions in the range of 0.00728 to 0.150.

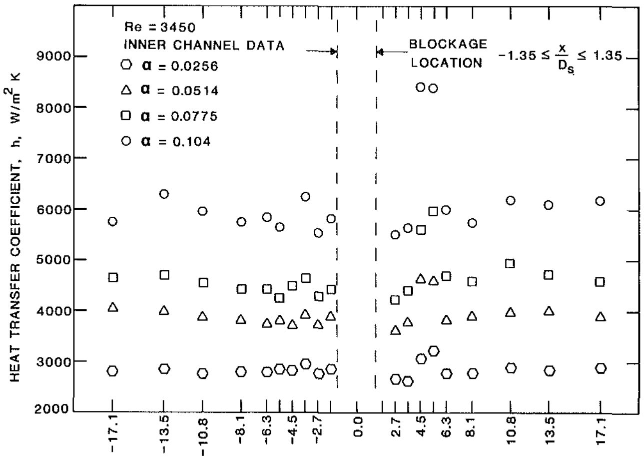

Fig. 10 Variation of the inner channel, two-phase heat transfer coefficient in the vicinity of the blockage, Re = 3450, $0.0256 \le \alpha \le 0.104$

The distribution of the heat transfer coefficient in the inner channel both upstream and downstream of the blockage is plotted in Fig. 10 for a Reynolds number of 3450 and for void fractions of 0.0256, 0.0514, 0.0775, and 0.104. A comparison of the undisturbed and fully developed heat transfer coefficient values far upstream of the blockage with the single-phase case presented in Fig. 5 shows that the addition of the discontinuous phase significantly enhances the heat transfer rate. The enhancement mechanisms here are the same as those discussed earlier for the case of two phase flow in tubes. The presence of the discontinuous gas phase leads to agitation and turbulence that increases the wall shear stress and the wall heat transfer rate. The enhancement is observed to increase with an increase in the void fraction.

Just upstream of the blockage, the heat transfer rate is depressed from its far upstream value. This reduction is the result of flow split. Similar to the single-phase case, a certain fraction of liquid and gas divert from the inner channel to the outer channel so as to avoid the high resistance region resulting from the blockage. At present no mechanistic model is known to exist which can describe how the two-phase flow split will occur near the blockage. Downstream of the blockage, significant enhancement in the heat transfer rate occurs. The enhancement is similar to that for the single-phase case; however, the regions of flow separation and redevelopment are very narrow. Starting with a value close to that calculated just upstream of the blockage, the heat transfer coefficient rapidly increases to a maximum value and then decreases equally rapidly to its initial value before asymptotically recovering back to the undisturbed and fully developed value found far upstream. The location of the maximum heat transfer coefficient is found to be slightly closer to the midplane of the blockage than that of single-phase flow with the same Reynolds number.

Correlation of Undisturbed and Fully Developed, Two-Phase Heat Transfer Data. Due to the varying length of the recovery region, the flow farthest downstream of the blockage was not always undisturbed. For this reason the observations made from thermocouples located at $X/D_s = -17.1$ (placed farthest upstream of the blockage) have been assumed to be representative of the undisturbed and fully developed two-phase flow conditions to be used in evaluating ψ. Figure 11 shows a plot of $\psi - 1$ as a function of $\alpha\text{Gr}/\text{Re}^2$ for both the

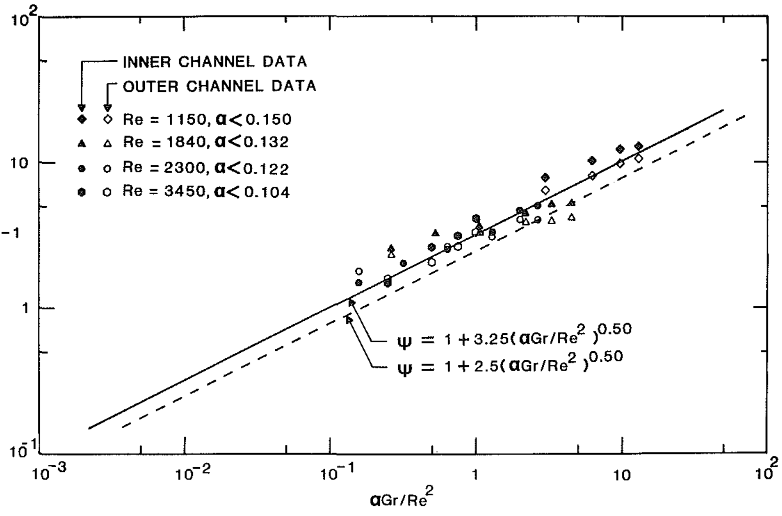

Fig. 11 Correlation of the two-component, two-phase heat transfer enhancement, ψ-1 for flow over a four-rod bundle

inner and the outer channel data. The present rod bundle data show the same functional dependence on $\alpha\mathrm{Gr}/\mathrm{Re}^2$ as the tube data but tend to be consistently higher than the correlation developed earlier for flow in tubes. The two-phase, rod bundle heat transfer data are correlated as

$$\psi = 1 + 3.25(\alpha\mathrm{Gr}/\mathrm{Re}^2)^{0.50} \qquad (25)$$

The constant 3.25 is 30 percent higher than the constant 2.5 used in correlating the tube data.

Correlation of Two-Phase Heat Transfer Data Downstream of the Blockage. In the inner channel, the enhancement in heat transfer includes both the effects of the blockage and the presence of the discontinuous phase. The ratio $X_{\max}$ is correlated as

$$\chi_{\max} \equiv \frac{\mathrm{Nu}_{max,tp}}{\mathrm{Nu}_o} = 1 + 3.0 \times 10^{-4}\mathrm{Re}^{0.9} + 3.5(\alpha\mathrm{Gr}/\mathrm{Re}^2)^{0.65} \qquad (26)$$

In writing equation (26), the average undisturbed values of Re and α have been used, since at this time considerable uncertainty about the flow split under two-phase flow conditions exists. Equation (26) correlates within +51 percent and −32 percent all of the present rod bundle data for the maximum heat transfer coefficient downstream of the blockage.

The ratio $\Theta_{\max}$ can be written by dividing equation (26) by equation (25) as

$$\Theta_{\max} \equiv \frac{\mathrm{Nu}_{\max,tp}}{\mathrm{Nu}_{00}} = \frac{\chi_{\max}}{\psi} = \frac{1 + 3.0 \times 10^{-4}\mathrm{Re}^{0.9} + 3.5(\alpha\mathrm{Gr}/\mathrm{Re}^2)^{0.65}}{1 + 3.25(\alpha\mathrm{Gr}/\mathrm{Re}^2)^{0.50}} \qquad (27)$$

Equation (27) correlates the present rod bundle data within +25 percent and −19 percent. Due to the cancellations of various uncertainties, the deviation of the data from correlation for $\Theta_{\max}$ is less than that for $\chi_{\max}$.

The location of the maximum two-phase heat transfer coefficient downstream of the blockage has been found to be slightly closer to the blockage midplane than that found for the single-phase case with the same Reynolds number. If the location of the maximum two-phase heat transfer coefficient downstream of the blockage is taken to be the same as for the single-phase case, the distribution of Θ in the redevelopment region downstream of the flow reattachment region can be correlated as

$$\Theta = 1 + (\Theta_{\max} - 1)\exp\left[-0.92\left(\frac{X - X_{\max}}{D_s}\right)\right] \qquad (28)$$

Equation (28) has been developed only for the flow redevelopment region prior to the start of the asymptotic recovery region far downstream.

All of the two phase correlations presented in this section have been derived for bubbly flow. However, it is postulated that similar equations will be valid for entrained flows in which the discontinuous liquid phase droplets do not wet the surface. For application of these correlations to entrained flows, α must be replaced by $(1-\alpha)$ and the Reynolds and Grashof numbers must be based on the gas or vapor properties. It must be mentioned that the empirical constants arrived at in this work will need to be verified with relevant data before they can be applied to disperse a flow.

5 Conclusions

1 The presence of a discontinuous gas phase in a continuous liquid phase significantly enhances turbulence and heat transfer.

2 Correlations have been developed to describe the enhancement for flow in tubes and over rod bundles.

3 Significant enhancement in heat transfer has been observed downstream of blockages in rod bundles for both single and two phase flows. The enhancement is caused by increased turbulence in the separation and reattachment regions.

4 Correlations have been developed to describe both the magnitude and location of the downstream enhancement. The magnitude of the enhancement depends on both Re and $\alpha\mathrm{Gr}/\mathrm{Re}^2$.

5 In entrained flows enhancement similar to that observed in present work will occur. However the empirical constants in the correlations will need to be verified with entrained flow data.

References

1 Collier, J. G., *Convective Boiling and Condensation*, McGraw-Hill, London, 1972.

2 Michiyoshi, I., "Two-Phase, Two-Component Heat Transfer," *Proceedings Sixth International Heat Transfer Conference*, Toronto, Vol. 6, 1978, pp. 219-233.

3 Shah, M. M., "Generalized Prediction of Heat Transfer During Two Component Gas-Liquid Flow in Tubes and Other Channels," *AIChE Symposium Series 208*, Vol. 77, 1981, pp. 140-151.

4 Serizawa, A., Kataoka, I., and Michiyoshi, I., "Turbulence Structure of Air-Water Bubbly Flow—II. Local Properties," *International Journal of Multiphase Flow*, Vol. 2, 1975, pp. 235-246.

5 Serizawa, A., Kataoka, I., and Michiyoshi, I., "Turbulence Structure of Air-Water Bubbly Flow—III. Transport Properties," *International Journal of Multiphase Flow*, Vol. 2, 1975, pp. 247-259.

6 Theofanous, T. G., and Sullivan, J., "Turbulence in Two-Phase Dispersed Flows," *Journal of Fluid Mechanics*, Vol. 116, 1982, pp. 343-362.

7 Hall, P. C., and Duffey, R. B., "A Method of Calculating the Effect of Clad Ballooning on Loss-of-Coolant-Accident Temperature Transients," *Nuclear Science and Engineering*, Vol. 58, No. 1, 1975, pp. 1-20.

8 Koram, K. K., and Sparrow, E. M., "Turbulence Heat Transfer Downstream of an Unsymmetric Blockage in a Tube," ASME JOURNAL OF HEAT TRANSFER, Vol. 100, 1978, pp. 588-594.

9 Murakami, S., Kikuchi, Y., and Michiyoshi, I., "Heat Transfer in Downstream of Blockage with Discrete Permeability in Rectangular Channel," *Journal of Nuclear Science and Technology*, Vol. 16, 1979, pp. 929-931.

10 Dhir, V. K., Catton, I., Ornedo, R., Drucker, M., Yaung, J., and Murrin, J., "Reflood Experiments with a 4-Rod Bundle," *EPRI Report NP-1277*, Dec. 1979.

11 Drucker, M. I., and Dhir, V. K., "Effects of High Temperature and Flow Blockage on the Reflood Behavior of a 4-Rod Bundle," *EPRI Report NP-2122*, Nov. 1981.

12 Simonich, J. C., and Bradshaw, P., "Effect of Free Stream Turbulence on Heat Transfer Through a Turbulent Boundary Layer," ASME JOURNAL OF HEAT TRANSFER, Vol. 100, 1978, pp. 671-672.

13 Verschoor, H., and Stemerding, S., "Heat Transfer in Two-Phase Flow," *Proceedings General Discussion on Heat Transfer*, Institute of Mechanical Engineers, Sept. 1951, pp. 201-204.

14 Kudirka, A. A., "Two-Phase Heat Transfer with Gas Injection Through a Porous Boundary Surface," *ANL-6862*, 1964.

15 Kudirka, A. A., Grosh, R. J. and McFadden, P. W., "Heat Transfer in Two-Phase Flow of Gas-Liquid Mixtures," *I&EC Fundamentals*, Vol. 4, No. 3, 1965, pp. 339-344.

16 Michiyoshi, I., "Heat Transfer in Air-Water Two-Phase Flow in a Concentric Annulus," *Proceedings Sixth International Heat Transfer Conference*, Toronto, Vol. 1, 1978, pp. 499-504.

17 Fedotkin, I. M., and Zarudnev, L. P., "Correlation of Experimental Data on Local Heat Transfer in Heating of Air-Liquid Mixtures in Pipes," *Heat Transfer-Soviet Research*, Vol. 2 Mo. 1, 1970, pp. 175-181.

18 Goothuis, H., and Hendal, W. P., "Heat Transfer in Two-Phase Flow," *Chemical Engineering Science*, Vol. 11, No. 3, 1959, pp. 212-220.

19 Drucker, M. I., "Studies of Single and Two Phase Heat Transfer in a Blocked Four Rod Bundle," M.S. thesis, UCLA Engineering, 1982.

20 Wallis, G. B., *One-Dimensional Two-Phase Flow*, McGraw-Hill, New York, 1969.

21 Kim, J. H., "Heat Transfer in Longitudinal Laminar Flow along Circular Cylinders in Square Arrays," *Fluid Flow and Heat Transfer over Rod or Tube Bundles*, ASME Winter Annual Meeting, New York, Dec. 1979, pp. 155-161.

22 Weisman, J., "Heat Transfer to Fluid Flowing Parallel to Tube Bundles," *Nuclear Science and Engineering*, Vol. 6, No. 1, 1959, pp. 78-79.

23 Dorresteijn, W.R., "Experimental Study of Heat Transfer in Upward and Downward Two-Phase Flow of Air and Oil Through 70-mm Tubes," *Proceedings Fourth International Heat Transfer Conference*, Paris-Versailles, 1970, Paper B5.9.

N. K. Tutu

T. Ginsberg
Assoc. Mem. ASME
Department of Nuclear Energy,
Brookhaven National Laboratory,
Upton, N.Y. 11973

J. C. Chen
Chemical Engineering Department,
Lehigh University,
Bethlehem, Pa. 18015
Mem. ASME

Interfacial Drag for Two-Phase Flow Through High Permeability Porous Beds[1]

Pressure drop and void fraction measurements in two-phase (air–water) flow through porous beds of randomly packed spheres have been used to determine the interfacial gas–liquid drag and the gas–solid drag for the case of zero net liquid flux through the bed. The results, presented for beds of 3.18-, 6.35-, and 12.7-mm spheres, show that the interfacial gas–liquid drag term is of the same order as the gas-solid drag term when the particle size is greater than 6 mm.

1 Introduction

Two-phase flow through porous beds of packed particles occurs in a number of applications, including oil and gas production, multiphase catalytic reactors, and synfuel processing. In recent years, such flows have also become of concern in nuclear reactor safety analyses, where emergency coolant injection after formation of a hot debris bed can result in steam–water flow through a packed bed of core debris. Engineering analyses of these situations require a fluid dynamic model of the two-phase flow in porous beds. A current difficulty in modeling such flows is the lack of information on interfactial drag (gas–solid, liquid–solid, and gas–liquid). In particular, there are no experimental data for the interfacial gas–liquid drag and this force is sometimes neglected in analysis of two-phase flows through porous beds.

Numerous investigations (eg., Vasiliev and Maiorov [1]; Maron and Cohen [2]; Naik and Dhir [3]; Lipinski [4], and Gabor et al. [5]) have undertaken analytical and experimental studies of evaporative cooling of internally heated porous beds (for an extensive list of references, see Lipinski [6]). The two-phase frictional pressure drop is usually based on some modified form of the single-phase Ergun equation

$$-\frac{dP}{dz}\bigg|_{\text{friction}} = \frac{\mu j}{\kappa} + \frac{\rho j^2}{\eta} \tag{1}$$

Vasiliev and Maiorov [1], for example, use a defined mixture viscosity and density in equation (1) within the two-phase region of the bed without any physical or experimental justification. On the other hand, Naik and Dhir [3] treat the gas and liquid phases using separate momentum equations. A modified form of equation (1) is used for each of the two phases. However, no direct experimental verification of these models showing a comparison between the measured and predicted frictional pressure drops is available to date.

The separated flow treatment (two momentum equations) of two-phase flow in porous media is based upon extensive experimental work by many investigators (summarized by Scheidegger [7]). This work has demonstrated that when a two-phase, gas–liquid mixture flows through a porous medium of low specific permeability ($\kappa < 10^{-10}$ m^2) at a low Reynolds number (Darcy flow regime), the frictional pressure drop encountered by each phase can be described by the Darcy law provided the permeability is modified. Thus the second term on the right-hand side of equation (1) is neglected, and κ is replaced by $\kappa\kappa_g$ in the equation for the gas phase, and by $\kappa\kappa_l$ in the equation for the liquid phase. The relative permeabilities κ_g and κ_l have experimentally been found to be a function of void fraction only. However, the authors are unaware of any experimental measurements[2] of relative permeabilities for porous beds of large specific permeability ($\kappa \geq 10^{-8}$ m^2) at large Reynolds numbers where the inertia term (the second term on the right-hand side of equation (1)) cannot be neglected. In the absence of such data, Lipinski [6], for example, simply extends the foregoing result to large permeability beds even beyond the Darcy flow regime. His model replaced η in equation (1) by $\eta\kappa_g$ for the gas phase, and by $\eta\kappa_l$ for the liquid phase. In addition, this model negelcts the gas–liquid interfacial drag.

The purpose of this investigation was to obtain measurements of the gas–liquid interfacial drag and the gas–solid drag for two-phase flow in porous beds of high specific permeability ($\kappa \geq 10^{-8}$ m^2). Spherical particles of various sizes were used to form the porous bed.

2 Analysis

Consider a one-dimensional flow of gas-liquid mixture through a porous bed of constant cross-sectional area A flowing upwards against gravity. Let j_g and j_l be the constant superficial gas and liquid velocities through the bed. Neglecting the density change in the gas phase due to the pressure gradient, the momentum flux of each phase across the bed is constant throughout the bed. Thus the net force balance for the gas phase across a section dz of the bed yields

$$dz\left(\frac{dP}{dz}\right)A\ \epsilon\ \alpha + \rho_g A\epsilon\alpha g dz + F^i_{gl}A\epsilon dz + F^*_{gs}A\epsilon dz = 0$$

or

$$-\left(\frac{dP}{dz}\right)\alpha = \rho_g\alpha g + F^i_{gl} + F^*_{gs} \tag{2}$$

where F^i_{gl} is the interfacial drag per unit volume of free space in the bed on the gas phase due to the presence of liquid, and F^*_{gs} is the force per unit volume of free space on the gas phase due to the solid particles of the bed. All drag forces are positive when downwards. Similarly, the force balance on the liquid phase gives

$$-\left(\frac{dP}{dz}\right)(1-\alpha) = \rho_l(1-\alpha)g - F^i_{gl} + F_{ls} \tag{3}$$

where F_{ls} is the particle-liquid drag force.

By adding, and later by eliminating the pressure gradient, equations (2) and (3) can be replaced by an alternate pair

$$-\frac{dP}{dz} = \left[\rho_g\alpha + \rho_l(1-\alpha)\right]g + F^*_{gs} + F_{ls} \tag{4}$$

---

[1] Work performed under the auspices of the U.S. Nuclear Regulatory Commission.

Contributed by the Heat Transfer Division for publication in the JOURNAL OF HEAT TRANSFER. Manuscript received by the Heat Transfer Division September 17, 1983.

[2] Footnote added after the manuscript was submitted. Dhir, Chu, Lee, and Catton [8] have recognized the lack of experimental data for relative permeabilities for high permeability porous beds. Using pressure drop measurements, they have determined bounds for the relative permeabilities.

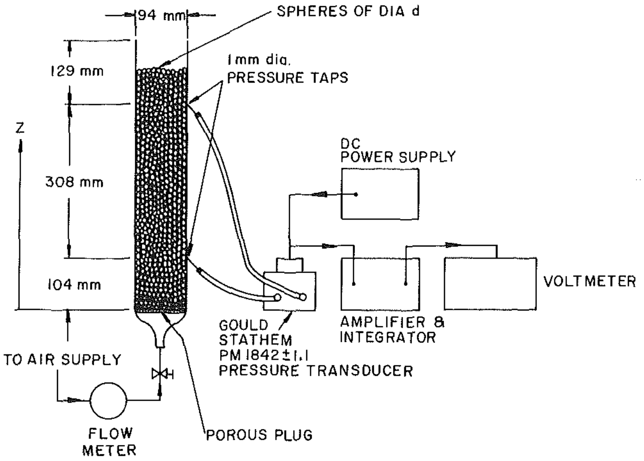

Fig. 1 Schematic of experimental setup

$$F^i_{gl} + (1-\alpha)F^*_{gs} - \alpha F_{ls} = \alpha(1-\alpha)g(\rho_l - \rho_g) \tag{5}$$

Given j_g and j_l, before one can predict α and dP/dz, all the drag terms in equations (2) and (3) need to be modeled.

3 Experimental Apparatus and Method

As shown in Fig. 1, the experiments were carried out in a vertical cylindrical glass vessel with a 94 mm dia. Stainless steel spheres were packed to a depth of 460 mm to form the porous bed. The glass vessel had two 1-mm-dia pressure taps 308 mm apart, and these were connected to a Gould-Stathem model PM8142 ± 1.1 differential pressure transducer with water-filled lines. The output of the transducer was amplified and integrated with a time constant of 26 s to measure the mean pressure drop.

At the beginning of each test, the bed was filled with a known amount of water to the top surface of the bed. Air was then injected at a constant flow rate at the bottom of the bed and flowed upward through the liquid-filled bed. At steady state, the void fraction of gas within the bed could be determined simply by measuring the volume of liquid displaced into the free-board space above the packed particles. This was done by physically removing the displaced liquid by means of a syringe during the experimental run and weighing it. A flowmeter in the air supply line was used to measure the air flow rate. So by changing the air flow rate, an experimental evaluation of void fraction and pressure drop could be made as a function of the superficial air velocity j_g. Experiments were carried out for particle sizes of 3.18 mm, 6.35 mm, and 12.7 mm dia. In addition, experiments were carried out with the glass vessel devoid of particles (two-phase pipe flow).

4 Results

4.1 Void Fraction and Pressure Gradient. Figures 2, 3, and 4 show the measured void fraction and dimensionless pressure gradient as a function of superficial gas velocity for beds of different particle sizes. For small j_g, the pressure gradient decreases with increasing j_g because the increase in the gas-solid force F^*_{gs} is smaller than the reduction in the hydrostatic pressure gradient. It will be noticed that we measure a finite void fraction α_o at $j_g = 0$. This shows that once the flow of gas within the liquid-filled bed has been started, turning off the gas supply leaves some gas trapped within the bed. The gas can remain trapped in the porous bed due to surface tension effects, due to a simple mechanical blockage, or a combination of the two.

4.2 Interfacial Gas-Liquid Drag and Gas-Solid Drag. Since the average liquid superficial velocity is zero in our experiments, the net liquid-solid drag term F_{ls} is assumed to be zero. Having measured the pressure gradient and the void fraction, we can then solve equations (2) and (3) for the two unknowns F^*_{gs} and F^i_{gl}. The results are presented in Figs. 5, 6, and 7. It is observed that for low values of j_g, the interfacial gas-liquid drag is of the same order as the gas-solid force. The importance of the interfacial gas-liquid drag increases with increasing particle size in the bed. For 3.18 mm particles, the interfacial drag force is small compared with the gas-solid force. The interfacial gas-liquid drag for particle sizes greater than 6 mm is, however, significant compared with the gas-solid force and must be accounted for in the models of two-phase flow behavior. Figures 5-7 show that $F^*_{gs} \neq 0$ as $j_g \rightarrow 0$. This finite gas-solid force at no gas flow is to be viewed in terms of the gas trapped within the bed when the gas flow is shut off. With $j_g = j_l = 0$ in the bed, we would expect $F^i_{gl} = 0$, and $(-dP/dz) = \rho_l g$. Substituting these in equation (2), we have

Nomenclature

a_i = gas-liquid interfacial area concentration
A_w = wall factor due to Coulson = $[6(1-\epsilon)/\{6(1-\epsilon)+2d/D\}]^2$
a_w = $(-1 + 1/A_w)$
A = cross-sectional area of the porous bed
C_D = drag coefficient
C^*_d = modified drag coefficient
d = diameter of the particles constituting the porous bed
d_b = bubble diameter
D = vessel diameter
F_{gs} = dynamic gas-solid drag per unit volume of free space
F^*_{gs} = force per unit volume of free space on the gas phase due to solid particles
$F_{g\sigma}$ = surface binding force on the gas phase
F_{ls} = drag per unit volume of free space on the liquid phase due to solid particles in the bed
F^i_{gl} = interfacial drag on the gas phase due to the liquid phase per unit volume of free space
g = acceleration due to gravity
j = superficial velocity upwards = volumetric flow rate/A
P = average cross-sectional pressure
r_D = drag radius
r_{sm} = Sauter mean radius
v_g = gas velocity
v_l = liquid velocity
v_r = $v_g - v_l$
z = vertical coordinate upwards
α = void (gas volume) fraction in the free space of the porous bed
α_0 = void fraction due to trapped gas at no gas flow
ϵ = bed porosity
η_g = inertial relative permeability of the gas phase
η = $\dfrac{d\,\epsilon^3}{1.75(1-\epsilon)}$
κ = $\dfrac{d^2\epsilon^3}{150(1-\epsilon)^2}$, specific permeability of porous bed
κ_g = relative permeability of the gas phase
κ_l = relative permeability of the liquid phase
μ = absolute viscosity
ρ = density
ρ_c = continuous phase density
σ = surface tension of the liquid-gas pair

Subscripts

g = gas phase
l = liquid phase
m = "measured" value

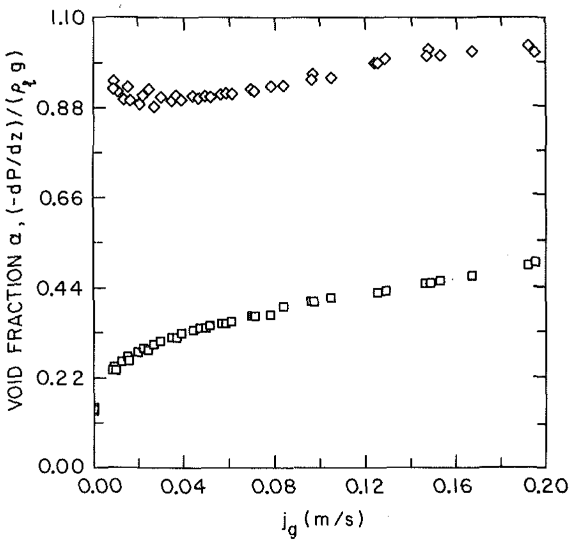

Fig. 2 Void fraction and pressure gradient for 3.18 mm spheres. □ : α; ◇ : dimensionless pressure gradient; α_o = 0.144, ϵ = 0.39, κ = 1.05 × 10^{-8} m^2.

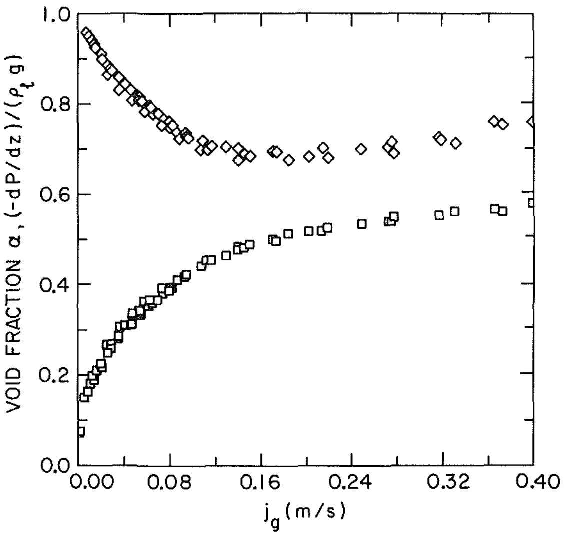

Fig. 3 Void fraction and pressure gradient for 6.35 mm spheres. □ : α; ◇ : dimensionless pressure gradient; α_o = 0.07, ϵ = 0.38, κ = 3.67 × 10^{-8} m^2.

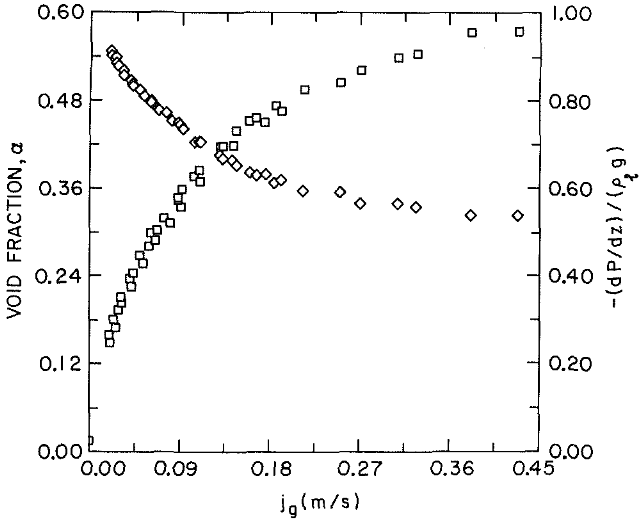

Fig. 4 Void fraction and pressure gradient for 12.7 mm spheres. □ : α; ◇ : dimensionless pressure gradient; α_o = 0.0165, ϵ = 0.42, κ = 2.44 × 10^{-7} m^2.

$$F_{gs}^{*}\big|_{j_g=0}=F_{g\sigma}=g\,\alpha_o(\rho_l-\rho_g) \qquad (6)$$

Thus α_o is an important quantity and must be modeled before one can hope to model the gas-solid force, F_{gs}^{*}, appropriately. However, it must be emphasized that these measurements of α_o, and hence of $F_{g\sigma}$ have been made for the special case of no net liquid flow. The dependence of α_o on j_l remains to be investigated. $F_{g\sigma}$, which is the force responsible for trapping the gas bubbles within the bed, will be referred to as the "surface binding force."

5 Discussion

5.1 The Gas-Solid Force. In view of the foregoing discussion about $F_{g\sigma}$ and the experimental data, it is appropriate to model F_{gs}^{*} as the sum of the surface binding force and the dynamic gas-solid drag, F_{gs}

$$F_{gs}^{*}=F_{g\sigma}+F_{gs} \qquad (7)$$

It is now interesting to see the result of assuming F_{gs} to be given by Lipinski's [6] model for the gas phase frictional pressure drop. Lipinski's model is, of course, based on a simple extension of the Ergun equation. Thus

$$F_{gs}=\frac{\mu_g j_g}{\kappa\kappa_g}+\frac{\rho_g j_g^2}{\eta\eta_g} \qquad (8)$$

where

$$\kappa_g=\eta_g=\left(\frac{\alpha}{0.83}\right)^3 \quad 0\leq \alpha<0.83$$
$$=1 \qquad\qquad \alpha\geq 0.83$$

The foregoing expression for the relative permeability, κ_g was found to give reasonable agreement with the measurements reported by Scheidegger [7]. Lipinski simply assumed η_g to be equal to κ_g. Thus the extended Lipinski model for the gas-solid force F_{gs}^{*} becomes

$$\frac{F_{gs}^{*}}{g(\rho_l-\rho_g)}=\alpha_o+\frac{0.5718}{\alpha^3 g(\rho_l-\rho_g)}\left\{\frac{\mu_g i_g}{\kappa}+\frac{\rho_g j_g^2}{\eta}\right\} \qquad (9)$$

To compute $F_{g\sigma}$, instead of the measured α_o, the following expression for α_o was used

$$a_o=0.00161(\sigma/\kappa\rho_l g)^{0.7} \qquad (10)$$

This was found to give reasonable agreement with the measured α_o for the air-water system and for the three particle sizes tested. It is not, however, intended to be a general model for α_o. In fact, this equation did a very poor job of predicting α_o for the kerosene-air system.

The gas-solid force, F_{gs}^{*} as predicted by equation (9) is plotted as a solid line in Figs. 5, 6, and 7. Experimentally measured values of j_g and α have been used in these computations. Although this modified Lipinski model for F_{gs}^{*} shows reasonable agreement with the data for 6.35 mm spheres, the agreement is poor for 3.18 mm and 12.7 mm particles. It should be noted that if $F_{g\sigma}$ were not added to the Lipinski model, the agreement with the data would be much worse.

5.2 Interfacial Gas-Liquid Drag Force. Figures 5-7 indicate that the interfacial gas-liquid drag force is comparable to the gas-solid force for at least part of the range of gas velocity considered in the experiments. A model for F_{gl}^{i} is, therefore, required in order to complete the mathematical formulation described in section 2. The objective of the present section is to discuss an analytical framework for interfacial gas-liquid drag in porous media. The anaytical model (Ishii [9]) developed for pipe flow is compared qualitatively to experimental data for porous media flows presented here. Research needs required to complete the model for interfacial drag for two-phase flow in porous media are identified.

Interfacial Drag in Two-Phase Pipe Flow. Consider the

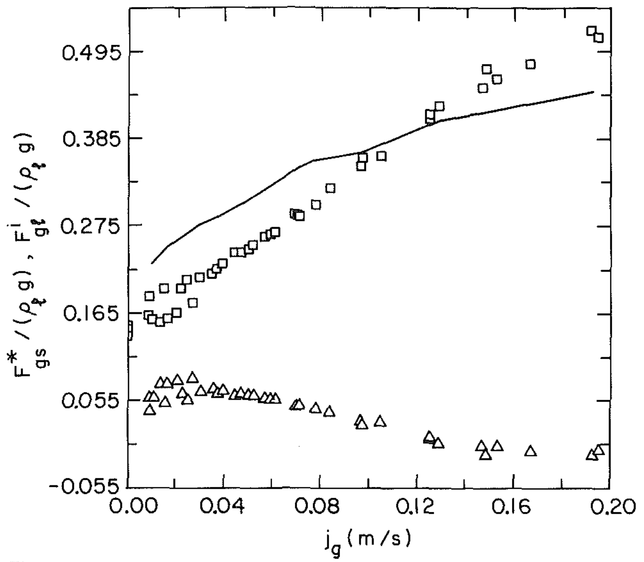

Fig. 5 Gas-solid force, interfacial gas-liquid drag, and modified Lipinski model for the gas-solid force. d = 3.18 mm; □: $F^*_{gs}/(\rho_l g)$; △: $F^i_{gl}/(\rho_l g)$; ___: modified Lipinski model, equation (9).

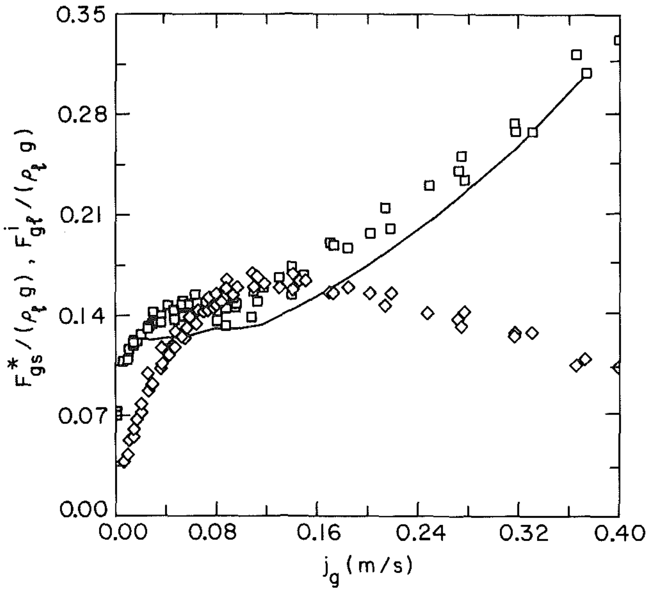

Fig. 6 Gas-solid force, interfacial gas-liquid drag, and modified Lipinski model for the gas-solid force. d = 6.35 mm; □: $F^*_{gs}/(\rho_l g)$; ◇: $F^i_{gl}/(\rho_l g)$; ___: modified Lipinski model, equation (9).

special case of gas bubbling through a stagnant pool of liquid (no porous bed) with negligible wall shear. For this case, $F^*_{gs} = F_{ls} = 0$, and equation (5) yields

$$F^i_{gl}=\alpha(1-\alpha)g(\rho_l-\rho_g) \tag{11}$$

Since both the void fraction and pressure gradient were measured for each experimental condition, the interfacial gas-liquid drag could be determined experimentally either from equations (2) or (3). The F^i_{gl} computed using both of these equations is plotted in Fig. 8, together with the theoretical value given by equation (11). The agreement is good, which is taken to establish the reliability of the experimental methods used in the study.

In general case where wall shear is significant, equation (11) is expected to be inaccurate. A more general approach is, therefore required. Ishii [9] has proposed a formulation based upon the drag of liquid and vapor fluid elements. The interfacial drag force is given by

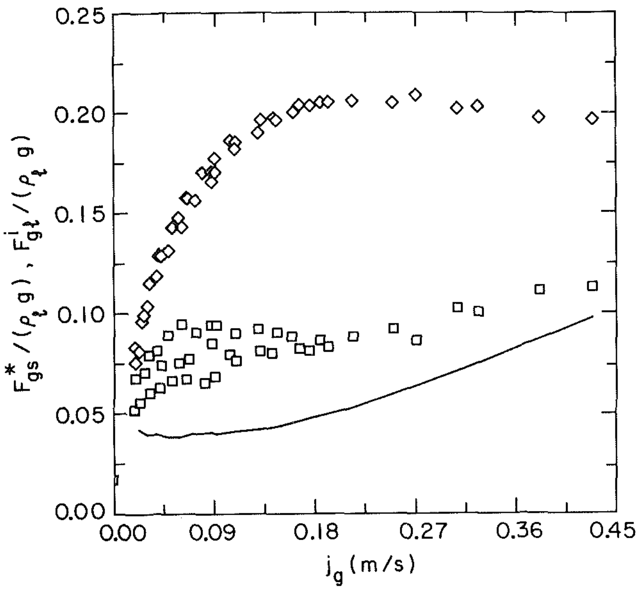

Fig. 7 Gas-solid force, interfacial gas-liquid drag, and modified Lipinski model for the gas-solid force. d = 12.7 mm; □: $F^*_{gs}/(\rho_l g)$; ◇: $F^i_{gl}/(\rho_l g)$; ___: modified Lipinski model, equation (9).

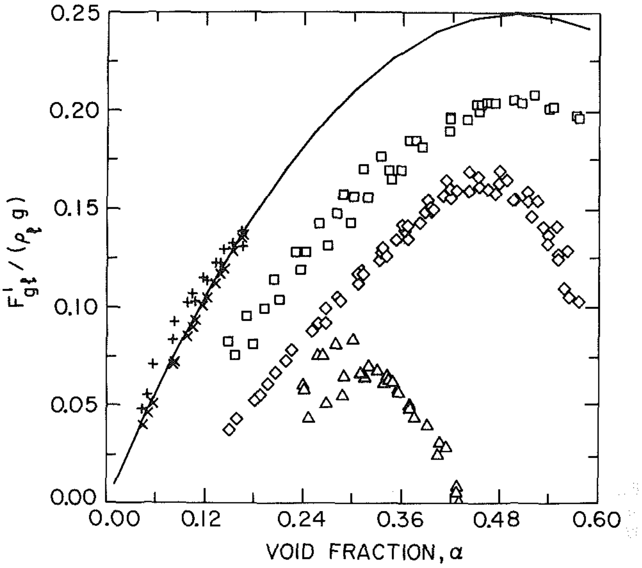

Fig. 8 The interfacial gas-liquid drag as a function of void fraction. ___: $\alpha(1-\alpha)$; X: no porous bed, F^i_{gl} from equation (2); +: no porous bed, F^i_{gl} from equation (3); □: d = 12.7 mm; ◇: 6.35 mm; d = 3.18 mm.

$$F^i_{gl}=a_i\left[\frac{C_D}{4}\left(\frac{r_{sm}}{r_D}\right)\frac{\rho_c|v_r|v_r}{2}\right] \tag{12}$$

In order to use equation (12), relationships for the interfacial area concentration and drag coefficients are required as functions of flow parameter. Ishii has presented recommendations for a_i and C_D that depend upon the two-phase flow regime. For bubbly flow, Ishii recommends

$$C_D=\frac{2}{3}d_b\sqrt{\frac{g(\rho_l-\rho_g)}{\sigma}}\left\{\frac{1+17.67[f(\alpha)]^{\frac{6}{7}}}{18.67f(\alpha)}\right\}^2$$

where

$$f(\alpha)=(1-\alpha)^{1.5}$$

For churn-turbulent flow, the drag coefficient is proposed to be

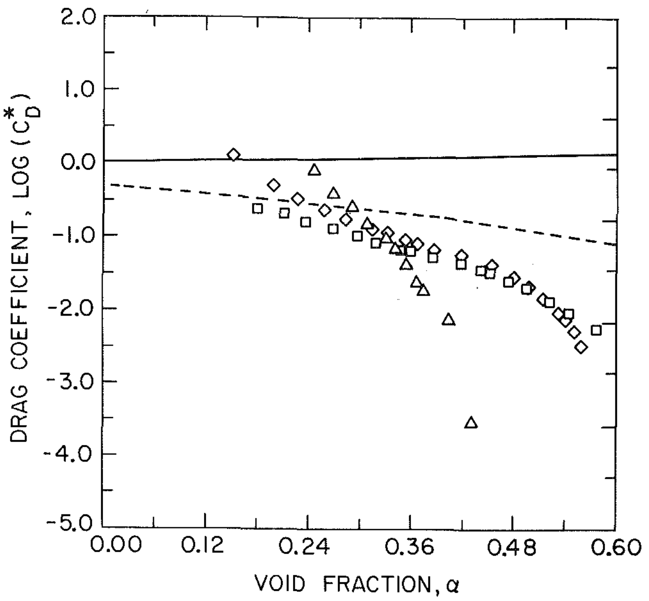

Fig. 9 Computed (Ishii [9]) and measured fluid drag coefficient; No bed: ___bubbly flow; ..... churn flow (d_b = 5 mm); porous bed: △, d = 3.18 mm; ◇, d = 6.35 mm; □, d = 12.7 mm.

$$C_D = \frac{8}{3}(1-\alpha)^2$$

Figure 9 shows the drag coefficient, defined by

$$C_D^* = \frac{C_D}{\frac{2}{3} d_b \sqrt{\frac{g(\rho_l - \rho_g)}{\sigma}}}$$

plotted as a function of void fraction. For the churn-turbulent regime, the bubble radius is chosen as 5 mm. Clearly the behavior of the drag coefficient, as proposed by Ishii for two-phase flow in pipes, is dependent on the flow regime. Similarly, the interfacial area density a_i is also a function of flow regime.

Interfacial Gas-Liquid Drag in Porous Media. The interfacial drag force data for the porous beds are presented in Fig. 8, together with the data for the two-phase pipe flow. The results suggest that as the bed particle size increases, the interfacial drag approaches the prediction given by equation (11) for the case of negligible wall shear. Data for larger particle sizes are required in order to substantiate this apparent trend. The peak value of the interfacial drag for the 12.7 mm particle bed appears to occur for $\alpha = 0.5$, as it is for the pipe flow. The peak in the drag curves shifts to smaller void fraction as the particle size decreases. The interfacial drag force decreases with decreasing particle size. The data of Fig. 8 suggest no simple analog to equation (11) that would be applicable to all three particle beds considered here.

The model proposed by Ishii may also prove to be useful in application to porous bed flows. The applicability of the model represented by equation (12) to two-phase porous media flows is, however, difficult to establish since no relevant data have previously been published for F_{gl}^i, a_i, or C_D. The approach taken here is to assume that the flow regime in the experiments was bubbly and that the bubbles were spheres of some characteristic diameter d_b. Equation (12) is then used to compute the drag coefficient from the basic experimental data. It is further assumed that $r_{sm}/r_D = 1$, $\rho_c = \rho_l$ and that $v_g >> v_l$. For bubbly flow of uniform diameter bubbles, $a_i = 6\alpha/d_b$. Equation (12) can then be written as

$$\frac{F_{gl}^i}{\rho_l g} = \frac{3\, j_g^2}{4\, d_b g \epsilon^2 \alpha} C_D \qquad (13)$$

The drag coefficient C_D^* is, then,

$$C_D^* = \frac{2\,\alpha\epsilon^2}{j_g^2} \frac{F_{gl}^i}{\rho_l g} \sqrt{\frac{\sigma g}{(\rho_l - \rho_g)}} \qquad (14)$$

This quantity was computed from the data using j_g, α, and F_{gl}^i, which were measured for each particle bed experimental condition.

The interfacial drag coefficients for porous beds of three particle sizes, computed from the data using equation (14), are presented in Fig. 9 along with the drag coefficients for two-phase flow in pipes. The 12.7 mm and 6.35 mm data follow each other closely over most of the range of void fraction considered, but appear to deviate at the low and high end of the void fraction range. The drag coefficients for the 3.18 mm particles deviate markedly from the remaining data. This observation suggests that the two-phase flow regime for the 3.18 mm particles was different from the flow regime in the other particle beds.

The drag coefficient results shown in Fig. 9 are difficult to interpret. A major reason for this difficulty is the lack of flow regime information associated with each of the data points. This is due to two factors: (*i*) the interfacial area density implicit in equation (14) is characteristic of the bubbly flow regime, (*ii*) the difference in behavior between the results for different particle size beds may be attributable to changes in flow regime. Further basic experiments, which would provide data on the interfacial area density and drag coefficients, and the flow regimes associated with each measurement, are required. This additional research is necessary in order to complete the development and evaluation of the interfacial gas-liquid drag model for two-phase flow in porous media.

The interfacial drag model represented by equation (12) is, at this time, of limited usefulness because of the difficulties in interpretation discussed. While it is possible to use the data shown in Fig. 9 together with equation (12) to predict the interfacial drag, additional work is required it order to evaluate and further develop the basic approach. The work presented here, however, should provide a basic framework for future development.

5.3 Wall Effect. Since the ratio of vessel diameter to particle diameter is only 7.4 for 12.7 mm spheres, the errors in the measured values of F_{gs}^* and F_{gl}^i could be large due to wall effects in this case. For single-phase flows through a porous medium, Coulson [10] has recommended an empirical wall correction factor A_w, which is defined as the ratio of the frictional pressure drop in an infinite diameter vessel to the frictional pressure drop as actually measured in the finite vessel. Although there is no reason to expect the same wall correction factor to be valid for two-phase flow, we could use this to get a qualitative estimate of the errors due to the wall effect. Since $F_{ls} = 0$ for our experiments, equation (4) and the foregoing defintion of A_w implies

$$(F_{gs}^*)_m = F_{gs}^* + a_w F_{gs}^*$$

where the subscripts m denotes the measured value (as opposed to the true value) and $a_w = (-1 + 1/A_w)$. Here we have neglected the surface binding force $F_{g\sigma}$ which should not contribute to the frictional pressure drop. Using equations (3) and (4) it is now easy to show that

$$\left\{ (F_{gl}^i)_m - F_{gl}^i \right\} / F_{gl}^i = -(1-\alpha) a_w F_{gs}^* / F_{gl}^i$$

or

$$\left| \text{Relative Error in } F_{gl}^i \right| \leq (1-\alpha) a_w (F_{gs}^*)_m / (F_{gl}^i)_m$$

Now for 12.7 mm spheres $A_w = 0.865$, $a_w = 0.156$, and $(F_{gs}^*)_m / (F_{gl}^i)_m \approx 0.5$. This implies an error of less than 4.7 percent (assuming $\alpha = 0.4$) in $(F_{gl}^i)_m$, which is well within the scatter in the data. Of course the relative error in $(F_{gs}^*)_m$ could be rather large at 15.6 percent. However, since F_{gs}^* is small for

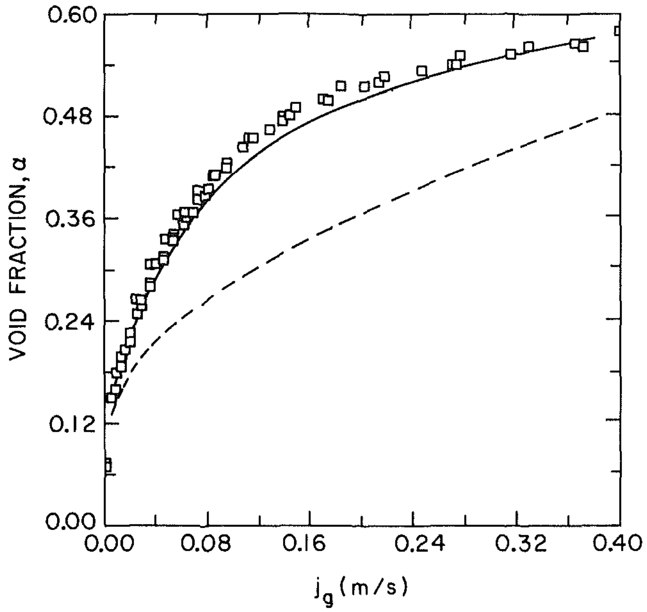

Fig. 10 Void fraction prediction for 6.35 mm spheres. □: data; ___: prediction with F^i_{gl} from equation (15); -----: prediction with $F^i_{gl} = 0$; F^*_{gs} as modeled by equation (9).

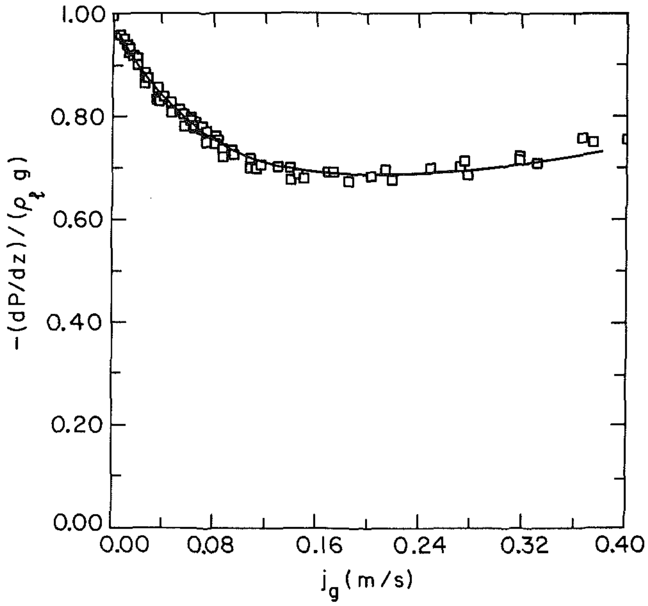

Fig. 11 Pressure gradient prediction for 6.35 mm spheres. □: data; ___: prediction with F^i_{gl} with equation (15); $-(dP/dz)/(\rho_l g) \equiv 1.0$ if $F^i_{gl} = 0$; F^*_{gs} as modeled by equation (9).

12.7 mm spheres, the scatter in the measured values of $(F^*_{gs})_m$ is of the same order (see Fig. 7).

5.4 Prediction of α and dP/dz. In this section we demonstrate the importance of including the interfacial gas-liquid drag in predicting the void fraction and pressure gradient accurately. For our experiments, $F_{ls} = 0$, and therefore, if F^i_{gl} is neglected, equation (3) predicts that $-(dP/dz) = \rho_l g$. This obviously does not agree with our measurements, although for 3.18 mm spheres the deviation is small. Since the F^*_{gs}, as predicted by equation (9), shows reasonable agreement with the data for 6.35 mm spheres, and also because for this case F^i_{gl} and F^*_{gs} are of the same order, this case was selected for prediction of α and dP/dz. The following expression was found to give good agreement with the measurements of F^i_{gl} for 6.35 mm spheres

$$\frac{F^i_{gl}}{\rho_l g} = 1.531(\alpha-\alpha_0)^{1.5}\left\{1-1.772(\alpha-\alpha_0)\right\}^{0.7} \tag{15}$$

where α_0 is given by equation (10). Equations (2) and (3) were then solved for the two unknowns α and dP/dz both by including this expression for F^i_{gl} and by neglecting it. The results shown in Figs. 10 and 11 clearly demonstrate that the interfacial gas-liquid drag must be included in a two-fluid model describing a two-phase flow through a high permeability porous bed.

6 Conclusions

Experiments involving the measurement of two-phase pressure drop and void fraction during a two-phase (air-water) flow through porous beds of randomly packed spheres have been performed for the case of zero net liquid flux through the bed. These measurements, together with the fundamental momentum balance equations for the two phases, were used to compute the gas-solid drag, and the gas-liquid interfacial drag as a function of the gas flux.

The following conclusions are drawn from the results presented here:

(*i*) For beds of large particle size (dia ≥ 6 mm), the gas-liquid interfacial drag term is of the same order as the gas-solid term and cannot, in general, be neglected. For a given particle bed, the interfacial gas-liquid drag term is important, in particular at low superficial velocities.

(*ii*) A finite gas-solid surface binding force F_{g_o} is measured at zero gas flux. This is attributed to the gas trapped within the bed when the gas is shut off. The volume fraction of trapped gas decreases with increasing bed particle diameter.

(*iii*) The measured gas-solid force agrees reasonably well with a form of the Lipinski [6] model, which was modified to account for the volume fraction of trapped gas.

(*iv*) The behavior of the gas-liquid interfacial drag force with void fraction approaches that of a two-phase flow with negligible wall shear as the bed particle size increases. This conclusion applies to a maximum bed particle size tested of 12.7 mm.

(*v*) A fluid drag model (application of Ishii [9] approach) to characterize the gas-liquid interfacial drag force was evaluated. The computed drag coefficients display features which suggest that the two-phase porous bed flow regimes must be identified experimentally.

References

1 Vasiliev, L. L., and Maiorov, V. A., "An Analytical Study of Resistance, Heat Transfer and Stability in Evaporative Cooling of a Porous Heat Producing Element," *International Journal of Heat and Mass Transfer*, Vol. 22, 1979, pp. 301-307.

2 Maron, D. M., and Cohen, S., "Non-Darcy Flow with Change of Phase in Internally Energized Flat Shaped Porous Element," *International Journal of Heat and Mass Transfer*, Vol. 22, No. 8, Aug. 1979, pp. 1165-1174.

3 Naik, A. S., and Dhir, V. K., "Forced Flow Evaporative Cooling of a Volumetrically Heated Porous Layer," *International Journal of Heat and Mass Transfer*, Vol. 25, No. 4, 1982, pp. 541-552.

4 Lipinski, R. J., "A Particle-Bed Dryout Model with Upward and Downward Boiling," *Trans. Am. Nucl. Soc.*, Vol. 35, 1980, pp. 358-360.

5 Gabor, J. D., Epstein, M., Jones, S. W., and Cassulo, J. C., "Status Report on Limiting Heat Fluxes in Debris Beds," ANL/RAS 80-21, Sept. 1980, Argonne National Laboratory, Argonne, Ill.

6 Lipinski, R. J., "A Model for Boiling and Dryout in Particle Beds," NUREG/CR-2646, SAND 82-0765, 1982, Sandia National Laboratory, Albuquerque, N.M.

7 Scheidegger, A. E., *The Physics of Flow Through Porous Media*, University of Toronto Press, 1974.

8 Dhir, V. K., Chu, W., Lee, H., and Catton, I., "On the Hydrodynamic Characteristics of Two-Phase Flow Through Porous Media," Presented at the Joint NRC/ANS Meeting on Basic Thermal-Hydraulic Mechanism in LWR Analysis, Sept. 14-15, 1982, Bethesda, Md.

9 Ishii, M., and Mishima, K., "Study of Two Fluid Model and Interfacial Area," NUREG/CR-1873, ANL-80-111, 1980, Argonne National Laboratory, Argonne, Ill.

10 Coulson, J. M., "The Flow of Fluids Through Granular Beds: Effect of Particle Shape and Voids in Steamline Flow," *Trans. Inst. Chem. Eng.*, Vol. 27, 1949, pp. 237-257.

Optimization of Cooled Shields in Insulations

J. C. Chato
Fellow ASME

J. M. Khodadadi
Student Mem. ASME

Department of Mechanical
and Industrial Engineering,
University of Illinois at Urbana-Champaign,
Urbana, Ill. 61801

A relatively simple method has been developed to optimize the location, temperature, and heat dissipation rate of each cooled shield inside an insulation layer. The method is based on the minimization of the entropy production rate, which is proportional to the heat leak across the insulation. The results show that the maximum number of shields to be used in most practical applications is three. However, cooled shields are useful only at low values of the overall, cold wall to hot wall absolute temperature ratio. The performance of the insulation system is relatively insensitive to deviations from the optimum values of temperature and location of the cooling shields. Design curves are presented for rapid estimates of the locations and temperatures of cooling shields in various types of insulations, and an equation is given for calculating the cooling loads for the shields.

Introduction

The search for the ultimate, energy-efficient insulation system has led in the past few years to a fascinating rediscovery and application of some fundamental concepts of thermodynamics: specifically, the second law and the use of entropy production rates and availability (or exergy) for design optimization purposes. The classical approach has been to minimize the heat flow between surfaces at different temperatures.

The concept of a single, vapor-cooled shield in an insulation has been treated theoretically as far back as 1959 in Scott's classic textbook on cryogenics [1], and designs employing them were described not much later [2]. Paivanas et al. obtained a patent [3] and later reported on the use of uniformly spaced multiple shields that were cooled by the boil-off from the insulated dewar [4]. Eyssa and Okasha [5] considered only radiative heat exchange between shields and minimized the total refrigeration power required. Hilal et al. [6, 7] used a similar minimization of refrigeration power as the design basis. Related works were reported by Bejan et al. [8-11].

Recently, Bejan [12] proposed a new point of view, based on the second law of thermodynamics, which considers thermal insulations as dissipators of useful mechanical power (i.e., the availability or exergy) or, alternately, as generators of irreversibility or entropy. Thus, in this method, optimization of an insulation corresponds to minimization of either the entropy production rate or the irreversibility, or the decrease of availability. Various applications of this concept to insulation systems have been documented subsequently [13, 14].

Our work grew out of an examination of Cunnington's paper [13], who utilized a numerical technique to find optimum temperatures at given locations for one and two shields for a thermal conductivity function of the form $k_1 T^{0.6}$. Although several equations seemed to be incorrectly printed, we have found two of the design curves to be essentially correct. Thus our purpose was:

1 To develop a simple optimization technique
2 To generalize the results to a broader class of insulations
3 To develop simple design methods for cooled shields

Analysis

We accept the previously developed concept that to optimize an insulation system is equivalent to minimizing the entropy production rate. In addition, we assume one-dimensional heat flow and that the heat capacity of the boil-off gas is adequate to do the cooling for all shields and does not impose a restriction on the optimization. In contrast to Bejan [9, 11], who has developed a constrained optimization based on the heat capacity of the boil-off, we employ the argument that in most practical systems the boil-off is generated by cooling of some equipment in addition to the heat leakage across the insulation.

Parallel heat paths, e.g., supports, have not been considered. However, each path can be optimized separately using its own thermal conductivity function. Then a decision has to be made whether the two structures should be independently cooled at their respective optimum conditions.

We examine the general situation of an insulation where equivalent thermal conductivity k can be expressed as a two-term function of the absolute temperature

$$k = k_1 T^m + k_2 T^n \tag{1}$$

where, typically, the first term represents actual conduction with $m \cong 1$ and the second term represents radiation with $n \cong 3$. In the following, m and n can be any value except -1.

The heat flow across a layer of insulation can be expressed in terms of Fourier's law (see Fig. 1)

$$q\,dx = Ak\,dT \tag{2}$$

Substituting k from equation (1) and integrating across a layer from one end at 1, to the other at 2, yields

$$q = \frac{A}{x_2 - x_1}\left[\frac{k_1}{m+1}\left(T_2^{m+1} - T_1^{m+1}\right) + \frac{k_2}{n+1}\left(T_2^{n+1} - T_1^{n+1}\right)\right] \tag{3}$$

Now consider the insulation with a cooled shield at T_S located at x between a hot surface at T_H and a cold one at T_C, separated by the insulation thickness t, as shown in Fig. 1(*a*). The entropy production rate for the insulation can be determined from the heat flows and temperatures as follows

$$\dot{S} = -\frac{q_H}{T_H} + \frac{q_C}{T_C} + \frac{q_S}{T_S} \tag{4}$$

where $q_S = q_H - q_C$.

The heat flow terms can be expressed in the form of equation (3) and the resulting expression can be nondimensionalized using the following terms

$$s \equiv \frac{\dot{S}t}{Ak_H} \quad \text{where } k_H = k \text{ at } T_H \tag{5}$$

Contributed by the Heat Transfer Division and presented at the ASME Winter Annual Meeting, Boston, Massachusetts, November 13-18, 1983. Manuscript received by the Heat Transfer Division July 25, 1983. Paper No. 83-WA/HT-57.

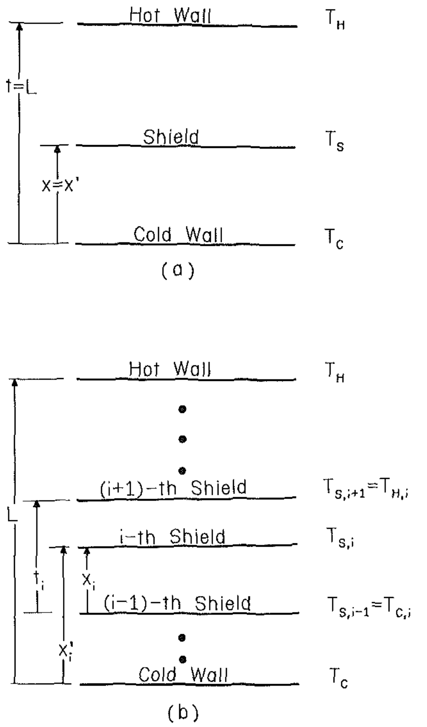

Fig. 1 Schematic of the nomenclature for (*a*) single and (*b*) multiple shields

$$P \equiv \frac{T_S}{T_C} \tag{6}$$

$$R \equiv \frac{T_C}{T_H}, \tag{7}$$

$$\gamma \equiv \frac{k_2(m+1)}{k_1(n+1)} T_H^{n-m} \tag{8}$$

and

$$X \equiv \frac{x}{t} \tag{9}$$

The resulting equation is

$$\begin{aligned} s(m+1)\left(1+\gamma\frac{n+1}{m+1}\right) &= \frac{1}{1-X}\{[(PR)^{m+1}-(PR)^m-1+(PR)^{-1}] \\ &\quad +\gamma[(PR)^{n+1}-(PR)^n-1+(PR)^{-1}]\} \\ &\quad +\frac{1}{X}\{R^m[P^{m+1}-P^m-1+P^{-1}] \\ &\quad +\gamma R^n[P^{n+1}-P^n-1+P^{-1}]\} \end{aligned} \tag{10}$$

Since R, the overall temperature ratio, is generally known, s is a function of P and X, and its extreme value can be found by differentiating it with respect to each variable separately and setting the results equal to zero. This procedure yields two equations to be solved simultaneously: $\partial s/\partial P=0$ and $\partial s/\partial X=0$. Because of the regular form of the expressions, one of the final two equations contains only a single unknown as follows

$$\frac{R^m F(m,P)+\gamma R^n F(n,P)}{[R^{m-1}D(m,P)+\gamma R^{n-1}D(n,P)]^2} = \frac{F(m,PR)+\gamma F(n,PR)}{[D(m,PR)+\gamma D(n,PR)]^2} \tag{11}$$

$$\frac{X}{1-X} = -\frac{R^{m-1}D(m,P)+\gamma R^{n-1}D(n,P)}{D(m,PR)+\gamma D(n,PR)} \tag{12}$$

where the following functionals were used

$$F(b,B) \equiv B^{b+1}-B^b-1+B^{-1} \tag{13}$$

$$D(b,B) \equiv (b+1)B^b - bB^{b-1} - B^{-2} \tag{14}$$

Thus, to find the optimum temperature and location for a shield, equation (11) can be solved for P, and then X can be calculated from equation (12). The heat to be removed by the shield $q_S=q_H-q_C$ can be found, as before, from equation (3). In dimensionless form the equation becomes

$$\begin{aligned} \frac{q_S t}{Ak_H T_H}(m+1)\left(1+\gamma\frac{n+1}{m+1}\right) &= \frac{1-(PR)^{m+1}+\gamma[1-(PR)^{n+1}]}{1-X} \\ &\quad - \frac{(PR)^{m+1}-R^{m+1}+\gamma[(PR)^{n+1}-R^{n+1}]}{X} \end{aligned} \tag{15}$$

For multiple shields t_i represents the distance between the two surfaces surrounding the ith shield on either side, $T_{H,i}$ and $T_{C,i}$ are the temperatures of these two surfaces, $X_i=x_i/t_i$ is the location of the shield relative to t_i, and x'_i is the location of the shield relative to the cold wall as shown in Fig. 1(*b*). To determine the optimum temperatures and locations for multiple shields, first we assumed a temperature for the first shield next to the cold wall, then we used equations (11) and (12) to find the temperature and location of the second shield. This process was repeated for the rest of the shields and the hot wall. Thus each shield was optimized consecutively with respect to the two surfaces on either side. With given values of

Nomenclature

A = area of heat flow, m^2
D = functional defined by equation (14)
F = functional defined by equation (13)
k = thermal conductivity, W/m-K; with subscripts, coefficients in equation (1)
L = overall thickness of insulation, m^1
m,n = exponents in conductivity function, equation (1)
P = T_S/T_C, temperature ratio
q = heat flow rate, W
R = T_C/T_H, overall temperature ratio
s = dimensionless entropy production rate defined by equation (5)
$\dot{S}$ = entropy production rate, W/K
t = thickness between walls with single shield between, m^1
T = absolute temperature, K
x = distance from cold wall, m^1
x' = distance from cold wall in a multi-shield configuration, m^1
X = x/t, dimensionless distance^1
X' = x'/L, dimensionless distance^1
γ = defined by equation (8)

Subscripts

C = cold wall
H = hot wall
i = ith shield
min = minimum
opt = optimum
S = shield

---

[1] For systems with single shield $L=t$, $x=x'$, $X=X'$

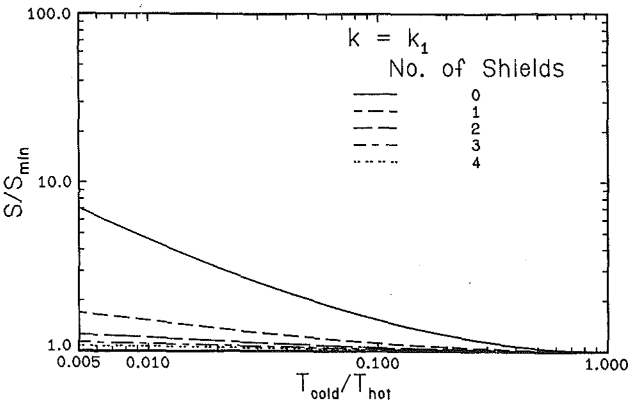

Fig. 2 The effect of optimally cooled shields on the entropy production rates for $k = k_1$

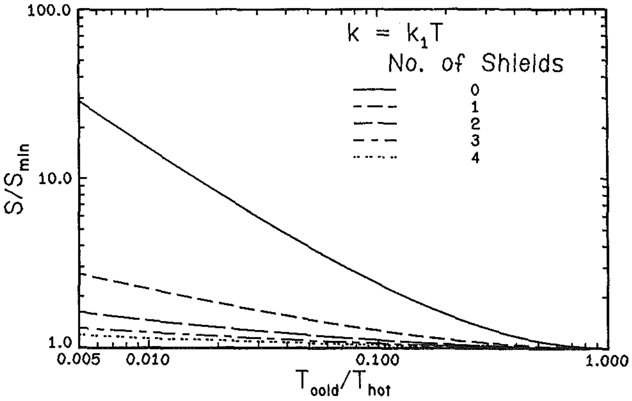

Fig. 3 The effect of optimally cooled shields on the entropy production rates for $k = k_1 T$

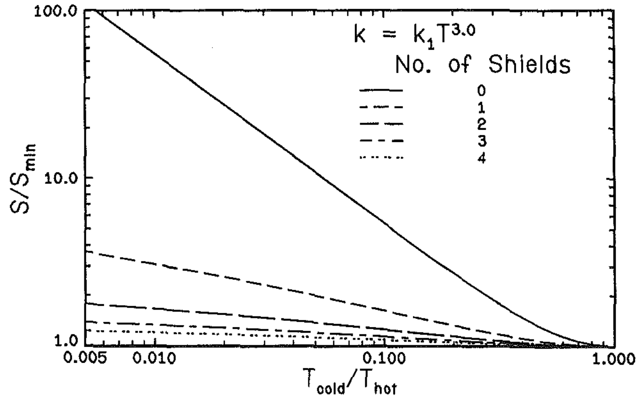

Fig. 4 The effect of optimally cooled shields on the entropy production rates for $k = k_1 T^3$

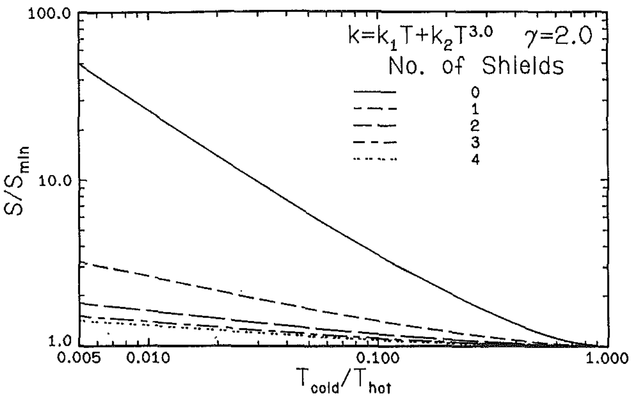

Fig. 5 The effect of optimally cooled shields on the entropy production rates for $k = k_1 T + k_2 T^3$ with $\gamma = 2$

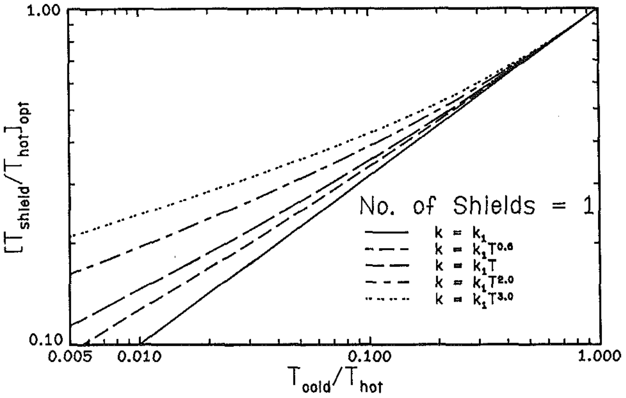

Fig. 6 The effect of the exponent m in $k = k_1 T^m$ on the optimal shield temperature

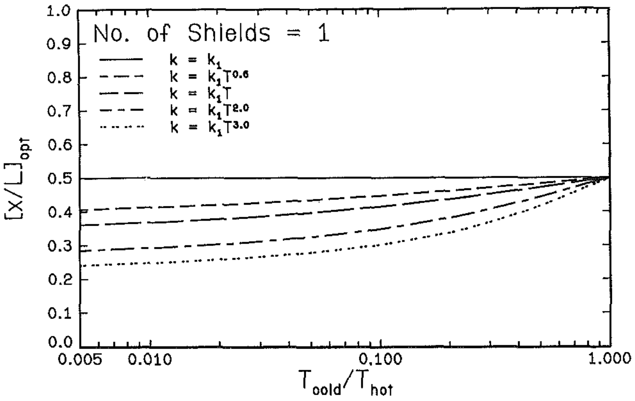

Fig. 7 The effect of the exponent m in $k = k_1 T^m$ on the optimal shield location

the overall temperature ratio R and of the number of shields, the process requires iterative solution.

To put the results into proper perspective, the entropy production rates can be compared to the thermodynamically minimum rate obtainable through spatially continuous cooling. According to Bejan [12], this rate is

$$\dot{S}_{\min} = \frac{A}{t}\left[\int_{T_C}^{T_H} (k)^{1/2} T^{-1} dT\right]^2 \tag{16}$$

This expression was evaluated analytically for the single-term functions of k, i.e., for $\gamma = 0$, and numerically otherwise.

Results and Discussion

Figures 2–5 show the relative entropy production rates for various thermal conductivity functions and for up to four optimally cooled shields as functions of the overall temperature ratio $R \equiv T_C/T_H$. The curves show that the entropy production rate increases with decreasing values of the temperature ratio R and with increasing values of the exponents m and n. Adding shields, of course, reduces the entropy production rate; but for most of the practical temperature range, say $0.01 < R < 1.0$, only three shields contribute to significant decreases and adding a fourth shield can be considered unnecessary. No shields are useful at high values of R; but this "high" range is strongly dependent on the exponent of the temperature as can be seen in Figs. 2–5. Similar curves developed with $k = k_1\ T^{0.6}$ for one and two shields were very close to those given by Cunnington [13], converted appropriately.

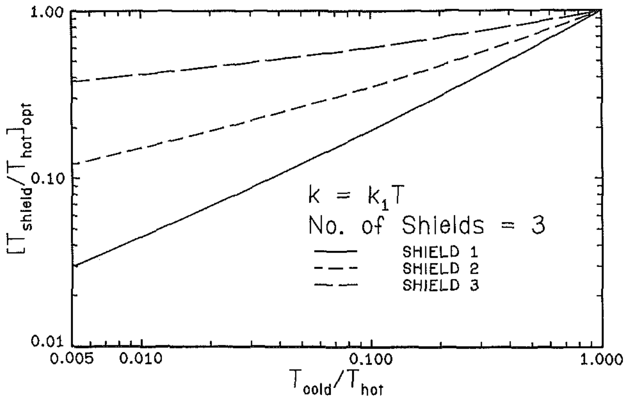

Fig. 8 Optimal shield temperatures for three shields with $k = k_1T$

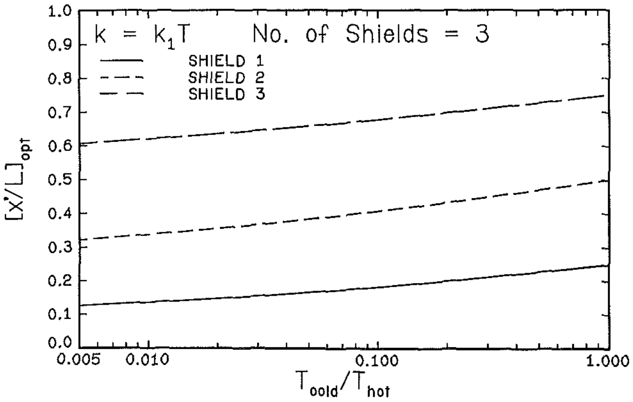

Fig. 9 Optimal shield locations for three shields with $k = k_1T$

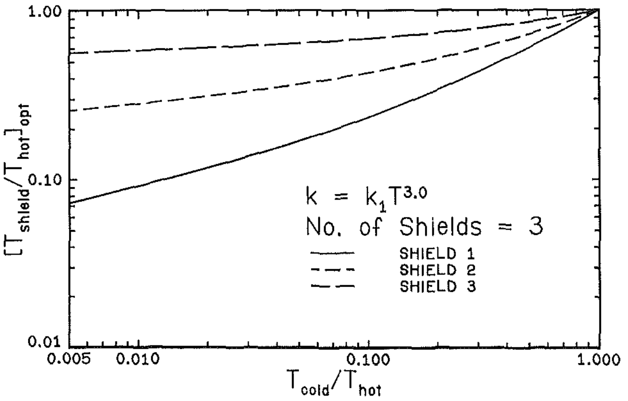

Fig. 10 Optimal shield temperatures for three shields with $k = k_1T^3$

Study of the results of two-term conductivities, e.g., Fig. 5, reveals that the curves fall between those obtained for each of the two terms alone. If γ is small the first term, T^m, dominates; whereas if γ is large (>10), the second term, T^n, controls. Thus general conclusions can be drawn from examining the results of the single-term conductivities.

Figures 6 and 7 show the optimum, single-shield temperature ratios $PR=T_S/T_H$ and locations $X=x/L$ for five conductivity functions. Both of these quantities generally decrease with decreasing R. Figures 8-11 show typical shield temperatures and locations for systems with three shields and for two single-term conductivities, k_1T and k_1T^3. The results are strongly nonlinear. For example, for k_1T^3 and $R=0.01$, the optimum temperature ratios are about 0.09, 0.3, and 0.6, and the optimum locations are about 0.05, 0.2, and 0.5. As is to be expected, our unconstrained optimization yields a somewhat better performance per shield than Bejan's [9, 11] constrained method.

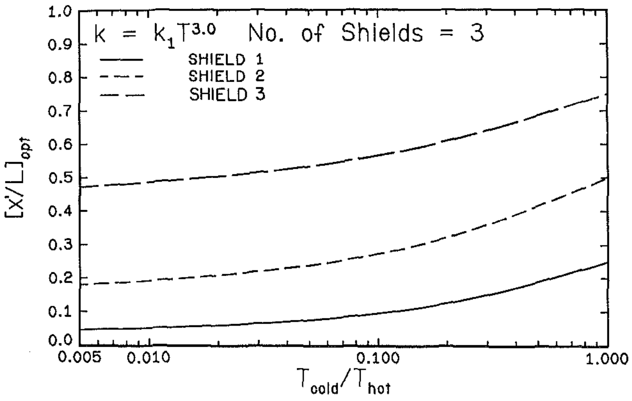

Fig. 11 Optimal shield locations for three shields with $k = k_1T^3$

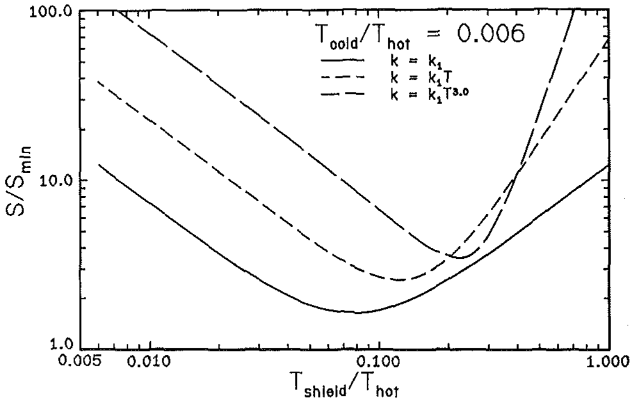

Fig. 12 System sensitivity to deviations from the optimum shield temperature for one shield

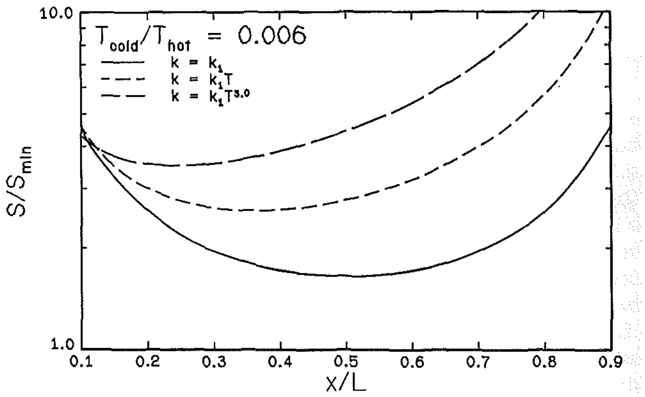

Fig. 13 System sensitivity to deviations from the optimum shield location for one shield

The sensitivities of the entropy production rates to deviations from the optimum values of PR and X are demonstrated in Figs. 12 and 13 for single shields. The sensitivity increases with the value of the exponents m and n, but the curves are relatively flat near the minima. A ±20 percent change from optimum, for example, has negligible effect. Thus the system is relatively tolerant of deviations from the optimum design conditions.

Calculations with two different conductivities on the two sides of a cooled shield show that using the better insulator on both sides always yields the optimum condition. However, if for some reason two types of insulations have to be used, then the better insulator should be placed on the warm side of the shield.

Conclusions

A relatively simple method has been developed to optimize the temperatures, locations, and heat dissipation rates for cooled shields inside an insulation layer. The method consists of solving one nonlinear algebraic equation for the optimum temperature, equation (11), then substituting into equation (12) to obtain the optimum location for a cooled shield with respect to the two surfaces on either side. For multiple shields, the same calculations are performed consecutively for each cooled shield starting from one boundary, preferably the cold wall. A series of design curves have been presented for a range of thermal conductivity functions and number of cooled shields to facilitate estimates for optimum configurations.

The main conclusions are:

1 The maximum number of useful shields is generally three. Additional shields improve the system only marginally but add complexity and weight, and should be considered only if additional, nonthermodynamic conditions warrant.

2 For high values of the overall temperature ratio R, even a single shield can be superfluous.

3 The results are relatively insensitive to the exact values of the temperature ratios PR and locations X. Deviations of ±20 percent can easily be tolerated.

4 If two different insulations have to be used on the two sides of a cooled shield, then the better insulator should be on the warm side. However, using only the better insulator on both sides will provide a lower heat leak.

Acknowledgments

This work was supported in part by NASA Grant No. NAG2-219. Dr. Peter Kittel of NASA-Ames Research Center provided invaluable help.

References

1 Scott, R. B., *Cryogenic Engineering*, D. Van Nostrand Co., Princeton, N.J., 1959.

2 Murto, P. J., "A Gas-Shielded Storage and Transport Vessel for Liquid Helium," *Advances in Cryogenic Engineering*, Vol. 7, 1962, pp. 291–295.

3 Paivanas, J. A., Francis, A. W., and Wang, D. I-J., "US Patent No. 3, 133, 422, "Insulation Construction," May 19, 1964.

4 Paivanas, J. A., Roberts, O. P., and Wang, D. I-J., "Multishielding—An Advanced Superinsulation Technique," *Advances in Cryogenic Engineering*, Vol. 10, 1965, pp. 197–207.

5 Eyssa, Y. M., and Okasha, O., "Thermodynamic Optimization of Thermal Radiation Shields for a Cryogenic Apparatus," *Cryogenics*, Vol. 18, 1978, pp. 305–307.

6 Hilal, M. A., and Boom, R. W., "Optimization of Mechanical Supports for Large Superconductive Magnets," *Advances in Cryogenic Engineering*, Vol. 22, 1977, pp. 224–232.

7 Hilal, M. A., and Eyssa, Y. M., "Minimization of Refrigeration Power for Large Cryogenic Systems," *Advances in Cryogenic Engineering*, Vol. 25, 1980, pp. 350–357.

8 Bejan, A., and Smith, J. L., Jr., "Thermodynamic Optimization of Mechanical Supports for Cryogenic Apparatus," *Cryogenics*, Vol. 14, 1974, pp. 158–163.

9 Bejan, A., "Discrete Cooling of Low Heat Leak Supports to 4.2K," *Cryogenics*, Vol. 15, 1975, pp. 290–292.

10 Bejan, A., and Smith, J. L., Jr., "Heat Exchangers for Vapor-Cooled Conducting Supports of Cryostats," *Advances in Cryogenic Engineering*, Vol. 21, 1976, pp. 247–256.

11 Bejan, A., *Entropy Generation through Heat and Fluid Flow*, ch. 9, Wiley-Interscience, N.Y., 1982.

12 Bejan, A., "A General Variational Principle for Thermal Insulation System Design," *International Journal of Heat and Mass Transfer*, Vol. 22, 1979, pp. 219–227.

13 Cunnington, G. R., "Thermodynamic Optimization of a Cryogenic Storage System for Minimum Boiloff," No. AIAA-82-0075, AIAA 20th Aerospace Sciences Meeting, Orlando, Fla., 1982.

14 Schultz, W., and Bejan, A., "Exergy Conservation in Parallel Thermal Insulation Systems," *International Journal of Heat and Mass Transfer*, Vol. 26, 1983, pp. 335–340.

Boundary Elements for Static Optimal Heating of Solids

R. A. Meric

Marmara Scientific and Industrial
Research Institute,
Applied Mathematics Division,
Gebze, Kocaeli, Turkey

The static optimal heating of solids by a boundary heat flux has been formulated for a solid of arbitrary geometry. Through the use of a Lagrange multiplier the problem is reduced to an unconstrained optimization problem. The necessary conditions for optimality of a performance index that characterizes the physical objectives are first found by calculus of variations. An iterational numerical procedure is then proposed in which the elliptic equations for the temperature and the Lagrange multiplier are solved by the boundary element method, and better estimates for the boundary heat flux are found by the minimization of the performance index through the conjugate gradient method of optimization. Numerical results are also provided for a two-dimensional problem.

Introduction

Optimal heating of solids is an important branch of engineering in which a solid material is optimally heated by boundary heat fluxes or distributed heat sources inside the body such that some desired distributions of temperature and/or its gradients are achieved in the body with a minimum amount of "applied energy." Such optimization problems may find their applications mostly in manufacturing industries, e.g., in iron-and-steel and glass technologies [1, 2].

In the case of nontransient, i.e., static, optimization problems the time variable does not appear and the physical systems to be optimized are usually described by elliptic partial differential equations (PDE). Such static optimization problems fall into the realm of optimal control problems of distributed parameter systems (DPS), which generally deal with elliptic, parabolic, or hyperbolic systems [3].

In optimization problems, the desired physical objectives of the problem are usually cast into an integral functional, the so-called performance index. The necessary conditions for the minimization of this performance index under the system equation constraint (e.g., the heat conduction equation) may be found by using the Lagrange multiplier method and the calculus of variations. In the end, coupled elliptic PDE are obtained in terms of the state function system variable (in this case, the temperature of the body) and the Lagrange multiplier function.

For a solid body of arbitrary geometry the solution of PDE and the minimization of an integral functional is impossible by analytical means. Appropriate numerical methods must be introduced in order to discretize the problem spatially. The finite difference methods (FDM) and the finite element methods (FEM) are two numerical methods that can be applied to such problems [4-8]. In [5], a two-dimensional static optimization problem has been analyzed by solving the necessary conditions for optimality directly via the FEM without formulating the problem as a mathematical programming (MP) problem as in the present investigation. Furthermore, both the "control" and the "observation" in the optimization problem have been taken in the solution domain. In [6-8], on the other hand, one-dimensional transient or dynamic optimal control problems are solved by adopting different numerical solution strategies in order to minimize performance indices.

The boundary element method (BEM) has recently proven to be another powerful numerical discretization technique, especially for problems governed by elliptic PDE [9]. This technique has some special advantages over the "domain" type of methods, such as the FDM and FEM. Using the BEM, any arbitrarily shaped geometry, including infinite boundaries, can be handled easily. In addition, since the discretizations are only made on the boundary surface of the problem domain the dimensionality of the problem is practically reduced by one involving less number of unknown variables (thus, savings in computer storage). Ease of data preparation and checking in computer programming can also be mentioned as other advantages of the BEM.

In this investigation, first, the static optimal heating problem of an arbitrary solid will be described in general terms. The formulation of the problem will encompass two- or three-dimensional problems. A boundary heat flux will constitute the controlling "applied energy" function in the problem. The physical objectives of the optimization problem will be the desired distributions of temperature in the whole solid body and of the heat flux in some parts of the boundary. The necessary conditions for optimality of the performance index will then be obtained through the calculus of variations.

The space discretization of the resulting PDE will be achieved by means of the BEM [10]. In [10], the heat optimization problem investigated is of the type called boundary-control and -observation. Thus no domain integrations are needed in the numerical procedure. Also the coupling of the variables in the necessary conditions for optimality occurs only in the boundary conditions and not in the PDE's.

The adopted numerical method, i.e., the BEM, will enable us to obtain accurate solutions of temperature and also the normal temperature gradients on the boundary that are needed in the evaluation of the performance index. In the BEM the temperature and its normal gradient are both interpolated over the boundary elements independently. Hence the same order of accuracy is maintained for the gradient values as for the variables, themselves, as contrast to the other methods. Therefore, the direct and efficient numerical solution of the normal temperature gradients by the BEM is of much significance in this optimization problem, and hence distinguishes the BEM from the other numerical methods, namely, the FDM and FEM.

After spatial discretization the problem may be treated as an MP problem in which the minimization of the performance index will be achieved by means of the conjugate gradient method (CGM) of optimization. The CGM is an iterational technique that utilizes the first-order derivatives of the function with respect to the minimizing set of variables, in this case, the discretized applied boundary heat flux distribution.

A simple model problem in two dimensions with a square plate taken as the solid body is then numerically investigated after the general formulation of the problem. Numerical

---

Contributed by the Heat Transfer Division for publication in the JOURNAL OF HEAT TRANSFER. Manuscript received by the Heat Transfer Division March 14, 1984.

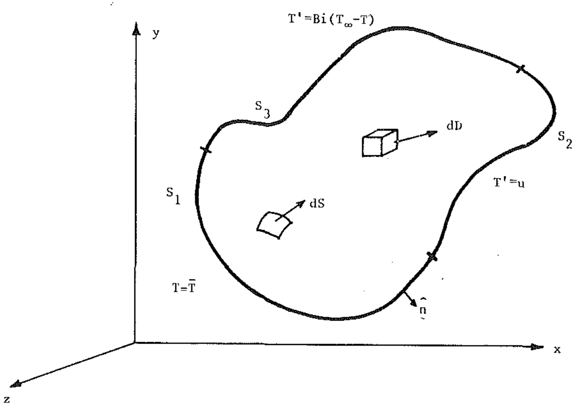

Fig. 1 Problem geometry and boundary conditions

solutions are provided for various values of the physical parameters and also for weighting parameters appearing in the performance index.

Statement of the Optimization Problem

Consider a homogeneous isotropic solid body of arbitrary geometry in three-dimensions (see, Fig. 1). The steady-state heat conduction in the body is governed by

$$\nabla^2 T = 0 \text{ in } D \tag{1}$$

where T is the temperature and D denotes the arbitrary physical domain of interest. The boundary surface S of the solid body may be divided into three parts S_i (i = 1, 2, 3) on which different kinds of boundary conditions may be applied, hence

$$T = \bar{T} \text{ on } S_1 \tag{2}$$

$$T' = u \text{ on } S_2 \tag{3}$$

$$T' = \mathrm{Bi}\,(T_\infty - T) \text{ on } S_3 \tag{4}$$

where $\bar{T}$ is a given temperature distribution; T' is the temperature gradient normal to the surface:, Bi is the Biot number; and T_∞ is the ambient temperature.

The quantity denoted by u in equation (3) may describe an applied boundary heat flux on S_2. This heat flux distribution is, however, not given a priori in the problem. Hence the stated problem described by equations (1-4) does not constitute a classic heat transfer problem. The boundary heat flux u will play the role of the control function in an optimization problem, which controls the system state (i.e., the temperature in the body) such that some physical objectives are achieved.

The physical objectives of the optimization problem may be given as:

(*i*) Achieve a temperature distribution in the whole solid body as close as possible to a desired distribution

(*ii*) Achieve a temperature gradient on S_1 normal to the boundary surface as close to zero as possible

by utilizing a minimum amount of applied heat flux on S_2. These objectives may be cast into a mathematical form in terms of an integral functional $J[u, T]$, the so-called performance index of the optimization problem, i.e.,

$$J[u,T] = \frac{1}{2}\int_D (T - T_d)^2 dD + \frac{r_1}{2}\int_{S_1} T'^2 dS + \frac{r_2}{2}\int_{S_2} u^2 dS \tag{5}$$

where T_d is the desired temperature distribution in the solid body; r_1 and r_2 are given weighting parameters. The performance index $J[u, T]$ takes on different numerical values depending on the distribution of u on S_2, since T is an implicit function of u. On the other hand, the physical objectives will be obtained with a relative degree of achievement according to the prescribed values of the weighting parameters r_1 and r_2. The physical objectives are achieved also in an average sense, since they are described in terms of domain or boundary integrals in $J[u, T]$.

The static optimization problem of optimal heating of solids may be formally described as a steady-state optimal control problem. By adopting the control problem terminology it can be stated as follows:

Find the optimal control function u such that the performance index $J[u, T]$ is minimized under the state equation constraint (1) and the boundary constraints (2-4).

By noting the domains of definition of the three integrals in $J[u, T]$ expression, equation (5), in the reverse order, the control problem may also be classified as a boundary control-boundary and domain observation problem. The unknowns of the control problem are the control function u (i.e., the boundary heat flux on S_2) and the corresponding state function T (i.e., the temperature in the solid body).

Necessary Conditions for Optimality

The optimization problem at hand has been stated as a control problem under the system equation constraint (1). It is possible, however, to adjoin this constraint with $J[u, T]$ by means of a Lagrange multiplier function λ as follows:

$$J^*[u,T,\lambda] = J[u,T] + \int_D \lambda\, \nabla^2 T\, dD \tag{6}$$

The necessary condition for the modified (or augmented) performance index J^* to be stationary is that its first variation should be equal to zero for permissible values of δu, δT, and $\delta\lambda$, hence

Nomenclature

Bi = dimensionless Biot number
D = domain of problem
$\{g\}$ = gradient vector of the performance index
J = performance index
J^* = modified performance index
m = iteration number
$\{N\}$ = shape function vector
r_1, r_2 = weighting parameters
S = boundary of domain
$S_i\,(i = 1,2,3)$ = part of the domain boundary
T = temperature (the state function)
$\bar{T}$ = prescribed temperature on S_1
T_d = desired temperature distribution
T_∞ = ambient temperature
u = boundry heat flux on S_2 (the control function)
x,y,z = Cartesian coordinates

Greek Letters

λ = Lagrange multiplier function
$\delta(\,.\,)$ = first variation of (.)
ϕ = dummy variable

Subscripts

m = iterational level
0 = zeroth iterational level

Superscripts

$(\,.\,)'$ = normal outward derivative of (.) on the boundary
e = for the boundary element
T = transpose

$$\delta J^*[u,T,\lambda]=0 \tag{7}$$

By combining equations (5) and (6) the foregoing equation may be written as

$$\delta J^* = \int_D (T-T_d)\,\delta T\,dD + r_1\int_{S_1} T'\,\delta T'\,dS + r_2\int_{S_2} u\,\delta u\,dS$$

$$+\int_D [\delta\lambda\,\nabla^2 T + \lambda\,\delta(\nabla^2 T)]dD = 0 \tag{8}$$

The only constraints left in the problem are the boundary constraints (2–4), which will be incorporated into the variational formulation by means of Green's second identity. Thus, by employing this identity, the last domain integral term in equation (8) may be written as

$$\int_D \lambda\,\nabla^2(\delta T)dD = \int_D \nabla^2\lambda\,\delta T\,dD + \int_S (\lambda\delta T' - \lambda'\delta T)dS \tag{9}$$

Introduction of equation (9) into (8) now gives the following expression

$$\delta J^* = \int_D [(\nabla^2\lambda + T - T_d)\delta T + \nabla^2 T\,\delta\lambda]dD$$

$$+\int_{S_1} [(\lambda + r_1 T')\delta T' - \lambda'\delta T]dS$$

$$+\int_{S_2} (r_2 u\,\delta u + \lambda\,\delta T' - \lambda'\delta T)dS$$

$$+\int_{S_3} (\lambda\delta T' - \lambda'\delta T)dS = 0 \tag{10}$$

The first variational expressions of the boundary conditions (2–4) may then be introduced into equation (10) yielding

$$\delta J^* = \int_D [(\nabla^2\lambda + T - Td)\delta T + \nabla^2 T\,\delta\lambda]dD$$

$$+\int_{S_1} (\lambda + r_1 T')\delta T'\,dS$$

$$+\int_{S_2} (r_2 u\,\delta u + \lambda\,\delta T' - \lambda'\delta T)dS$$

$$+\int_{S_3} (\lambda\delta T' - \lambda'\delta T)dS = 0 \tag{11}$$

In equation (11), the variations δu, δT, and $\delta\lambda$ are independent of each other, hence their coefficients can be set equal to zero separately. This yields the stationary conditions for J^* (i.e., the Euler-Lagrange equations of calculus of variations) together with the essential boundary conditions (2–4) of the modified variational formulation as

$$\text{in } D: \quad \nabla^2 T = 0; \quad \nabla^2\lambda = T_d - T \tag{12}$$

$$\text{on } S_1: \quad T = \bar{T}; \quad \lambda = -r_1 T' \tag{13}$$

$$\text{on } S_2: \quad T' = u; \quad \lambda' = 0 \tag{14}$$

$$\text{on } S_3: \quad T' = \text{Bi}(T_\infty - T); \quad \lambda' = -\text{Bi}\lambda \tag{15}$$

and

$$\text{on } S_2: \quad \lambda + r_2 u = 0 \tag{16}$$

Equations (12–16) are also the necessary conditions for optimality of the performance index J subject to equations (1–4). The equations constitute a boundary value problem (BVP) in mathematical physics in terms of the unknown functions u, T, and λ. In the present analysis, a "direct" method of solution will be employed as opposed to an "indirect" method in which the coupled BVP is solved for $u = -\lambda/r_2$ on S_2.

Method of Solution

An iterational numerical method of solution will be adopted in order to find the optimal solutions. Treating u as known momentarily, the first set of equations in equations (12–15) would describe a BVP for T, and this will be denoted as the T-problem. Similarly, treating T as known this time, the second set of equations would describe a BVP for λ, and this will be referred to as the λ-problem. Both the T- and λ-problem have to be discretized in space by using an appropriate numerical method of solution. In the present study the BEM is chosen since the method produces solutions for the variables and their normal derivatives with the same order of accuracy and without any need for extraneous procedures [9].

Through the space discretization of the unknown variables the static optimization problem can be treated as a standard MP problem in which the function to be minimized is given by the discretized J^*. Starting with an initial guess for the discretized control function u, better estimates will be obtained by using the CGM of optimization.

Boundary Element Method. At any iterational level of the numerical procedure, both the T- and λ-problem represent a BVP with mixed boundary conditions. First of all, the boundary surface S of the domain is divided into boundary elements [9, 11]. The elements are triangular or quadrilateral in shape in the case of three-dimensional problems, while line elements are taken for two-dimensional problems. In each case, the unknown functions u, T, and λ are interpolated by linear functions, similar to the application of the FEM. In addition, the normal derivatives of T and λ are also linearly interpolated over the same boundary elements. Thus, over each boundary element e, the interpolations may be given as

$$\phi = \{\mathbf{N}\}^T\{\phi\}^e \tag{17}$$

where ϕ denotes any of the unknown variables or their normal derivatives defined over e; $\{\mathbf{N}\}$ is the linear shape function vector, and the $\{\phi\}^e$ vector contains the nodal values for the element.

An initial guess for the nodal values of the control function u is taken over the S_2 part of the boundary, and is denoted by $\{\mathbf{u}\}_0$, where the subscript 0 indicates that the vector is for the 0th iterational level. The T-problem can then be solved by the BEM using standard procedures for the nodal values of temperature and its normal derivative on S [9, 11]. Inner temperature values are also found by numerical quadratures.

Since there is a "source" term present in the Poisson's equation for the λ-problem, equation (12), the problem domain D has to be divided into inner cells. Knowing the temperature values at the current iterational level and also the desired temperature T_d in D, the source integrals can easily be evaluated by numerical means, namely, by the seven-point, Gauss-Legendre rule. These integrals appear in the application of the BEM for the λ-problem solution of which now yields the nodal values of λ and its normal derivative along the boundary S. At this point, it may be noted that the BEM solution of both the T- and λ-problem involve the same "influence" matrices [9], which do not change from one iterational level to another. Hence savings in computer storage and time can be achieved by simply decomposing and storing a single matrix.

Conjugate Gradient Method. Starting with an initial guess for u, the corresponding discrete values of T and its normal derivative on S have been found by using the BEM. The modified performance index J_0^* and its gradient $\{\mathbf{g}\}_0$ with respect to the discrete control vector $\{\mathbf{u}\}_0$ can now be found from equation (11). Since equations (12–15) have already been satisfied by the BEM solution of the T- and λ-problem, the gradient vector $\{\mathbf{g}\}_0$ may be given by the first S_2-term in

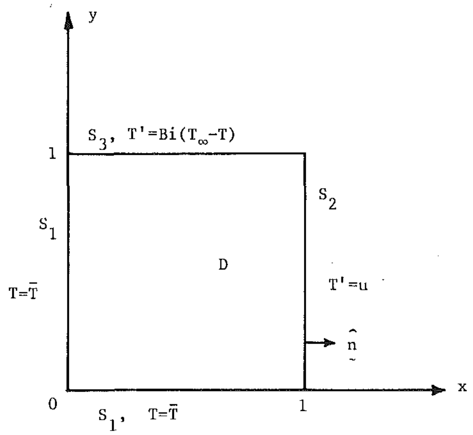

Fig. 2 Two-dimensional example problem geometry and boundary conditions

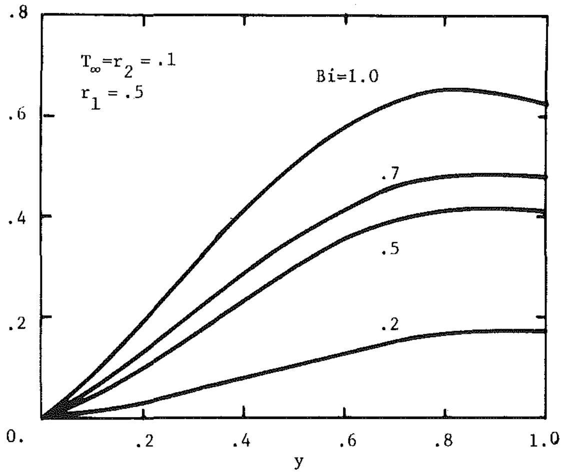

Fig. 3 Optimum boundary heat flux u for $\bar{T} = T_d = 1.0$, $T_\infty = r_2 = 0.1$, and $r_1 = 0.5$

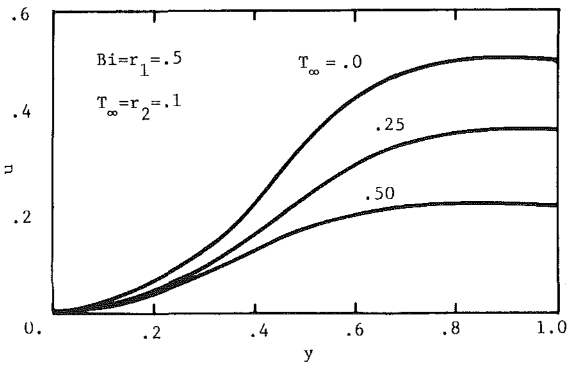

Fig. 4 Optimum boundary heat flux u for $\bar{T} = T_d = 1.0$, Bi $= r_1 = 0.5$, and $r_2 = 0.1$

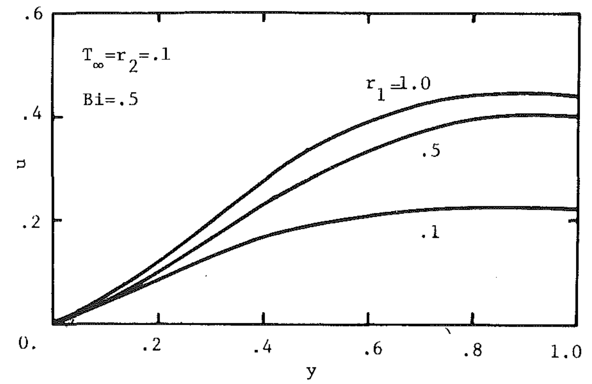

Fig. 5 Optimum boundary heat flux u for $\bar{T} = T_d = 1.0$, Bi $= 0.5$, and $T_\infty = r_2 = 0.1$

equation (11) after substituting the interpolations for λ and u over each element, i.e., equation (17), and then differentiating with respect to the $\{\mathbf{u}\}_0$ vector, hence

$$\{\mathbf{g}\}_0=\frac{\partial J_0^*}{\partial\{u\}_0}=\sum_e\int_{S_2^e}\{\mathbf{N}\}\{\mathbf{N}\}^T[\{\lambda\}^e+r_2\{\mathbf{u}\}^e]dS \qquad (18)$$

where the summation is over the elements on S_2.

Knowing the gradient $\{\mathbf{g}\}_0$ vector, the function J_0^* can be minimized by using any first-order unconstrained optimization technique. The conjugate gradient method (CGM) is adopted in the present study [11], since the computer storage requirement for the method is relatively low. A computer program for the CGM written in FORTRAN is available in [12].

Outline of Numerical Procedure. The iterational method of solution for the static optimization problem can be summarized as follows:

1. For $m = 0$, guess the initial control vector $\{\mathbf{u}\}_m$.
2. Solve the T-problem by the BEM.
3. Solve the λ-problem by the BEM.
4. Calculate J_m^* and $\{\mathbf{g}\}_m$.
5. Update the control vector by the CGM, i.e., obtain $\{\mathbf{u}\}_{m+1}$.
6. Increase m and repeat steps 2–5 until convergence is achieved.

Numerical Results and Discussion

A model problem in two-dimension has been analyzed by the numerical procedure just outlined. The problem consists of the optimal heating of a square plate by a boundary heat flux. The problem geometry is shown in Fig. 2. The temperature parameters of the problem were set as $\bar{T} = T_d = 1$ and $T_\infty = 1$, while the Biot number Bi and the weighting parameters r_1 and r_2 have been varied.

For the BEM solution of the T- and λ-problem, the boundary of the domain was divided into 44 "linear" elements, which were dispositioned over S uniformly except near the four corners where the double-node technique [9] has been utilized.

During the iterative solution procedure, several initial guesses were tried in order to make sure that the numerical results corresponded to the global minimum of the performance index. Computations have been performed on a DEC VAX-11/780 computer system. The first part of a FORTRAN program, in which the "influence" matrices of the BEM were evaluated and then decomposed, took 14 s of run time. The iterative numerical procedure typically took 6 iterations for convergence when the Euclidean norm of the gradient vector was set equal to 10^{-6}. Successive solutions of two BVP's (i.e., the T- and λ-problem) by the BEM were needed in an iterational loop whose typical run time was approximately .75 s.

In Fig. 3, the optimal heat flux u on S_2 (where $x = 1$) is given as a function of position for various Bi. When Bi = 0, the trivial solution for u would be equal to zero identically, as there will be no need for boundary heating of the plate for the given case $\bar{T} = T_d$. Increasing values of Bi, which results in higher amounts of boundary convection, necessitates higher values of u when $T_\infty < T_d$ in order to keep the temperature of the plate close to the desired level T_d.

The effect of the ambient temperature T_∞ on u is depicted in Fig. 4 as a function of position. As can be expected, smaller amounts of u are needed as T_∞ increases towards T_d.

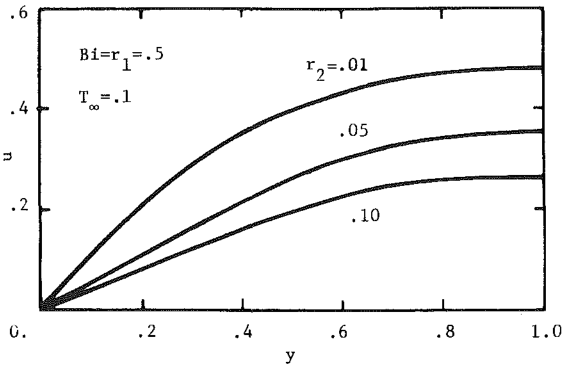

Fig. 6 Optimum boundary heat flux u for $\bar{T} = T_d = 1.0$, $T_\infty = 0.1$, and Bi = r_1 = 0.5

The values of the weighting parameters r_1 and r_2 indicate the relative importance we give to the achievement of the physical objectives that have been stated previously. For example, if $r_1 = 0$ is taken it means that we are not concerned with what the normal temperature gradient on S_1 will be as long as the other objectives are satisfied. Setting $r_1 = 1$, on the other hand, would mean, that we give the same order of importance to both achieving $T \rightarrow T_d$ in D and $T' \rightarrow 0$ on S_1. The behavior of the optimal u for various values of r_1 is shown in Fig. 5.

The value of r_2 is, on the other hand, an indicator of how much "fuel" we are willing to spend. If we set $r_2 = 0$, that means we are ready to spend any amount of fuel (i.e., boundary heat flux) as long as the desired objectives are met up to their maximum levels of achievement. Higher values of r_2 indicate that we make a compromise between spending minimum amount of fuel and achieving the objectives more closely. Figure 6 shows the relative trends of u as r_2 is given different numerical values.

Conclusion

In this investigation, the static optimal heating of solids by a boundary heat flux has been analyzed. The formulation of the problem and the proposed numerical solution procedure are such that they can be applied to either two- or three-dimensional problems. Numerical results are given for a two-dimensional square plate example problem.

The basic steps in the solution method is the successive solution of some elliptic PDE's by the BEM and the minimization of the performance index by the CGM of optimization. The BEM is, in particular, to be recommended for the optimization problem since accurate solutions can be obtained for the normal derivatives of the variables, as they are needed in the solution procedure. The method also retains its standard advantages over the domain type of methods, i.e., for arbitrary problem geometries, boundaries at infinity, reduction of dimensions, etc. Thus the proposed numerical approach appears to be well suited to this class of problems and provides an effective means of solution.

References

1 Butkovskiy, A. G., "Distributed Control Systems," American Elsevier Publishing, New York, 1969.

2 Bourne, D. E., Huntley, E., Hendrie, I. J., and Hunter, B. P., "Temperature control of Poiseuille flow with particular application to flow of molten glass," *International Journal of Heat and Mass Transfer*, Vol. 19, 1976, pp. 1045-1055.

3 Lions, J. L., *Optimal Control of Systems Governed by Partial Differential Equations*, Springer Verlag, Berlin, 1971.

4 Sage, A. P., *Optimum Systems Control*, Prentice-Hall, Englewood Cliffs, N.J., 1968.

5 Meric, R. A., "Finite element methods for an optimal steady-state control problem," *Int. J. Numer. Meth. Engn*, Vol. 12, 1978, pp. 1375-1382.

6 Meric, R. A., "Finite elements for an optimal control problem governed by a parabolic equation," *Int. J. Numer. Meth. Engn.*, Vol. 14, 1979, pp. 624-628.

7 Meric, R. A., "Finite element and conjugate gradient methods for a nonlinear optimal heat transfer control problem," *Int. J. Numer. Meth. Engn*, Vol. 14, 1979, pp. 1851-1863.

8 Meric, R. A., "Finite element analysis of optimal heating of a slab with temperature dependent thermal conductivity," *International Journal of Heat and Mass Transfer*, Vol. 22, 1979, pp. 1347-1353.

9 Brebbia, C. A., *The Boundary Element Method for Engineers*, Pentech Press, London, 1978.

10 Meric, R. A., "Boundary integral equation and conjugate gradient methods for optimal boundary heating of solids," *International Journal of Heat and Mass Transfer*, Vol. 26, 1983, pp. 261-267.

11 Fletcher, R., and Reeves, C. M., "Function minimization by conjugate gradients," *Computer J.*, Vol. 7, 1964, pp. 149-154.

12 Kuester, J. L., and Mize, J. H., "Optimization Techniques with FORTRAN," McGraw-Hill, New York, 1973.

E. F. Thacher
Mechanical and Industrial Engineering
Department,
Clarkson University,
Potsdam, N.Y. 13676

Entropy Production and Thermoelectric Device Performance

Integral forms for the thermal efficiency of thermoelectric generators, the coefficient of performance of thermoelectric refrigerators, and the coefficient of performance of thermoelectric heat pumps are derived. These forms are obtained for the isotropic material, nonsteady-state, nonadiabatic leg surface case. An example of the use of these forms is given.

Introduction

Study of the relationship between the entropy production rate and the performance parameters of thermoelectric devices has yielded insights into the performance and optimum shape of these devices.

When constant material properties, adiabatic leg surfaces, one-dimensional processes, steady state, and equal leg lengths are assumed, direct optimization of the thermoelectric generator efficiency gives a ratio between the cross-sectional areas of the two legs, which maximizes the thermal efficiency. Heikes et al. [1], showed that, for the same case, this ratio may be obtained by minimizing the total entropy production rate per unit power.

Clingman [2] analyzed a generalized, isotropic thermoelectric device with adiabatic leg surfaces operating at steady state. He showed that the thermal efficiency and the coefficient of performance are related to an entropy production rate, but one defined differently from that of [1] and [5]. He obtained exponential integral equations for these performance measures. Using variational calculus and assuming that the electric current density **J** is a known function of position, he derived from these equations a generalized form for the thermoelectric figure-of-merit, among other relations.

Thacher [3], using the entropy production rate derived in [5], and assuming steady state, obtained integral forms for the thermal efficiency and coefficient of performance, including heat loss from the leg surfaces. Thacher used the integral equation for the generator efficiency to investigate the influence of generator leg shape on the generator efficiency.

Efficiency

Figure 1 shows a nonuniformly shaped thermoelectric device operating as a generator. Heat flows into the hot junction of the generator at temperature T_h and is rejected at temperature T_c. The leg surfaces exchange heat with the surroundings at temperature T_∞. Losses in the bus bars and in the bus bar-to-leg joints are neglected. According to [4], if the legs are modeled as isotropic continua, then the rate of change of the local entropy per unit volume in the n-leg, say, is

$$\frac{\partial S_{vn}}{\partial t} = -\nabla \cdot \mathbf{J}_{sn} + \sigma_n \tag{1}$$

where $\mathbf{J}_{sn}$, the entropy flux, is given by

$$\mathbf{J}_{sn} = -\frac{k_n}{T_n}\nabla T_n - \frac{\pi_n}{T_n}\mathbf{J}_n \tag{2}$$

and σ is given by equation (A16). If the pressure and the mole fraction of all species are assumed to be constant, then equation (1) may be written [5]

$$\frac{\rho_n c_{pn}}{T_n}\frac{\partial T_n}{\partial t} = -\nabla \cdot \mathbf{J}_{sn} + \sigma_n \tag{3}$$

Equation (3) is now integrated over the leg volume, and the divergence theorem is applied to the divergence of the entropy flux, giving

$$\int_{\mathbf{R}_n} \frac{\rho c_p}{T}\frac{\partial T}{\partial t}\,dV = -\int_{\Omega_n} \mathbf{J}_s \cdot \mathbf{n}\,dV + \int_{\mathbf{R}_n} \sigma\, dV. \tag{4}$$

Let the leg surface be divided into three zones, one for the region in contact with the heat source, one for the region exchanging heat with the surroundings, and one for the region in contact with the heat sink. The temperature of the surface in contact with the heat source is assumed uniform at T_h and that of the surface in contact with the heat sink is assumed uniform at T_c. Then, because of equation (2), the surface integral in equation (4) may be written

$$-\int_{\Omega_n} \mathbf{J}_s \cdot \mathbf{n}\,d\Omega = \frac{Q_{hn}}{T_h} + \int_{\Omega_{an}} \frac{q\,d\Omega}{T} - \frac{Q_{cn}}{T_c} \tag{5}$$

where q is the normal component of the local energy flux into the leg across the leg surface, Ω_n. Over surface Ω_{an}

$$q\,d\Omega = -h_n(T_n - T_\infty)\,d\Omega \tag{6}$$

Substituting equation (6) into equation (5) and solving the result for Q_{hn}, the magnitude of the rate of energy transfer into the leg at the hot junction, gives

$$Q_{hn} = T_h \int_{\mathbf{R}_n} \frac{\rho c_p}{T}\frac{\partial T}{\partial t}\,dV + T_h \int_{\Omega_{an}} \frac{h}{T}(T - T_\infty)\,d\Omega + \frac{T_h}{T_c} Q_{cn} - T_h \int_{\mathbf{R}_n} \sigma\, dV \tag{7}$$

Equation (7) has the same form in the p-leg. The thermal efficiency is defined by

$$\eta = \frac{W_o}{Q_h} \tag{8}$$

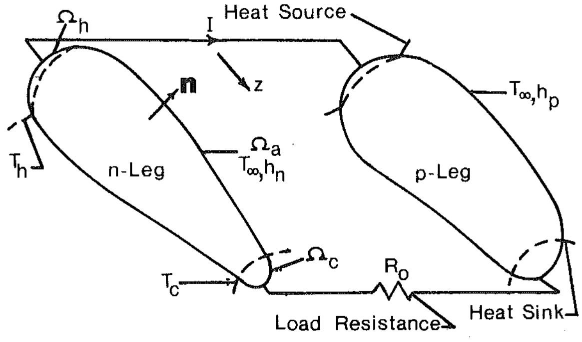

Fig. 1 Thermoelectric generator

Contributed by the Heat Transfer Division for publication in the JOURNAL OF HEAT TRANSFER. Manuscript received by the Heat Transfer Division September 8, 1983.

Combining equations (7), (A10), and (8) gives

$$\eta = \frac{\eta_c}{1 + \dfrac{\int_{\mathbf{R}} \left[c_p \left(1 - \frac{T_c}{T}\right) \frac{\partial T}{\partial t} + T_c \sigma \right] dV + \int_{\Omega_a} \left(1 - \frac{T_c}{T}\right) h (T - T_\infty) d\Omega}{W_o}} \tag{9}$$

for the thermal efficiency of a thermoelectric generator where

$$\eta_c = 1 - \frac{T_c}{T_h}$$

is the Carnot efficiency and

$$\begin{aligned} Q_h &= Q_{hn} + Q_{cn} \\ \mathbf{R} &= \mathbf{R}_n + \mathbf{R}_p \\ \Omega_a &= \Omega_{an} + \Omega_{ap} \end{aligned} \tag{10}$$

Coefficient of Performance

Peltier Refrigerator. The coefficient of performance (COP) of a refrigerator is given by

$$\beta_r = \frac{Q_c}{W} \tag{11}$$

where W is the power input to the refrigerator. Equation (7) for the legs of the refrigerator is the same as for the generator except that the signs of Q_h and Q_c are reversed. With this change, combining equations (11), (A11), and (7) gives

$$\beta_r = \beta_{cr} \left\{ 1 - \frac{\int_{\mathbf{R}} \left[\left(1 - \frac{T_h}{T}\right) \rho c_p \frac{\partial T}{\partial t} + T_h \sigma \right] dV + \int_{\Omega_a} \left(1 - \frac{T_h}{T}\right) h (T - T_\infty) d\Omega}{W} \right\} \tag{12}$$

where

$$\beta_{cr} = \frac{T_c}{T_h - T_c} \tag{13}$$

is the coefficient of performance of a Carnot refrigerator.

Heat Pump. The definition of the coefficient of performance is

$$\beta_p = \frac{Q_h}{W} \tag{14}$$

By steps similar to the above it can be shown that

$$\beta_p = \beta_{cp} \left\{ 1 - \frac{\int_{\mathbf{R}} \left[\left(1 - \frac{T_c}{T}\right) \rho c_p \frac{\partial T}{\partial t} + T_c \sigma \right] dV + \int_{\Omega_a} \left(1 - \frac{T_c}{T}\right) h (T - T_\infty) d\Omega}{W} \right\} \tag{15}$$

gives the coefficient of performance of a heat pump where

$$\beta_{cp} = \frac{T_h}{T_h - T_c} \tag{16}$$

is the coefficient of performance of a Carnot heat pump.

Remarks. Equation (9) shows that the thermal efficiency depends inversely upon the ratio of the total entropy production rate per unit output power when $h = 0$, as asserted by [1] for the constant property, uniform cross-sectional area steady-state case. When steady state exists, but $h \neq 0$, then the efficiency also depends inversely upon the ratio of a term related to the total leg surface heat transfer to the output power. This term can be called the "reduced" total leg surface heat transfer, because $1 - T_c/T \leq 1$. Allowing nonsteady-state conditions adds an additional ratio: that of a term representing the "reduced" energy storage to the output power. Similar dependencies are shown by equations (12) and (15), except that the ratios in those cases involve the input power.

Note that the form of equations (9), (12), and (15) is independent of the actual processes going on, except for the necessity of accounting for the two legs as separate regions. Therefore these three equations can be applied to any heat engine, refrigerator, or heat pump that can be modeled as an isotropic region (or regions) operating between two reservoirs

Nomenclature

A = cross-sectional area
c_p = specific heat at constant pressure
H = defined by equation (A14)
h = heat transfer coefficient
I = total conventional electric current
$\mathbf{J}$ = electric current density
$\mathbf{J}_s$ = entropy flux
k = thermal conductivity at zero electric field
L = leg length
$\mathbf{n}$ = unit outward normal to Ω
P = perimeter
q = normal component of the local energy flux
Q = total energy flow rate over a specified area
$\mathbf{R}$ = a region of space
R = resistance
r = radius
S_v = entropy per unit volume
T = absolute temperature
t = time
V = volume; total generator volume
W = input power
W_0 = output power
z = space coordinate

Greek Variables

α = Seebeck coefficient
β = coefficient of performance
ρ = resistivity
∇ = gradient operator
η = thermal efficiency
Ω – surface of region $\mathbf{R}$
τ = Thomson coefficient, $-Td\alpha/dT$
λ – constant Lagrange multiplier
μ = Lagrange multiplier function
π = Peltier coefficient; 3.1415926 . . .
σ = entropy production rate per unit volume
Φ = electrochemical potential divided by the Faraday constant, $96487 \dfrac{\text{coul}}{\text{mol}}$

Subscripts

a = ambient
c = Carnot; cold end of leg
h = hot end of leg
n = n-leg
o = load
p = p-leg; heat pump; constant pressure
r = refrigerator
s = entropy
T = total resistance of legs

at fixed temperatures and to which the performance definitions used above apply.

Because

$$\eta_c \geq 1 - T_c/T \geq 0 \tag{17}$$

the heat storage term in equation (9) will increase or decrease the thermal efficiency, depending on the sign of $\partial T/\partial t$. The surface loss term increases the thermal efficiency if $T - T_\infty$ is negative, and decreases it otherwise. Similarly, in the case of the refrigerator, for example,

$$-1/\beta_{cr} \leq 1 - T_h/T \leq 0 \tag{18}$$

and again the effects of the storage and heat transfer terms depend on the signs of $\partial T/\partial t$ and $T - T_\infty$, respectively.

Application

As an example of the possible uses of the foregoing results consider the problem of finding the shape of a thermoelectric generator which maximizes its thermal efficiency when operating at steady state. This problem has been examined by [6], [7], [8] and [9], but without determining the optimum shape. The present work will derive necessary conditions which must be satisfied by the optimum shape.

Variational Problem

One-Dimensional Assumption. The assumption that the processes occurring in the legs depend only on one space coordinate, z, is doubly anomalous. Either shape variation or surface heat transfer will certainly give at least an axisymmetric problem. However, as in the study of shaped fins, where it has been widely used, and as in most of the studies previously mentioned, the great simplification that the assumption introduces overrides objections. The processes in the generator will therefore be assumed one-dimensional. The error thereby introduced will be small as long as dA/dz or h is not "too large."

Problem Statement. Equation (9) shows that, if η_c is fixed, the thermal efficiency will be maximized when the denominator of equation (9) is minimized. If the load resistance R_o and the leg length L are assumed to be fixed, the variational problem selected may be stated as:

Minimize

$F(T_c, T_h, T_\infty, L, R_o) =$

$$\frac{\left[T_c \int_o^L \left[kA\left(\frac{1}{T}\frac{dT}{dz}\right)^2 + \frac{\rho I^2}{TA}\right]dz + \int_o^L \left(1 - \frac{T_c}{T}\right)hP(T - T_\infty)dz\right]_{n+p}}{I^2 R_o} \tag{19}$$

subject to boundary conditions

$$T(o) = T_h \tag{20}$$

$$T(L) = T_c \tag{21}$$

and with isoperimetric constraint

$$V = \int_o^L A_n(z)dz + \int_o^L A_p(z)dz \tag{22}$$

where V, the total volume, is constant, and differential constraints in each leg

$$G_i = \left[\frac{d}{dz}\left(kA\frac{dT}{dz}\right) \pm \tau\frac{dT}{dz}I + \frac{\rho I^2}{A} - hP(T - T_\infty)\right]_i = 0$$

$$i = n, p \tag{23}$$

where the "+" is taken in the p-leg and the "−" is taken in the n-leg. The total conventional electric current I is given by

$$I = \frac{\int_{T_c}^{T_h} (\alpha_p - \alpha_n)dT}{R_o + \int_o^L \left(\frac{\rho_n}{A_n} + \frac{\rho_p}{A_p}\right)dz} \tag{24}$$

and ρ_p and ρ_n are functions of T_p and T_n, respectively.

In the integrand of the functional, equation (19), the temperature, and the cross-sectional area are unknown functions of z, whereas the current is a constant for any particular temperature and area distribution. The perimeter P may be regarded as a known function of A. The intrinsic Seebeck coefficients, α_p and α_n, in equation (24) are independent of the temperature distributions in the legs.

To simplify the notation, the discussion will be continued in terms of the n-leg. Subscripts will therefore be omitted unless required for clarity.

Euler-Lagrange Equations. The variation of the functional with respect to the leg cross-sectional areas and temperatures, and after including the constraints using the method of Lagrange multipliers, gives Euler-Lagrange equations in the n-leg and p-leg. These equations are cumbersome and so are contained in the Appendix as equations (A12) and (A13).

They contain the Lagrange multiplier function μ, which is a function of z and satisfies the boundary conditions

$$\mu(o) = 0 \tag{25}$$

$$\mu(L) = 0 \tag{26}$$

These equations, plus equations (20) and (21) leave $A(0)$ and $A(L)$ free because the associated natural boundary condition is satisfied at $z = (0, L)$ without prescribing the cross-sectional area there [3].

Character of Extremum. The Euler-Lagrange equations constitute necessary conditions that must be satisfied at an extremum. Establishing sufficient conditions for a minimum is much more difficult. A theoretical development of sufficiency tests for application to functionals with more than one unknown variable is given by [10] for the case when no higher than first-order derivatives appear in the functional, and by [11] for the case when higher-order derivatives are present. The application of these developments to the present case is not attempted.

First Integral. When a functional is explicitly independent of the independent variable, as is equation (19), a first integral of the system of Euler-Lagrange equations for the functional can be obtained. A formula for the first integral for a functional with integrand f containing unknown functions $y_k(x)$, $k = 1, 2, 3, \ldots, n$, together with the first and second derivatives of the y_k with respect to x was derived in [3]. It is

$$\sum_{k=1}^{n}\left[\frac{\partial f}{\partial y_k'} - \frac{d}{dx}\left(\frac{\partial f}{\partial y_k''}\right)\right]y_k' + \sum_{k=1}^{n}\frac{\partial f}{\partial y_k''}y_k'' - f = C_1 \tag{27}$$

where the primes indicate differentiation with respect to x, and C_1 is a constant.

If $\partial f/\partial y_k'' = 0$, $k = 1, 2, 3, \ldots, n$, equation (27) reduces to the first integral for functionals containing only first-order derivatives, which may be found in [12].

Application. Applying equation (27) yields the following first integral

$$T_c kA\left(\frac{1}{T}\frac{dT}{dz}\right)^2 - kA\frac{dT}{dz}\frac{d\mu}{dz} - \frac{T_c \rho I^2}{TA} - \left(1 - \frac{T_c}{T}\right)H$$

$$-\theta(L)\frac{\rho}{A} - \mu\frac{\rho I^2}{A} + \mu H - \lambda A = C_1 \qquad (28)$$

Equation (A13) is multiplied by $A(z)$ and then is subtracted from equation (28); applying equations (21) and (26) to the result gives

$$\left(1 - \frac{T_c}{T} - \mu\right)\left(H + A\frac{\partial H}{\partial A}\right) + 2\lambda(A - A(L)) = 0 \qquad (29)$$

Equation (29) will be called the "shape relation."

Suppose that $h = 0$. This implies perfect insulation, a frequently used idealization. Equation (29) then requires that the cross-sectional area be constant because both H and $\partial H/\partial A$ are zero. Thus, if one is to obtain optimum performance, regardless of the temperature dependence of the material properties, the cross-sectional area must be constant if h is zero. On the other hand, if $h \neq 0$ (the physically real case), the cross-sectional area varies with z in order to satisfy the shape relation at each z.

When written in the form of equation (29), the shape relation is independent of the choice of the independent variable, r or z. Therefore, the results just obtained also apply when the independent variable is r. The legs of the generator would then be disks, and electric current and heat would flow in the radial direction, as shown in Fig. 2. Suppose $h = 0$, and u is the coordinate of the surface in the z-direction, measured from the $(r, 0)$-plane, equation (29) requires that

$$ur = \frac{A(r_0)}{4\pi} \qquad (30)$$

where r_0 is the inner radius. That is, the shape in the (r, z)-plane is hyperbolic.

Discussion of Results

Landecker Connection. The theoretical and experimental work of Landecker [13] indirectly supports the foregoing conclusion. Landecker experimented with disk-shaped Peltier refrigerators, giving them hyperbolic shapes in the (r, z)-plane, as shown in Fig. 2. The refrigerators were tested under nearly adiabatic conditions.

He writes (p. 152):

> . . . the efficiency of this design as revealed by the maximum temperature difference is the highest . . . ever experienced in this laboratory with radial or with linear current junctions.

If the variation of equation (12) is taken as previously given, Euler-Lagrange equations identical in form to those for a generator are obtained, but with T_c replaced by T_h($\theta(L)$ is given by a somewhat different relation from equation (A15)), as shown in [3]. Therefore, because of this identity of form, the shape relation also applies to Peltier refrigerators. It applied to heat pumps, too, because equation (15) is of the same form as equation (12), except that T_c takes the place of T_h and β_{cp} replaces β_{cr}.

The independence of the shape relation of the choice of the independent variable, already discussed, means that for Landecker's configuration to satisfy the necessary conditions for a maximum β_r, the shape of the legs must be hyperbolic in the (r, z)-plane, as previously shown.

This conclusion is only indirectly supported by Landecker's statement because it has not been shown that the shape relation must be satisfied in order to maximize the temperature difference of a Peltier refrigerator.

Rollinger Connection. In his numerical study of shaped Peltier refrigerators with z as the independent variable ("linear" legs, to use Landecker's term), Rollinger [14] found that the maximum heat-pumping rate and the maximum temperature difference were unaffected by shaping unless $h \neq 0$. He did not present results for β_r, so that his work again only indirectly supports the conclusions drawn from the shape relation.

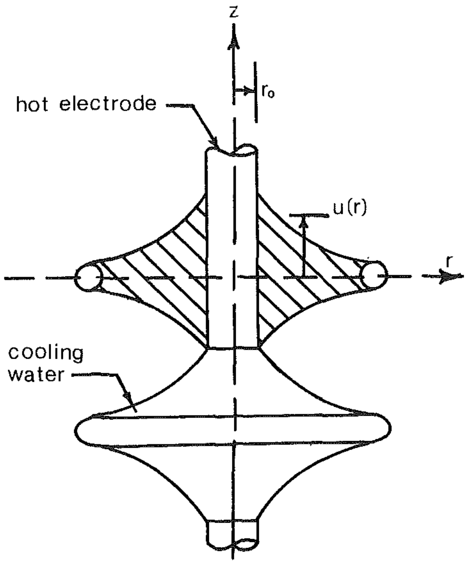

Fig. 2 Landecker configuration

Conclusions

The major conclusion of this paper is that reached in the discussion of the shape relation: if the thermoelectric device (generator or refrigerator) legs are adiabatic, the cross-sectional area distribution that maximizes the thermal efficiency, or COP, cannot be a function of the space coordinate. When the space coordinate is z, this requires a uniform shape, but when it is r, it requires a hyperbolic shape. If the legs are not adiabatic, then the shape must satisfy equation (29) for an extremum. If the same rule also applies to the maximum temperature difference of a refrigerator, then it cancels the apparent contradiction between the results of Landecker [13] and Rollinger [14]. Landecker showed, experimentally, that the temperature difference of an adiabatic hyperbolic disk Peltier refrigerator could be made much larger than that of a corresponding conventionally shaped refrigerator, as previously mentioned. On the other hand Rollinger, who did not consider disk-shaped legs, concluded that if $h = 0$, then shaping would have no effect on the temperature difference. The rule given herein, if applicable, would predict a maximum temperature difference when the cross-sectional area is not a function of the space coordinate. In this sense, Landecker's adiabatic hyperbolic disk is a "uniform shape," and both results are correct for their respective geometries.

References

1 Heikes, R. R., Sherman, B., and Ure, R., Jr., "Calculation of Efficiency of Thermoelectric Devices," *J. of Applied Physics*, Vol. 31, No. 1, Jan. 1960, pp. 1-16.

2 Clingman, W. H., "Entropy Production and Optimum Device Design," *Advanced Energy Conversion*, Vol. 1, 1961, pp. 61-79.

3 Thacher, E. F., "Optimal Thermoelectric Generator Shapes," Ph.D. dissertation, New Mexico State University, Las Cruces, New Mexico, 1980.

4 DeGroot, S. R., and Mazur, P., *Non-Equilibrium Thermodynamics*, North-Holland Publishing, Amsterdam, The Netherlands, 1962.

5 Hasse, Rolf, *Thermodynamics of Irreversible Processes*, Addison-Wesley Publishing, Reading, Mass., 1969.

6 Gehloff, P. O., Justi, E., and Kohler, M., "Verfeinerte Theorie der elektrothermischen Kälteerseugung," *Abhandl. Braunschweig. Wiss. Ges.*, Vol. 2, 1950, pp. 149-164.

7 Boerdijk, A. H., "Contribution to a General Theory of Thermocouples," *J. Applied Physics*, Vol. 30, 7, July 1959, pp. 1080-1083.

8 Brandt, J. A., "Solutions to a Differential Equations Describing the Temperature Distribution, Thermal Efficiency, and Power Ouput of a Thermoelectric Element with Variable Properties and Cross-sectional Area," *Advanced Energy Conversion*, Vol. 2, 1962, pp. 219-230.

9 Rollinger, C. N., "Effects of Geometric Shape and Convective Heat Transfer on the Performance of a Thermoelement," Ph.D. dissertation, Northwestern University, 1961.

10 Sagan, Hans, *Introduction to the Calculus of Variations*, McGraw-Hill, New York, 1969.

11 Forsyth, A. R., *Calculus of Variations*, University Press, Cambridge, England, 1927.

12 Weinstock, Robert, *Calculus of Variations with Applications to Physics and Engineering*, Dover Publications, New York, 1974.

13 Landecker, K., "Some Recent Developments in Thermoelectric Junctions for Refrigeration and Power Production," *Proc. International Conference on Thermoelectric Energy Conversion, Arlington, Texas, Sept. 1-3, 1976*, IEEE, 1976, p. 150.

14 Rollinger, C. N., "Convectively Cooled Thermoelements With Variable Cross-sectional Area," ASME JOURNAL OF HEAT TRANSFER, Vol. 87, No. 2, May 1965, pp. 259-265.

15 Domencali, C. A., "Irreversible Thermodynamics of Thermoelectricity," *Rev. of Modern Physics*, Vol. 26, No. 2, Apr. 1954, pp. 237-275.

APPENDIX

First Law

It is shown in [5] that in region **R**, which may be the *n*-leg or the *p*-leg,

$$\rho c_p \frac{\partial T}{\partial t} = \nabla \cdot k \nabla T - \tau \nabla T + \rho J^2 \tag{A1}$$

Because of electro-neutrality in **R** [4], [5]

$$\nabla \cdot \mathbf{J} = 0 \tag{A2}$$

Also

$$\tau \nabla T \cdot \mathbf{J} = -\nabla \cdot (\pi \mathbf{J}) + \alpha \mathbf{J} \cdot \nabla T \tag{A3}$$

and from [15]

$$\int_{\mathbf{R}} \rho J^2 dV = \int_{\mathbf{R}} \mathbf{J} \cdot \nabla \Phi dV + \int_{\mathbf{R}} \alpha \nabla T \cdot \mathbf{J} dV \tag{A4}$$

Integrating equation (A1) over **R** and using the divergence theorem and equations (A2), (A3), and (A4) gives

$$\int_{\mathbf{R}} \rho c_p \frac{\partial T}{\partial t} dV = \int_{\Omega_{\mathbf{R}}} k \nabla T \cdot \mathbf{n} d\Omega + \int_{\Omega_{\mathbf{R}}} \pi \mathbf{J} \cdot \mathbf{n} d\Omega + \int_{\mathbf{R}} \mathbf{J} \cdot \nabla \Phi dV \tag{A5}$$

Current flows only through subsurfaces Ω_h and Ω_c, and it is assumed that Φ is uniform over Ω_h and Ω_c. This allows equation (A5) to be written

$$-\int_{\Omega_{\mathbf{R}}} (-k \nabla T - \pi \mathbf{J}) \cdot \mathbf{n} d\Omega = \int_{\mathbf{R}} \rho c_p \frac{\partial T}{\partial t} dV - \Phi_h \int_{\Omega_{h\mathbf{R}}} \mathbf{J} \cdot \mathbf{n} d\Omega - \Phi_c \int_{\Omega_{c\mathbf{R}}} \mathbf{J} \cdot \mathbf{n} d\Omega \tag{A6}$$

The left-hand side of equation (A6) is the net rate of energy transport into **R**. Hence

$$Q_{h\mathbf{R}} - \int_{\Omega_{a\mathbf{R}}} -k \nabla T \cdot \mathbf{n} d\Omega - Q_{c\mathbf{R}} = \int_{\mathbf{R}} \rho c_p \frac{\partial T}{\partial t} dV - \Phi_h \int_{\Omega_{h\mathbf{R}}} \mathbf{J} \cdot \mathbf{n} d\Omega - \Phi_c \int_{\Omega_{c\mathbf{R}}} \mathbf{J} \cdot \mathbf{n} d\Omega \tag{A7}$$

Note that on Ω_a

$$-k \nabla T \cdot \mathbf{n} = h(T - T_\infty) \tag{A8}$$

Also

$$\int_{\Omega_h} \mathbf{J} \cdot \mathbf{n} d\Omega = \begin{cases} I, & n\text{-leg} \\ -I, & p\text{-leg} \end{cases} \qquad \int_{\Omega_c} \mathbf{J} \cdot \mathbf{n} d\Omega = \begin{cases} -I, & n\text{-leg} \\ I, & p\text{-leg} \end{cases} \tag{A9}$$

Making use of equations (A7), (A8), and (A9) and neglecting bus-bar and contact resistances, gives for the complete generator

$$Q_h = \int_{\mathbf{R}} \rho c_p \frac{\partial T}{\partial t} dV + Q_c + W_0 + \int_{\Omega_a} h(T - T_\infty) d\Omega \tag{A10}$$

For a refrigerator or heat pump, it is only necessary to set $W = -W_0$ and to reverse the signs of Q_h and Q_c, giving

$$Q_c + W = Q_h + \int_{\Omega_a} h(T - T_\infty) d\Omega + \int_{\mathbf{R}} \rho c_p \frac{\partial T}{\partial t} dV \tag{A11}$$

where now

$$\Omega_a \equiv \Omega_{an} + \Omega_{ap}$$
$$\mathbf{R} \equiv \mathbf{R}_n + \mathbf{R}_p$$

Euler-Lagrange Equations

Equations (A12) and (A13) are the Euler-Lagrange equations for the *n*-leg of the thermoelectric generator (*n* subscript omitted) [3]. The equations for the *p*-leg are identical, except that the sign of the Thomson coefficient, τ, is reversed.

$$-\frac{2T_c kA}{T^2} \frac{dT}{dz} - T_c A \left(\frac{dT}{dz}\right)^2 \frac{d}{dT}\left(\frac{k}{T^2}\right) + \frac{T_c I^2}{A} \frac{d}{dT}\left(\frac{\rho}{T}\right) + \frac{\theta(L)}{A} \frac{d\rho}{dT} + \frac{\partial}{\partial T}\left[\left(1 - \frac{T_c}{T}\right) H\right] + \mu\left(\frac{I^2}{A} \frac{d\rho}{dT} - \frac{\partial H}{\partial T}\right) + \frac{d\mu}{dz}\left(k \frac{dA}{dz} + \tau I\right) + kA \frac{d^2 \mu}{dz^2} = 0 \tag{A12}$$

$$T_c k \left(\frac{1}{T} \frac{dT}{dz}\right)^2 - \frac{T_c \rho}{T}\left(\frac{I}{A}\right)^2 + \frac{\partial}{\partial A}\left[\left(1 - \frac{T_c}{T}\right) H\right] - \theta(L) \frac{\rho}{A^2} - \mu\left(\frac{\rho I^2}{A^2} + \frac{\partial H}{\partial A}\right) - k \frac{d\mu}{dz} \frac{dT}{dz} + \lambda = 0 \tag{A13}$$

where

$$H = hP(T - T_\infty) \tag{A14}$$

and

$$\theta(L) = \frac{2}{R_T}\Bigg\{-I^2 \int_o^L \left[\left(\frac{\mu\rho}{A}\right)_n + \left(\frac{\mu\rho}{A}\right)_p\right] dz - \frac{I}{2} \int_o^L \left[-\left(\mu\tau \frac{dT}{dz}\right)_n + \left(\mu\tau \frac{dT}{dz}\right)_p\right] dz + T_c \int_o^L \left[k_n A_n \left(\frac{1}{T} \frac{dT}{dz}\right)_n^2 + k_p A_p \left(\frac{1}{T} \frac{dT}{dz}\right)_p^2\right] dz + \int_o^L \left[\left(1 - \frac{T_c}{T}\right)_n H_n + \left(1 - \frac{T_c}{T}\right)_p H_p\right] dz\Bigg\} \tag{A15}$$

Local Entropy Production Rate

According to [5] the entropy production rate per unit volume in the legs of a thermoelectric device is

$$\sigma = (k/T^2) \nabla T \cdot \nabla T + (\rho/T) \mathbf{J} \cdot \mathbf{J} \tag{A16}$$

Journal of Heat Transfer

Technical Notes

This section contains shorter technical papers. These shorter papers will be subjected to the same review process as that for full papers.

Radiative Heat Fluxes Near Turbulent Buoyant Methane Diffusion Flames

S-M. Jeng[1] and G. M. Faeth[1,2]

Introduction

The objective of this investigation was to develop and evaluate methods for predicting total radiation heat fluxes produced by buoyant, turbulent, diffusion flames – motivated by the fact that flame radiation significantly influences rates of fire spread and burning during unwanted fires. The investigation was limited to round methane-fueled diffusion flames burning in still air, since their structure and spectral radiation properties had been studied earlier in this laboratory [1-3]. Another advantage of these methane flames is that they radiate primarily in the infrared gas bands and the absence of continuum radiation from soot avoids current difficulties in predicting soot concentrations in flames.

Recent work treating gaseous radiation from turbulent flames includes methanol-fueled furnaces, considered by Grosshandler and Sawyer [4], and hydrogen-fueled flames, considered by Fishburne and Pergament [5]. Grosshandler and Sawyer [4] consider the spectral properties of flames along particular radiation paths through the flames, analogous to the earlier methane flame study in this laboratory [3]. Fishburne and Pergament [5] treat spectral radiation properties over an entire flame, but flame structure was not well known for the conditions they consider. The present study extends consideration to total radiative heat fluxes at various positions near flames whose structure was well known from earlier work [1-3].

Past methods used to compute radiative heat fluxes from flames include zone, Monte Carlo, and multiflux techniques. Lockwood and Shah [6] discuss the relative merits of these techniques and propose a new "discrete transfer" method which they successfully evaluate using test problems involving gray gases. The discrete transfer method has several advantages for practical applications, e.g., computational economy, geometric adaptability, and ability to return any desired degree of precision [6]. In addition, the approach involves summing predictions of intensities so that it is a direct extension of methods used in [3]. Therefore, the discrete transfer method was chosen for study during the present investigation. Present work extends examination of the method to nongray gases and evaluation of predictions using data from buoyant turbulent fires.

The discussion begins with a description of experimental and theoretical methods used in the study and concludes with a comparison of predictions and measurements. The following description is brief, more details and a complete tabulation of data are presented in [7]. Additional details concerning flame properties and theoretical methods can also be found in [1-3].

Experimental Methods

The test flames were produced with a burner having an exit diameter of 5 mm injecting vertically upward in still air. The flames were attached at the burner exit using a small coflow of hydrogen. Three flames were considered, having burner exit Reynolds numbers of 2920, 5850, and 11700 – all with visible flame heights of roughly 500 mm (mean position). The flames were turbulent, with buoyancy dominating much of the visible flame region – particularly for the lowest burner Reynolds number. Other properties of the test flames, burner exit Richardson numbers, total radiative heat losses, etc., are summarized in [1].

Measurements of total radiative heat flux distributions were made along the base and height of the flames using a gas-purged, water-cooled sensor (Medtherm Radiation Heat Flux Transducer, type 64F-10-22, 150 deg viewing angle). The sensor was traversed in the radial direction, looking vertically upward, in the exit plane of the burner. The sensor was also traversed parallel to the axis of the flames, facing the axis at a radial distance of 575 mm. The flame boundaries were entirely within the viewing angle of the sensor, except points far from the injector where contributions to radiative heat flux are small. The uncertainty and repeatability of the measurements were within 10 percent of the reported reading.

Theoretical Methods

The discrete transfer method involves determining the spectral radiation intensity along several paths passing through the point in question (the sensor location in this instance) and then summing over both the points and wavelength to find the total radiative heat flux [6]. The computation of spectral radiation intensity followed [3]. Present intensity predictions were based on time-averaged mean properties within the flames, since earlier work had shown that this yielded good intensity predictions even though the flames were turbulent [3].

Structure predictions needed for intensity calculations were based on numerical solution of the boundary layer equations using a Favre, (mass)-averaged k-ϵ-g model, followed by computation of time-averaged scalar properties. The conserved-scalar (mixture fraction) method was used to find all scalar properties, fixing instantaneous scalar properties as a function of instantaneous mixture fraction using the laminar flamelet method of Bilger [8]. This approach ignores effects of local radiation absorption and emission on the scalar

---

[1] Department of Mechanical Engineering, The Pennsylvania State University, University Park, Pa. 16802

[2] Fellow ASME

Contributed by the Heat Transfer Division for publication in the JOURNAL OF HEAT TRANSFER. Manuscript received by the Heat Transfer Division, January 9, 1984.

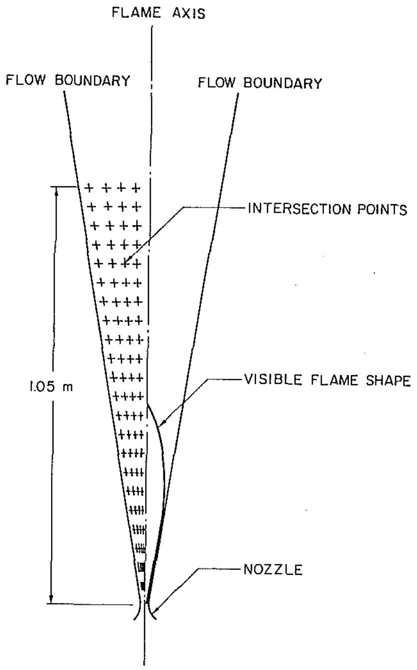

Fig. 1 Intersection of radiation paths used in the computations with a normal plane through the axis of symmetry of the flames

structure predictions, treating radiation as a perturbation of the flow process. The approximation is reasonable for the test flames, since total radiative heat losses were less than 20 percent of the chemical energy release rate. Furthermore, earlier work showed that this approach yielded satisfactory scalar structure predictions for the test flames [2].

For present test conditions, scattering can be ignored with little error. The spectral radiation intensity I_λ at wavelength λ along a particular path can then be determined from the integral form of the equation of transfer, assuming that I_λ is small at the position where the integration is initiated ($s=0$)

$$I_\lambda(s)=\int_0^s \frac{e_{\lambda b}(s')}{\pi}\,\frac{\partial}{\partial s'\tau_\lambda}(s,s')ds' \qquad (1)$$

where $e_{\lambda b}$ is the blackbody spectral emissive power, s is the position of the sensor, and $\tau_\lambda(s,s')$ is the spectral transmittance between s' and s. The spectral radiance at the surface of the sensor, J_λ is then given by summing over all paths i

$$J_\lambda=\sum_{i=1}^{n}(I_\lambda \cos\theta\Delta_\omega)_i \qquad (2)$$

where θ_i is the angle between path i and a normal to the surface of the sensor, and $\Delta\omega_i$ is the solid angle of the path viewed from the sensor. The total radiance, or radiative heat flux from the flame, is obtained by summing equation (2) over all wavelengths.

The spectral radiation intensity calculations considered all gas bands observed in the flames [3]: 1.87, 2.7, and 6.3 microns for H_2O; 2.7 and 4.3 μm for CO_2; 2.3 and 3.3 μm for CH_4; and 4.7 μm for CO. The CO_2, H_2O, and CO bands were treated using the Goody statistical narrow-band model in conjunction with the Curtis-Godson approximation to account for an inhomogeneous path following Ludwig et al. [9]. CH_4 is not a major contributor to the radiation heat flux and properties of this band were found using Beer's law – based on extrapolation of Lee and Happel's [10] high-temperature data (transmittivities of CH_4 generally exceeded 85 percent, which justifies this approximation [9]).

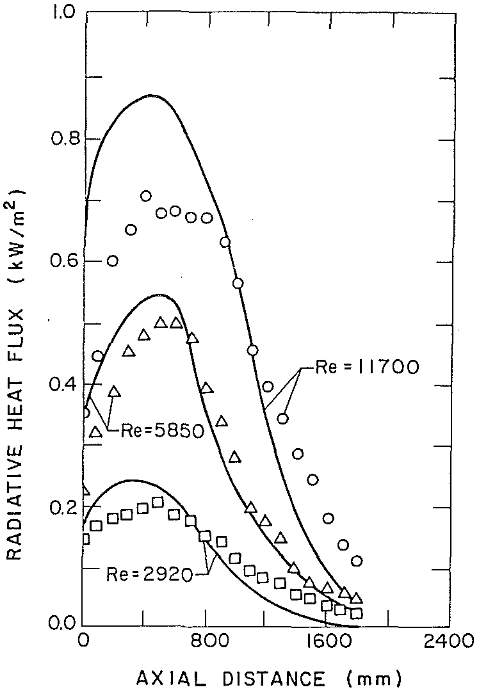

Fig. 2 Total radiative heat flux distribution parallel to the flame axis at a distance of 575 mm

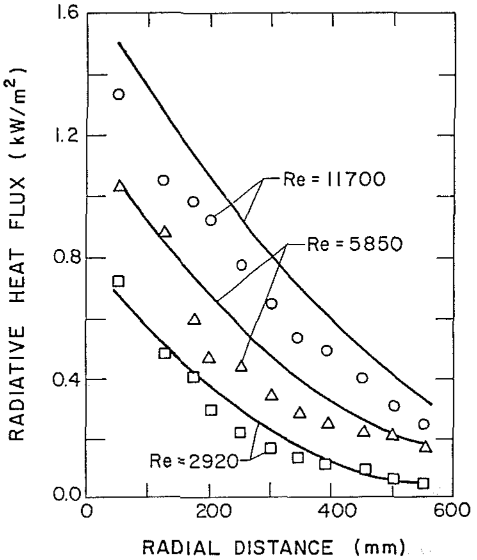

Fig. 3 Total radiative heat flux distribution along the flame base

The arrangement of the radiation paths used in the computations is illustrated in Fig. 1. The figure shows the point where each path from the sensor intersects a plane through the flame axis and normal to the plane of the sensor and the axis. With this arrangement, the incremental solid angle needed in equation (2) for path i is given by

$$\Delta\omega_i=(\Delta A\cos\phi/r^2)_i \qquad (3)$$

where ϕ_i is the angle between the path and the normal to the incremental area ΔA_i in the axial plane; while r_i is the length between the sensor and the point of intersection with the axial plane. The problem is symmetrical about the plane through the sensor and the flame axis for present conditions – 84 paths were used on the side computed as shown in Fig. 1.

The underlying flame structure calculation was numerically closed as before [2], involving 33 radial nodes and about 1000 axial steps to cover the range $x/d<400$ – where x is distance from the burner having exit diameter d. Time-averaged scalar properties were then computed and retained at 80 axial stations for the radiation calculations, since integration of equation (1) is less sensitive to discretization errors than the solution of the differential equations for structure predictions. Results for these 80 stations were then interpolated to find properties at 20 stations along each path through the flame. The calculations were summed over the wavelength range 1.25–12.5 μm, using wavelength increments of 0.10 μm. Richardson extrapolation suggests that the overall descretization error for computations reported here is less than 10 percent, which is well within the accuracy of the structure model, the narrow-band model, and potential effects of turbulent fluctuations.

Results and Discussion

Measurements and predictions of total radiative heat flux are illustrated in Figs. 2 and 3. The measurements are in qualitative agreement with earlier findings for methane flames, in this laboratory [11]. The radiative heat flux distribution parallel to the axis, Fig. 2, reaches a maximum near the height where the mean temperature along the axis is maximum, e.g., roughly $x/d = 100$ [2]. Radiative heat fluxes along the base plane, however, decrease monotonically with increasing radial distance. Although peak mean temperatures and species concentrations are similar for the three flames, flame dimensions tend to decrease with decreasing initial Reynolds number due to effects of buoyancy [2], which causes radiative heat fluxes to decrease at lower Reynolds numbers as well.

The comparison between predictions and measurements is reasonably good, e.g., discrepancies are generally less than 10–30 percent. Predictions also represent trends with respect to position and Reynolds number reasonably well. The differences between predictions and measurements are comparable to errors observed during an earlier study of spectral intensities for these flames and are attributable uncertainties in the structure model, effects of turbulent fluctuations, and uncertainties in the narrow-band model itself [3]. In addition, interaction between radiation and the flow, particularly for the 4.3-μm band of CO_2 which approaches optically thick conditions in these flames, could also be a factor.

While these results are encouraging, the present approach is computationally intensive and use of a wide-band radiation model should be considered for practical calculations. Unlike the test methane flames, most unwanted fires exhibit significant continuum radiation from soot which presents new problems. Work in this laboratory on methods for considering soot radiation phenomena is currently underway.

Acknowledgment

This research was supported by the United States Department of Commerce, National Bureau of Standards, Grant No. NB81NADA2044, with H. Baum of the Center for Fire Research serving as Scientific Officer.

References

1 Jeng, S-M., Chen, L-D., and Faeth, G. M., "The Structure of Buoyant Methane and Propane Diffusion Flames," *Nineteenth Symposium (International) on Combustion*, The Combustion Institute, 1982, pp. 349–358.

2 Jeng, S-M., and Faeth, G. M., "Species Concentrations and Turbulence Properties in Buoyant Methane Diffusion Flames," ASME JOURNAL OF HEAT TRANSFER, in press.

3 Jeng, S-M., Lai, M-C., and Faeth, G. M., "Nonluminous Radiation in Turbulent Buoyant Axisymmetric Flames," *Comb. Sci. and Tech.*, in press.

4 Grosshandler, W. L., and Sawyer, R. F., "Radiation from a Methanol Furnace," JOURNAL OF HEAT TRANSFER, Vol. 100, 1978, pp. 247–252.

5 Fishburne, E. S., and Pergament, H. S., "The Dynamics and Radiant Intensity of Large Hydrogen Flames," *Seventeenth Symposium (International) on Combustion*, The Combustion Institute, Pittsburgh, Pa., 1979, pp. 1063–1073.

6 Lockwood, F. C., and Shah, N. B., "A New Radiation Solution Method for Incorporation in General Combustion Prediction Procedures," *Eighteenth Symposium (International) on Combustion*, The Combustion Institute, Pittsburgh, Pa., 1981, pp. 1405–1414.

7 Jeng, S. M., "An Investigation of the Structure and Radiation Properties of Turbulent Buoyant Diffusion Flames," Ph.D. thesis, The Pennsylvania State University, May 1984.

8 Bilger, R. W., "Reaction Rates in Diffusion Flames," *Combustion and Flame*, Vol. 30, 1977, pp. 277–284.

9 Ludwig, C. B., Malkmus, W., Reardon, J. E., and Thomson, J. A., *Handbook of Infrared Radiation from Combustion Gases*, NASA SP-3080, 1973.

10 Lee, R. H. C., and Happel, J., "Thermal Radiation of Methane Gas," *I&EC Fundamentals*, Vol. 3, 1964, pp. 167–176.

11 You, H-Z., and Faeth, G. M., "Buoyant Axisymmetric Turbulent Diffusion Flames in Still Air," *Combustion and Flame*, Vol. 44, No. 1-3, 1982, pp. 251–275.

A Finite Difference Solution to Transient Combined Conductive and Radiative Heat Transfer in an Annular Medium

F. Gordaninejad[1] and J. Francis[2]

Nomenclature

c_p = specific heat at constant pressure
I = radiative intensity
k = thermal conductivity
N = conduction radiation parameter
q_i = flux at the inner surface
Q_r = radiative flux
r = radius
$R, \tilde{R}$ = outer radius
t = time
T = temperature
X = coordinate along the horizontal projection of a ray
α = angle a ray makes with the horizon
β = horizontal projection of the angle between the direction of intensity and a line from the point of entry into the medium to the center of the cylinder
ϵ = emissivity at inner surface
$\bar{\epsilon}$ = thermal diffusivity
θ = angle between the direction of the intensity and the outward drawn normal to the surface
κ = absorption coefficient
ν = frequency
ρ = density
σ_s = Stefan-Boltzmann constant
ϕ = radiation potential
ω = solid angle

Nondimensional Variables

$$N = \frac{k\kappa}{4\sigma_s T^3_{\text{reference}}}$$

$$Q^* = \frac{Q_r}{\sigma_s T^4_{\text{reference}}}$$

$$r^* = \kappa r$$

$$t^* = \frac{4k\ \sigma_s T^3_{\text{reference}} t}{\rho\ c_p}$$

$$X^* = kx$$

$$\phi = \frac{\pi I}{\sigma_s T^4_{\text{reference}}}$$

---

[1] Assistant Professor, Aerospace, Department of Mechanical Engineering, University of Nevada, Reno, Nevada 89557

[2] Professor, Aerospace, Mechanical and Nuclear Engineering, University of Okla., Mem. ASME

Contributed by the Heat Transfer Division for publication in the JOURNAL OF HEAT TRANSFER. Manuscript received by the Heat Transfer Division July 18, 1983.

equation (1) is less sensitive to discretization errors than the solution of the differential equations for structure predictions. Results for these 80 stations were then interpolated to find properties at 20 stations along each path through the flame. The calculations were summed over the wavelength range 1.25–12.5 μm, using wavelength increments of 0.10 μm. Richardson extrapolation suggests that the overall descretization error for computations reported here is less than 10 percent, which is well within the accuracy of the structure model, the narrow-band model, and potential effects of turbulent fluctuations.

Results and Discussion

Measurements and predictions of total radiative heat flux are illustrated in Figs. 2 and 3. The measurements are in qualitative agreement with earlier findings for methane flames, in this laboratory [11]. The radiative heat flux distribution parallel to the axis, Fig. 2, reaches a maximum near the height where the mean temperature along the axis is maximum, e.g., roughly $x/d = 100$ [2]. Radiative heat fluxes along the base plane, however, decrease monotonically with increasing radial distance. Although peak mean temperatures and species concentrations are similar for the three flames, flame dimensions tend to decrease with decreasing initial Reynolds number due to effects of buoyancy [2], which causes radiative heat fluxes to decrease at lower Reynolds numbers as well.

The comparison between predictions and measurements is reasonably good, e.g., discrepancies are generally less than 10–30 percent. Predictions also represent trends with respect to position and Reynolds number reasonably well. The differences between predictions and measurements are comparable to errors observed during an earlier study of spectral intensities for these flames and are attributable uncertainties in the structure model, effects of turbulent fluctuations, and uncertainties in the narrow-band model itself [3]. In addition, interaction between radiation and the flow, particularly for the 4.3-μm band of CO_2 which approaches optically thick conditions in these flames, could also be a factor.

While these results are encouraging, the present approach is computationally intensive and use of a wide-band radiation model should be considered for practical calculations. Unlike the test methane flames, most unwanted fires exhibit significant continuum radiation from soot which presents new problems. Work in this laboratory on methods for considering soot radiation phenomena is currently underway.

Acknowledgment

This research was supported by the United States Department of Commerce, National Bureau of Standards, Grant No. NB81NADA2044, with H. Baum of the Center for Fire Research serving as Scientific Officer.

References

1 Jeng, S-M., Chen, L-D., and Faeth, G. M., "The Structure of Buoyant Methane and Propane Diffusion Flames," *Nineteenth Symposium (International) on Combustion*, The Combustion Institute, 1982, pp. 349–358.

2 Jeng, S-M., and Faeth, G. M., "Species Concentrations and Turbulence Properties in Buoyant Methane Diffusion Flames," ASME JOURNAL OF HEAT TRANSFER, in press.

3 Jeng, S-M., Lai, M-C., and Faeth, G. M., "Nonluminous Radiation in Turbulent Buoyant Axisymmetric Flames," *Comb. Sci. and Tech.*, in press.

4 Grosshandler, W. L., and Sawyer, R. F., "Radiation from a Methanol Furnace," JOURNAL OF HEAT TRANSFER, Vol. 100, 1978, pp. 247–252.

5 Fishburne, E. S., and Pergament, H. S., "The Dynamics and Radiant Intensity of Large Hydrogen Flames," *Seventeenth Symposium (International) on Combustion*, The Combustion Institute, Pittsburgh, Pa., 1979, pp. 1063–1073.

6 Lockwood, F. C., and Shah, N. B., "A New Radiation Solution Method for Incorporation in General Combustion Prediction Procedures," *Eighteenth Symposium (International) on Combustion*, The Combustion Institute, Pittsburgh, Pa., 1981, pp. 1405–1414.

7 Jeng, S. M., "An Investigation of the Structure and Radiation Properties of Turbulent Buoyant Diffusion Flames," Ph.D. thesis, The Pennsylvania State University, May 1984.

8 Bilger, R. W., "Reaction Rates in Diffusion Flames," *Combustion and Flame*, Vol. 30, 1977, pp. 277–284.

9 Ludwig, C. B., Malkmus, W., Reardon, J. E., and Thomson, J. A., *Handbook of Infrared Radiation from Combustion Gases*, NASA SP-3080, 1973.

10 Lee, R. H. C., and Happel, J., "Thermal Radiation of Methane Gas," *I&EC Fundamentals*, Vol. 3, 1964, pp. 167–176.

11 You, H-Z., and Faeth, G. M., "Buoyant Axisymmetric Turbulent Diffusion Flames in Still Air," *Combustion and Flame*, Vol. 44, No. 1-3, 1982, pp. 251–275.

A Finite Difference Solution to Transient Combined Conductive and Radiative Heat Transfer in an Annular Medium

F. Gordaninejad[1] **and J. Francis**[2]

Nomenclature

c_p = specific heat at constant pressure
I = radiative intensity
k = thermal conductivity
N = conduction radiation parameter
q_i = flux at the inner surface
Q_r = radiative flux
r = radius
$R, \tilde{R}$ = outer radius
t = time
T = temperature
X = coordinate along the horizontal projection of a ray
α = angle a ray makes with the horizon
β = horizontal projection of the angle between the direction of intensity and a line from the point of entry into the medium to the center of the cylinder
ϵ = emissivity at inner surface
$\bar{\epsilon}$ = thermal diffusivity
θ = angle between the direction of the intensity and the outward drawn normal to the surface
κ = absorption coefficient
ν = frequency
ρ = density
σ_s = Stefan-Boltzmann constant
ϕ = radiation potential
ω = solid angle

Nondimensional Variables

$$N = \frac{k\kappa}{4\sigma_s T^3_{\text{reference}}}$$

$$Q^* = \frac{Q_r}{\sigma_s T^4_{\text{reference}}}$$

$$r^* = \kappa r$$

$$t^* = \frac{4k\ \sigma_s T^3_{\text{reference}} t}{\rho\ c_p}$$

$$X^* = kx$$

$$\phi = \frac{\pi I}{\sigma_s T^4_{\text{reference}}}$$

---

[1] Assistant Professor, Aerospace, Department of Mechanical Engineering, University of Nevada, Reno, Nevada 89557

[2] Professor, Aerospace, Mechanical and Nuclear Engineering, University of Okla., Mem. ASME

Contributed by the Heat Transfer Division for publication in the JOURNAL OF HEAT TRANSFER. Manuscript received by the Heat Transfer Division July 18, 1983.

Subscripts

i = inner surface
m = node number
r = radiative
ν = monochromatic

Introduction

Numerous authors have analyzed combined conduction and radiation in various geometries. Lick [1] studied the transient conduction and radiation in a planar medium using a kernel substitution technique. Howell [2] analyzed combined radiation and conduction in an annular region using exchange factors. Viskanta and Merriam [3] investigated combined conduction and radiation in spherical geometries for an absorbing, emitting, and scattering medium with various boundary conditions. Chang and Smith [4] analyzed transient and steady-state combined radiation and conduction between coaxial cylinders using the Eddington approximation. Lii and Özisik [5] studied transient heat transfer in an absorbing, emitting, and scattering medium for a planar geometry using the Case normal mode expansion technique. Anderson and Viskanta [6] have studied coupled radiation/conduction problems in a planar medium, both analytically and experimentally. Saito et al. [7], investigated the hot-wire thermal conductivity method analytically with combined radiative and conduction heat transfer. Their approach was a finite difference approximation to the problem where the radiative contribution is analyzed using absorbing wedges of various dimensions.

In this paper, a modified finite difference approach to the problem of transient combined conduction and radiation in an absorbing and emitting annular medium is presented. Fernandes and Francis [8] subsequently expanded the problem to include isotropic scattering using the finite element method but, did not include the step flux boundary condition.

Theory and Formulation

The governing equation for a conducting diathermanous medium is

$$\rho c_p \frac{\partial T}{\partial t} = \nabla \cdot (K \nabla T) - \nabla \cdot \mathbf{Q}_r \tag{1}$$

Assuming constant thermal conductivity and nondimensionalizing, equation (1) becomes

$$\frac{\partial T^*}{\partial t^*} = N \nabla^2 T^* - \frac{1}{4} \nabla \cdot \mathbf{Q}_r^* \tag{2}$$

For an annular geometry with cylindrical symmetry, the net radiant heat flux at any radial distance r is

$$Q_r(r) = \int_0^\infty \int_\omega I_\nu(r) \cos\theta \, d\omega \, d\nu \tag{3}$$

For the gray case, the nondimensional form of equation (3) becomes

$$Q_r^*(r^*) = \frac{1}{\pi} \int_\omega \phi(r^*) \cos\theta \, d\omega \tag{4}$$

The transport equation is written in terms of the angle β, the horizontal projection of the angle between the intensity direction and a radius from the point of entry for two different regions

$$\frac{dI^-}{dr^*} - \frac{I^-}{\cos\alpha \, F(r^*,\beta)} = - \frac{I_b}{\cos\alpha \, F(r^*,\beta)} \qquad \le x^* < R^* \cos\beta \tag{5}$$

$$\frac{dI^+}{dr^*} + \frac{I^+}{\cos\alpha \, F(r^*,\beta)} = \frac{I_b}{\cos\alpha F(r^*,\beta)} \qquad R^*\cos\beta < x^* \le 2R^*\cos\beta \tag{6}$$

where

$$F(r^*,\beta) = \frac{\sqrt{r^{*2} - R^{*2}\sin^2\beta}}{\rho\kappa r^*} \tag{7}$$

To compute the radiation potential ϕ, the transport equation is recast in terms of the dimensionless variable solved subject to the appropriate boundary conditions and substituted into the energy equation. However, the transport equation includes the local blackbody radiation potential ϕ_b, which requires knowledge of the unknown temperature distribution. To obtain a numerical solution, an initial temperature distribution is assumed, and the transport equation is solved relative to this assumed temperature distribution. The resulting net radiative flux is then substituted into the energy equation, and the temperature distribution is found by suitable numerical means. To simplify the problem, a coordinate change is made following the procedure of Kesten [9].

The radiative boundary conditions imposed are that at the inner radius the surfaces is specular and at the outer radius the radiation field is black. This is similar to what might be found in a hot-wire thermal conductivity apparatus. The governing equations in terms of these variables are presented in [8] and [10].

Finite Difference Formulations

The energy equation is formulated in a finite difference format using the explicit form of the time derivative. Simpson's method is used to approximate the integrals. Since the angle β is varying, the limit $R^*\sin\beta$ will not always fall on integer multiple of Δr^*. Therefore, for this type of integrals, the temperature distribution is treated as linear across the ring of thickness Δr^* that encompasses $r^* = R^*\sin\beta$, and a Gauss quadrature is applied over that portion of the integral from $R^*\sin\beta$ to the next integer multiple of Δr^*. Simpson's rule is used for the remainder of the integral. Since the radiation intensity is discontinuous at $r^* = R^*\sin\beta$, using the Gauss quadrature (five point) just described, the difficulty of integration over this discontinuity is overcome.

When a small number of nodes are used (large Δr^*), the linear approximation just mentioned can cause considerable error. This is particularly true for the first node, where considerable changes in temperature are occurring near time zero. To eliminate this difficulty (only when $r^* = R^*\sin\beta$ falls within the first two nodes and near time zero), a second-order curve is assumed to represent the temperature distribution across the first node, and the procedure aforementioned is then followed. The integrals over the angles α and β are found to be well represented with a five-point Gauss quadrature.

Two different boundary conditions were studied. The first one is a step change in temperature on both inner and outer surfaces. The second type of boundary condition studied here is a step flux at the inner surface, which results in the following finite difference equation

$$Q_R^*(r^*) + 2N\left(\frac{1}{r_m^*} + \frac{2}{\Delta r^*}\right)[T^*(r_m^*) - T^*(r_1^*)] - Q_r^*(r_m^*) = 2r_m^* \frac{\Delta T^*}{\Delta t^*} \tag{8}$$

were net radiative flux is

$$Q_r^*(r_m^*) = \epsilon\sigma_s T_i^{*4} - \frac{4\epsilon R^*}{\pi\sigma r_i^*} \left\{ \int_0^{\frac{\pi}{2}} \int_0^{\sin^{-1}\frac{r_i^*}{R^*}} \cos\beta\cos^2\alpha e^{\frac{1}{\cos\alpha}\left[\sqrt{r_i^{*2} - R^{*2}\sin^2\beta} - R^*\cos\beta\right]} d\beta d\alpha \right.$$

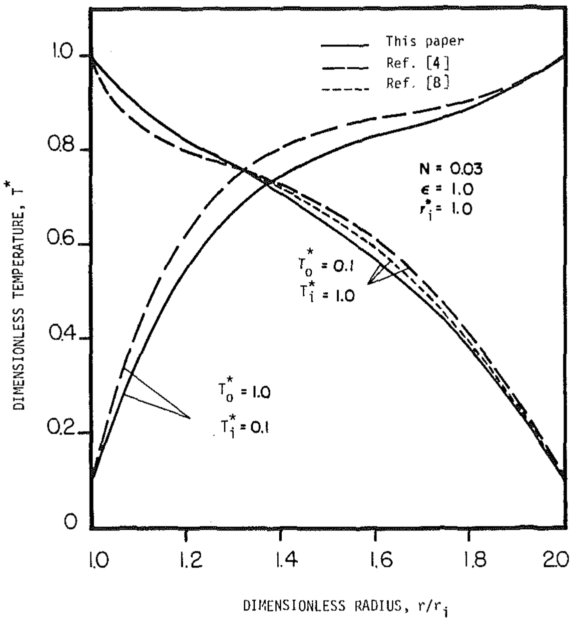

Fig. 1 Steady-state temperature distribution comparisons among Eddington first approximation [4], finite element method [8] and finite difference solutions

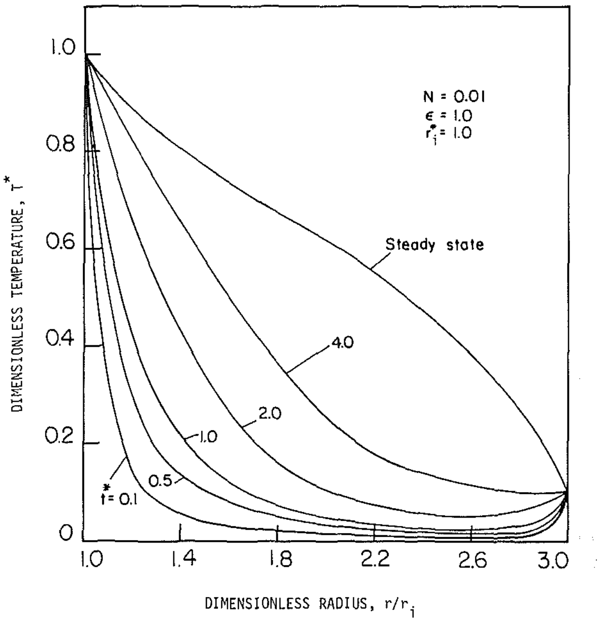

Fig. 3 Transient temperature distribution in the annulus for $r_i^* = 1.0$, $\epsilon = 1.0$, and $N = 0.01$

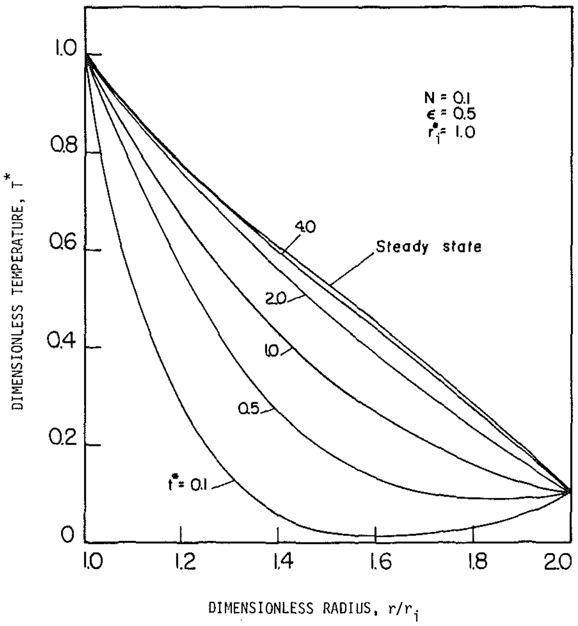

Fig. 2 Transient temperature distribution in the annulus for $r_i^* = 1.0$, $\epsilon = 0.5$ and $N = 0.1$

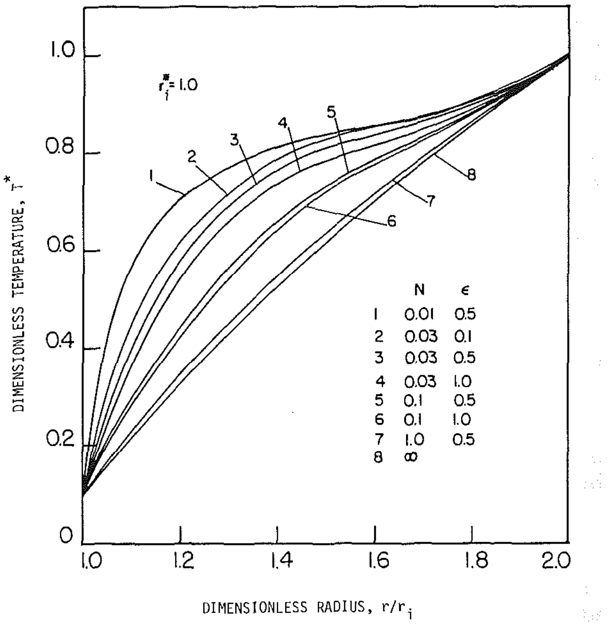

Fig. 4 Effects of inside surface emissivity and conduction radiation parameter on the steady-state temperature distribution in the annulus

$$+\int_0^{\frac{\pi}{2}}\int_0^{\sin^{-1}\frac{r^*{}_i}{R^*}}\int_{r_i^*}^{R^*}\frac{r'^*T^{*4}\cos\beta\cos\alpha}{\sqrt{r'^{*2}-R^{*2}\sin^2\beta}}$$

$$e^{\frac{1}{\cos\alpha}[\sqrt{r_i^{*2}-R^{*2}\sin^2\beta}-\sqrt{r'^{*2}-R^{*2}\sin^2\beta}]dr'}\ \mu\beta d\alpha\Big\} \qquad (9)$$

where $T_{\text{reference}} = T_i$.

For the flux boundary condition, the problem can be simplified by taking note of the exact analytical solution for pure conduction. Carslaw and Jaeger [11] have shown that the line source pure conduction solution is

$$T - T_{\text{initial}} = -\frac{q_i}{4\pi k}E_i\left(\frac{r^2}{4\bar{\epsilon}t}\right) \qquad (10)$$

Note that for pure conduction if $r^2/4\bar{\epsilon}t > 3$, a small change in temperature occurs. Therefore, for studies that include radiation but are not optically thin, the procedure of [7] is followed (for $r^2/4\bar{\epsilon}t = 7$ or $\tilde{R} = \sqrt{28\bar{\epsilon}t_{\max}}$ there is very small variation in temperature). This allows the reduction of the physical dimension of the problem and therefore a medium of greater optical density can be analyzed.

Numerical Results

In this analysis only *five* nodes are used (computer runs were made with ten and twenty nodes but the results did not vary substantially). It should be noted that for more than five nodes it is necessary to reduce the time step appreciably. To validate the results, comparisons are made with published results. For the step temperature change boundary condition, comparisons are made among a solution based on the Eddington's first approximation [4], *twenty* element finite element solution [8], and this study (see Fig. 1). The comparisons are quite good with predicted temperatures never differing by more than 10 percent from [4] and, even better with finite element solution.

The transient temperature distributions with two different emissivities and three different values of N are shown in Figs. 2 and 3. As expected, for larger values of N, the solution approaches the pure conduction solution. Also results for an optically thicker sample and dimensionless radius values from 1.0–3.0 are shown in Fig. 3. As one would expect, the effect of a black inside surface is to give the highest temperature and the effect of a perfectly reflecting one is to give the lowest temperatures throughout the medium. The effect of inside surface emissivities and conduction radiation parameter on the steady-state temperature distribution with different step boundary temperature changes are shown in Fig. 4.

Using the properties of toluene, the step flux solution is compared to results of [7][3]; these differed by less than 1 percent. The comparison is seen to be quite good.

Conclusions

This paper resulted in a finite difference solution of the transient combined conductive and radiative heat transfer in an annular geometry. The solution was shown to closely represent the exact solution for the case of pure conduction. Both the step temperature boundary condition and the step flux boundary condition problems were found to compare quite favorably with approximate solutions using only five nodes. The study included ten and twenty node models but the results did not change appreciably.

In the initial time step, a second-order temperature distribution across the first element was required in order to obtain meaningful results. For the step flux boundary condition, since at $r > \sqrt{28\bar{\epsilon}t}$ the temperature changes very little, the physical size was reduced to $r = \sqrt{28\bar{\epsilon}t}$. These modifications were important in obtaining the results presented.

The excellent results for a small number of nodes from a relatively simple approach render this a very useful means of solving problems of this type.

References

1 Lick, W., "Transient Energy Transfer by Radiation and Conduction," *Int. Journal of Heat and Mass Transfer*, Vol. 8, 1965, pp. 119–127.

2 Howell, J. R., "Determination of Combined Conduction and Radiation of Heat Absorbing Media by the Exchange Factor Approximation," *Chemical Engineering Progress Symposium Series*, Vol. 61, No. 59, 1965.

3 Viskanta, R., and Merriam, R. L., "Heat Transfer by Combined Conduction and Radiation Between Concentric Spheres Separated by a Radiating Medium," ASME JOURNAL OF HEAT TRANSFER, May 1968, pp. 248–256.

4 Chang, Y. P., and Smith, R. S., "Steady and Transient Heat Transfer by Radiation and Conduction in a Medium Bounded by Two Coaxial Cylindrical Surfaces," *International Journal of Heat and Mass Transfer*, Vol. 13, 1970, pp. 69–80.

5 Lii, C. C., and Özisik, M. N., "Transient Radiation and Conduction in an Absorbing, Emitting, and Scattering Slab with Reflective Boundaries," *International Journal of Heat and Mass Transfer*, Vol. 15, 1972, pp. 1175–1179.

6 Anderson, E. E., and Viskanta, R., "Effective Thermal Conductivity for Heat Transfer Through Semi-Transparent Solids," *Journal of American Ceramic Society*, Vol. 56, No. 10, 1973, pp. 541–546.

7 Saito, A., Mani, N., and Venart, J. E. S., "Combined Transient Conduction/Radiation Effects with the Lime Source Technique of Measuring Thermal Conductivity," Paper No. 76-CSME/CSchE-6, presented at the 16th National Heat Transfer Conference, St. Louis, Mo., Aug. 8–11, 1976.

8 Fernandes, R., and Francis, J., "Combined Conductive and Radiative Heat Transfer in an Absorbing, Emitting and Scattering Cylindrical Medium," ASME JOURNAL OF HEAT TRANSFER, Vol. 104, 1982, pp. 594–601.

9 Kesten, A. S., "Radiant Heat Flux Distribution in a Cylindrically-Symmetric Nonisothermal Gas with Temperature Dependent Absorption Coefficient," *Journal of Quant. Spectrosc. and Radiative Heat Transfer*, Vol. 8, 1968, pp. 419–434.

10 Gordaninejad, F., *Analytical Analysis of Combined Conductive and Radiative Heat Transfer as Applied to the Hot Wire Thermal Conductivity Method*, M.S. thesis, Mechanical Engineering, The University of Oklahoma, Norman, Okla, 1980.

11 Carslaw, H. S., and Jaeger, J. C., *Conduction of Heat in Solids*, Oxford University Press, 1947.

---

[3] Reference [7] uses *forty* radial nodes and *twenty* angular elements.

Predictions of Mean Scalar Properties in Turbulent Propane Diffusion Flames

S-M. Jeng[1] and G. M. Faeth[2]

Introduction

In order to estimate convective and radiative heat transfer from turbulent diffusion flames, which controls the growth of unwanted fires, the structure of these flames must be understood. We recently completed an evaluation of a Favre-averaged κ-ϵ-g turbulence model for turbulent methane flames that yielded encouraging results [1, 2]. The objective of this note is to extend the evaluation to turbulent propane flames by using existing measurements from axisymmetric flames burning in still air [2–4].

Liew et al. [5] have also treated turbulent propane flames using a laminar flamelet technique, examined here, with encouraging results. The present contribution extends the evaluation to treat all mean scalar properties of the flames as well as considering an alternative partial equilibrium method, which has advantages for practical applications. The following description of the study is brief – complete details are available elsewhere [6].

Theoretical Methods

General Description. The analysis which is fully presented in [1], uses many features of the Favre-averaged, κ-ϵ-g turbulence model described by Bilger [7]. The major assumptions are steady, axisymmetric turbulent diffusion flame in a stagnant environment; boundary layer approximations; low Mach number flow; radiation only perturbs the structure; and exchange coefficients of all species and heat are identical. These assumptions are typical of most models of turbulent flames [1–3, 5–7]. In this case, instantaneous scalar properties (density, temperature, and species concentrations) are only functions of mixture fraction (the fraction of total mass at a point which is fuel) – termed state relationships. Solution of the governing equations for mixture fraction f and the square of its fluctuations g can then be combined with the state relationships to yield predictions of scalar properties in turbulent flows [1–3, 5–7].

State Relationships

Bilger [8] and Liew et al. [5] suggest a laminar flamelet method to find state relationships. This rests on Bilger's observation that scalar properties in laminar diffusion flames are nearly universal functions of mixture fraction for a given fuel and surroundings – relatively independent of shear rate and position. Correlation of these measurements is then used in turbulent flame calculations, implying that turbulent flames consist of a succession of laminar flamelets.

A second approach is the partial equilibrium method used earlier in this laboratory [1, 2]. Properties are found as a function of mixture fraction using conventional thermodynamic equilibrium calculations for f less than a critical value f_c and by frozen adiabatic mixing calculations of the

---

[1] Research Assistant, Department of Mechanical Engineering, The Pennsylvania State University, University Park, Pa. 16802.

[2] Professor, Department of Mechanical Engineering, The Pennsylvania State University, University Park, Pa., 16802, Fellow ASME.

Contributed by the Heat Transfer Division for publication in the JOURNAL OF HEAT TRANSFER. Manuscript received by the Heat Transfer Division August 25, 1983.

element solution [8], and this study (see Fig. 1). The comparisons are quite good with predicted temperatures never differing by more than 10 percent from [4] and, even better with finite element solution.

The transient temperature distributions with two different emissivities and three different values of N are shown in Figs. 2 and 3. As expected, for larger values of N, the solution approaches the pure conduction solution. Also results for an optically thicker sample and dimensionless radius values from 1.0–3.0 are shown in Fig. 3. As one would expect, the effect of a black inside surface is to give the highest temperature and the effect of a perfectly reflecting one is to give the lowest temperatures throughout the medium. The effect of inside surface emissivities and conduction radiation parameter on the steady-state temperature distribution with different step boundary temperature changes are shown in Fig. 4.

Using the properties of toluene, the step flux solution is compared to results of [7][3]; these differed by less than 1 percent. The comparison is seen to be quite good.

Conclusions

This paper resulted in a finite difference solution of the transient combined conductive and radiative heat transfer in an annular geometry. The solution was shown to closely represent the exact solution for the case of pure conduction. Both the step temperature boundary condition and the step flux boundary condition problems were found to compare quite favorably with approximate solutions using only five nodes. The study included ten and twenty node models but the results did not change appreciably.

In the initial time step, a second-order temperature distribution across the first element was required in order to obtain meaningful results. For the step flux boundary condition, since at $r > \sqrt{28\bar{\epsilon}t}$ the temperature changes very little, the physical size was reduced to $r = \sqrt{28\bar{\epsilon}t}$. These modifications were important in obtaining the results presented.

The excellent results for a small number of nodes from a relatively simple approach render this a very useful means of solving problems of this type.

References

1 Lick, W., "Transient Energy Transfer by Radiation and Conduction," *Int. Journal of Heat and Mass Transfer*, Vol. 8, 1965, pp. 119–127.

2 Howell, J. R., "Determination of Combined Conduction and Radiation of Heat Absorbing Media by the Exchange Factor Approximation," *Chemical Engineering Progress Symposium Series*, Vol. 61, No. 59, 1965.

3 Viskanta, R., and Merriam, R. L., "Heat Transfer by Combined Conduction and Radiation Between Concentric Spheres Separated by a Radiating Medium," ASME JOURNAL OF HEAT TRANSFER, May 1968, pp. 248–256.

4 Chang, Y. P., and Smith, R. S., "Steady and Transient Heat Transfer by Radiation and Conduction in a Medium Bounded by Two Coaxial Cylindrical Surfaces," *International Journal of Heat and Mass Transfer*, Vol. 13, 1970, pp. 69–80.

5 Lii, C. C., and Özisik, M. N., "Transient Radiation and Conduction in an Absorbing, Emitting, and Scattering Slab with Reflective Boundaries," *International Journal of Heat and Mass Transfer*, Vol. 15, 1972, pp. 1175–1179.

6 Anderson, E. E., and Viskanta, R., "Effective Thermal Conductivity for Heat Transfer Through Semi-Transparent Solids," *Journal of American Ceramic Society*, Vol. 56, No. 10, 1973, pp. 541–546.

7 Saito, A., Mani, N., and Venart, J. E. S., "Combined Transient Conduction/Radiation Effects with the Lime Source Technique of Measuring Thermal Conductivity," Paper No. 76-CSME/CSchE-6, presented at the 16th National Heat Transfer Conference, St. Louis, Mo., Aug. 8–11, 1976.

8 Fernandes, R., and Francis, J., "Combined Conductive and Radiative Heat Transfer in an Absorbing, Emitting and Scattering Cylindrical Medium," ASME JOURNAL OF HEAT TRANSFER, Vol. 104, 1982, pp. 594–601.

9 Kesten, A. S., "Radiant Heat Flux Distribution in a Cylindrically-Symmetric Nonisothermal Gas with Temperature Dependent Absorption Coefficient," *Journal of Quant. Spectrosc. and Radiative Heat Transfer*, Vol. 8, 1968, pp. 419–434.

10 Gordaninejad, F., *Analytical Analysis of Combined Conductive and Radiative Heat Transfer as Applied to the Hot Wire Thermal Conductivity Method*, M.S. thesis, Mechanical Engineering, The University of Oklahoma, Norman, Okla, 1980.

11 Carslaw, H. S., and Jaeger, J. C., *Conduction of Heat in Solids*, Oxford University Press, 1947.

---

[3] Reference [7] uses *forty* radial nodes and *twenty* angular elements.

Predictions of Mean Scalar Properties in Turbulent Propane Diffusion Flames

S-M. Jeng[1] and G. M. Faeth[2]

Introduction

In order to estimate convective and radiative heat transfer from turbulent diffusion flames, which controls the growth of unwanted fires, the structure of these flames must be understood. We recently completed an evaluation of a Favre-averaged κ-ϵ-g turbulence model for turbulent methane flames that yielded encouraging results [1, 2]. The objective of this note is to extend the evaluation to turbulent propane flames by using existing measurements from axisymmetric flames burning in still air [2–4].

Liew et al. [5] have also treated turbulent propane flames using a laminar flamelet technique, examined here, with encouraging results. The present contribution extends the evaluation to treat all mean scalar properties of the flames as well as considering an alternative partial equilibrium method, which has advantages for practical applications. The following description of the study is brief – complete details are available elsewhere [6].

Theoretical Methods

General Description. The analysis which is fully presented in [1], uses many features of the Favre-averaged, κ-ϵ-g turbulence model described by Bilger [7]. The major assumptions are steady, axisymmetric turbulent diffusion flame in a stagnant environment; boundary layer approximations; low Mach number flow; radiation only perturbs the structure; and exchange coefficients of all species and heat are identical. These assumptions are typical of most models of turbulent flames [1–3, 5–7]. In this case, instantaneous scalar properties (density, temperature, and species concentrations) are only functions of mixture fraction (the fraction of total mass at a point which is fuel) – termed state relationships. Solution of the governing equations for mixture fraction f and the square of its fluctuations g can then be combined with the state relationships to yield predictions of scalar properties in turbulent flows [1–3, 5–7].

State Relationships

Bilger [8] and Liew et al. [5] suggest a laminar flamelet method to find state relationships. This rests on Bilger's observation that scalar properties in laminar diffusion flames are nearly universal functions of mixture fraction for a given fuel and surroundings – relatively independent of shear rate and position. Correlation of these measurements is then used in turbulent flame calculations, implying that turbulent flames consist of a succession of laminar flamelets.

A second approach is the partial equilibrium method used earlier in this laboratory [1, 2]. Properties are found as a function of mixture fraction using conventional thermodynamic equilibrium calculations for f less than a critical value f_c and by frozen adiabatic mixing calculations of the

---

[1] Research Assistant, Department of Mechanical Engineering, The Pennsylvania State University, University Park, Pa. 16802.

[2] Professor, Department of Mechanical Engineering, The Pennsylvania State University, University Park, Pa., 16802, Fellow ASME.

Contributed by the Heat Transfer Division for publication in the JOURNAL OF HEAT TRANSFER. Manuscript received by the Heat Transfer Division August 25, 1983.

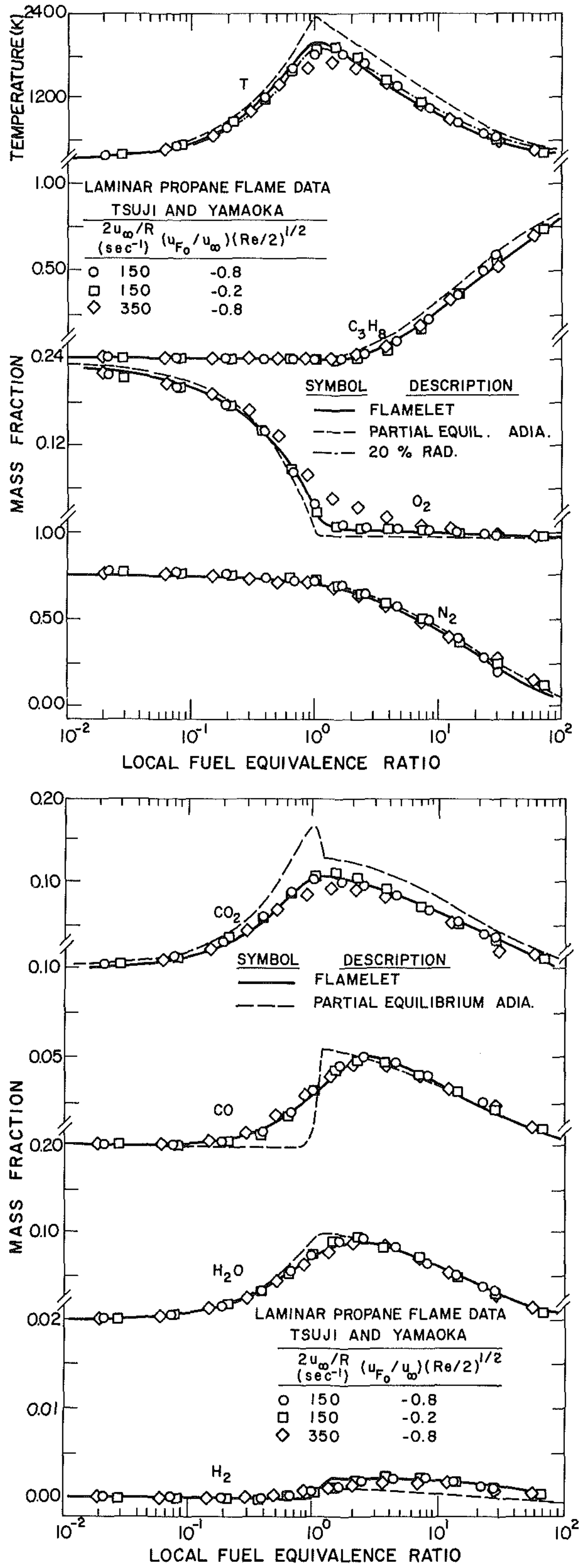

Fig. 1 State relationships for propane diffusion flames burning in air

mixture at f_c and pure fuel for $f>f_c$. Freezing reaction in this way helps account for low rates of equilibration at the low mixture temperatures found at high mixture fractions. Effects of radiant heat losses are either ignored (adiabatic) or a fixed fraction of the chemical energy released during equilibration is assumed to be lost by radiation [1].

State relationships found with these methods, for propane burning in air, are illustrated in Fig. 1. The independent variable is local fuel equivalence ratio, which is directly related to mixture fraction. The laminar flame measurements were obtained from Tsuji and Yamaoka [9-11]. Fuel concentrations shown on the plots omit minor species, which comprise roughly 5 percent (by mass) of the mixture for fuel-rich conditions. A reasonable correlation of the data is achieved – yielding laminar flamelet state relationships. The partial equilibrium method provides a reasonable approximation of these results for a critical fuel equivalence ratio, $\phi_c = 1.2$, which is the same value used earlier for methane [1]. Allowing for 20 percent radiative heat loss, which is reasonable for a propane flame, provides a good estimate of mixture temperature.

Results and Discussion

Predictions of mean momentum flux along the flame axis were in good agreement with measurements of Becker and Yamazaki [4] for propane flames having various degrees of buoyancy – similar to results for methane reported in [1] (see [2] for plots).

Predicted and measured mean temperatures and the concentrations of major gas species (C_3H_8, N_2, O_2, CO_2, H_2O, CO, and H_2) are illustrated in Figs. 2-4. The measurements were obtained from Mao et al. [3], for a flame having a burner exit Reynolds number of 23560, at three axial stations $x/d = 75$, 170, and 340, where x is distance above a burner having exit diameter d. These locations are before, near, and after the point where mean temperature reaches a maximum along the axis (the flame tip). Results are plotted as a function of r/x, where r is radial distance, so that predictions of flow widths can be evaluated. Only predictions for the laminar flamelet model are shown – results for the partial equilibrium methods are essentially the same.

Favre-averaged predictions are plotted in Figs. 2-4, while measurements generally are between Favre- and time-averages [1, 7]. Differences between these averages and experimental uncertainties for mean temperatures are less than 200 K at the flame tip and generally less than 100 K elsewhere. For data appearing in Figs. 2-4, mass fraction sums were within 2 percent of unity and element mass ratios had the following mean values and standard deviations: C/H, 3.5 and 0.8; O/N, 0.31 and 0.07. Allowing for hydrogen added at the injector, the flame should have a C/H mass ratio of 4.3 while the O/N mass ratio of dry air is 0.304. The discrepancies are due to effects of ambient humidity and sampling errors. Based on these checks, uncertainties of composition measurements are estimated to be on the order of 20 percent.

The comparison between predictions and measurements is reasonably good, resolving earlier problems of Mao et al. [3] in predicting species concentrations with a more ad hoc partial equilibrium method. An apparent exception is the H_2O concentrations, where predictions underestimate the measurements. These data appear to be in error, however, since some measurements exceed values expected for stoichiometric combustion. Therefore, further measurements are needed to test this aspect of the predictions. The remainder of the predictions are within expectations based on uncertainties of the measurements.

Bilger [7] finds that the laminar flamelet correlation for n-heptane is also satisfactory – based on measurements of Abdel-Khalik et al. [12]. Use of the partial equilibrium method, with $\phi_c = 1.2$, yields similar results, except that measured CO_2 mass fractions are underestimated by about 20 percent. This suggests that the present partial equilibrium method might provide an approach for estimating state relationships in the many instances where appropriate laminar flame data are unavailable. More work is needed to adequately assess this potential.

In summary, the present Favre-averaged κ-ϵ-g model, using

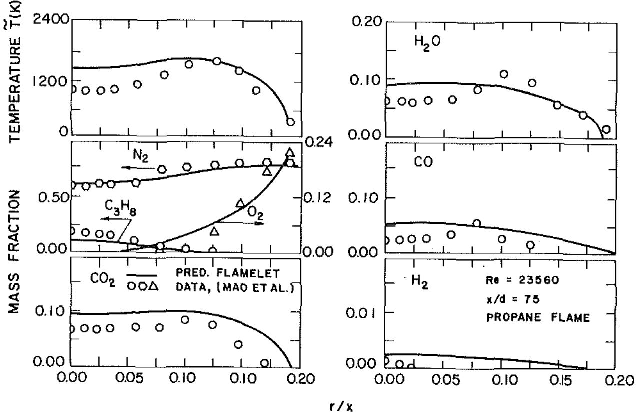

Fig. 2 Radial variation of mean temperature and species concentrations at $x/d = 75$

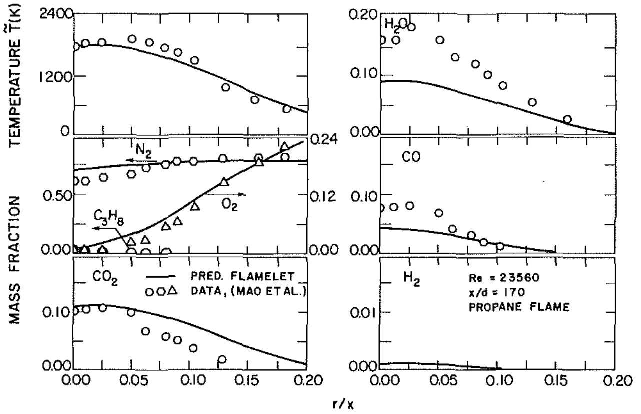

Fig. 3 Radial variation of mean temperature and species concentrations at $x/d = 170$

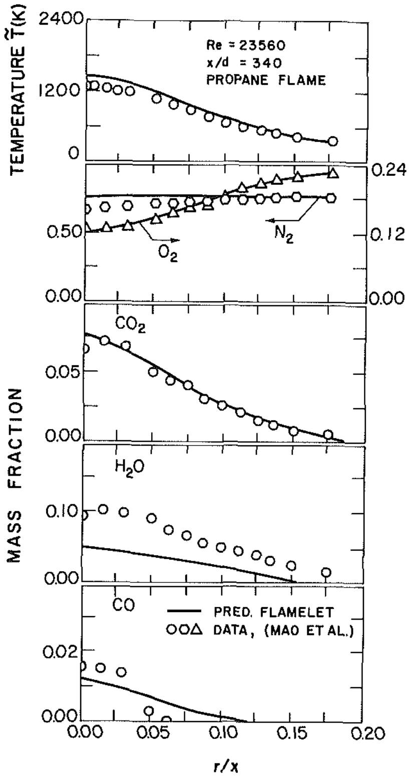

Fig. 4 Radial variation of mean temperature and species concentrations at $x/d = 340$

either the laminar flamelet or partial equilibrium methods to find state relationships, provided reasonably good predictions of mean momentum flux, temperature, and the concentrations of major gas species for existing data in propane flames. The model involves a single set of empirical constants, found in noncombusting flows [1, 6]. The success of the laminar flamelet method suggests that routine measurements in laminar flames might be used to predict properties of turbulent diffusion flames – where rational methods for treating finite reaction rates have been elusive thus far. The partial equilibrium method provides an alternative in the many instances where data in laminar diffusion flames are unavailable.

Acknowledgment

This research was supported by the United States Department of Commerce, National Bureau of Standards, Grant No. NB81NADA2044, with H. Baum of the Center for Fire Research serving as Scientific Officer.

References

1 Jeng, S-M., and Faeth, G. M., "Species Concentrations and Turbulent Properties in Buoyant Methane Diffusion Flames," to be published.

2 Jeng, S-M., Chen, L-D., and Faeth, G. M., "The Structure of Buoyant Methane and Propane Diffusion Flames," *Nineteenth Symposium (International) on Combustion*, The Combustion Institute, 1982, pp. 349-358.

3 Mao, C-P., Szekely, G. A., Jr., and Faeth, G. M., "Evaluation of a Locally Homogeneous Flow Model of Spray Combustion," *J. Energy*, Vol. 4, 1980, pp. 78-87.

4 Becker, H. A., and Yamazaki, S., "Entrainment, Momentum Flux and Temperature in Vertical Free Turbulent Diffusion Flames," *Combustion and Flame*, Vol. 33, 1976, pp. 123-148.

5 Liew, S. K., Bray, K. N. C., and Moss, J. B., "A Flamelet Model of Turbulent Non-Premixed Combustion," *Comb. Sci. and Tech.*, Vol. 27, 1981, pp. 69-73.

6 Jeng, S-M., "An Investigation of the Structure and Radiation Properties of Turbulent Buoyant Diffusion Flames," Ph.D. thesis, the Pennsylvania State University, Dec. 1983.

7 Bilger, R. W., "Turbulent Jet Diffusion Flames," *Prog. Energy Combust. Sci.*, Vol. 1, 1976, pp. 87-109.

8 Bilger, R. W., "Reaction Rates in Turbulent Flames," *Combustion and Flame*, Vol. 30, 1977, pp. 277-284.

9 Tsuji, H., and Yamaoka, L., "Structure Analysis of Counterflow Diffusion Flames in the Forward Stagnation Region of a Porous Cylinder," *Thirteenth Symposium (International) on Combustion*, The Combustion Institute, Pittsburgh, 1971, pp. 723-731.

10 Tsuji, H., and Yamaoka, I., "The Counterflow Diffusion Flame in the Forward Stagnation Region of a Porous Cylinder," *Eleventh Symposium (International) on Combustion*, The Combustion Institute, Pittsburgh, 1967, pp. 970-984.

11 Tsuji, H., and Yamaoka, I., "The Structure of Counterflow Diffusion Flames in the Forward Stagnation Region of a Porous Cylinder," *Twelfth Symposium (International) on Combustion*, The Combustion Institute, Pittsburgh, 1969, pp. 997-1005.

12 Abdel-Khalik, S. I., Tamaru, T., and El-Wakil, M. M., "A Chromatographic and Interferometric Study of the Diffusion Flame Around a Simulated Drop," *Fifteenth Symposium (International) on Combustion*, The Combustion Institute, Pittsburgh, 1975, pp. 389-399.

Performance and Design Charts for Heat Exchangers

R. Turton,[1] C. D. Ferguson,[2] and O. Levenspiel[1]

Nomenclature

A = heat exchanger surface area (m^2)

c = specific heat capacity, tube or cold side (kJ/kg•K)

C = specific heat capacity, shell or hot side (kJ/kg•K)

---

[1] Chemical Engineering Department, Oregon State University, Corvallis, Ore. 97331

[2] C. D. Ferguson is currently employed as a Process Engineer for Georgia Pacific Corporation.

Contributed by the Heat Transfer Division for publication in the JOURNAL OF HEAT TRANSFER. Manuscript received by the Heat Transfer Division, October 19, 1983.

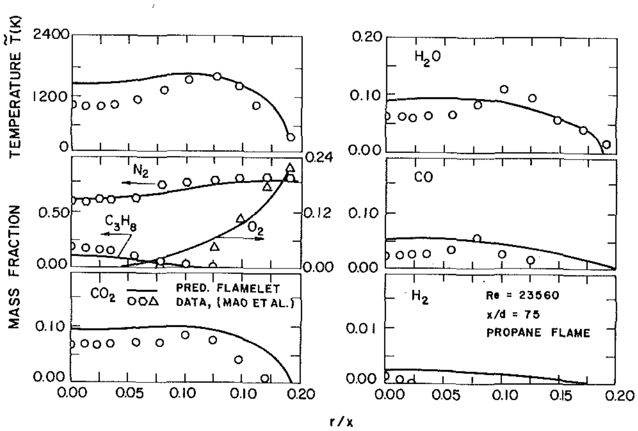

Fig. 2 Radial variation of mean temperature and species concentrations at x/d = 75

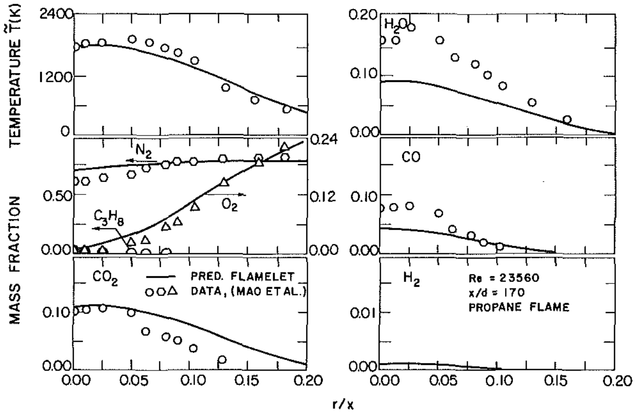

Fig. 3 Radial variation of mean temperature and species concentrations at x/d = 170

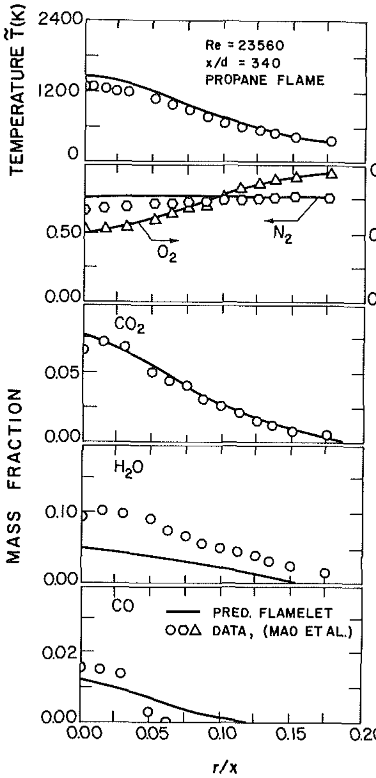

Fig. 4 Radial variation of mean temperature and species concentrations at x/d = 340

either the laminar flamelet or partial equilibrium methods to find state relationships, provided reasonably good predictions of mean momentum flux, temperature, and the concentrations of major gas species for existing data in propane flames. The model involves a single set of empirical constants, found in noncombusting flows [1, 6]. The success of the laminar flamelet method suggests that routine measurements in laminar flames might be used to predict properties of turbulent diffusion flames—where rational methods for treating finite reaction rates have been elusive thus far. The partial equilibrium method provides an alternative in the many instances where data in laminar diffusion flames are unavailable.

Acknowledgment

This research was supported by the United States Department of Commerce, National Bureau of Standards, Grant No. NB81NADA2044, with H. Baum of the Center for Fire Research serving as Scientific Officer.

References

1 Jeng, S-M., and Faeth, G. M., "Species Concentrations and Turbulent Properties in Buoyant Methane Diffusion Flames," to be published.

2 Jeng, S-M., Chen, L-D., and Faeth, G. M., "The Structure of Buoyant Methane and Propane Diffusion Flames," *Nineteenth Symposium (International) on Combustion*, The Combustion Institute, 1982, pp. 349-358.

3 Mao, C-P., Szekely, G. A., Jr., and Faeth, G. M., "Evaluation of a Locally Homogeneous Flow Model of Spray Combustion," *J. Energy*, Vol. 4, 1980, pp. 78-87.

4 Becker, H. A., and Yamazaki, S., "Entrainment, Momentum Flux and Temperature in Vertical Free Turbulent Diffusion Flames," *Combustion and Flame*, Vol. 33, 1976, pp. 123-148.

5 Liew, S. K., Bray, K. N. C., and Moss, J. B., "A Flamelet Model of Turbulent Non-Premixed Combustion," *Comb. Sci. and Tech.*, Vol. 27, 1981, pp. 69-73.

6 Jeng, S-M., "An Investigation of the Structure and Radiation Properties of Turbulent Buoyant Diffusion Flames," Ph.D. thesis, the Pennsylvania State University, Dec. 1983.

7 Bilger, R. W., "Turbulent Jet Diffusion Flames," *Prog. Energy Combust. Sci.*, Vol. 1, 1976, pp. 87-109.

8 Bilger, R. W., "Reaction Rates in Turbulent Flames," *Combustion and Flame*, Vol. 30, 1977, pp. 277-284.

9 Tsuji, H., and Yamaoka, L., "Structure Analysis of Counterflow Diffusion Flames in the Forward Stagnation Region of a Porous Cylinder," *Thirteenth Symposium (International) on Combustion*, The Combustion Institute, Pittsburgh, 1971, pp. 723-731.

10 Tsuji, H., and Yamaoka, I., "The Counterflow Diffusion Flame in the Forward Stagnation Region of a Porous Cylinder," *Eleventh Symposium (International) on Combustion*, The Combustion Institute, Pittsburgh, 1967, pp. 970-984.

11 Tsuji, H., and Yamaoka, I., "The Structure of Counterflow Diffusion Flames in the Forward Stagnation Region of a Porous Cylinder," *Twelfth Symposium (International) on Combustion*, The Combustion Institute, Pittsburgh, 1969, pp. 997-1005.

12 Abdel-Khalik, S. I., Tamaru, T., and El-Wakil, M. M., "A Chromatographic and Interferometric Study of the Diffusion Flame Around a Simulated Drop," *Fifteenth Symposium (International) on Combustion*, The Combustion Institute, Pittsburgh, 1975, pp. 389-399.

Performance and Design Charts for Heat Exchangers

R. Turton,[1] C. D. Ferguson,[2] and O. Levenspiel[1]

Nomenclature

A = heat exchanger surface area (m^2)
c = specific heat capacity, tube or cold side (kJ/kg•K)
C = specific heat capacity, shell or hot side (kJ/kg•K)

---

[1] Chemical Engineering Department, Oregon State University, Corvallis, Ore. 97331

[2] C. D. Ferguson is currently employed as a Process Engineer for Georgia Pacific Corporation.

Contributed by the Heat Transfer Division for publication in the JOURNAL OF HEAT TRANSFER. Manuscript received by the Heat Transfer Division, October 19, 1983.

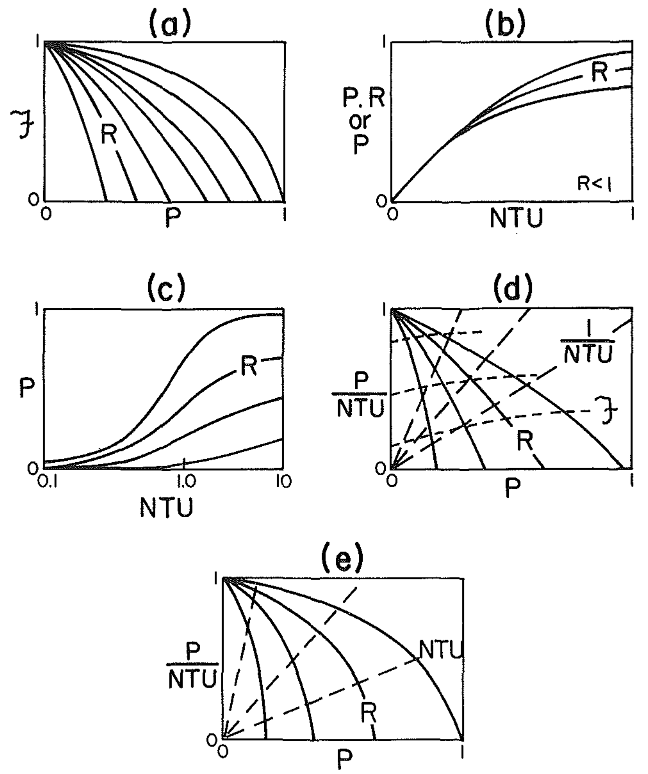

Fig. 1 The various ways of displaying the relationships between variables in heat exchangers: (*a*) from Bowman et al. [1]; (*b*) from Kays & London [2]; (*c*) from TEMA [3]; (*d*) from Mueller [4]; and (*e*) from Reference [5]

$\dot{m}$ = mass flow rate, tube or cold side (kg/s)
$\dot{M}$ = mass flow rate, shell or hot side (kg/s)
$\dot{q}$ = rate of heat transfer (W)
t = temperature of tube side fluid (K)
T = temperature of shell side fluid (K)
$\overline{\Delta T}$ = mean temperature difference in exchanger (K)
$\Delta T_{\rm lm}$ = log mean temperature difference in exchanger (K)
U = overall heat transfer coefficient in exchanger (W/m^2•K)

Subscripts

1 = inlet
2 = outlet

The behavior of heat exchangers is always compared to that of ideal countercurrent contacting. Most often an efficiency factor $\mathfrak{F}$ is used and thus we can write

$$\dot{q} = UA\mathfrak{F}\Delta T_{\rm lm}$$

where $\mathfrak{F} = 1$ for countercurrent contacting, but is smaller than unity for all other contacting patterns.

Broadly speaking, there are two types of heat exchanger problems. First, there is the *design* problem of calculating the required exchanger surface area for a given duty. Second, there is the *performance* problem of determining the fluid outlet temperatures from a given exchanger. To solve either of these problems from first principles is a laborious task. Hence graphical design charts for the various shell-and-tube and compact exchanger arrangements were introduced many years ago and have gained wide acceptance throughout industry.

Five types of heat exchanger design charts are found in the literature. These are shown in Fig. 1. The dimensionless variables used in these charts are defined as follows:

$$P = \frac{t_2 - t_1}{T_1 - t_1}$$

$$R = \frac{T_1 - T_2}{t_2 - t_1} = \frac{\dot{m}c}{\dot{M}C}$$

$$NTU = \frac{UA}{\dot{m}c}$$

and

$$\mathfrak{F} = \frac{\overline{\Delta T}}{\Delta T_{\rm lm}}$$

Figure 1(*a*) is the most widely used of these charts and was introduced by Bowman et al. [1] in 1940. The design problem can be solved directly using this chart, but the performance problem requires a trial and error solution.

Figure 1(*b*), due to Kays and London [2], and Fig. 1(*c*), prepared by TEMA [3], can be used to solve both the design and performance problem. However, neither of these charts displays the $\mathfrak{F}$-values, which must be found by an additional calculation.

Mueller [4] later proposed the charts of Fig. 1(*d*) with its triple family of curves. This chart can be used to solve both the design and performance problem and in addition gives the $\mathfrak{F}$-values. However, Fig. 1(*d*) is somewhat cramped and difficult to read accurately and introduces yet another parameter – P/NTU. The Mueller charts have been redrawn recently [5] and are shown in their new form in Fig. 1(*e*). The main difference between Figs. 1(*d*) and 1(*e*) is that the $\mathfrak{F}$ parameter curves have been omitted in the latter, thus the problem of having to separately calculate the $\mathfrak{F}$-values has been reintroduced.

In a system with four variables, $\mathfrak{F}$, P, R, and NTU, any chart that displays just one family of curves, such as Figs. 1(*a–c*), does not give all the interrelationships directly. On the other hand, a chart with three families of curves, as is Fig. 1(*d*), has one set which is redundant. To show all the interrelationships between these four variables requires a chart with two families of curves. Although Fig. 1(*e*) satisfies this criterion, it does not show directly the four parameters of interest.

The purpose of this paper is to introduce a new set of charts that extend the easy-to-read Bowman charts of Fig. 1(*a*) to include a second family of curves representing the NTU parameter. Both the design and performance problems can be solved using these charts and $\mathfrak{F}$- values can be found directly for both types of problem. Thus to find exchanger surface area, use P and R to evaluate $\mathfrak{F}$ and NTU. To find terminal temperatures, use NTU and R to evaluate P and $\mathfrak{F}$.

The charts in Figs. 2 and 3 were calculated and drawn by computer. The curves in Fig. 2 were computed from the appropriate equations given by Bowman et al. [1]. The curves in Fig. 3 were generated numerically although analytical solutions are given by Nusselt [6] and Bačlić [7], the latter being in closed form and easier to use.

Summary

This paper introduces a new form of heat exchanger design chart. This chart displays both design and performance parameters. Its advantages over other charts are its clear, concise, and simple presentation of the information.

Although only two exchanger configurations are given here, a more comprehensive set of charts will be published by Levenspiel [8].

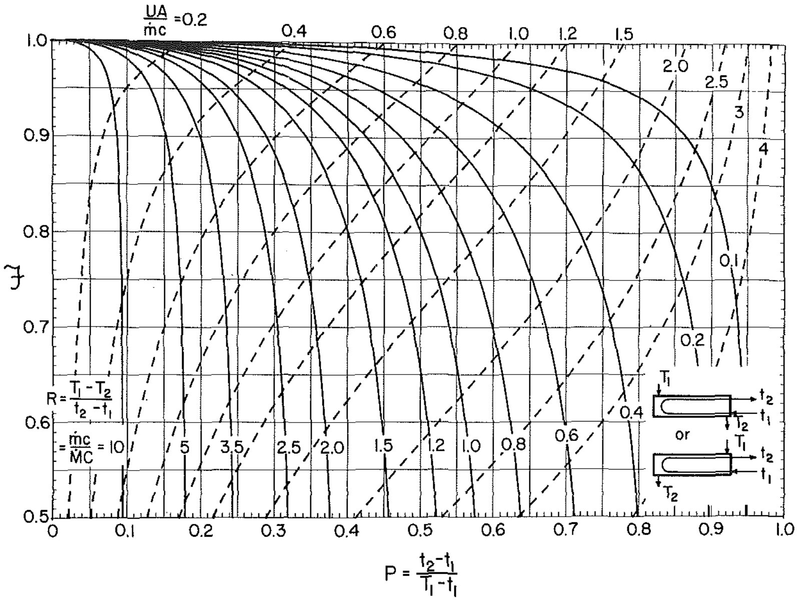

Fig. 2 Performance and design chart for a shell and the tube exchanger with one shell and two tube passes

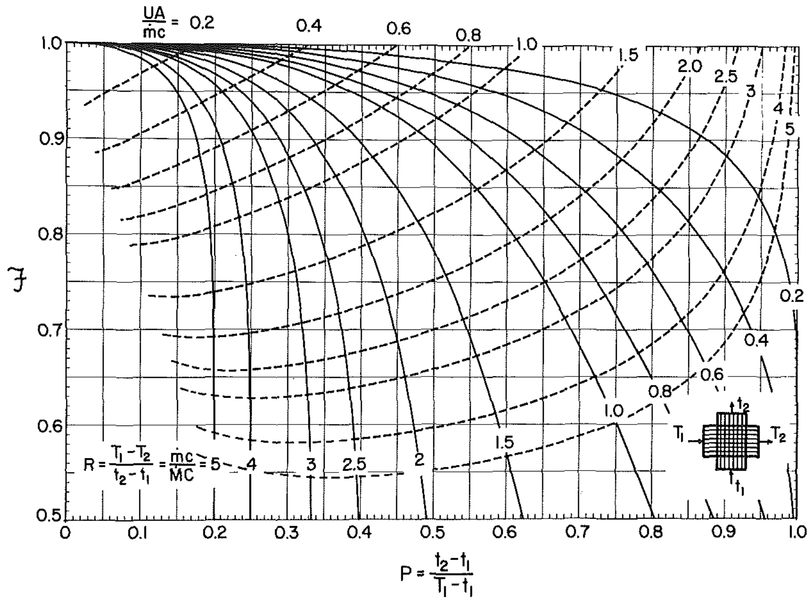

Fig. 3 Performance and design chart for a crossflow exchanger with both fluids unmixed

Acknowledgments

The authors would like to acknowledge that the work done for this paper was carried out under NSF Grant No. CPE 8026799.

References

1 Bowman, R. A., Mueller, A. C., and Nagle, W. M., "Mean Temperature Difference in Design," ASME *Transactions*, Vol. 62, 1940, pp. 283-294.

2 Kays, W. M., and London, A. L., *Compact Heat Exchangers*, 2d ed., McGraw-Hill, New York, 1964.

3 *TEMA, Standards of Tubular Exchanger Manufacturers Association*, 6th ed., Tubular Exchanger Manufacturers Association, Inc., New York, 1978.

4 Mueller, A. C., *Handbook of Heat Transfer*, sect. 18, edited by W. H. Rohsenow, and J. P. Hartnett, McGraw-Hill, 1973.

5 Schlünder, E. U., Editor-in-Chief, *Heat Exchanger Design Handbook*, Vol. 1, Hemisphere Publishing, 1983.

6 Nusselt, W., "Der Warmeubergang im Kreuzstron," *Zeitschrift Des Vereines Deutscher Ingenieur*, Vol. 55, 1911, pp. 2021-2024.

7 Bačlić, B. S., "A Simplified Formula for Crossflow Heat Exchanger Effectiveness," ASME Journal of Heat Transfer, Vol. 100, 1978, pp. 746-747.

8 Levenspiel, O., *Engineering Flow and Heat Exchange*, Plenum, in press.

Heat Transfer in the Fully Developed Region of Elliptical Ducts With Uniform Wall Heat Flux

M. S. Bhatti[1]

Nomenclature

a = semimajor axis of the duct wall
b = semiminor axis of the duct wall
c_p = specific heat
D = $\pi b/E(m)$, hydraulic diameter of the elliptical duct

$$E(m) = \int_0^{\pi/2} \sqrt{1 - m^2 \sin\theta}\, d\theta, \text{ complete}$$

elliptic integral of the second kind

Contributed by the Heat Transfer Division for publication in the Journal of Heat Trasnfer. Manuscript received by the Heat Transfer Division January 5, 1984.

[1] Owens-Corning Fiberglas Corp., Research and Development Division, Technical Center, Granville, Ohio 43023, Mem. ASME

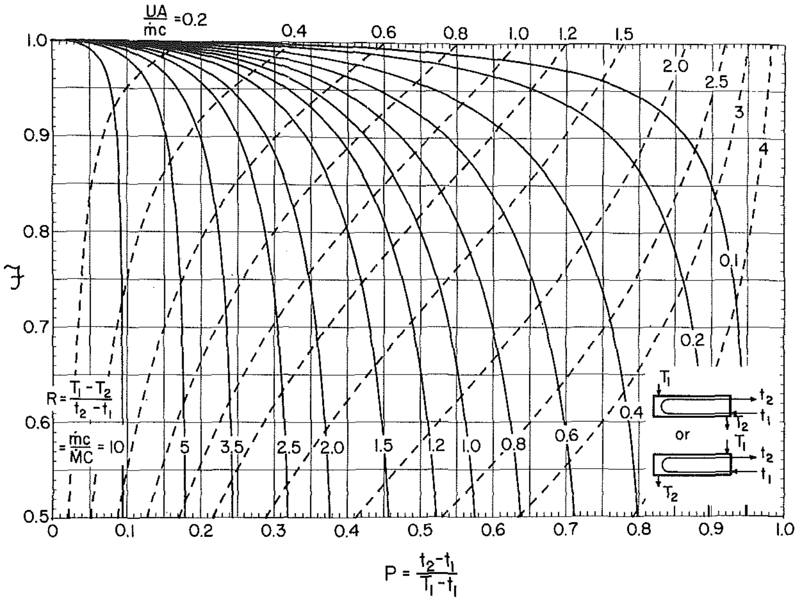

Fig. 2 Performance and design chart for a shell and the tube exchanger with one shell and two tube passes

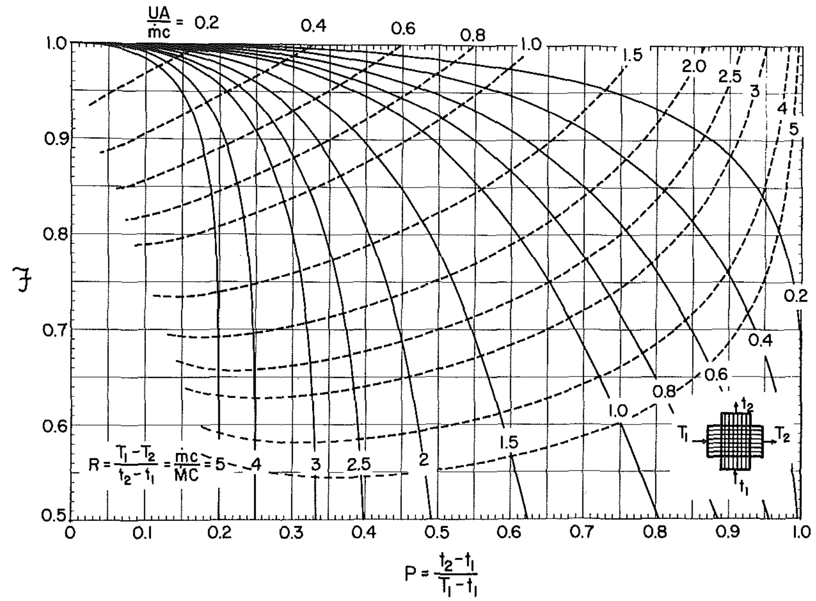

Fig. 3 Performance and design chart for a crossflow exchanger with both fluids unmixed

Acknowledgments

The authors would like to acknowledge that the work done for this paper was carried out under NSF Grant No. CPE 8026799.

References

1 Bowman, R. A., Mueller, A. C., and Nagle, W. M., "Mean Temperature Difference in Design," ASME *Transactions*, Vol. 62, 1940, pp. 283-294.

2 Kays, W. M., and London, A. L., *Compact Heat Exchangers*, 2d ed., McGraw-Hill, New York, 1964.

3 *TEMA, Standards of Tubular Exchanger Manufacturers Association*, 6th ed., Tubular Exchanger Manufacturers Association, Inc., New York, 1978.

4 Mueller, A. C., *Handbook of Heat Transfer*, sect. 18, edited by W. H. Rohsenow, and J. P. Hartnett, McGraw-Hill, 1973.

5 Schlünder, E. U., Editor-in-Chief, *Heat Exchanger Design Handbook*, Vol. 1, Hemisphere Publishing, 1983.

6 Nusselt, W., "Der Warmeubergang im Kreuzstron," *Zeitschrift Des Vereines Deutscher Ingenieur*, Vol. 55, 1911, pp. 2021-2024.

7 Bačlić, B. S., "A Simplified Formula for Crossflow Heat Exchanger Effectiveness," ASME Journal of Heat Transfer, Vol. 100, 1978, pp. 746-747.

8 Levenspiel, O., *Engineering Flow and Heat Exchange*, Plenum, in press.

Heat Transfer in the Fully Developed Region of Elliptical Ducts With Uniform Wall Heat Flux

M. S. Bhatti[1]

Nomenclature

a = semimajor axis of the duct wall
b = semiminor axis of the duct wall
c_p = specific heat
D = $\pi b/E(m)$, hydraulic diameter of the elliptical duct
$E(m)$ = $\int_0^{\pi/2} \sqrt{1 - m^2 \sin\theta}\, d\theta$, complete elliptic integral of the second kind

---

Contributed by the Heat Transfer Division for publication in the Journal of Heat Trasnfer. Manuscript received by the Heat Transfer Division January 5, 1984.

[1] Owens-Corning Fiberglas Corp., Research and Development Division, Technical Center, Granville, Ohio 43023, Mem. ASME

h = $\dot{q}_w''/(T_w - T_b)$, heat transfer coefficient
k = thermal conductivity
m = $\sqrt{1-\lambda^2}$, modulus of the complete elliptic integral of the second kind
Nu = hD/k, the Nusselt number
$\dot{q}_w''$ = uniform wall heat flux
r = radial coordinate
R = r/a or r/b dimensionless radial coordinate for the circular duct
T = local temperature
T_b = bulk fluid temperature
T_c = duct center line temeprature
T_w = duct wall temperature
w = local axial velocity
w_0 = mean axial velocity
W = w/w_0, dimensionless axial velocity
x,y,z = Cartesian coordinates
X,Y = x/a, y/b dimensionless spanwise coordinates
Z = $\alpha z/w_0 ab$, dimensionless streamwise coordinate
α = $k/\rho c_p$, thermal diffusivity
θ = $(T-T_c)/(\dot{q}_w'' b/k)$, dimensionless local temperature
λ = b/a, duct aspect ratio
ρ = fluid density

Introduction

The problem of heat transfer in the fully developed region of elliptical pipes with uniform wall heat flux is of interest in the piping industry, where short lengths of elliptical pipes are occasionally employed as transitional sections between long lengths of circular pipes. This problem is also of interest in the design of certain heat exchangers requiring modest increase in the heat transfer rate over that achievable by the circular heat exchanger elements. Previously, this problem was investigated by Tao [1] and Tyagi [2], using the method of complex variables. This method is quite involved and cumbersome. The resulting expressions for the temperature distribution and the Nusselt number are rather unwieldly for rapid computations. The motivation for the present analysis was to provide a compact and usable solution whose accuracy is on par with that of the complex variable solution.

Analysis

For the purpose of the present analysis, the origin of the coordinate system is placed at the duct axis and accordingly the elliptical duct wall is described by $X^2 + Y^2 = 1$. The fully developed velocity distribution in the duct is given by [3]

$$W = 2(1 - X^2 - Y^2) \tag{1}$$

In order to find the fully developed temperature distribution in the duct, we will assume the quartic temperature profile

$$\theta = A(X^2+Y^2) + B(X^2+Y^2)^2 \tag{2}$$

where A and B are the constants to be determined from the appropriate conditions. The first of these conditions will be taken as stemming from satisfaction of the energy differential equation along the duct axis and the second as stemming from satisfaction of the integrated form of the energy equation. This latter condition implies that the energy differential equation is satisfied in an overall sense over every cross section rather than at every pont over the cross section.

Now in terms of the dimensionless variables, the energy differential equation can be written as

$$\lambda W \frac{dT_b}{dZ} = \lambda^2 \frac{\partial^2 T}{\partial X^2} + \frac{\partial^2 T}{\partial Y^2} \tag{3}$$

Equation (3) follows from the usual boundary layer theory form of the energy equation when the local axial temperature gradient $\partial T/\partial z$ is replaced by the bulk temperature gradient dT_b/dZ. This is permissible for the thermally developed flows [4]. It may also be noted that in writing equation (3) the axial heat conduction and the viscous dissipation effects are neglected.

The bulk temperature gradient appearing in equation (3) can be expressed in terms of the uniform wall heat flux by performing a simple energy balance on a duct segment lying between z and $z + dz$. To that end, it is noted that the amount of the thermal energy entering the segment from the duct wall is $4aE(m)\ \dot{q}_w'' dz$ where $4a(Em)$ is the duct perimeter. Furthermore, the amount of the thermal energy entering the segment at the cross section at z is $\pi abw_0\rho c_p T_b$. Finally, the amount of the thermal energy leaving the segment at the cross section at $z + dz$ is $\pi abw_0\rho c_p\ [T_b + (dT_b/dz)dz]$. Equating the total amount of the energy entering the segment to that leaving it, we get

$$\dot{q}_w'' = \frac{\pi abw_0\rho c_p}{4aE(m)}\left(\frac{dT_b}{dz}\right) \tag{4}$$

Combining equations (3) and (4) and introducing the dimensionless variables, we obtain

$$\lambda^2 \frac{\partial^2\theta}{\partial X^2} + \frac{\partial^2\theta}{\partial Y^2} = \frac{4E(m)}{\pi} W \tag{5}$$

We are now in a position to derive the necessary conditions to determine the constants A and B in equation (2). Firstly, along the duct axis $X = Y = 0$ and according to equation (1), $W = 2$. Thus, along the duct axis, equation (5) reduces to

$$\lambda^2\left[\frac{\partial^2\theta}{\partial X^2}\right]_{X=Y=0} + \left[\frac{\partial^2\theta}{\partial Y^2}\right]_{X=Y=0} = \frac{8E(m)}{\pi} \tag{6}$$

Secondly, the integrated form of the energy equation follows directly from equation (5) when equation (1) is introduced into it and the resulting equation integrated over the duct cross section. This leads to

$$\lambda^2 \int_{Y=0}^{1}\left(\frac{\partial\theta}{\partial X}\right)_{X=\sqrt{1-Y^2}} dY + \int_{X=0}^{1}\left(\frac{\partial\theta}{\partial Y}\right)_{Y=\sqrt{1-X^2}} dX = E(m) \tag{7}$$

In arriving at equation (7), the symmetry conditions $(\partial\theta/\partial X) = 0$ at $X = 0$ and $(\partial\theta/\partial Y) = 0$ at $Y = 0$ have been utilized.

Introducing equation (2) into equations (6) and (7) successively, we get two simultaneous algebraic equations whose solution yields the values of A and B. When these values are introduced in equation (2), we get the desired temperature profile

$$\theta = \frac{E(m)}{\pi(1+\lambda^2)}\left[4(X^2+Y^2) - (X^2+Y^2)^2\right] \tag{8}$$

The temperature profile obtained by Tao [1] and Tyagi [2] is presented in the cited references in an extremely complex form in terms of the axial pressure and the axial temperature gradients. By expressing the pressure gradient in terms of the mean axial velocity and the temperature gradient in terms of the wall heat flux, the temperature profile derived by Tao [1] and Tyagi [2] can be reduced to the following simpler form

$$\begin{aligned}\theta = \frac{2E(m)}{3\pi(1+\lambda^2)(1+6\lambda^2+\lambda^4)}\{&(1+\lambda^2)(\lambda^2+5)X^2 \\ &+ (1+\lambda^2)(1+5\lambda^2)Y^2 - [(1+\lambda^2)(\lambda^2+5)X^2 \\ &+ (1+\lambda^2)(1+5\lambda^2)Y^2 - (5\lambda^4+26\lambda^2+5)](X^2+Y^2)\}\end{aligned} \tag{9}$$

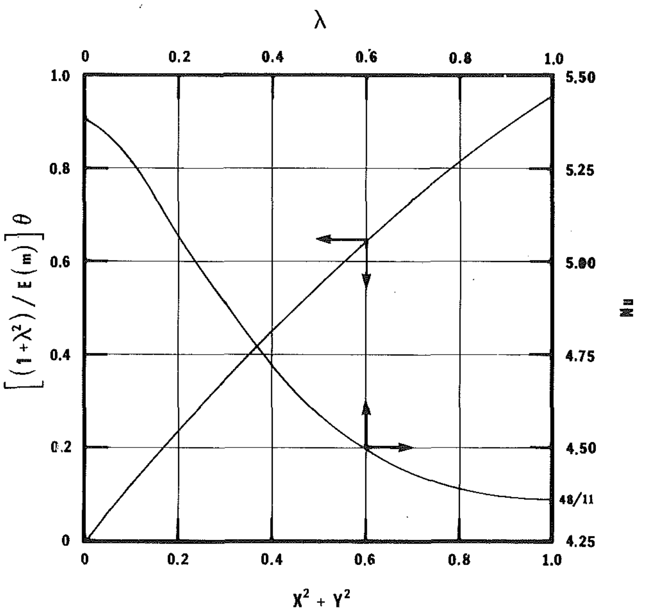

Fig. 1 Fully developed temperature distribution and nusselt numbers in elliptical ducts with uniform wall heat flux

An examination of equation (8) reveals that λ together with $E(m)$, which is a function of λ, can be absorbed in θ on the left-hand side yielding a temperature profile independent of λ. This temperature profile can be viewed as a universal profile applicable to elliptical ducts of all aspect ratios. The temperature distribution given by equation (9), on the other hand, does not lend itself for concise presentation as a universal profile.

For the limiting case of the circular tube $\lambda = 1$, $E(m) = \pi/2$, and $X^2 + Y^2 = R^2$. Introducing these values into equations (8) and (9), we notice that both reduce to the known exact temperature profile for the circular tube $\theta = R^2 - R^4/4$. It is often suggested that $\lambda = 0$ may correspond to the case of the flat duct. Now $\lambda = 0$ when either $b = 0$ or $a = \infty$. The case of $b = 0$ clearly does not correspond to any duct as it implies absence of a gap between two surfaces. The case of $a = \infty$ does permit presence of a gap between two surfaces. However, the resulting duct is not a true flat duct with the hydraulic diameter $4b$. Rather, it is a narrow lenticular passage with the hydraulic diameter πb. Consequently, for $\lambda = 0$, $E(m) = 1$, and $X = 0$, neither equation (8) nor equation (9) reduces to the flat duct temperature profile $\theta = (6Y^2 - Y^4)/8$.

The duct wall temperature T_w required for the determination of the heat transfer coefficient h can be found from equation (8) by setting $X^2 + Y^2 = 1$.

$$\frac{T_w - T_c}{(\dot{q}_w''b/k)} = \frac{3E(m)}{\pi(1+\lambda^2)} \tag{10}$$

The bulk fluid temperature T_b also entering the determination of the heat transfer coefficient h can be found from the defining relation

$$T_b = \frac{1}{A_c w_0}\int_{A_c} wT\,dA_c \tag{11}$$

where A_c is the duct cross section area. Introducing equations (1) and (8) into equation (11) and noting that for elliptical duct $A_c = \pi ab$ and $dA_c = dxdy$, the indicated surface integral in equation (11) can be evaluated. This leads to

$$\frac{T_b - T_c}{(\dot{q}_w''b/k)} = \frac{7E(m)}{6\pi(1+\lambda^2)} \tag{12}$$

Table 1 Comparison of the Nusselt number predictions

	Nu	
λ	Present analysis	Analysis of [1] and [2]
0.0	5.3834	5.2251
0.1	5.2674	5.1238
0.2	5.0724	4.9609
0.3	4.8805	4.8027
0.4	4.7170	4.6668
0.5	4.5878	4.5575
0.6	4.4939	4.4770
0.7	4.4301	4.4218
0.8	4.3902	4.3870
0.9	4.3749	4.3741
1.0	4.3636	4.3636

Noting that the hydraulic diameter D for elliptical ducts can be expressed as $\pi b/E(m)$, we can form the Nusselt number $\mathrm{Nu} = hD/k$ with the help of equations (10) and (12) and the defining relation for h, viz., ,$\dot{q}_w'' = h(T_w - T_b)$. This yields

$$\mathrm{Nu} = \frac{6}{11}\left[\frac{\pi}{E(m)}\right]^2 (1+\lambda^2) \tag{13}$$

The Nusselt number expression developed by Tao [1] and Tyagi [2] is given by

$$\mathrm{Nu} = 9\left[\frac{\pi}{E(m)}\right]^2 \left[\frac{1+6\lambda^2+\lambda^4}{17+98\lambda^2+17\lambda^4}\right](1+\lambda^2) \tag{14}$$

For the limiting case of $\lambda = 1$ and $E(m) = \pi/2$ both equations (13) and (14) yield $\mathrm{Nu} = 48/11$ which is the exact known value for a circular tube. For the other limiting case of $\lambda = 0$ and $E(m) = 1$, equations (13) and (14) predict the Nusselt number values of 5.3834 and 5.2251, respectively. These values do not agree with the value for a flat duct, viz., 140/17. As already discussed, the reason for this is that $\lambda = 0$ corresponds to a narrow lenticular passage rather than to a true flat duct.

Results and Discussion

The temperature distribution in the fully developed region is calculated from equation (8) and displayed in Fig. 1 as a universal curve applicable to elliptical ducts of all aspects ratios. This curve starts at the origin and slopes upward. Note that the duct aspect ratio λ as well as the complete elliptic integral of the second kind $E(m)$, which is a function of λ, is absorbed in the dimensionless temperature θ while constructing Fig. 1. The temperature distribution of equation (9) developed by Tao [1] and Tyagi [2] does not lend itself for presentation as a universal curve. The extreme simplicity of the present analysis stems from effective elimination of the duct aspect ratio as a parameter in the temperature distribution. This approach can be very valuable in developing compact solutions to problems involving complex ducts.

The Nusselt numbers of the present analysis calculated from equation (13) are presented in Table 1 as well as in Fig. 1. Included in Table 1 are the Nusselt numbers due to Tao [1] and Tyagi [2] calculated from equation (14). Comparison of the two sets of the Nusselt numbers shows that they are in remarkably close agreement. The present analysis numbers are slightly higher than those of Tao [1] and Tyagi [2], since the present analysis wall temperatures are slightly lower. However, the maximum deviation between the two sets of numbers is only 3 perent corresponding to $\lambda = 0$. Thus, in spite of its extreme simplicity, accuracy of the present analysis in predicting the Nusselt numbers is on par with that of the complex variable analysis. The present analysis is a good illustration how some simple and approximate solutions turn out to be just as valuable as complex and perhaps more accurate solutions.

Concluding Remarks

The problem of heat transfer in the fully developed region of elliptical ducts with uniform wall heat flux is solved in closed form by the simple integral method. The resulting solution is extremely compact and of a usable form. Moreover, its accuracy in predicting the Nusselt numbers is on par with that of the complex variable solution. A unique feature of the present analysis is generation of the universal temperature profile applicable to elliptical ducts of all aspect ratios. A generalization of this temperature profile can be extremely valuable in developing a manageable solution to hitherto unsolved problem of simultaneous development of velocity and temperature fields in elliptical ducts.

References

1 Tao, L. N., "On Some Laminar Forced Convection Problems," ASME Journal of Heat Transfer, Vol. 83, Nov. 1961, pp. 466–473.

2 Tyagi, V. P., "Laminar Forced Convection of a Dissipative Fluid in a Channel," ASME, Journal of Heat Transfer, Vol. 88, May 1966, pp. 161–169.

3 Bhatti, M. S., "Laminar Flow in the Entrance Region of Elliptical Ducts," ASME *Journal of Fluids Engineering*, Vol. 105, No. 3, Sept. 1983, pp. 290–296.

4 Kays, W. M., and Crawford, M. E., *Convective Heat and Mass Transfer*, McGraw Hill, New York, 2nd ed., 1980, pp. 92–95.

An Analysis of the Heat Transfer to Drag Reducing Turbulent Pipe Flows

H. K. Yoon[1] and A. J. Ghajar[2]

Nomenclature

A^+ = constant that characterizes thickness of wall layer in Van Driest's law

c = specific heat

E = nondimensional momentum eddy diffusivity, $E = \epsilon_m/\nu$

F = Fanning friction factor, $F = 2\tau_0/\rho U_m^2$

h = heat transfer coefficient

j = Colburn j factor, $j = \mathrm{St}\,\mathrm{Pr}^{2/3}$

K = von Karman constant, $K = 0.4$

k = thermal conductivity

$\overline{p^*}$ = mean pressure

$\bar{p}$ = nondimensional mean pressure, $\bar{p} = \overline{p^*}/\rho U_m^2$

Pr = apparent Prandtl number, $\mathrm{Pr} = \nu/\alpha = \mu c/k$

$\dot{q}_0''$ = heat flux at surface

Re = Reynolds number, $\mathrm{Re} = (2r_0)U_m/\nu$

R = Reynolds number based on pipe radius, $\mathrm{R} = r_0 U_m/\nu$

r_0 = radius of pipe

r_0^+ = nondimensional pipe radius, $r_0^+ = r_0 U_\tau/\nu$

r = radial coordinate direction

$\bar{r}$ = nondimensional radial coordinate, $\bar{r} = r/r_0$

St = Stanton number, $\mathrm{St} = h/\rho c U_m$

$\overline{T^*}$ = mean temperature

T_m = mixed mean temperature

T_0 = fluid temperature at surface

$\overline{U^*}$ = streamwise mean velocity

$\bar{U}$ = nondimensional streamwise mean velocity, $\bar{U} = \overline{U^*}/U_m$

U_m = mass average velocity

U_τ = shear velocity, $U_\tau = (\tau_0/\rho)^{1/2}$

x = streamwise coordinate direction

$\bar{x}$ = nondimensional streamwise coordinate direction, $\bar{x} = x/r_0$

y = coordinate direction normal to wall, $y = r_0 - r$

$\bar{y}$ = nondimensional direction normal to wall, $\bar{y} = y/r_0$

y^+ = nondimensional distance normal to wall, $y^+ = y\,U_\tau/\nu$

ν = apparent kinematic viscosity, $\nu = \mu/\rho$

μ = apparent absolute viscosity (solution viscosity at the wall)

ρ = fluid density

ϵ_m = turbulent eddy diffusivity of momentum

ϵ_h = turbulent eddy diffusivity of heat

τ_0 = wall shear stress

α = molecular thermal diffusivity, $\alpha = k/\rho c$

1 Introduction

The fascinating effects of long-chain polymer molecules on the friction drag and heat transfer coefficient of turbulent flows have stimulated numerous studies of the phenomenon known as drag reduction or Toms effects. The better understanding of friction factor and heat transfer coefficient reduction phenomena has direct applications in designs of more efficient heat exchangers for food processing, chemical and biochemical industires, of increased capacity pipelines, and of faster ships for shipping industries.

Most heat transfer models take advantage of the Reynolds analogy to correlate heat and momentum transfer phenomena. However, recent studies [1, 2] have shown that Reynolds analogy is not applicable to drag reducing turbulent pipe flows. These studies have revealed that eddy diffusivity of heat is smaller than that of momentum. Objectives of the current study were to clarify the validity and limitations of Reynolds analogy for viscoelastic fluids and to investigate various eddy diffusivity models of heat by comparing the predicted results with heat transfer experiments of Kwack et al. [3]. Their experimental data are the only available data that are reliable and well documented. Their experiments take into account such important effects as thermal entrance length, polymer degradation, and solvent chemistry.

2 Mathematical Background

The analysis begins with the Navier-Stokes equation in the x-direction for an axisymmetic flow in a circular tube written in terms of mean velocity and fluctuations from the mean. After averaging with respect to time, this equation becomes

$$\frac{1}{r}\frac{\partial}{\partial r}\left[r(\nu+\epsilon_m)\frac{d\overline{U^*}}{dr}\right] = \frac{1}{\rho}\frac{\partial \overline{P^*}}{\partial x} \tag{1}$$

Before integrating equation (1), first nondimensionalize such that

$$\bar{U} = \frac{\overline{U^*}}{U_m}, \quad \bar{P} = \frac{\overline{P^*}}{\rho U_m^2}$$

$$E = \frac{\epsilon_m}{\nu}, \quad \bar{x} = \frac{x}{r_0}, \quad \bar{r} = \frac{r}{r_0} \tag{2}$$

where

---

[1] Graduate Student, School of Mechanical and Aerospace Engineering, Oklahoma State University, Stillwater, Okla. 74078.

[2] Assistant Professor, School of Mechanical and Aerospace Engineering, Oklahoma State University, Stillwater, Okla. 74078. Mem. ASME.

Contributed by the Heat Transfer Division for publication in the Journal of Heat Transfer. Manuscript received by the Heat Transfer Division April 26, 1984.

of elliptical ducts with uniform wall heat flux is solved in closed form by the simple integral method. The resulting solution is extremely compact and of a usable form. Moreover, its accuracy in predicting the Nusselt numbers is on par with that of the complex variable solution. A unique feature of the present analysis is generation of the universal temperature profile applicable to elliptical ducts of all aspect ratios. A generalization of this temperature profile can be extremely valuable in developing a manageable solution to hitherto unsolved problem of simultaneous development of velocity and temperature fields in elliptical ducts.

References

1 Tao, L. N., "On Some Laminar Forced Convection Problems," ASME JOURNAL OF HEAT TRANSFER, Vol. 83, Nov. 1961, pp. 466–473.

2 Tyagi, V. P., "Laminar Forced Convection of a Dissipative Fluid in a Channel," ASME, JOURNAL OF HEAT TRANSFER, Vol. 88, May 1966, pp. 161–169.

3 Bhatti, M. S., "Laminar Flow in the Entrance Region of Elliptical Ducts," ASME *Journal of Fluids Engineering*, Vol. 105, No. 3, Sept. 1983, pp. 290–296.

4 Kays, W. M., and Crawford, M. E., *Convective Heat and Mass Transfer*, McGraw Hill, New York, 2nd ed., 1980, pp. 92–95.

An Analysis of the Heat Transfer to Drag Reducing Turbulent Pipe Flows

H. K. Yoon[1] **and A. J. Ghajar**[2]

Nomenclature

A^+ = constant that characterizes thickness of wall layer in Van Driest's law
c = specific heat
E = nondimensional momentum eddy diffusivity, $E = \epsilon_m/\nu$
F = Fanning friction factor, $F = 2\tau_0/\rho U_m^2$
h = heat transfer coefficient
j = Colburn j factor, $j = \mathrm{St}\,\mathrm{Pr}^{2/3}$
K = von Karman constant, $K = 0.4$
k = thermal conductivity
$\overline{p^*}$ = mean pressure
$\bar{p}$ = nondimensional mean pressure, $\bar{p} = \overline{p^*}/\rho U_m^2$
Pr = apparent Prandtl number, $\mathrm{Pr} = \nu/\alpha = \mu c/k$
$\dot{q}_0''$ = heat flux at surface
Re = Reynolds number, $\mathrm{Re} = (2r_0)U_m/\nu$
R = Reynolds number based on pipe radius, $\mathrm{R} = r_0 U_m/\nu$
r_0 = radius of pipe
r_0^+ = nondimensional pipe radius, $r_0^+ = r_0 U_\tau/\nu$
r = radial coordinate direction
$\bar{r}$ = nondimensional radial coordinate, $\bar{r} = r/r_0$
St = Stanton number, $\mathrm{St} = h/\rho c U_m$
$\overline{T^*}$ = mean temperature
T_m = mixed mean temperature
T_0 = fluid temperature at surface
$\overline{U^*}$ = streamwise mean velocity
$\bar{U}$ = nondimensional streamwise mean velocity, $\bar{U} = \overline{U^*}/U_m$
U_m = mass average velocity
U_τ = shear velocity, $U_\tau = (\tau_0/\rho)^{1/2}$
x = streamwise coordinate direction
$\bar{x}$ = nondimensional streamwise coordinate direction, $\bar{x} = x/r_0$
y = coordinate direction normal to wall, $y = r_0 - r$
$\bar{y}$ = nondimensional direction normal to wall, $\bar{y} = y/r_0$
y^+ = nondimensional distance normal to wall, $y^+ = y\,U_\tau/\nu$
ν = apparent kinematic viscosity, $\nu = \mu/\rho$
μ = apparent absolute viscosity (solution viscosity at the wall)
ρ = fluid density
ϵ_m = turbulent eddy diffusivity of momentum
ϵ_h = turbulent eddy diffusivity of heat
τ_0 = wall shear stress
α = molecular thermal diffusivity, $\alpha = k/\rho c$

1 Introduction

The fascinating effects of long-chain polymer molecules on the friction drag and heat transfer coefficient of turbulent flows have stimulated numerous studies of the phenomenon known as drag reduction or Toms effects. The better understanding of friction factor and heat transfer coefficient reduction phenomena has direct applications in designs of more efficient heat exchangers for food processing, chemical and biochemical industires, of increased capacity pipelines, and of faster ships for shipping industries.

Most heat transfer models take advantage of the Reynolds analogy to correlate heat and momentum transfer phenomena. However, recent studies [1, 2] have shown that Reynolds analogy is not applicable to drag reducing turbulent pipe flows. These studies have revealed that eddy diffusivity of heat is smaller than that of momentum. Objectives of the current study were to clarify the validity and limitations of Reynolds analogy for viscoelastic fluids and to investigate various eddy diffusivity models of heat by comparing the predicted results with heat transfer experiments of Kwack et al. [3]. Their experimental data are the only available data that are reliable and well documented. Their experiments take into account such important effects as thermal entrance length, polymer degradation, and solvent chemistry.

2 Mathematical Background

The analysis begins with the Navier-Stokes equation in the x-direction for an axisymmetic flow in a circular tube written in terms of mean velocity and fluctuations from the mean. After averaging with respect to time, this equation becomes

$$\frac{1}{r}\frac{\partial}{\partial r}\left[r(\nu+\epsilon_m)\frac{d\overline{U^*}}{dr}\right]=\frac{1}{\rho}\frac{\partial\overline{P^*}}{\partial x} \qquad (1)$$

Before integrating equation (1), first nondimensionalize such that

$$\bar{U}=\frac{\overline{U^*}}{U_m},\quad \bar{P}=\frac{\overline{P^*}}{\rho U_m^2}$$

$$E=\frac{\epsilon_m}{\nu},\quad \bar{x}=\frac{x}{r_0},\quad \bar{r}=\frac{r}{r_0} \qquad (2)$$

where

---

[1] Graduate Student, School of Mechanical and Aerospace Engineering, Oklahoma State University, Stillwater, Okla. 74078.

[2] Assistant Professor, School of Mechanical and Aerospace Engineering, Oklahoma State University, Stillwater, Okla. 74078. Mem. ASME.

Contributed by the Heat Transfer Division for publication in the JOURNAL OF HEAT TRANSFER. Manuscript received by the Heat Transfer Division April 26, 1984.

$$U_m=\frac{2}{r_0^2}\int_0^{r_0}\overline{U^*}r\,dr \qquad (3)$$

Thus equation (1) becomes

$$\frac{1}{\bar{r}}\frac{\partial}{\partial\bar{r}}\left[\bar{r}(1+E)\frac{d\bar{U}}{d\bar{r}}\right]=\mathrm{R}F \qquad (4)$$

where

$$R=\frac{r_0U_m}{\nu} \quad \text{and} \quad F=\frac{d\bar{P}}{d\bar{x}} \qquad (5)$$

Equation (4) may be integrated twice with the aid of boundary conditions

$$\frac{d\bar{U}}{d\bar{r}}=0 \quad \text{at} \quad \bar{r}=0$$

and

$$\bar{U}=0 \quad \text{at} \quad \bar{r}=1 \qquad (6)$$

Finally, we can obtain the nondimensionalized form of the mean velocity profile from equations (3) and (4)

$$1=\mathrm{R}F\int_0^1\int_1^{\bar{r}}\left[\frac{r_1}{1+E(r_1)}dr_1\right]\bar{r}\,d\bar{r} \qquad (7)$$

The eddy diffusivity expression in equation (7) must be chosen so that this equation is satisfied. Consequently, the eddy diffusivity must be determined such that the product of RF determined from equation (7) agrees with experimental conditions. Details concerning the eddy diffusivity expression for momentum will be given in section 3.

With the obtained time-mean velocity profiles, we are ready to solve the time-mean energy equation in the x-direction

$$\frac{1}{r}\frac{\partial}{\partial r}\left[r(\alpha+\epsilon_h)\frac{\partial\overline{T^*}}{\partial r}\right]=\overline{U^*}\frac{dT_m}{dx} \qquad (8)$$

The heat transfer coefficient is defined by

$$\dot{q}_0''=h(T_0-T_m) \qquad (9)$$

where

$$\dot{q}_0''=+k\left(\frac{\partial\overline{T^*}}{\partial r}\right)_{r=r_0} \qquad (10)$$

Some mathematical manipulations of equations (8), (9), and (10), with well-defined boundary conditions result in a Stanton number, which can be expressed by

$$\mathrm{St}=\frac{\int_1^0\bar{U}(1-\bar{y})\,d\bar{y}}{\mathrm{Re}\int_0^1\bar{U}(1-\bar{y})\left\{\int_0^{\bar{y}}\left[\frac{\int_1^{\bar{y}_1}\bar{U}(1-\bar{y}_2)d\bar{y}_2}{\left(\frac{\epsilon_h}{\nu}(\bar{y}_1)+\frac{1}{\mathrm{Pr}}\right)(1-\bar{y}_1)}\right]d\bar{y}_1\right\}d\bar{y}} \qquad (11)$$

Additional details of mathematical derivations may be found in [4, 5]. Details concerning an eddy diffusivity expression for heat will be discussed in section 4.

3 Predictions of Mean Velocity Profile

In the proposed heat transfer analysis, the Cess eddy diffusivity model was used to predict the mean velocity profile. Cess [6] combined the wall region eddy diffusivity of Van Driest with Reichardt's expression for the diffusivity in the center portion of a pipe flow to obtain a single, continuous expression for eddy diffusivity of momentum ϵ_m. The eddy diffusivity expression proposed by Cess is

$$\frac{\epsilon_m}{\nu}=\frac{1}{2}\left\{1+\frac{K^2r_0^{+2}}{9}\left[1-\left(\frac{r}{r_0}\right)^2\right]^2\left[1+2\left(\frac{r}{r_0}\right)^2\right]^2\right.$$
$$\left.\times\left[1-\exp\left\{\frac{-(1-r/r_0)}{A^+/r_0^+}\right\}\right]^2\right\}^{1/2}-\frac{1}{2} \qquad (12)$$

The unique feature of this model is that in drag reducing flows, it is not possible to determine one of the constants in the eddy diffusivity model a priori. An iterative scheme proposed by Tiederman and Reischman [7] was used to determine the constant A^+ that characterizes the thickness of the near-wall region of the flow. This iterative scheme requires as inputs an experimental value for the von Karman contant K and some initial guess for A^+. The procedure then determines an exact value for A^+ and integrates the equations to yield velocity profiles.

The Cess model has proved to be able to predict the mean velocity profile excellently when compared with experimentally measured profiles in both Newtonian and drag reducing flows. The simplicity of using the Cess model should not be overlooked. It is an explicit technique and the distribution is continuous. Consequently, there is no "patching" of diffusivity expressions at arbitrary locations. Finally, it combines the best features of two good diffusivity models so that the final diffusivity has the correct behavior both at the wall and in the center portion of the pipe.

4 Prediction of Heat Transfer Coefficients

In order to predict heat transfer coefficients, the differential energy equation should be solved based on an accurate and general eddy diffusivity model for heat ϵ_h. It is common to assume that Reynolds analogy is valid for viscoelastic fluids. In this section, an attempt will be made to define the validity and limitations of Reynolds analogy. Additionally, to close the gap between analytical predictions and experimental data, depending on the Prandtl number of polymer solutions, three different eddy diffusivities of heat were employed. For dilute (Pr < 6.5) polymer solutions, Reynolds analogy was used and for intermediate (6.5 ≤ Pr < 8.2) and high concentration (Pr ≥ 8.2) polymer solutions, heat eddy diffusivity models proposed by Mizushina and Usui [2] were adopted. The proposed models are

$$\epsilon_h/\epsilon_m=1 \quad \text{for} \quad \mathrm{Pr}<6.5 \qquad (13)$$

$$\epsilon_h/\epsilon_m=1.5\{1-\exp[-y^+(42+120/\mathrm{Pr}^{1/2})^{-1}]\}$$
$$\text{for } 6.5\le\mathrm{Pr}<8.2 \qquad (14)$$
$$\times[1-\exp(-y^+/26)]^{-1}$$

$$\epsilon_h/\nu=\mathrm{C}y^{+3} \quad \text{for} \quad \mathrm{Pr}\ge 8.2 \qquad (15)$$

where $C=1.7\times10^{-6}-2.5\times10^{-6}$

These models were used to predict Colburn j-factors, using experimental data of Kwack et al. [3]. The results are summarized in Figs. 1 and 2. In these calculations, the Cess eddy diffusivity model for momentum was used to predict mean velocity profiles. As shown in Fig. 1, Reynolds analogy is valid only for Pr < 6.5, and considerable error (as much as 150 percent) can be introduced in the calculations for Pr ≥ 6.5 if Reynolds analogy is assumed. However, as shown in Fig. 2, the employment of different eddy diffusivities of heat depending on the Prandtl number of polymer solutions, ushered the predicted heat transfer results into the ± 20 percent error bound, with the exception of three points, which is believed to be due to the inconsistency in the reported experimental data.

5 Closure

Based on the observations made in the previous section, the following heat eddy diffusivity models are proposed:

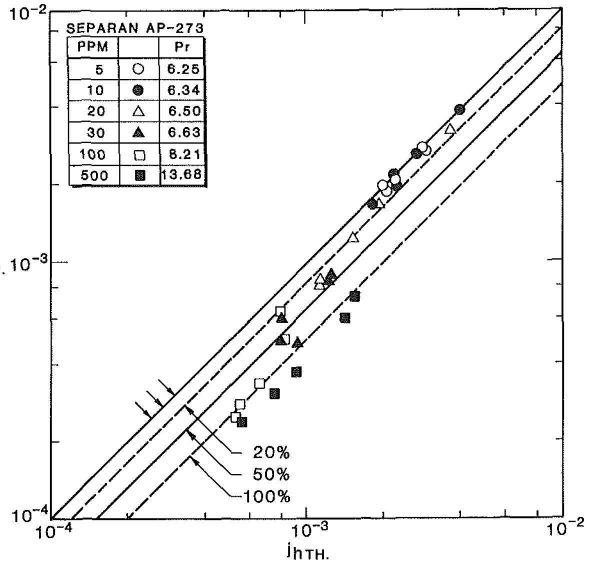

Fig. 1 Comparison of the predicted Colburn *j*-factors based on Reynolds analogy with measurements [3]

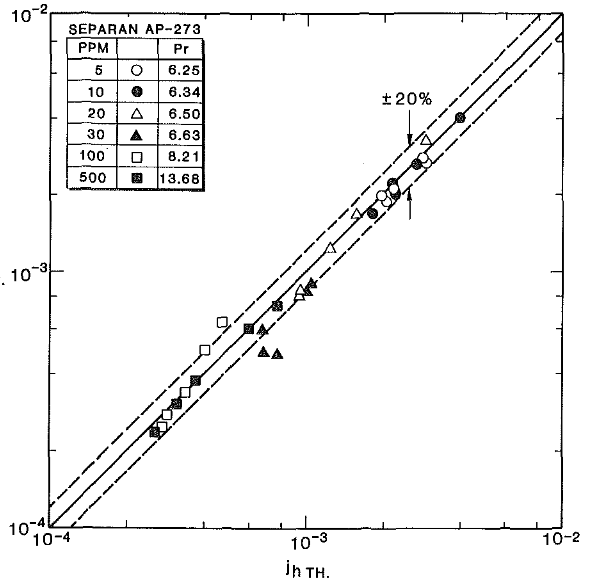

Fig. 2 Comparison of the predicted Colburn *j*-factors using three different heat eddy diffusivities, depening on polymer concentration, with measurements [3]

1 for $Pr < 6.5$, the model proposed in equation (13).
2 for $6.5 \leq Pr < 8.2$, the model proposed in equation (14).
3 for $Pr \geq 8.2$, the model proposed in equation (15).

However, there are shortcomings associated with the use of these heat eddy diffusivity models for future work. The validity and limitations of the diffusivity models are not fully known. The models should be evaluated further with more reliable experimental data that cover wide ranges of polymer concentrations and different types of polymers. Unfortunately, presently this type of data is not available. In addition, no relationship exists that would relate the models to one another. To remedy these shortcomings and increase the predictive capability of the proposed analytical model, the eddy diffusivities of momentum and heat must be expressed as a function of Deborah number (ratio of the elastic forces to the viscous forces). The Deborah number must be determined experimentally for different types of polymers at different concentrations. Presently, this type of information is not available. Efforts are now underway to generate this type of data.

References

1 Cho, Y. I., and Hartnett, J. P., "Analogy for Viscoelastic Fluids—Momentum, Heat, and Mass Transfer in Turbulent Pipe Flow," *Letters in Heat and Mass Transfer*, Vol. 7, 1980, pp. 339-346.

2 Mizushina, T., and Usui, H., "Reduction of Eddy Diffusion for Momentum and Heat in Viscoelastic Fluid Flow in a Circular Tube," *The Physics of Fluids*, Vol. 20, No. 10, Pt. 11, Oct. 1977, pp. S100-S108.

3 Kwack, E. Y., Cho, Y. I., and Hartnett, J. P., "Heat Transfer to Polyacrylamide Solutions in Turbulent Pipe Flow: The Once-Through Mode," *AIChE J.*, Vol. 27, 1981, pp. 123-130.

4 Ghajar, A. J., "Prediction of Heat Transfer Coefficients in Drag Reducing Turbulent Pipe Flows," M.S. thesis, Oklahoma State University, Stillwater, Okla., 1975.

5 Ghajar, A. J., and Tiederman, W. G., "Predictions of Heat Transfer Coefficients in Drag Reducing Turbulent Pipe Flows," *AIChE J.*, Vol. 23, No. 1, Jan. 1977, pp. 128-131.

6 Cess, R. D., "A Survey of the Literature in Heat Transfer in Turbulent Tube Flows,"' Westinghouse Research Report 8-0529-R24, Philadelphia, Pa., Westinghouse Corp., 1958.

7 Tiederman, W. G., and Reischman, M. M., "Calculation of Velocity Profiles in Drag-Reducing Flows," ASME *Journal of Fluids Engineering*, Vol. 98, No. 3, Sept. 1976, pp. 563-566.

Stability of Steam-Water Countercurrent Flow in an Inclined Channel: Part II—Condensation-Induced Waterhammer[1]

S. C. Lee[2] and S. G. Bankoff[2,3]

Introduction

Two important instabilities have been observed in inclined countercurrent flow of steam and cold water [1]: condensation-induced waterhammer and flooding. Flooding has been discussed in detail in a preceding paper [2]. Condensation-induced waterhammer, considered to be a combined thermal and hydraulic instability of countercurrent stratified flow, is characterized by significant pressure drop oscillations, probably due to unsteady collapse or near-collapse of local vapor pockets. The initiating mechanism of this condensation-induced instability is not clear yet, although work has been done on particular situations, such as waterhammer in PWR steam generators [3] or in horizontal pipes containing steam and subcooled water [4].

The present study deals with condensation-induced waterhammer in stratified steam-water flow in rectangular ducts inclined at two different angles, approximately 30 and 4.5 deg, to the horizontal. A stability map is constructed, with distinct regions of waterhammer, flooding, and stable operation. The necessary conditions for waterhammer are established and analyses of these conditions are presented on a basis of interfacial wave stability and heat transfer considerations.

Experimental System and Procedure

The experimental apparatus includes a test section, two water storage tanks, heat exchanger, and two circulating pumps. The test section is a rectangular channel approximately 2.13 m long and 0.38 m wide with adjustable depth. The distance between the water inlet and outlet is 1.27 m. The test section has its own support system which permits any inclination between 0 and 90 deg. Two channel depths ($H = 0.076$ m and 0.038 m) and two inclination angles were employed. Measurements of temperatures, pressure drops,

---

[1] Work supported by a grant from the U. S. Nuclear Regulatory Commission.

[2] Department of Mechanical Engineering, Northwestern University, Evanston, Ill. 60210.

[3] Mem. ASME.

Contributed by the Heat Transfer Division for publication in the JOURNAL OF HEAT TRANSFER. Manuscript received by the Heat Transfer Division May 18, 1983.

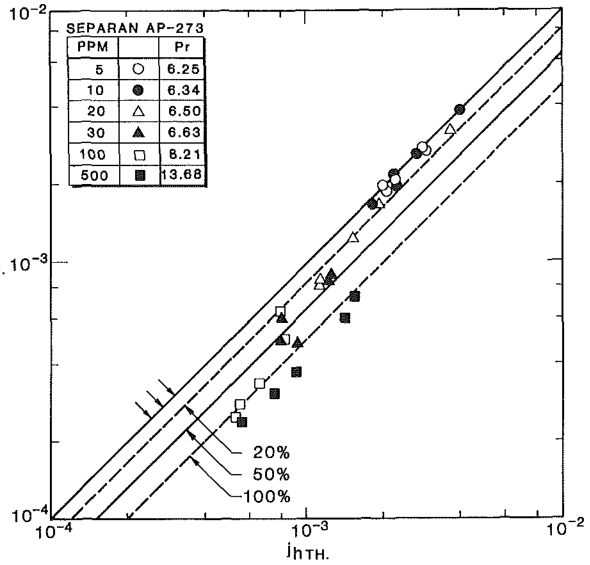

Fig. 1 Comparison of the predicted Colburn *j*-factors based on Reynolds analogy with measurements [3]

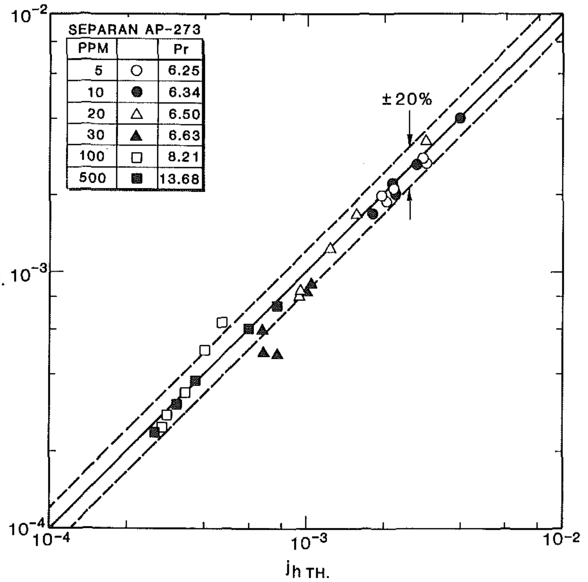

Fig. 2 Comparison of the predicted Colburn *j*-factors using three different heat eddy diffusivities, depening on polymer concentration, with measurements [3]

1 for $\mathrm{Pr} < 6.5$, the model proposed in equation (13).
2 for $6.5 \leq \mathrm{Pr} < 8.2$, the model proposed in equation (14).
3 for $\mathrm{Pr} \geq 8.2$, the model proposed in equation (15).

However, there are shortcomings associated with the use of these heat eddy diffusivity models for future work. The validity and limitations of the diffusivity models are not fully known. The models should be evaluated further with more reliable experimental data that cover wide ranges of polymer concentrations and different types of polymers. Unfortunately, presently this type of data is not available. In addition, no relationship exists that would relate the models to one another. To remedy these shortcomings and increase the predictive capability of the proposed analytical model, the eddy diffusivities of momentum and heat must be expressed as a function of Deborah number (ratio of the elastic forces to the viscous forces). The Deborah number must be determined experimentally for different types of polymers at different concentrations. Presently, this type of information is not available. Efforts are now underway to generate this type of data.

References

1 Cho, Y. I., and Hartnett, J. P., "Analogy for Viscoelastic Fluids—Momentum, Heat, and Mass Transfer in Turbulent Pipe Flow," *Letters in Heat and Mass Transfer*, Vol. 7, 1980, pp. 339–346.

2 Mizushina, T., and Usui, H., "Reduction of Eddy Diffusion for Momentum and Heat in Viscoelastic Fluid Flow in a Circular Tube," *The Physics of Fluids*, Vol. 20, No. 10, Pt. 11, Oct. 1977, pp. S100–S108.

3 Kwack, E. Y., Cho, Y. I., and Hartnett, J. P., "Heat Transfer to Polyacrylamide Solutions in Turbulent Pipe Flow: The Once-Through Mode," *AIChE J.*, Vol. 27, 1981, pp. 123–130.

4 Ghajar, A. J., "Prediction of Heat Transfer Coefficients in Drag Reducing Turbulent Pipe Flows," M.S. thesis, Oklahoma State University, Stillwater, Okla., 1975.

5 Ghajar, A. J., and Tiederman, W. G., "Predictions of Heat Transfer Coefficients in Drag Reducing Turbulent Pipe Flows," *AIChE J.*, Vol. 23, No. 1, Jan. 1977, pp. 128–131.

6 Cess, R. D., "A Survey of the Literature in Heat Transfer in Turbulent Tube Flows,"' Westinghouse Research Report 8-0529-R24, Philadelphia, Pa., Westinghouse Corp., 1958.

7 Tiederman, W. G., and Reischman, M. M., "Calculation of Velocity Profiles in Drag-Reducing Flows," ASME *Journal of Fluids Engineering*, Vol. 98, No. 3, Sept. 1976, pp. 563–566.

Stability of Steam–Water Countercurrent Flow in an Inclined Channel: Part II—Condensation-Induced Waterhammer[1]

S. C. Lee[2] and S. G. Bankoff[2,3]

Introduction

Two important instabilities have been observed in inclined countercurrent flow of steam and cold water [1]: condensation-induced waterhammer and flooding. Flooding has been discussed in detail in a preceding paper [2]. Condensation-induced waterhammer, considered to be a combined thermal and hydraulic instability of countercurrent stratified flow, is characterized by significant pressure drop oscillations, probably due to unsteady collapse or near-collapse of local vapor pockets. The initiating mechanism of this condensation-induced instability is not clear yet, although work has been done on particular situations, such as waterhammer in PWR steam generators [3] or in horizontal pipes containing steam and subcooled water [4].

The present study deals with condensation-induced waterhammer in stratified steam–water flow in rectangular ducts inclined at two different angles, approximately 30 and 4.5 deg, to the horizontal. A stability map is constructed, with distinct regions of waterhammer, flooding, and stable operation. The necessary conditions for waterhammer arc established and analyses of these conditions are presented on a basis of interfacial wave stability and heat transfer considerations.

Experimental System and Procedure

The experimental apparatus includes a test section, two water storage tanks, heat exchanger, and two circulating pumps. The test section is a rectangular channel approximately 2.13 m long and 0.38 m wide with adjustable depth. The distance between the water inlet and outlet is 1.27 m. The test section has its own support system which permits any inclination between 0 and 90 deg. Two channel depths (H = 0.076 m and 0.038 m) and two inclination angles were employed. Measurements of temperatures, pressure drops,

---

[1] Work supported by a grant from the U. S. Nuclear Regulatory Commission.

[2] Department of Mechanical Engineering, Northwestern University, Evanston, Ill. 60210.

[3] Mem. ASME.

Contributed by the Heat Transfer Division for publication in the JOURNAL OF HEAT TRANSFER. Manuscript received by the Heat Transfer Division May 18, 1983.

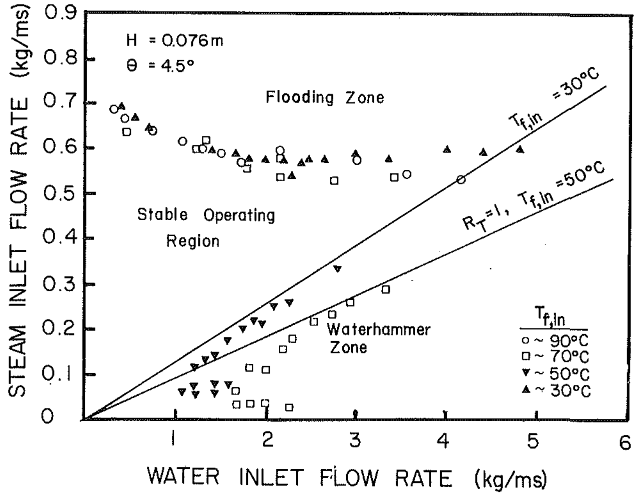

Fig. 1 Stability map of countercurrent stratified steam—water flow in a nearly horizontal duct

and flow rates were made. Details on the apparatus and measurement are found elsewhere [1, 5].

The data for the boundary separating the waterhammer zone from the stable operating region in a stability map were obtained by monitoring the occurrence of weak pressure waves while varying the steam supply rate at a fixed water inlet flow rate. The pressure drop of the vapor phase started to fluctuate wildly, with periodic noises caused by impacts upon the channel walls. Visual observations indicated sudden increases of the interfacial wave heights near the water exit. These probably resulted from the suction effect of the steam void caused by rapid condensation.

Results and Analysis

Figure 1 shows a stability map of countercurrent steam–water flow in a rectangular duct (H = 0.076 m) inclined at θ = 4.5 deg to the horizontal. Three distinct regions are noted: waterhammer, flooding, and stable operating region. The ideal complete condensation line, defined by Rothe et al. [6], is

$$R_T \triangleq \frac{C_{pl}(T_s - T_{f,\text{in}})W_{f,\text{in}}}{i_{fg}W_{g,\text{in}}} \tag{1}$$

It is seen that in stratified flow waterhammer cannot exist when the water flow rate is insufficient to condense all the incoming steam. This is consistent with the experimental result of Rothe et al. [6] that $R_T > 1$ is a necessary condition for initiating condensation-induced transients in horizontal countercurrent flow of steam and subcooled water.

One may note in Fig. 1 that the actual data points for complete condensation deviate slightly from $R_T = 1$ because of nonideal condensation efficiency, which is dependent upon geometry and flow conditions. From a simple analysis based on mass and energy balances [1], the data can be represented by the following equation

$$W_{g,\text{in}} = fKW_{f,\text{in}} \tag{2}$$

where the dimensionless subcooling number K and the condensation efficiency f are defined by

$$K = C_{pl}(T_s - T_{f,\text{in}})/i_{fg} \tag{3}$$

$$f = 1 - \exp\left[-\frac{\bar{h}_L L}{(1+K)C_{pl}W_{f,\text{in}}}\right] \tag{4}$$

In equation (4), the average heat transfer coefficient, $\bar{h}_L$ may be obtained either from direct empirical correlations or by a finite-difference calculation based on empirical correlations of the local condensation heat transfer coefficient.

Another interesting feature of the condensation-induced waterhammer zone is the appearance of the wavy interface. The lower boundary in Fig. 1 may be related to the transition from a smooth film to a wavy interface. Some previous analyses [7–9] show that when the pressure work done by the gas flow over the liquid film is equal to, or more than, the energy dissipated in the liquid, the surface wave tends to be sustained or grow with time. Of basic significance in the interactions of the gas and liquid flow is the separation of flow that occurs at the wave crests, which was considered first by Jeffreys [7, 8] in terms of a sheltering coefficient. Taitel and Dukler [10] suggested that this effect accounts for the transition between the stratified smooth and stratified wavy regimes in horizontal, or near-horizontal, cocurrent flow. With vapor condensation, an additional force acts on the liquid film owing to the momentum loss of the condensing vapor, although this effect, as pointed out by Bankoff [11] for evaporating films, is likely to be small. Considering the condensation effect, a criterion for this transition can be obtained in a rather straightforward manner [1]

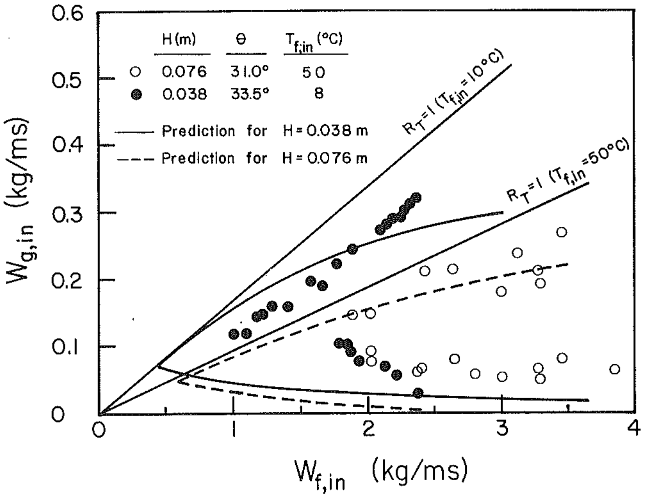

Fig. 2 Predicted boundaries of condensation-induced waterhammer zone

$$ns\rho_g(U_g + c)^2 c + \frac{1}{4}\rho_g V_g^2 c \geq \nu_f(\rho_f - \rho_g)g\cos\theta \tag{5}$$

where the constant n is given as 1/2 based on a two-dimensional wave assumption and 1/4 for a three-dimensional wave, and V_g is the average velocity of the condensing vapor normal to the interface, given by

$$V_g = \frac{h(T_s - T_f)}{\rho_g i_{fg}} \tag{6}$$

or calculated approximately from the overall energy balance as follows:

$$V_g \cong \frac{W_{g,\text{in}}}{\rho_g L} \tag{7}$$

One may assume that the wave celerity c in equation (5) is approximately equal to the average liquid velocity for high liquid Reynolds number [1].

Typical data for the boundaries of the waterhammer zone are compared with the calculated result in Fig. 2. The upper boundary representing the actual complete condensation line $R_T = f$ was obtained by a finite difference approximation, based on empirical correlations for the local heat transfer coefficient developed in the present apparatus [12]

$$\text{Nu} = A\ \text{Re}_g^{e_1}\text{Re}_f^{e_2}\ \text{Pr}^{e_3} \tag{8}$$

where the constants for H = 0.038 m and θ = 33.5 deg are given by

$A = 0.173$; $e_1 = 0.027$; $e_2 = 0.49$; $e_3 = 0.42$

and for $H = 0.076$ m and θ = 31 deg,

$A = 1.35 \times 10^{-4}$; $e_1 = 0.35$; $e_2 = 1.0$; $e_3 = 0.56$

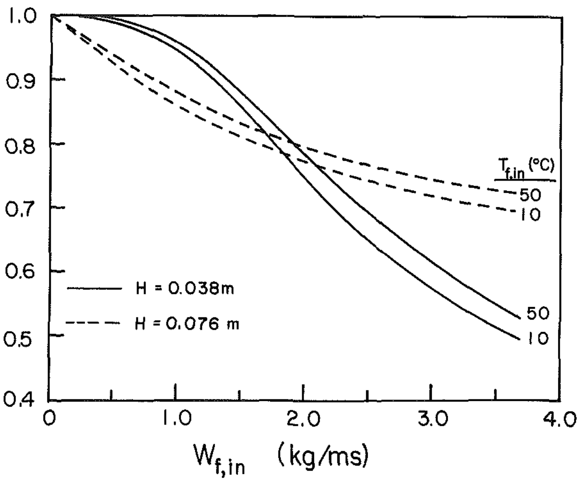

Fig. 3 Calculated condensation efficiency for complete condensation

The numerical procedure is summarized in [1]. The condensation efficiency calculated by this method may be underestimated slightly because of the entrance effect at both ends. The lower boundary in Fig. 2 was calculated from equation (5), with $n = 1/4$. The sheltering coefficient s is chosen as 0.01, following Benjamin [9]. It is shown that the data points lie, in general, above the predicted boundary. This may be partly because the stabilizing surface tension term in the dispersion equation was ignored in deriving the dissipation rate in equation (5).

The condensation efficiency calculated by a finite difference approximation, when complete condensation takes place inside the test section, is shown in Fig. 3. It decreases as the water inlet flow rate increases, and the rate of decrease is steeper for $H = 0.038$ m. It is also shown that the increase of the water temperature tends to increase the condensation efficiency.

The present experimental result is comparable to the "universal" flow regime map proposed by Block [13]. The appearance of a wavy interface in the present stability map apparently corresponds to the upper boundary of the relatively smooth interface region (Boundary A) in this "universal" map. No flow instability can exist below Boundary A. On the other hand, the lower boundary of the high-frequency fluctuation region (Boundary B) may be replaced by the flooding line in Fig. 1, because this region reflects the presence of an unsteady plug, according to the experimental result of Rothe et al. [6] for horizontal countercurrent steam/subcooled-water flow. As described in the preceding paper [2], the onset of flooding was characterized by the formation of liquid slugs and bridging in inclined countercurrent flow. It is shown that the onset of flooding can take place in the region $R_T < 1$ in Fig. 1, but this is not reflected in this "universal" flow regime map.

References

1 Lee, S. C., "Stability of Steam-Water Countercurrent Stratified Flow," Ph.D. thesis, Northwestern University, Evanston, Ill., 1983.

2 Lee, S. C., and Bankoff, S. G., "Stability of Steam-Water Countercurrent Flow in an Inclined Channel: Part I—Flooding," ASME JOURNAL OF HEAT TRANSFER, Vol. 105, 1983, pp. 713–718.

3 Saha, P., Ginsberg, T., Wu, B. J. C., and Jones, Jr., O. C., "An Evaluation of Condensation-Induced Waterhammer in Preheat Steam Generators," NUREG/CR-1606, 1980.

4 Bjorge, R. W., and Griffith, P., "Initiation of Waterhammer in Horizontal and Nearly Horizontal Pipes Containing Steam and Subcooled Water," submitted to ASME JOURNAL OF HEAT TRANSFER, 1982.

5 Lee, S. C., and Bankoff, S. G., "Stability of Steam-Water Countercurrent Flow in an Inclined Channel," ASME 82-WA/HT-6, 1982.

6 Rothe, P. H., Wallis, G. B., and Block, J. A., "Cold Leg ECC Flow Oscillations," *Proceedings of the Symposium on the Thermal and Hydraulic Aspects of Nuclear Reactor Safety*, Vol. 1, ASME, New York, 1977, pp. 133–150.

7 Jeffreys, H., "On the Formation of Water Waves by Wind," *Proc. Roy. Soc. A.*, Vol. 107, 1925, pp. 189–205.

8 Jeffreys, H., "On the Formation of Water Waves by Wind (second paper)," *Proc. Roy. Soc. A.*, Vol. 110, 1926, pp. 241–247.

9 Benjamin, T. B., "Shearing Flow over a Wavy Boundary," J. Fluid Mechanics," Vol. 6, 1959, pp. 161–205.

10 Taitel, Y., and Dukler, A. E., "A Model for Predicting Flow Regime Transitions in Horizontal and Near Horizontal Gas-Liquid Flow," *AIChE Journal*, Vol. 22, 1976, pp. 47–55.

11 Bankoff, S. G., "Stability of Liquid Flow Down a Heated Inclined Plane," *International Journal of Heat and Mass Transfer*, Vol. 14, 1971, pp. 377–385.

12 Bankoff, S. G., and Kim, H. J., "Direct-Contact Condensation of Steam on Cold Water in Stratified Countercurrent Flow," Topical Report to U.S. NRC, 1983.

13 Block, J. A., "Condensation-Driven Fluid Motions," *Int. J. Multiphase Flow*, Vol. 6, 1980, pp. 113–129.

Some Characteristics of the Conduction Heat Flux at the Surface of a Wedge Enclosure

C. Wei[1] and J. T. Berry[2]

Nomenclature

E = edge function
Fo = Fourier number
$_1F_1$ = confluent hypergeometric function
J = Bessel function of the first kind
K = thermal conductivity
q = heat flow per unit time and area
r = radial coordinate
t = time
T = temperature
α = thermal diffusivity
Γ = gamma function
$\Delta(\theta_0)$ = wedge invariant
$\eta = \dfrac{1}{2\sqrt{\mathrm{Fo}}}$
θ = angular coordinate
θ_0 = wedge angle

Introduction

The classical problem of heat conduction in wedges was analyzed by Jaeger [1] some 40 years ago. The knowledge of this subject has recently been expanded via a transformation technique [2]. It has been found [2] that, for an infinite wedge enclosure subjected to an instantaneously imposed constant temperature boundary condition, the *difference* between the heat flow rate across the wedge surface, per unit time and unit depth along the edge, and the heat flow rate when the wedge takes the shape of a corner-free, semi-infinite solid, does *not* vary with time. The term "wedge invariant" was used to define the invariability [2].

The edge or corner effect on heat transport within the wedge is best represented by the transient distribution of the heat flux at the surface. The surface heat flux derived from Jaeger's solution [1] can be decomposed into the product of the time-dependent surface heat flux over a semi-infinite solid and an edge function that is governed only by a Fourier

---

[1] Assistant Professor, Department of Mechanical and Aerospace Engineering, Polytechnic Institute of New York, Brooklyn, N.Y. 11201, Assoc. Mem. ASME

[2] Professor, School of Mechanical Engineering, Georgia Institute of Technology, Atlanta, GA. 30332, Mem. ASME

Contributed by the Heat Transfer Division for publication in the JOURNAL OF HEAT TRANSFER. Manuscript received by the Heat Transfer Division, October 6, 1983.

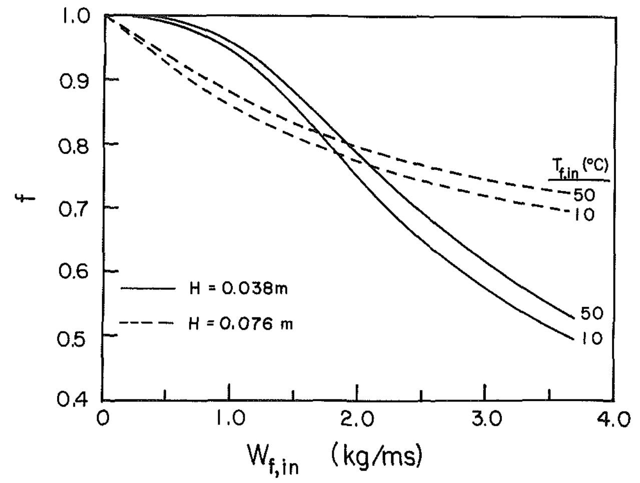

Fig. 3 Calculated condensation efficiency for complete condensation

The numerical procedure is summarized in [1]. The condensation efficiency calculated by this method may be underestimated slightly because of the entrance effect at both ends. The lower boundary in Fig. 2 was calculated from equation (5), with $n = 1/4$. The sheltering coefficient s is chosen as 0.01, following Benjamin [9]. It is shown that the data points lie, in general, above the predicted boundary. This may be partly because the stabilizing surface tension term in the dispersion equation was ignored in deriving the dissipation rate in equation (5).

The condensation efficiency calculated by a finite difference approximation, when complete condensation takes place inside the test section, is shown in Fig. 3. It decreases as the water inlet flow rate increases, and the rate of decrease is steeper for $H = 0.038$ m. It is also shown that the increase of the water temperature tends to increase the condensation efficiency.

The present experimental result is comparable to the "universal" flow regime map proposed by Block [13]. The appearance of a wavy interface in the present stability map apparently corresponds to the upper boundary of the relatively smooth interface region (Boundary A) in this "universal" map. No flow instability can exist below Boundary A. On the other hand, the lower boundary of the high-frequency fluctuation region (Boundary B) may be replaced by the flooding line in Fig. 1, because this region reflects the presence of an unsteady plug, according to the experimental result of Rothe et al. [6] for horizontal countercurrent steam/subcooled-water flow. As described in the preceding paper [2], the onset of flooding was characterized by the formation of liquid slugs and bridging in inclined countercurrent flow. It is shown that the onset of flooding can take place in the region $R_T < 1$ in Fig. 1, but this is not reflected in this "universal" flow regime map.

References

1 Lee, S. C., "Stability of Steam-Water Countercurrent Stratified Flow," Ph.D. thesis, Northwestern University, Evanston, Ill., 1983.

2 Lee, S. C., and Bankoff, S. G., "Stability of Steam-Water Countercurrent Flow in an Inclined Channel: Part I—Flooding," ASME JOURNAL OF HEAT TRANSFER, Vol. 105, 1983, pp. 713–718.

3 Saha, P., Ginsberg, T., Wu, B. J. C., and Jones, Jr., O. C., "An Evaluation of Condensation-Induced Waterhammer in Preheat Steam Generators," NUREG/CR-1606, 1980.

4 Bjorge, R. W., and Griffith, P., "Initiation of Waterhammer in Horizontal and Nearly Horizontal Pipes Containing Steam and Subcooled Water," submitted to ASME JOURNAL OF HEAT TRANSFER, 1982.

5 Lee, S. C., and Bankoff, S. G., "Stability of Steam-Water Countercurrent Flow in an Inclined Channel," ASME 82-WA/HT-6, 1982.

6 Rothe, P. H., Wallis, G. B., and Block, J. A., "Cold Leg ECC Flow Oscillations," *Proceedings of the Symposium on the Thermal and Hydraulic Aspects of Nuclear Reactor Safety*, Vol. 1, ASME, New York, 1977, pp. 133–150.

7 Jeffreys, H., "On the Formation of Water Waves by Wind," *Proc. Roy. Soc. A.*, Vol. 107, 1925, pp. 189–205.

8 Jeffreys, H., "On the Formation of Water Waves by Wind (second paper)," *Proc. Roy. Soc. A.*, Vol. 110, 1926, pp. 241–247.

9 Benjamin, T. B., "Shearing Flow over a Wavy Boundary," J. Fluid Mechanics," Vol. 6, 1959, pp. 161–205.

10 Taitel, Y., and Dukler, A. E., "A Model for Predicting Flow Regime Transitions in Horizontal and Near Horizontal Gas-Liquid Flow," *AIChE Journal*, Vol. 22, 1976, pp. 47–55.

11 Bankoff, S. G., "Stability of Liquid Flow Down a Heated Inclined Plane," *International Journal of Heat and Mass Transfer*, Vol. 14, 1971, pp. 377–385.

12 Bankoff, S. G., and Kim, H. J., "Direct-Contact Condensation of Steam on Cold Water in Stratified Countercurrent Flow," Topical Report to U.S. NRC, 1983.

13 Block, J. A., "Condensation-Driven Fluid Motions," *Int. J. Multiphase Flow*, Vol. 6, 1980, pp. 113–129.

Some Characteristics of the Conduction Heat Flux at the Surface of a Wedge Enclosure

C. Wei[1] and J. T. Berry[2]

Nomenclature

E = edge function
Fo = Fourier number
${}_1F_1$ = confluent hypergeometric function
J = Bessel function of the first kind
K = thermal conductivity
q = heat flow per unit time and area
r = radial coordinate
t = time
T = temperature
α = thermal diffusivity
Γ = gamma function
$\Delta(\theta_0)$ = wedge invariant
$\eta = \dfrac{1}{2\sqrt{\text{Fo}}}$
θ = angular coordinate
θ_0 = wedge angle

Introduction

The classical problem of heat conduction in wedges was analyzed by Jaeger [1] some 40 years ago. The knowledge of this subject has recently been expanded via a transformation technique [2]. It has been found [2] that, for an infinite wedge enclosure subjected to an instantaneously imposed constant temperature boundary condition, the *difference* between the heat flow rate across the wedge surface, per unit time and unit depth along the edge, and the heat flow rate when the wedge takes the shape of a corner-free, semi-infinite solid, does *not* vary with time. The term "wedge invariant" was used to define the invariability [2].

The edge or corner effect on heat transport within the wedge is best represented by the transient distribution of the heat flux at the surface. The surface heat flux derived from Jaeger's solution [1] can be decomposed into the product of the time-dependent surface heat flux over a semi-infinite solid and an edge function that is governed only by a Fourier

---

[1] Assistant Professor, Department of Mechanical and Aerospace Engineering, Polytechnic Institute of New York, Brooklyn, N.Y. 11201, Assoc. Mem. ASME

[2] Professor, School of Mechanical Engineering, Georgia Institute of Technology, Atlanta, GA. 30332, Mem. ASME

Contributed by the Heat Transfer Division for publication in the JOURNAL OF HEAT TRANSFER. Manuscript received by the Heat Transfer Division, October 6, 1983.

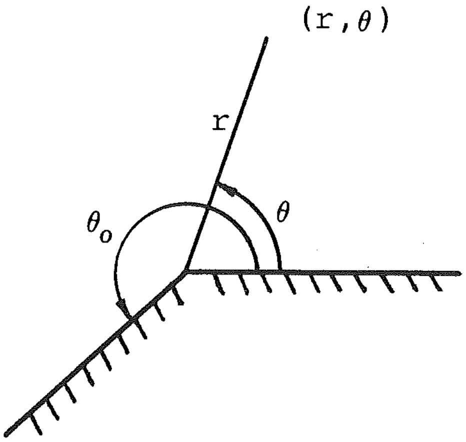

Fig. 1 Coordinates utilized in deriving solution (1); $0<\theta<\theta_0$, $0<r<\infty$

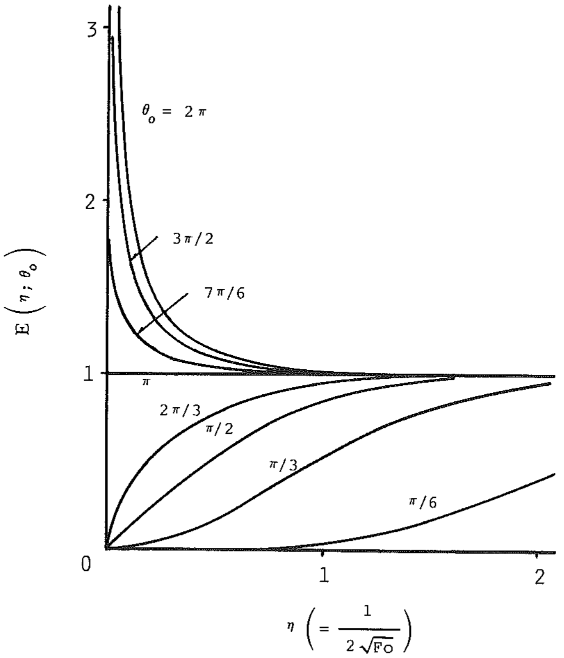

Fig. 2 Graphical representation of the *E*-function versus $1/2\sqrt{\text{Fo}}$

number. This note presents the mathematics and a practical application of such similarity characteristic.

Analysis

In 1942, Jaeger [1] gave the following analytical solution for the transient temperature within an infinite, constant-property wedge enclosure subjected to zero initial temperature and unit surface temperature.

$$T(r,\theta,t;\theta_0)=1-\frac{4}{\theta_0}\sum_{n=0}^{\infty}\sin(\nu\theta)\int_0^{\infty}e^{-u^2\text{Fo}}\,\frac{J_\nu(u)\,du}{u} \tag{1}$$

where Fo is the Fourier number $\alpha t/r^2$, J_ν is the Bessel function of the first kind of order ν, and $\nu=(2n+1)\pi/\theta_0$ for $n=0, 1, 2, \ldots$ Fig. 1 shows the coordinate system used in deriving the foregoing solution.

One can conveniently derive the heat flux function at the wedge surface from equation (1) as follows:

$$q(r,\text{o},t;\theta_0)=-\frac{K}{r}\frac{\partial T}{\partial\theta}\bigg|_{\theta=0}$$

$$=\frac{4K}{r\theta_0}\sum_{n=0}^{\infty}\nu\int_0^{\infty}e^{-u^2\text{Fo}}\,\frac{J_\nu(u)\,du}{u} \tag{2}$$

where K is the thermal conductivity of the wedge enclosure. Initial inspection of the foregoing equation does not readily provide any clue for characterization of the heat flux function in terms of time (t) and position (r).

The definition of the wedge invariant [2] suggests that a certain similarity exists in the foregoing heat flux function. By dividing (2) with the corresponding one-dimensional form [3], one obtains

$$E(\text{Fo};\,\theta_0)=\frac{q(r,\text{o},t;\theta_0)}{q(r,\text{o},t;\pi)}$$

$$=4\sqrt{\pi\text{Fo}}\sum_{n=0}^{\infty}\frac{\nu}{\theta_0}\int_0^{\infty}e^{-u^2\text{Fo}}\,\frac{J_\nu(u)\,du}{u} \tag{3}$$

The foregoing similarity function is termed the edge function. The infinite series in (3) can be evaluated using the result [1, 4]

$$\int_0^{\infty}e^{-u^2\text{Fo}}\,\frac{J_\nu(u)\,du}{u}$$

$$=\frac{\Gamma(\nu/2)}{2^{\nu+1}\text{Fo}^{\nu/2}\Gamma(f+1)}\,{}_1F_1(\nu/2;\nu+1;-1/4\text{Fo}) \tag{4}$$

The confluent hypergeometric function, ${}_1F_1$, can further be expanded into the following series [5]:

$${}_1F_1(u;v;w)=1+\frac{uw}{v}+\frac{(u)_2w^2}{(v)_2 2!}+\ldots+\frac{(u)_nw^n}{(v)_n n!}+\ldots \tag{5}$$

where

$$(u)_n=u(u+1)(u+2)\ldots(u+n-1)$$

and

$$(u)_0=1$$

For positive values of u and v in the above equation, the well-behaved confluent hypergeometric function in (4) and hence the E-function in (3) can be readily evaluated. Figure 2 shows a graphical representation of the E-function plotted against $1/2\sqrt{\text{Fo}}$, which is equivalent to another convenient parameter $r/2\sqrt{\alpha t}$, with θ_0 as a parameter. The similarity curves in Fig. 2 reveal, concisely, the interrelation among edge effect, location, time, and thermal diffusivity of the enclosure. The rather extensive spreading of the edge influence in acute wedges, as illustrated by the similarity curves for $\theta_0=\pi/3$ and $\pi/6$, is due mainly to thermal saturation near the edges. Note that for $\theta_0=\pi/2$ the E-function can be reduced to an error function and that the solution is also valid for the boundary conditions of $T=1$ at $\theta=0$ and $\delta T/\delta\theta=0$ at $\theta=\theta_0/2$. It should also be noted that the E-curves presented are "exact" in that the infinite series involved converge rapidly.

Application

Numerical simulation of casting solidification has been accepted as an effective approach to optimal casting system designs [6]. Practically accurate simulation of production-scale systems requires discretization of the system into sufficiently small volume elements that can be fed into a finite difference or finite element routine. The fact that sand molds are much larger in size than castings often results in 70 to 90 percent of the volume elements being located on the mold side. Since the temperature history of the mold is, in practice, of little interest to foundrymen, an economical simulation scheme can be achieved if the heat dissipation into the mold can be represented by an artificial convective heat transfer coefficient acting at the mold-casting interface, instead of a continuity in temperature and heat flux across the interface. Thus only the volume elements in the casting need to be manipulated.

It is well-known that, in sand-casting systems, the release of latent heat during solidification of molten metals helps the mold-casting interface maintain a temperature near the solidus. The heat flow pattern in a wedge-shaped sand mold will thus resemble that of the wedge-shaped sand mold subjected to an isothermal heat source. It follows that distribution of the artificial heat transfer coefficient will resemble the *E*-curve. The advantages of using and *E*-function-based heat transfer coefficient in computation of sand casting solidification profiles have been reported elsewhere [7].

Concluding Remarks

The foregoing analysis quantifies the two-dimensional corner effect on the conduction heat flux at the surface of a wedge enclosure. The results are directly applicable to other diffusion-related problems. The simple relationship between corner-free and corner-induced surface heat fluxes has made possible an economical computation scheme for simulating solidification profiles in shaped sand-casting systems.

Acknowledgment

This research was performed at Georgia Institute of Technology under the auspices of the National Science Foundation (grant DAR 78-24301, Project Manager Dr. W. S. Spurgeon). The report presented was prepared at the Polytechnic Institute of New York. The authors would also like to acknowledge the constructive comments provided by the reviewers and the editors.

References

1 Jaeger, J. C., "Heat Conduction in a Wedge or an Infinite Cylinder Whose Cross-Section is a Circle or a Section of a Circle," *Philosophical Magazine*, Vol. 33, 1982, pp. 527-536.

2 Wei, C., and Berry, J. T., "An Analysis of the Transient Edge Effect on Heat Conduction in Wedges," *International Journal of Heat and Mass Transfer*, Vol. 25, 1982, pp. 590-592.

3 Carslaw, H. S., and Jaeger, J. C., *Conduction of Heat in Solids*, 2d ed., Clarendon Press, Oxford, 1959.

4 Watson, G. N., *Theory of Bessel Functions*, University Press, Cambridge, 1962.

5 Abramowitz, M., and Stegun, I. A., *Handbook of Mathematical Functions*, Dover, New York, 1970.

6 Erickson, W. C., "Computer Simulation of Solidification," AFS *International Cast Metals Journal*, Vol. 5, 1980, pp. 30-41.

7 Wei, C., and Berry, J. T., "Solidification Simulation Based on the Edge Function Approach," presented at the annual American Foundrymen's Society Casting Congress, Illinois, Apr. 1983, and accepted for publication in the AFS Transactions.

Journal of Heat Transfer
Discussion

Enhancement of Natural Convection Heat Transfer From a Horizontal Cylinder Due to Vertical Shrouding Surfaces[1]

R. M. Fand.[2] Presented in this paper by Sparrow and Pfeil is the following empirically determined correlation equation for an unshrouded cylinder

$$\mathrm{Nu} = 0.605\ \mathrm{Ra}^{0.225} \tag{5}$$

Equation (5) is based on data taken in air in the limited range of Rayleigh numbers from 2×10^4 to 2×10^5. It is pointed out in the paper that at $\mathrm{Ra} = 10^5$ this equation yields a Nusselt number that is in remarkably close agreement (difference less than 1 percent) with Kuehn and Goldsmith's finite difference solution [4]. The authors then go on to state:

> The most recent and encompassing literature correlations of experimental data for unshrouded horizontal cylinders are those of [1] and [5]. In the latter, a single algebraic equation is used to correlate Nusselt number data which span a Rayleigh number range of 10^{15}. Such a single-equation representation affords convenience but tends to sacrifice accuracy and, in particular, in the present Rayleigh number range falls below the data on which it is based. In contrast, [1] offers several correlation equations, each specific to a given Rayleigh number range. For the present range, [1] gives
>
> $$\mathrm{Nu} = 0.480\mathrm{Ra}^{1/4} \tag{6}$$
>
> from which equation (5) deviates by 2 to 7 percent – a level of agreement that is quite satisfactory.

The objective of this communication is to call attention to a single-equation representation of the Nusselt number that has been published – namely, equation (9) in [1] – for heat transfer by natural convection from horizontal cylinders that spans a Rayleigh number range of 10^{16} and yields Nusselt numbers that deviate from values calculated via equation (5) throughout the range $2 \times 10^4 \leq \mathrm{Ra} \leq 2 \times 10^5$ by less than 3 percent, which is somewhat better than what is deemed satisfactory by the authors. Thus the convenience of single-equation representation referred to by the authors is available without an attendant sacrifice in accuracy.

Further References

1 Fand, R. M., and Brucker, J., "A Correlation for Heat Transfer by Natural Convection From Horizontal Cylinders that Accounts for Viscous Dissipation," *International Journal of Heat and Mass Transfer*, Vol. 26, No. 5, 1983, pp. 709–726.

Authors' Closure

We are grateful to Professor Fand for calling our attention to the new correlation which he has formulated. It is especially gratifying that the agreement between the correlation and the data is within 3 percent.

On the Presentation of Performance Data for Enhanced Tubes Used in Shell-and-Tube Heat Exchangers[1]

H. Soumerai.[2] The purpose of this Discussion is to provide some of the information lacking on one of the commercially available enhanced tubes listed in Table 1 and to use the opportunity to make a couple of relevant comments on this highly interesting and informative paper.

1 The Dunham Bush Inner-Fin is listed without any "references for data source" in Table 1. Actually, a number of technical papers and publications have been released since the 1950s, when this new type of enhanced tube was introduced on the market, which include performance data as well as essential parameters to completely characterize the geometry. Some of these publications also show drawings and pictures to highlight a unique feature of this design, i.e., in addition to providing extended internal surface as indicated in Table 1, the discontinuous and "skewed" fins also ensure continuous mixing of the fluid, which is particularly significant in two-phase flow evaporator and condenser applications for which this enhanced tube design was initially developed.

These early publications in all probability were overlooked in the authors' literature survey because they were either considered too old or published in highly specialized refrigeration journals and transactions, some of them outside the United States. In the hope this may be of interest to some readers and the authors I have listed below a few of these 1950s and 1960s references. I am sure more up-to-date information is available on request from the manufacturers' headquarters in West Hartford, Connecticut.

2 Standardized Presentation Format. I would be interested to know the basic rationale for proposing two different sets of standards for the presentation of the heat transfer performance, i.e., $\tilde{\mathrm{Nu}}_i$ for tube flow and $\tilde{J}_0$ for shell side flow? Or to put it differently: what were the overriding

---

[1] By E. M. Sparrow and D. R. Pfeil, published in the February 1984 issue of ASME JOURNAL OF HEAT TRANSFER, Vol. 106, No. 1, pp. 709–726.

[2] Professor of Mechanical Engineering, University of Hawaii at Manoa, Mem. ASME.

[1] By W. J. Marner, A. E. Bergles, and J. M. Chenoweth, published in the May 1983 issue of ASME JOURNAL OF HEAT TRANSFER, Vol. 105, No. 2, pp. 358–364.

[2] Private Consultant, CH-5442 Fislisbach, Switzerland